UNITED STATES DEPARTMENT OF THE INTERIOR

GEOLOGICAL SURVEY

Office of Earthquake Studies

PROCEEDINGS OF

CONFERENCE IX

MAGNITUDE OF DEVIATORIC STRESSES IN THE EARTH'S CRUST AND UPPER MANTLE

VOLUME II

Convened Under Auspices of

NATIONAL EARTHQUAKE HAZARDS REDUCTION PROGRAM

29 July 1979 – 2 August 1979

OPEN-FILE REPORT 80-625

Menlo Park, California

1980

CONFERENCES TO DATE

Conference I	Abnormal Animal Behavior Prior to Earthquakes,I Not open-filed
Conference II	Experimental Studies of Rock Friction with Application to Earthquake Prediction Not open-filed
Conference III	Fault Mechanics and Its Relation to Earthquake Prediction Open-File No. 78-380
Conference IV	Use of Volunteers in the Earthquake Hazards Reduction Program Open-File No. 78-336
Conference V	Communicating Earthquake Hazard Reduction Information Open-File No. 78-933
Conference VI	Methodology for Identifying Seismic Gaps and Soon-to-Break Gaps Open-File No. 78-943
Conference VII	Stress and Strain Measurements Related to Earthquake Prediction Open-File No. 79-370
Conference VIII	Analysis of Actual Fault Zones in Bedrock Open-File No. 79-1239
Conference IX	Magnitude of Deviatoric Stresses in the Earth's Crust and Upper Mantle Open-File No. 80-625

Open-File Service Section
Branch of Distribution
U.S. Geological Survey
Box 25425
Federal Center
Denver, Colorado 80225

UNITED STATES

DEPARTMENT OF THE INTERIOR

GEOLOGICAL SURVEY

PROCEEDINGS OF CONFERENCE IX

MAGNITUDE OF DEVIATORIC STRESSES IN THE EARTH'S CRUST AND UPPER MANTLE

VOLUME II

Convened Under Auspices of

NATIONAL EARTHQUAKE HAZARDS REDUCTION PROGRAM

29 July 1979 - 2 August 1979

Co-Organizers

Thomas Hanks
United States Geological Survey
Office of Earthquake Studies
Menlo Park, California 94025

Barry Raleigh
United States Geological Survey
Office of Earthquake Studies
Menlo Park, California 94025

Convener

Jack F. Evernden
United States Geological Survey
Office of Earthquake Studies
Menlo Park, California 94025

OPEN-FILE REPORT 80-625

Compiled by
Pamela Andriese

Menlo Park, California

1980

Table of Contents

VOLUME II

VOLUME II

CRUSTAL EARTHQUAKE STRESS DROPS

Thomas C. Hanks
U.S. Geological Survey
345 Middlefield Road
Menlo Park, California 94025

INTRODUCTION

Earthquake stress drop data almost always frequent discussions of the state of stress in the Earth's crust and uppermost mantle but not for any particularly good reason. Indeed, the equations of motion in a deformable medium guarantee that we can learn nothing at all about absolute stresses from the radiated field of earthquakes. Yet the notion that earthquake stress drops represent absolute stresses has persisted and even thrived since Chinnery (1964) and dates back at least to Tsuboi (1956).

In the first place, three important early papers (Tsuboi, 1956; Chinnery, 1964; McKenzie, 1967) simply assumed that earthquake stress drops represented the ultimate strength of the crust and uppermost mantle. The difficulty with this assumption is that it violates everything that is known about the brittle failure of candidate rock types under the appropriate conditions of pressure and temperature, unless nearly lithostatic fluid pressures are an ambient condition of the Earth's crust. Secondly, the apparent stress $\eta\bar{\sigma}$ (Aki, 1966; Wyss, 1970), where $\bar{\sigma}$ is the average tectonic stress and η is seismic efficiency, has offered the possibility of estimating $\bar{\sigma}$ for earthquakes if η could otherwise be determined. The apparent stress, however, is only apparent since it is easy to show that $\eta \sim \Delta\sigma/\bar{\sigma}$ (Hanks and Thatcher, 1972), where $\Delta\sigma$ is the earthquake stress drop. Thus $\eta\bar{\sigma}$ is a stress difference, as it must be, not an absolute stress.

Third, crustal earthquake stress drops are remarkably constant, showing in general little if any dependence on external geological or geophysical conditions, including "size" of the earthquake, depth of focus, mode of tectonic accommodation, geologic province, ... The question, then, is how can earthquake stress drops be so sensibly constant if they

do not in fact represent the total tectonic stress? At the present time, there is no consensus answer to this question, although this need not mean that earthquake stress drops are the same as tectonic stresses. We shall defer this question to the DISCUSSION that concludes this correspondence.

Finally, the absence of a heat flow anomaly localized to the San Andreas fault has been used to infer that frictional stresses do not exceed 100 bars or so (Brune et al., 1969; Lachenbruch and Sass, 1973), a value coincident with the upper bound of earthquake stress drops (Figure 1). Earthquake stress drops are certainly a minimum estimate of the causative tectonic stresses; the studies of Brune et al (1969) and Lachenbruch and Sass (1973) then suggest that they are near maximum estimates as well for the upper crust--or at least the larger stress drops are. But the heat flow argument is largely beyond the implications of crustal earthquake stress drops alone and will be addressed elsewhere at this conference. It is perhaps worth noting in passing that Scholz et al (1979) have estimated from thermal observations expressed as metamorphic grade and K-Ar ages that frictional stresses along the Alpine fault are unlikely to be less than a kilobar.

EARTHQUAKE STRESS DROPS

Earthquake stress drops are determined from separate estimates of seismic moment M_o (or average faulting displacement $\bar{u}$) and characteristic source dimension r (or fault area A). Stress drops $\Delta\sigma$ are then formed from relations of the type

$$\Delta\sigma = k_1 M_o/r^3 \qquad (1)$$

$$\Delta\sigma = k_2 M_o/A^{3/2} \qquad (2)$$

or

$$\Delta\sigma = k_3 \mu\bar{u}/r \qquad (3)$$

where μ is the shear modulus. In the case of the larger events ($M \gtrsim 6\frac{1}{2}$), r or A is usually determined from direct observations of the length of surface faulting and/or dimensions of the aftershock zone. In the case of the smaller shocks ($M \lesssim 6$), r is almost always estimated from the spectral corner frequency f_o, usually of the S-wave. This, in turn, is mapped most often to r by the Brune (1970, 1971) relation

$$r = \frac{2.34\beta}{2\pi f_o}. \qquad (4)$$

Dozens of studies have resulted in the determination of more than a thousand earthquake stress drops. Figure 1a and 1b are representative of the results for larger and smaller earthquakes, respectively. The principal and widely acknowledged result of these investigations is that earthquake stress drops, in their average value $\overline{\Delta\sigma}$, are remarkably constant over the entire range of earthquakes accessible to instrumental recording (Aki, 1972; Thatcher and Hanks, 1973; Abe, 1975; Kanamori and Anderson, 1975; Hanks, 1977). $\overline{\Delta\sigma}$ is of the order of several tens of bars, although individual values vary through a range of an order of magnitude on either side of $\overline{\Delta\sigma}$. For these results, the following caveats are generally recognized:

First, most of the spectrally determined source parameter data ($M_o \lesssim 10^{25}$ dyne-cm) are obtained from single-station estimates, and $\Delta\sigma$ so obtained is subject to a fairly large uncertainty (a factor of 3 to 5). It is not surprising, then that a significantly larger variation exists for stress drops of the smaller (Figure 1b) than for the larger earthquakes (Figure 1a). If it should be the case that the smaller earthquakes have a wider variation in $\Delta\sigma$ (that is real) than the larger events, most of the presently available determinations are poorly disposed to resolve it.

Second, in any spectrally determined data set, there is a natural

size threshold below which stress drops will be biased to low values, through an inability to recover corner frequencies above a certain value. The data set of Thatcher and Hanks (1973) in Figure 1b is almost certainly so affected and perhaps the set of Tucker and Brune (1973) as well. Plainly, this can introduce a fictitious dependence on magnitude in any one data set (or disguise a real one). For the larger earthquakes also, there is a bias to overestimate source dimensions (and thus to underestimate stress drops) with aftershock zones, both because of earthquake location errors and because of the tendency of aftershock zones to grow in time.

The coincidence of stress drops for mining-induced seismogenic shear failure with those of crustal earthquakes is an intriguing but poorly understood problem. Figure 2 presents such data for events occurring at 3½ km depth in the East Rand Proprietary Mines of South Africa (Spottiswoode and McGarr, 1975). These events span much the same range in M_o as the San Fernando aftershock data of Tucker and Brune (1973) in Figure 1b. The mining-induced shocks are known to have occurred in a shear stress field ranging from 0.5 to 2 kbar (McGarr et al., 1975), and if these events occurred in places where local inhomogeneities of the stress field exist, as seems likely, the local shear stresses causing failure are higher.

Finally, as an historical footnote, there is very little in the principal conclusion extracted from the data set as a whole, that $\overline{\Delta\sigma}$ is of the order of several tens for crustal earthquakes, that was not apparent to and explicitly stated by Tsuboi (1956) and Chinnery (1964) on the basis of very limited observations.

RESULTS OF SOME RECENT STUDIES

The remarks given in the previous section could have been--and were

(Hanks, 1977)--an appropriate summary of crustal earthquake stress drops as of several years ago. Since then, several studies have indicated that crustal earthquake stress drops are not entirely independent of all geological and geophysical conditions, at least in specific source regions and through limited variations in source strength. Typically, these studies involve earthquakes within a small volume measured at close distances ($R \lesssim 20$ km); it is also true that the source parameters are largely determined, as in the past, from one or two station measurements, but the uncertainties usually associated with this condition are mitigated to some extent by the coincidence of focal mechanisms and propagation paths for the events in each study.

Work to date on determining source parameters for the larger ($2.8 \leq M_L \leq 4.9$) and smaller ($M_L \lesssim 2\frac{1}{2}$) aftershocks of the Oroville, California earthquake (Aug. 1, 1975; $M_L = 5.7$) reveals a clear difference in the stress drops for the two sets of events (Figure 3, prepared by J. B. Fletcher from soon-to-be published results of J. Boatwright, J. B. Fletcher, T. C. Hanks, and A. McGarr). The stress drops of the three largest earthquakes are particularly well-determined, these events having been recorded by as many as eleven strong-motion accelerographs, all at $R \lesssim 15$ km. That for event F (0350 Aug. 6; $M_L = 4.7$) is 420 ± 110 bars (Fletcher *et al.*, 1979).

The stress drops for the smaller events (Fletcher, 1979) are 1 to 2 orders of magnitude smaller than those for the three larger events. While the former set of data was recorded on a single-station three component system, P-wave estimates are in reasonable accord with S-wave estimates. There is no likely reason to suspect that the magnitude dependence of $\Delta\sigma$ indicated in Figure 3 is fictitious.

The significance of this magnitude dependence is less clear, however, since the smaller aftershocks were recorded ten months after the larger ones, and the stress drops of the larger events are among the greatest ever reported (compared with Figure 1). Moreover, this magnitude-dependence occurs within a set of aftershocks whose b-value is markedly less than 1 (0.61, according to Morrison et al (1976)), and virtually all of the smaller events have high-frequency ($f > f_o$) spectral decay rates (γ) greater than 2, possibly an observational example of the associations between the constancy of earthquake stress drops, b-values near 1, and $\gamma = 2$ (or variations from these normative conditions) suggested by Hanks (1979).

Magnitude dependence of stress drop has been inferred for earthquakes in the Bear Valley region of the San Andreas fault in central California by Johnson and McEvilly (1974) and Bakun et al (1976). Figure 4, from Bakun (1979), summarizes these results as do Chouet et al (1978). With $\log M_o \sim 1.5$ magnitude, lines of constant stress drop have a slope of +2 in this figure. Since the f_o estimates of Johnson and McEvilly (1974) are obtained from whole record spectra (up to 40 seconds), it is reasonable to suspect that the very weak dependence of f_o on magnitude results from a resonant frequency near 1 Hz of the crustal structure rather than from the intrinsic source effect. In the case of the S-wave data of Bakun et al (1976), the analyzed sample is restricted to the S-wave window. A strong dependence of $\Delta\sigma$ on magnitude can only be escaped by supposing an attenuation structure that transmits little $f \gtrsim 10$ to 20 Hz information to $R \lesssim 15$ km.

As a final example, the data of Hartzell and Brune (1977) (Figure 5a) reveal an unusual set of high stress drop earthquakes in the course

of the Brawley, California, swarm of January-February, 1975, and, at least for a partial set of the data, an indicated dependence on M_o. A dependence on depth is also indicated (Figure 5b).

Thus, in contrast to what was said in the previous section about the constancy of earthquake stress drops, there is accumulating evidence, at least in specific areas and for limited ranges in source strength, that significant differences in stress drops exist that correlate with source strength. With only several exceptions, however, the data do not make significant excursions outside the observational limits suggested by Figure 1b. In the case of the Brawley swarm, the stress drops are also a function of depth (for a restricted data set allowing only a small variation in M_o), but this was not the case at Oroville or for San Fernando aftershocks (Tucker and Brune, 1973).

INHOMOGENEOUS FAULTING AND ASSOCIATED STRESS DIFFERENCES

It has been known for decades that when a large enough earthquake is viewed through a short enough period seismic recording system, the earthquake no longer appears as a single, simple faulting event but as a multiplicity of shorter duration events that may be, collectively, of almost arbitrary complexity. This multiple, complex event phraseology is generally applied to great earthquakes as seen through conventional (i.e., WWSSN) instrumentation, but it seems likely that the process itself is scale-independent. That is, a $M \sim 8$ earthquake ($\sim$ 100-second duration) at 1 Hz is probably no more or less complicated than a $M \sim 6$ earthquake ($\sim$ 10-second duration) at 10 Hz or a $M \sim 4$ earthquake ($\sim$ 1-second duration) at $\sim$ 100 Hz. Strong-motion accelerograms written at close distances for $M \gtrsim 4$ earthquakes provide, in general, ample evidence for this likelihood.

The stress drops of the individual elements--or at least of some of them--will inevitably be associated with higher stress differences than the stress drop of the faulting event as a whole, simply because the dimension of such elements is so much smaller than that of the final faulting event. In most cases, however, it is probably not correct to assume that these stress differences are a minimum estimate of the pre-existing tectonic stress even over this limited dimension, since dynamic loading effects must almost certainly be important. Moreover, it is not easy to analyze such events when they occur in the midst of the entire seismogram. In the case of the initial rupture event, however, it is more likely that the associated stress differences are related to the pre-existing tectonic stress at least as a minimum estimate, and moreover they are intrinsically easier to analyze.

Hanks (1974) studied the initial rupture event of the San Fernando, California, earthquake (Feb. 9, 1971; M_L = 6.4) and estimated that it was associated with stress differences of 350 to 1400 bars. Although the numbers are subject to some uncertainty, there is a consensus developed in numerous studies since then that the initial rupture event was especially energetic, with source parameters not at all representative of those associated with the final faulting configuration. Burdick and Mellman (1976) and Heaton and Helmberger (1977) have studied teleseismic and local records of the Borrego Mt. earthquake (Apr. 9, 1968; M_L = 6.4) to conclude that most of the radiated energy emanated from rupture across a surface much smaller than that of the plane of aftershocks. Hartzell and Brune (1979) suggest that the Horse Canyon, California, earthquake (Aug. 2, 1975; M_L = 4.8) was initiated with stress differences of 225 bars, although $\Delta\sigma$ = 90 bars. Hanks and Johnson (1976) have argued that the larger peak acceler-

ations recorded at R $\lesssim$ 10 km correspond to dynamic stress differences of $\sim$ 2 kbar which develop in the hypocentral region.

In these and in related observational (e.g. Wyss and Brune, 1967; Kanamori and Stewart, 1978) and theoretical (e.g. Das and Aki, 1978; Madariaga, 1979) studies, then, there is ample evidence that stress differences considerably larger than the earthquake stress drop can and do accompany crustal faulting. Their physical significance, however, is yet to be determined.

"HIGH-FREQUENCY" EARTHQUAKE STRESS DROPS

As given by equations (1) to (3), the earthquake stress drop is an average, static parameter of the source that is measurable in principle and occasionally in fact in the absence of any inertial recording of the earthquake; in particular, it tells us nothing about localized, perhaps transient stress differences that may develop in the course of crustal faulting, as discussed in the last section. If we regard f_o as the frequency dividing the long-period and high-frequency portions of the source spectrum, the spectrally determined stress drops are then long-period quantities. But $\Delta\sigma$ also controls the high-frequency excitation, at least implicitly, and some interesting results have developed with respect to stress drops inferred from the high-frequency ground motion.

Largely because of its utility as a measure of high-frequency strong ground motion for engineering purposes, it is convenient to express the theoretical and observational measures of high-frequency ground motion in terms of the root-mean-square acceleration, a_{rms}. For the Brune (1970, 1971) model of the far-field shear wave displacement spectrum in the presence of anelastic attenuation, the result is (Hanks, 1979; McGuire and Hanks, 1979)

$$a_{rms} = \sqrt{2}\, R_{\theta\phi}\, \frac{(2\pi)^2}{106}\, \frac{\Delta\sigma}{\rho R^{3/2}} \sqrt{\frac{Q\beta}{\pi f_o}} \qquad (5)$$

where $R_{\theta\phi}$ is the radiation pattern; $\Delta\sigma$ and f_o are, as before, the earthquake stress drop and spectral corner frequency; and ρ, β, and Q are the density, shear-wave velocity, and quality factor respectively. The leading $\sqrt{2}$ accounts for free-surface amplification of shear waves (2.0) and vectorial partition onto two horizontal components of equal amplitude.

Figure 6 presents record estimates of a_{rms} in the 10-second window beginning with direct shear arrival for both horizontal components of the numerous strong motion accelerograms of the San Fernando earthquake at southern azimuths, together with (5) evaluated for $\Delta\sigma$ = 50 bars, f_o = 0.1 Hz, $R_{\theta\phi}$ = 1, ρ = 2.8 gm/cm^3, β = 3.2 km/sec, and Q = 300. The 10-second window used for the observations is based on estimates of faulting duration for this earthquake and corresponds to teleseismic determinations of $f_o \simeq 0.1$ Hz. $R_{\theta\phi}$ is taken equal to 1 since southern azimuths are on a near maximum of the radiation pattern.

By conventional seismological standards in estimating high frequency seismic amplitudes, the agreement between the record and model a_{rms} estimates in Figure 6 is remarkable. The observations are in reasonable accord with the predicted $R^{-3/2}$ dependence, although the data are high with respect to the model by a factor of about 2. The San Fernando earthquake, then, appears slightly more energetic than the simple model allows (by a factor of about 4), and the reason for this almost certainly lies in the localized but highly energetic initial rupture event mentioned in the last section.

Encouraged by this success, R. McGuire and I have investigated this matter for other significant earthquakes that have written strong-motion

accelerograms in the western U.S., using published source parameter determinations in the model estimates. This didn't work out so well, and Figure 7 indicates why. Here, the mismatch between the record/model a_{rms} values is expressed as that ratio and plotted against $\Delta\sigma$, as it was taken from the literature and used in the appropriate theoretical estimate. To a first approximation, the ratio mismatch is inversely proportional to $\Delta\sigma$; that is, had we chosen a $\Delta\sigma$ of $\sim$ 120 bars instead of whatever we took from the literature the agreement between the model and record estimates would have been quite good (a factor of 3 difference in the worst cases). Note that the same phenomenon apparently occurs in Figure 6; the model a_{rms} is low by a factor of $\sim$ 2 because the chosen $\Delta\sigma$ (50 bars) is less than $\sim$ 120 bars by about the same amount.

Evidently, the stress drops of the Borrego Mt. (Model A), Parkfield, Long Beach, and Wheeler Ridge earthquakes are significantly underestimated. The stress drops for the first three of these earthquakes are from Kanamori and Anderson (1975) who give dimensions based principally on aftershock areas. The stress drop for the Wheeler Ridge earthquake was taken from Thatcher and Hanks (1973), is apparently underestimated by a factor of about 10, and underscores again the limitations of single-station spectral measurements.

In view of the explicit caveats mentioned earlier that are generally applicable to earthquake stress drop data, it should come as no great surprise that the stress drops of four selected earthquakes should be biased significantly to low values. At least in the case of the Borrego Mt. and Parkfield earthquakes, there is evidence that the source dimension responsible for the bulk of the radiated energy is indeed smaller than that of the aftershocks (Burdick and Mellman, 1976, and Lindh, 1979, respectively).

What is surprising is that when $\Delta\sigma$ is greater than 100 bars, as is the case for three of four Oroville aftershocks studied to date, the model a_{rms} is greater than the record a_{rms} (Figure 8) in just the same way that when $\Delta\sigma$ is lower than 100 bars the model a_{rms} is less than the record value. These results, while preliminary, are bizarre, and I do not understand them. The implication to be drawn from them, however, is that earthquake stress drops, as measured by the high-frequency excitation, are remarkably similar, considerably more so than we might expect on the basis of the previous three sections.

NON-CONTEMPORANEOUS STRESS DROP MEASUREMENTS

Zoback (1979) has determined shear stress at 4 sites along a profile aligned approximately normal to the San Andreas fault near Palmdale from hydrofracture measurements at $\sim$ 200 m depth (Figure 9, top) and has interpreted them in terms of an ambient shear stress model of the San Andreas fault (Figure 9, bottom). The model itself is an idealized and special case, and the data themselves are poorly disposed to determine shear stresses at depth (McGarr, 1979). Although Zoback (1979) chose to discount them because of the effects of near-surface fracturing, the near-surface gradients of shear stress would extrapolate to about a kilobar at 10 km depth in three of the four holes, consistent with extrapolations based on a large set of data presented by McGarr (1979).

An alternate interpretation of these data is that they represent the remnant stress drop of the 1857 earthquake which has partially reaccumulated in the intervening 122 years. The curve labled 3 in Figure 9 (top) has been obtained from the equation

$$\tau_{xy}(x, z = 0) = 54 - 46\ (1 + \frac{x^2}{h^2})^{-1}, h = 5\ \text{km} \qquad (6)$$

with units of bars. The second term on the right-hand side is obtained from the standard expression for the surface ($z = 0$) stress (τ_{xy}) change away from an infinitely long fault that occupies the plane $x = 0$ to depth $z = h$ with displacement U:

$$\Delta\tau_{xy}(x, z = 0) = \frac{\mu U}{\pi h}\left(1 + \frac{x^2}{h^2}\right)^{-1} \qquad (7)$$

where μ is the shear modulus.

The face-value interpretation of model 3, then, is that the observed surface τ_{xy} arose from an earthquake that involved a great length and 230 cm of displacement over the upper 5 km in the presence of a uniform τ_{xy} ($z \lesssim 0$) of 54 bars. This uniform stress, however, may be any function of depth, so long as its $\sim$ 200 m depth value is 54 bars. It didn't happen this way, of course. The observations do not represent such an earthquake, but rather the 1857 earthquake stress drop and the affects of strain accumulation since then.

At Pallett Creek, approximately 25 km south of Palmdale, Sieh (1978) has estimated that 4½ meters of displacement took place at the time of the 1857 earthquake. Assuming that the displacement deficit relative to that existing just prior to the 1857 earthquake is 230 cm implies that the intervening 122 years represents about one-half of the interval to the next comparably sized shock, in reasonable accord with Sieh's (1978) estimates of 160 to 230 year recurrence intervals for shocks of the size and location of the 1857 earthquake.

While the elements of this interpretation of Zoback's (1979) observations are reasonably consistent, its non-uniqueness is worth re-emphasizing. Nevertheless the possibility of estimating partially reaccumulated stress drops and recurrence intervals for large to great earthquakes in the pre-

instrumental (either geodetic or seismic) era with present-day hydrofracture measurements has such important implications for earthquake hazards analysis that it is certainly worth exploring for other events, in particular the San Francisco earthquake of 1906 for which considerable seismic and geodetic observations are available (Thatcher, 1975).

DISCUSSION

As the preceding sections should indicate, there is yet considerable uncertainty about the stress differences that accompany crustal faulting, especially those associated with localized (relative to r), high-frequency (relative to f_o), and perhaps transient conditions. Similarly, there is also considerable ambiguity about the physical significance of magnitude-dependent stress drops, such as they exist for certain sets of data from specific areas within a limited range of M_o. Nevertheless, it seems likely that the "constancy" of earthquake stress drops, in their average value of several tens to perhaps 100 bars that is generally independent of source strength, does mean something in terms of the deviatoric stress-or stresses-operating on active crustal fault zones. But what?

Almost certainly, the answer involves the nature of the stress system driving plate motions and, in particular, relative motion across vertical strike-slip (transform) faults. In simple plate models with stress-free basal surfaces, there is, essentially, just one stress (say τ_{xy}) in the system: the plate is more or less in simple shear as the result of the equilibrium between the driving force on one edge and the frictional resisting stress on the other (fault) edge. In such a model, earthquake stress drops must be comparable to τ_{xy}, if the stress drop is complete. If only because the plate is attached to the rest of the Earth, however, such a model is undoubtedly naive. In this case, at least two stresses exist in

the system, say τ_{xy} as before and a τ_{zy} that arises from a basal shear across horizontal planes (that may either drive or resist plate motions), . Hanks (1977) noted that if the frictional resistance to plate motions across the upper tens of kilometers is of the order of a kilobar or so, the only viable mechanism for driving plate tectonics is a basal shear stress of several tens of bars and suggested that it is the local release of this stress that appears as earthquake stress drops. But it is the phrase immediately following "if" that is the one to be decided, and the stress drop data themselves cannot do it; that is, earthquake stress drop data will be consistent with whatever may be the correct model in this connection (and the range of possibilities is far larger then the two given above), but they cannot, alone, allow us to decide what the model is.

Two subsidiary but potentially important issues with respect to the resolution of this issue are worth recounting. First, naturally occurring shear failure can proceed without total (or anywhere near total) release of the maximum deviatoric stresses causing failure, if we may regard the mining-induced shocks as naturally occurring in the sense that fundamentally it is the deviatoric stress field that is induced by the mining operations, not the material failure itself. Second, despite the constancy of earthquake stress drops at a value of several tens to perhaps 100 bars, it seems likely that considerably larger stress differences can and do accompany crustal faulting.

REFERENCES

Abe, K., Reliable estimation of the seismic moment of large earthquakes, J. Phys. Earth. 23, 381-390, 1975.

Aki, K., Generation and propagation of G waves from the Niigata earthquake of June 16, 1964. Part 2. Estimation of earthquake moment, released energy and stress-strain drop from the G wave spectrum, Bull. E. Res. Inst. 44, 73-88, 1966.

Aki, K., Earthquake mechanism, Tectonophysics, 13, 423-446, 1972.

Bakun, W. H., C. G. Bufe, and R. M. Stewart, Body-wave spectra of central California earthquakes, Bull. Seismol. Soc. Amer., 66, 363-384, 1976.

Bakun, W. H., C. G. Bufe, and R. M. Stewart, Do P- and S- corner frequencies measure different source parameters? Bull. Seismol. Soc. Amer. in press, 1979.

Brune, J. N., Tectonic stress and the spectra of seismic shear waves, J. Geophys. Res., 75, 4997-5009, 1970.

Brune, J. N., Correction, J. Geophys. Res., 76, 5002, 1971.

Brune, J. N., Henyey, T. L. and Roy, R. F. (1969), Heat flow, stress, and rate of slip along the San Andreas fault, California, J. Geophys. Res. 74, 3821-3827.

Burdick, L. J., and G. R. Mellman, Inversion of the body waves from the Borrego Mountain earthquake to the source mechanism, Bull. Seismol. Soc. Amer., 66, 1485-1499, 1976.

Chinnery, M. A. (1964), The strength of the Earth's crust under horizontal shear stress, J. Geophys. Res. 69, 2085-2089.

Chouet, B., K. Aki, and M. Tsujiura, Regional variations of the scaling law of

earthquake source spectra, Bull. Seismol. Soc. Amer. 68, 49-79, 1978.

Das, S., and K. Aki, Fault plane with barriers: A versatile earthquake model, J. Geophys. Res., 82, 5658-5670, 1977.

Fletcher, J. B., Spectra from high-dynamic range digital recordings of Oroville, California, aftershocks and their source parameters, Bull. Seismol. Soc. Amer., submitted, 1979.

Fletcher, J. B., A. G. Brady, and T. C. Hanks, Strong motion accelerograms of the Oroville aftershocks: data processing and the aftershock of 0350 August 6, 1975, Bull. Seismol. Soc. Amer., in press, 1979.

Hanks, T. C., The faulting mechanism of the San Fernando earthquake, J. Geophys. Res., 79, 1215-1229, 1974.

Hanks, T. C., Earthquake stress drops, ambient tectonic stresses, and stresses that drive plate motions, Pure Appl. Geophys., 115, 441-458, 1977.

Hanks, T. C., b-values and $\omega^{-\gamma}$ seismic source models: Implications for tectonic stress variations along active crustal fault zones and the estimation of high-frequency strong ground motion, J. Geophys. Res., 84, 2235-2242, 1979.

Hanks, T. C., and D. A. Johnson, Geophysical assessment of peak accelerations, Bull. Seismol. Soc. Amer., 66, 959-968, 1976.

Hanks, T. C., and W. R. Thatcher, A graphical representation of seismic source parameters, J. Geophys. Res., 77, 4393-4405, 1972.

Hartzell, S. H., and J. N. Brune, Source parameters for the January 1975 Brawley-Imperial Valley earthquake swarm, Pure Appl. Geophys., 115, 333-355, 1977.

Hartzell, S., and J. N. Brune, The Horse Canyon earthquake of August 2, 1975-two-stage stress-release process in a strike-slip earthquake, Bull. Seismol. Soc. Amer., in press, 1979.

Heaton, T. H., and D. V. Helmberger, A study of the strong ground motion of the Borrego Mountain, California, earthquake, Bull. Seismol. Soc. Amer., 67, 315-330, 1977.

Johnson, L. R., and T. V. McEvilly, Near-field observations and source parameters of central California earthqukes, Bull. Seismol. Soc. Amer., 64, 1855-1886, 1974.

Kanamori, H., and D. L. Anderson, Theoretical basis of some empirical relations in seismology, Bull. Seismol. Soc. Amer., 65, 1073-1096, 1975.

Kanamori, H., and G. S. Stewart, Seismological aspects of the Guatemala earthquake of February 4, 1976, J. Geophys, Res., 83, 3427-3434, 1978.

Lachenbruch, A. H., and Sass, J. H., Thermo-mechanical aspects of the San Andreas fault system in Proceedings of the Conference on Tectonic Problems of the San Andreas fault system (eds. R. L. Kovach and A. Nur)(Stanford University Publications, Stanford, 1973), pp. 192-205.

Lindh, A.

Madariaga, R., On the relation between seismic moment and stress drop in the presence of stress and strength heterogeneity., J. Geophys. Res., 84, 2243-2250, 1979.

McGarr, A., S. M. Spottiswoode, and N. C. Gay, Relationship of mine tremors to induced stresses and to rock properties in the local region, Bull. Seismol. Soc. Amer., 65, 981-993, 1975.

McGarr, A., Some constraints on levels of shear stress in the crust from observations and theory, this volume 1979.

McGuire, R. K., and T. C. Hanks, rms-accelerations and spectral amplitudes of strong ground motion during the San Fernando, California, earthquake,

Bull. Seismol. Soc. Amer, submitted, 1979.

McKenzie, D. P., Some remarks on heat flow and gravity anomalies, J. Geophys. Res., 72, 6261-6273, 1967.

Morrison, R. W., B. W. Stump, and R. Uhrhammer, The Oroville earthquake sequence of August 1975, Bull, Seismol. Soc. Amer., 66, 1065-1084, 1976.

Scholz, C. H., J. Beavan, and T. C. Hanks, Frictional metamorphism, argon depletion and tectonic stress on the Alpine Fault, New Zealand, J. Geophys. Res., in press, 1979.

Sieh, E. E., Prehistoric large earthquakes produced by slip on the San Andreas Fault at Pallett, Creek, California, J. Geophys. Res., 83, 3907-3939, 1978.

Spottiswoode, S. M., and A. McGarr, Source parameters of tremors in a deep-level gold mine, Bull. Seismol. Soc. Amer., 65, 93-112, 1975.

Thatcher, W., and T. C. Hanks, Source parameters of southern California earthquakes, J. Geophys. Res., 78, 8547-8576, 1973.

Tsuboi, C., Earthquake energy, earthquake volume, aftershock area, and strength of the Earth's crust, J. Phys. Earth 4, 63-66, 1956.

Tucker, B. E., and Brune, J. N., Seismograms, S-wave spectra, and source parameters for aftershocks of San Fernando earthquake in San Fernando, California Earthquake of February 9, 1971, Vol. III (Geological and Geophysical Studies, 69-122, U.S. Dept. of Commerce, 1973).

Wyss, M., Stress estimates for South American shallow and deep earthquakes, J. Geophys. Res., 75, 1529-1544, 1970.

Wyss, M., and J. N. Brune, The Alaska earthquake of 28 March 1964: a complex multiple rupture, Bull. Seismol. Soc. Amer., 57, 1017-1023, 1967.

Zoback, M. D., and J. C. Roller, Magnitude of shear stress on the San Andreas Fault: implications from a stress measurement profile at shallow depth, Science, in press, 1979.

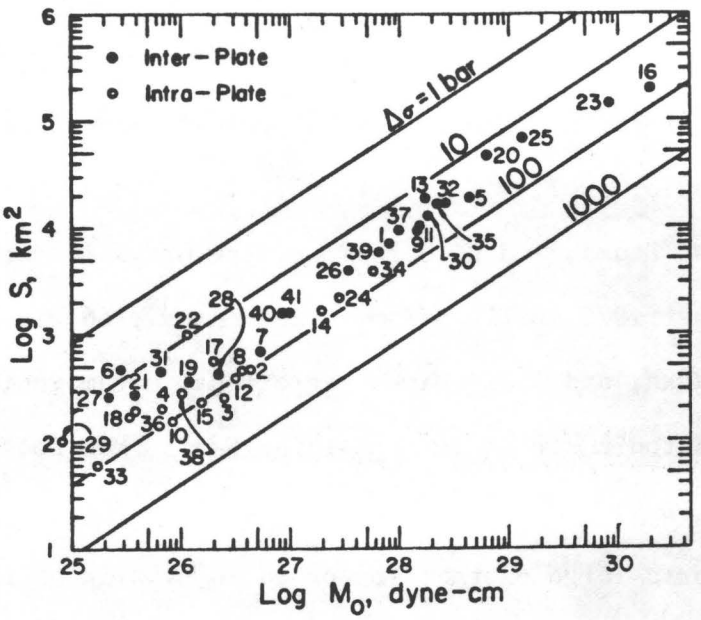

(a)
Kanamori and Anderson (1975)

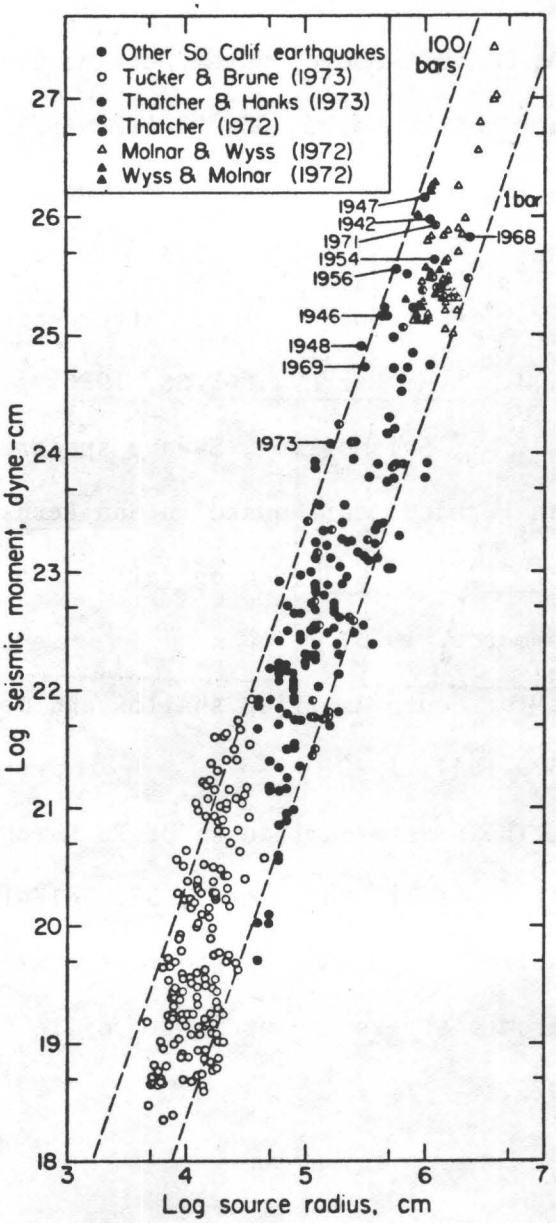

(b)
Hanks (1977)

Figure 1

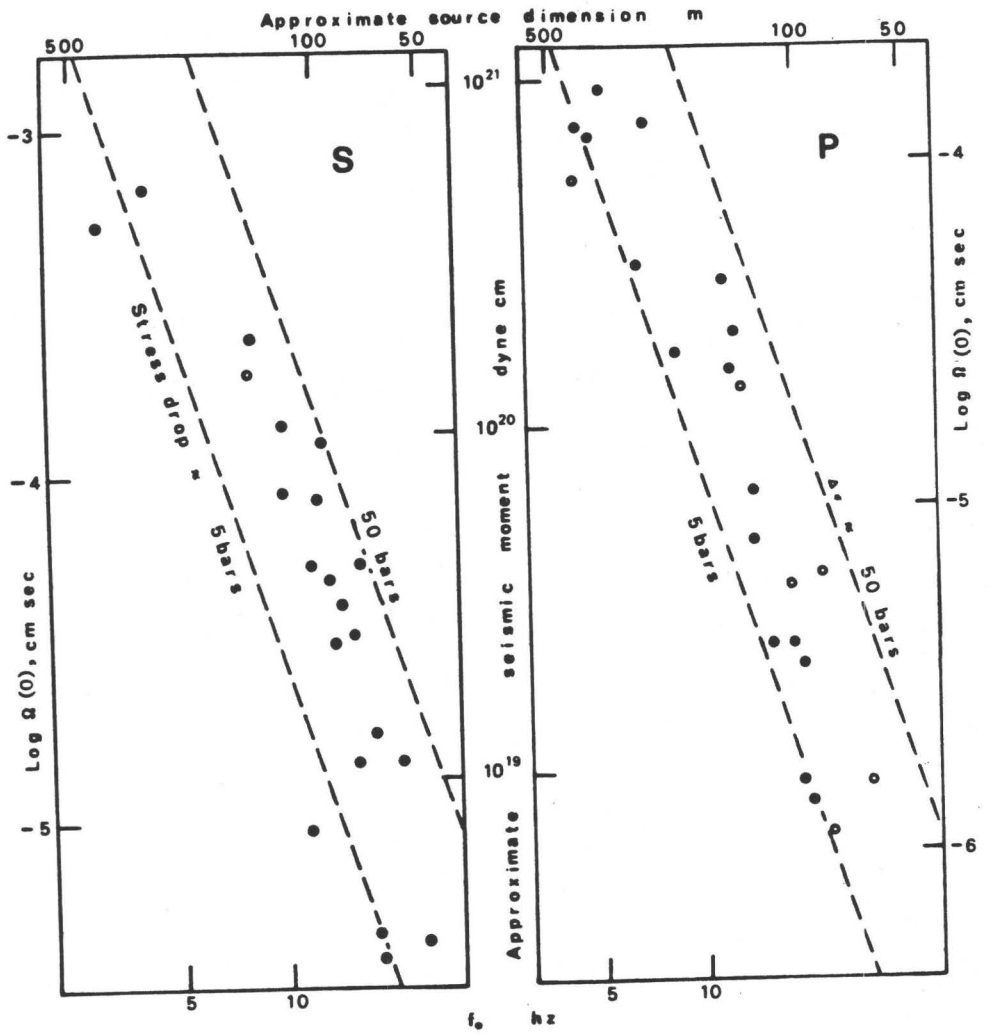

Spottiswoode & McGarr (1975)

Figure 2

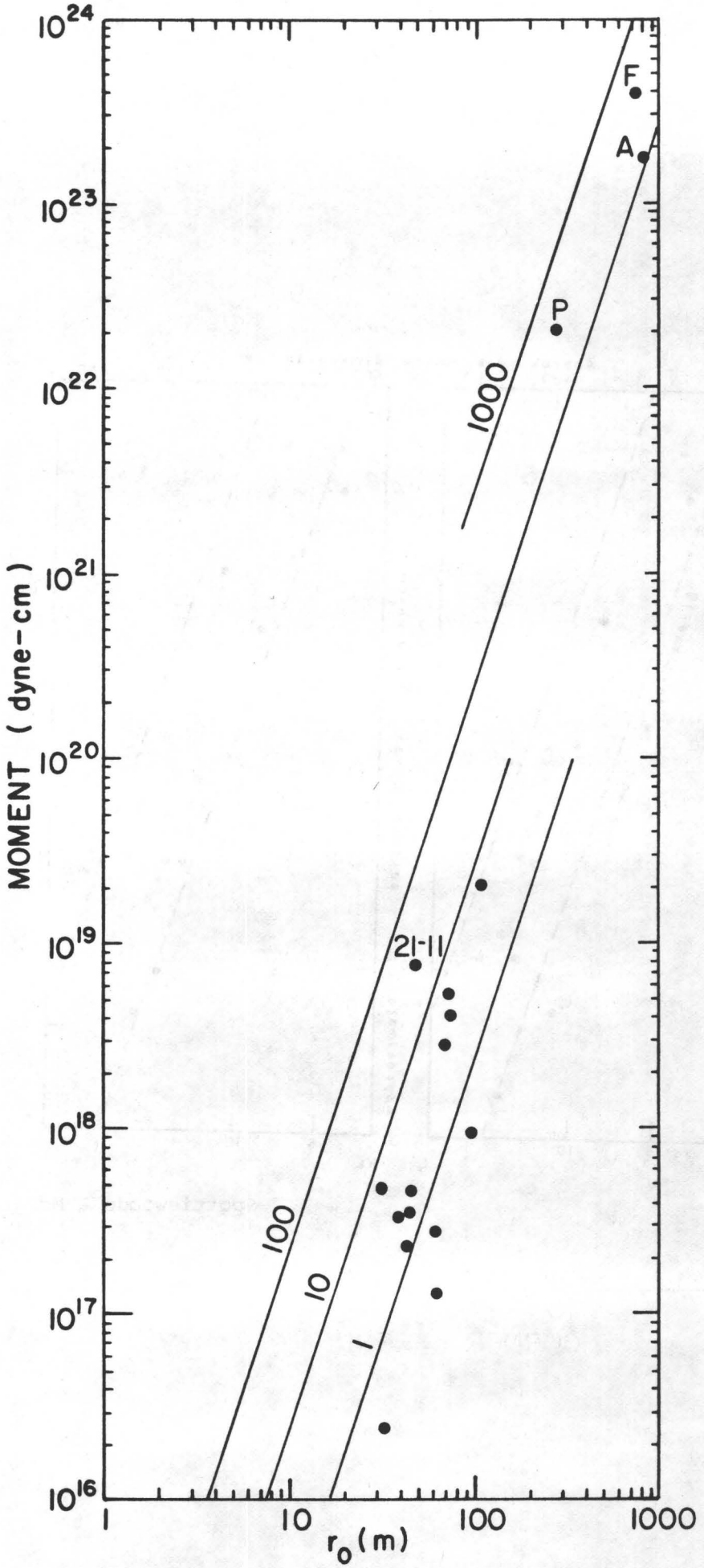

Unpublished Oroville aftershock data compiled by J.B. Fletcher

Figure 3

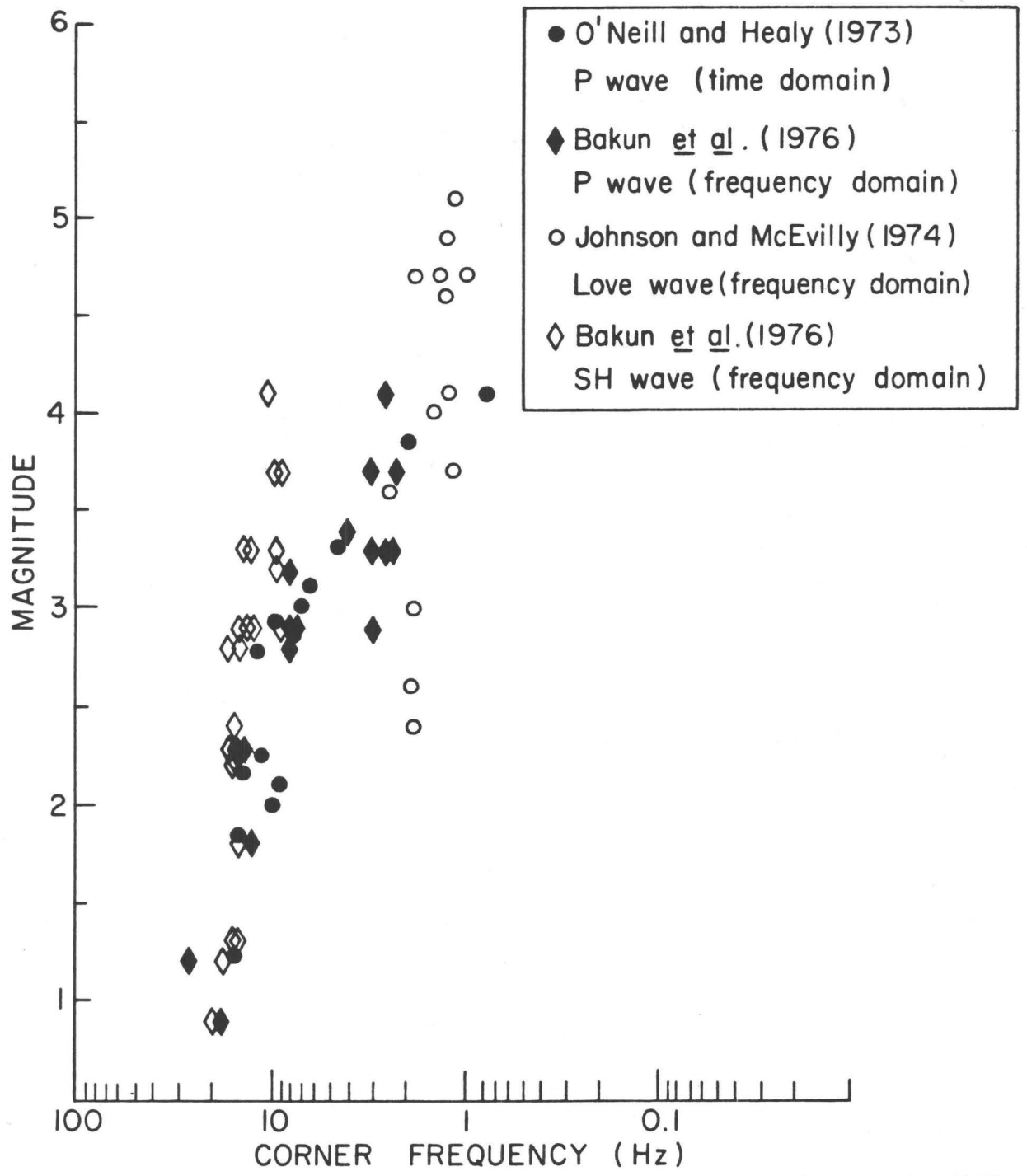

Bakun et al (1979)

Figure 4

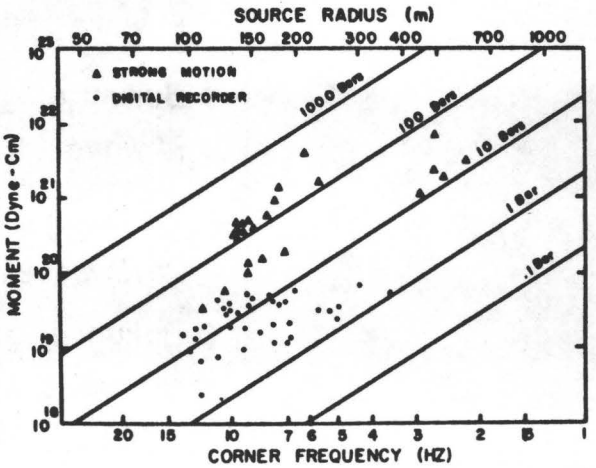

(a)

Hartzell & Brune (1977)

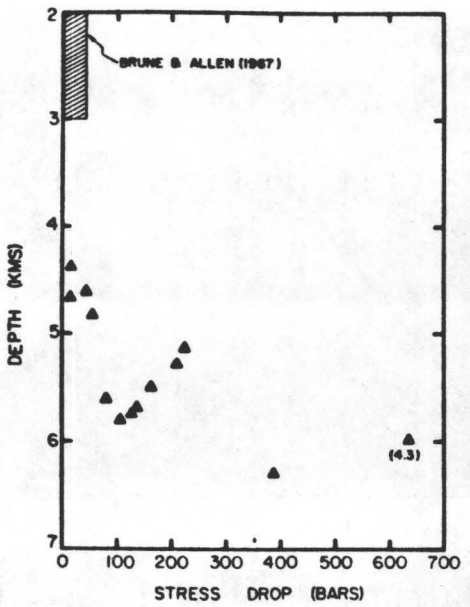

(b)

Figure 5

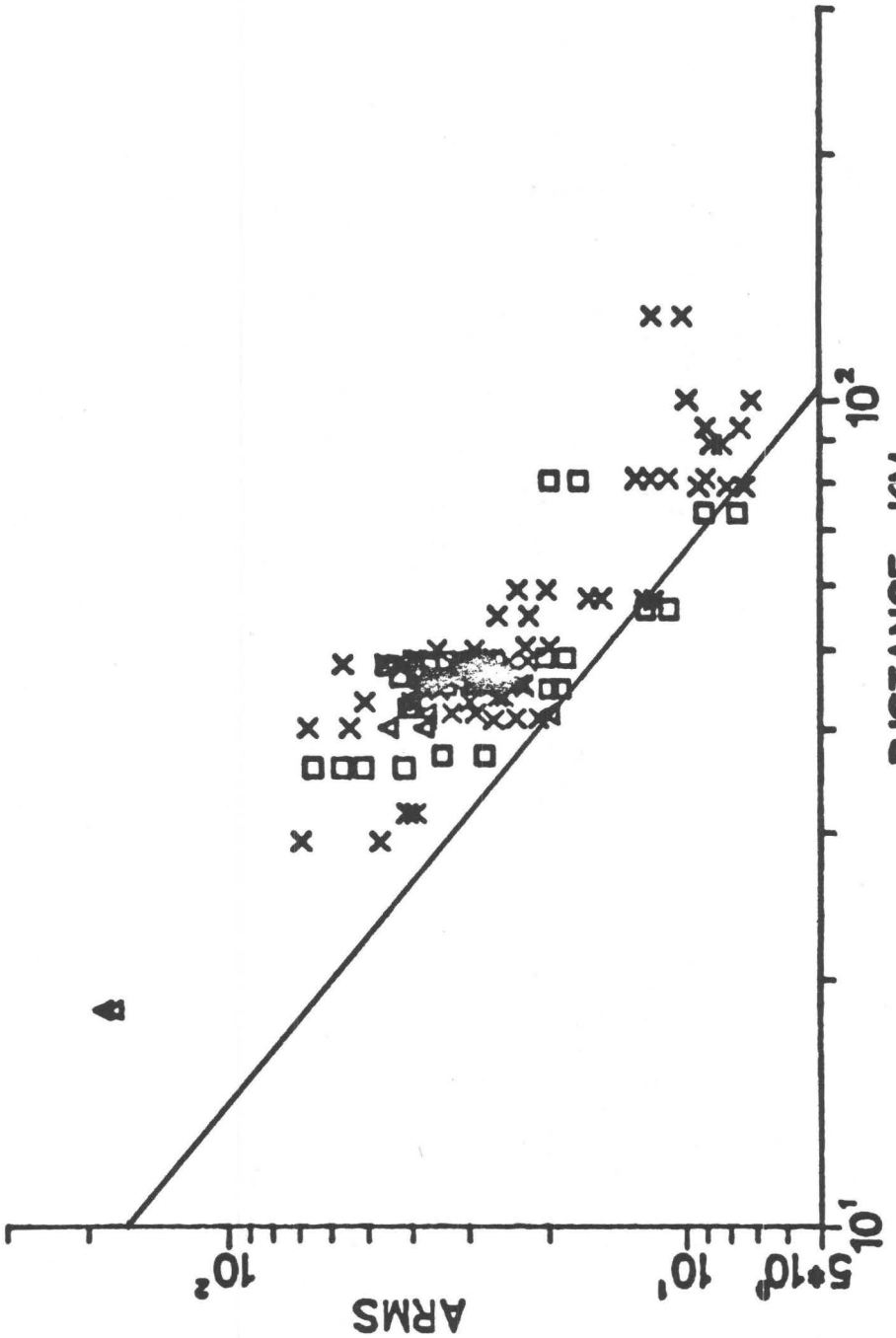

McGuire & Hanks (1979)

Figure 6

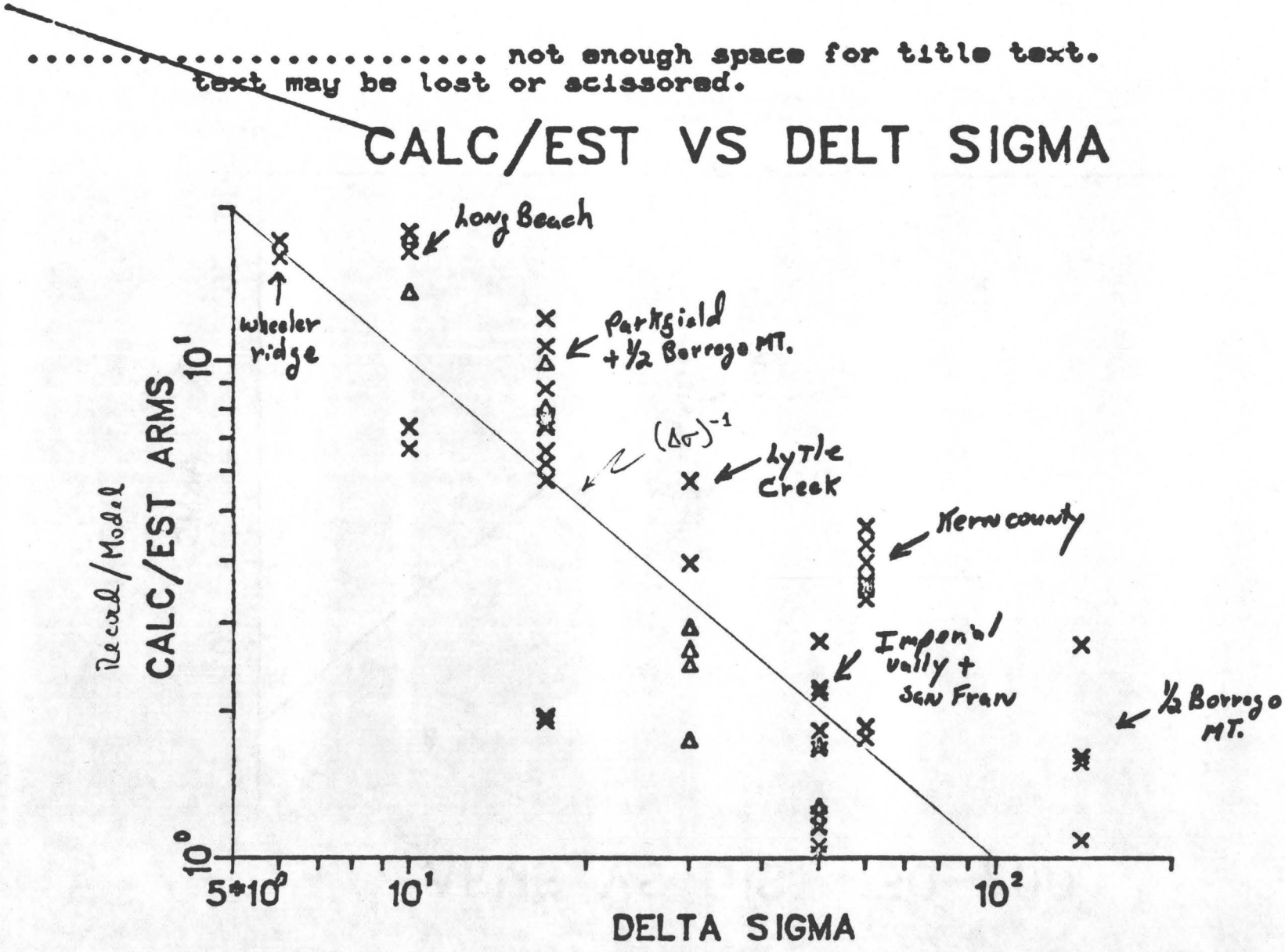

Unpublished data of
T. C. Hanks and R.K. McGuire

Figure 7

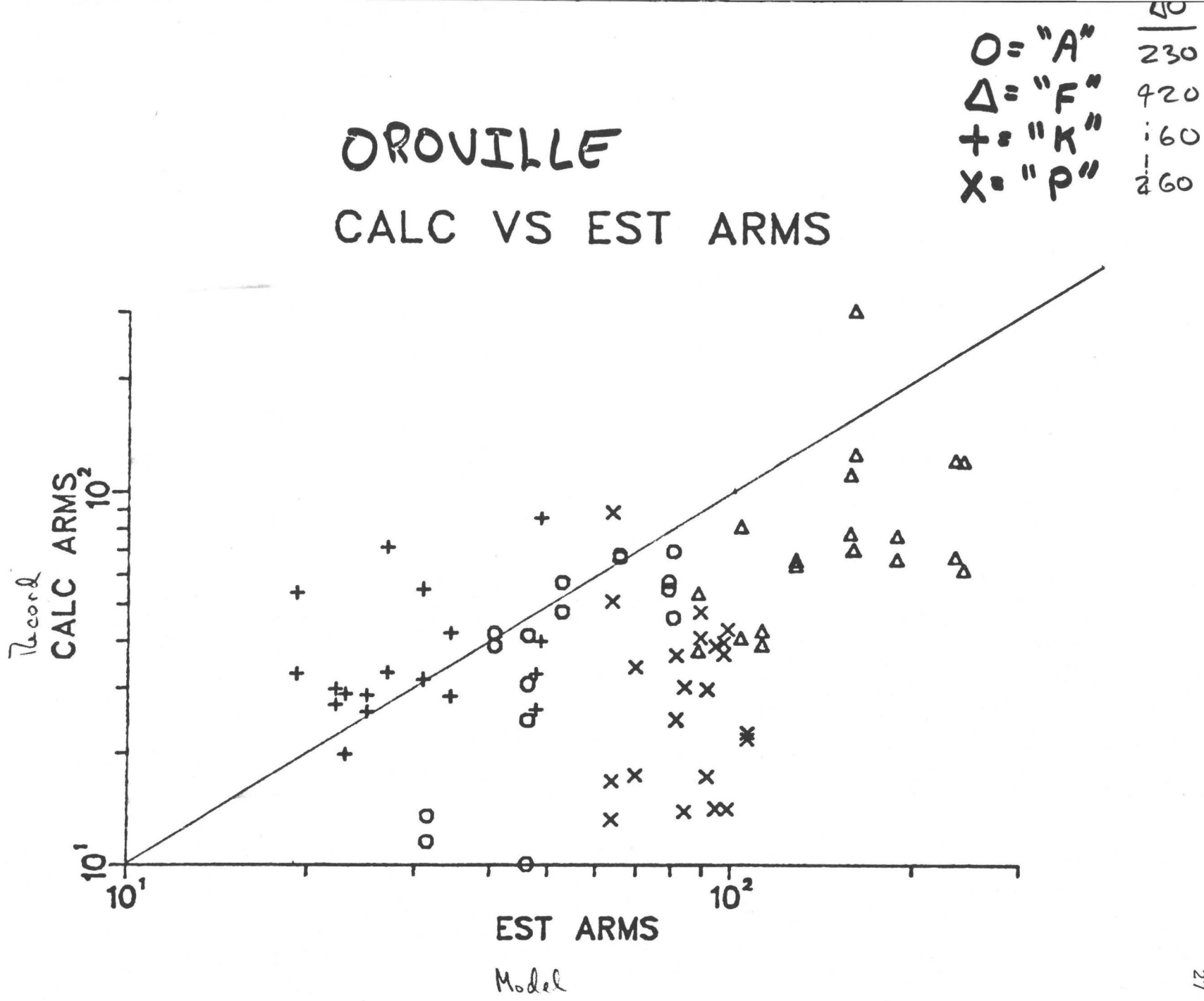

Unpublished data of T.C. Hanks and R.K. McGuire.

Figure 8

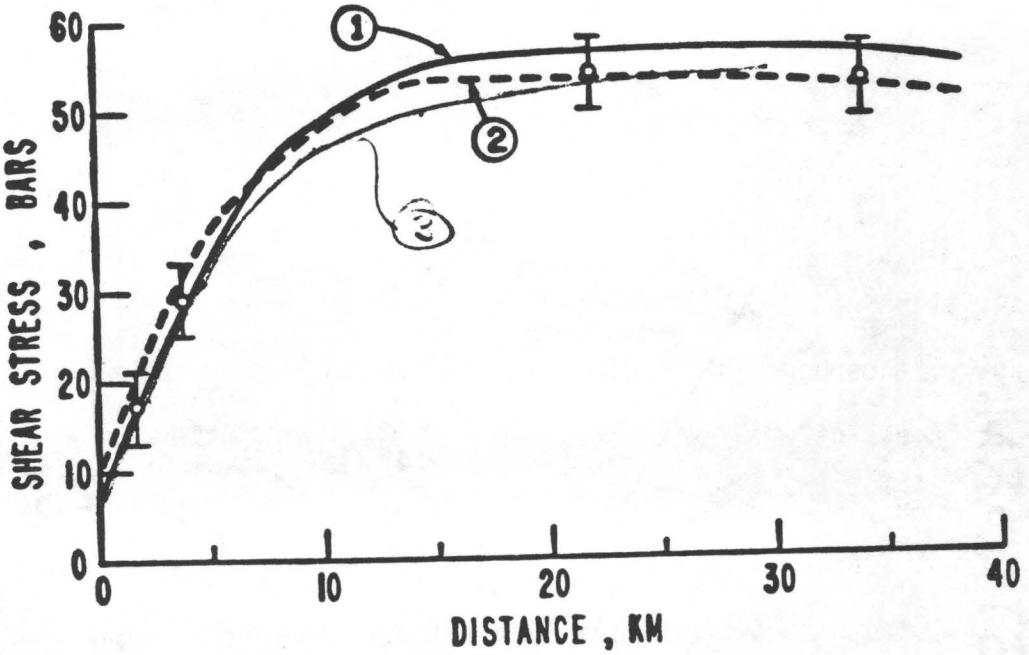

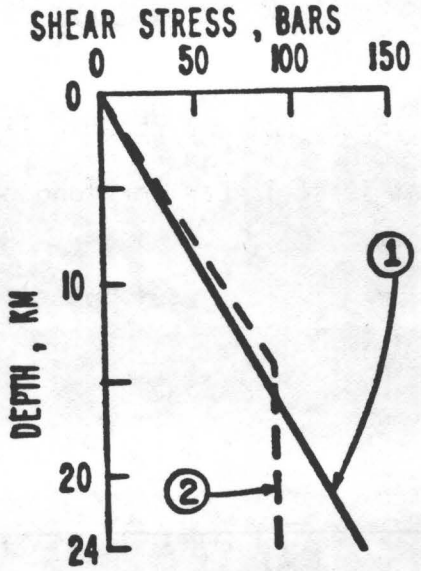

Modified from Zoback (1979)

Figure 9

OBSERVATIONS OF FLEXURE AND THE STATE OF STRESS IN THE OCEANIC LITHOSPHERE

by

A. B. Watts, J. H. Bodine and M. S. Steckler

Abstract

Observations of flexure indicate the effective elastic thickness of the oceanic lithosphere is 2 to 3 times smaller than the seismic or thermal thickness of oceanic lithosphere. The effective elastic thickness is a function of temperature gradient and hence age of the lithosphere at the time of loading. Recent results of experimental rock mechanics indicate that the strength of rocks is a strong function of temperature and that on loading the oceanic lithosphere would thin rapidly from its seismic thickness to its rheologic thickness. We have used a yield stress envelope based on experimental rock mechanics to estimate the maximum stresses associated with the load of the Hawaiian Islands near Oahu. These results indicate that the oceanic lithosphere is capable of supporting stresses of at least 1 kbar for long periods of geological time (>50 m.y.).

Introduction

There is currently much geological and geophysical interest in determining the state of stress in the oceanic lithosphere. Unfortunately, it is still not possible to reliably estimate regional stress fields associated with the driving mechanism of plate tectonics. Recent advances in experimental rock mechanics, however, now make it possible to estimate the local stress fields associated with the flexure of the lithosphere due to long-term (>10^6 years) surface loads.

The earliest evidence for the existence of a strong rigid lithosphere came from observations of large volumes of sediments at the mouths of rivers (Barrell, 1914) and the observation that large scale surface inequalities on the Earth's surface, such as mountain ranges and valleys, were supported by large stress-differences (>1.5 kbar) for long periods of geological time (Jeffreys, 1932). More recent evidence has come from quantitative studies of lithospheric flexure in the vicinity of long-term (>10^6 years) surface loads. These surface loads include ice sheets (Walcott, 1970a), seamount chains (Vening Meinesz, 1941; Walcott, 1970b; Watts and Cochran, 1974; Watts, 1978), isolated seamounts (Watts et al., 1975; McNutt and Menard, 1978) and sediments (Walcott, 1972; Cochran, 1973). In addition, a number of studies have been made of the oceanic lithosphere as it approaches an island arc-trench system (Hanks, 1971; Watts and Talwani, 1974; Dubois et al., 1975; Parsons and Molnar, 1976; Caldwell et al., 1976; Caldwell, 1979). These studies have shown that in a number of cases the oceanic lithosphere responds to long-term surface loads in a manner similar to a thin elastic plate overlying a weak fluid.

The most useful parameter in flexure studies is the flexural rigidity which in the elastic plate model (for example, Walcott, 1970c) is related to the elastic thickness of the plate. The flexural rigidity determines

both the amplitude and wavelength of flexure associated with a surface load. By comparing free-air gravity anomaly profiles, seismic refraction data, patterns of uplift and subsidence, or elevation and bathymetry data to calculations based on elastic or viscoelastic plate models, a number of estimates of the flexural rigidity have now been obtained. The flexural rigidity for oceanic lithosphere is in the range 5×10^{27} to 1×10^{31} dyne-cm (for example, McKenzie and Bowin, 1976; Watts et al., 1975; Watts and Cochran, 1974; Walcott, 1970c; McNutt and Menard, 1978; Caldwell, 1979; Cochran, 1979; McNutt, in press) and for continental lithosphere is $\lesssim 4 \times 10^{31}$ dyne-cm (Molnar et al., in press; Haxby et al., 1976; Banks et al., 1977; McNutt and Parker, 1978). These values imply the effective elastic thickness, T_e, is in the range 3 to 47 km for oceanic lithosphere and $\lesssim 77$ km for continental lithosphere.

The elastic model requires large bending stresses, in the range of a few kbar (Walcott, 1970a) to several kbar (Cochran, 1973; Hanks, 1971; Watts and Talwani, 1974), to fit the observations of flexure. The largest bending stresses (>5 kbar) occur at island arc-trench systems where the associated strains are as large as a few percent. The bending stresses deduced from these studies are somewhat limited in their geological application, however, since they are based on a simple homogeneous elastic plate model. Data from experimental rock mechanics (for example, Goetze and Brace, 1972; Weertman and Weertman, 1975; Kohlstedt and Goetze, 1974) indicate that under the large stresses associated with the elastic model, rocks would yield by fracture near the Earth's surface and will deform by flow at great depths. A major difficulty in applying these experimental results to the crust and upper mantle, however, is in extrapolating high experimental strain rates ($\gtrsim 10^{-8}$/sec) to the slower rates (10^{-18} to 10^{-14}/sec) applicable to the lithosphere.

Attempts to model lithospheric flexure using a more complex rheology have been made by Turcotte et al. (1978), McAdoo et al. (1978) and Bodine and Watts (1979). These studies considered an elastic plate model in which the oceanic lithosphere responds elastically to an applied load until some yield stress criterion are met. For bending stresses greater than the yield stress, portions of the plate deform plastically. Turcotte et al. (1978) and McAdoo et al. (1978) assumed a yield stress that is uniform with depth and Bodine and Watts (1979) assumed a yield stress that varied with depth. Although these models produce flexure curves similar to the elastic models they do not produce as large bending stresses. The yield stress required in these models, however, is large (several kbar) and is assumed to be independent of both temperature and strain rate.

The purpose of this paper is to summarize the results of recent studies of lithospheric flexure and extrapolations of experimental rock mechanics in order to examine their implications for the state of stress in the oceanic lithosphere. There are three main objectives to the study: (1) to determine the relationship between effective elastic thickness and age of the oceanic lithosphere, (2) to use this relationship together with the results of experimental rock mechanics to provide constraints on the long-term mechanical thickness of the oceanic lithosphere, (3) to use this information to estimate the magnitude of the stresses which can be supported by the oceanic lithosphere.

Lithospheric flexure

The results of a number of recent studies of oceanic plate flexure

are summarized in Figure 1. In this figure the effective elastic thickness T_e is plotted against the age of the lithosphere at the time of loading. Each estimate of T_e is based on an assumed Young's Modulus of $E = 10^{12}$ dyne/cm^2. The age of the oceanic lithosphere at the time of loading was determined by subtracting the age of the load from the estimated age of the oceanic crust underlying the load. For example, the age of the Great Meteor Seamount in the North Atlantic based on dredge hauls is 11 to 16 m.y. B.P (Wendt et al., 1976) and the age of the underlying oceanic crust is 80 m.y.B.P. (Pitman and Talwani, 1972). Thus the age of the oceanic lithosphere at the time of loading is in the range 64 to 69 m.y.

We have plotted in Figure 1 estimates of the elastic thickness determined from different surface loads on the oceanic lithosphere. These include the topography of oceanic layer 2 (McKenzie and Bowin, 1976; Cochran, 1979; McNutt, in press), seamount chains (Walcott, 1970b; Watts and Cochran, 1974; Watts, 1978), isolated seamounts (Watts et al., 1975; McNutt and Menard, 1978) and deep-sea trench outer rise systems (Caldwell et al., 1976; Caldwell, 1979). The dashed lines in Figure 1 represent studies (Watts, 1978; McNutt and Menard, 1978) in which a single estimate of the elastic thickness was obtained for a wide range of ages of the lithosphere at the time of loading (<60 m.y.). Also shown as a dashed line is the estimate by Caldwell (1979) for the Aleutian trench-outer rise system since it is difficult at this trench system to separate the outer rise from regional changes in sea-floor topography between Hawaii and the Aleutian trench.

The parameter that has been most widely used in flexure studies is the free-air gravity anomaly (for example, Walcott, 1970b; Watts and

Cochran, 1974; McKenzie and Bowin, 1976; McNutt, in press; Cochran, 1979; Watts, 1978). The gravity anomaly can be relatively easily measured on a surface-ship and depends strongly on the effective elastic thickness T_e of the oceanic lithosphere. For example, Figure 2 compares an observed gravity anomaly profile of the Hawaiian ridge near Oahu to calculated profiles for T_e = 10, 30, 50 and 75 km. The most satisfactory fit between observed and calculated gravity anomaly profiles is for T_e=30 km. The computed profiles with T_e=10 and 20 km predict too small an amplitude for the anomaly over the crest of the ridge and too short wavelengths in flanking regions compared to the observed profile. Furthermore, the computed profiles with T_e=50 and 75 km predict too large an amplitude for the anomaly over the crest and too long wavelengths in flanking regions.

Although free-air gravity anomaly data generally supports the flexure models at deep-sea trench outer rise systems (Watts and Talwani, 1974), most estimates of the elastic thickness at trenches (Walcott, 1970c; Caldwell et al., 1976; Turcotte et al., 1978; Caldwell, 1979) have been based on bathymetry and seismic reflection profile data. These data have shown (for example, Walcott, 1970c; Watts and Talwani, 1974) that seaward of a number of deep-sea trenches is a broad (a few hundred km) small amplitude ($\lesssim$700 meters) regional rise in sea-floor topography. Caldwell et al. (1976) and Caldwell (1979) used the amplitude and wavelength of the topographic rise to estimate the elastic thickness of oceanic lithosphere. There are, however, two main difficulties with estimating the elastic thickness from the topographic rise seaward of deep-sea trenches. First, the amplitude of the rise is relatively small

(for example, Fig. 3) and it is sometimes difficult to separate from the normal depth of the ocean floor. Second, the oceanic lithosphere seaward of trenches may be subject to horizontal boundary loads (for example, Turcotte et al., 1978; Bodine and Watts, 1978) which may, depending on the rheology of the lithosphere assumed, modify the shape of the topographic rise.

The main result, shown in Figure 1, is that surface loads formed on young oceanic lithosphere, such as the topography of oceanic Layer 2, are associated with relatively small values of the effective elastic thickness while loads formed on old oceanic lithosphere, such as the Hawaiian-Emperor seamount chain, are associated with relatively high values. The simplest interpretation of these results is that as the oceanic lithosphere increases in age, it cools, thickens, and becomes more rigid in its response to surface loads. Figure 1 shows there is good general agreement between T_e and the 300°C to 600°C oceanic isotherms based on the cooling plate model.

There are three main conclusions which can be drawn from the flexure studies shown in Figure 1.

1. The effective elastic thickness of the oceanic lithosphere based on long-term ($>10^6$ years) loads is 2 to 3 times smaller than the seismic thickness based on short-term (up to several tens of seconds) seismic wave periods.

2. The effective elastic thickness depends on the temperature gradient and hence age of the oceanic lithosphere at the time of loading.

3. The effective elastic thickness does not relax appreciably with time as evidenced, for example, by the long duration of the Emperor seamount load (50 m.y.).

These studies of lithospheric flexure have important implications in models for the rheology of the oceanic lithosphere. Apparently, on application of a surface load there is a rapid ($\lesssim 10^6$ years) relaxation of the lithosphere from its short-term or seismic thickness to its long-term ($>10^6$ years) mechanical thickness*. Subsequent relaxation is not observed but may exist on very long time-scales (>50 m.y.). The effective elastic thickness and the corresponding stresses therefore appear to be acquired at the time of loading and do not change appreciably with time.

The results of lithospheric flexure studies are not in conflict with thermal cooling models (for example, Parsons and Sclater, 1977) which predict that the thickness of the oceanic lithosphere increases with age. The material added to the lower part of the plate as it cools was not deformed by the surface load and would not be expected to alter the elastic thickness acquired at the time of loading. The oceanic lithosphere however, would deform in response to subsequent loads with an effective elastic thickness dependent on the new depth to the 300 to 600°C isotherm. Thus, by determining the effective elastic thickness at an oceanic island or seamount of unknown origin it should be possible to estimate whether it formed on young (mid-ocean ridge crest) or old (off-ridge) sea floor.

Rheology of the oceanic lithosphere

Recent studies in experimental rock mechanics (for example, Goetze, 1978; Ashby and Verrall, 1977) indicate the oceanic lithosphere is more

*Footnote: The mechanical thickness defined here is the upper layer of the oceanic lithosphere which is capable of supporting the stresses associated with surface loads for long periods of geological time (>1 m.y.).

complex than the simple elastic plate assumed in lithospheric flexure studies. The strength of the lower part of the lithosphere is highly temperature and strain rate dependent while the uppermost lithosphere yields through pressure-dependent frictional sliding and faulting.

Murrell (1976) made one of the first attempts to compare the results of lithospheric flexure to the predictions of experimental rock mechanics. He used both diffusional and dislocation creep mechanisms to construct viscosity profiles as a function of depth and stress in the lithosphere. The resulting viscosity profiles suggested that the lower part of the lithosphere could only support small stresses (of the order of 10 to 100 bars) while the upper part could support stresses greater than 1 kbar. Thus the uppermost part of the lithosphere could be considered elastic on long time scales.

Anderson and Minster (in press) examined dislocation creep and found that the characteristic time for the relaxation of stress by movement of dislocations to be a strong function of temperature. In the hotter part of the lithosphere, stresses will relax more rapidly. Thus, for loads of short duration (ie. seismic wave periods) the lithosphere appears relatively thick while loads of long duration (>1 m.y.) are supported by a relatively thin strong lithosphere. This suggests that on application of a surface load the lithosphere would initially thin rapidly from its seismic thickness and then more slowly as it approaches its rheologic thickness. The rheologic thickness as defined by Anderson and Minster (in Press) is the mechanically upper strong layer of the lithosphere whose flexural rigidity is similar to the effective elastic thickness of flexure studies.

A detailed study of the deformation mechanisms dominant at different depths in the lithosphere has been carried out by Ashby and Verrall (1978). They showed that the dominant mechanism at shallow depth is pressure-dependent cataclastic flow and the dominant mechanism at greater depth is power-law creep. The transitional region between cataclastic and ductile flow will effectively be elastic except in the presence of very large stresses ($\gtrsim$6 kbar).

Goetze and Evans (in press) defined a yield strength envelope for the oceanic lithosphere in which the yield stress increases and then decreases with depth. For the upper part of the envelope the yield stress is defined by Coulomb failure criteria for frictional sliding and in the lower part by dislocation creep. The dislocation creep is represented by a power-law with n = 3 for stresses less than 2 kbar and by the Dorn law (Goetze, 1978) for higher stresses. At any depth the plate will deform elastically for stresses less than the yield stress and plastically for greater stresses.

The yield strength envelope was applied by Goetze and Evans (in press) to deep-sea trench-outer rise systems. Previous elastic or elastic-plastic models at trenches (for example, Hanks, 1971; Caldwell et al., 1976; McAdoo et al., 1978) produce large bending stresses (several kbar) in the upper part of the lithosphere. Seismic reflection profiling with large air-guns (for example, Fig. 3) at trenches, however, show evidence of faulting and therefore stress relaxation in the upper part of the lithosphere. By specifying the strain rate at trenches Goetze and Evans (in press) showed that the yield strength envelope can support bending moments and curvatures consistent with those determined by Caldwell et al. (1976) at trenches.

The maximum stresses developed in their preferred model, however, although smaller than developed in the elastic or elastic-plastic plate model, were large and of the order of several kbar.

Flexure at the Hawaiian Islands

The Hawaiian Islands, which have been one of the most studied surface loads on the oceanic lithosphere, are a particularly satisfactory load for flexure studies. 1) They represent the largest surface load on oceanic lithosphere. 2) Both the age of individual islands and the age of the underlying sea-floor are reasonably well known (Clague and Jarrard, 1973; Larson and Chase, 1972). 3) The islands are located in the center of the Pacific plate away from the complexities of plate boundaries.

The earliest submarine gravity measurements (Vening Meinesz, 1941) showed that the load of the Hawaiian Islands were not supported by the Airy model but were regionally supported. More recent studies using gravity and bathymetry data (Walcott, 1970b; Watts and Cochran, 1974; Watts, 1978) show that the compensation of the islands can be explained by a simple elastic plate model. However, the applicability of flexural models to the Hawaiian Islands has been questioned. For example, they assume the "normal" Pacific oceanic crust (Shor et al., 1970) is simply flexed beneath the islands. Woollard (1967, 1970) has argued that oceanic Layer 3 may thicken beneath the islands and therefore that the Layer 2/Layer 3 boundary may be a better measure of flexure rather than the 'Moho'.

An independent test of the flexure models is to compare the calculated crustal flexure to seismic evidence of the configuration of the Layer 2/Layer 3 boundary and the 'Moho' beneath the islands. Unfortunately,

only a limited number of reliable seismic refraction measurements have been carried out on the islands or in peripheral oceanic regions (Shor, 1960; Shor and Pollard, 1964; Furumoto and Woollard, 1965) and these provide only general constraints on flexure models. Although available seismic refraction measurements northeast of Oahu (Shor and Pollard, 1964) are in general agreement with the elastic model (Fig. 4), measurements beneath the islands (Furumoto et al., 1968) are in poor agreement. The discrepancy beneath the islands could be due to uncertainties in the flexure model (for example, Models A and B in Watts and Cochran, 1974) or the crustal structure. Most of the available seismic measurements in the region of the Hawaiian Islands were obtained during the late 1950's and 1960's and were hampered (in sea areas) by drifting surface receivers, poor navigation and large shot spacing.

Figure 4c shows the bending stresses associated with the upper surface of the best fitting elastic model for the Hawaiian Islands near Oahu. The largest compressive stresses (6.8 kbar) occur directly beneath the island load and the largest tensile stresses (2.8 kbar) occur in flanking regions. The problem with stresses estimated using an elastic model is that the largest stresses are developed at the top and bottom of the plate where the lithosphere would be expected to be the weakest.

A better approach is to use a yield strength envelope (Goetze and Evans, in press) to estimate the stresses developed in the plate. For this purpose it is most convenient to consider surface loads in terms of an applied bending moment. We have used the bending moments calculated for the elastic models which best fit available geophysical data in the region of Oahu. The bending moments beneath Oahu, based on the best

fitting elastic model (Fig. 4), are in the range 6.5×10^{21} to 1.9×10^{22} dyne (Table 1).

The bending moment can be expressed as an integral of the vertical stress profile through the plate. We have therefore used the yield stress envelope of Goetze and Evans (in press) and the observed range of bending moments beneath Oahu to estimate a likely range of stresses which are developed in the plate (Fig. 5).

In order to define the lower part of the yield stress envelope the temperature profile and strain rate must be specified. For the temperature profile we have used the cooling plate model (Parsons and Sclater, 1977) for a thermal age of 80 m.y. An estimate of the present day strain rate can be obtained from the age of the load and strains developed during flexure. This strain rate will be a maximum value since most of the relaxation occurs early in the loading history. The age of Oahu is 3 m.y. ($\sim 10^{14}$ secs) (Clague and Jarrard, 1973) and the maximum strains are about 0.7% (Table 1), thus the maximum strain rate is about 1×10^{-16}/sec. The maximum strain rate will be associated with a minimum estimate of the stress needed to support the load at Oahu.

We applied the best fitting range of bending moments determined beneath Oahu to this yield envelope (Fig. 5). The maximum stresses occur at the top and bottom of the central elastic core and are in the range of 1.3 to 5.7 kbar. Table 2 shows the results for the range of possible bending moments at the maximum strain rate of 1×10^{-16}/sec and a strain rate an order of magnitude smaller.

These estimates of the maximum stresses may be uncertain, however, because the bending moments are poorly constrained beneath Oahu. The

only constraint on the elastic model beneath Oahu is free-air gravity anomaly data since there are no reliable seismic refraction determinations of crustal thickness or velocity.

The elastic model is reasonably well constrained, however, by bathymetry, gravity anomaly and seismic refraction data in the region of the Hawaiian arch northeast of Oahu (Fig. 4). The maximum bending moments based on the best fitting elastic model (T_e = 30 km) in the region of the arch is 4.5×10^{21} dyne and the corresponding maximum stresses based on the yield stress envelope with $\dot{\varepsilon} = 1 \times 10^{16}$/sec are in the range 1.0 to 1.1 kbar. These results suggest that stresses of at least 1.0 kbar are required to support the load of the Hawaiian ridge in the region of Oahu. If the crustal structure predicted by the elastic model beneath Oahu (Fig. 4) is correct, then stresses in the range 1.3 to 5.7 kbar are required. While these stresses are smaller than those determined using the elastic model (Table 1) they indicate that the oceanic lithosphere is capable of supporting stresses of at least 1 kbar.

Summary and Conclusions

The principal results of this study are illustrated in Figure 6.

1. The mechanical thickness of the oceanic lithosphere is 2 to 3 times smaller than the seismic thickness or the thermal thickness of plate tectonics.

2. The mechanical thickness is a strong function of temperature and hence age of the oceanic lithosphere.

3. The results of lithospheric flexure due to long-term surface loads are in general agreement with extrapolations of data based on the results of experimental rock mechanics.

4. The oceanic lithosphere is capable of supporting stresses of at least 1 kbar.

5. These stresses can apparently be maintained for long periods of geologic time (>50 m.y.).

Acknowledgments

The studies of lithospheric flexure at Lamont-Doherty have been supported by National Science Foundation grant OCE 77-07941 and Office of Naval Research contract N00014-75-C-210 Scope C.

TABLE 1

HAWAIIAN RIDGE PARAMETERS

Elastic Thickness T_e km	Maximum Deflection km	Flexural Rigidity D Dyne-cm	Maximum Bending Stress kbar	Maximum Strain %	Maximum Bending Moment Dyne
10	6.1	8.9×10^{28}	-10.96	1.09	-1.9×10^{21}
20	4.0	7.1×10^{29}	- 9.10	0.91	-6.5×10^{21}
30	2.8	2.4×10^{30}	- 6.83	0.68	-1.1×10^{22}
50	2.0	1.1×10^{31}	- 4.42	0.44	-1.9×10^{22}

All parameters assume the seismic Young's Modulus E = 10^{12} dyne/cm^2.

TABLE 2

STRESS DIFFERENCES AT THE TOP (σ_1) AND BOTTOM (σ_2) OF THE CENTRAL ELASTIC CORE FOR DIFFERENT APPLIED BENDING MOMENTS AND STRAIN RATES

Maximum Bending Moment	Strain Rate			
	$\dot{\varepsilon} = 1.16 \times 10^{-17}$/sec		$\dot{\varepsilon} = 1.16 \times 10^{-16}$/sec	
M (dyne)	σ_1 (kbar)	σ_2 (kbar)	σ_1 (kbar)	σ_2 (kbar)
-1.9×10^{21}	-0.4	0.3	-0.3	0.3
-6.5×10^{21}	-1.7	1.6	-1.5	1.3
-1.1×10^{22}	-3.3	3.1	-2.8	2.6
-1.9×10^{22}	-6.9	6.7	-5.7	5.4

References

Anderson, D.L. and J.B. Minster, Seismic velocity, attenuation and rheology of the upper mantle, Physics Earth & Planet. Inter., Prof. Jean Coulonb Symp., (in press).

Ashby, M.F. and R.A. Verrall, 1978. Micromechanisms of flow and fracture and their relevance to the rheology of the upper mantle, Phil. Trans. R. Soc. Lond. A., 288, 59-95.

Banks, R.J., R.L. Parker and S.P. Heustis, 1977. Isostatic compensation on a continental scale: local versus regional mechanisms, Geophys. J. R. astr. Soc., 50, 431-452.

Barrell, J., 1914. The strength of the Earth's crust, Part VIII. Physical conditions controlling the nature of lithosphere and asthenosphere, J. Geology, 22, 425-443.

Bodine, J.H. and A.B. Watts, 1979. On lithospheric flexure seaward of the Bonin and Mariana trenches, Earth Planet Sci. Lett., 43, 132-148.

Bowie, W. 1927. Isostasy, Dutton and Co., N.Y., 275p.

Caldwell, J.G., 1978. The mechanical behavior of the oceanic lithosphere near subduction zones, Ph. D. Thesis, Cornell University.

Caldwell, J.G., W.F. Haxby, D.E. Karig and D.L. Turcotte, 1976. On the applicability of a universal elastic trench profile, Earth Planet. Sci. Lett., 31, 239.

Cochran, J.R., 1979. An analysis of isostasy in the world's ocean, Part 2. Mid-ocean ridge crests, J. Geophys. Res., 84, 4713-4729.

Cochran, J.R., 1973. Gravity and magnetic investigations in the Guiana Basin, Western Equatorial Atlantic, Geol. Soc. Am. Bull., 84, 3249-3268.

Clague, D.A. and R.D. Jarrard, 1973. Tertiary Pacific plate motion deduced from the Hawaiian-Emperor chain, Geol. Soc. Am. Bull., 84, 1135-1154.

Dubois, J., J. Launay and J. Recy, 1975. Some new evidence on lithospheric bulges close to island arcs, Tectonophysics 26, 189.

Forsyth, D.W., 1977. The evolution of the upper mantle beneath mid-ocean ridges, Tectonophysics, 38, 89-118.

Furumoto, A.S. and G.P. Woollard, 1965. Seismic refraction studies of the crustal structure of the Hawaiian Archipelago, Pacific Sci., 19, 315-319.

Furumoto, A.S., G.P. Woollard, J.F. Campbell and D.M. Hussong (1968). Variations in the thickness of the crust in the Hawaiian archipelago, in The Crust and Upper Mantle of the Pacific Area, Geophys. Mono. 12, AGU, 94-111.

Goetze, C., 1978. The mechanisms of creep in Olivine, Phil. Trans. R. Soc. Lond., 288, 99.

Goetze, C., and W.F. Brace, 1972. Laboratory observations of high-temperature rheology of rocks, Tectonophysics 13, 583.

Goetze, C. and B. Evans, Stress and temperature in the bending lithosphere as constrained by experimental rock mechanics, Geophys. J. R. astr. Soc., in press.

Gunn, R., 1947. Isostasy - Extended, J. Geology, 57, 263-279.

Hanks, T.C., 1971. The Kuril trench - Hokkaido Rise System: large shallow earthquakes and simple models of deformation, Geophys. J. R. astr. Soc., 23, 173.

Haxby, W.F., D.L. Turcotte, and J.M. Bird, 1976. Thermal and mechanical evolution of the Michigan basin, Tectonophysics, 36, 57-75.

Jeffreys, H., 1932. On the stresses in the Earth's crust required to support surface inequalities, Mon. Nots. Geophys. Soc., 3, 30-41.

Kohlstedt, D.L. and C Geotze, 1974. Low-stress high-temperature creep in olivine single crustals, J. Geophys. Res., 79, 2045.

Larson, R.L. and C.G. Chase, 1972. Late Mesozoic evolution of the Western Pacific ocean, Geol. Soc. Am. Bull., 83, 3627-3644.

McAdoo, D.C., J.G. Caldwell and D.L. Turcotte, 1978. On the elastic-perfectly plastic bending of the lithosphere under generalized loading with application to the Kuril trench, Geophys. J. R. astr. Soc., 54, 11.

McKenzie, D.P. and C. Bowin, 1976. The relationship between bathymetry and gravity in the Atlantic ocean, J. Geophys, Res., 81, 1903-1915.

McNutt, M., Compensation of oceanic topography: An application of the response function technique to the SURVEYOR area, J. Geophys. Res., in press.

McNutt, M., H.W., Menard, 1978. Lithospheric flexure and uplifted atolls, J. Geophys. Res., 83, 1206-1212.

Molnar, P., W.P. Chen, T.J. Fitch, P. Tapponnier, W.E.R. Warsi, and F.T. Wu, The Indian shield as an outer bulge, CNRS Colloquium on the Himalaya, in press.

Murrell, S.A.F., 1976. Rheology of the lithosphere-experimental indications, Tectonophysics, 36, 5.

Parsons, B. and P. Molnar, 1976. The origin of outer topographic rises associated with trenches, Geophys. J. R. astr. Soc., 45, 707.

Parsons, B. and J.G. Sclater, 1977. An analysis of the variation of ocean floor bathymetry and heat flow with age, J. Geophys. Res., 82, 803-827.

Pitman, W.C. and M. Talwani, 1972. Sea-floor spreading in the North Atlantic, Geol. Soc. Am. Bull., 83, 619-646.

Shor, G.G. and D.D. Pollard, 1964. Mohole site selection studies north of Maui, J. Geophys. Res., 69, 1627.

Shor, G.G., 1960. Crustal structure of the Hawaiian ridge near Gardner Pinnacles, Bull Seismo. Soc. of Am., 50, 563-573.

Shor, G.G., H.W. Menard, and R.W. Riatt, 1970. Structure of the Pacific basin, in The Sea, 4, A.E. Maxwell (ed), Interscience, N.Y., 3-27.

Solomon, S.C., 1972. On Q and seismic discrimination, Geophys. J. R. astr. Soc., 31, 163-177.

Suyenaga, W., 1977. Earth deformation in response to surface loading: Application to the formation of the Hawaiian Ridge, Ph. D. Thesis, Univ. of Hawaii.

Turcotte, D.L., D.C. McAdoo and J.C. Caldwell, 1978. An elastic-perfectly plastic analysis of the bending lithosphere, Tectonophysics 47, 193.

Vening Meinesz, F.A., 1941. Gravity over the Hawaiian Archipelago and over the Madiera Area; Conclusions about the Earth's crust, Proc. Kon. Ned. Akad. Wetensia, 44p.

Watts, A.B. and M. Talwani, 1974. Gravity anomalies seaward of deep-sea trenches and their tectonic implications, Geophys. J. R. astr. Soc., 36, 57-90.

Watts, A.B. and J.R. Cochran, 1974. Gravity anomalies and flexure of the lithosphere along the Hawaiian-Emperor Seamount Chain, Geophys. J. R. astr. Soc., 38, 119-141.

Watts, A.B., J.R. Cochran and G. Selzer, 1975. Gravity anomalies and flexure of the lithosphere: A three-dimensional study of the Great Meteor Seamount, Northeast Atlantic, J. Geophys. Res., 80, 1391-1398,

Watts, A.B., 1978. An analysis of isostasy in the world's oceans, Part 1. Hawaiian-Emperor seamount chain, J. Geophys. Res., 83, 5989-6004.

Walcott, R.I., 1970a. Isostatic response to loading of the crust in Canada, Can. J. Earth Sci., 7, 716-727.

Walcott, R.I., 1970b. Flexure of the lithosphere at Hawaii, Tectonophysics, 9, 435-466.

Walcott, R.I., 1970c. Flexural rigidity, thickness and viscosity of the lithosphere, J. Geophys. Res., 75, 3941-3954.

Walcott, R.I., 1972. Gravity, flexure and the growth of sedimentary basins at a continental edge, Geol. Soc. Am. Bull., 83, 1845.

Weertman, J. and J.R. Weertman, 1975. High-temperature creep of rock and mantle viscosity, Ann. Rev. Earth Planet. Sci. 3, 293.

Wendt, I., H. Kreuzer, P. Müller, U. von Rad and H. Raschka, 1976. K-Ar age of basalts from Great Meteor and Josephine seamounts (eastern North Atlantic), Deep-Sea Research, 23, 849-862.

Woollard, G.P., 1966. Crust and mantle relations in the Hawaiian area, in Continental margins and island arcs, W.M. Poole (ed), Geol. Surv. Can. Paper, 66-15, 294-310.

Woollard, G.P., 1970. Evaluation of Isostatic Mechanism and Role of mineralogic transformations from seismic and gravity data, Phys. Earth Planet. Interiors, 3, 484-498.

FIGURE CAPTIONS

Figure 1. Plot of T_e, the effective elastic thickness of the oceanic lithosphere against age of the lithosphere at the time of loading. 1- East Pacific rise crest (Cochran, 1979). 2- Juan da Fuca rise crest (McNutt, in press). 3-Mid-Atlantic ridge crest (McKenize and Bowin, 1976). 4- Deep-sea trench-outer rise systems (Caldwell, 1979). 4a- Nankai trough, 4b- Middle America trench, 4c- Kuril trench, 4d- Mariana trench, 4e- Aleutian trench. 5- Hawaiian-Emperor seamount chain (Watts, 1978). 5a- Emperor seamounts north of 40°N, 5b- Hawaiian ridge and Emperor seamounts south of 40°N. 6- Uplifted Pacific ocean atolls from the Cook, Tuamotu, Austral and Pitcairn island groups (McNutt and Menard, 1978). 7- Great Meteor seamount (Watts et al., 1975). 8- Kuril trench (McAdoo et al., 1978). 9- Deep-Sea trench-outer rise systems (Caldwell et al., 1976). 9a- Aleutian trench, 9b- Kuril trench, 9c- Bonin trench, 9d- Mariana trench. 10- Hawaiian ridge (Suyenaga, 1977). 11- Hawaiian ridge (Walcott, 1970b). Symbols indicate ridge crest (squares), seamounts and oceanic islands (circles) and deep-sea trench outer rise systems (triangles). Dashed lines and open symbols indicate either studies based on a wide range of ages (5, 6) or uncertain values (4e). The elastic thickness has been computed assuming Young's Modulus $E = 10^{12}$ dyne/cm^2. The solid lines are the 300° and 600°C oceanic isotherms based on the cooling plate model of Parsons and Sclater (1977).

Figure 2. Comparison of observed and computed free-air gravity anomaly profiles of the Hawaiian ridge near Oahu. The observed profile was obtained during R/V Vema cruise 21 leg 5 and R/V Robert D. Conrad cruise 12 leg 20. The computed profiles are based on the elastic plate model and assumed values of T_e of 10, 20, 30, 50 and 75 km. The best overall fit to the observed data is for T_e = 30 km.

Figure 3. Bathymetry and seismic reflection profile of the northern Japan trench at latitude 39.9° North. The seismic reflection profile illustrates sedimentary and basement structure of a portion of the seaward wall of the trench. The profiles were obtained on R/V Vema cruise 32 leg 13.

Figure 4. Free-air gravity anomaly profile and crustal model of the Hawaiian ridge near Oahu. a) Comparison of observed free-air gravity anomaly profile (solid line) and computed gravity anomaly profile based on the elastic plate model with T_e = 30 km (dots). b) Comparison of crustal flexure based on seismic refraction stations 22, 23, 25, and 30 (Shor and Pollard, 1964) to a calculated flexure curve (dashed line) with T_e = 30 km. c) Bending stresses associated with the calculated flexure curve in (b).

Figure 5. Stress difference as a function of depth for oceanic lithosphere of 80 m.y. age (modified from Goetze and Evans, in press). The dashed lines show the maximum stress differences which can be supported before brittle failure occurs and the dash-dot lines show stress limits for ductile flow with strain-rate $\dot{\varepsilon}$ = 1.16 x

10^{-16}/sec. The solid lines a and b give the stress difference - depth profile for curvatures corresponding to bending moments obtained from computed flexure curves associated with the Hawaiian Islands (Fig. 3b). 'a' corresponds to a bending moment 0.6 x 10^{22} dyne (T_e = 20 km, Table 1) and 'b' corresponds to a bending moment 1.9 x 10^{22} dyne (T_e = 50 km, Table 1).

Figure 6. Summary plot of elastic thickness of the oceanic lithosphere T_e against age of the lithosphere at the time of loading. The elastic thickness values (Fig. 1) have been re-computed using the relaxed Young's Modulus E = 0.65 x 10^{12} dyne/cm^2 The open symbols represent seismic surface wave estimates of lithospheric thickness (Forsyth, 1977) and the solid lines is the seismic thickness based on a summary by Solomon (1972). The vertical arrows schematically illustrate the relaxation of the oceanic lithosphere from its short-term seismic thickness to its long-term rheologic thickness.

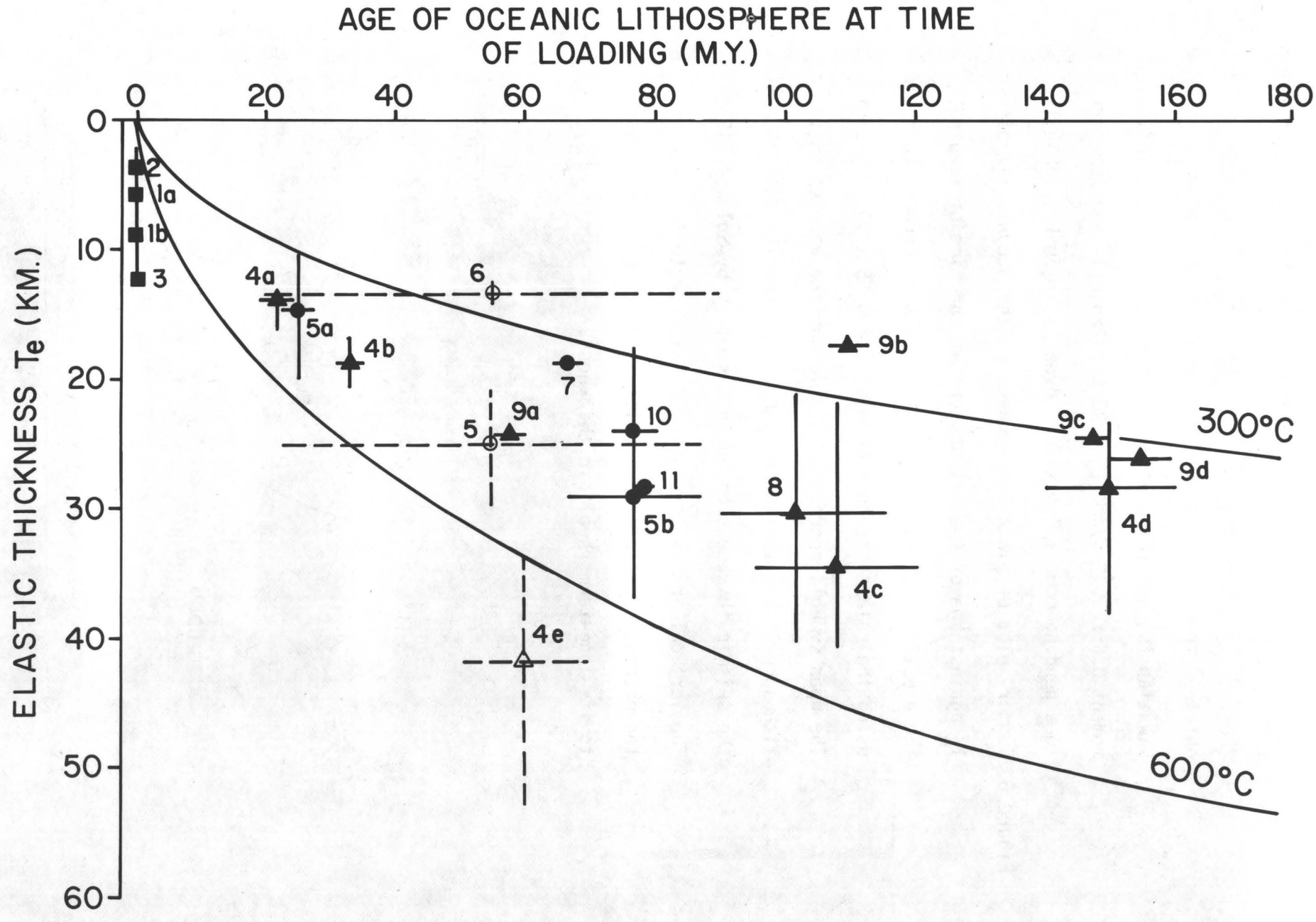
AGE OF OCEANIC LITHOSPHERE AT TIME OF LOADING (M.Y.)
0
20
40
60
80
100
120
140
160
180
ELASTIC THICKNESS Te (KM.)
0
10
20
30
40
50
60
1a
1b
2
3
4a
5a
4b
6
7
9a
5
10
11
5b
8
4c
4e
9b
9c
9d
4d
300°C
600°C

Figure 1

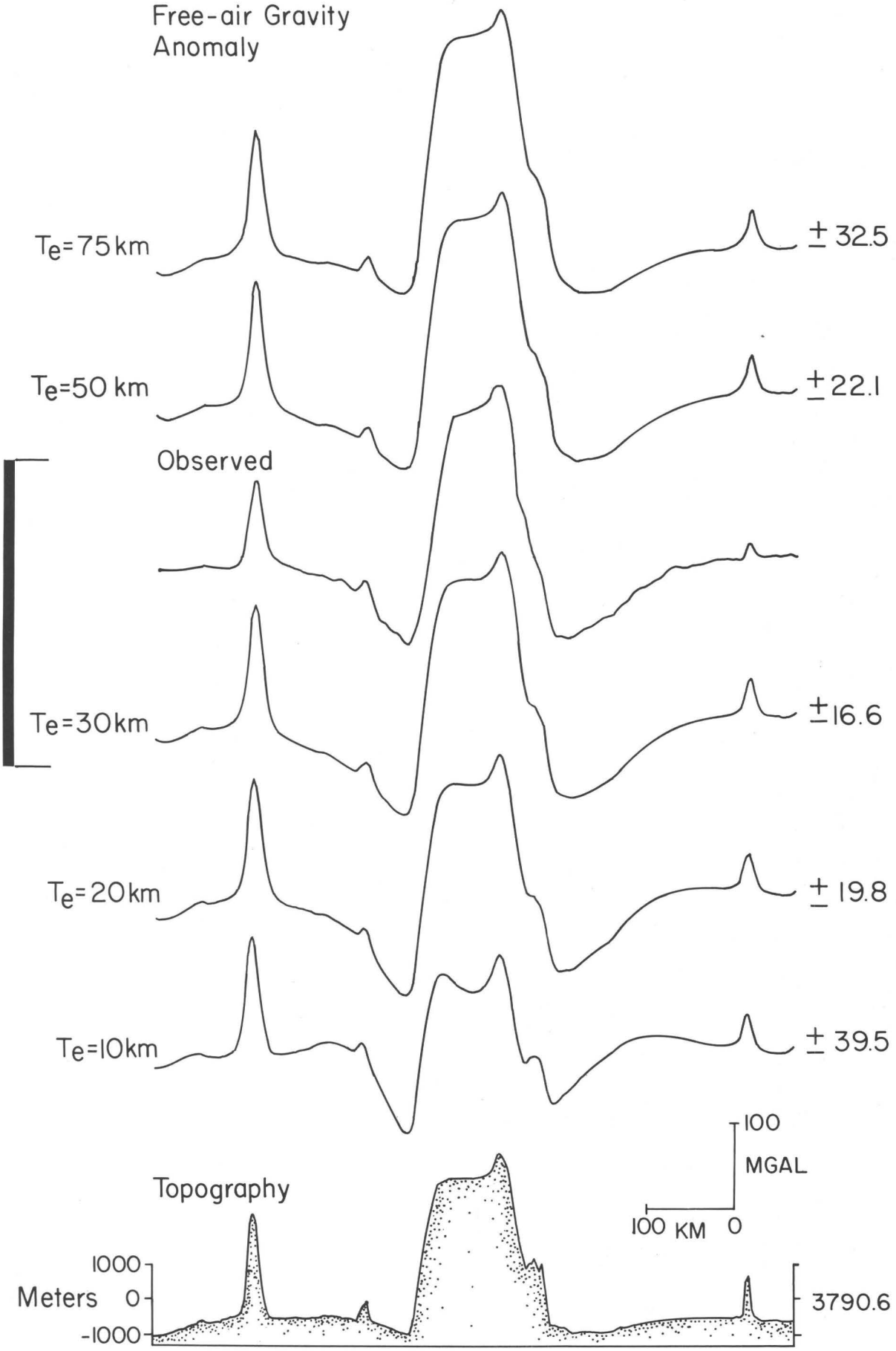
Free-air Gravity
Anomaly
Te=75km
±32.5
Te=50 km
±22.1
Observed
Te=30km
±16.6
Te=20km
±19.8
Te=10km
±39.5
100
MGAL
100 KM 0
Topography
1000
Meters 0
-1000
3790.6

Figure 2

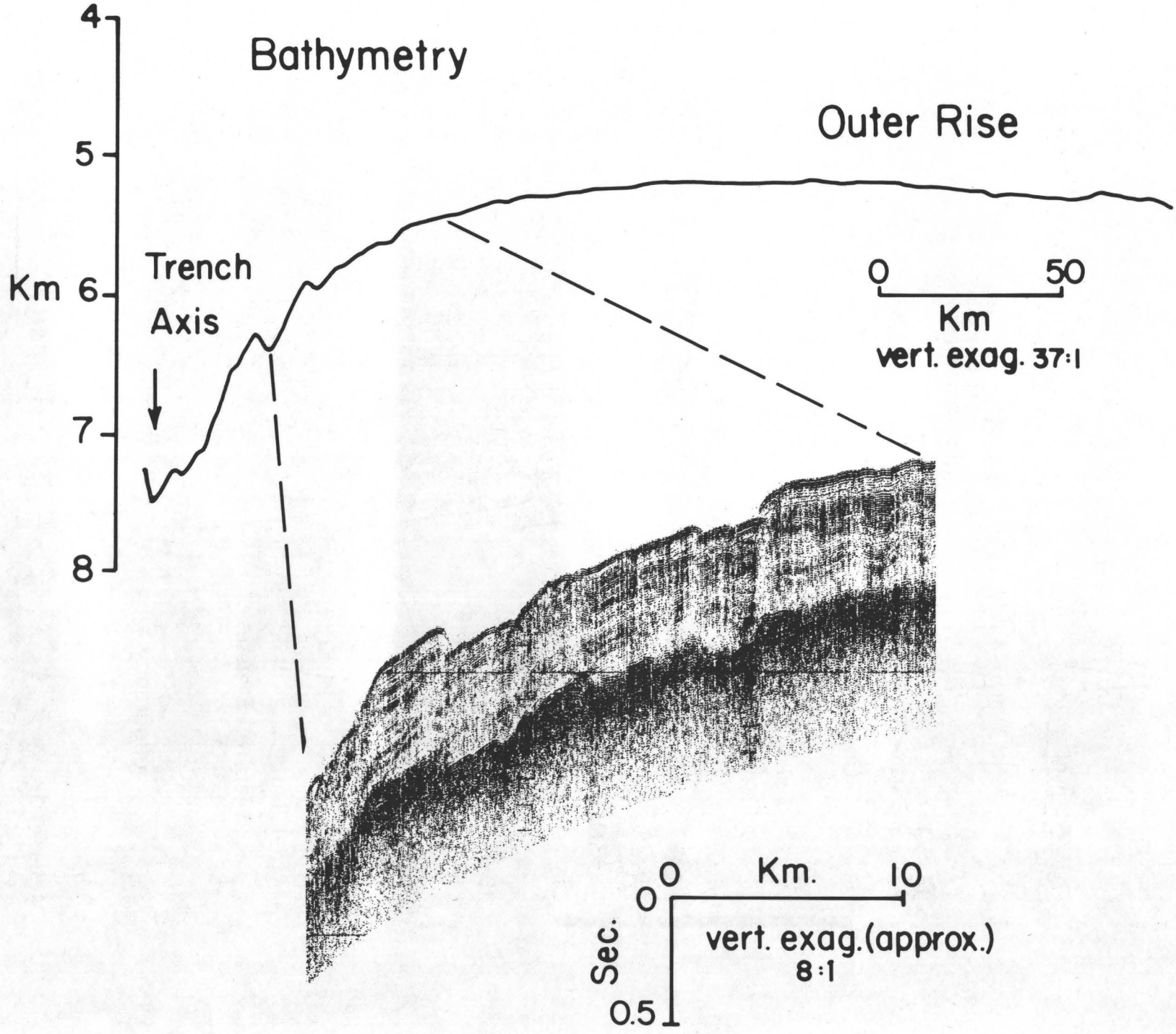
Bathymetry
Outer Rise
Trench
Axis
Km
4
5
6
7
8
0
50
Km
vert. exag. 37:1
0
Km.
10
0
Sec.
0.5
vert. exag.(approx.)
8:1

Figure 3

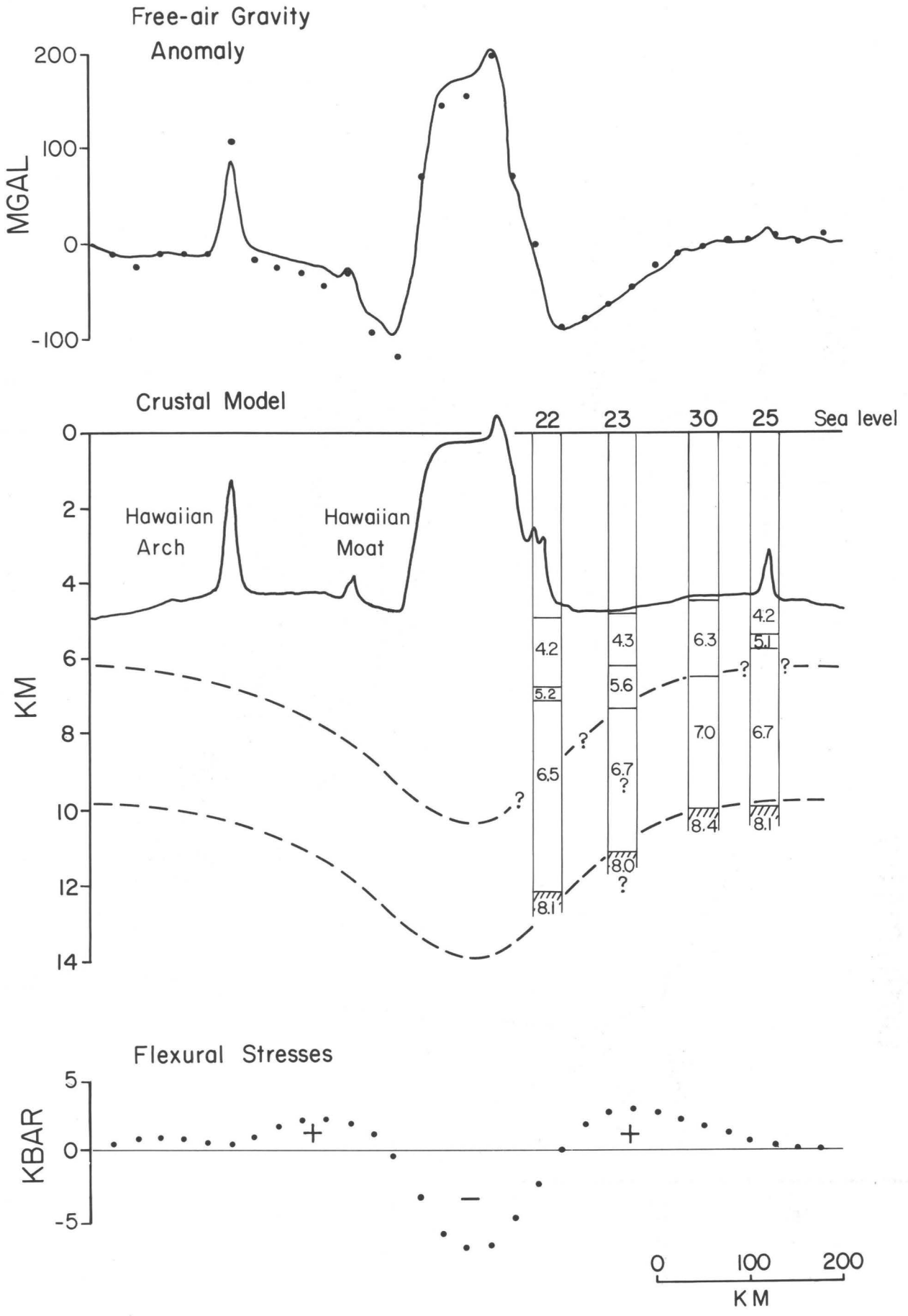
Free-air Gravity
Anomaly
200
100
0
-100
MGAL
Crustal Model
22
23
30
25
Sea level
0
2
4
6
8
10
12
14
KM
Hawaiian
Arch
Hawaiian
Moat
4.2
5.2
6.5
8.1
4.3
5.6
6.7
?
8.0
?
6.3
7.0
8.4
4.2
5.1
6.7
8.1
?
?
?
Flexural Stresses
5
0
-5
KBAR
+
+
−
0
100
200
KM

Figure 4

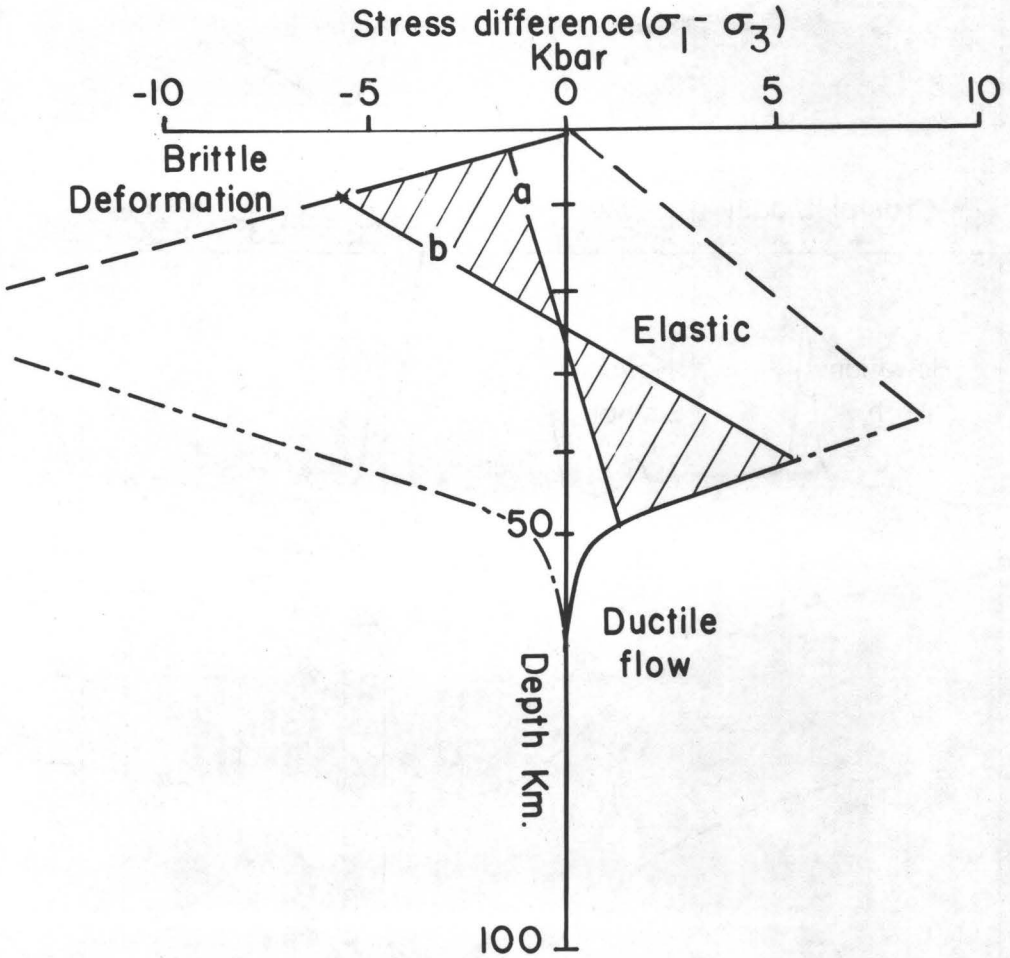
Stress difference ($\sigma_1 - \sigma_3$)
Kbar
-10
-5
0
5
10
Brittle
Deformation
a
b
Elastic
50
Ductile
flow
Depth Km.
100

Figure 5

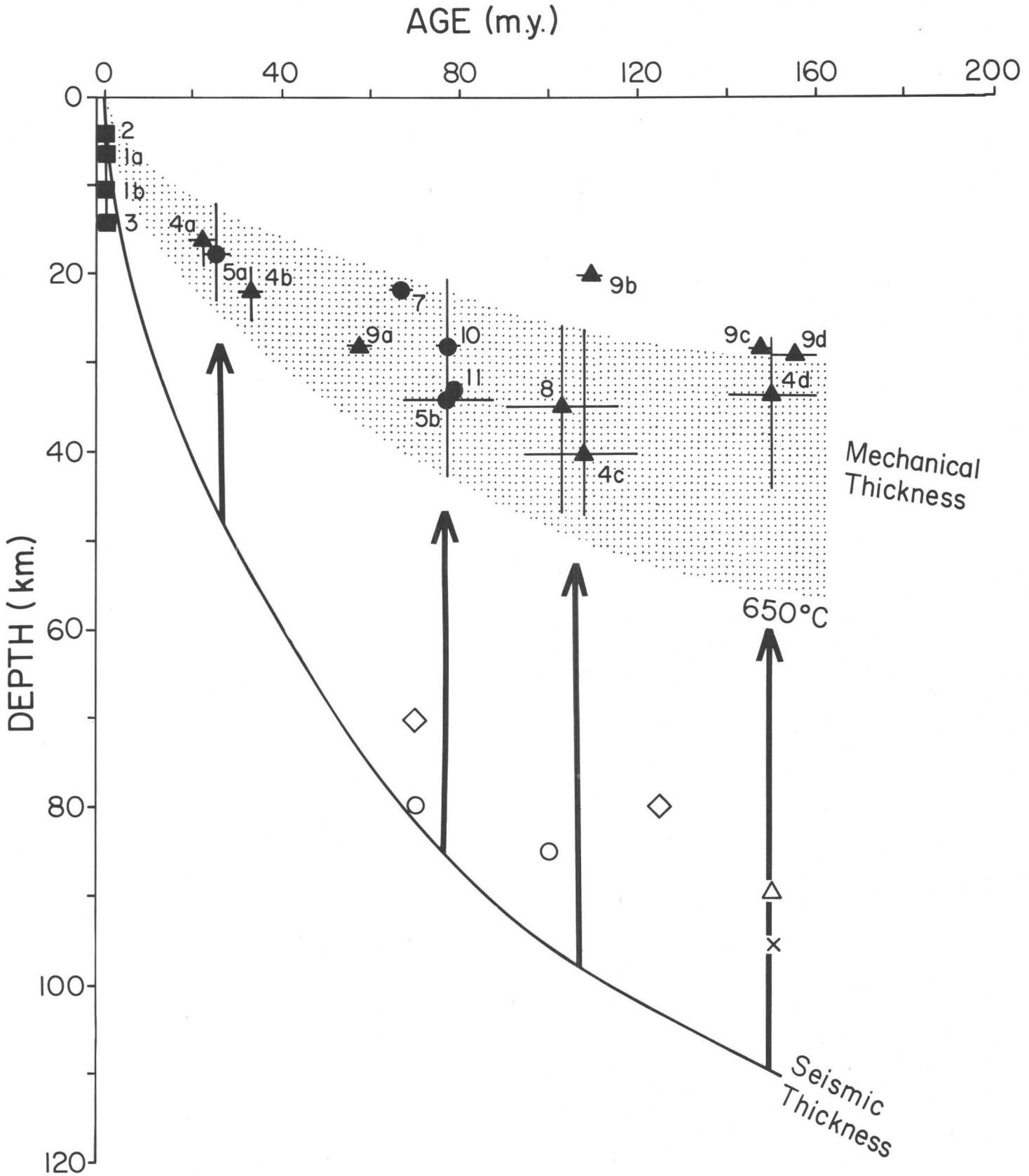
AGE (m.y.)
0
40
80
120
160
200
0
20
40
60
80
100
120
DEPTH (km.)
2
1a
1b
3
4a
5a
4b
7
9a
10
11
5b
8
9b
4c
9c
9d
4d
Mechanical Thickness
650°C
Seismic Thickness

Figure 6

COMPARISON OF MECHANICAL MODELS OF THE OCEANIC LITHOSPHERE

Donald W. Forsyth
Department of Geological Sciences
Brown University
Providence, Rhode Island 02912

INTRODUCTION

Several authors have suggested that large, regional compressive stresses averaging several kilobars over the thickness of the lithosphere are required to produce the shape of oceanic plates as they bend before subduction (Hanks, 1971; Watts and Talwani, 1974; McAdoo et al, 1978; Bodine and Watts, 1979). Others have responded with models which do not require regional stresses to fit the topography of the trench and outer rise (LePichon, et al, 1973; Parsons and Molnar, 1976; Caldwell et al, 1976; Chapple and Forsyth, 1979). Both families of models have in common deviatoric bending stresses of several kilobars, with plates assigned either elastic or elastic-plastic rheology. Recently, DeBremaecker (1977), McKenzie (1977) and Melosh (1978) have suggested that viscous relaxation may reduce the required bending stresses by an order of magnitude. Since the deformation of the plates is one of the few means available for assessing the absolute level of stress within the lithosphere, it is worth reviewing the characteristics of these diverse models and the observational tests which may serve to distinguish between them.

Six basic models are considered. In each, a mechanically strong lithosphere is assumed to float on a much weaker asthenosphere and horizontal and vertical loads or bending moments may be applied to the lithosphere (Figure 1). The six models of the plate are: 1) A uniform elastic plate with no regional stress. The model variables are flexural rigidity (controlled by the thickness of the plate) and either elevation of the outer rise (Caldwell et al, 1976) or bending moment at the trench axis (Parsons and Molnar, 1976). 2) A uniform elastic plate under regional compression. The model variables are horizontal load (regional stress), plate thickness, and either elevation of the outer rise (Caldwell et al,

1976) or vertical force at the trench axis (Hanks, 1971). 3) A uniform plate with elastic-perfectly plastic rheology. The plate behaves elastically until the yield stress is reached, beyond which it yields plastically at a constant stress level. The variables are yield stress, plate thickness, and amplitude of the outer rise (Turcotte et al, 1978). 4) A uniform plate with elastic-perfectly plastic rheology under regional compression. Added variable is the level of regional stress (McAdoo et al, 1978). 5) A plate with elastic-perfectly plastic rheology in which yield stress is a function of depth. Variables are plate thickness, variation of yield stress with depth, and maximum bending moment (Chapple and Forsyth, 1979). 6) A uniform viscous plate with no regional stress. Variables are viscosity of the plate, plate thickness, and amplitude of the outer rise (DeBremaecker, 1977) (It should be noted that there are two errors in the original version of DeBremaecker's paper. He uses an incorrect value for the viscous analogue to the flexural rigidity and an incorrect relation between moment and rate of change of curvature. To correct these errors in his Table 2 while keeping the same shape, divide viscosity by 9 and multiply maximum bending stress by 12/9.)

OBSERVATIONAL TESTS

Each of the six basic models are tested against observations of the shape of the bending plates before subduction at trenches, the distribution of earthquakes associated with bending, the bending of the plate under seamount loads, and the deformation of mantle rocks in the laboratory. The results of these tests are summarized in Table 1.

Trench and Outer Rise Topography. All the models fit typical topographic profiles of the trench and outer rise. In a typical profile, the outer rise has an amplitude of 300 to 500 m peaking about 120 to 150 km

from the trench axis, which has a depth about 3000 m below the equilibrium level. In Figure 2a, we compare the shapes of four of the models, with the variables in each model adjusted to give similar results: outer rise amplitude about 350 m, trench depth 3 to 3.5 km, and distance from trench axis to crest of outer rise about 125 km. Although there are minor differences in predicted shape, it is obvious that topography alone is not an effective discriminant between rheological models.

Some profiles seem to have significantly shorter wavelength topography within the trench than on the outer rise (Turcotte et al, 1978). Simple elastic models cannot fit these profiles because their shape is simply a damped sinusoid. They can satisfy the distance from the axis to the first zero-crossing point and the length of the outer rise, but only at the expense of excessive amplitude of the rise. Since adding a compressive stress decreases both the damping factor and the wavelength, it is more difficult to fit these profiles with regional compression than without it. The profiles can be fit fairly well with a large regional tensile stress (~10 kbars), but only if unreasonably large bending moments are applied, involving bending stresses on the order of 15 kbars or more.

The shape of uniform viscous plate is also described by a damped sinusoid, but because the damping factor resembles that of an elastic plate under a large tensile force (DeBremaecker, 1977) the viscous model can be adjusted to fit the short-wavelength trench profile fairly well. Viscous relaxation keeps the bending stresses low and no regional stress is required. Elastic-plastic models can match this type of profile because the characteristic wavelength decreases toward the trench axis as the bending increases and more of the plate yields plastically (Turcotte et al, 1978). An applied compressive stress forces the plate to yield sooner,

further reducing the distance from the peak of the outer rise to the trench axis. McAdoo et al (1978) found that several kilobars of regional compression were required to fit some profiles. However, Bodine and Watts (1979) and Chapple and Forsyth (1979) showed that the required regional stress can be greatly reduced or eliminated if the yield stress is allowed to vary with depth.

One further test of the bending models is provided by the Puerto Rican trench. The amplitude and wavelength of the outer rise is very similar to that of trenches in the western Pacific, yet, at present, motion between the North American and Caribbean plates along the trench is almost pure strike-slip (Molnar, 1978). The similarity of the topographic profiles from the two areas is inconsistent with viscous plate models, which rely on continual motion of the plate toward the trench to restore the stresses needed to support the outer rise. As pointed out by Parsons and Molnar (1976), the strike-slip motion also may be inconsistent with models requiring large regional compression.

Earthquake Data. Normal faulting earthquakes associated with the bending of the oceanic plate before subduction are found in nearly every major trench system. Chapple and Forsyth (1979) give a list of events with known focal mechanism. Although a few earthquakes occur as far as 50 to 75 km seaward of the trench axis, the great majority of events is concentrated within 25 km of the trench axis (Figure 3). On the average, the epicenters are likely to be mislocated by 10 to 20 km toward the trench, resulting from the uneven distribution of stations and ray paths through the faster, subducted lithosphere. A normal-faulting event whose bulletin location was landward of the axis was accepted as a bending event only if there was a clear gap between its position and the

position of nearby underthrusting events or if pwP-pP delay times indicated the event was beneath the trench axis. Since regional variations in mislocation would tend to smear out any true concentration, the observed concentration is assumed to be real. Any model of the bending plate should then predict a strong concentration of seismicity near the trench axis.

The normal faulting earthquakes are assumed to be associated with extension in the upper part of the plate as the curvature increases. As the plate moves toward subduction, the curvature at a point along a profile across the trench describes the total deformation or extension that has been accomplished by bending up to that point. The derivative of the curvature with respect to distance along the profile describes where this deformation is achieved, i.e., the rate of deformation along the profile. To predict the seismicity from a given theoretical model, the distribution of the rate of extension within the model plate must be mapped. Once the maximum bending point is reached, no more extension and presumably no more normal faulting earthquakes occur, even though the slope and absolute depth of the bathymetry continue to increase.

The second and third derivatives of the topography, representing curvature and rate of extension, respectively, are plotted in figure 2 for four mechanical models of the plate. The subtle differences in topography appear as dramatic differences in the higher order derivatives. The simple elastic plate model predicts that seismicity would be distributed over a broad region peaking about 75 km from the trench axis. This predicted pattern is clearly not consistent with observation. The elastic plate under regional compression is even worse. One of the primary effects of adding a regional compression is to reduce the bending moments required

to produce the amplitude of the outer rise, and in particular, it reduces the bending moment at the trench axis to near zero (Hanks, 1971). (Note that in an elastic plate, bending moment is directly proportional to curvature.) Consequently, in this model the plate has almost completely unbent at the trench axis and the point with the maximum rate of extension is moved even farther seaward.

The viscous plate model does satisfactorily predict that the greatest activity should be near the axis, but the peak in strain rate is significantly broader than the peak in seismicity. Only elastic-plastic models, which may exhibit hinge-like bending at the maximum moment point just before unbending, correctly predict both the location and concentration of earthquake activity.

Another test is provided by the depth of extensional earthquakes. Chapple and Forsyth (1979) showed that normal faulting extends at least to a depth of 25 km, even in the Kurile trench, an area which Hanks (1971) and McAdoo et al. (1978) suggested was under strong regional compression. A model can pass this test only if horizontal deviatoric tension is present down to a depth of 25 km or more. The stress patterns as a function of depth in the six basic models are illustrated in figure 4. The stress profiles shown correspond to the stress state at the point of maximum curvature in each model; the point at which the depth extent of the tensile regime is greatest. Only the viscous model and the elastic-plastic model with variable yield strength satisfy this test. It has been suggested that the upper 10 km of crust and upper mantle may be incompetent under tension and the effective, mechanically strong plate that controls the shape of the bending begins below this weak layer. Adding ten kilometers to the

extensional zone in this manner makes the uniform elastic and elastic-plastic models marginally acceptable.Models with large regional compression fail the test.

A successful model should also be able to account for the cumulative seismic moment of the normal faulting earthquakes (Hanks, 1979; Chapple and Forsyth, 1979). Although these events are relatively rare, their net seismic moment is significant. Estimates range from a minimum of about 5×10^{26} dyn-cm/yr to 27×10^{26} dyn-cm/yr, depending on whether or not large normal faulting events such as the 1933 Sanrika and 1977 Java earthquakes are included in the total. There must be sufficient deformation within the extensional regime to account for the minimum deformation and strain energy associated with the earthquake. As formulated by Hanks, Chapple and Forsyth, this condition is

$$h^2 \left. \frac{d^2 w}{dx^2} \right|_{max} \geq \frac{\Sigma M_o / yr}{\mu L v}$$

where h is the depth of the extensional regime, μ is the shear modulus, L is the total length of all the trenches, and v is the average rate of subduction. The curvature used is the maximum reached in the model. The elastic-plastic models satisfy this condition unless there is strong regional compression. The viscous model also meets the condition. An elastic model under no regional stress satisfies the condition only if deformation of a weak surface layer is included. If this layer has a low effective μ , then the test is again failed.

Seamount loads A rheological model of the oceanic lithosphere should be capable of reproducing the topography associated with loads other than subduction. The flexure associated with seamount chains has been successfully modeled with elastic (Walcott, 1970, 1976; Watts and Cochran, 1974; Watts et al., 1975; Watts, 1978; McNutt and Menard, 1978) and elastic-plastic (Liu and Kosloff, 1978) rheologies, although the effective flexural rigidities are significantly less than in subduction models of sea floor of the same age. If the hypothesis that the response to a load reflects the flexural rigidity of the lithosphere at the time of loading rather than the current rigidity (Watts, 1978; McNutt, 1979) is accepted, then reheating and thinning of the lithosphere accompanying the formation of seamount chains (Detrick and Crough, 1978; Withjack, 1979) provides a natural explanation of the difference in flexual rigidity. Forsyth (1979) pointed out that the rigidity reported for seamounts is comparable to the rigidity reported for subducting lithosphere 25-30 m.y. in age (Caldwell and Turcotte, 1979), the same effective age Detrick and Crough proposed for reheated lithosphere. Elastic and elastic-plastic models of the lithosphere thus appear to be consistent with topography of both trench and seamount loads simultaneously.

The persistence of seamount loads for tens of millions of years has frequently been cited as evidence against viscous or viscoelastic models of the lithosphere. However, Jones (1979) suggests that the effective viscoelastic plate thickness increases with time as the plate cools and that this offsets to some extent the effects of viscous relaxation, resulting in a deformation that is very similar to that of an elastic plate with constant properties. The viscous relaxation time required to fit the

Hawaiian-Emperor seamount chain is 10^6 to 10^7 years, according to Jones, one to two orders of magnitude greater than the relaxation time needed to explain trench topography. Thus, there remains some doubt whether a viscous model can explain the topography of both trench and seamount loads.

DISCUSSION

Only the elastic-plastic model with variable yield strength is consistent in detail with the predictions of experimental rock mechanics, as summarized by Kirby (1977) and Goetze and Evans (1979). The uppermost lithosphere should yield cataclastically under extension, with the yield strength increasing with depth. At some depth, thermally activated ductile flow begins, with the stress level which can be maintained rapidly decreasing again with increasing depth. The center of the plate is capable of supporting kilobars of stress elastically. Although the uniform elastic and elastic-plastic models do not explicitly represent this behavior, it could justifiably be argued that they are reasonable simplifications and the plate thicknesses are roughly consistent with laboratory data and oceanic geotherms. Viscous models have little resemblance to the predictions of experimental rock mechanics, but since there are many orders of magnitude difference in strain rate between experiments and natural systems, there remains some doubt as to the relevance of this test.

The least successful models are those with large regional compressive stresses. Of the models published to date, the most successful are those with elastic-perfectly rheology and little or no regional compression. Bending stresses within the lithosphere are predicted to reach about 5 kb, but horizontal stresses averaged over the thickness of the lithosphere should be on the order of 1 kb or less.

ACKNOWLEDGEMENTS

The author benefited greatly from many discussions with William M. Chapple. This material is based upon work supported by the National Science Foundation under Grant EAR78-14761. The author was also supported as an Alfred P. Sloan Research Fellow.

REFERENCES

Bodine, J. H. and A. B. Watts, On lithospheric flexure seaward of the Bonin and Mariana trenches, Earth Planet. Sci. Lett., in press, 1979.

Caldwell, J. G. and D. L. Turcotte, Dependence of the thickness of the elastic oceanic lithosphere on age, Earth Planet. Sci. Lett., in press, 1979.

Caldwell, J. G., W. F. Haxby, D. E. Karig, and D. L. Turcotte, On the applicability of a universal elastic trench profile. Earth Planet. Sci. Let., 31, 239-246, 1976.

Chapple, W. M. and D. W. Forsyth, Earthquakes and bending of plates at trenches, J. Geophys. Res., in press, 1979.

DeBremaecker, J.-C., Is the oceanic lithosphere elastic or viscous? J. Geophys. Res., 82, 2001-2004, 1977.

Detrick, R. S. and S. T. Crough, Island Subsidence, hot spots and lithospheric thinning, J. Geophys. Res., 83, 1236-1244, 1978.

Forsyth, D. W., Lithospheric flexure, Rev. Geophys. Space Phys., 17, 1109-1114, 1979.

Goetze, C. and B. Evans, Stress and temperature in the bending lithosphere as constrained by experimental rock mechanics, Geophys. J. R. Astr. Soc., in press, 1979.

Hanks, T. C., The Kurile trench - Hokkaido rise system: Large shallow earthquakes and simple models of deformation, Geophys. J. R. Astr. Soc., 23, 173-189, 1971.

Hanks, T. C., Deviatoric stresses and earthquake occurrence at the outer rise, J. Geophys. Res., 84, 2343-2347, 1979.

Jones, G. M., Visco-elastic flexure of oceanic lithosphere, Geophys. J. R. Astr. Soc., in press, 1979.

Kirby, S. H., State of stress in the lithosphere: Inferences from the flow law of olivine, PAGEOPH 115, 245-258, 1977.

Liu, H.-P. and D. Kosloff, Elastic-plastic bending of the lithosphere incorporating rock deformation data, with application to the structure of the Hawaiian archipelago, Tectonophys., 50, 249-274, 1978.

McAdoo, D. C., J. G. Caldwell, and D. L. Turcotte, On the elastic-perfectly plastic bending of the lithosphere under generalized loading with application to the Kurile trench, Geophys. J. R. Astr. Soc., 54, 11-26, 1978.

McKenzie, D., Surface deformation, gravity anomalies and convention, Geophys. J. R. Astr. Soc., 48, 211-238, 1977.

McNutt, M., Compensation of oceanic topography: An application of the response function technique to the Surveyor area, J. Geophys. Res., in press, 1979.

McNutt, M., and H. W. Menard, Lithospheric flexure and uplifted atolls, J. Geophys. Res., 83, 1206-1212, 1978.

Melosh, H. J., Dynamic support of the outer rise, Geophys. Res. Lett., 5, 321-324, 1978.

Molnar, P., Gravity anomalies and the origin of the Puerto Rico trench, Geophys. J. R. Astr. Soc., 51, 701-708, 1978.

Parsons, B., and P. Molnar, The origin of outer topographic rises associated with trenches, Geophys. J. Roy. Astr. Soc., 45, 707-712, 1976.

Turcotte, D. L., McAdoo, D. C. and J. G. Caldwell, An elastic-perfectly plastic analysis of the bending of the lithosphere at a trench, Tectonophys., 47, 193-206, 1978.

Walcott, R. I., Flexure of the lithosphere at Hawaii, Tectonophys., 9, 435-446, 1970a.

Walcott, R. I., Lithospheric flexure, analysis of gravity anomalies and the propagation of seamount chains, International Woollard Symposium, AGU, Mono. 19, 431-438, 1976.

Watts, A. B., An analysis of isostasy in the world's oceans: Part 1. Hawaiian-Emperor seamount chain; J. Geophys. Res., 83, 5939-6004, 1978.

Watts, A. B. and J. R. Cochran, Gravity anomalies and flexure of the lithosphere along the Hawaiian-Emperor Seamount Chain, Geophys. J. R. Astr. Soc., 38, 119-141, 1974.

Watts, A. B., J. R. Cochran, and G. Selzer, Gravity anomalies and flexure of the lithosphere: A three-dimensional study of the Great Meteor Seamount, northeast Atlantic, J. Geophys. Res., 80, 1391-1398, 1975.

Watts, A. B. and M. Talwani, Gravity anomalies seaward of deep-sea trenches and their tectonic implications, Geophys. J. R. Astr. Soc., 36, 57-90, 1974.

Withjack, M., A convective heat transfer model for lithospheric thinning and crustal uplift, J. Geophys. Res., 84, 3008-3022, 1979.

Table 1. Tests of Mechanical Models of the Oceanic Lithosphere

TEST	PLATE MODEL					
	Elastic	Elastic Regional Compression	Elastic-Plastic	Elastic-Plastic Regional Compression	Elastic-Plastic Variable Strength	Viscous
Typical Trench Topography	yes	yes	yes	yes	yes	yes
Short-wave-length trench	no	no	?	yes	yes	yes
Puerto-Rican Trench	yes	?	yes	?	yes	no
Concentration of seismicity	no	no	yes	yes	yes	?
Depth of Normal Faulting	?	no	?	no	yes	yes
Seismic moment	?	no	yes	no	yes	yes
Topography of Seamount loads	yes	yes	yes	yes	yes	?
Lab Rock Mechanics	?	?	?	?	yes	?
~bending stress level	5-10 kb	5-10	5	5	5	<1
~regional stress level	—	5-10 kb	—	3-5	≤1	—

FIGURE CAPTIONS

Figure 1. Schematic diagram of the bending of the lithosphere at a trench (after McAdoo et al., 1978). Applied loads at the trench include vertical force Q, bending moment M, and horizontal force T. Restoring buoyancy forces are proportional to the elevation, w, and to the difference between the density of the mantle and water layers, ρ_m and ρ_w, respectively. The elevation of the highest point on the forebulge, w_b, is typically 300 to 500 m above the equilibrium level. Variables include the thickness of the plate, h, and its rheological properties.

Figure 2. Shape of the bending lithosphere. First column gives the topography, second column the curvature, and third column the rate of extension as a function of distance from the trench axis. First row gives the shape for a uniform elastic plate 28 km thick; second row, uniform elastic plate 28 km thick under 5 kb regional compression; third row, elastic-perfectly plastic plate 50 km thick with yield stress 1 kb in upper 20 km, 5 kb in lower 30 km; bottom row, viscous plate 100 km thick with viscosity 1.1×10^{23} P.

Figure 3. Distribution of known normal faulting earthquakes with respect to trench axis. See text for discussion of mislocation errors.

Figure 4. Horizontal deviatoric stress as a function of depth at the maximum moment point. Numbering of models corresponds to that given in the introduction. Negative sign indicates deviatoric tension, positive, deviatoric compression.

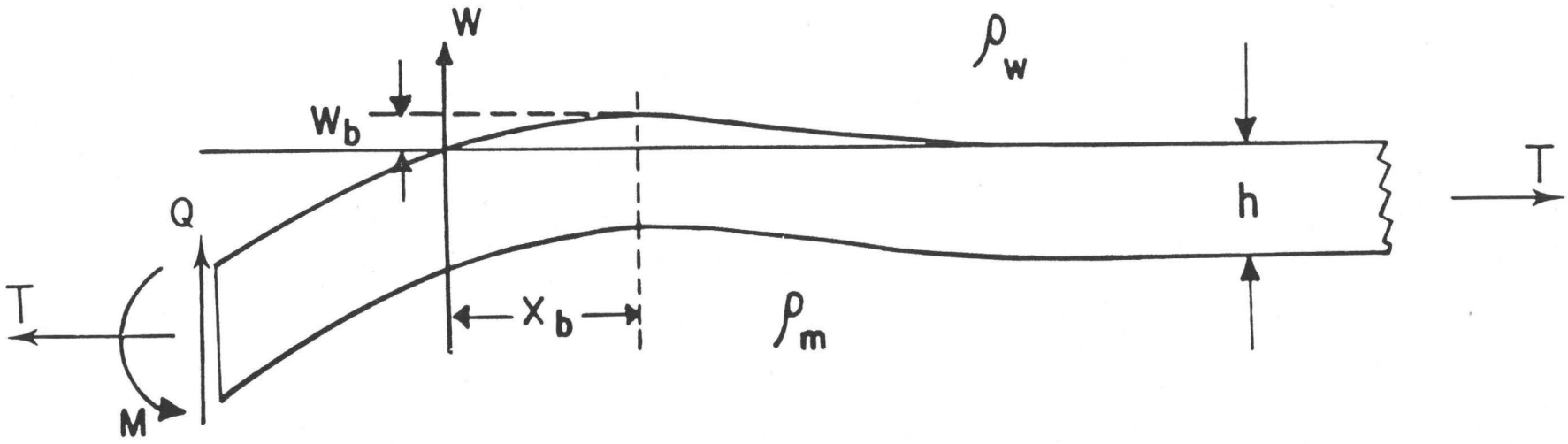

Figure 1.

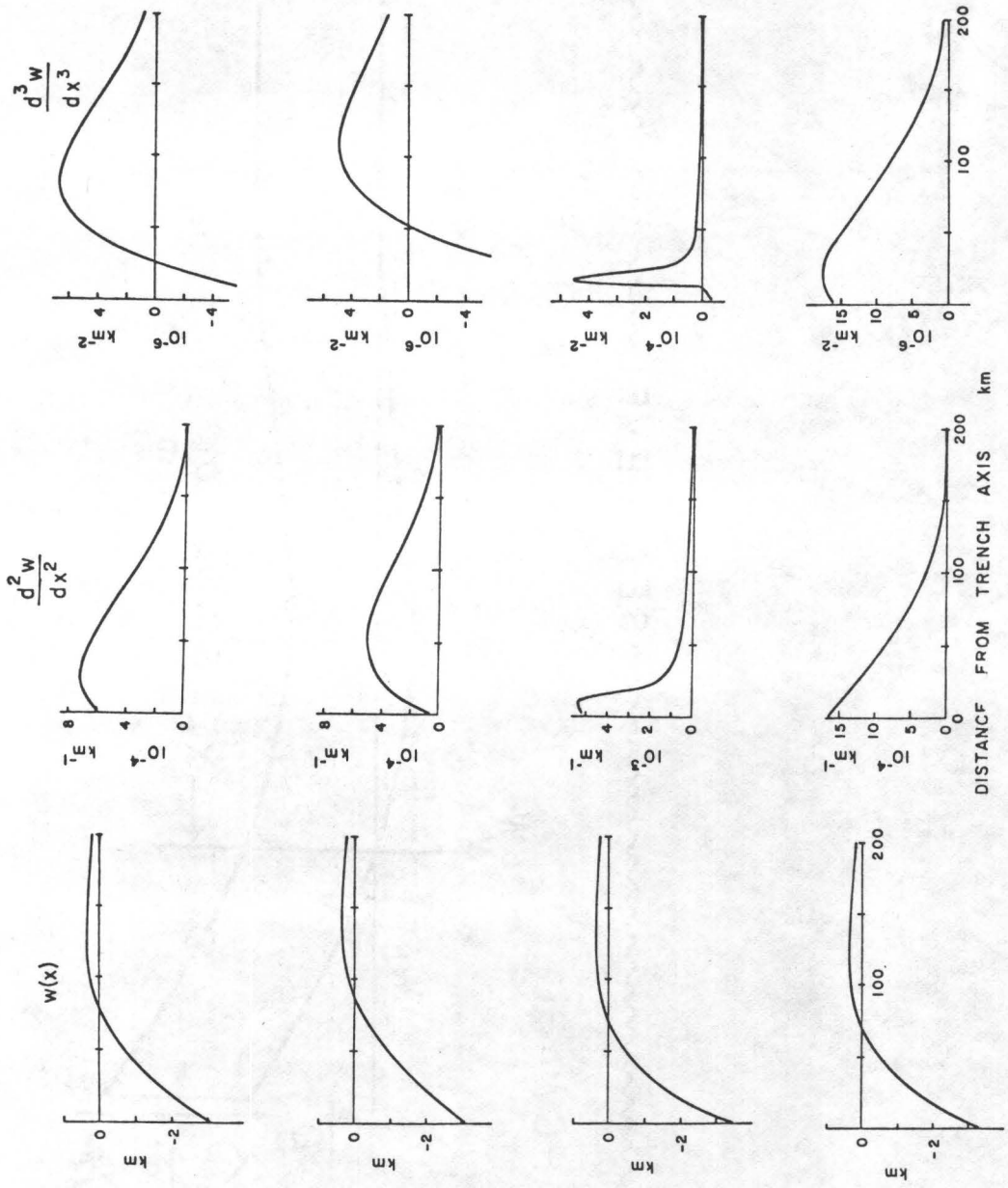

Figure 2.

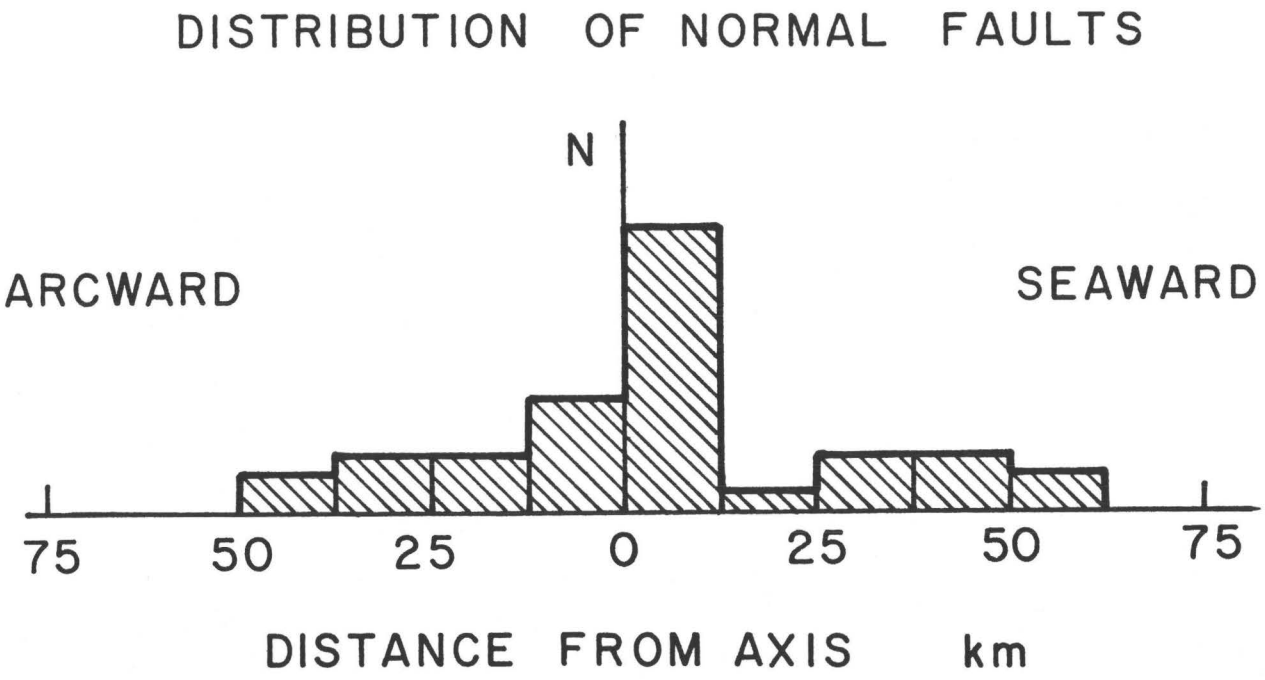
DISTRIBUTION OF NORMAL FAULTS
N
ARCWARD
SEAWARD
75
50
25
0
25
50
75
DISTANCE FROM AXIS km

Figure 3.

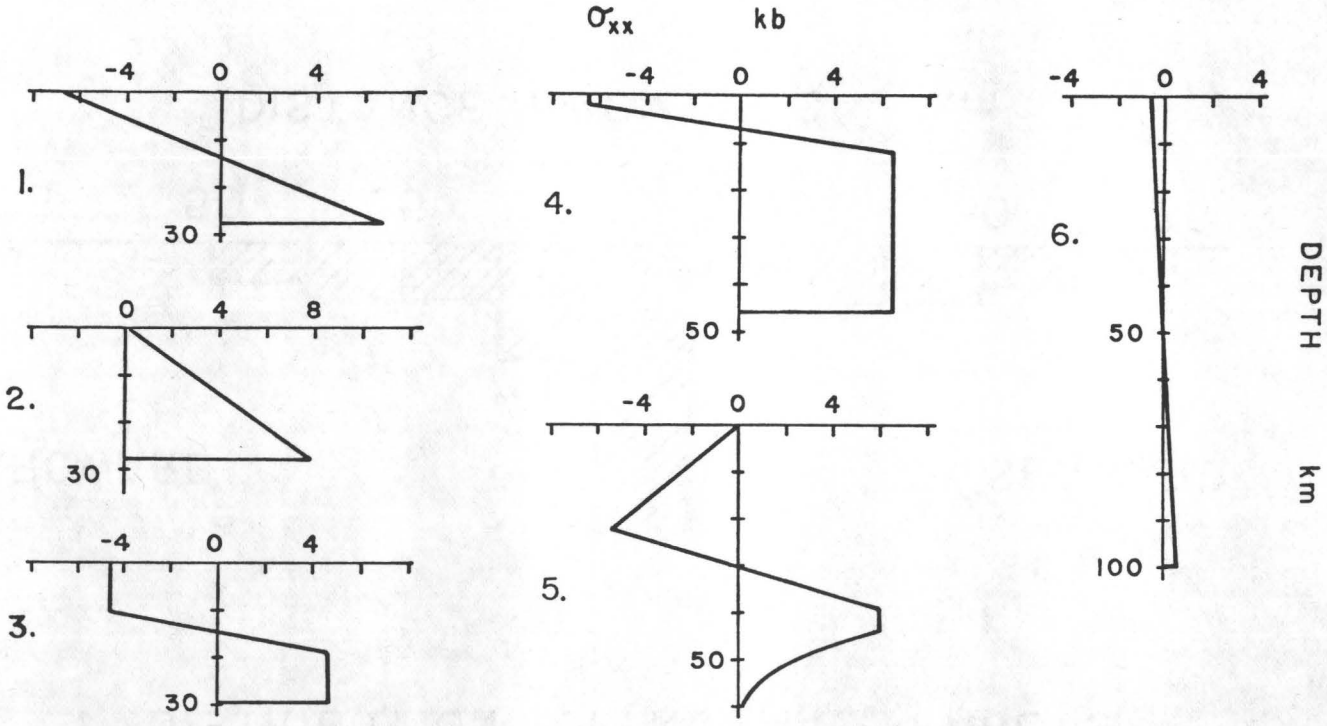
σ_{xx} kb
-4
0
4
1.
30
0
4
8
2.
30
-4
0
4
3.
30
-4
0
4
4.
50
-4
0
4
5.
50
-4
0
4
6.
50
100
DEPTH
km

Figure 4.

THE STRUCTURE OF THE KURILE TRENCH-HOKKAIDO RISE SYSTEM COMPUTED BY AN ELASTIC TIME-DEPENDENT PLASTIC PLATE MODEL INCORPORATING ROCK DEFORMATION DATA

Hsi-Ping Liu
U. S. Geological Survey
345 Middlefield Road
Menlo Park, California 94025

The flexure profile of the Kurile trench-Hokkaido rise system has been fitted numerically to observational accuracy by an elastic time-dependent plastic plate model. The elastic part of the constitutive relation is derived from seismology (relaxed moduli = 56% of the seismic values) while the strain-rate-dependent plastic part is derived from dunite deformation data extrapolated to the appropriate loading rates. The numerical fit of the flexure profile depends on a number of parameters such as the rock flow law parameters, the temperature distribution inside the lithosphere, and the state of pre-stress of the plate before it enters into the subduction zone. Two examples of fitting, one with Kirby-Raleigh flow-law parameters and one with Carter-Ave'Lallement flow-law parameters, are given. The oceanic crust is considered to be made of strong and competent rocks in the former example, and it is considered to be made of fractured rocks with negligible strength in the latter. Because the solution is nonunique, conclusions regarding the values of the individual parameters cannot be drawn from the flexure profile alone. The present calculation, however, demonstrates the consistency between the rock deformation data and the observed plate flexure profile.

INTRODUCTION

The mechanical model of plate tectonics consists in part of strong lithosphere plates floating on a weak layer of asthenosphere. The hypothesis of plate tectonics states also that oceanic lithosphere is created at the accreting plate margin and subducted at the consuming plate boundaries where oceanic trench and rise systems often exist (e.g. Le Pichon, et al., 1973). The relaxation time on the order of 2×10^3 years of vertical movements in shield areas unloaded by late Quaternary ice sheets (e.g., O'Connell, 1971) suggests that the asthenosphere can be modeled as an inviscid fluid for loading times exceeding 10^6 years. The lithosphere is often modeled as an elastic sheet (Gunn, 1947; Walcott, 1970; Hanks, 1971; Watts and Talwani, 1974; Caldwell et al., 1976; Parsons and Molnar, 1976), a viscous sheet (De Bremaecker, 1977), or an elastic perfectly-plastic sheet (McAdoo et al., 1978) subjected to various vertical loads, bending moments, and end thrusts due to in-plane compression to explain the surface topography and gravity anomalies of the trench and rise systems in the subduction zones. Although computations based on these models can satisfy the observed data of flexure profile and gravity anomaly, there are several difficulties associated with them, specifically: (1) The maximum bending stress at the base of the 120 km-thick lithosphere of De Bremaecker's (1977) plate model is on the order of 600 bars. The yield stresses assumed by McAdoo et al. (1978) in their elastic perfectly-plastic plate model depend neither on temperature nor on strain rate and are all greater than 4.7 kilobars. The strength of the possible mantle rocks at a depth of 60 km or more, on the other hand, is on the order of 50 bars or less on the geologic loading time scale as inferred from laboratory deformation experiments (e. g. Carter, 1976). (2) The flexure rigidity obtained from the elastic plate models implies a plate thickness considerably different from that determined from seismology. For example, Watts et al. (1976) give a flexure rigidity of 3×10^{29} dyne-cm for the Pacific plate near the trenches. If we adopt for the relaxed elastic moduli for lithosphere flexure a 50% reduction from their seismic values, the above flexure rigidity would imply a plate thickness of 16 km. This value differs by a factor of nearly five from the plate thickness of 70 km for the oceanic lithosphere as determined from seismology (e.g. Kanamori and Press, 1970). The implication is that the mechanical behavior of the lithosphere differs considerably between time scales on the order of 1 m.y. and time scales of seismic surface wave periods. As a consequence, Hanks (1977) suggested a demarcation of the lithosphere into two parts, an upper elastic plate and a significantly weaker lower lithosphere, for the consideration of plate tectonics on a time scale of 1 m.y. Such an ad hoc demarcation, however, is less fruitful than seeking an explanation of the apparent difference in lithosphere thickness in the strain-rate dependent and nonlinear rheological behavior of the upper mantle rocks. (3) Lateral thrust due to in-plane compression is often not included in the computation of lithosphere flexure. For example, except for Hanks (1971), Watts and Talwani (1974), and McAdoo et al. (1978), the lateral thrust is either neglected or considered to be unnecessary in the calculation of trench profiles. However, the lateral thrust, equal to the magnitude of the integral of the normal stress over the vertical lithosphere cross-section parallel to the trench axis, can be neglected only under the unlikely

situation that the lateral stress due to overburden stress is balanced by a tensile tectonic stress of the same magnitude (Denkhaus, 1966). The lateral stress due to the overburden normal stress averages to several kilobars inside the lithosphere and has an appreciable effect on the flexure profile.

A more complete treatment of the lithosphere flexure problem in the vicinity of the subduction zone than those already given in the litherature requires the consideration of the strain-rate-dependent and nonlinear deformation behavior of the lithosphere rocks, the temperature distribution inside the lithosphere, and the tectonic loading history including the state of pre-stress inside the plate before it enters into the subduction zone. the present work is an attempt at such a treatment. It parallels the development of the plate flexure calculation for loading by a linear island chain as given by Liu and Kosloff (1978).

THEORY

Equations Describing Large Deflection of Plates

A well-known theory of large deflection of plates is due to Von Karman (e.g. Fung, 1965). This theory takes into account finite deformation in plate bending and is based on the Lagrangian description of the strain tensor (i.e. description of the plate is with respect to the initial undeformed configuraton). Consideration of finite deformation is necessary in the plate flexure calculations since the bending moment produced by the lateral thrust depends on the amount of deflection of the plate. Several assumptions are invoked in this theory: (1) the plate thickness is small compared with the typical plate dimensions; (2) the magnitude of plate deflection, w, can be of the same order of magnitude as the plate thickness, h, but is small compared with the typical plate dimensions L; (3) the slope is everywhere small, i. e., $\left|\frac{\partial w}{\partial x}\right| \ll 1$ $\left|\frac{\partial w}{\partial y}\right| \ll 1$; (4) the tangential displacements u, v are small comared with the plate thickness; (5) there exists a traction-free neutral surface, and strains very linearly within the plate. The first four assumptions are justified by observation in the trench profiles. The fifth assumption has been proved as a theory for pure bending in one direction by Fazekas (1967) regardless of the material behavior. The one-dimensional bending equations are (Fung, 1965)

$$\frac{d^2 M_x}{dx^2} = -q - \frac{dm_x}{dx} - N_x \frac{d^2 w}{dx^2} + f_x \frac{dw}{dx} \tag{1}$$

$$M_x = \int_{z_t}^{z_b} S_{xx}\, \zeta dz \tag{2}$$

$$N_x = \int_{z_t}^{z_b} S_{xx}\, dz \tag{3}$$

$$q = \left(S_{zz} + S_{zx} \frac{dw}{dx}\right)_{z_t}^{z_b} + \int_{z_t}^{z_b} Z dz \tag{4}$$

$$m_x = h \left[S_{zx}(z_b) + S_{zx}(z_t)\right]/2 + \int_{z_t}^{z_b} X\, \zeta dz \tag{5}$$

$$f_x = S_{zx}(z_b) - S_{zx}(z_t) + \int_{z_t}^{z_b} X\, dz \qquad (6)$$

where S_{ij} is the Kirchhoff stress tensor, z is the vertical coordinate in the undeformed plate measured positive downward, z_b and z_t are the undeformed plate bottom and plate top coordinates respectively, ζ is the vertical coordinate centered at the neutral plane and X, Z, are the body forces. We now apply this set of equations to the lithosphere flexure. The body force in the horizontal direction, X, is zero since z is taken to be the vertical direction. Since the plate is overlain by ocean water and underlain by the asthenosphere modeled as an inviscid fluid, the shear stress components $S_{zx}(z_b) = S_{xx}(z_t) = 0$. Therefore, $m_x = f_x = 0$ and the set of equations (1) - (6) becomes

$$\frac{d^2M_x}{dx^2} = -q - N_x \frac{d^2w}{dx^2} = -S_{zz}(z_b) + S_{zz}(z_t) - N_x \frac{d^2w}{dx^2} - \int_{z_t}^{z_b} Z dz \qquad (7)$$

The Kirchhoff stress tensor S_{ij}, the stress resultant N_x, and the moment M_x are defined with respect to the original undeformed configuration of the plate. However, since all slopes in the plate bending are assumed to be small compared to unity, the values S_{ij}, N_x, and M_x in the first-order approximation are equal respectively to the Eulerian stress tensor, the stress resultant, and the moment defined in the deformed configuration (Fung, 1965). The distributive load on the plate top is therefore

$$S_{zz}(z_t) = -\rho_w g B(x) = -\rho_w g\{B(x) - z_t\} - \rho_w g z_t = -(\rho_w g w + \rho_w g z_t) \qquad (8)$$

where ρ_m is the density of seawater, B(x) is the bathmetry and g is the gravitational acceleration. The distributive load on the plate bottom is

$$S_{zz}(z_b) = -\rho_m g w \qquad (9)$$

where is the asthenosphere density immediately below the lithosphere. Substituting equations (8) and (9) into equation (7)

$$\frac{d^2M_x}{dx^2} + N_x \frac{d^2w}{dx^2} - (\rho_m - \rho_w) g w = -\int_{z_t}^{z_b} Z dz - \rho_w g z_t = -\int_{0}^{z_b} Z dz \qquad (10)$$

Assuming that the lithosphere has zero curvature at distance far away from the trench, the constant loading term in the above equation can be satisfied by a constant vertical displacement $w^{(0)} = -\int_0^{z_b} Z dz/(\rho_m - \rho_w)g$, and is left out from further plate flexure calculations. The assumption that the lithosphere has zero curvature at distances far away from the trench implies that the bending moment caused by the pre-stresses before flexure is balanced by an opposite moment of equal magnitude at the confinement boundaries. The equation for plate bending in one direction becomes, after dropping the subfix x

$$\frac{d^2M}{dx^2} + N\frac{d^2w}{dx^2} - (\rho_m - \rho_w)gw = 0 \qquad (10a)$$

where in equation (10a) the moment is due only to the bending fiber stresses during plate flexure. Equation (10a) together with the appropriate boundary conditions and the moment-curvature relation $M = M(d^2w/dx^2)$ can be integrated to give the flexure profile. The moment-curvatur relation $M=M(\kappa)$ of the lithosphere, because of the rate-dependent and nonlinear rheological behavior of mantle rocks, depends on the state of pre-stress existing inside the lithosphere before bending takes place. This point will be discussed in detail later in this paper. A shematic diagram illustrating lithosphere flexure at the trench is shown in Figure 1.

Boundary conditions

The boundary conditions are (in reference to Figure 2)

either $\frac{dM}{dx} + N\frac{dw}{dx} = Q_v$ or $\delta w = 0$ (11)

and

either $M\left(\frac{d^2w}{dx^2}\right) = M$ or $\delta\left(\frac{dw}{dx}\right) = 0$ (12)

Equation (11) means that either the quantity $\frac{dM}{dx} + N\frac{dw}{dx}$ evaluated at the boundary is given by the known vertical shear force Q_v or that the displacement is fixed at the boundary. Equation (12) means that either the moment, expressed through the moment-curvature relation, is given by the known moment at the boundary or that the slope is fixedat the boundary. For example, for linearly elastic behavior, the boundary conditions are:

either $-\frac{d}{dx}\left(D\frac{d^2w}{dx^2}\right) + N\frac{dw}{dx} = Q_v$ or $\delta w = 0$ (11a)

and

either $-D\frac{d^2w}{dx^2} = M$ or $\delta\left(\frac{dw}{dx}\right) = 0$ (12a)

where D is the flexure rigidity.

These boundary conditions are derived in Hetenyi (1946) and in Fung (1965).

Material behavior. Ductile rock deformation under lithospheric temperature and confining pressure ranges have been carried out extensively in the laboratory and the results have been summarized in e.g., Carter (1976). The loading stress-strain curve of dunite at 5 kb confining pressure, 800 ^{0}C temperature, and a strain rate of 5×10^{-4} s^{-1} measured by Griggs et al. (1960) is illustrated in Figure 3. The loading stress-strain curve starts as a straight line, and after a curved region, approaches another horizontal straight line. The first straight segment represents reversible elastic behavior and the second straight line segment represents rate-dependent perfect plastic behavior. The ductile behavior is representative of general rock deformation behavior under the lithospheric conditions except for approximately the first 20 km where brittle and semibrittle behavior are

encountered (Carter and Kirby, 1978). To facilitate mathematical analysis, the experimentally determined stress-strain curve represented by the solid line in Figure 3 is approximately by the elastic-perfect plastic behavior represented by the dashed curve in the same figure. The unloading line in the perfect plastic region is approximated by a straight line parallel to the elastic part of the loading curve. The stress-strain cruve in Figure 3 is for one particular strain rate. Both elastic part (the slope of the first straight line segment in the stress-strain curve) and the plastic part (the yield stress level) of the constitutive relation are rate-dependent. The rate dependence of the elastic moduli is generally known as anelasticity and for linear attentuation mechanisms, the moduli become smaller at lower strain rates (e.g., Liu et al., 1976). Attenuation data of lithosphere rocks at strain rates lower than those of the Chandler wobble do not exist. It is assumed in the present calculation that for strain rates lower than 10^{-14} s^{-1}, the elastic moduli have reached their relaxed values of 56% of their corresponding values at seismic surface wave frequencies (Anderson and Minster, 1979). The rate dependence of the plastic yield stress is thought to be controlled by dislocation motions and it is extrapolated from laboratory deformation experiments to geologic loading rates by the power law equation (Carter, 1976)

$$\dot{\varepsilon} = A \exp(-Q/TR\ 10^{-3})\ \sigma^n \qquad (13)$$

where $\dot{\varepsilon}$ is the total strain rate in s^{-1}, A is a material constant in $s^{-1}kb^{-n}$, n is a positive numerical constant, σ is the yield stress or strength in kb, Q is an activation energy in kcal/mole, R is the gas constant and T is the absolute temperature. For a given strain rate, the yield stress as given by equation (13) depends only on the temperature and is independent of the confining pressure.

Plate Tectonics Model

The plate tectonics model for the plate flexure calculation of the trench-rise system is as follows: The plate is assumed to be in a steady state motion toward the subduction margins. Flexure loading begins on a segment of the plate parallel to the trench axis when it approaches the vicinity of the plate margin and its curvature is changed by the downward thrust or bending moment exerted by the neighboring plate. Different segments parallel to the trench axis are therefore under different states of flexure loading depending on their distances from the trench axis. Since plastic yielding depends on the total deviatoric stress acting on the material, it is necessary to consider the state of pre-stress existing inside the lithosphere before it enters the vicinity of the trench-rise system. Assume that in this pre-stressed state the greatest and the least principal stresses lie in the plane of bending, one in the vertical direction and the other in the horizontal direction. This assumption is made only to simplify the calculation of the yield criterion. (See eq. (16).) In the elastic part of the lithosphere, the principal stresses are:

$$S_1^{(p)}(z) = \begin{cases} -\rho_w g z_t - \rho_c g(z - z_t), & z \leq z_2 \\ -\rho_w g z_t - \rho_c g(z_2 - z_t) - \rho_p g(z - z_2), & z > z_2 \end{cases}$$

$$S_{2e}^{(p)}(z)$$

$$S_{3e}^{(p)}(z) = S_{30} + \beta S_1^{(p)}(z) \qquad \begin{matrix} \text{for } z>z_2 \text{ (fractured oceanic crust)} \\ \text{for } z>z_t \text{ (competent oceanic crust)} \end{matrix} \tag{14}$$

where ρ_c is the crust density, z_2 is the Moho depth measured from sea level, is the average plate density below the Moho, and β is the lateral stress confinement coefficient (Denkhaus, 1966). The vertical principal stress $S_1(p)(z)$ is due to overburden pressure, and the horizontal principal stress $S_{3e}(z)$ consists of a part $\beta S_1^{(p)}(z)$ induced by the overburden pressure and another part S_{30} of tectonic origin. The value of β depends on the condition of emplacement of the lithosphere material. These principal stresses satisfy the stress equilibrium equation $\partial S_3 / \partial x = 0$, $S_2 e/\partial y = 0$ and $\partial S_1/\partial z + Z = 0$. The intermidiate principal stress $S_2(p)(z)^2$ is not specified since it does not enter the problem. (See equation (16).) The yield stress as a function of depth, $\sigma_y(p)(z)$, is an unknown which depends not only on the material properties and temperature distribution inside the lithosphere, but also on the confinement boundary conditions. For example, take a plate made out of rigid perfectly plastic material with yield stress given by equation (13). If the plate is under rigid confinement, there can be no plastic yielding anywhere. On the other hand if the part of the plate under consideration has zero lateral confinement stress at the boundaries, there will eventually be yielding everywhere inside the region. Without knowing the exact confinement boundary conditions, we can nevertheless arrive at the form of the depth dependence of the yield stress function $\sigma_y(p)(z)$ from equation (13) and from assumptions about plastic yielding inside the lithosphere. Rewrite equation (13) as

$$\sigma_y^{(p)}(z) = (\dot{\varepsilon}^{(p)}(z)/A)^{1/n} \exp\left(Q/R \cdot T(z) \cdot 10^{-3} n\right) \tag{15}$$

where $T(z)$ is the temperature as a function of depth from sea level inside the lithosphere. Assume that plastic yielding in the lower lithosphere is by horizontal extension under a positive value of $S_3(p) - S_1(p)$. This mode of plastic flow corresponds to a horizontal spreading in the lower lithosphere toward its boundaries. Assume also that $\dot{\varepsilon}^{(p)}(z)$ is a slow varying function of z as compared with the term $\exp(Q/R\ T(z)\ 10^{-3})$. $\dot{\varepsilon}^{(p)}(z)$ can therefore be replaced by its average value over the plastically yielded part of the lithosphere.

$$\sigma_y^{(p)}(z) = (\dot{\varepsilon}^{(p)}/A)^{1/n} \exp\left(Q/R \cdot T(z) \cdot 10^{-3} n\right) \tag{15a}$$

where $\dot{\varepsilon}^{(p)}$ is now a numerically constant parameter. The principal stresses in the plastically yielded part are:

$$S_1^{(p)} = -\rho_w g z_t - \rho_c g (z_2 - z_t) - \rho_p g (z - z_2), \quad z > z_2 \qquad 8$$

$$S_{2p}^{(p)}(z) \qquad (14a)$$

$$S_{3p}^{(p)}(z) - S_1^{(p)}(z) = \sigma_y^{(p)}(z)$$

Here the Tresca yield condition is adopted and the plastic yield depth is assumed to lie below the Moho depth z . The principal stresses as given by equation (14a) also satisfy the stress equilibrium equations. We require also that $S_2(p)$ and $S_3(p)$ be continuous across the elastic-plastic boundary. The yield depth z_5 of the pre-stressed plate is given by the solution of the equation.

$$\sigma_y^{(p)}(z_5) = S_{3e}^{(p)}(z_5) - S_1^{(p)}(z_5) \qquad (16)$$

The horizontal resultant N in equation (10a) is the integral over the plate thickness of the horizontal normal stress S_{xx}. In the pre-stressed state, S_{xx} is given by S_3 in equations (14) and (14a). During flexure of the lithosphere, additional normal horizontal stresses (the bending fiber stresses) are induced inside the plate. The resultant of these bending fiber stresses, however, is zero for one-dimensional plate flexure by the condition of static equilibrium. The horizontal resultant N therefore depends on the pre-stresses only. Specifically,

$$N = \int_{z_o}^{z_5} (S_{30} + \beta S_1^{(p)})\, dz + \int_{z_5}^{z_b} (S_1^{(p)} + \sigma_y^{(p)})\, dz \qquad (17)$$

(where $z_o = z_t$ (competent oceanic crust) and $z_o = z_2$ (fractured oceanic crust).

Construction of Moment-Curvature Relation. The moment-curvature relation can now be constructed from the material behavior and the plate tectonics model. This moment-curvature relation is needed in conjunction with the equilibrium equation (equation (10a) and the boundary conditions (equations (11) and (12) to determine the flexure profile of the trench-rise system. It is necessary at first to write down the plastic yield functions during flexure of the lithosphere. These plastic yield functions are given in accordance with the rock deformation behavior as shown in Figure 3 and equation (13).

Bending fiber stress is tensile and flexure strain rate is positive.

(1) Previously yilded part: Since yielding in the pre-stressed state is by a positive value of the stress difference $S_3(p) - S_1(p)$ (i.e., horizontal extension), this represents an additional loading over the pre-stessed state. The plastic yield function becomes

$$\sigma_y^{(T)}(x,z) = \{(\dot{\varepsilon}^{(p)}(z) + \dot{\varepsilon}^{(f)}(x,z)\}^{1/n} A^{-1/n} \exp(Q/R \cdot T(z) \cdot 10^{-3} \cdot n) \qquad (18)$$

where $\dot{\varepsilon}^{(f)}(x,z)$ is the strain rate due to flexure of the lithosphere. (2) Previously unyielded part: The strain rate is zero in the initial state before plate flexure. The plastic yield function during plate flexure is therefore

$$\sigma_y^{(T)}(x,z) = |\dot{\varepsilon}^{(f)}(x,z)|^{1/n} A^{-1/n} \exp(Q/R \cdot T(z) \cdot 10^{-3} \cdot n) \tag{19}$$

Bending fiber stress is compressive. (1) Previously yielded part: As soon as plate flexure begins, the material is in the unloading state. It becomes elastic. Plastic yielding occurs again when

$$S_3^{(f)} + S_3^{(p)} - S_1^{(p)} = -\sigma_y^{(C)}(x,z)$$

where the yeild stress function $\sigma_y^{(C)}(x,z)$ is given by

$$\sigma_y^{(C)}(x,z) = |\dot{\varepsilon}^{(f)}(x,z)|^{1/n} A^{-1/n} \exp(Q/R \cdot T(z) \cdot 10^{-3} \cdot n) \tag{20}$$

(2) Previously unyielded part: The yield stress function is also given by equation (20).

The flexure strain rate $\dot{\varepsilon}^{(f)}(x,z)$ for a steady state flexure profile is given by

$$\dot{\varepsilon}^{(f)}(x,z) = -(z - z_3) \frac{d\kappa}{dx} \cdot \frac{dx}{dt} = (z - z_3) \cdot \frac{d\kappa}{dx} \cdot sr \tag{21}$$

where κ is the curvature of the cross section in which the point under consideration is located, z_3 is the depth of the neutral axis and sr is the plate spreading rate. The expression $(z - z_3)$ in equation (21) is a slowly varying function of depth as compared with the term $\exp(Q/R\ T(z)\ 10^{-3})$ and can be replaced by its average value in the plastically yielded part duirng plate bending.

Moment-Curvature relation. The sign convention is illustrated in Figure 2. Curvature is negative when the bending fiber stress is compressive above the neutral axis and tensile below the neutral axis. Curvature is positive when the bending fiber stress is tensile above the neutral axis and compressive below the neutral axis. The moment has the opposite sign of the curvature. (1) Negative curvature: The maximum tensile bending fiber stress in addition to the pre-stress that can be sustained by the lithosphere is given by:

$$\sigma_y^{(1)}(x,z) = \begin{cases} \sigma_y^{(T)}(x,z) - (S_{3e}^{(p)} - S_1^{(p)}), & z \leq z_5 \\ \sigma_y^{(T)}(x,z) - \sigma_y^{(p)}(z) & z > z_5 \end{cases} \tag{22}$$

where z_5, as given by equation (16), is the yield depth in the pre-stressed state of the lithosphere. Denote the yield depth during plate bending by z_4. Continuity of stess at z_4 implies:

$$-\kappa (z_3 - z_4) E = \sigma_y^{(1)}(x,z_4) \tag{23}$$

Notice that z_4 varies with the distance from the trench axis through the yield function $\sigma_y^{(1)}(x, z)$.

Static force equilibrium implies:

$$\int_{z_1}^{z_2} \kappa E_c (z - z_3)\, dz + \int_{z_2}^{z_3} \kappa E (z - z_3)\, dz = -\int_{z_3}^{z_4} \kappa E (z - z_3)\, dz + \int_{z_4}^{z_b} \sigma_y^{(1)}(x,z)\, dz \tag{24}$$

where in equations (23) and (24) E_c is the crustal Young's modulus, E is the plate Young's modulus below the crust, and z_3 is the depth of the neutral axis below sea level. The two unknows z_3 and z_4 can be solved in terms of the curvature from the equations (22), (23), nd (24) for each cross section. The moment acting on the corresponding cross section is then given by:

$$M = -\kappa E_c \left[(z_3 - z_1)^3 - (z_3 - z_2)^3\right]/3 - \kappa E \left[(z_4 - z_3)^3 + (z_3 - z_2)^3\right]/3 + \int_{z_4}^{z_b} \sigma_y^{(1)}(x,z)\,(z - z_3)\, dz \tag{25}$$

(2) Positive curvature: The maximum compressive bending fiber stress in addition to the pre-stress that can be sustained by the lithosphere is given by:

$$\sigma_y^{(2)}(x,z) = \begin{cases} -\sigma_y^{(C)}(x,z) - (S_{3e}^{(p)} - S_1^{(p)}), \text{ if } \sigma_y^{(C)}(x,z) > -(S_{3e}^{(p)} - S_1^{(p)}) \\ 0, \text{ if } 0 < \sigma_y^{(C)}(x,z) \leq -(S_{3e}^{(p)} - S_1^{(p)}) \end{cases} \quad \text{for } z < z_5$$

$$\sigma_y^{(2)}(x,z) = -\sigma_y^{(C)}(x,z) - \sigma_y^{(p)}(z), \quad z > z_5 \tag{26}$$

Denote the yield depth during plate bending by z_4. Continunity of stress at z_4 gives:

$$-\kappa E (z_4 - z_3) = \sigma_y^{(2)}(x, z_4) \tag{27}$$

Static force equilibrium implies

$$\int_{z_1}^{z_2} \kappa E_c (z - z_3)\, dz + \int_{z_2}^{z_3} \kappa E (z - z_3)\, dz = \int_{z_3}^{z_4} -\kappa E (z - z_3)\, dz + \int_{z_4}^{z_b} \sigma_y^{(2)}(x,z)\, dz \tag{28}$$

where z_3 is again depth of the neutral axis. Solution of equations (26), (27), and (28) yields the unknowns z_3 and z_4 in terms of the curvature for each lithosphere cross section. The bending moment acting on the corresponding cross section is:

$$M = -\kappa E_c \left[(z_3 - z_1)^3 - (z_3 - z_2)^3\right]/3 - \kappa E \left[(z_3 - z_2)^3 + (z_4 - z_3)^3\right]/3 + \int_{z_4}^{z_b} \sigma_y^{(2)}(x,z) \cdot (z - z_3)\, dz \tag{29}$$

NUMERICAL COMPUTATION OF THE TRENCH PROFILE

The numerical computation of the trench profile is carried out by the finite-element numerical method. The system of equations to be solved is:

$$\frac{d^2M}{dx^2} + N\frac{d^2x}{dx^2} - (\rho_m - \rho_w)\, gw = 0 \qquad (10a)$$

and

$$M = M\left(\frac{d^2w}{dx^2};\ E_c,\ E,\ \sigma_y^{(p)}(z),\ \sigma_y^{(C)}(x,z),\ \sigma_y^{(T)}(x,z),\ z_t,\ z_2,\ z_b,\ S_1^{(p)},\ S_3^{(p)}\right) \qquad (30)$$

The solution scheme is as follows: A smoothed profile constructed from the bathymetry data is used as an input flexure profile to compute the local strain rate. (See equation (21).) Start from $M(o) = -D(o)d^2W/dx^2$, i. e. the moment-curvature relation of an elastic lithosphere where the starting flexure rigidity $D^{(0)}$ is computed from equation (30) with $d^2w/dx^2 = -1 \times 10^{-9} m^{-1}$ and $D^{(0)} = M\left(\frac{d^2w}{dx^2} = -1 \times 10^{-9}\ m^{-1};\ x = 45\ km\right) \times 1.2/(1 \times 10^{-9})$. Equation (10a) is then solved by a finite-elements scheme using Galerkin's method of approximation and a third-order shape function. Both nodal displacement and slope are treated as unknowns (Zienkiewicz, p. 171, 1971). Twenty elements, covering a distance from 30 km seaward of the trench axis to 630 km seaward of the trench axis, are employed in the computation. The element sizes are unequal, being smaller near the outer rise. Figure 4 shows the nodal coordinates and the element sizes. The first nodal coordinate is chosen at 30 km away from the trench axis for the reason that there exist stress concentrations near the trench axis where two plates come together. Such stress concentrations will invalidate the simple pre-stress distribution (equaitons (14) and (14a)) assumed for the lithosphere. This complication can be avoided by applying the present analysis only to the section of the lithosphere starting at about one elastic plate thickness seaward of the trench axis, since by Saint Venant's principle, the stress concentration at the trench axis is localized in a volume whose linear dimension is on the order of one elastic plate thickness. The bending moment $M(x_1)$ and the vertical shear force $Q_v(x_1)$ acting on node 1 are treated as unknown loading parameters. Details of the finite-element computation of flexure of an elastic plate are given in an Appendix. The solution with the flexure rigidity $D(o)$ is denoted by $w(1)$. the curvature $\kappa(1) = d^2w(1)/dx^2$ can be computed from the element shape function. From the nonlinear moment-curvature relation, equation (30), the new flexure rigidity for each element is computed by $D^{(1)} = -M^{(1)}/\kappa(1)$ Subsequent approximations are computed according to the Newton-Raphson scheme for solving nonlinear differential equations (e.g. Kosloff, 1978). The new flexure rigidity in each iteration is given by

$$D^{(i)} = \frac{M^{(i)} - M^{(i-1)}}{\kappa^{(i)} - \kappa^{(i-1)}} \qquad i = 2, 3, 4, \ldots \qquad (31)$$

Details of the Newton-Raphson scheme in solving the present plate flexure problem are also given in an Appendix. Convergence is judged by the criterion $\Sigma(w_j^{(i)} - w_j^{(i-1)})^2/\Sigma(w_j^{(i)})^2 < 10^{-5}$ where j is the nodal index and i is the iteration index. The entire numerical procedure was checked out by the problem of a point load applied at the free end of a cantilever beam made of an elastic perfectly-plastic material. The results agree with the analytic solution to within 0.3% with 20 elements. The pre-stress and loading parameters are adjusted such that the computed flexure profile fits the observed bathymetry. However, the computed profile differs in detail from the starting profile which was used to calculate the local strain rate. The computed profile is now used as the new input profile for local strain rate calculation. The entire solution procedure is then repeated. This process is continued until the computed profile agrees uniformly with the input profile for local strain rate computation to 1%.

DATA AND RESULTS

Data. The bathymetry of the Kurile trench-Hokkaido rise system (Figure 5) is from Chase et al. (1971) (Prfile B). This profile lies approximately half way between the Kamchatka and Hokkaido islands and is taken in a course perpendicular to the Kurile trench axis. This particular bathymetry profile has the parameters $w_b \simeq 390$ m and $x_b \simeq 65$ km where w_b is the amplitude of the forebulge and x_b is the position of the highest point on the forebulge relative to a point trenchward of the forebulge with zero flexure displacement. (See Figure 1.) McAdoo et al. (1978) examined 11 flexure profiles distributed along the entire Kurile trench (the present profile coincides with profile 5 of McAdoo et al. (1978)). The value of w_b varies between 250 and 500 m and the value of x_b varies between 50 and 80 km. The present flexure profile therefore represents an average profile for the one-dimensional plate flexure model.

Results. The computed results of the two flexure profiles are listed in Table 2. Flexure profile a is computed with Kirby-Raleigh dunite flow-law parameters (Kirby and Raleigh, 1973) with a strong crust whereas flexure profile b is computed with Carter-Ave'Lallement dunite flow-law parameters (Carter and Ave'Lallement, 1970; Carter, 1976) with a fractured crust of negligible strength. Flexure profile a is also plotted in Figure 5. Flexure profile b has not been plotted separately since it agrees closely with flexure profile a. (See Table 2.) The pertinent parameters for these two flexure profiles are listed in Table 1. The symbols in Table 1 are defined in the NOTATION section of this paper. Temperature in the lower lithosphere is approximated by a linear function of depth

$$T(z) = 178.86 + 17.868 \times 10^{-3} z \qquad (32)$$

where T is in degrees Kelvin and z is in meters. Equation (32) is constructed from the oceanic lithosphere temperature profile by Sclater and Francheteau (1970). The bending stress distribuion at two locations, one with positive

curvature and the other with negative curvature, are shown in Figure 6 (Kirby and Raleigh rheology). The plastic yield depth and maxima in bending stresses and total principal stress differences in the cross sections along the flexure profiles a and b are listed in tables 3 and 4 respectively. The moment-curvature relation computed for a lithosphere cross section at a distance of 45 km from the trench axis for flexure profile a is shown in Figure 7. Note that the moment-curvature relation of a particular cross-section depends on its distance from the trench axis.

DISCUSSION AND CONCLUSION

(1) Gravity anomaly profiles associated with the trench-rise systems are well developed and have been reported in the literature (Watts and Talwani, 1974). The principal term in the gravity effect is given by (e.g. Watts and Talwani, 1974):

$$\Delta g = - 2\pi G(\rho_m - \rho_w) w \qquad (33)$$

where G is the gravitational constant. Watts and Talwani (1974) and McAdoo et at. (1978) showed that equation (33) holds for the Kurile trench-Hokkaido rise system, i. e., the observed gravity anomaly is proportional to the observed flexure amplitude. Since the results of the present calculation fit closely to the observed flexure profile, the fit to the gravity anomaly has not been displayed by a further calculation according to equation (33). (2) The cause of the trench-rise topography of the present work is attributed to the bending of the lithosphere with an elastic strain-rate-dependent plastic rheology. No large-scale flow is assumed to exist inside the lithosphere. This is in contrast with the model adopted by Melosh (1978) in which both large-scale flow and a discontinuous viscosity boundary are assumed to exist inside the lithosphere. (3) The boundary between the lithosphere and the asthenosphere is defined by change in rheological properties (le Pichon et al., 1973). The asthenosphere is thought to begin with the seismic high attenuation low velocity zone. For example, Kanamori and Press (1970) determined form the seismic surface wave group velocity data a sharp decrease in rigidity near a depth of 70 km and suggested this depth to be the solidus as well as the bottom of the oceanic lithosphere. The thickness of the lithosphere influneces the present plate flexure clculation in two respects. The thrust as calculated by equation (17) depends on the depth of the bottom of the lithosphere. However, the thrust is independent of the bending stresses and enters into the flexure calculation as a single parameter. A change in the plate thickness can be matched by a change in the pre-stress distribution inside the lithosphere to give the same value of the total thrust. The other influence of the lithospheric plate thickness on the flexure profile is on the moment-curvature relation calculations. However, as shown by Figure 6, the bending fiber stress at a depth of 60 km is negligibly small as compared with the bending fiber stresses in the elastic part of the lithosphere. The exact location of the lithosphere and the asthenosphere boundary below a depth of 60 km is therefore immaterial as far as bending stress is concerned. To summarize, the exact depth of the bottom of the lithosphere does not affect the resuls of the present calcuation provided that it is deeper than 60 km and the thrust is treated as an independent parameter. (4) The value of the lateral stress confinement coefficient β is chosen to be 1/3 and 1/2 for flexure profiles a and b respectively. Objection may be raised that stress relaxation in the lithosphere would imply a higher value of β. Also, the plate tectonics assumption that the plate is formed at the ridge by cooling from hot asthenosphere materials seems to imply a high value of β. The answer to these objections are: (a) While it is true that β approaches 1 with time for a viscoelastic material exhibiting indefinite primary creep such as the Maxwellian solid, this is not the case with the present assumed viscoelastic

behavior. The assumed viscoelastic behavior has a finite absorption band and a relaxed modulus which is 56% of its corresponding seismic value. The relaxed modulus has the value 0 for the viscoelastc material with indefinite primary creep. (b) The stress condition in the hot material at the ridge is likely to be nearly hydrostatic ($\beta = 1$). However, when the material cools to form the lithosphere, thermal stresses produce by volume contraction tend to make the lateral stress less compressive, therefore decrease the value of β. (5) A large horizontal compressive pre-stress is assumed to exist inside the lithosphere, -5 kb for profile a and -6.5 kb for profile b. These values are consistent with the focal-plane solutions of large shallow earthquakes occurring near the outer rise of the Kurile trench-Hokkaido rise system (Hanks, 1971; Stuader and Maulchin, 1976). Without such large compressive stress the tensile bending stress near the surface (on the order of 4 kb) in the vicinity of the outer rise where the curvatures are the greatest would have caused tensile fracture in the lithosphere. The seismological observation, however, indicate that the few large shallow earthquakes occurring near the outer rise have their compressive axis nearly horizontal and perpendicular to the trench axis. The large horizontal compressive pre-stress is therefore a result of the seismological constraints. However, this large compressive pre-stress, while overcoming the tensile bending fiber stress near the outer rise, gives rise to a principal stress difference approaching -4.6 kb at ocean bottom depths away from the trench (Table 3) for plate flexure model a. Such a large stress difference at the confining pressure of -0.54 kb at ocean bottom depth can be sustained only if the oceanic crust is made of unfractured competent rocks. Recent evidences suggest the contrary that fractures (joints, faults, and foliations) exists extensively throughout the crust (e.g. Brace, 1972). Plate flexure model b takes into account the fractured nature of the oceanic crust by neglecting the crustal strength in the plate flexure calculations. The stress differences of plate flexure model b in Table 4 all lie within the failure envelopes consistent with rock fracture and deformation data. (6) The explantion of the more numerous earthquakes occurring near the trench axis is beyond the scope of the simple plate flexure model used in the present calculation. Indeed, the possible stress concentrations at the trench axis where two lithospheric plates converge provide the very reason the first node of the present finite-element calculationis chosen at 30 km from the trench axis. The earthquake occurring near the trench axis and the deep focus earthquakes occurring beneath the island arc have been considered in terms of friction between the continental and the oceanic lithospheres and gravity sinking of the oceanic lithosphere (e.g. Kanamori, 1971). (7) A power law flow equation (equation (13)) describing strain rate as a function of yield stress has been used in the present calculations. Kirby (1977) pointed out that the power law holds only at low stress levels. The maximum stress at which the power law remains valid was estimated to lie between 1 and 4 kilobars. The maximum yield stress in the present calculation does not exceed 4 kb. The uncertainties in the water content of the lithosphere affect the computed results more severely than the exact dependence of strain rate on the yield stress. The power law rheology therefore serves adequately to illustrate the use of realistic rheology in plate flexure calculations. (8) A large number of parameters are employed in the present plate flexure calculation (See Table 1). All these parameters are necessary for the lithosphere model to be

consistent with the known seismic observations and laboratory deformation data. The flexure profile, on the other hand, is a relatively simple curve that can be characterized by far fewer number of parameters than the input paramters. The problem is therefore mathematically underdetermined. Conclusions regarding the values of the individual parameters therefore cannot be drawn from the flexure profile alone. This fact has been demonstrated by the two similar profiles a and b with quite dissimilar input pre-stress parameters. The present work, however, demonstrates the consistency between the laboratory rock deformation data and the observed plate flexure profile. (9) A deformation plasticity theory is used in the present treatment to approximate the material plastic behavior. The more complete and rigorously correct treatment by an incremental plasticity theory remains to be attempted in the future.

APPENDIX A: FINITE ELEMENT FOR SOLVING ONE-DIMENSIONAL ELASTIC PLATE FLEXURE PROFILE

Both nodal displacements and slopes must be considered to be unknows in the plate flexure problems (Zienkiewicz, p. 171, 1971). The displacement w(x) is given in the terms of shape functions $P_{i,1}(x)$, $P_{i,2}(x)$, the nodal displacements w_i, and the nodal slopes $(\frac{dw}{dx})_i$ by

$$w(x) = \sum_i \{ P_{i,1}(x)\ w_i + P_{i,2}(x)\ (\frac{dw}{dx})_i \} \tag{A1}$$

where i is the nodal index.
Consider the i th element between the i th and the i + 1 the nodes. For a third order displacement interpolation function.

$$w = \alpha_o + \alpha_1 x + \alpha_2 x^2 + \alpha_3 x^3, \qquad x_i \leqslant x \leqslant x_{i+1}\ , \tag{A2}$$

and

$$\frac{dw}{dx} = \alpha_1 + 2\alpha_2 x + 3\alpha_3 x^2.$$

The Four parameters $\alpha_0, \alpha_1, \alpha_2$, and α_3 can be solved in terms of the nodal displacements w_i, w_{i+1} and the nodal slopes $(\frac{dw}{dx})_i$, $(\frac{dw}{dx})_{i+1}$. Equation (A2) becomes

$$w(x) = (1, x, x^2, x^3)\ \underline{\underline{C}}^e{}_i\ (w_i, (\frac{dw}{dx})_i, w_{i+1}, (\frac{dw}{dx})_{i+1})^T \tag{A3}$$

where

$$\underline{\underline{C}}^e{}_i = \begin{pmatrix} x_{i+1}^2(x_{i+1} - 3x_i)/(\Delta x_i)^3, & -x_i x_{i+1}^2/(\Delta x_i)^2, & x_i^2(3x_{i+1} - x_i)/(\Delta x_i)^3, & -x_i^2 x_{i+1}/(\Delta x_i)^2 \\ 6x_i x_{i+1}/(\Delta x_i)^3, & x_{i+1}(x_{i+1} + 2x_i)/(\Delta x_i)^2, & -6x_i x_{i+1}/(\Delta x_i)^3, & x_i(x_i + 2x_{i+1})/(\Delta x_i)^2 \\ -3(x_i + x_{i+1})/(\Delta x_i)^3, & -(x_i + 2x_{i+1})/(\Delta x_i)^2, & 3(x_i + x_{i+1})/(\Delta x_i)^3, & -(x_{i+1} + 2x_i)/(\Delta x_i)^2 \\ 2/(\Delta x_i)^3, & 1/(\Delta x_i)^2, & -2/(\Delta x_i)^3, & 1/(\Delta x_i)^2 \end{pmatrix}$$

and $\Delta x_i = x_{i+1} - x_i$

Compare equation (A3) with equation (A1). the shape functions $P_{i,1}(x)$ and $P_{i,2}(x)$ are given by:

$$P_{i,k}(x) = P^{e_{i-1}}_{i,k}(x) + P^{e_i}_{i,k}(x)\ , \qquad x_{i-1} \leqslant x \leqslant x_{i+1} \qquad k = 1,2$$

where $P^{e_{i-1}}_{i,k}(x)$ and $P^{e_i}_{i,k}(x)$ are computed by

$$(P^{e_i}_{i,1}(x), P^{e_i}_{i,2}(x), P^{e_i}_{i+1,1}(x), P^{e_i}_{i+1,2}(x)) = (1, x, x^2, x^3)\ \underline{\underline{C}}^{e_i}, \tag{A4}$$
$$x_i \leqslant x \leqslant x_{i+1}$$

$$P_{i,k}(x) = 0 \qquad x < x_{i-1},\ x > x_{i+1}$$

The one-dimensional plate flexure equation (10) is solved by the Galerkin method of approximation (e.g., Fung. 1965) as follows:

$$\int_{x_1}^{x_n} P_{i,k}(x) \left[(\frac{d^2}{dx^2})\ (D\frac{d^2w}{dx^2}) + T_h \frac{d^2w}{dx^2} + \gamma w \right] dx \quad + \tag{A5}$$

$$\delta_{i,1} \left\{ - \left[D(\frac{d^2w}{dx^2})_{x_1} + M(x_1) \right] \left(\frac{dP_{1,k}}{dx} \right) + \right.$$

$$\left[\frac{d}{dx}\left(D\frac{d^2w}{dx^2}\right)_{x_1} + Q_v(x_1) + T_h\left(\frac{dw}{dx}\right)_{x_1}\right] P_{1,k}(x_1)\Bigg\} = 0$$

$k = 1, 2; \quad i = 1, 2, \ldots, n$

where $T_h \equiv N =$ thrust, $\gamma = (\rho_m - \rho_w)$ and $\delta_{i,j}$ is the kronecker delta. The terms outside of the integral sign come from the boundary conditions (equations (11a), (12a)) at x_1 (30 km seaward from the trench axis). The boundary conditions at $x = x_n$, i.e. at distances far away from the trench axis d not enter into equation (A5) becuase $\delta(w)_{x_n} = \delta(dw/dx)_{x_n} = 0$. Integrating equation (A5) by parts and assuming vanishing loads far away from the trench axis, the result is:

$$\int_{x_1}^{x_n} \left[D\frac{d^2w}{dx^2}\frac{d^2P_{i,k}(x)}{dx^2} - T_h\frac{dP_{i,k}(x)}{dx}\frac{dw}{dx} + \gamma w P_{i,k}(x)\right] dx$$

$$= \delta_{i,1}\left[M(x_1)\left(\frac{dP_{i,k}}{dx}\right)_{x_1} - Q_v(x_1) P_{1,k}(x_1)\right] \quad \begin{matrix} i = 1, 2, 3, \ldots n \\ k = 1, 2 \end{matrix}$$

It can be shown from equation (A4)

$$P_{1,1}(x_1) = 1, \qquad P_{1,2}(x_1) = 0$$

$$\left(\frac{dP_{1,1}}{dx}\right)_{x_1} = 0, \qquad \left(\frac{dP_{1,2}}{dx}\right)_{x_1} = 1$$

Therefore

$$\int_{x_1}^{x_n} \left[D\frac{d^2w}{dx^2}\frac{d^2P_{i,k}}{dx^2} - T_h\frac{dP_{i,k}}{dx}\frac{dw}{dx} + \gamma w P_{i,k}(x)\right] dx$$

$$= \delta_{i,1}\left[M(x_1)\,\delta_{k,2} - Q_v(x_1)\,\delta_{k,1}\right] \qquad \text{(A6)}$$

Equation (A6) is a set of 2n linear equations with the 2n unknowns w_i, $(dw/dx)_i$, $i = 2, 2, \ldots\ldots n$. The bending moment $M(x_1)$ and the vertical shear force $Q_v(x_1)$ acting on node 1 are the loading parameters.

APPENDIX B: Newton-Raphson method for solving nonlinear differential equations as applied to the plate flexure problem.

A flow chart showing the Newton-Raphson scheme is shown below:

STARTING SOLUTION $w^{(1)}$, $\frac{dw}{dx}^{(1)}$

↓

FIND CURVATURE $\kappa^{(1)}$ FROM INTERPOLATION FUNCTION

↓

FIND MOMENT $M^{(1)}$ FROM THE NONLINEAR MOMENT-CURVATURE RELATION

↓

COMPUTE THE FLEXURE RIGIDITY

$$D^{(1)} = -M^{(1)}/\kappa^{(1)}$$

COMPUTE THE RESIDUE $R^{(1)}$ FROM

$$R^{(1)}(x) = -\frac{d^2M^{(1)}}{dx^2} + T_h \frac{dw}{dx}^{(1)} + \gamma w^{(1)}$$

↓

SOLVE FOR THE CORRECTION TERM $\Delta w^{(1)} = w^{(2)} - w^{(1)}$ BY THE GALERKIN APPROXIMATION

$i = 1, 2, \ldots, n$; and $k = 1, 2$

$$\int_{x_1}^{x_n} P_{i,k} \left[\frac{d^2}{dx^2} D^{(1)} \frac{d^2\Delta w^{(1)}}{dx^2} + T_h \frac{d^2\Delta w^{(1)}}{dx^2} + \gamma\Delta w^{(1)} + R^{(1)}(x)\right] dx \qquad \text{(A7)}$$

$$+\delta_{i,1} \left\{-\left(D^{(1)} \frac{d^2\Delta w^{(1)}}{dx^2}\right)_{x_1} \left(\frac{dP_{i,k}}{dx}\right)_{x_1} + \left[\frac{d}{dx}\left(D^{(1)} \frac{d^2\Delta w^{(1)}}{dx^2}\right)_{x_1}\right.\right.$$

$$\left.\left. + T_h \left(\frac{d\Delta w^{(1)}}{dx}\right)_{x_1}\right] P_{1,k}\right\} = 0$$

↓

FIRST ITERATION RESULT $w^{(2)} = w^{(1)} + \Delta w^{(1)}$, $\frac{dw}{dx}^{(2)} = \frac{d}{dw}(w^{(1)} + \Delta w^{(1)})$

↓

TEST CONVERGENCE $\sum_i (w_i^{(2)} - w_i^{(1)})^2 / \sum_i (w_i^{(2)})^2 < 10^{-5}$?

YES → STOP

NO ↓

REPEAT ITERATION WITH NEW FLEXURE RIGIDITY

$$D^{(i)} = -(M^{(i)} - M^{(i-1)})/(\kappa^{(i)} - \kappa^{(i-1)}) \quad i \geq 2$$

Notice that in the boundary conditon terms in equation (A7) the external loads $M(x_1)$, $Q(x_1)$ are set to zero for the calculation of the correction term $\Delta w^{(1)}$. This is demanded by the condition when $R^{(1)}(x)=0$, $\Delta w^{(1)}=0$. Equation (A7) can be rearranged to give (for the n-th iteration)

$$\int_{x_1}^{x_n} P_{i,k} \left[-\frac{d^2 M^{(n)}}{dx^2} + T_h \frac{d^2 w^{(n+1)}}{dx^2} + \gamma w^{(n+1)} \right] dx$$

$$= \int_{x_1}^{x_n} P_{i,k} \left[\frac{d^2}{dx^2} D^{(n)} \frac{d^2}{dx^2} (w^{(n+1)} - w^{(n)}) \right] dx$$

$$-\delta_{i,1} \left\{ \left[-D^{(n)} \frac{d^2 (w^{(n+1)} - w^{(n)})}{dx^2} \right] \frac{dP_{1,k}}{dx} + \left[\frac{d}{dx} (D^{(n)} \frac{d^2 (w^{(n+1)} - w^{(n)})}{dx^2}) + T_h \frac{d(w^{(n+1)} - w^{(n)})}{dx} \right] P_{1,k} \right\} \quad \text{(A8)}$$

It is found for the present plate flexure problem that when the convergence criterion is satisfied both $w^{(n+1)} \to w^{(n)}$ and $dw^{(n+1)}/dx \to dw^{(n)}/dx$. From the interpolation funtion $d^2 w^{(n+1)}/dx^2 \to d^2 w^{(n)}/dx^2$ and $d^3 w^{(n+1)}/dx^3 \to d^3 w^{(n)}/dx^3$. The right-hand side of equation (A8) therefore vanished. $d^2 w^{(n+1)}/dx^2 \to d^2 w^{(n)}/dx^2$ implies $M^{(n+1)} \to M^{(n)}$. (A8) therefore implies

$$-\frac{d^2 M^{(n+1)}}{dx^2} + T_h \frac{d^2 w^{(n+1)}}{dx^2} + \gamma w^{(n+1)} = 0$$

i.e., the static equilibrium equation is satisfied.

NOTATION

A : material constant in rock deformation flow law

$B(x)$: bathymetry

$D^{(i)}$: flexure rigidity of the i-th iteration

E : average plate Young's modulus below the Moho

E_c : crustal Young's modulus

G : gravitational constant

M, M_x : bending moment in one-dimensional plate flexure

N, N_x : horizontal stress resultant in one-dimensional plate flexure

$P_{i,1}^{(x)}$, $P_{i,2}^{(x)}$: one-dimensional finite-element shape functions

Q : activation energy in rock deformation flow law

Q_v : vertical shear force in one-dimensional plate flexure

R : gas constant

S_{ij}: Kirchhoff stress tensor

$S_1^{(p)}(z)$: vertical principal pre-stress in the plate before flexure

$S_{2e}^{(p)}(z)$: horizontal principal pre-stress along the y-axis in the elastic part of the plate before the flexure

$S_{2p}^{(p)}(z)$: horizontal principal pre-stress along the y-axis in the plastic part of the plate before flexure

$S_{3e}^{(p)}(z)$: horizontal principal pre-stress along the x-axis in the elastic part of the plate before flexure

$S_{3p}^{(p)}(z)$: horizontal principal pre-stress along the x-axis in the plastic part of the plate before flexure

S_{30}: horizontal principal pre-stress of tectonic origin along the x-axis in the elastic part of the plate before flexure

T: absolute temperature

T_h : thrust in one-dimensional plate bending

X, Z : body forces in the x and z directions respectively

f_x : external load per unit area tangential to the plate in one-dimensional plate flexure

g : gravitational acceleration

m_x : resultant external moment per unit area in one-dimensional plate flexure

q : lateral load per unit area in one-dimensional plate flexure

sr : plate spreading rate

u, v, w : displacements in the x, y, z, directions respectively

w_b : amplitude of the forebulge in the flexure profile

x, y, z : coordinates in three dimensions: x = horizontal and perpendicular to the trench axis; y = horizontal and parallel to the trench axis; and z = vertical and positive downward

x_b : position of the highest point on the forebulge relative to a point trenchward of the forebulge with zero displacement

z_b : undeformed plate bottom profile

z_t : undeformed plate top profile

z_2 : Moho depth

z_3 : depth of bending neutral axis

z_4 : plastic yield depth during plate flexure

z_5 : yield depth in the plate before flexure

β : lateral stress confinement coefficient

γ : $(\rho_m - \rho_w)g$

$\delta_{i,j}$: kronecker delta

$\dot{\varepsilon}$: total strain rate in the rock deformation flow law

$\dot{\varepsilon}^{(f)}(x,z)$: plastic strain rate due to plate flexure

$\dot{\varepsilon}^{(p)}(z)$: total strain rate in the plate before flexure

κ : curvature

ρ_c : crustal density

ρ_m : asthenosphere density immediately below the lithosphere

ρ_p : average plate density below the Moho

ρ_w : density of ocean water

σ : yield strength in rock deformation flow law

$\sigma_y^{(C)}(x,z)$: plastic yield function during plate flexure when bending fiber stress is compressive

$\sigma_y^{(T)}(x,z)$: plastic yield function during plate flexure when bending fiber stress is tensile

$\sigma_y^{(p)}(z)$: yield stress as a function of depth in the plate before flexure

$\sigma_y^{(1)}(x,z)$: maximum tensile bending fiber stress in addition to the pre-stress that can be supported during plate flexure

$\sigma_y^{(2)}(x,z)$: maximum compressive bending fiber stress in addition to the pre-stress that can be supported during plate flexure

ζ : vertical coordinate centered at the neutral plane

All units are in MKS system.

ACKNOWLEDGEMENT: The author wishes to thank D. Kosloff, T. Hanks, J. Dieterich, and an anonymous reviewer whose comments improved this paper.

TABLE 1. PARAMETERS USED IN THE COMPUTATION OF PROFILES A AND B IN FIGURE 5

	Flexure Profile a	Flexure Profile b
z_t(km)	5.356	5.356
z_b(km)	60.000	60.000
z_2(km)	10.756	10.756
z_5(km)	32.345	45.115
ρ_w(g/cm^3)	1.03	1.03
ρ_c(g/cm^3)	2.70	2.70
ρ_p(g/cm^3)	3.30	3.30
ρ_m(g/cm^3)	3.40	3.40
E_c(Mb)	0.4978	-*-
E(Mb)	0.9539	0.9539
$\dot{\varepsilon}^{(p)}$(s^{-1})	3.171×10^{-20}	3.171×10^{-20}
$\overline{z - z_3}$ (km)	25.000	25.000
Q(kcal/mole)	96	111
A(kb^{-n} s^{-1})	1.8×10^{8}	5.1×10^{9}
n	3.0	3.3
β	1/3	1/2
sr(cm/y)	7.2	7.2
S_{30}(kb)	-5.0	-6.5
T_h(N/m)	5.4558×10^{13}	5.8301×10^{13}
$Q_v(x_1)$ (N/m)	7.1×10^{11}	7.2×10^{11}
$M(x_1)$ (N·m/m)	-6.4×10^{16}	-6.256×10^{16}

* The strength of the oceanic crust is neglected in flexure profile b calculations.

TABLE 2. COMPUTED RESULTS OF PROFILES A AND B

Profile a

Distance from trench axis (km)	Displacement (m)	Slope
30.000	868.24	-0.2775×10^{-1}
45.000	483.52	-0.2343×10^{-1}
60.000	171.77	-0.1811×10^{-1}
75.000	-61.43	-0.1303×10^{-1}
90.000	-223.65	-0.8693×10^{-2}
105.000	-326.09	-0.5085×10^{-2}
120.000	-379.99	-0.2225×10^{-2}
135.000	-396.41	-0.8197×10^{-4}
150.000	-385.60	0.1419×10^{-2}
190.000	-285.56	0.3103×10^{-2}
230.000	-159.78	0.3044×10^{-2}
270.000	-53.15	0.2198×10^{-2}
310.000	10.35	0.1002×10^{-2}
350.000	33.88	0.2422×10^{-3}
390.000	34.87	-0.1339×10^{-3}
430.000	26.20	-0.2460×10^{-3}
470.000	16.33	-0.2378×10^{-3}
510.000	7.91	-0.1767×10^{-3}
550.000	2.64	-0.8748×10^{-4}
590.000	0.44	-0.2753×10^{-4}
630.000	0.00	0.0000

w_b = 396.41 m

x_b = 65.05 km

TABLE 2 (Continued)

Profile b

Distance from trench axis (km)	Displacement (m)	Slope
30.000	877.87	-0.2765×10^{-1}
45.000	492.55	-0.2360×10^{-1}
60.000	177.14	-0.1841×10^{-1}
75.000	-58.85	-0.1310×10^{-1}
90.000	-221.78	-0.8716×10^{-2}
105.000	-324.53	-0.5102×10^{-2}
120.000	-378.73	-0.2251×10^{-2}
135.000	-395.68	-0.1286×10^{-3}
150.000	-385.79	0.1342×10^{-2}
190.000	-289.86	0.2982×10^{-2}
230.000	-168.24	0.2971×10^{-2}
270.000	-62.48	0.2229×10^{-2}
310.000	-3.90	0.1102×10^{-2}
350.000	31.41	0.3312×10^{-3}
390.000	35.31	-0.7949×10^{-4}
430.000	28.52	-0.2252×10^{-3}
470.000	19.03	-0.2374×10^{-3}
510.000	10.26	-0.1935×10^{-3}
550.000	4.02	-0.1168×10^{-3}
590.000	0.82	-0.4588×10^{-4}
630.000	0.00	0.0000

w_b = 395.75 m

x_b = 65.35 km

TABLE 3. PLASTIC YIELD DEPTH DURING BENDING, z_4, BENDING STRESS, σ_B, AND TOTAL PRINCIPAL STRESS DIFFERENCE, $\sigma_3 - \sigma_1$, AT OCEAN BOTTOM (z_t), MOHO (z_2), AND PLASTIC YIELD DEPTH (z_4)

(Along flexure profile A (Kirby & Raleigh Rheology, Strong Oceanic Crust))

Distance from trench axis* (km)	z_4 (km)	σ_B at z_1 (kb)	σ_B at z_2 (kb)	σ_B at z_4 (kb)	$\sigma_3 - \sigma_1$ at z_1 (kb)	$\sigma_3 - \sigma_1$ at z_2 (kb)	$\sigma_3 - \sigma_1$ at z_4 (kb)
33.170	36.015	2.424	3.227	-3.401	-2.216	-0.460	-3.224
41.830	35.817	2.640	3.505	-3.702	-2.000	-0.182	-3.509
48.170	34.679	2.965	3.872	-4.144	-1.674	0.185	-3.826
56.830	34.642	3.018	3.939	-4.215	-1.621	0.252	-3.891
63.170	34.942	2.931	3.843	-4.099	-1.708	0.156	-3.816
71.830	35.014	2.839	3.726	-3.969	-1.801	0.039	-3.695
78.170	35.652	2.617	3.467	-3.668	-2.022	-0.220	-3.461
86.830	35.817	2.437	3.236	-3.416	-2.203	-0.451	-3.223
93.170	36.157	2.251	3.003	-3.157	-2.389	-0.684	-2.990
101.830	36.408	2.024	2.709	-2.841	-2.616	-0.978	-2.691
108.170	36.663	1.843	2.475	-2.590	-2.797	-1.212	-2.455
116.830	37.003	1.602	2.161	-2.253	-3.038	-1.526	-2.135
123.170	37.234	1.432	1.937	-2.014	-3.208	-1.750	-1.907
131.830	37.676	1.199	1.632	-1.688	-3.440	-2.055	-1.598

TABLE 3. (Continued)

138.170	37.915	1.046	1.427	-1.474	-3.594	-2.260	-1.392
146.830	38.486	0.837	1.151	-1.181	-3.802	-2.537	-1.116
158.453	38.983	0.606	0.837	-0.856	-4.034	-2.850	-0.802
181.547	41.795	0.222	0.316	-0.316	-4.417	-3.371	-0.296
198.453	45.128	0.053	0.077	-0.075	-4.587	-3.610	-0.068
221.547	43.048	0.082	-0.117	0.116	-4.721	-3.804	0.130
238.453	40.361	-0.173	-0.243	0.245	-4.813	-3.930	0.278
261.547	39.416	-0.244	-0.339	0.345	-4.884	-4.026	0.391
278.453	37.728	-0.288	-0.392	0.406	-4.927	-4.079	0.493
301.547	37.901	-0.269	-0.367	0.379	-4.908	-4.054	0.461
318.453	39.484	-0.215	-0.298	0.304	-4.854	-3.985	0.348
341.547	40.283	-0.161	-0.225	0.227	-4.800	-3.912	0.261
358.453	40.911	-0.122	-0.171	0.172	-4.761	-3.858	0.199
381.547	42.429	-0.073	-0.104	0.103	-4.712	-3.791	0.120
398.453	42.491	-0.054	-0.078	0.077	-4.694	-3.765	0.093
421.547	50.039	-0.006	-0.009	0.009	-4.646	-3.696	0.011
438.453	50.495	-0.003	-0.004	0.004	-4.643	-3.691	0.006
461.547	48.836	0.008	0.012	-0.011	-4.632	-3.675	-0.009

TABLE 3. (Continued)

478.453	46.509	0.015	0.022	-0.021	-4.625	-3.665	-0.016
501.547	45.351	0.021	0.030	-0.029	-4.619	-3.657	-0.023
518.453	43.245	0.025	0.035	-0.035	-4.615	-3.652	-0.023
541.547	43.349	0.024	0.034	-0.034	-4.616	-3.653	-0.022
558.453	45.294	0.019	0.029	-0.028	-4.620	-3.659	-0.021
581.547	46.195	0.015	0.022	-0.022	-4.625	-3.665	-0.016
598.453	47.375	0.011	0.016	-0.016	-4.629	-3.671	-0.012
621.547	49.840	0.006	0.009	-0.008	-4.634	-3.678	-0.006

*These distances coincide with the Gaussian integration points within each element.

Table 4. Plastic Yield Depth During Bending, z_4, Bending Stress, σ_B, And Total Principal Stress Difference, $\sigma_3 - \sigma_1$, At MOHO (z_2), And At Plastic Yield Depth (z_4) Along Flexture Profile B (Carter & Ave Lallement Rheology, Fractured Oceanic Crust With Negligible Strength).

Distance from trench axis*	z_4	σ_B at z_2	σ_B at z_4	$\sigma_3 - \sigma_1$ at z_2	$\sigma_3 - \sigma_1$ at z_4
(km)	(km)	(kb)	(kb)	(kb)	(kb)
33.170	39.514	3.821	-3.164	-1.694	-2.879
41.830	39.278	4.232	-3.512	-1.283	-3.200
48.170	38.109	4.831	-4.064	-0.684	-3.567
56.830	38.047	4.969	-4.185	-0.546	-3.676
63.170	37.898	5.034	-4.247	-0.481	-3.706
71.830	37.951	4.915	-4.141	-0.600	-3.611
78.170	38.859	4.428	-3.691	-1.087	-3.324
86.830	39.007	4.141	-3.449	-1.375	-3.102
93.170	39.422	3.807	-3.153	-1.708	-2.859
101.830	39.661	3.432	-2.837	-2.083	-2.568
108.170	39.947	3.124	-2.570	-2.392	-2.329
116.830	40.280	2.718	-2.260	-2.798	-2.014
123.170	40.516	2.429	-1.981	-3.086	-1.787
131.830	40.966	2.033	-1.645	-3.482	-1.480
138.170	41.192	1.775	-1.427	-3.741	-1.276
146.830	41.813	1.416	-1.126	-4.100	-1.005
158.453	42.148	1.032	-0.807	-4.483	-0.699
181.547	46.655	0.384	-0.320	-5.131	-0.294
198.453	49.925	0.107	-0.090	-5.408	-0.080
221.547	48.708	-0.115	0.096	-5.631	0.111

Table 4. (continued)

238.453	45.423	-0.265	0.221	-5.781	0.258
261.547	44.753	-0.391	0.335	-5.906	0.381
278.453	43.684	-0.473	0.427	-5.988	0.492
301.547	43.743	-0.457	0.413	-5.972	0.476
318.453	44.628	-0.377	0.327	-5.892	0.374
341.547	44.933	-0.296	0.251	-5.811	0.294
358.453	45.382	-0.230	0.190	-5.745	0.228
381.547	46-866	-0.147	0.122	-5.662	0.146
398.453	47.668	-0.099	0.083	-5.614	0.102
421.547	50.623	-0.044	0.037	-5.559	0.046
438.453	52.672	-0.018	0.015	-5.533	0.020
461.547	60.000	0.005	-0.005	-5.510	-0.004
478.453	54.295	0.017	-0.015	-5.498	-0.012
501.547	52.073	0.030	-0.026	-5.485	-0.020
518.453	50.100	0.038	-0.032	-5.478	-0.022
541.547	49.834	0.040	-0.034	-5.475	-0.023
558.453	50.175	0.039	-0.033	-5.477	-0.023
581.547	50.660	0.034	-0.029	-5.481	-0.020
598.453	51.798	0.028	0.024	-5.487	-0.018
621.547	53.066	0.021	-0.018	-5.495	-0.013

*These distances coincide with the Gaussian integration points within each element.

REFERENCES

Anderson, D. L., and J. B. Minster, Seismic velocity, attenuation and rheology of the upper mantle, Phys. Earth Planet, Interiors, in press, 1979.

Brace, W. F., Pore pressure in Geophysics, Amer. Geophys. Un. Monograph No. 16 265-273, 1972.

Caldwell, J. G., W. F. Haxby, D. E. Karig, and D. L. Turcotte, On the applicability of a universal trench profile. Earth Plan. Sci. Lett., 31, 239-246, 1976.

Carter, N. L., Steady state flow of rocks, Rev. Geophys. Space Phys., 14, 301-360, 1976.

Carter, N. L., and H. G. Ave'Lallement, High temperature flow of dunite and peridotite, Geol. Soc. Amer. Bull., 81, 2181-2202, 1970.

Carter, N. L., and S. H. Kirby, Transient creep and semibrittle behavior of crystalline rocks, Pageoph, 116, 807-839, 1978.

Chase, T. E., H. W. Menard, and J. Mammerikx, Topography of the north Pacific, Institute of Marine Resources, University of California, San Diego, Calif. 1971.

De Bremaecker, J. C., Is the oceanic lithosphere elastic or viscous? J. Geophys. Res., 82, 2001-2004, 1977.

Denkhaus, H. G., Residual stresses in rock masses, Proc. Congr. Int. Soc. Rock Mechanics, 1st. Lisbon, 311-331, 1966.

Fazekas, G. A., A note on the bending of Euler beams, J. Eng. Educ., 57, 393-394, 1967.

Fung, Y. C., Foundations of Solid Mechanics, Prentice Hall, Englewood Cliffs (N. J.), 525 pages, 1965.

Griggs, D. T., F. J. Turner, and H. C. Heard, Deformation of rocks at 500 - 800 C, Geol. Soc. Am. Mem., 79, 39-104, 1960.

Gunn, R., Quantitative aspects of juxtaposed ocean deeps, mountain chains, and volcanic ranges, Geophysics, 12, 238-255, 1947.

Hetenyi, M., Beams on Elastic Foundation, The University of Michigan Press, Ann Arbor, Michigan, 255 pages, 1946.

Hanks, T. C., The Kurile trench-Hokkaido Rise system: large shallow earthquakes and simple models of deformation, Geophys. J. R. Astr. Soc, 23, 173-189, 1971.

Hanks, T. C., Earthquake stress drops, ambient tectonic stresses and stresses that drive plate motions, Pageoph., 115, 441-458, 1977.

Kanamori, H. Great earthquakes at island arcs and the lithosphere, Tectonophysics, 12, 187-198, 1971.

Kanamori, H., and F. Press, How thick is the lithosphere? Nature, 226, 330-331, 1970.

Kirby, S. H., and C. B. Raleigh, Mechanisms of high-temperature, solid-state flow in minerals and ceramics and their bearing on the crep behavior of the mantle, Tectonophysics, 19, 165-194, 1973.

Kosloff, D., Numerical Modeling of Crustal Deformation, Thesis, California Institute of Technology, 218 pages, 1978.

Le Pichon, X., J. Francheteau, and J. Bonnin, Plate Tectonics, Elsevier, Amsterdam, 300 pages, 1973.

Liu, H. P., and D. Kosloff, Elastic-plastic bending of the lithosphere incorporating rock deformation data, with application to the structure of the Hawaiian Archipalago, Tectonophysics, 50, 249-274, 1978.

Liu, H. P., D. L. Anderson, and H. Kanamori, Velocity dispersion due to anelasticity: Implication for seismology and mantle composition, Geophys. J. R. astr. Soc., 47, 41-58, 1976.

McAdoo, D. G., J. G. Caldwell and D. L. Turcotte, on the elastic-perfectly plastic bending of the lithosphere under generalized loading with application to the Kurile trench, Geophys. J. R. astr. Soc., 54, 11-26, 1978.

Melosh, G. H., Dynamic support of the outer rise, Geophys. Res. Lett., 5, 321-324, 1978.

O'Connell, R. J., Pleistocene glaciation and the viscosity of the lower mantle, Geophys. J. R. astr. Soc., 23, 299-327, 1971.

Parsons, B. and P. Molnar, The origin of outer topographic rises associated with trenches, Geophys. J. R. astr. Soc., 45, 707-712, 1976.

Sclater, J. G. and J. Francheteau, The implication of terrestial heat-flow observations on current tectonic and geochemical models of the crust and upper mantle of the earth, Geophys. J. R. astr. Soc., 20, 509-542, 1970.

Stauder, W., and L. Mualchin, Fault motion in the larger earthquakes of the Kurile-Kamchatka Arc and of the Kurile-Hokkaido corner, J. Geophys. Res., 81, 297-308. 1976.

Walcott, R. J., Flexute rigidity, thickness, and viscosity of the lithosphere, J. Geophys. Res., 75, 3941-3954, 1970.

Watts, A. B. and M. Talwani, Gravity anomalies seaward of deep sea trenches and their tectonic implications, Geophys. J. R. astr. Soc., 36, 57-90, 1974.

Watt, A. B., M. Talwani, and J. R. Cochran, Gravity field of the Northwest Pacific Ocean basin and its margin, In: G. H. Sutton, M. H. Manghnani, and R. Moberly (editors), The Geophysics of the Pacific Ocean Basin and Its Margin, 17-34, AGU, Washington, D. C. 1976.

Zienkiewicz, O. C., The Finite Element Method in Engineering Science, McGraw-Hill, London, 521, 1971.

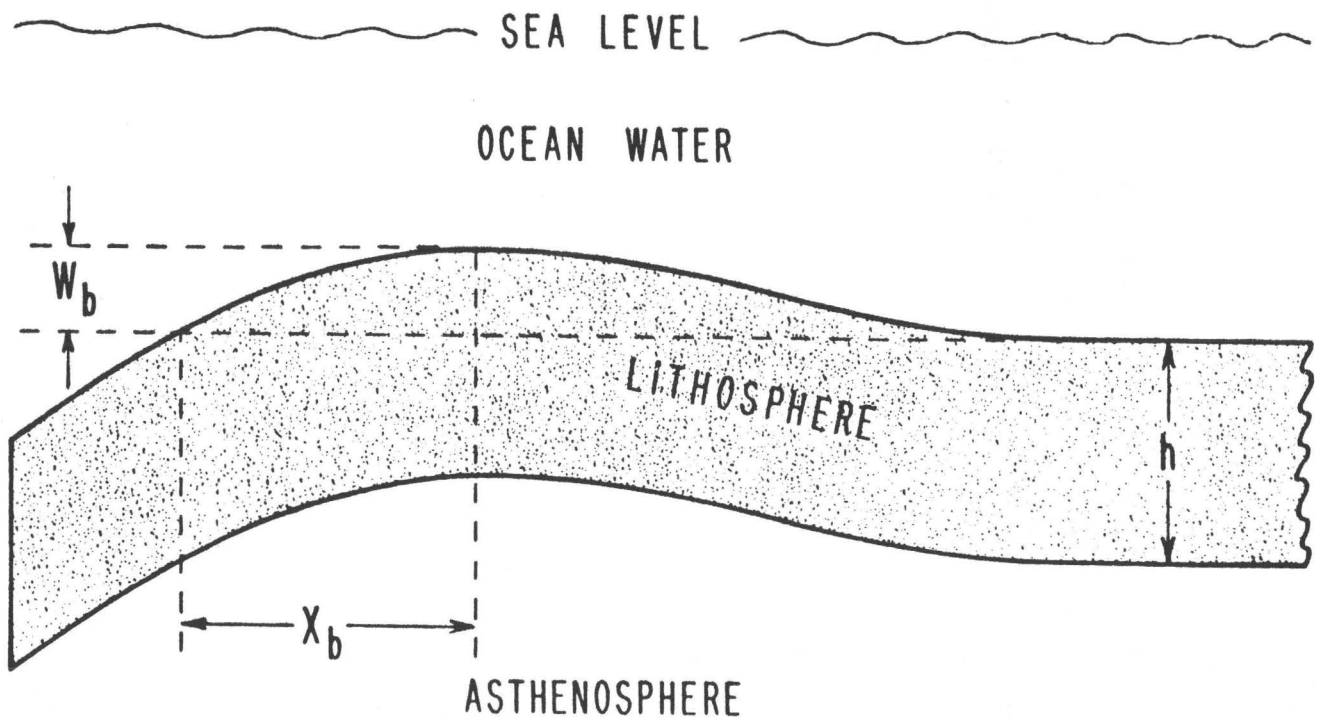

Figure 1. Schematic diagram illustrating lithosphere flexure at a trench.

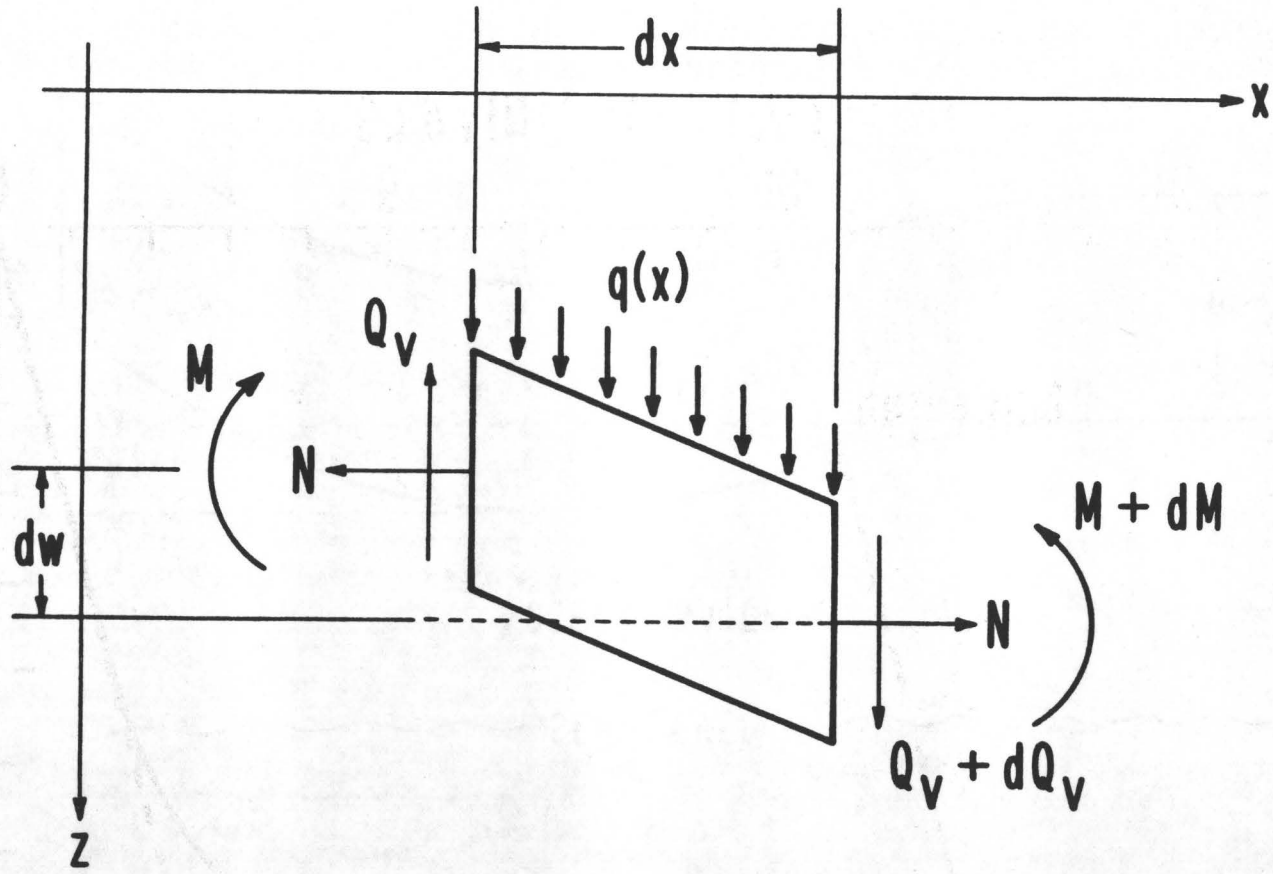

Figure 2. Coordinates and sign convention used in the present calculation. The moment M, horizontal resultant N, shear force Q , and distributive load q(x) are shown in their positive sense.

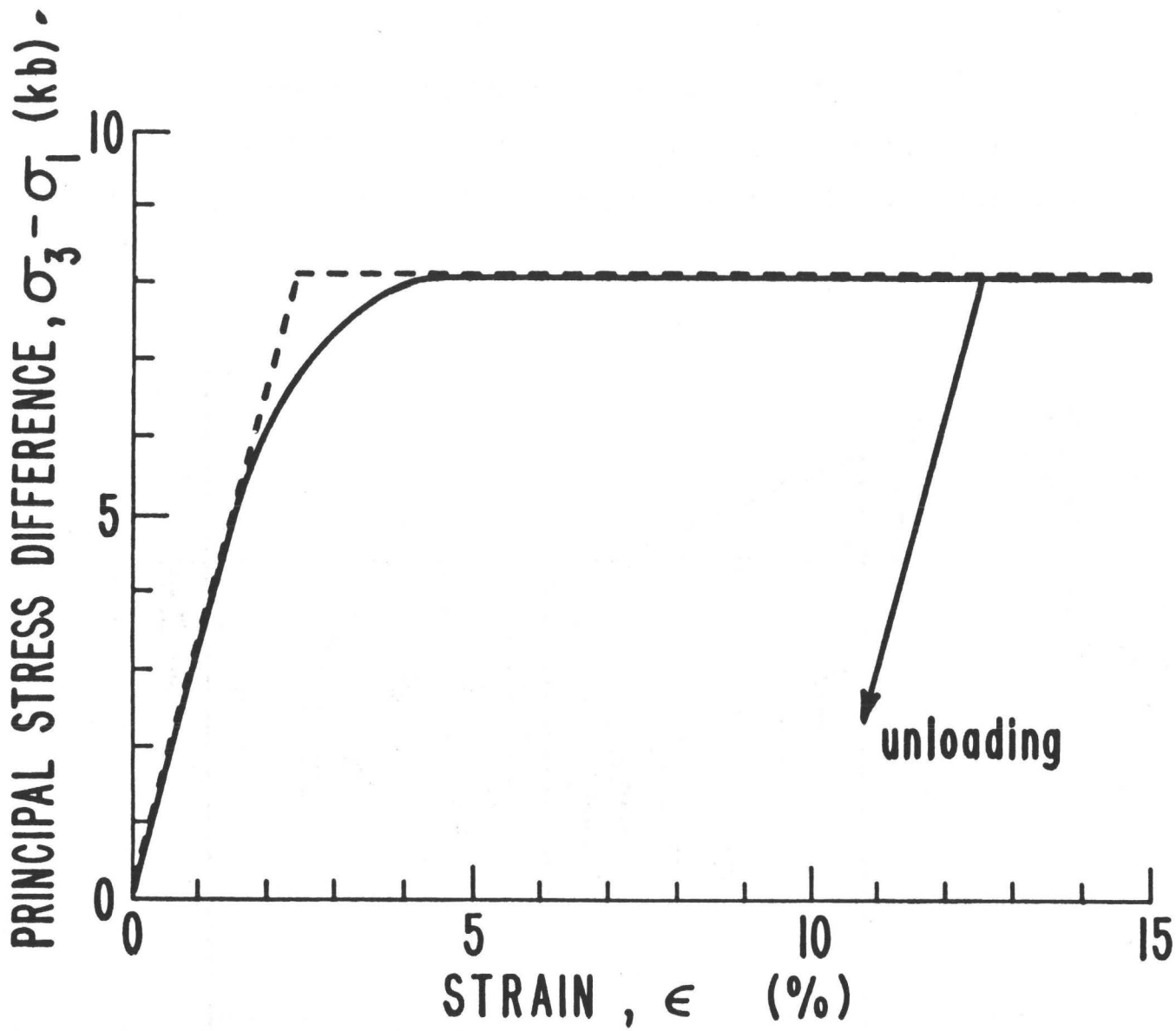

Figure 3. Stress-strain curve of dunite at 5 kb confining pressure, 800°C and 5 x 10^{-4} s^{-1} strain rate (after Griggs et al., 1960).

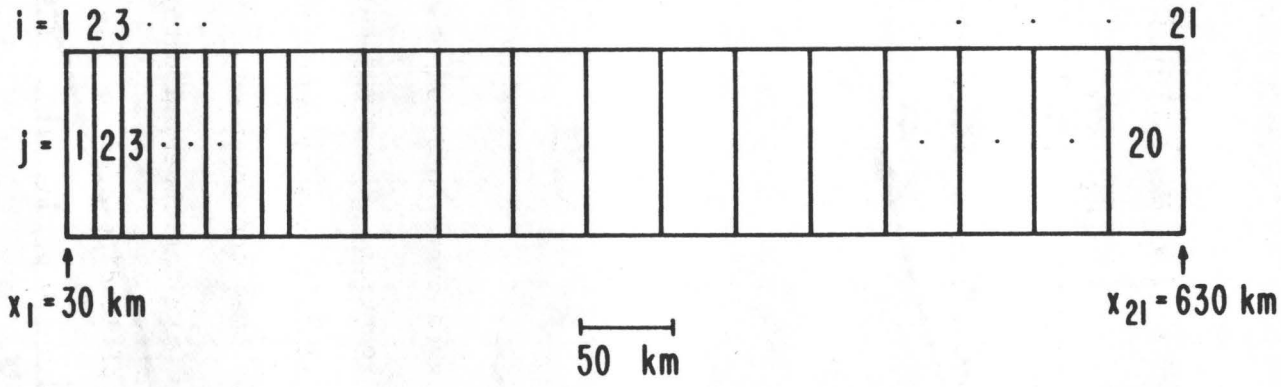

Figure 4. Nodal coordinates and element sizes employed in the numerical computation of the plate flexure profle. i: Nodal index; j: Element index.

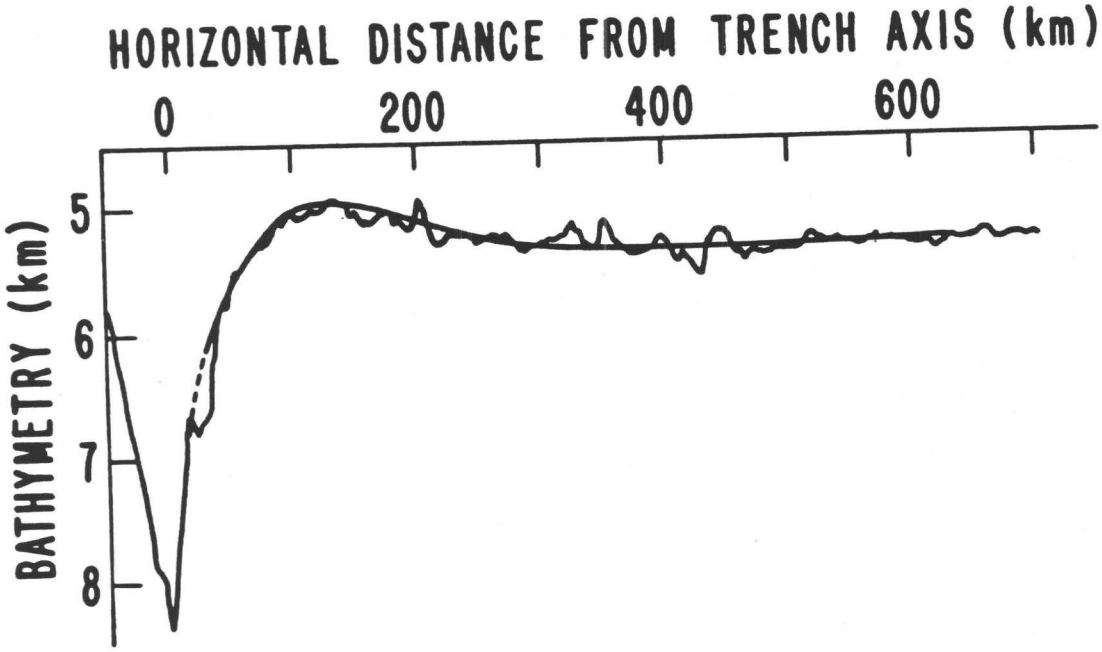

Figure 5. Observed bathymetry (jagged curve) and computed lithosphere top surface profile (smooth curves). The computed profile range from 30 km to 630 km in horizontal distance measured from the trench axis. Dashed line shows that continuation of the computed profile joints smoothly with the observed bathymetry.
The computed flexure profile displayed in this figure is profile a (Kirby and Raleigh flow-law parameters). The computed profile b agrees closely with this profile. (See Table 2.)

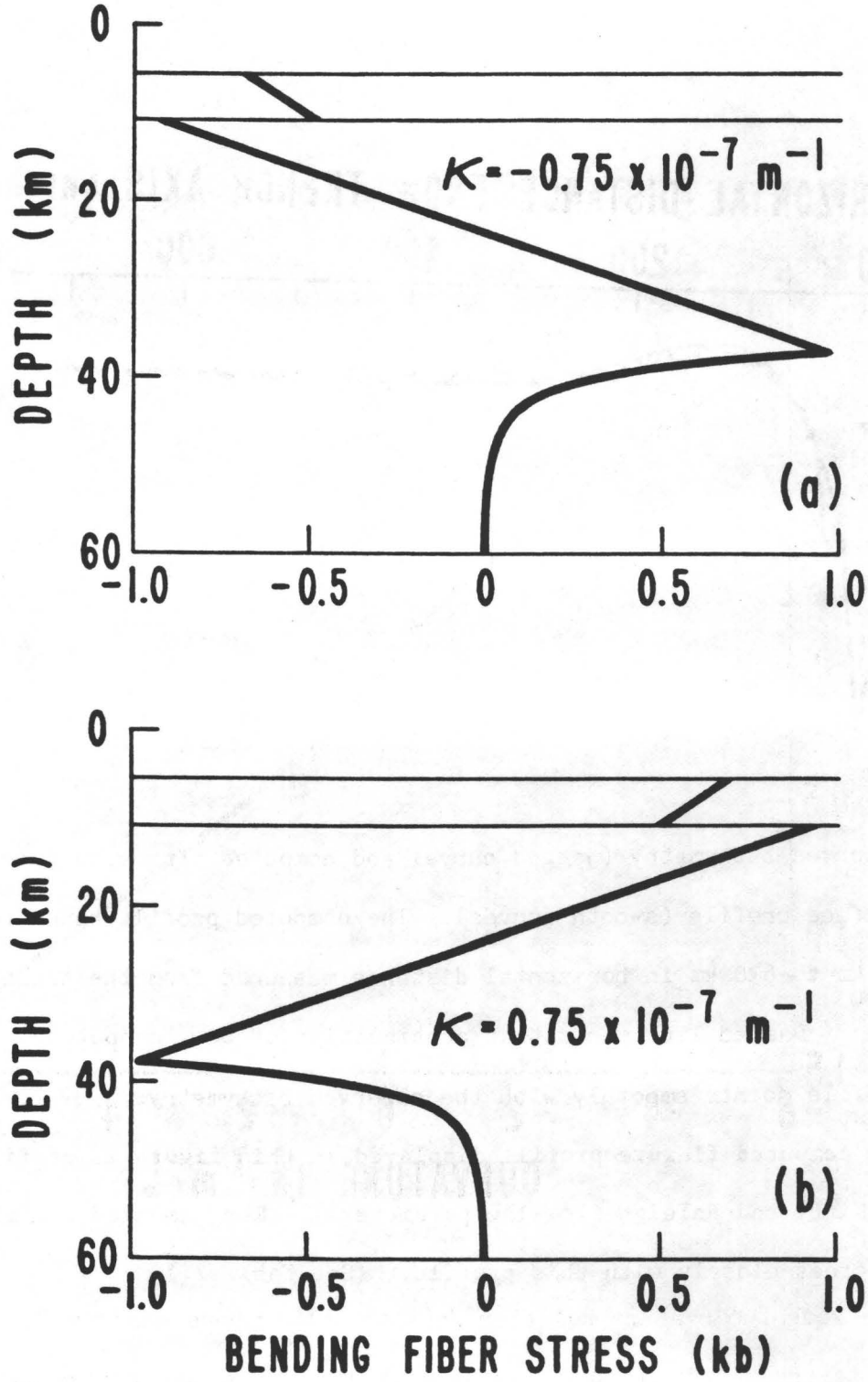

Figure 6. Bending stress distribution with depth at (a) 181.54 km and (b) 278.45 km from the trench axis (plate flexure model a).

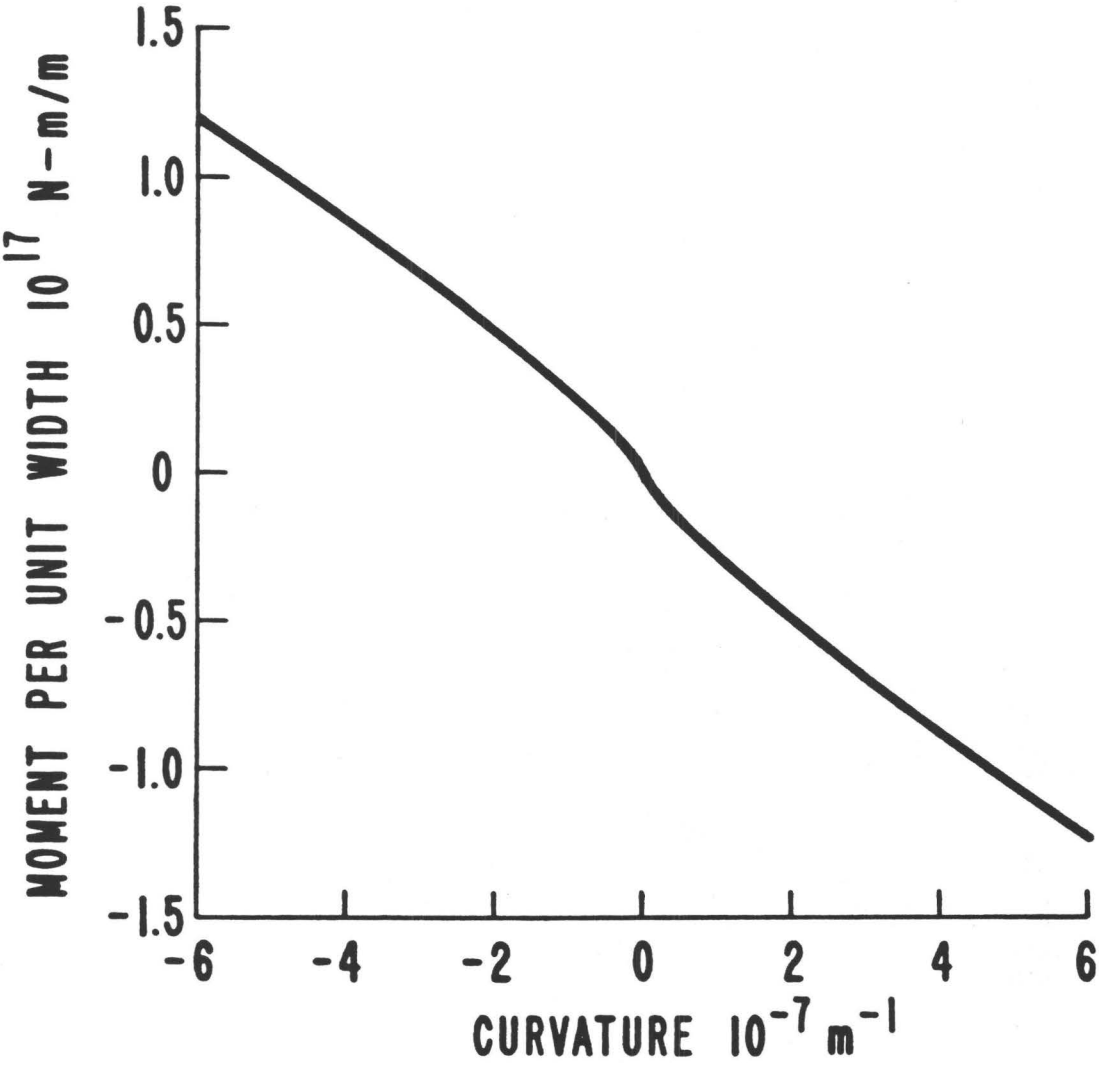

Figure 7. The moment-curvature relation for the lithosphere bending for a plate cross-section at a distance of 45 km from the trench axis (plate flexure model a).

SEAMOUNT LOADING OF THE OCEANIC LITHOSPHERE

Kurt Lambeck and S.M. Nakiboglu*
Research School of Earth Sciences
Australian National University
Canberra 2600 Australia

ABSTRACT

The modelling of lithospheric flexure due to seamounts has been examined in some detail to try to evaluate the stress differences that can exist in the oceanic crust over long time intervals. Most published models result in stress-differences that are of the order 2-3 kbar per km of deflection and maximum values approach 10 kbars. Geophysical support for the elastic plate theory comes mainly from gravity which requires a broad negative anomaly on the flanks of the actual seamount. The anomaly, however, is not very sensitive to the density structure of the crust and to the density of the fill-in or to the degree of fill-in. The stress in the plate is sensitive to these parameters. In consequence, the stress-differences can be significantly reduced by adopting a lower density for the fill-in, rather than the usual 2.8 gcm^{-3}, without modifying the gravity anomaly. The stress can be further reduced, particularly at the base of the plate, by introducing a non-elastic rheology. For large loads, such as Oahu Island discussed by Watts (1978), the maximum stress under the load can be reduced to about 2-2.5 kbars near the upper surface of the plate and the maximum stress-differences $\sigma_{rr}-\sigma_{zz}$ are of the order 1-1.5 kbars. The introduction of the non-elastic rheology results in a stress and time dependence of the flexural rigidity. Large loads or loads of long duration will result in a thinner apparent plate thickness than small loads or loads of a short duration, all other factors being equal.

---

* On leave from University of Queensland, Department of Surveying, St. Lucia 4067, Australia.

SEAMOUNT LOADING OF THE OCEANIC LITHOSPHERE

Introduction

The existence of the Hawaiian Archipelago and other seamount chains have, since the work by Vening Meinesz (1941), usually been interpreted as being regionally rather than locally compensated features and they have often been invoked as evidence that the ocean lithosphere is capable of supporting deviatoric stresses that reach several kilobars (e.g. Walcott, 1970; 1976). The regional compensation is usually modelled as the elastic support of the load by an elastic plate overlying a fluid medium (Gunn, 1943). These models typically indicate stress-differences of about 2kbars per kilometer of deflection (e.g. Walcott, 1976; see below) while the total deflection may attain several kilometers. Hence stress-differences of up to 10kbars are not uncommon in these models.

The elastic plate theory goes back at least as far as the work of Hertz in 1889 (Hertz, 1895) and early applications were by Vening Meinesz (1941) and by Gunn (1943). The theory is well developed in the engineering mechanics literature (e.g. Reisner, 1944; 1946; Frederick, 1956; Timoshenko and Woinowsky-Krieger, 1959) and in the recent geophysical literature by Brotchie and Silvester (1969) and Brotchie (1971). Most geophysical applications have used the thin plate theory even though the computed deflections reach a significant fraction of the elastic plate thickness. In the subsequent sections we will address ourselves to (i) the thin plate theory, (ii) the geophysical applications of this theory, (iii) consequences of seamount loading on the stress state in the ocean crust, and (iv) review some published results in light of the above analyses.

Thin plate theory

The basic equation expressing the deformation $w(x,y)$ of an elastic plate of flexural rigidity D, loaded at its upper surface $z = -H/2$ by $q(x,y)$ is

$$D\Delta\Delta w + \rho_s g w = q. \qquad (1)$$

The vertical coordinate z is measured downwards from the middle plane of the undeformed infinite plate whose surfaces are given by $z = \pm H/2$. ρ_s is the density of the underlying fluid-like medium.

This equation expresses the force balance between the surface load q, the elastic response of the plate and the reaction $\rho_s gw$ of the substratum on the base of the plate, assuming that a static situation has been attained. Apart from assumptions of homogeneous elastic properties and an initial hydrostatic equilibrium state, equation (1) assumes that: (i) the effect on bending of shearing stresses and normal pressures on planes parallel to the x-y plane have been ignored and (ii) deflections are small compared with the plate thickness.

Equation (1) are solved for the specified load q(x,y) and appropriate boundary conditions. For a load of finite dimensions, specified by a boundary $r = R_A(x,y)$, frequently used boundary conditions are:

w and dw/dr are finite at r = 0 (2a)

w and dw/dr are continuous at $r = R_A$ (2b)

moments and shears are continuous at $r = R_A$ (2c)

w and $r^{-1}dw/dr = 0$ at infinity. (2d)

This last condition follows from the requirement that the moments vanish at infinity.

In some geophysical problems, it may be desirable to restrict the loading deformation to occur only over a finite radius $r = R_B > R_A$. This could be the case where the seamount, a result of an endogenic thermal process, sits on a plate that is of higher average temperature and is therefore weaker than the plate further away. The boundary conditions would then be (2a-2c) and

$w = dw/dr = 0$ at $r = R_B$. (2e)

For a point load and a response that is symmetrical about the point of loading, the deformation w(r) can be readily expressed in terms of zero-order Kelvin-Bessel functions as

$$w(\frac{r}{\ell}) = - \frac{q\ell^2}{2\pi D} \text{kei}(\frac{r}{\ell}) \tag{3a}$$

where $\ell^4 = D/\rho_s g$. ℓ is the "radius of relative stiffness". The

solution (3a) is equivalent to that given by Hertz (1895). At the origin r=0

$$w(0) = -\frac{q\ell^2}{8D} . \tag{3b}$$

The solution (3a) behaves as a damped sinusoid with the sign of w changing about every 4ℓ but with a rapid decrease in the maximum amplitudes between successive zeros. The maximum negative w value, occurring at about 5ℓ, is only about 1.5% of w(0) and the next maximum, occurring at about 9.5ℓ, is only 0.4% of w(0). Thus for a 1km downward deflection at z=0, the maximum upward deflection will be only of the order of 15m and will occur at about 5ℓ from the point of loading.

Solutions for equation (1) take a particularly simple form for simple axisymmetrical loads (see, for example, Brotchie and Silvester, 1969). For a uniform disc load of density ρ, height h and radius A the deflection at $r \leq A$ is

$$w = \frac{\rho h}{\rho_s} \{1 + C_1 \, \mathrm{ber}(\tfrac{r}{\ell}) + C_2 \, \mathrm{bei}(\tfrac{r}{\ell})\} \tag{4a}$$

and at $r \geq A$

$$w = \frac{\rho h}{\rho_s} \{C_1' \, \mathrm{ber}(\tfrac{r}{\ell}) + C_2' \, \mathrm{bei}(\tfrac{r}{\ell}) + C_3' \, \mathrm{ker}(\tfrac{r}{\ell}) + C_4' \, \mathrm{kei}(\tfrac{r}{\ell})\} \tag{4b}$$

The constants C_i and C_i' are evaluated from the appropriate boundary conditions (2). With (2a-2d) and writing $x=r/\ell$, $a=A/\ell$

$$\begin{Bmatrix} C_1 \\ C_2 \\ C_1' \\ C_2' \\ C_3' \\ C_4' \end{Bmatrix} = a \begin{Bmatrix} \mathrm{ker}'a \\ -\mathrm{kei}'a \\ 0 \\ 0 \\ \mathrm{ber}'a \\ -\mathrm{bei}'a \end{Bmatrix} \tag{4c}$$

The algebra for the constants C_i and C_i' subject to the conditions (2a-2c) and (2e) is more tedious and the effect of the change in boundary conditions can be readily seen by considering the appropriate point load solutions. For the load q at r=0, and for $r \leq R_B$

$$w = -\frac{q\ell^2}{2\pi D} (\text{kei } x + C_i \text{ ber } x + C_2 \text{ bei } x) \tag{5a}$$

with

$$\begin{aligned} x &= r/\ell, \quad b=R_B/\ell \\ C_1 &= (\text{bei } b \text{ kei}'b - \text{bei}'b \text{ kei } b)/\alpha \\ C_2 &= (\text{kei } b \text{ ber}'b - \text{kei}'b \text{ ber } b)/\alpha \\ \alpha &= (\text{ber } b \text{ bei}'b - \text{ber}'b \text{ bei } b). \end{aligned} \tag{5b}$$

At x=0.

$$w(o) = \frac{q\ell^2}{8D} \left(1 - \frac{4}{\pi} C_1\right) \tag{5c}$$

compared with (3b). For b=2 ($R_B=2\ell$) the reduction in the maximum deflection is more than 40%.

For an axisymmetric parabolic load of radius r_A at z=-H/2, the solution with the boundary conditions (2a-2d) is, for $r \leq r_A$,

$$w = \frac{\rho h}{\rho_s} \left[\left(1 - \frac{x^2}{a^2}\right) + C_1 \text{ ber } x + C_2 \text{ bei } x\right] \tag{6a}$$

and for $r \geq r_A$

$$w = \frac{\rho h}{\rho_s} [C_3 \text{ ker } x + C_4 \text{ kei } x] \tag{6b}$$

with

$$\left.\begin{matrix} C_1 \\ C_2 \\ C_3 \\ C_4 \end{matrix}\right\} = 2 \left\{\begin{matrix} \text{ker } a - \frac{2}{a} \text{ kei}'a \\ -\text{kei } a - \frac{2}{a} \text{ ker}'a \\ \text{ber } a - \frac{2}{a} \text{ bei}'a \\ -\text{bei } a - \frac{2}{a} \text{ ber}'a \end{matrix}\right. \tag{6c}$$

In the above solutions ρ is the density of the material loading the plate while ρ_s is the density of the substratum. If the load is below water the effective density of the load is $\rho-\rho_o$, where ρ_o is the density of water. Beyond the load proper, the upper surface of the plate is subjected to the water load $\rho_o gw$. Equations (1) now are, within the load,

$$D\Delta\Delta w + \rho_s gw = (\rho-\rho_o)gh\,, \tag{7a}$$

and outside the load,

$$D\Delta\Delta w + \rho_s gw = \rho_o gw. \tag{7b}$$

The solution is of the form (4) but now the constants are evaluated numerically, subject to the appropriate boundary conditions.

In the seamount problems there is usually little bathymetric evidence for large depressions of the seafloor about the foot of the load and it is assumed that the deflected lithosphere is filled with sediments or with the volcanic rock that also made up the load. If this fill-in has a density ρ_f, equations (1) become within the load

$$D\Delta\Delta w + \rho_s gw = (\rho-\rho_o)gh + \rho_f gw \tag{8a}$$

and outside the load

$$D\Delta\Delta w + \rho_s gw = \rho_f gw \tag{8b}$$

where h is now measured with respect to the sea floor and not, as before, with respect to the top of the deformed plate. The simplest solution follows when $\rho = \rho_f$, for then

$$D\Delta\Delta w + (\rho_s-\rho)gw = (\rho-\rho_o)gh \tag{9}$$

and the solution is as for (1), except that ℓ is now defined by

$$\ell^4 = \frac{D}{(\rho_s-\rho)g} \tag{10}$$

This solution immediately resolves the problem of knowing only the visible part of the load above the seafloor. This assumption concerning the fill-in is one of mathematical convenience rather than for their physical reality and if the fill-in is only partially completed, or if the fill-in is of a density different from the

load, iterative solutions will generally be required. In particular, the fill-in up to the original undeformed level of the plate is an ad-hoc one, for if such large sedimentation rates have occurred, the fill-in would not have stopped at the level corresponding to the original undeformed plate surface z = -H/2 but would have gone up to the level corresponding to the maximum uplift of the plate before spilling over onto the surrounding seafloor.

Figure 1 illustrates the deflections for both disc and parabolic loads. The parameters A and h for the latter have been selected such that both loads have the same surface area and both loads exert the same mean pressure on the plate. Both loads are underwater and two cases are considered, where the depressions have, and have not been filled with sediments of the same density as the load itself. The results of the disc and equivalent parabolic loads are quite comparable, and for most of the present illustrative examples it will suffice to consider only the disc load. In the fill-in models the maximum deformation is increased by a factor of about 3 relative to the no-fill model. The width of the deflection is also much increased in the second model. In both cases the maximum negative values for w remain small, less than 100m for a maximum positive deflection of 5km. Depending on the degree of fill-in and on the density of the fill-in the actual solutions will generally lie between the two limits.

As the radius of the load increases, the maximum deflections occurring under the center of the load approach the isostatic limits of $h(\rho-\rho_o)/(\rho_s-\rho)$ for the fill-in case although, due to the oscillatory behaviour of the solution (4) for w(r), the maximum deflection is somewhat greater than this limit (Figure 2).

Apart from the density of the load and of the fill-in, the key parameters defining the magnitude and wavelength of the deflection are the flexural rigidity D and the density contrast $\rho-\rho_s$. For a uniform plate D is defined as

$$D = \frac{\mu}{3}\,\frac{\lambda+\mu}{\lambda+2\mu}\,H^3 = \frac{E}{12(1-\nu 2)}\,H^3 \qquad (11a)$$

where μ,λ are the Lamé parameters and H is the thickness of the plate. E is Young's modulus and ν is Poison's ratio. Table 1 summarizes some typical parameters for the ocean lithosphere. If μ and λ (or E and ν) are variable with depth

$$D = 4 \int_{-H/2}^{H/2} \frac{\mu(\lambda+\mu)}{\lambda+2\mu} z^2 dz \qquad (11b)$$

The usual and convenient procedure is to assume that D is uniform, giving an equivalent flexural rigidity or an equivalent elastic plate thickness H . D and H can subsequently be interpreted in terms of more realistic plate properties. Figure 3 illustrates the deflection for different D. In the limit $D \to 0$, $\ell \to 0$ and w approaches the isostatic limit $h(\rho-\rho_o)/(\rho_s-\rho)$. As D decreases, the wavelength of the deflection decreases and the magnitude of the negative deflections increase.

The density contrast $\rho_s-\rho$ affects both the magnitude of the deflection and the wavelength; the larger the contrast the smaller ℓ and the smaller the magnitude of the deflection (Figure 5b).

Stress-state of the plate

The stresses in the x-y plane for axisymmetric loads follow from (e.g. Timoshenko and Woinowsky-Krieger, 1959)

$$\sigma_{rr} = \frac{12D}{H^3\ell^2} z\left(\frac{d^2w}{dx^2} + \frac{\nu}{x}\frac{dw}{dx}\right) \qquad (12a)$$

$$\sigma_{\theta\theta} = \frac{12D}{H^3\ell^2} z\left(\nu\frac{d^2w}{dx^2} + \frac{1}{x}\frac{dw}{dx}\right) \qquad (12b)$$

$$\sigma_{rz} = \frac{3D}{2H^3\ell^3} (H^2-4z^2) \frac{d}{dx}\left(\frac{d^2w}{dx^2} + \frac{1}{x}\frac{dw}{dx}\right) \qquad (12c)$$

$$\sigma_{r\theta} = 0$$

where ν is Poisson's ratio. σ_{rr} and $\sigma_{\theta\theta}$ reach maxima at $z = \pm H/2$.

The vertical stress is (e.g. Frederick, 1956)

$$\sigma_{zz} = \frac{q_1+q_2}{2} + (q_2-q_1)\left[\frac{3}{2}\frac{z}{h} - 2\left(\frac{z}{h}\right)^3\right] \qquad (12d)$$

where $q_1 = -\rho g(h + w)$ is the load on the upper surface of the deformed plate and $q_2 = -\rho_s g w$ is the load on the lower surface of the plate. The maximum value for σ_{zz} is reached at the upper surface. The remaining stress-tensor elements σ_{rz}, $\sigma_{\theta z}$ are everywhere small and σ_{rr}, $\sigma_{\theta\theta}$, σ_{zz} can be considered as principal stresses near the surface of the plate. On the middle plane $\sigma_{zz} = q_1+q_2/2$ and σ_{rz} are the only non-zero elements, both of which never exceed 1kbar for the examples considered here.

With the deflection solutions (4a,4b;6a,6b) and (12a-c) analytical expressions for the stresses are readily obtained. Figure 1 illustrate results for the disc and parabolic loads discussed previously for the two cases of fill-in and no fill-in. For small A, both σ_{rr} and $\sigma_{\theta\theta}$ reach maxima below the center of the load that significantly exceed σ_{zz} and the maximum stress-difference in the plate is essentially given by $\sigma_{rr}(\pm H/2)$ or $\sigma_{\theta\theta}(\pm H/2)$ at x=0. With equations (4, 12) at x=0

$$\sigma_{rr|max} = \sigma_{\theta\theta|max} = \frac{3D}{H^2\ell^2}\,\frac{\rho-\rho_o}{\rho_s-\rho}\,h(1+\nu)\,\frac{A}{\ell}\,\mathrm{kei}'\,\frac{A}{\ell} \qquad (13a)$$

$$= 3g\left(\frac{\ell}{H}\right)^2 (\rho-\rho_o)\,h(1+\nu)\,\frac{A}{\ell}\,\mathrm{kei}'\,\frac{A}{\ell}.$$

For the parameters given in table (1) and a disc of 60km radius, a nominal estimate of the maximum stress is

$$\sigma_{max} \simeq 2.6h \text{ kbar} \qquad (14a)$$

for h in km. This result is for the case of fill-in. For the no fill-in but submerged case

$$\sigma_{max} \simeq 1.3h \text{ kbar}. \qquad (14b)$$

For the parabolic load with fill-in

$$\sigma_{rr|max} = \sigma_{\theta\theta|max} = 6g\left(\frac{\ell}{H}\right)^2 (\rho-\rho_o)h(1+\nu)\cdot$$

$$\left[\text{kei}\left(\frac{A}{\ell}\right) + \frac{2}{a}\ \text{ker}'\left(\frac{A}{\ell}\right) + \frac{2}{a^2}\right] \qquad (13b)$$

and for A=60 km and other parameters as in table 1

$$\sigma_{max} \simeq 1.9h \text{ kbar} \qquad (14c)$$

and for the no fill-in case

$$\sigma_{max} \simeq 1.0h \text{ kbar}. \qquad (14d)$$

As the radius R_A increases $\sigma_{rr|max}$ and $\sigma_{\theta\theta|max}$ under the center of the load reach an isostatic limit of $(\rho-\rho_o)gh$ when R_A is of the order of 4ℓ. The maximum deviatoric stresses now occur towards the edge of the load. Seamounts are generally much smaller than this, and the maximum stress-differences occurring in the plate are given by (13), if other aspects of the above model are valid. As D decreases the magnitudes of the stresses also decrease and the maximum stresses occur near the edge of the load. Figure 4 illustrates some examples.

Gravity and geoid anomalies

The principal geophysical evidence for the regional compensation of seamounts has been gravity, and estimates for the flexural rigidity of the plate have been deduced mainly by matching the model with gravity observations in either the spatial domain (e.g. Walcott, 1970; Watts and Cochran, 1974) or in the frequency domain (e.g. Watts, 1978). More recently it has been possible to compare these models with observations of the geometric form of the geoid (e.g. Cazenave et al. 1979).

The gravity and geoid anomalies over seamounts are a consequence of several lateral density anomaly sources associated with (1) the load itself, of effective density $\rho-\rho_o$ (in realistic models the load will be quite complex in its density structure), (ii) the fill-in,

of density ρ_f in the fill-in case or of density ρ_o in the no-fill case, (iii) the deformation of surfaces of equal density within the plate due to the bending, particularly the interface between ocean crustal layers 2 and 3 and layer 3 and the mantle, (iv) compression of material under the load, (v) an eventual density contrast at the base of the elastic plate. The base of the plate will usually be defined as an isotherm and there will be no density discontinuity here. The density of the fill-in is usually very similar to that of the upper ocean crust while compression effects can probably be ignored. Thus the main contribution to gravity, Δg, or geoid anomalies come from (i) and (iii).

The above-used axisymmetric loads lend themselves to relatively simple analytical expressions for the perturbations in gravity and in geoid height. Consider a homogeneous mass bounded by a surface $z=z(r)$ and the plane $z=0$. The gravity perturbation at $P_o(r_o, \alpha=0, z_o)$ due to a mass element of this load at $P(r,\alpha,z)$ is

$$\delta g = -G\rho \int_{r=0}^{\infty} \int_{\alpha=0}^{2\pi} \int_{z=0}^{z(r)} \frac{(z_o-z)\,dz\; r\,dr\; d\alpha}{[r^2+r_o^2-2rr_o\cos\alpha + (z_o-z)^2]^{3/2}}.$$

Integrating, first over z and then over α,

$$\delta g = 4G\rho \int_{r=0}^{\infty} \frac{K(\frac{\pi}{2}, m)}{[(r+r_o)^2 + (z-z_o)^2]^{1/2}} \Bigg|_{z=0}^{z(r)} r\,dr, \qquad (15)$$

where $K(\pi/2,m)$ is a complete elliptic integral of the first kind with modulus

$$m = \frac{4rr_o}{(r+r_o)^2 + (z-z_o)^2}.$$

The elliptic integrals can be expanded into series for $0 \leq m < 1$ (e.g. Abramowitz and Segun, 1968; p.591) and the gravity perturbation is integrated numerically for different shapes of the boundary $z=z(r)$. The geoid heights, for the plane approximation, follow from

$$N = \frac{1}{2\pi g} \int_{r=0}^{\infty} \int_{\alpha=0}^{2\pi} \frac{\delta g\; r\; dr\; d\alpha}{[r_o^2+r^2-2rr_o\cos\alpha]^{1/2}} \qquad r \neq r_o$$

or, because δg is a function of r only,

$$N = \frac{2}{\pi g} \int_{r=0}^{\infty} \frac{K(\frac{\pi}{2}, n)\delta g}{r+r_o} \, r \, dr \qquad (16a)$$

where $n = 4rr_o/(r+r_o)^2$. Strictly the gravity anomaly,

$$\Delta g = \delta g - \frac{2g}{R} N,$$

should be introduced into the above integral instead of the gravity perturbation δg. Either an interative procedure can be adopted to solve for N from δg, or the geoid height term is simply ignored since its contribution is small in the present problems. N does not exceed about 10m and $\Delta g - \delta g \simeq 3$mgal. Since $\lim_{r \to r_o} K \to \infty$, the inner zone effects of the above integrals are evaluated by a limiting process

$$N(r_o) = \frac{\varepsilon \, \delta g \, (r_a)}{g} + \frac{2}{\pi g} \int_{0}^{r \gtrless r} \frac{K \, \delta g \, r \, dr}{r+r_o} \, , \qquad (16b)$$

where ε is the size of the inner zone area. Equations (16) are integrated numerically using trapezoidal and Ramberg rules.

Figure 1 illustrates the gravity anomalies over the nominal disc loads. In the fill-in model, the gravity perturbation is the sum of the short wavelength positive Bouguer correction and the broad wavelength negative anomaly associated with the density contrasts within the crust and with the crust-mantle interface. The resultant profiles are quite typical of gravity anomalies seen over many seamounts and provide the main observational evidence in support of the elastic plate model. The no fill-in case gives a similar gravity anomaly except that the negative anomaly is due to (i) the density contrast in the crust and at the crust-mantle interface, effects that now are less than before since the deformation is reduced in both magnitude and wavelength, and (ii) the nearer-the-surface crust-water interface. The total anomaly is not very different from the fill-in case.

A number of other general observations on the gravity anomalies follow directly from Figure 1. For a given load and crustal model, the increase in flexural rigidity will result in a decrease in amplitude and an increase in wavelength of the anomaly. Figure 5a

illustrates some examples for the same load and crustal model as in Figure 1. A reduction in D by one order of magnitude reduces δg by about 50 mgal and increases the width of the negative anomaly by about 100km although the magnitudes of the negative anomalies do not differ by more than about 20mgal. The effect on gravity of a change in density contrast $\Delta\rho$ between the load and mantle is even less marked (Figure 5b). A decrease in $\Delta\rho$ results in a significant increase in the deflection but the change in gravity due to two competing effects, the increase in the deflection and a decrease in density contrast, is slight.

The characteristics of the gravity anomalies suggest that a comparison in the frequency domain may be more helpful in discriminating between the various models, using, for example, the linear transfer function techniques developed in applied geophysics. These models have been applied with some success in a number of recent studies of the Earth's gravity field (e.g. Dorman and Lewis, 1970; McKenzie and Bowen, 1976; Watts, 1978). In so far as the bathymetry is an invariant in the present models we considered only the Fourier spectrum of the gravity anomalies (e.g. Figure 6). The spectra for the disc loads are not very sensitive to D and $\Delta\rho$.

These results, explored further below, indicate that the discriminatory power of gravity anomalies depends rather strongly on the fine detail, both amplitude and wavelength, of the gravity signal, a detail that will frequently be lost amongst the observational and geological noise of the data. As also indicated in Figure 5, the stresses differ quite significantly from one model to the next, confirming that not only is gravity a poor indicator of deformation (i.e. of w) but also of stress.

Physical properties of the ocean lithosphere

In so far as the previous results have shown that gravity anomalies are not very sensitive to several physical parameters but that stress is, an appraisal of relevant parameters is appropriate.

Rheology

The Flexural rigidity defined by (11.a) is a function of the elastic parameters λ and μ or E and ν and are normally deduced from seismic velocities. The actual response of the lithosphere can be considered as an initial elastic response followed by creep or, very generally

$$\varepsilon = \frac{\sigma}{2\mu} + \frac{\sigma}{2\eta} f(t) \qquad (17a)$$

where σ is the applied deviatoric stress and η the viscosity which itself may be stress dependent. Since loading takes place over a finite time, typically of the order of 10^6 years, the relaxed modulus rather than the unrelaxed modulus, measured at seismic frequencies, is an appropriate choice for μ, and Anderson and Minster (1979) propose a reduction of about 50%. The corresponding elastic parameters given in table 1 are based on this assumption. As the bulk modulus is little affected by these dispersion effects both λ and ν will increase.

In the plate model used above the viscous element is ignored and strain is described by

$$\varepsilon = \sigma/2\mu^* \qquad (17b)$$

where μ^* is an apparent or equivalent rigidity. Equating this with (17a) gives

$$\mu^* = \frac{\mu}{1 + \frac{\mu}{\eta} f(t)} . \qquad (18)$$

In the upper crust the response will be dominated by the elastic term of (17a). Also μ^* can be expected to increase with depth due to the effects of (i) the increasing confining pressure, (ii) possibly a decrease in water content, and (iii) compositional changes, particularly in the passage from the ocean crustal layer 2 to layer 3. At some depth, due to increasing temperatures, the flow term will become dominant and

$$\mu^* = \frac{\eta}{f(t)} .$$

In so far as η will be temperature dependent through the general creep law

$$\dot{\varepsilon} = A\sigma^n \exp[-(E^* + PV^*)/RT] \equiv \frac{\sigma}{\eta} \qquad (19)$$

the apparent rigidity μ^*, will be depth dependent. A schematic variation of μ^* with depth is illustrated in figure 7 where an ad-hoc transition from elastic to plastic flow has been introduced. Laboratory experiments suggest that flow will be the dominant deformation mechanism at temperatures exceeding about one half the melting

point temperature but in geological situation flow is likely to occur at much lower temperatures (e.g. Carter, 1976). Also much of the experimental results are based on geological materials not appropriate for the oceanic crust and perhaps not even for the upper mantle. The most significant experimental results are based on olivine single crystals or on dunite aggregates but while Othello would like the Earth to consist of a single perfect crystal, the actual Earth is undoubtedly more complex. Recent results on Websterite indicate that at relatively shallow depths, <60km, the equivalent viscosities are less than those of dry dunite (Ave' Lallemant, 1977). The problems of scaling from the laboratory measurements to the geological problems are such that the experimental results can, for the present purposes, only be considered as gross upper-limits and while the scale of μ^* cannot be established, the trend of μ^* in figure (7) can be anticipated to reflect conditions in the lithosphere.

The variation of the bulk modulus with depth can be expected to be much less than that of μ so that the function $F \equiv E/(1-\nu^2)$ will exhibit a similar variation with depth. Mathematically, this depth dependence is conveniently represented by the error function

$$F = F_o e^{-a[(z-z_o)/z_o]^2} \tag{20a}$$

where, as before, z is measured with respect to the mid-plane of the undeformed equivalent plate and z_o is the value of z at which the maximum F_o is attained. With (11a) and (20a) the flexural rigidity becomes

$$D = \frac{F_o}{12} \int_{-H/2}^{\infty} z^2 e^{-a[(z-z_o/z_o]^2} dz. \tag{20b}$$

If the maximum value of F is assumed to occur at some z_o, typically at a depth of about 5 km, or the middle of ocean layer 3, and we equate (20b) with the observed flexural rigidity, we obtain an estimate of F_o. Alternatively we can fix F_o and determine z_o. Once these parameters are known the stresses follow directly from equations (12). That is, writing σ_{rr}, as

$$\sigma_{rr} = -\sigma_o(z) \left(\frac{d^2w}{dr^2} + \frac{\nu}{r}\frac{dw}{dr}\right),$$

and similarly for the other stresses, we obtain

$$\sigma_o(z) = F_o z e^{-a[(z-z_o)/z_o]^2} \tag{21a}$$

as compared with

$$\sigma_o(z) = -F_o' z \tag{21b}$$

where F_o' is the depth independent value for the equivalent plate. The implications of (21) are immediately obvious in that the maximum stress-differences can be confined to the upper and cooler part of the plate and will be significantly reduced at the lower depths, where temperatures are higher and the material is less resistant to flow deformation. The analytical evaluation of (20b) and the solution for the parameters is cumbersome and for the present purposes we approximate (20a) by a parabolic function

$$F = F_o[A + B\,(\tfrac{z}{H}) + C\,(\tfrac{z}{H})^2]. \tag{22a}$$

With (11a)

$$D = \frac{F_o}{4} H^3\,(\frac{A}{3} + \frac{C}{20}). \tag{22b}$$

Figure 8 illustrates an example in which $E=0.75E_o$ at the surface $z=-H/2$ and $E=E_o$ at $z=-H/4$. The constants are

$$A = \frac{23}{24}, \qquad B = -\frac{9}{12}, \qquad C = -\frac{7}{3}$$

and

$$D = 0.61\,\frac{E_o}{12(1-\nu_o^2)} H^3.$$

If this is compared with (11a), and the same elastic parameters are adopted, the plate with variable rigidity will be somewhat thicker than the uniform plate. With (22a)

$$\sigma_o(z) = -\frac{E_o}{1-\nu_o^2}\,(A + B\,(\tfrac{z}{H}) + C(\tfrac{z}{H})^2)z \tag{23a}$$

which compares with

$$\sigma_o(z) = - \frac{E_o}{1-\nu_o^2} \qquad (23b)$$

for the uniform plate. Figure 8 illustrates σ_o as a function of depth. While this model does not have the more attractive characteristics of the error function model (20) it does illustrate clearly that the stresses in the plate can be quite significantly reduced by introducing a depth dependent rheology. In this particular case the reduction is by a factor of 2.5 near the base of the plate.

The stress dependence of the flexural rigidity follows directly from the flow law (19) and the apparent rigidity (18) and in the domain where deformation is mainly by creep

$$\mu^* = \frac{\sigma^{-(n-1)}}{A \; f(t)} \exp[(E^* + PV^*)/RT].$$

The effective flexural rigidity will exhibit a similar stress dependence. Thus if σ is increased the effective D is decreased and the apparent plate thickness will be decreased, and large loads should give thinner elastic thicknesses than small loads, all other parameters being equal. Equivalently, in terms of the flexural rigidity function (21a) large loads will result in a shallower z_o than small loads, as is schematically illustrated in Figure 8.

The time dependence of the effective flexural rigidity is also obvious from (18), with time D decreases according to $f^{-1}(t)$. Typically $f(t) \sim t^{\alpha}$ where α varies from 0.25 to 0.3, or $f(t) \sim \ell n(t)$ but in both cases the time dependence of D will be compounded by the thermal evolution of the lithosphere (Watts, 1978; Cazenave et al., 1979).

Crustal densities

The models in the preceding sections have also demonstrated the importance of the choice of crustal densities and layer thickness. The flexure estimates for the elastic thickness are of the order of a few tens of kilometers and this suggests that the plate can be largely assimilated with the crust and uppermost part of the mantle. Broadly speaking, the oceanic crust can be characterized by a three layer model although considerable regional variation in crustal structure occurs from one location to the next. Figure 9a illustrates

a number of models of seismic velocities. Models 1 to 3 are average models due to Raitt (1963), Christensen and Salisbury (1975) and Woollard (1975) and there is a general consensus of (i) layer 1, a thin (a few hundred meters) sedimentary layer, (ii) layer 2, of about 1.5-2 km thickness of average V_P velocity ranging from 4.6 to 5.1 km s^{-1}, (iii) layer 3, of about 5 km thickness with a velocity ranging from 6.4 to 6.7 km s^{-1}, (iv) an upper mantle of velocity of about 8.2 km s^{-1}. Some regional models (models 3 and 4 in Figure 9a) suggest that layer 3 may be divided into two parts but there is no universal agreement on this. Layer 2 is believed to consist mainly of unconsolidated basalts possessing considerable porosity and subjected to large scale fracturing, submarine weathering and intercalated with sediments. Seismic velocities for the basalts, as determined in the laboratory, are of the order 5.3-5.8 km s^{-1} and densities are of the order 2.60-2.75 gcm^{-3}. In-situ densities may be somewhat less than this. Ocean layer 3 is believed to be mainly of mafic composition of metagabbro and gabbro whose seismic velocities range from about 6.5 to 7.2 km s^{-1} and whose densities range from about 2.8 to 3.0 (e.g. Christensen, 1977). The mantle velocities correspond approximately to that of peridotites with densities in the range 3.25-3.40 gcm^{-3}. To simplify the gravity calculations, layers 1 and 2 have been combined into an equivalent layer of the same thickness but of a depth weighted density. Likewise the two layers making up layer 3 in models 4 and 5 have been combined. Figure 9b illustrates the adopted density models. Model 1 corresponds to the average model of Raitt (1963) and is similar to that deduced from the other averaged models. Model 2 corresponds to one of the regional models of Christensen and Salisbury (1975) (model 2 of Figure 9a). When averaged in the above-mentioned manner, this model does not differ greatly from density model 1. Added to this is model 3, deduced from figures given by Watts and Cochran (1974) and used by them in their analyses of the Hawaiian-Emperor seamounts, and model 4, used by Watts (1978) in a more recent study of these seamounts. These models differ from the others in that layer 2 has been given a higher density than would be expected from the seismic evidence. Watts' model also gives a thinner layer 3 and a higher mantle density than some of the other models.

Finally, one requires an estimate of the density of the load. An appropriate choice seems to be in the range 2.65-2.75 in that the volcano is presumably similar in composition to the basaltic layer 2 but freer from the various factors that appear to decrease the density of the in-situ layer 2 materials. Possibly the central region is of

higher density and clearly the density of the load may exceed that of the crust upon which it immediately rests.

Discussion

Figure 10 illustrates the deflections, stress σ_{rr}, Bouguer gravity perturbation and total geoid anomaly for the constant geometry (R_n=60 km, h=4 km) disc loads with density, ρ_2, equal to that of layer 2. The adopted flexural rigidity is 5×10^{29} dyne-cm. The maximum deflection for these models is determined by $\rho_m - \rho_2$ and the two illustrated examples are for density models 1 and 3, with model 1 resulting in deflections that are about 50% of that of model 3. Density models 1 and 2 give very similar results while model 4 gives deflections that are about 80% of that of model 3. If, in model 1, the mantle density is increased to 3.4 gcm^{-3}, deflections will be decreased by about 10%. If the volcanic load, including the part below the surface z=0, is of higher density than the fill-in, the deflections will lie between those corresponding to models 1 and 3. Similar results for the deflection and σ_{rr} are illustrated for the equivalent parabolic load.

As expected from the earlier results, the stresses in the plate are quite different for density model 3 than for model 1, $\sigma_{rr/max}$ ranging from nearly 8 kbars for the former to about 12 kbars for the latter, for both the disc and parabolic loads. For a load of density 2.8 gcm^{-3} and fill-in density of 2.4 gcm^{-3}, the maximum stress is of the order of 10 kbars for these particular load geometries.

The lower part of figure 10 illustrates the gravity anomalies and geoid heights for the two density models. The Bouguer anomalies in the spatial domain are almost indistinguishable from each other for all four density models considered here, and their theoretical spectra also differ only marginally: any differences would probably be very minor in real situations of noisy data, irregular geometries, and variations in density within the load. These results indicate once again that the gravity anomalies are not very sensitive to the crustal densities but that the stresses are, and that a significant stress reduction can be obtained if the density of fill-in is taken to be of the order 2.3-2.4 gcm^{-3} instead of the usual but improbable 2.8 gcm^{-3}. If the fill-in is not complete, as seems to be the case

for the Hawaiian chain, the gravity anomalies will not differ very significantly from the case of complete fill-in (Figure 1) but the stresses will be further reduced. The introduction of an inelastic response for the lower part of the layer reduces the stresses near the lower surface of the plate and a very significant reduction can be achieved there. This also introduces both a stress and a time dependence of the response that needs closer investigation.

Watts (1978) computed the deflections for the Hawaiian-Emperor seamounts, for a number of profiles for which both gravity and bathymetry have been observed. The largest topographic load analysed, Oahu, can be approximated by an equivalent disc load of radius about 60 km at its base and a height of about 4 km above the average seafloor. Density model 4 has been used by Watts. He obtains, from two profiles, $D \sim 2.66 \times 10^{30}$ dyne-cm. This is larger than that used in the above calculations by a factor of 5. The corresponding maximum deflection for this load and density model will be about 2.2 km. If the fill-in is of a density less than 2.8, this deflection will be reduced to about 70% of this value, or less if the fill-in is not complete, as appears to be the case. Possibly as much as 1 km of unfilled moat remains if the top of the undeformed plate is taken to be the broad regional swell, characteristic of this Pacific region. Thus the total deflection may not exceed about 2 km below Oahu.

Seismic refraction observations for a thickening of layer 2 about the Hawaiian seamounts remains inconclusive. Models for the crust below Oahu indicate a rapid increase of crustal thickness but the seismic model of Furumoto et al. (1968) is much more indicative of local compensation than of regional compensation. A thickening of the crust is generally noted below the major islands (Furumoto et al. 1971), but the results do not appear to be very consistent from one refraction profile to the next.

Using Watt's parameters, the inferred maximum stress below the center of the load is of the order 5 kbars (equation 13b). If the density model 1 is adopted, implying that the gravity data is insensitive to the crustal model (figure 6), this stress is reduced to about 3.5 kbars. A further reduction may result if the fill-in is incomplete to about 2.5-3 kbars. Finally, if the apparent shear modulus is depth dependent according to (22), the maximum stresses σ_{rr}, $\sigma_{\theta\theta}$ on the upper surface are further reduced, to about 2-2.5 kbars

(Figure 8). The vertical stress σ_{zz} (equation 12d) is of the order of about 1 kbar at this surface and all stresses are compressive. Hence the maximum stress-difference on the upper surface beneath the load is of the order of 1-1.5 kbar. The maximum stress differences near the base of the plate can be reduced much more and need not exceed a few hundred bars or even less, in keeping with basalt shear stresses of the order of 100 bars that have been suggested for driving plate tectonics and with estimates by Crittenden (1967), from the Bonneville uplift, that stress-differences below the continental crust are less than 100 bars.

In summary, rules such as (14) may grossly overestimate the maximum stress-differences that occur in the plate below the seamounts and actual values need not exceed 1-3 kbars. If compensation is partly local, as suggested by Furumoto et al. (1971) then the stress-differences will not differ much from the simple ρgh formula for local isostatic compensation. These stresses are valid for loads that have persisted for up to 10^8 years, and they are not inconsistent with the estimate by Lambeck (1979) of about 500 bars, based on the analysis of global isostasy where loading times may be much longer.

REFERENCES

Abramowitz, M. and Segun, I.A., 1965. Handbook of Mathematical Functions, Dover Publ.Co., New York.

Anderson, D.L. and Minster, J.B., 1979. Seismic velocity, attenuation and rheology of the upper mantle, (This volume).

Ave'Lallemant, H.G., 1977. Experimental deformation of clinopyroxene, Trans.Am.Geophys.Un., EOS, 58, 513, (abstract).

Brotchie, J.F., 1971. Flexure of a liquid-filled spherical shell in a radial gravity field, Modern Geology, 3, 15-23.

Brotchie, J.F. and Silvester, R., 1969. On crustal flexure, J.Geophys.Res., 74, 5240-5252.

Carter, N.L., 1976. Steady state flow of rocks, Rev.Geophys. Space Phys., 14, 301-360.

Cazenave, A., Lago, B., Dominh, K. and Lambeck, K., 1979. On the response of the ocean lithosphere to seamount loads from GEOS 3 satellite radar altimetry observations, Submitted to Geophys.J.Roy.Astron.Soc.

Christensen, N.I., 1978. Ophiolites, seismic velocities and oceanic crustal structure, Tectonophysics, 47, 131-157.

Christensen, N.I. and Salisbury, M.H., 1975. Structure and constitution of the lower oceanic crust, Revs.Geophys.Space Phys., 13, 57-86.

Crittenden, M.D., 1967. Viscosity and finite strength of the mantle as determined from water and ice loads, Geophys.J. Roy.Astron.Soc., 14, 261-279.

Dorman, L.M. and Lewis, B.T.R., 1970. Experimental isostasy. I., J.Geophys.Res., 75, 3357-3365.

Frederick, D., 1956. On some problems in bending of thick circular plates on an elastic foundation. J.Appl.Mech., 23, 195-200.

Furumoto, A.S., Woollard, G.P., Campbell, J.F. and Hussong, D.S., 1968. Variations in the thickness of the crust in the Hawaiian Archipelago, in The Crust and Upper Mantle of the Pacific Area, Am.Geophys.Un., Geophysical Monograph 12, 94-111.

Furumoto, A.S., Campbell, J.F. and Hussong, D.M., 1971. Seismic refraction surveys along the Hawaiian ridge, Kauai to Midway Island, Bull.Seism.Soc.Am., 61, 147-166.

Gunn, R., 1943. A quantitative study of isobaric equilibrium and gravity anomalies in the Hawaiian Islands, J.Franklin Inst., 238, 373-396.

Hertz, H., 1895. Uber das gleichgewicht schwimmender elasticher platten, Gesammelte Werke von Heinrich Hertz, Volume 1, 288-294, Leipzig.

Lambeck, K., 1979. Estimates of the finite strength of the lithosphere from isostatic considerations, (This volume).

McKenzie, D.P. and Bowin, C., 1976. The relationship between bathymetry and gravity in the Atlantic Ocean, J.Geophys.Res., 81, 1903-1915.

Raitt, R.W., 1963. The crustal rocks, in The Sea, 3, edited by M.N. Hill, 85-102, J. Wiley, New York.

Reisner, E., 1944. On the theory of bending of elastic plates, J.Math.Phys., 23, 184-191.

Reisner, E., 1946. Stresses and small displacements of shallow spherical sheels, J.Math.Phys., 25, 279-300.

Timoshenko, S.P. and Woinowsky-Krieger, S., 1959. Theory of Plates and Shells, McGraw Hill, New York, 580 pp.

Vening Meinesz, F.A., 1941. Gravity over the Hawaiian Archipelago and over the Medeira area, Proc.K.Ned.Akad.Wet., 44, 1-12, 1941.

Walcott, R.I., 1970. Flexural rigidity, thickness and viscosity of the lithosphere, J.Geophys.Res., 75, 3941-3954.

Walcott, R.I., 1976. Lithospheric flexure, analysis of gravity anomalies and the propagation of seamount chains, in The Geophysics of the Pacific Ocean Basin and Its Margin, Amer. Geophys.Union Monograph, 19, 431-438.

Watts, A.B., 1978. An analysis of isostasy in the World's Oceans, 1. Hawaiian-Emperor Seamount Chain. J.Geophys.Res., 83, 5989-6004.

Watts, A.B. and Cochran, J.R., 1974. Gravity anomalies and flexure of the lithosphere along the Hawaiian-Emperor seamount chain, Geophys.J.Roy.Astron.Soc., 38, 119-141.

Woollard, G.P., 1975. The interrelationships of crustal and upper mantle parameter values in the Pacific. Revs.Geophys.Space Phys., 13, 87-137.

Parameter	Value in c.g.s.
Rigidity μ	3.67×10^{11}
Lamé constant λ	9.45×10^{11}
Young's modulus E	1.0×10^{12}
Poisson's ratio $\nu = \lambda/2(\lambda+\mu)$	0.36
Thickness of lithosphere H	1.76×10^{6}
Flexural rigidity $D = \frac{\mu}{3} \frac{(\lambda+\mu)H^3}{\lambda+2\mu}$	0.5×10^{30}
"radius of relative stiffness" ℓ	5.37×10^{6}
density of substratum ρ_s	3.3
effective density of load ρ	1.8

TABLE 1. Lithospheric parameters adopted in the deflection and stress calculations for the results illustrated in figures 1 to 4.

FIGURE CAPTIONS

Figure 1. Deflections, stress and gravity perturbations for disc and equivalent parabolic loads of density equal to the fill-in density (left hand side). The right hand side is for a disc load without sediment fill-in and the moat is filled with water. The gravity perturbations are for the disc loads only and the several contributions to gravity are shown.

Figure 2. Deflections of the elastic plate of flexural rigidity D due to a disc load of variable radius A and height h. The depressed surface is filled with sediments of density equal to that of the load.

Figure 3. Deflections of the elastic plate for different flexural rigidities and a constant load above the level of sediment fill-in.

Figure 4. a) Maximum stresses σ_{rr} and $\sigma_{\theta\theta}$ occurring in a plate loaded by a disc of radius A and height h. All parameters are as in Table 1.

b) Maximum stresses σ_{rr}, $\sigma_{\theta\theta}$ for plates of different D.

Figure 5. Left. Deflections, stress and gravity anomalies for the disc load on a plate of variable flexural rigidity ($D=5\times10^{28}$; $2, D=5\times10^{29}$; $3, D=5\times10^{30}$ dyne-cm) all other parameters are as in table 1.

Right. Deflections, stress and gravity for the disc load with variable density $\rho_m-\rho_c$ ($1, \Delta\rho=0.2$; $2, \Delta\rho=0.5$; $3, \Delta\rho=0.6$ gcm^{-3}). All other parameters are as in table 1.

Figure 6. Power spectra of the gravity anomalies corresponding to the models in Figure 5 for (a) variable D and (b) variable $\Delta\rho$.

Figure 7. Schematic variation with depth of the "apparent" shear modulus μ^* (equation 18). As the stress increases the lower part of the curve moves to the left (curve 2) and intersects the elastic response curve nearer the surface resulting in a stress dependent flexural rigidity.

Figure 8. Variation of $E/(1-\nu^2)$ with depth according to equations (22a) (upper figure) and the variation of the stress factor σ_o with depth (lower figure).

Figure 9. Summary of ocean crustal models discussed in text. Figure 9a summarizes seismic V_P velocities and figure 9b summarizes densities.

Figure 10. (Left) Deflections, stress σ_{rr}, Bouguer gravity perturbation and geoid height for crustal density models 1 and 3 subjected to a disc load and fill-in of density equal to load density.

(Right) Deflections and stress σ_{rr} for the parabolic load.

(Lower Right) Power spectra of the Bouguer gravity anomalies for the disc load.

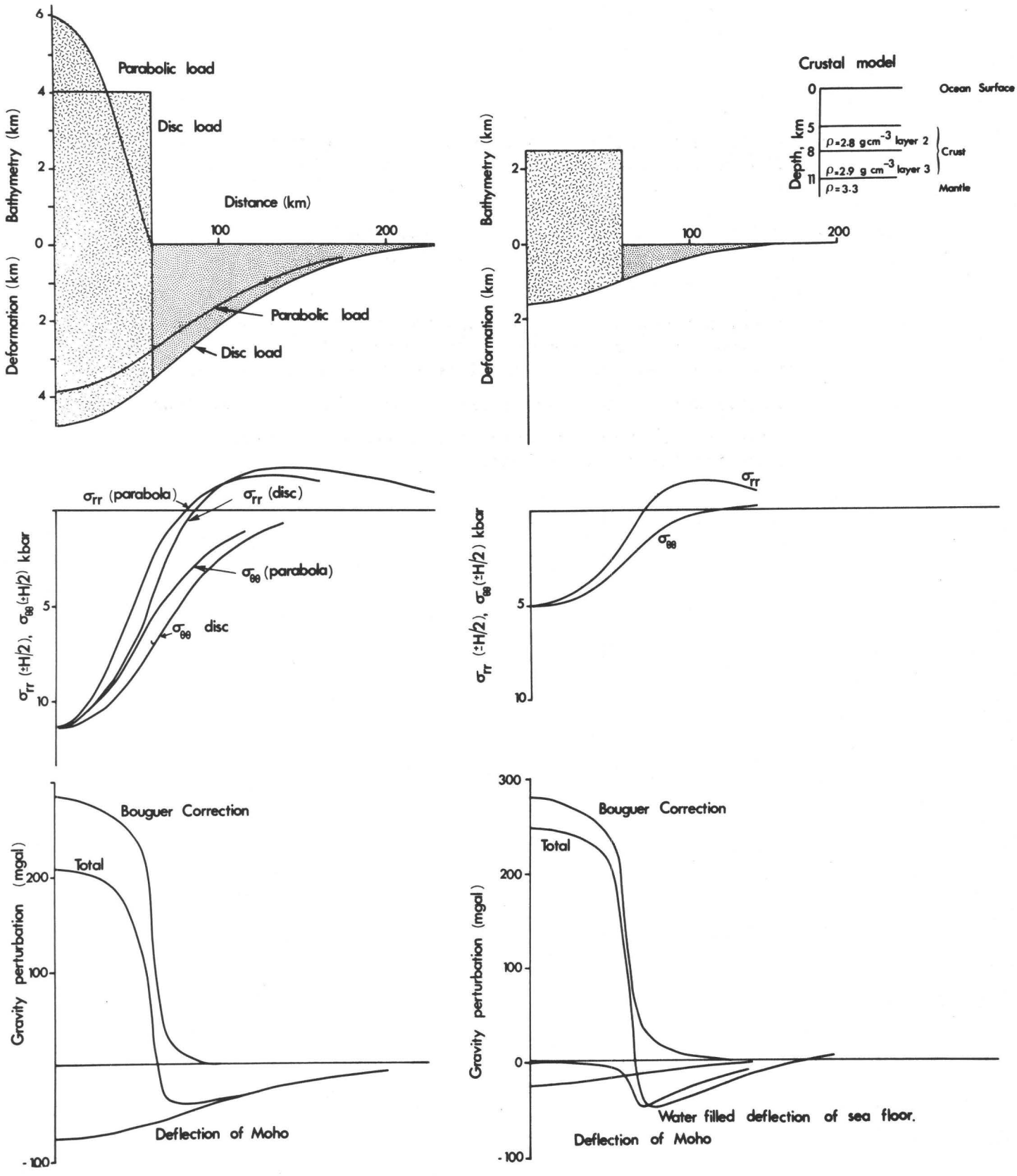
Parabolic load
Disc load
Distance (km)
Bathymetry (km)
Deformation (km)
Parabolic load
Disc load
Crustal model
Ocean Surface
Depth, km
ρ=2.8 g cm⁻³ layer 2
Crust
ρ=2.9 g cm⁻³ layer 3
ρ=3.3
Mantle
σrr (parabola)
σrr (disc)
σθθ (parabola)
σθθ disc
σrr (±H/2), σθθ(±H/2) kbar
σrr
σθθ
Bouguer Correction
Total
Gravity perturbation (mgal)
Deflection of Moho
Water filled deflection of sea floor.

Figure 1.

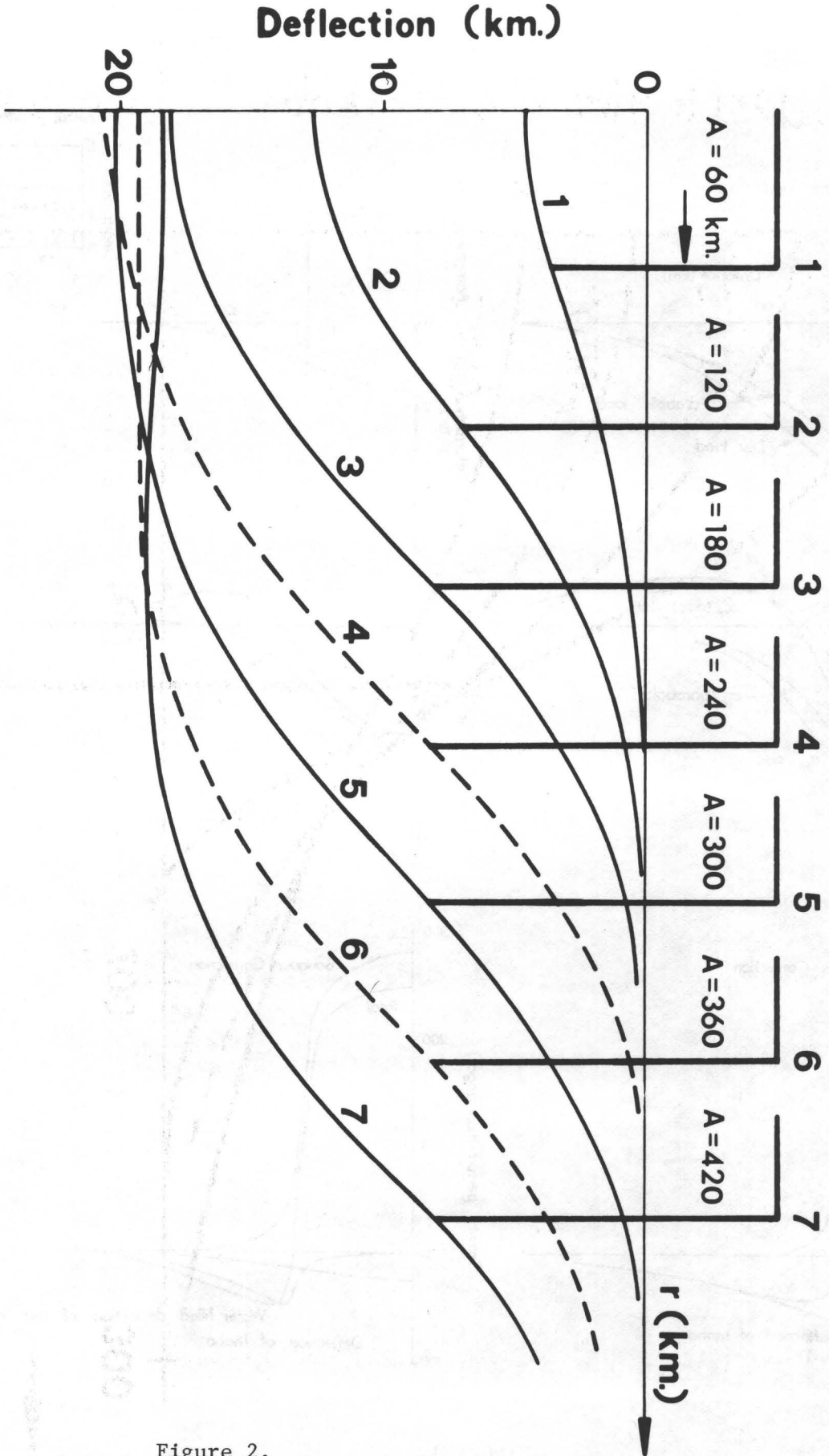
Deflection (km.)
20
10
0
A = 60 km.
A = 120
A = 180
A = 240
A = 300
A = 360
A = 420
1
2
3
4
5
6
7
r (km.)

Figure 2.

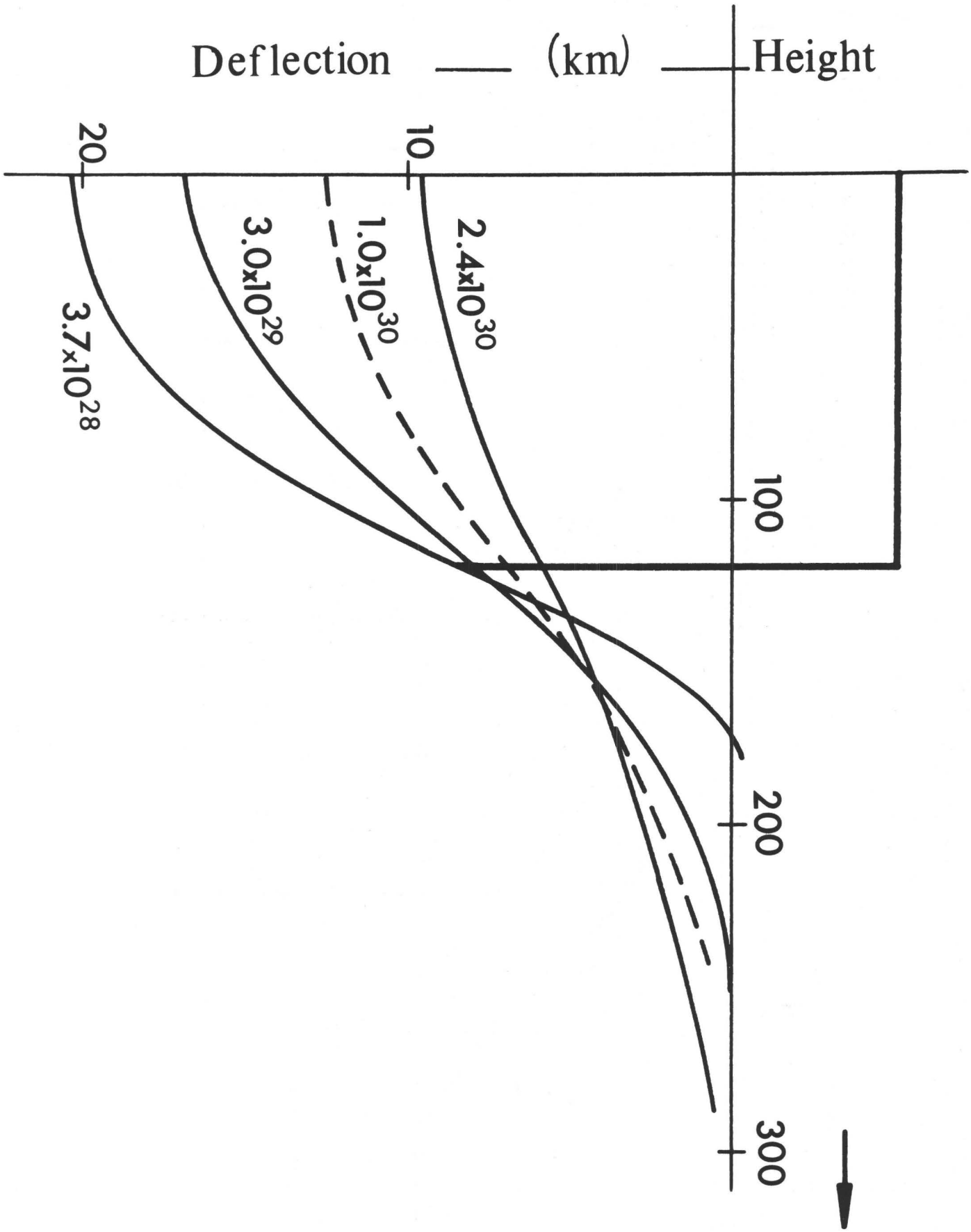
Deflection
(km)
Height
20
10
100
200
300
3.7x10^28
3.0x10^29
1.0x10^30
2.4x10^30

Figure 3.

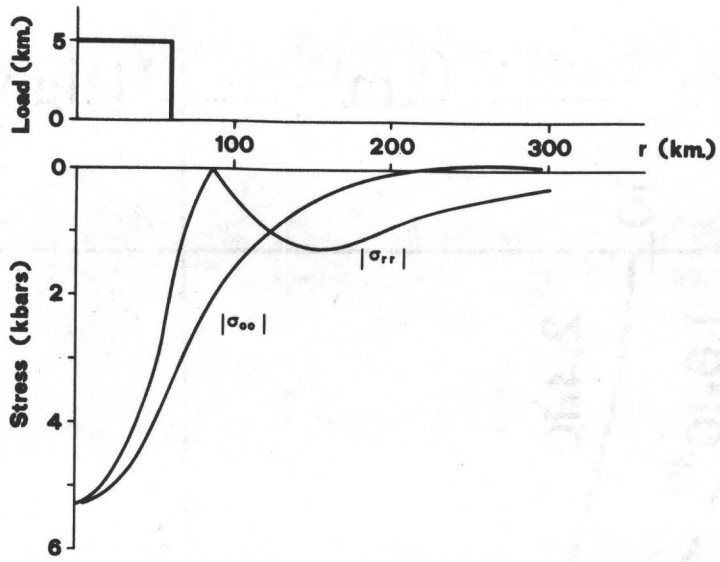
Load (km.)
5
0
100
200
300
r (km.)
0
2
4
6
Stress (kbars)
$|\sigma_{rr}|$
$|\sigma_{\theta\theta}|$

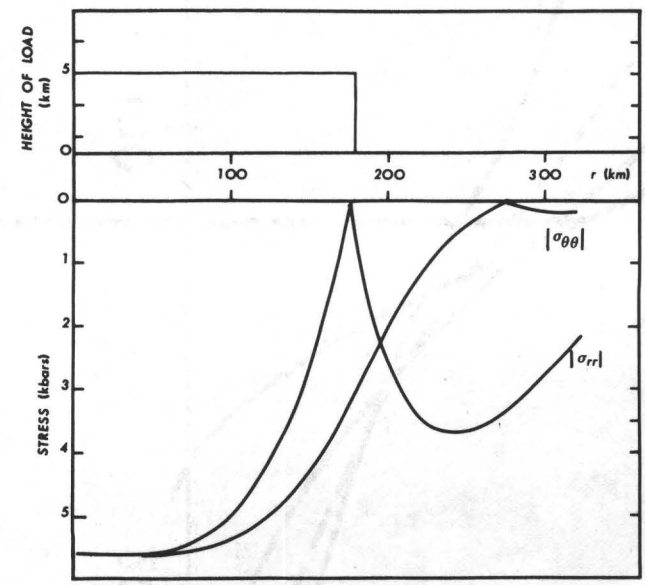
HEIGHT OF LOAD (km)
5
0
100
200
300
r (km)
0
1
2
3
4
5
STRESS (kbars)
$|\sigma_{\theta\theta}|$
$|\sigma_{rr}|$

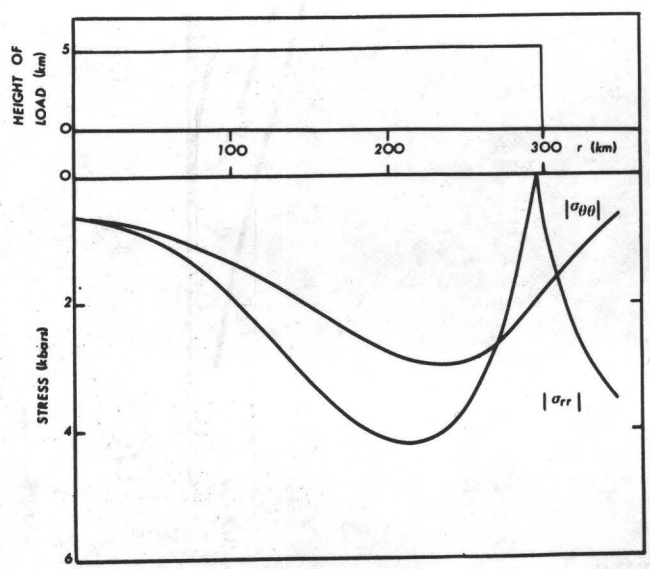
HEIGHT OF LOAD (km)
5
0
100
200
300
r (km)
0
2
4
6
STRESS (kbars)
$|\sigma_{\theta\theta}|$
$|\sigma_{rr}|$

Figure 4a.

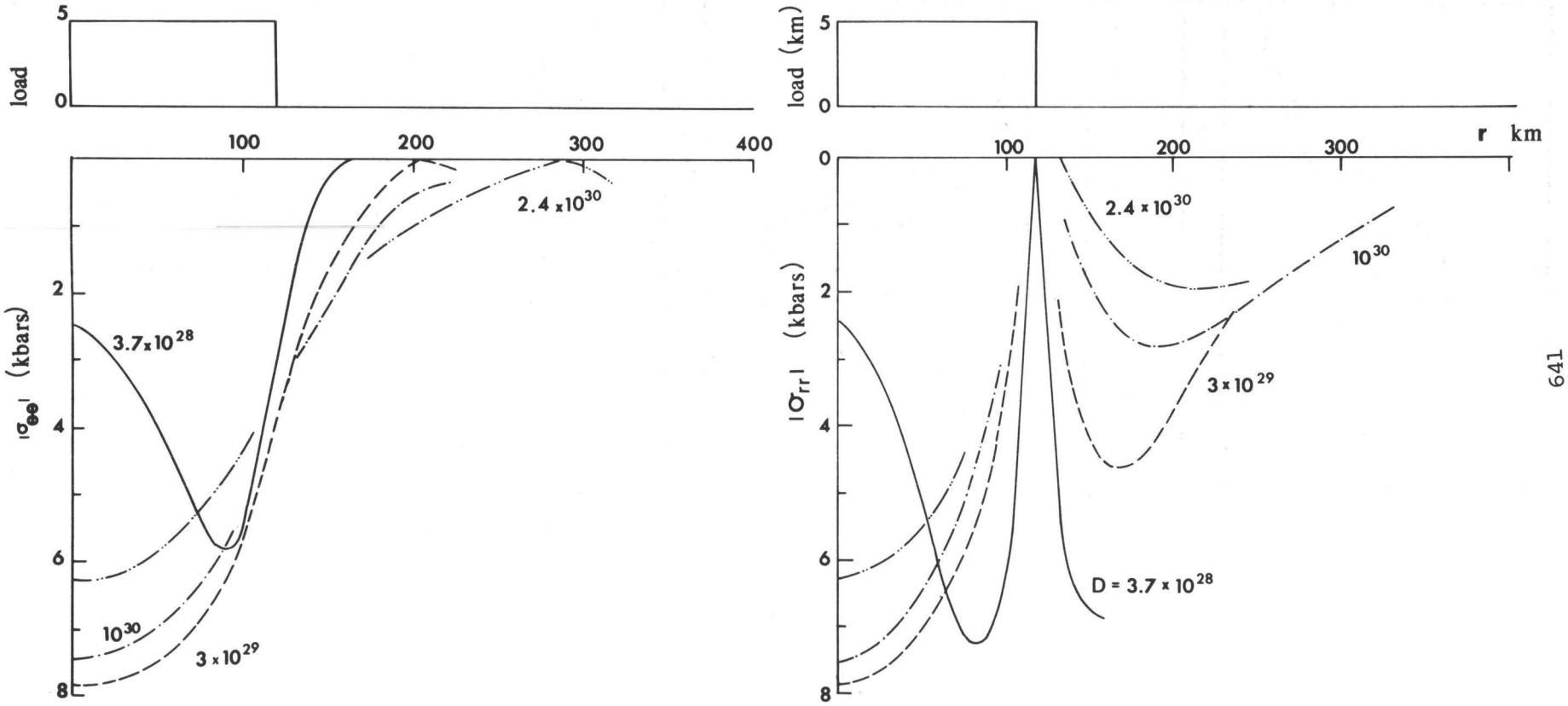
load
5
0
100
200
300
400
2.4 x10^30
3.7x10^28
10^30
3 x10^29
|σee| (kbars)
2
4
6
8
load (km)
r km
2.4 x 10^30
10^30
3 x 10^29
D = 3.7 x 10^28
|σrr| (kbars)

Figure 4b.

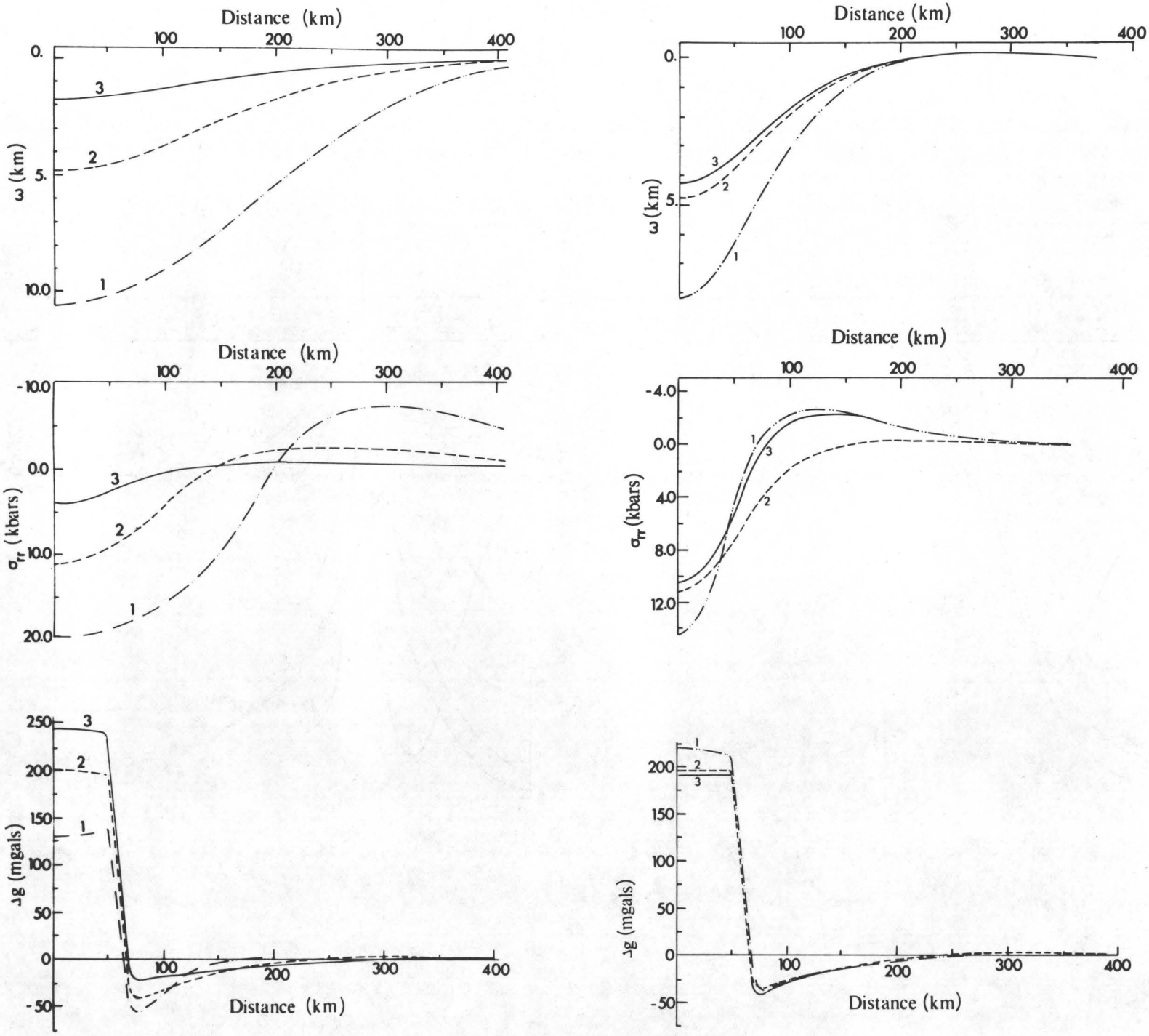
Distance (km)
100
200
300
400
0.
5.
10.0
ω (km)
3
2
1
Distance (km)
100
200
300
400
0.
5.
ω (km)
3
2
1
Distance (km)
100
200
300
400
-10.0
0.0
10.0
20.0
σ_{rr} (kbars)
3
2
1
Distance (km)
100
200
300
400
-4.0
0.0
4.0
8.0
12.0
σ_{rr} (kbars)
1
3
2
250
200
150
100
50
0
-50
Δg (mgals)
3
2
1
100
200
300
400
Distance (km)
200
150
100
50
0
-50
Δg (mgals)
1
2
3
100
200
300
400
Distance (km)

Figure 5.

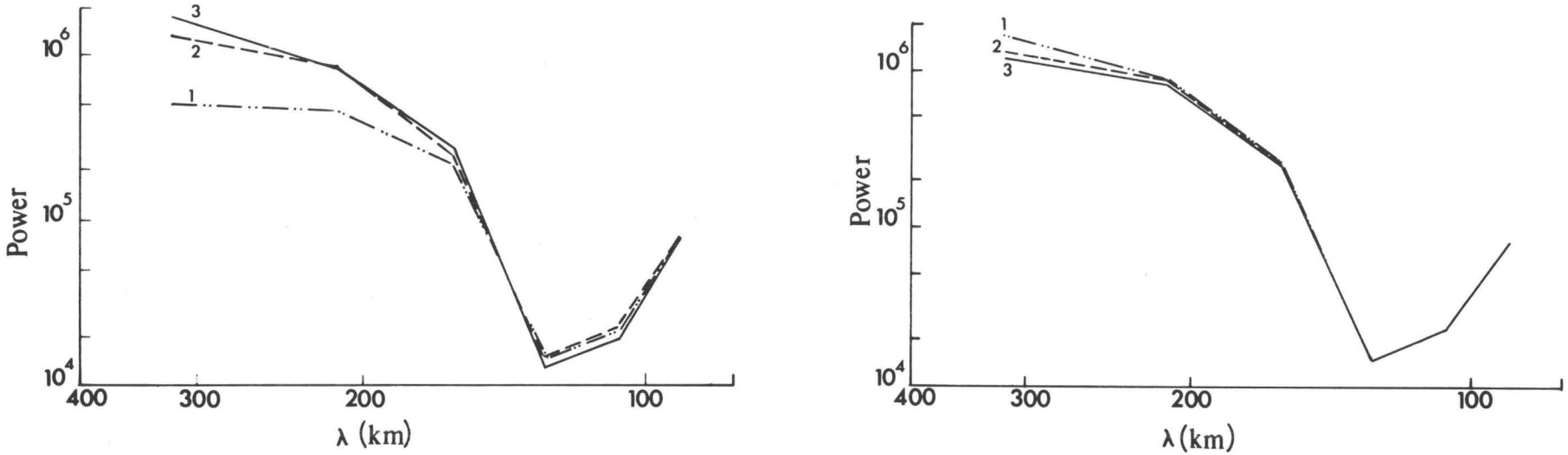
Power
10^6
10^5
10^4
400
300
200
100
λ (km)
3
2
1
Power
10^6
10^5
10^4
400
300
200
100
λ (km)
1
2
3

Figure 6.

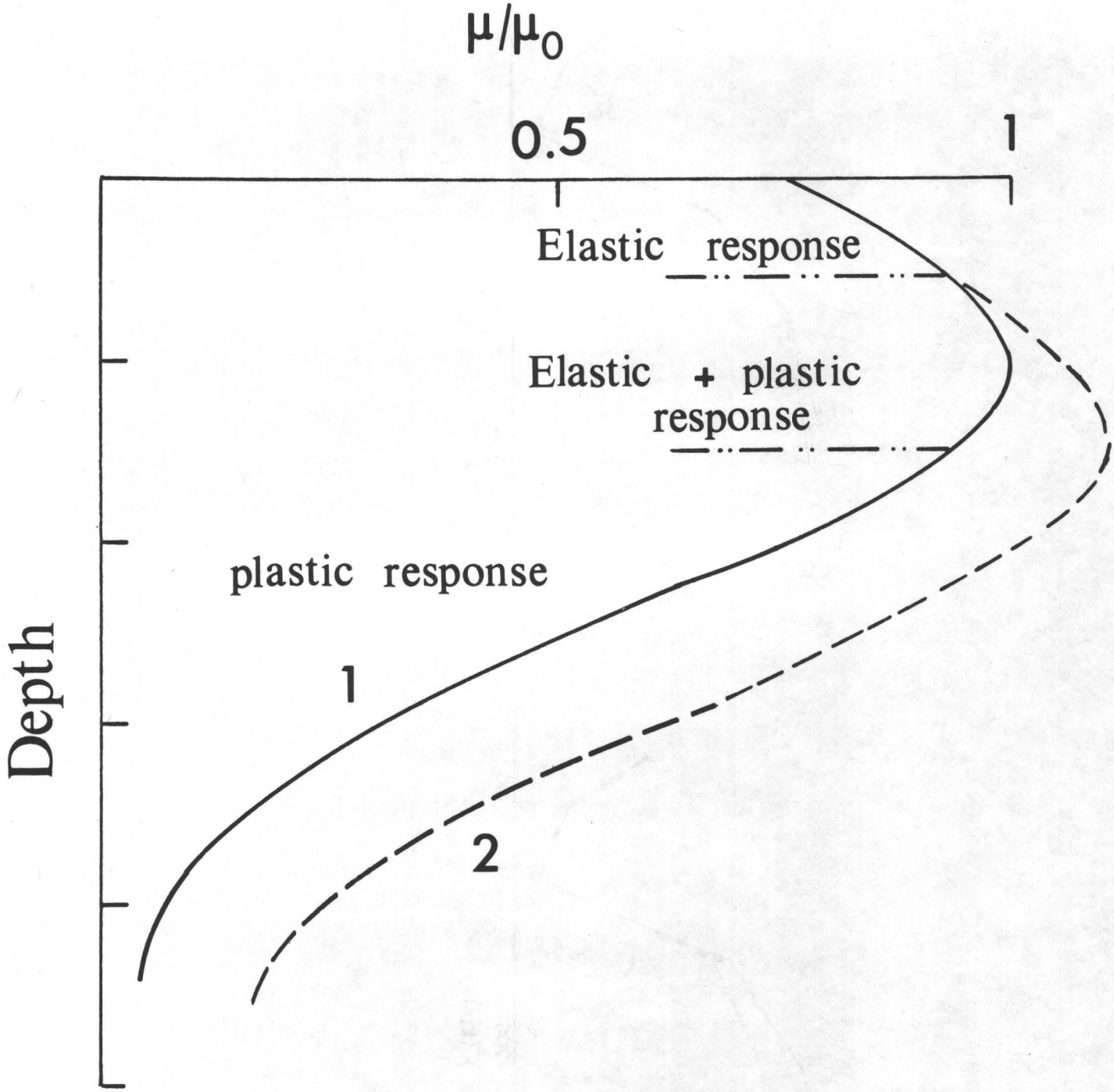
μ/μ0
0.5
1
Elastic response
Elastic + plastic response
plastic response
1
2
Depth

Figure 7.

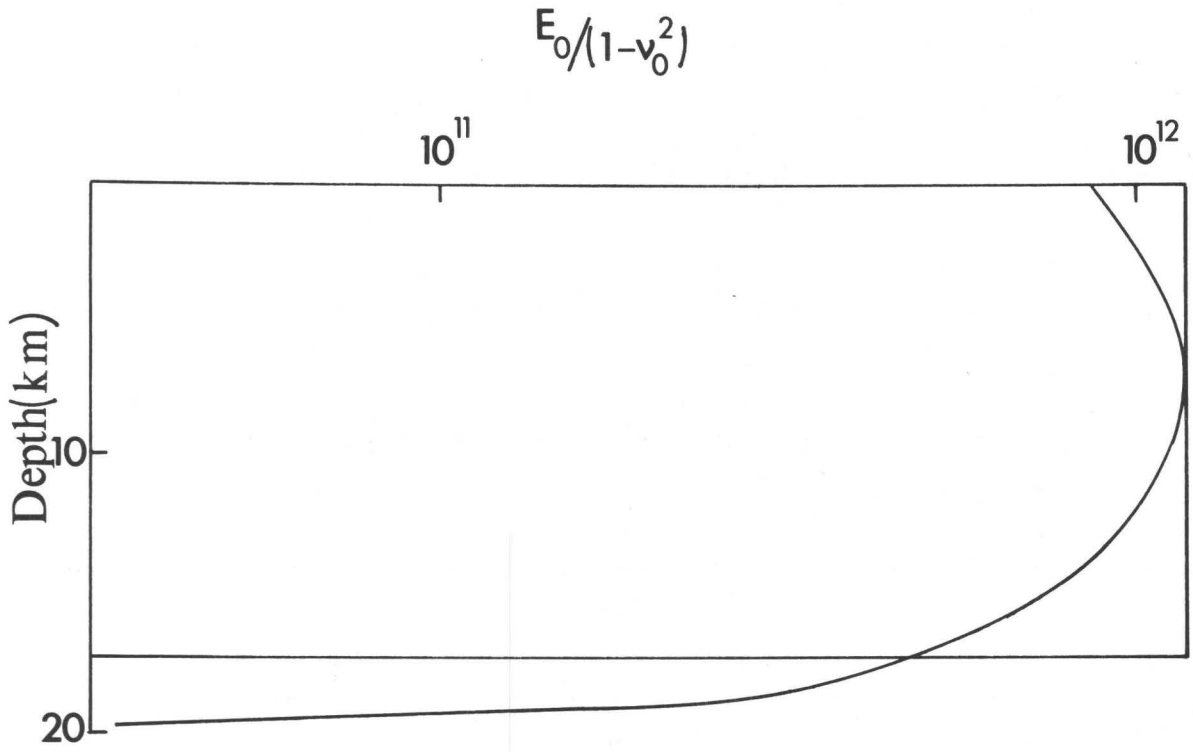
$E_0/(1-\nu_0^2)$
10^{11}
10^{12}
Depth(km)
10
20

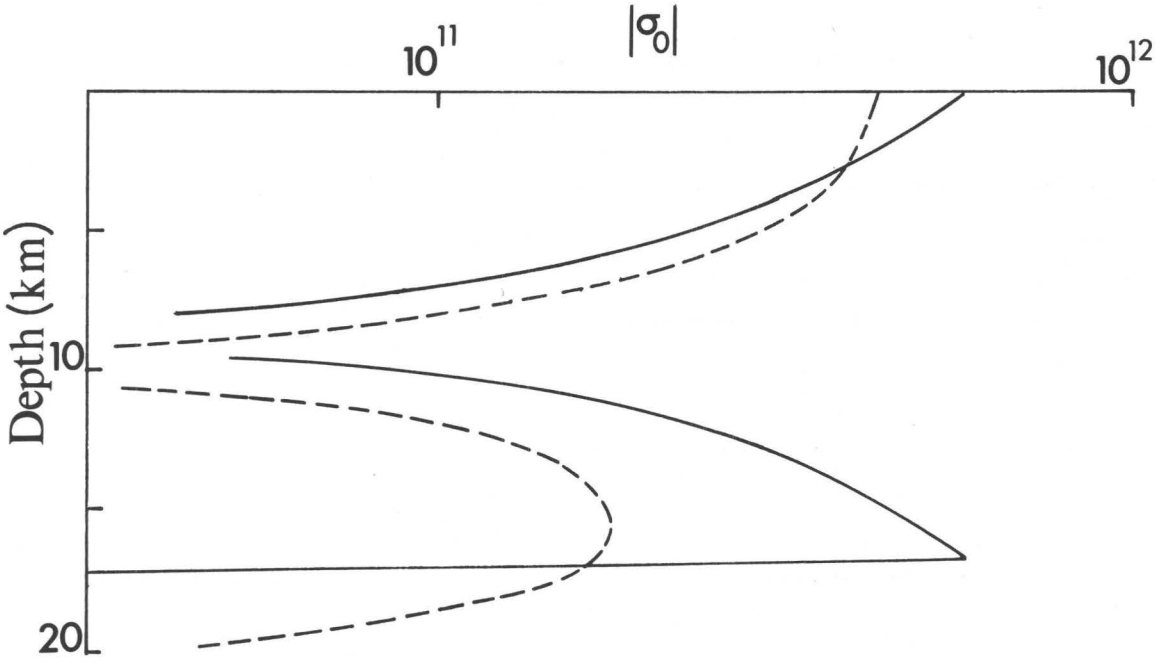
$|\sigma_0|$
10^{11}
10^{12}
Depth (km)
10
20

 Figure 8.

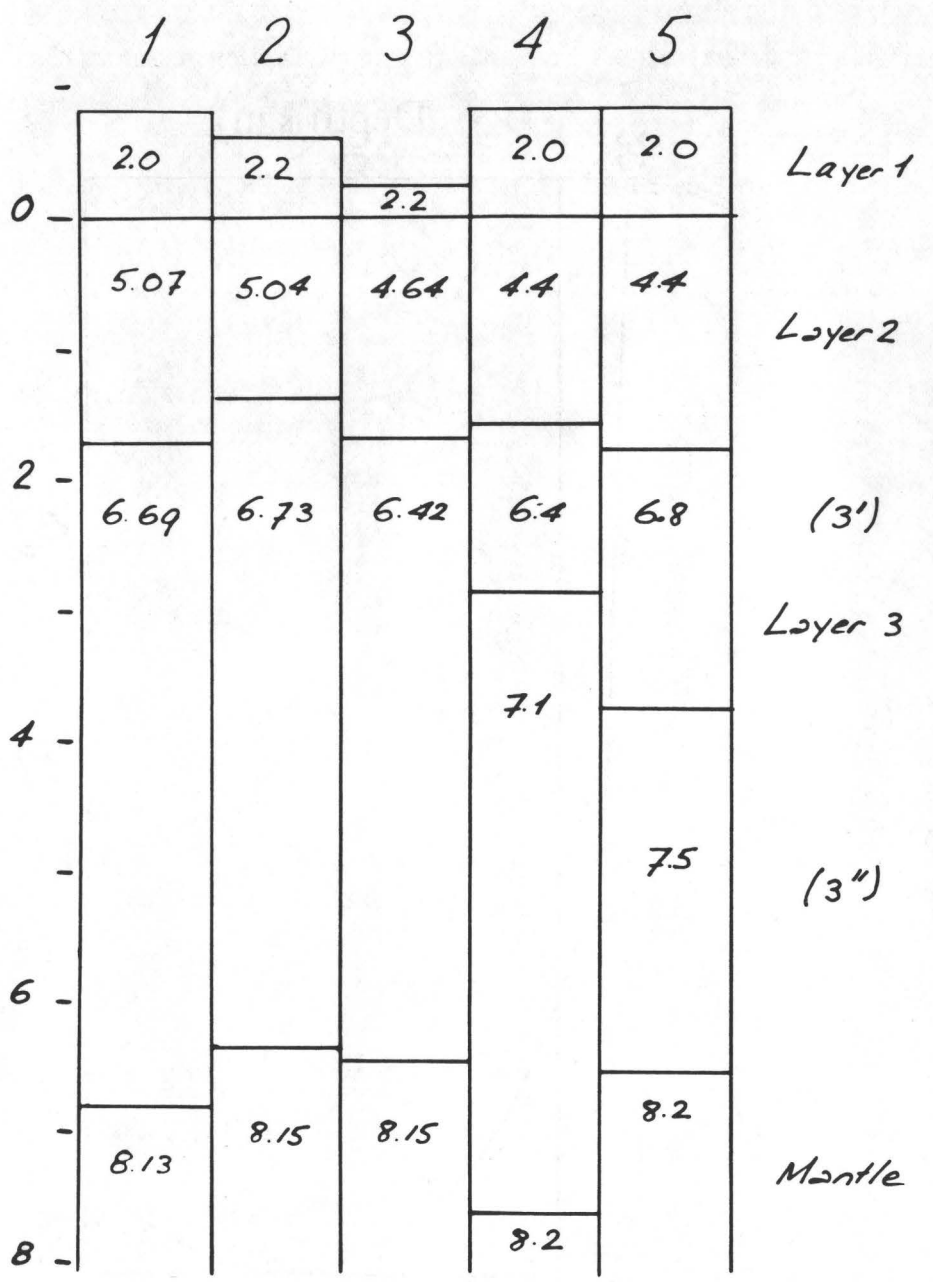

FIGURE a

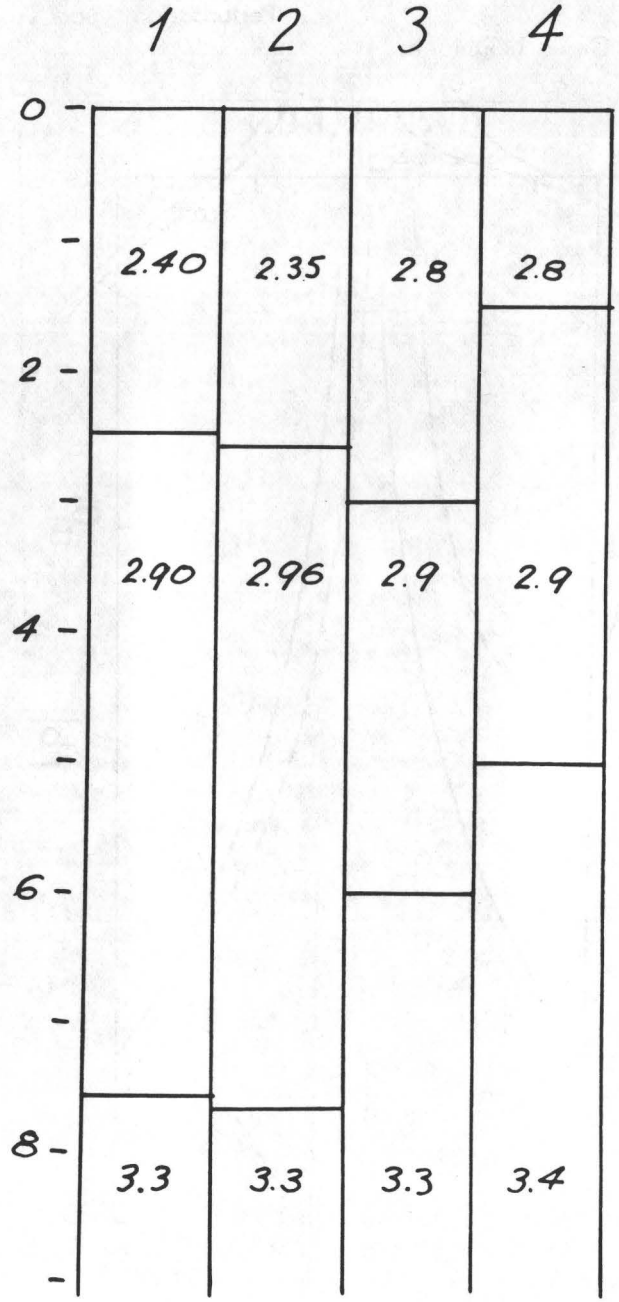

FIGURE b

Figure 9.

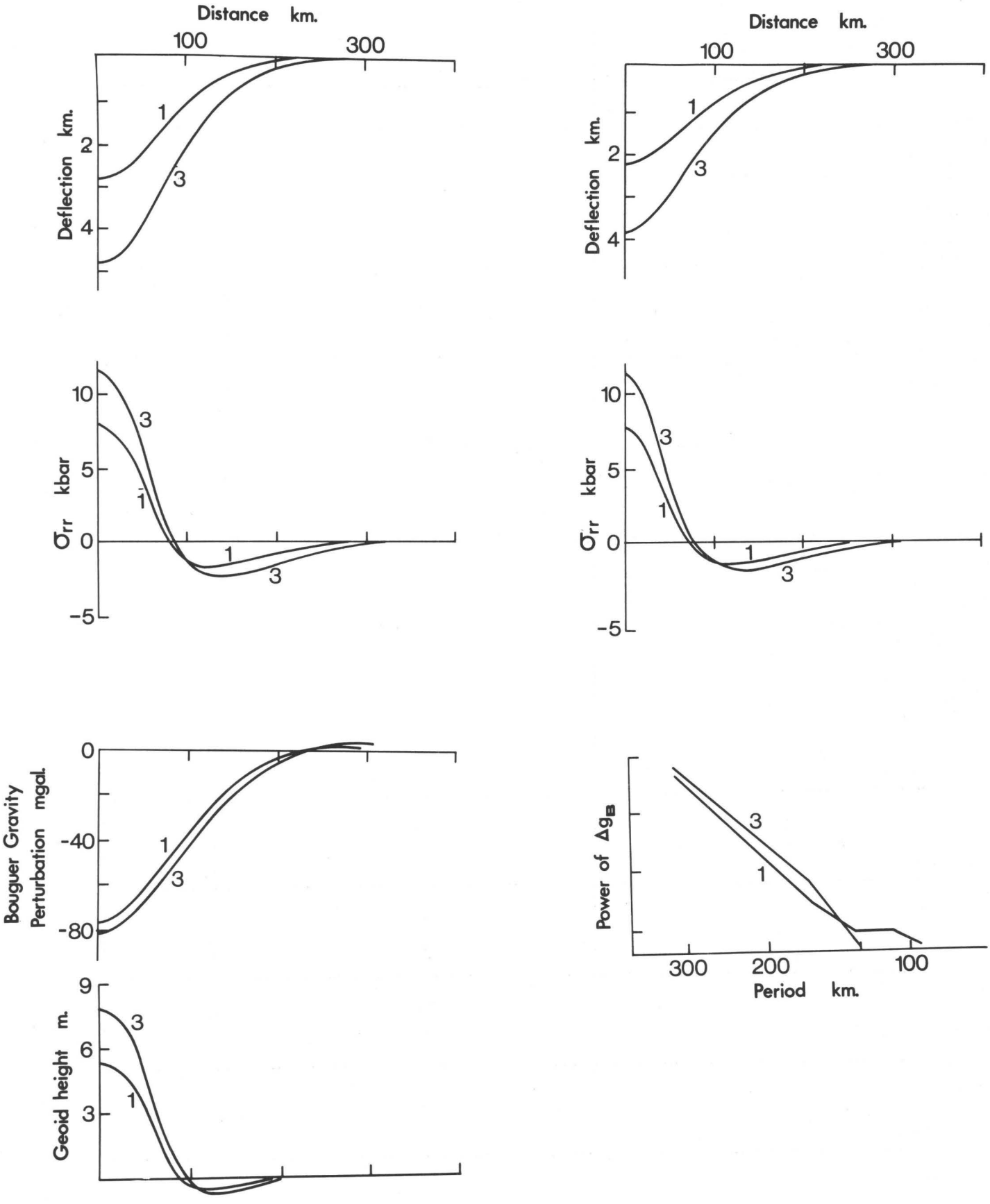
Distance km.
100
300
Deflection km.
2
4
1
3
Distance km.
100
300
Deflection km.
2
4
1
3
10
5
0
-5
σrr kbar
3
1
1
3
10
5
0
-5
σrr kbar
3
1
1
3
0
-40
-80
Bouguer Gravity Perturbation mgal.
1
3
9
6
3
Geoid height m.
3
1
Power of ΔgB
3
1
300
200
100
Period km.

Figure 10.

PALEOSTRESS LEVELS IN DEEPLY ERODED FAULT ZONES BASED ON ANALYSES OF DEFORMATION-INDUCED MICROSTRUCTURES

D. L. Kohlstedt

Department of Materials Science and Engineering

Cornell University, Ithaca, N.Y. 14853

1. INTRODUCTION

One approach to estimating the differential stress required to cause movement on the San Andreas fault is to determine the stress levels which existed during deformation in eroded faults zones. It now appears to be possible to calculate the paleostress levels in deeply exposed fault zones from the density of dislocations, size of subgrain, and/or size of grains if these deformation-induced parameters have not been altered by later annealing or deformation events.

In this paper, the theoretical arguments used to relate differential stress to dislocation density are reviewed, and some of the experimental data bearing on this point are summarized. The experimentally determined dependence of subgrain size and grain size on differential stress are also presented. The role of static recovery is then discussed in terms of recent laboratory studies. Finally, the published paleostress levels in ancient fault zones--determined from measured dislocation densities, subgrain size, and/or grain size--are reviewed.

2. DIFFERENTIAL STRESS AND DEFORMATION-INDUCED MICROSTRUCTURE

2.1. Differential Stress-Dislocation Density

Theoretical arguments which lead to a quantitative relationship between differential stress, $\sigma_1-\sigma_3$, and dislocation density, ρ, fall into two categories. The first group of models considers the stress required to cause dislocations on parallel slip planes to pass one another. The second class of models analyzes the effect of the internal stress or back stress on the stress required to operate Frank-Reed sources.

The central point in both lines of reasoning is the result from dislocation theory that the elastic stress field produced by a straight dislocation at r = 0 (in an elastically isotropic material) has components of the form (see for example, Dieter pp. 166-168 (1976))

$$\sigma_{ij} = \frac{\mu b}{2\pi K} f(\theta) \frac{1}{r} \qquad (1)$$

where $\sigma_{ij} \equiv$ ij component of the stress tension,

$\mu \equiv$ shear modulus,

$b \equiv$ Burgers vector,

K = 1 for screw dislocations and $(1-\nu)$ for edge dislocations,

$f(\theta)$ = 1 for screw dislocations and $-\sin\theta$ or $\cos\theta$ for edge dislocations,

$r \equiv$ distance from dislocation line.

This elastic stress field produces a force on the other dislocations in the crystal and, thus, provides the mechanism by which dislocations interact. The force of dislocation 1 on dislocation 2 is given by the Peach-Koehler equation (with summation from 1 to 3 over repeated subscripts)

$$F_i = \varepsilon_{ijk} P_j \ell_k \tag{2}$$

where $F_i \equiv$ component of force along i axis exerted by dislocation 1 on dislocation 2,

ε_{ijk} = 0 if i = j, j = k, or k = i

= +1 if ijk = 123 permutation

= -1 if ijk = 321 permutation,

$\ell_k \equiv$ component of dislocation line vector of dislocation 2 along k axis,

$P_j = b_\ell \sigma_{j\ell}$,

$b_\ell \equiv$ component of Burgers vector of dislocation 2 along axis,

$\sigma_{ij} \equiv$ ij component of stress field of dislocation 1.

In 1934, Taylor presented his classic analysis of the shear stress required to move edge dislocations past one another on parallel slip planes taking into account the interaction force between the dislocations. He considered several dislocation configurations. For the case of two straight, parallel dislocations of opposite sign on slip planes separated by a distance h, the dislocations can pass each other only if the applied shear stress

$$\tau > \frac{\mu b}{2\pi(1-\nu)h} . \tag{3}$$

(For a polycrystalline material, τ is set equal to $(\sigma_1-\sigma_3)/2$.) Taylor (1934) also treated the situation in which parallel positive and negative (i.e., opposite sign) dislocations lie on interpenetrating lattices. For a square lattice of repeat distance r, the dislocations can move past each other when

$$\tau > 0.174 \frac{\mu b}{(1-\nu)r} \tag{4}$$

where

$$\rho \cong 1/r^2. \tag{5}$$

when the dislocations lie on a net of equilateral triangles,

$$\tau > 0.030 \frac{\mu b}{(1-\nu)r} \tag{6}$$

is required to move the dislocations. The differential stress required to produce dislocation motion in a uniform array of edge dislocations is, therefore, of the form

$$\sigma_1-\sigma_3 > \alpha \frac{\mu}{(1-\nu)} \; b\rho^{1/2} \equiv \sigma_{int} \tag{7}$$

In Taylor's analysis, dislocations move in response to the locally acting effective stress

$$\sigma_{eff} = (\sigma_1-\sigma_3) - \sigma_{int} \tag{8}$$

where σ_{int} is the internal or back stress produced by the dislocation array. Thus, the internal stress screens each dislocation from the applied stress so that the local driving stress is σ_{eff}. The maximum dislocation density for a given applied stress, therefore, occurs when $\sigma_{eff} = 0$; that is, $\rho = \rho_{max}$ when

$$\sigma_1-\sigma_3 = \alpha\mu \; b\rho^{1/2}, \tag{9}$$

where the term $1/(1-\nu)$ is absorbed into the constant α; i.e.,

$$\alpha/(1-\nu) \rightarrow \alpha \; . \tag{10}$$

For experimentally deformed crystalline solids, $0.5 < \alpha < 5$ (Takeuchi and Argon, 1976). In the Taylor (1934) analysis, this range of values for α might arise for two reasons. First, the applied stress is found experimentally to be larger than the internal stress level (Lerner et al., 1979). The exact relation between $\sigma_1-\sigma_3$ and σ_{int} varies from one material to the next. Second, dislocation arrays in deformed grains are never the simple ones considered by

Taylor (1934). The arrays can involve both edge and screw dislocations which follow curved, non-planar paths through a grain.

In the second class of models which relate the deformation-induced dislocation density to the applied stress, the dislocation density in a well-annealed crystal or grain increases when a stress is applied until the locally acting effective stress falls below the critical stress required to operate the dislocation sources (such as Frank-Reed sources). (See Nicolas and Poirier, pp. 127-128 (1976).) Thus, dislocation multiplication ceases and a steady state dislocation density is established. If the density of free dislocations decreases due to dislocation-dislocation annihilation or dislocation climb into subboundaries or grain boundaries, the internal stress decreases and the local stress increases permitting dislocation sources to operate again. This model assumes that the rate of dislocation multiplication is fast compared to the rate at which dislocations are annihilated or absorbed into low angle boundaries. The dislocation density is determined as a function of the applied (differential) stress by assuming that the applied stress is proportional to the internal stress,

$$\sigma_1 - \sigma_3 \propto \sigma_{int} \tag{11}$$

Thus, from Eqs. 7, 10, and 11,

$$\sigma_1 - \sigma_3 = \propto \mu b \rho^{1/2} \ . \tag{12}$$

In non-dimensional terms,

$$\rho b^2 \propto \left(\frac{\sigma_1 - \sigma_3}{\mu}\right)^2 \ . \tag{13}$$

Clearly, the dislocation density depends strongly on differential stress, but only weakly on temperature through μ and b.

For the present discussion, the correctness of one model versus another is not the central issue. The important point is that because dislocations interact via their elastic stress fields, their density cannot increase indefinitely; and it is reasonable that a stress determined, steady-state density is obtained. Dislocation density-applied stress data for a large number of materials (well in excess of 50 (see Takeuchi and Argon, 1976)) clearly demonstrate that the steady-state dislocation density increases as the applied stress increases, although the increase in density may be less rapid than the square of the applied stress (Goetze, 1978).

Dislocation density versus applied stress data are plotted in Fig. 1 for experimentally deformed olivine and quartz grains. A least squares fit of these data to Eq. 12 yields $\propto = 3$. Durham et al. (1977) have fit a similar collection of data to the equation

$$\rho \propto (\sigma_1-\sigma_3)^m \qquad (14)$$

and obtained m = 1.6. The data on olivine presented in Fig. 1, which include the recent results of Zeuch and Green (1979), extend over four orders of magnitude in dislocation density and yield m = 1.5.

The stress-dislocation density data for olivine in Fig. 1 come from deformation experiments which cover a temperature range of 600°C, a strain rate range of 4 orders of magnitude, hydrostatic pressures between 1 and 15,000 bars, and different water contents. Clearly, the dislocation density is primarily determined by the differential stress. While the data may deviate from the anticipated $\rho \propto (\sigma_1-\sigma_3)^2$ behavior, the empirically derived dislocation density-differential stress relation, Fig. 1, provides a sound basis for estimating paleostresses.

Dislocation density-differential stress data for MgO are presented in Fig. 2. The data of Bilde-Sörensen (1972) and of Hüther and Reppich (1973) where obtained from samples deformed under high-temperature creep conditions. In contrast, the high-stress data point was obtained on a single crystal squeezed at room temperature by W. A. Barrett between diamond anvils to a pressure near 100 kbar and a differential stress of approximately 30 kbar (Kinsland and Bassett, 1977); the dislocation density was determined by this author. Yet, the data from these diverse conditions are in good agreement with the theoretical prediction, Eq. 12, and clearly demonstrate that the dislocation density is strongly dependent upon the applied stress.

Transmission electron micrographs of the dislocation structure in the sample deformed in the diamond anvils are presented in Fig. 3. The distribution of dislocations is very homogeneous, even though the density is high enough to cause extensive rotation of the crystal planes. The dislocation structure is dominated by an almost steel wool-like texture. Essmann and Mughrabi (1979) have recently treated in detail the problem of mutual annihilation of non-screw dislocations during glide at low temperatures. They conclude "that the dislocation densities introduced during deformation cannot exceed well-defined upper limits," as is required for a relationship such as Eq. 12 to be valid.

2.2. Differential Stress-Grain Size

For a number of materials, there is now experimental data which indicate that the size, d, of deformation-induced subgrains decreases as the differential stress increases (see Takeuchi and Argon, 1976). The stress-subgrain size relation is usually written

$$\sigma_1-\sigma_3 = K\frac{\mu b}{d}, \qquad (15)$$

where K is a constant found to lie in the range 20 to 200. Durham et al. (1977) report that Eq. 15 adequately describes available data for olivine.

The grain size generated during steady-state creep is also observed to decrease with increasing differential stress. The data for most materials fit

$$D \propto (\sigma_1-\sigma_3)^n \qquad (16)$$

with $1.2 < n < 1.7$. Twiss (1977) has summarized the available data, and Twiss (this volume) has presented theoretical justification for the power law relation given by Eq. 16. The reported stress-grain size relations for experimentally deformed olivine are summarized in Fig. 4; stress-grain size data for several naturally deformed olivine-rich rocks (where the stress level was calculated from the dislocation density using Fig. 1) are presented for comparison. The results of Post (1973), Mercier et al. (1977), Ross et al. (1979, dry) and Zeuch and Green (1979) are in quite good agreement with each other; and the data from the naturally deformed rocks is in good agreement with that from the samples deformed in the laboratory. Only the data on "wet" material deviates substantially from the other results. Additional work is needed to determine whether this deviation is simply an experimental problem, a result of "water" as suggested by Ross et al. (1979), or an indication of two distinct dynamic recrystallization mechanisms as observed by Guillope and Poirier (1979) in NaCl. The stress-grain size interrelation is a topic deserving thorough experimental investigation.

3. STATIC RECOVERY

The major criticism leveled at the use of deformation-induced microstructural parameters as measures of paleostress levels is that post-deformation, static recovery (or a deformation event post-dating the event of interest) could easily irradicate the essential data (see, for example, Christie, this volume). In complex geological processes, this point cannot be ignored.

Deformation or static annealing, following the event of interest, can obscure or irradicate the relevant microstructures. Dislocation density is the most easily altered of the three microstructural parameters; in olivine, for example, a few tenths of a percent strain at a new stress level (Durham, et al., 1977) or a few minutes of static annealing at 1300°C (Goetze and Kohlstedt, 1973) will result in large changes. Recent data for olivine from Kohlstedt et al. (1979) are presented in Fig. 5 to illustrate this point. In contrast, the subgrain size is quite refractory to static annealing (Goetze and Kohlstedt, 1973); it remains constant if the stress is decreased and decreases after approximately 10% strain if the stress is increased (Ross et al., 1979). Thus, the subgrain size records the maximum differential stress applied during deformation. The grain size is also very refractory to static annealing, and grains dynamically recrystallize under an increased stress level to a smaller size only after a relatively large strain ($\sim$10-50%). Some deviations from these general rules-of-thumb might be expected for very fine grained materials (e.g., a few microns or, at higher temperatures, a few

tens of microns). The short distances between grain boundaries, which can act as effective sources and sinks for dislocations, will possibly result in the absence of subgrain boundaries and in a dislocation density lower than that predicted by Eq. 9. Our experience with hot-pressing olivine indicates that recovery, recrystallization, and grain growth are extremely rapid for fine grained samples. Thus, we anticipate that, for fine grained rocks, the grain size will provide a lower bound for the differential stress.

In the most straight forward situation, all three parameters--dislocation density, subgrain size, and grain size--would all yield the same differential stress. At the moment, this point is difficult to test because the empirical curves relating stress and subgrain size are poorly calibrated, as are the empirical curves for stress and grain size (note the scatter amongst the several experimentally derived curves in Fig. 4, for example). Yet, as illustrated in Fig. 4, at least for some naturally deformed rocks the dislocation density and grain size yield comparable values of differential stress.

In more complex situations, the effects of static annealing and of a second deformation event can be tested for by comparing the three microstructural parameters for each specimen. Consider three examples. (i) A short-duration static anneal will reduce the dislocation density, which will then yield a low estimate of the stress level in comparison with that calculated from the grain size. (ii) A short-term, high-level stress pulse will result in a dislocation density that accurately indicates this new stress, while the grain size remains unchanged and provides an estimate of the previous stress level. (iii) A bimodal grain-size distribution would suggest a more prolonged, second stress pulse; the smaller grain size and the dislocation density in the larger grains should indicate the final stress level and the larger grain size should indicate the earlier stress level.

Goetze (1975) reported an excellent example of the use of the deformation-indiced microstructure in his analysis of the deformation history of olivine bearing kimerlite nodules. The olivine grains exhibited a bimodal size distribution with both the large and the small grain having similar dislocation densities. The size of the small (second generation) grains and the dislocation densities yield $\sigma_1-\sigma_3 \cong 3$ kbar; the size of the large (first generation) grains gives $\sigma_1-\sigma_3 \cong 100$ bars. Goetze (1975) concluded that the high ρ and small D (high $\sigma_1-\sigma_3$) were introduced during the explosive ascent of the nodule, while the large grain size (low $\sigma_1-\sigma_3$) was probably indicative of the differential stress level in the mantle.

The results of any paleostress analysis are constrained by the fact that the relation between dislocation density and differential stress and that between grain size and differential stress are based on relatively few data points. The uncertainty in the absolute values of the stress levels predicted from these parameters may be large. Yet, the uncertainty in the relative values of the differential stresses, determined for various localities or for multiple deformation events in one sample, is small.

4. PALEOSTRESS LEVELS IN DEEPLY ERODED FAULTS ZONES

Twiss (1977) surveyed published values for the sizes of grains produced by dynamic recrystallization in mylonites from four thrust fault zones. In all four fault zones, the size of the dynamically recrystallized quartz grains is in the range 10 to 40 μm which corresponds to $\sigma_1-\sigma_3$ in the range 500 to 1500 bars. Twiss (1977) concludes that "tectonic stresses on the order of 1000 bars are commonly associated with the emplacement of thrust sheets in crustal rocks."

Briegel and Goetze (1978) estimated the differential stress levels in the shear zone at the base of the Glarus overthrust from the dislocation density in the Lochseiten limestone. They calculated that $\sigma_1-\sigma_3 \cong 2$ kbar, and concluded that the dislocation structure was frozen-in during cooling.

Etheridge and Wilkie (1979) examined the microstructures of quartz-bearing rocks from mylonite zones from three distinct tectonic settings. They find that the size of recrystallized grains is independent of strain, and argue that it is "very sensitive to water content." I believe that the latter point is open for debate and that the main role of water may be to increase the kinetics of the recrystallization process (e.g. the grain boundary mobility) rather than the steady state grain size. They conclude from the size of recrystallized quartz grains that crustal stresses must be in the range 600 to 1500 bars.

Weathers et al. (1979) have studied the progressive development of the deformation-induced dislocation densities, grain elongation, and recrystallization in the basal quartzite unit at the Stack of Glencoul in the Moine thrust fault zone, Scotland. The dislocation density, $5 \times 10^8 cm^{-2}$, and the grain size after recrystallization, 15 μm, were found to be independent of distance from the fault, to the maximum sampling distance of ∿100 m. The differential stress level determined from the deformation-induced microstructures is on the order of 100 MPa. The quartz grains are progressively elongated and recrystallized approaching the fault, corresponding to a progressive increase in strain. At 100 m from the fault, the aspect ratio of relict quartz grains is ∿1:1; at 0.01 m, it is 85:1. A quantitative estimate of the strain, based on the aspect ratios of the relict quartz grains, as a function of distance from the fault was used to calculate strain rate and temperature profiles. For a creep activation energy of 0.19 MJ $mole^{-1}$, the temperature decreases away from the fault with a gradient of 7.5×10^{-3}°C cm^{-1}. At 100 m from the fault, 5% of the quartzite is recrystallized from 1 mm to 15 μm grains; at 0.01 m, it is 100% recrystallized to 15 μm grains. They argued that this small grain size probably favored grain-boundary deformation mechanisms over grain-matrix mechanisms and, thus, helped to concentrate the strain at the fault.

Acknowledgement: This research was supported by USGS Contract No. 14-08-0001-17772.

REFERENCES

Bilde-Sörensen, J. B., Dislocation structures in creep-deformed polycrystalline MgO, J. Amer. Ceram. Soc. 55, 606-610 (1972).

Briegel, U. and Goetze, C., Estimates of differential stress recorded in the dislocation structure of Lockseiten limestone (Switzerland), Tectonophys. 48, 61-76 (1978).

Dieter, G. E., Mechanical Metallurgy, McGraw-Hill, New York, 774 pp., 1976.

Durham, W. B., Goetze, C., and Blake, B., Plastic flow in oriented single crystals of olivine, Part II. Observations and interpretations of the dislocation structure, J. Geophys. Res. 82, 5755-5770 (1977).

Etheridge, M. A. and Wilkie, J. C., The geometry and microstructure of a range of QP-mylonite zones: A field test of the recrystallized grain size paleopiezometer, in Proceedings of Conference on Analysis of Actual Fault Zone in Bedrock, USGS, Open File Report 79-1239, 1-5 April 1979.

Essman, U. and Mughrabi, H., Annihilation of dislocations during tensile and cyclic deformation and limits of dislocation densities, Phil. Mag., in press (1979).

Goetze, C., Sheared Cherzolites: From the point of view of rock mechanics, Geology 3, 172-173 (1975).

Goetze, C., The mechanisms of creep in olivine, Phil. Trans. R. Soc. London A 288, 99-119 (1978).

Goetze, C. and Kohlstedt, D. L., Laboratory studies of dislocation climb and diffusion in olivine, J. Geophys. Res. 78, 5961-5971 (1973).

Guillope, M. and Poirier, J.-P., Dynamic recrystallization during creep of single crystalline halite, J. Geophys. Res., in press (1979).

Hüther, W. and Reppich, B., Dislocation structure during creep of MgO single crystals, Phil. Mag., 28, 363-371 (1973).

Kinsland, G. L. and Bassett, W. A., Strength of MgO and NaCl polycrystals to confining pressures of 250 kbar at 25°C, J. Appl. Phys. 48, 978-985 (1977).

Kohlstedt, D. L., Goetze, C., and Durham, W. B., Experimental deformation of olivine single crystals with application to mantle flow, in The Physics and Chemistry of Minerals and Rocks, ed. R. G. J. Streus, John Wiley and Sons, New York, pp. 35-49, 1976.

Kohlstedt, D. L. and Goetze, C., Low-stress high-temperature creep in olivine single crystals, J. Geophys. Res. 79, 2045-2051 (1974).

Kohlstedt, D. L., Nichols, H. P. K., and Hornack, P., The effect of pressure on the rate of dislocation recovery in olivine, J. Geophys. Res., accepted for publication (1979).

Lerner, I., Chiang, S.-W., and Kohlstedt, D. L., Load relaxation study of four alkali halides, Acta Met. 27, 1187-1196 (1979).

McCormick, J. W., Transmission electron microscopy study of experimentally deformed synthetic quartz, Ph.D. thesis, UCLA.

Mercier, J.-C. C., Anderson, D. A., and Carter, N. L., Stress in the lithosphere: Inferences from steady state flow of rocks, Pure Appl. Geophys. 115, 199-226 (1977).

Nicolas, A. and Poirier, J. P., Crystalline Plasticity and Solid State Flow in Metamorphic Rocks, John Wiley and Sons, New York, 444 pp., 1976.

Post, R. L., High Temperature Creep of Mt. Burnett Dunite, Ph.D. thesis, UCLA, 1973.

Ross, J. V., Ave'Lallemant, H. G., and Carter, N. L., Stress dependence of recrystallized grain and subgrain size in olivine, preprint (1979).

Takeuchi, S. and Argon, A. S., Review: Steady state creep of single-phase crystalline matter at high temperatures, J. Mater. Sci. 11, 1542-1566 (1976).

Taylor, G. I., The mechanisms of plastic deformation in crystals, Proc. Roy. Soc. London, Ser. A, 145, 362-404 (1934).

Twiss, R. J., Theory and applicability of a recrystallized grain size paleopiezometer, Pure Appl. Geophys. 115, 227-244 (1977).

Weathers, M. S., Bird, J. M., Cooper, R. F., and Kohlstedt, D. L., Differential stress determined from deformation-induced microstructures of the Moine thrust zone, J. Geophys. Res., in press (1979).

Zeuch, D. H., and Green, H. W., Experimental deformation in an "anhydrous" synthetic dunite, Bull. Mineral. 102, 185-187 (1979).

FIGURE CAPTIONS

Figure 1. Relation between ρb^2 and $(\sigma_1-\sigma_3)/\mu$ for experimentally deformed quartz and olivine. The slope of the line is 1.5. The data are from McCormick (1977), Kohlstedt and Goetze (1974), Durham et al. (1977), and Zeuch and Green (1979).

Figure 2. Relation between ρb^2 and $(\sigma_1-\sigma_3)/\mu$ for MgO.

Figure 3. Dislocation structure in MgO crystal squeezed in diamond anvils. TEM.

Figure 4. Relation between D/b and $(\sigma_1-\sigma_3)/\mu$ for olivine. The data are from Kohlstedt et al. (1976), Ross et al. (1979) for wet (w) and dry (d) samples, Mercier et al. (1977), Zeuch and Green (1979), and Post (1973).

Figure 5. Post-anneal dislocation density normalized against the starting dislocation density, ρ_o, for pre-deformed olivine crystals annealed for one hour at either 1 bar or 5000 bars confining pressure.

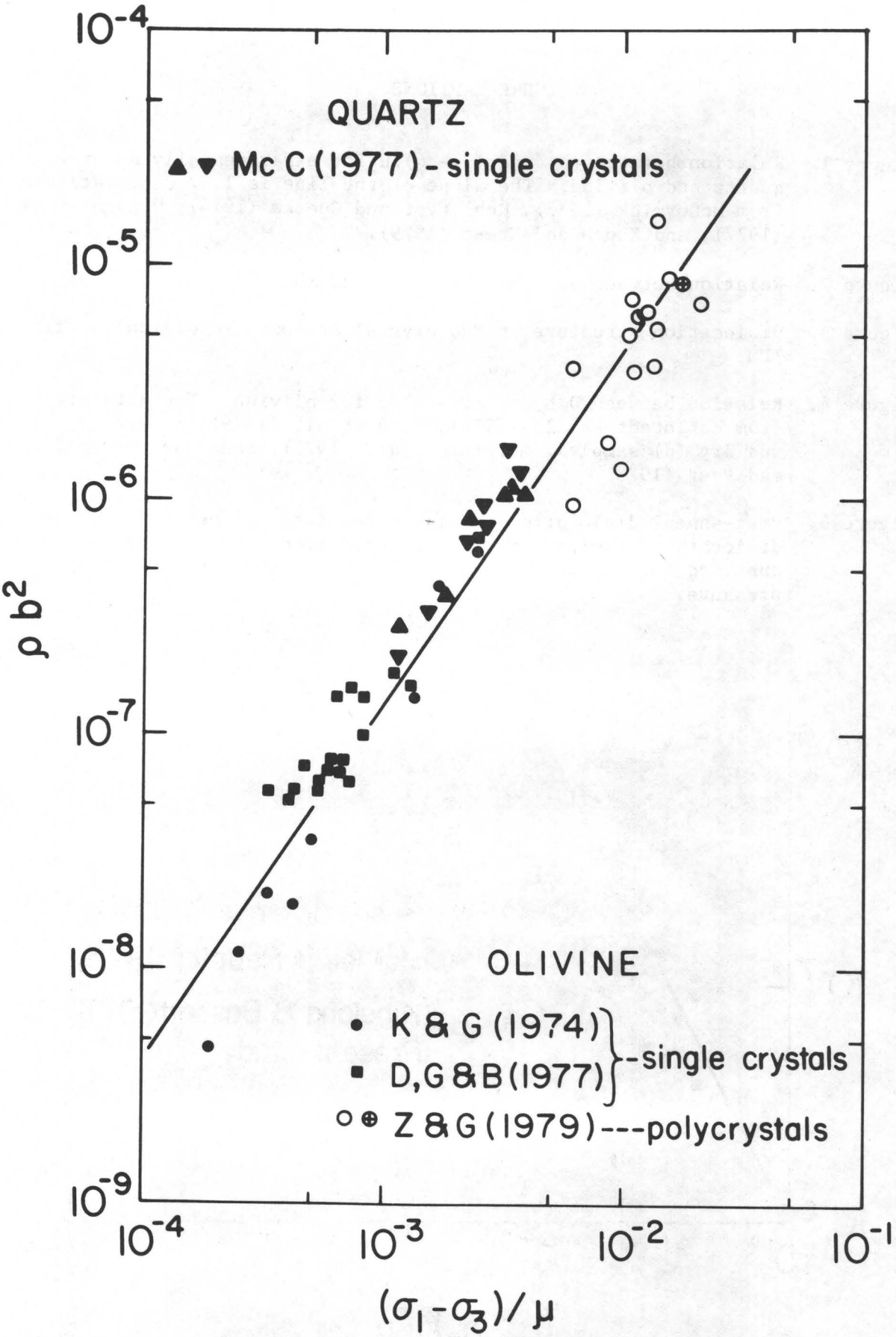
QUARTZ
▲ ▼ Mc C (1977) - single crystals
OLIVINE
• K & G (1974)
■ D,G & B (1977)
--single crystals
○ ⊕ Z & G (1979) ---polycrystals
10^{-4}
10^{-5}
10^{-6}
10^{-7}
10^{-8}
10^{-9}
ρb^2
10^{-4}
10^{-3}
10^{-2}
10^{-1}
$(\sigma_1 - \sigma_3)/\mu$

1

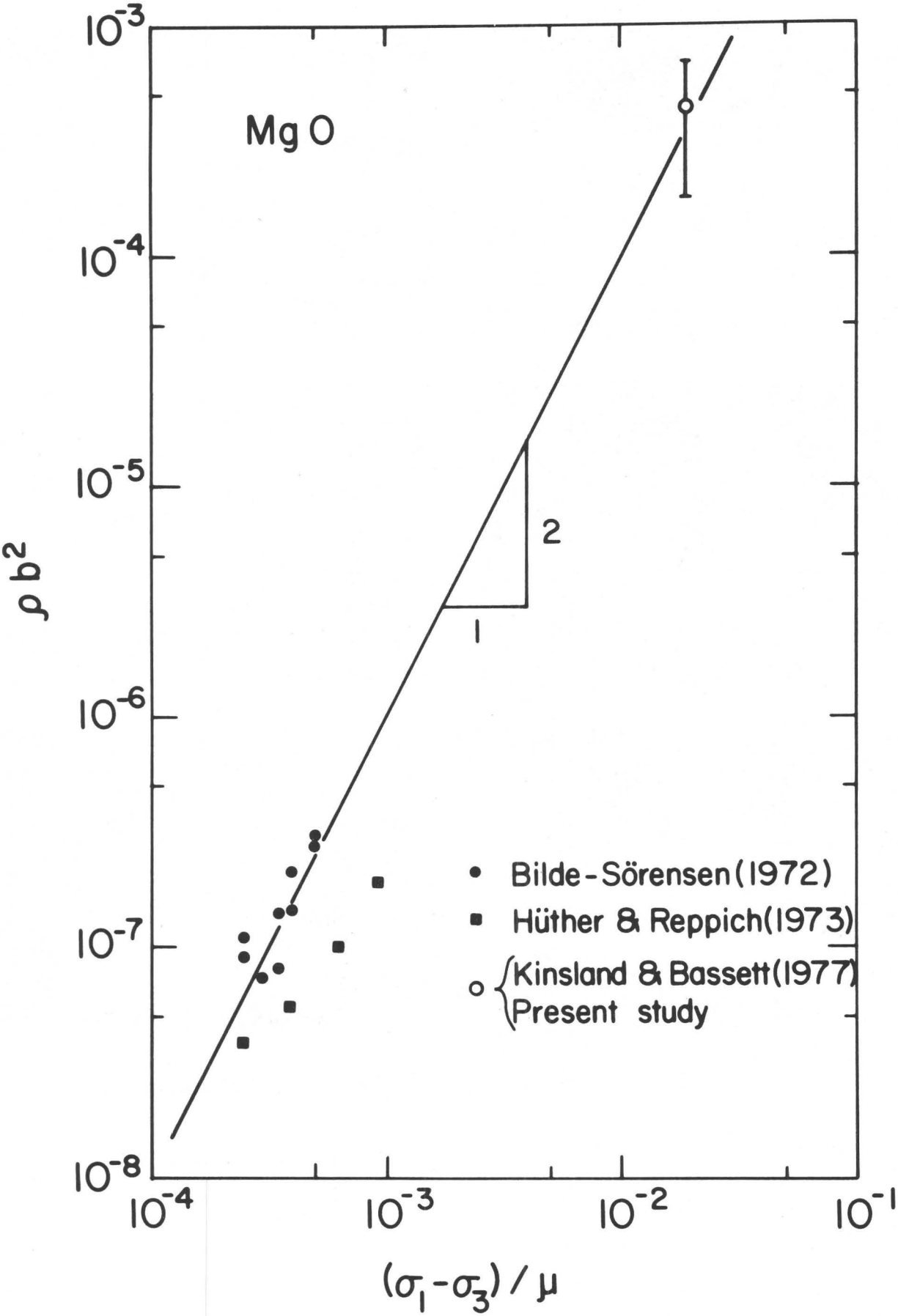
Mg O
10^{-3}
10^{-4}
10^{-5}
10^{-6}
10^{-7}
10^{-8}
ρb^2
2
1
Bilde-Sörensen (1972)
Hüther & Reppich (1973)
Kinsland & Bassett (1977)
Present study
10^{-4}
10^{-3}
10^{-2}
10^{-1}
$(\sigma_1 - \sigma_3) / \mu$

2

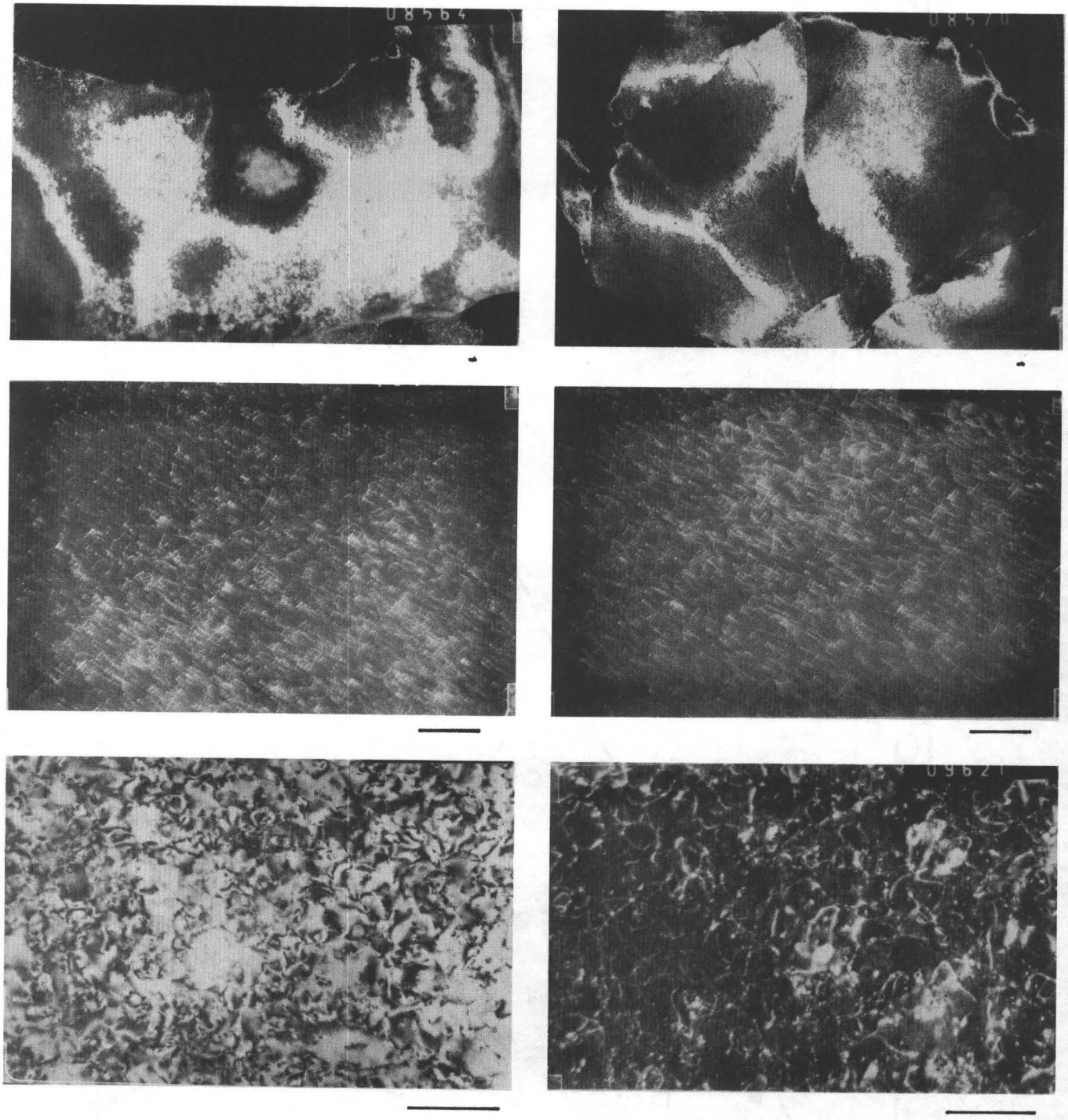

bar = 100 nm

3

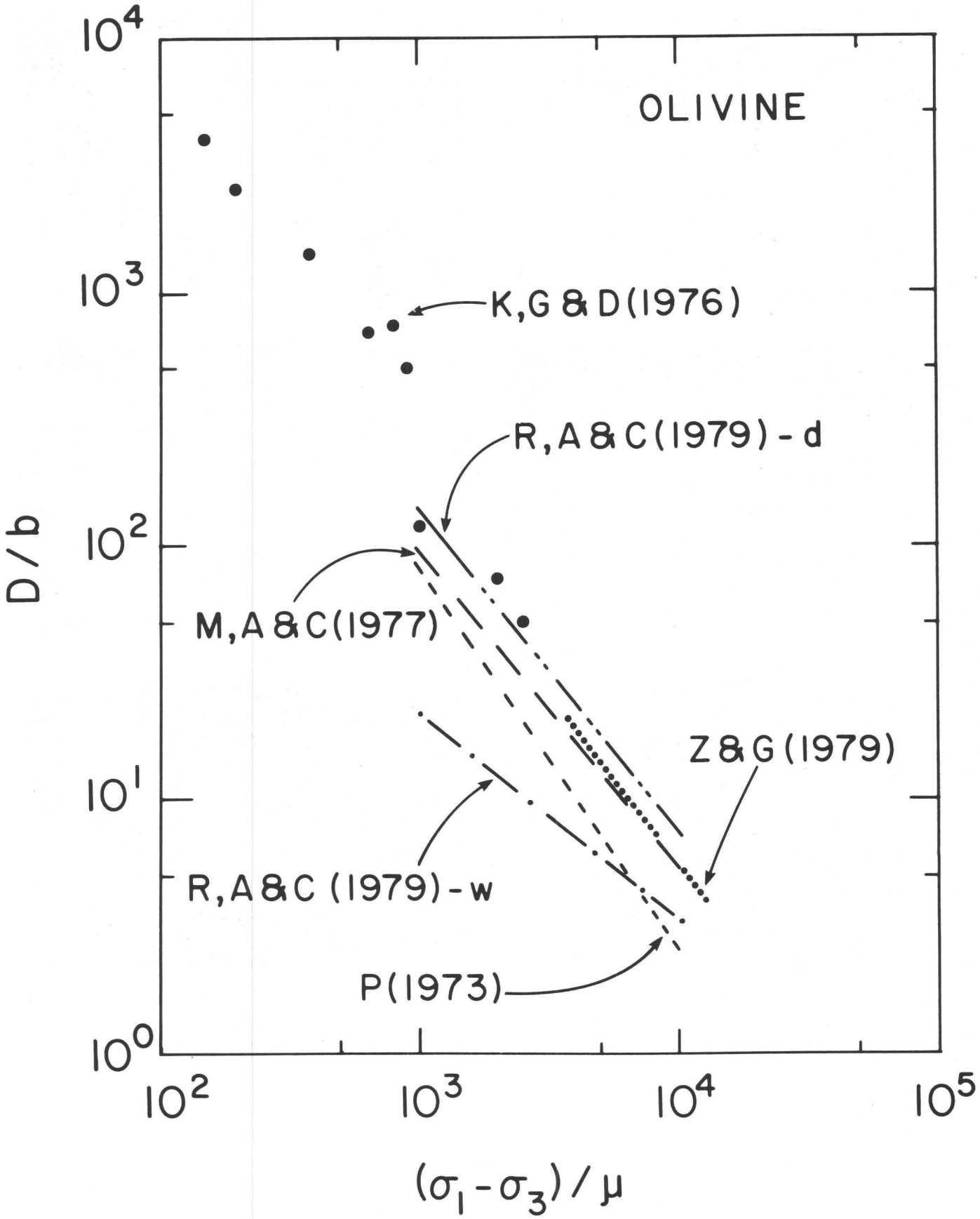
OLIVINE
K,G & D(1976)
R,A & C(1979) - d
M,A & C(1977)
Z & G(1979)
R,A & C (1979) - w
P(1973)
D/b
$(\sigma_1 - \sigma_3)/\mu$
10^0
10^1
10^2
10^3
10^4
10^5

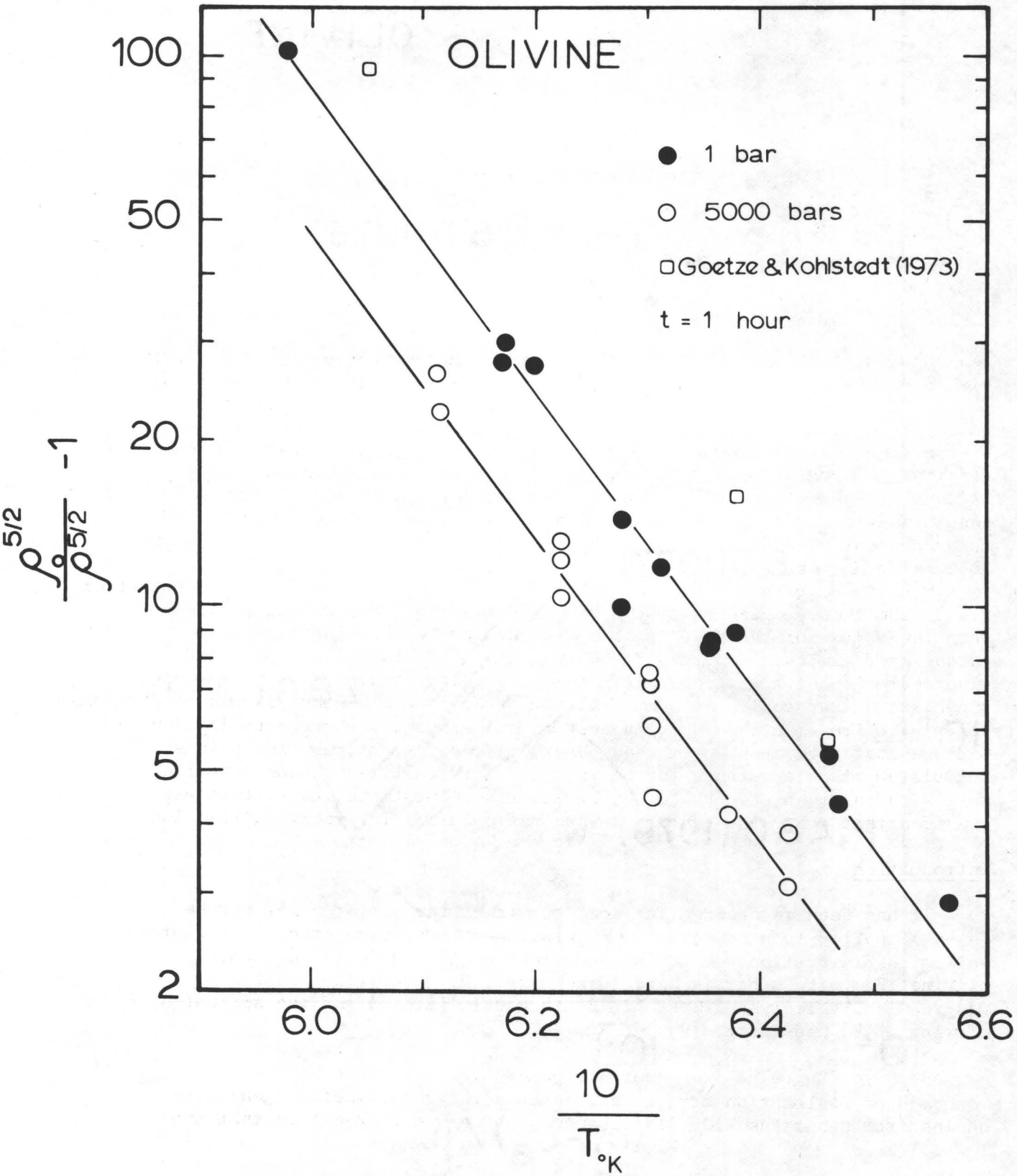
OLIVINE
1 bar
5000 bars
Goetze & Kohlstedt (1973)
t = 1 hour
100
50
20
10
5
2
6.0
6.2
6.4
6.6
$\frac{\rho_o^{5/2}}{\rho^{5/2}} - 1$
$\frac{10}{T_{°K}}$

STATIC THEORY OF SIZE VARIATION WITH STRESS FOR SUBGRAINS AND DYNAMICALLY RECRYSTALLIZED GRAINS

Project Title: Creep Properties of Ultrafine Grained Rocks
NSF Grants: EAR 75-21878, EAR 78-15206

Robert J. Twiss
Department of Geology
University of California
Davis, California 95616
Tel: (916) 752-1860

Abstract

Approximate theoretical equations relating stress to the steady state size of both subgrains and dynamically recrystallized grains are derived. The equations result from equating the strain energy of the dislocation walls defining the boundary of a nucleating grain, to the strain energy of the free dislocations in the grain volume at the steady state dislocations density. Subgrains and recrystallized grains are distinguished by the value of a parameter ϕ. This parameter is the ratio of dislocation length in the boundary to that in the volume of the nucleating grain and takes account of the assumption that a subgrain boundary encloses a volume containing a steady state density of dislocations, whereas a newly recrystallized grain boundary encloses a volume that is essentially dislocation free. The theory agrees closely with experimental data on grain sizes when the values of the adjustable parameters are within independently established limits. Subgrain boundaries act as dislocation sinks, and misorientation of a given boundary increases with strain until migration, annihilation and coalescense establish a steady state. Subgrain misorientations calculated from the theory apply only to the stage of subgrain nucleation and are therefore much lower than observed steady state misorientations. Calculated misorientations for nucleating recrystallized grains coincide well with observed steady state subgrain misorientations, consistent with the idea that subgrains can act as nucleation sites for recrystallization.

Introduction

It has been recognized for some time that the differential stress $(\sigma_1-\sigma_3)$ applied to a polycrystal undergoing steady state creep, correlates well with dislocation density in many metals [1] and in the silicate olivine [2]; with subgrain size in metals [1,3,4] and with the size of dynamically recrystallized grains in metals [5,6,7] and the silicates olivine [8,9] and quartz [9].

Because subgrains are generally bounded by low angle boundaries composed of dislocation arrays, and because recyrstallization generally begins from subgrains [10, 11] it seems reasonable to conclude that these

three features which correlate with differential stress are not independent of one another. Indeed, Bird et al. [1] have given an empirical relation between average dislocation spacing and subgrain size. In what follows, a static model is adopted as an approach to steady state features that allows the complexity of the dynamics to be ignored. Analysis of the strain energy of distributed dislocations and of dislocation arrays then leads rather simply to a first order theory which predicts the variation of subgrain and recrystallized grain size with stress. The theory fits available experimental data most satisfactorily. Different approaches have been given by Holt [12] and Gittus [13] for the derivation of the stress-subgrain size relation, and by Sandström and Lagneborg [14] for the stress-dynamically recrystallized grain size relation.

From this analysis, equations can also be derived relating stress to the misorientation of nucleating subgrains and recrystallized grains. Because the theory applies only to the stage of nucleation, the observational data available for the steady state misorientation of subgrains are very different from the theoretically predicted misorientation of the nuclei.

Analysis

The following assumptions are basic to the analysis:

1) It is assumed that the subgrains and recrystallized grains produced are of minimum possible size, subject to the following condition: The total strain energy of the dislocations in a closed boundary of a subgrain or recrystallized grain at nucleation is taken equal to the total strain energy of the dislocations distributed within the bounded volume (A. K. Mukherjee, 1975, pers. comm). The assumption of minimum possible size is justified because the probability of nucleation decreases with increasing size. The density of the dislocations in the volume is determined by the applied stress (equation 1). Whatever the process, the tendency of dislocations to order themselves into walls during steady state creep and annealing implies that the strain energy of ordered arrays is always less than or equal to that of the unordered distribution of dislocations in a volume. A trade-off exists, however, when the energy of dislocations ordered into a closed boundary is compared with the energy of unordered dislocations in the bounded volume. As the grain diameter d changes, the total energies of the surface and the volume change, respectively, as d^2 and d^3. Because the total volume energy changes more rapidly than the surface energy, a grain size exists at which the two energies are equal. Of course to drive the process, there must be a reduction of the internal strain energy, and a developing closed boundary must have a lower total energy than the enclosed volume. The equality, however, is the limiting case and is used in the equations below. Thus the critical size is taken to be the smallest subgrain or recrystallized grain size that can satisfy the energy equality under conditions of steady state. The manner in which subgrains and recrystallized grains are distinguished in the theory will become evident below.

2) The relation between differential stress and steady state dislocation density is accepted

$$\sigma = \alpha \Gamma b \rho^{1/2} \qquad \Gamma \equiv \frac{\mu}{1-\nu} \qquad (1)$$

TABLE 1
DEFINITION OF SYMBOLS WITH EQUATION NUMBERS OF FIRST OCCURRENCE ( ) AND DEFINITION [ ]

b	Burgers vector length $(1)_1$
D	spacing of dislocations in a simple tilt boundary (4)
d	steady state dimension of a subgrain or a newly recrystallized grain (2)
K	constant in the non-dimensional stress - grain size relation $(13)[14]_2$
p	exponent on the grain size in the non-dimensional stress - grain size relation $(13)[14]_1$
R	radius from a dislocation of a cylinder within which the dislocation strain energy is evaluated (3).
w	strain energy per unit length of an edge dislocation (3)
α	dislocation interaction parameter which describes the net effect of the interaction of a dislocation with its neighboring dislocations (1)
β	dislocation core energy parameter which accounts for the contribution of the core energy to the strain energy of a dislocation (3)
Γ	elastic parameter $(1)_1$, $[1]_2$
γ	energy per unit area in a simple tilt boundary (4)
η_o	compact notation for a four-term factor $(4)[5]_2$
θ	angle of tilt across a simple tilt boundary (17)
μ	shear modulus $(1)_2$
ν	Poisson's ratio $(1)_2$
ρ	dislocation density $(1)_1$
σ	differential stress: $\sigma_1-\sigma_3$ $(1)_1$
ϕ	dislocation length parameter. Ratio of the total dislocation length in a grain boundary to that in the grain volume. [9]

All symbols here and in subsequent equations are defined in Table 1. This equation is derived theoretically by assuming that, during steady state creep, the applied differential stress is equal to the back stress created by the dislocations [15]. The parameter α accounts for the complicated manner in which a large number of dislocations interact. It is of the order of 1. The experimental verification of this equation for a large number of different materials [1], and the theoretical understanding of its origin renders this assumption unproblematical.

3) It is assumed that all boundaries of subgrains and recrystallized grains can be approximated by simple tilt boundaries. Although this is an obvious oversimplication, the self energy of screw and edge dislocations differs only by a factor of $(1-\nu)$, and this assumption should therefore be a good first approximation. The application of a theory for low angle boundaries to recrystallized grains is believed appropriate for the early states of recrystallization. Recrystallized grains are observed to grow from subgrains [10, 11], and subgrain misorientation is generally less than 1° [1]. The equation for the strain energy of a low angle tilt boundary is appropriate for misorientations up to 10° or 15° [16], and therefore it should be applicable to recrystallized grains when they first form. After they form, recrystallized grains can rotate to form high angle boundaries, but this process is not relevant to the present theory.

4) Crystal anisotropy is neglected, and all dislocations are assumed to have equal Burgers vectors and the same energy per unit length. This assumption is made strictly to simplify the analysis. The requisite elastic moduli are taken to be those of a polycrystal of randomly oriented grains, and the Burgers vector is taken to be the smallest Burgers vector for a particular crystal. These simplifications are adequate for a first order theory.

Equating the dislocation strain energy of a closed boundary to the dislocation strain energy in the volume for a simple cubic grain of dimension d and dislocation density ρ gives:

$$6d^2\gamma = \rho d^3 w \tag{2}$$

For an edge dislocation in an infinite medium, the strain energy per unit length, within a cylinder of radius R about the dislocation, is given by [16, eq. 3-49]

$$w = \frac{\Gamma b^2}{4\pi} \ln \frac{\beta R}{b} \tag{3}$$

where β is the parameter that allows for the energy contribution from the dislocation core.

The energy per unit area in a simple tilt boundary composed of a single set of edge dislocations is given by [16, eq. 19-84]

$$\gamma = \frac{\Gamma b^2}{4\pi D} f(\eta_o) \tag{4}$$

$$f(\eta_o) \equiv \eta_o \coth \eta_o - \ln (2 \sinh \eta_o) \qquad \eta_o \equiv \frac{\pi b}{\beta D} \tag{5}$$

where D is the spacing of the dislocations in the boundary.

Introducing (3) and (4) into (2) gives:

$$f(\eta_o) = \frac{\rho dD}{6} \ln \frac{\beta R}{b} \tag{6}$$

An appropriate value for R in a crystal containing a large number of dislocations of both signs is half the distance between dislocations [16]. Beyond this distance the stresses associated with a dislocation are largely cancelled out by stresses from other dislocations. The dislocation density ρ has units of dislocation length per unit volume, or dislocations per unit area. Thus the mean distance between dislocations, 2R, is approximated by

$$R = 0.5\ \rho^{-0.5} = \frac{0.5\alpha\Gamma b}{\sigma} \tag{7}$$

where (1) was introduced to obtain the last expression in (7).

The total lengths of dislocation lines in the boundary (L_B) and in the volume (L_V) are, respectively

$$L_B = \frac{6d^2}{D} \qquad L_V = \rho d^3 \tag{8}$$

If the ratio of these two lengths is defined by

$$\phi \equiv \frac{L_B}{L_V} \tag{9}$$

then combining equations (8) with (9) yields

$$D = \frac{6}{\phi\rho d} \tag{10}$$

Introducing $(7)_2$ and (10) into (6), and substituting (10) and (1) into $(5)_2$ gives the complete form of the required relation between grain size and stress.

$$f(\eta_o) = \frac{1}{\phi} \ln \frac{0.5\alpha\beta\Gamma}{\sigma} \qquad \eta_o = \frac{\pi\phi}{6\alpha^2\beta} \left(\frac{d}{b}\right) \left(\frac{\sigma}{\Gamma}\right)^2 \tag{11}$$

where $f(\eta_o)$ is defined by $(5)_1$.

The form of $f(\eta_o)$ can be simplified considerably if $\eta_o << 1$. For the data considered below (Fig. 2), $\eta_o < 0.1$ which is sufficiently small to justify the use of the following approximations:

$$\coth \eta_o \simeq \frac{1}{\eta_o} \quad (\eta_o << 1) \qquad \sinh \eta_o \simeq \eta_o \quad (\eta_o << 1) \tag{12}$$

Combining (5), $(11)_1$, $(11)_2$, $(12)_1$, and $(12)_2$ and rearranging gives

$$\log \frac{\sigma}{\Gamma} = \log K - p \log \frac{d}{b}, \qquad \text{or} \qquad \frac{\sigma}{\Gamma} = K\left(\frac{d}{b}\right)^{-p} \tag{13}$$

where

$$p \equiv \frac{\phi}{2\phi - 1} \qquad \log K \equiv p\left\{\log \frac{3e\alpha^2\beta}{\pi\phi} - \frac{1}{\phi} \log 0.5\alpha\beta\right\} \tag{14}$$

and where e is the Napierian base.

The forms of (13) are essentially identical to the empirical equations found experimentally for the relation between stress and both subgrain size and recrystallized grain size. The exponent p is defined uniquely by the parameter ϕ, and the constant K is defined solely in terms of the material parameters α, β and ϕ. The relations are effectively independent of strain and temperature except insofar as the temperature affects the material parameters such as the elastic moduli and the Burgers vector.

It is possible to put fairly stringent limits on acceptable values for the parameters α, β and ϕ and thus to restrict the possible curves that the theoretical equation may describe. Experimentally determined values for the parameter α are between about 0.7 and 1.4 for many metals [1] and about 1.3 for the silicate olivine [17], where the values are appropriate for the use of the elastic parameters in Table (2) and the use of Γ rather than μ in (1). Theoretical considerations of the dislocation core energy [16] indicate values of the core energy parameter β could be in the range of approximately 1 to 8. Hirth and Lothe [16] suggest an average value of about 4 for non-metallic materials, and 1 to 2 for metals.

The only distinction between subgrains and recrystallized grains in this theory is the value of ϕ. The relevant difference between the two structures is that during steady state creep, a subgrain boundary encloses a volume having a relatively high dislocation density given by (1), whereas a newly recrystallized grain boundary encloses a volume that has been swept free of dislocations. Using a strictly heuristic argument, it is possible to associate the different structures with different, although approximate, values of ϕ. To deduce values for ϕ, note that equation $(11)_1$ can be written

$$D\gamma = \frac{1}{\phi} w \tag{15}$$

This means that the energy of a unit length of dislocation in the boundary ($D\gamma$) is equal to the energy of a length $1/\phi$ of dislocation in the volume.

We assume that during the development of a subgrain boundary, the dislocation density ρ remains constant at a value given by (1). The required minimization of the theoretically stable subgrain size is obtained by minimizing ϕ because at constant σ/Γ, equations (3) and (4) show that an increase in ϕ leads to an increase in the theoretically stable grain size. Thus we must take $\phi = 1$. Lower values would imply, from equation (15), that a dislocation would increase its self-energy by becoming part of the boundary, and the boundary would therefore never form. With this value for ϕ, equations (9) and (15) also imply that the energy of a unit length of dislocation in the boundary equals the energy of the same length of dislocation in the volume.

To produce a dislocation-free recrystallized grain, imagine that the dislocations in the volume all move outward by expansion of loops to form the grain boundary. In this case there is a net increase in the total dislocation length. Again the minimization of the theoretically stable grain size is achieved by minimizing ϕ. This requirement is satisfied if the boundary is formed by the expansion only of those dislocations originally in the volume when recrystallization began. The increase in the total dislocation

length is given by ϕ (equation 9) where $\phi > 1$. In this case, equation (15) means that the energy of a unit length of dislocation in the boundary after expansion of the dislocation loops is equal to the energy of a shorter length $(1/\phi)$ of dislocation in the volume before expansion of the loops.

According to the above model, the determination of a value for ϕ for recrystallized grains requires a knowledge of the average increase in dislocation length during the assumed expansion to the boundary. Given the complexity of dislocation structures, there seems no hope of actually calculating such a value. To obtain a first order approximation, however, assume all dislocations occur as planar circular loops in a spherical grain of diameter d, and take the mean diameter δ of all loops to be either half the grain diameter or that diameter which encloses half the area of a grain cross section. For these cases $\delta = 0.5d$ or $0.7d$ and $\phi = \pi d/\pi\delta = 2$ or 1.4.

Thus the independently expected limits on the material parameters can be summarized as

$$\begin{aligned} 0.7 \lesssim \alpha \lesssim 1.4 \\ 1 \lesssim \beta \lesssim 4 \\ \phi_s \simeq 1 \\ 1.4 \lesssim \phi_r \lesssim 2 \end{aligned} \qquad (16)$$

where the subscripts "s" and "r" refer to subgrains and recrystallized grains respectively.

The above argument indicates that a recrystallized grain boundary will have a higher total energy than a subgrain boundary under the same conditions because of the energy associated with the increase in total dislocation length. The equality of grain boundary energy with volume energy is therefore achieved at larger grain sizes for recrystallized grains than for subgrains.

Introducing the values of ϕ deduced above into equation $(14)_1$, the slope p of the curve represented by equation $(13)_1$ is found to be -1 for subgrains and in the approximate range of -0.67 to -0.78 for recrystallized grains. The variation of the intercept log K with p (or ϕ) for various values of α and β is illustrated in fig. 1.

The theory allows a calculation to be made concerning the misorientation across the boundary of a nucleating subgrain or recrystallized grain. In a tilt boundary, the angle of tilt θ is related to the spacing of the dislocations by [16, eq. 19-5]

$$D = b/(2 \sin 0.5\theta) \qquad (17)$$

Introducing equation (10) into (17) and using (1) gives

$$\theta = 2 \sin^{-1} \left[\frac{\phi}{12\alpha^2} \left(\frac{d}{b}\right)\left(\frac{\sigma}{\Gamma}\right)^2\right] \qquad (18)$$

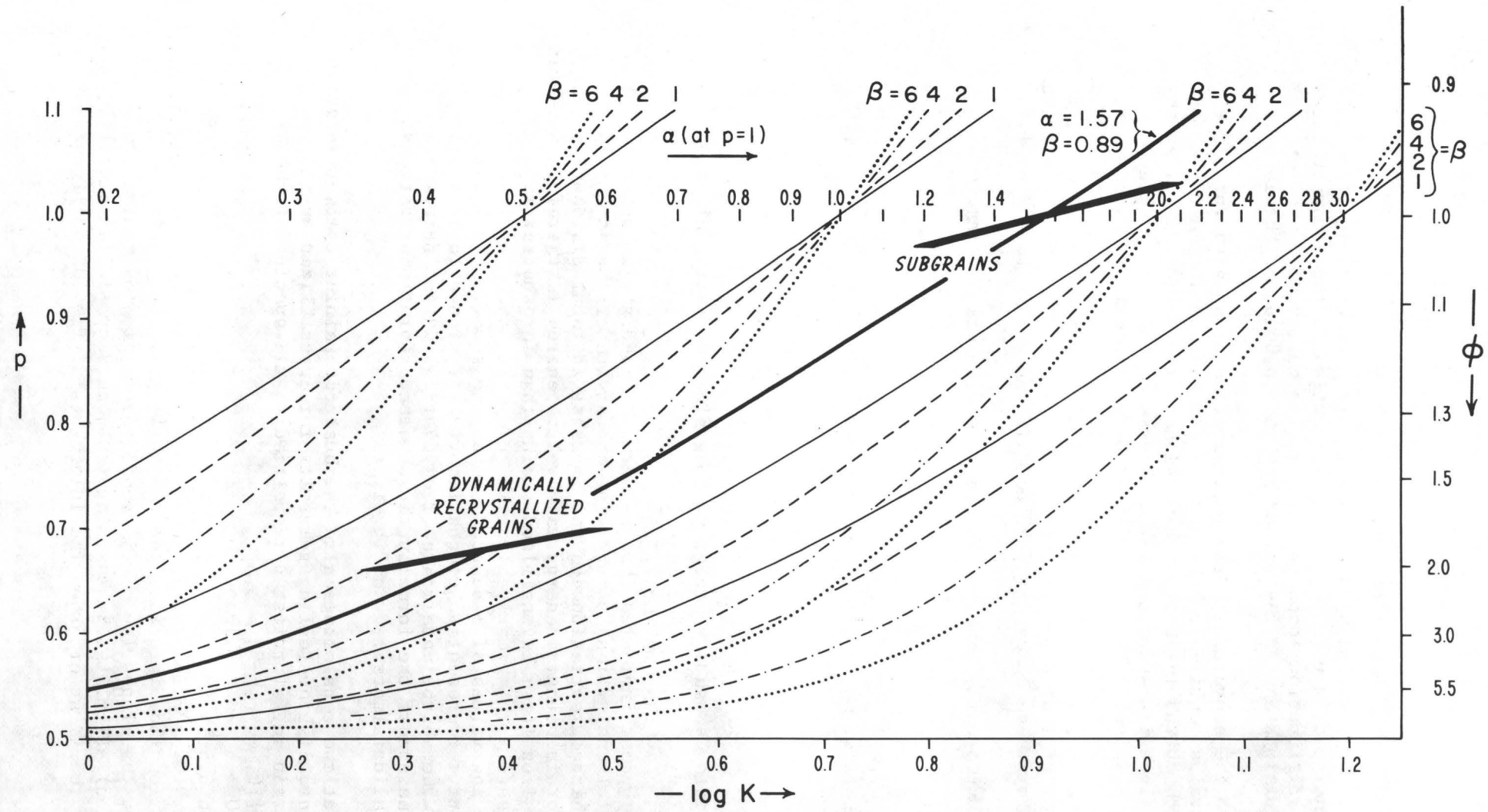

Figure 1. Variation of log K with p (or ϕ) for values of the parameters α and β. All curves having the same value of α intersect at p=1. These values of α are plotted along the p=1 line. For each of four values of α, curves are plotted for four values of β as indicated at the top ends of curves. Best values for subgrains and recrystallized grains are plotted as shaded parallelograms of error as given by equations (21). Values for the best fit are given in equations (26) and plotted as the heavy line.

Substituting $(13)_2$ into (18) then gives either of the following two equations

$$\theta = 2 \sin^{-1}\left[\frac{\phi K^2}{12\alpha^2} \left(\frac{d}{b}\right)^{1-2p}\right] \tag{19}$$

$$\theta = 2 \sin^{-1}\left[\frac{\phi K^{1/p}}{12\alpha^2} \left(\frac{\sigma}{\Gamma}\right)^{1/\phi}\right] \tag{20}$$

where p and K are defined in terms of α, β and ϕ in (14). These equations indicate that low stresses, which are associated with large subgrain or recrystallized grain sizes, result in small angles of misorientation for a nucleating subgrain or recrystallized grain. As stress increases and subgrain and recrystallized grain sizes decrease, the angles of misorientation of nucleating subgrains or recrystallized grains increase.

Equations (4) and (5) indicate that as the dislocation spacing in the boundary decreases, the energy per unit area of the boundary, γ, increases, and the energy per unit length of dislocations in the boundary, γD, decreases. This latter fact suggests that after the initial subgrain boundaries are nucleated, they could act as dislocation sinks, and the dislocation spacing would decrease and the misorientation would increase with increasing strain. In this case equations (19) and (20) would not be expected to describe the observed steady state subgrain misorientation.

Discussion

Some of the experimental data available from the literature for the variation of stress with both subgrain size and recrystallized grain size are plotted in Figure 2. The data were rendered non-dimensional using constants listed in Table 2, and the explanation of the symbols in Figure 2 is given in Table 3.

Unweighted linear regressions on each of the data sets are plotted as dashed lines. For the subgrain data, an unweighted linear regression on all the data gives a slope that is anomalously low and not characteristic of any of the data sets. This results from the predominance of different data sets at high and low stresses. The means of the slopes for the individual data sets are more representative of the data. For the subgrain data the mean slope is -1.00 ± 0.36, and for the recrystallized grain data it is -0.68 ± 0.05. The errors are formally the standard deviations of the slopes for the individual data sets.

Assuming that the mean slopes give the best fits to the data, unweighted linear regressions give the following results for the subgrain and recrystallized grain data (indicated respectively by subscripts s and r).

$$p_s = 1 \pm 0.03 \qquad \log K_s = 0.91 \pm 0.01 + 3.85\ \Delta p_s$$

$$p_r = 0.68 \pm 0.02 \qquad \log K_r = 0.38 \pm 0.01 + 5.30\ \Delta p_r \tag{21}$$

Here the error on the slopes is the 70% confidence limit (approximately 1 standard deviation) calculated by assuming the mean slope is the best fit to all the data; the first error on the intercepts is the 70% confidence

TABLE 2

ELASTIC PARAMETERS† AND BURGERS VECTORS FOR POLYCRYSTALLINE MATERIALS

MATERIAL	μ (10^4MPa)	ν	Γ (10^4MPa)	b (10^{-4} μm)
Aluminum	2.55	0.34	3.86	2.86
Copper*	4.62	0.35	7.11	2.56
Ice	0.34	0.36	0.53	4.5
Iron* α	7.65	0.28	10.6	2.48
γ				2.52
Nickel*	7.93	0.31	12.2	2.49
Olivine	7.8	0.24	10.3	6.98
Quartz	4.2	0.15	4.9	5.0

† Elastic parameters for metals are room temperature data from Smithells [18] Elastic parameters for polycrystalline olivine were calculated from wave velocities at 400 MPa pressure using formulas for isotropic bodies (Birch, Table 7-16 [19]

* The same data were used for all alloys of each metal

TABLE 3. KEY TO FIGURE 2

Curve No.	Material	Symbol	No. Data Points	Temperature Range °K	Slope*	Intercept*	Source
		RECRYSTALLIZED GRAIN SIZE DATA					
1	Cu	△	30	814-1220			
	Cu 1% Al	⧋	8	814-1220			
	Cu 4% Al	⧊	8	814-1220	-0.66	0.27	[6]
	Cu 8% Al	⧌	8	814-1220			
2	Ni	◇	19	1035-1552	-0.78	0.99	
3	Ni 5% Fe	◈	12	1207-1552	-0.66	0.21	
4	Ni 10% Fe	⟐	11	1207-1552	-0.71	0.44	[5]
5	Ni 20% Fe	⊕	11	1207-1552	-0.68	0.25	
6	α Fe	□	12	1023-1153	-0.63	-0.06	[7]
7	Olivine $(Mg_{.92}Fe_{.08})_2SiO_4$						
	wet	○	18	1073-1423	-0.67	0.37	[8]
	dry	⊕	12	1148-1699			
8	** Olivine $(Mg_{.92}Fe_{.08})_2SiO_4$		-NO DATA PLOTTED-		-0.81	1.15	[9]
9	** Quartz (SiO_2)		-NO DATA PLOTTED-		-0.71	0.23	
		SUBGRAIN SIZE DATA					
10	Ni	◆	2	923	-0.93	0.40	[20]
11	α Fe, vacuum melted	⬓	21	773-1123	-1.06	1.33	[7]
12	α Fe, zone refined	⬒	7	773-1123	-1.53	2.89	
13	low C Steel	◧	35	719-870 †	-0.95	0.66	[21]
14	Austenitic Stainless Steel	◨	16	977-1103	-1.33	2.60	[22]
15	316 Stainless Steel	◪	11	973-1173	-0.54	-0.84	
16	Fe 25% Cr	◩	7	773-1073	-0.80	-0.01	[24]
17	Fe 3% Si	◹	21	643-1373	-0.85	0.30	
18	Fe 3% Si	◹	7	916	-0.54	-0.87	[25]
19	Al	▼	12	528-889	-0.85	0.44	[26]
20	Al	▼	7	433-573	-1.62	3.22	[27]
21	Cu	▲	5	273	-1.02	0.92	[28]

*Slopes and intercepts are from my unweighted linear regressions on the reported data.
**These data were not used in determining the overall best fit to the data.
†Each of the data points in this set represents an average over the temperature range studied.

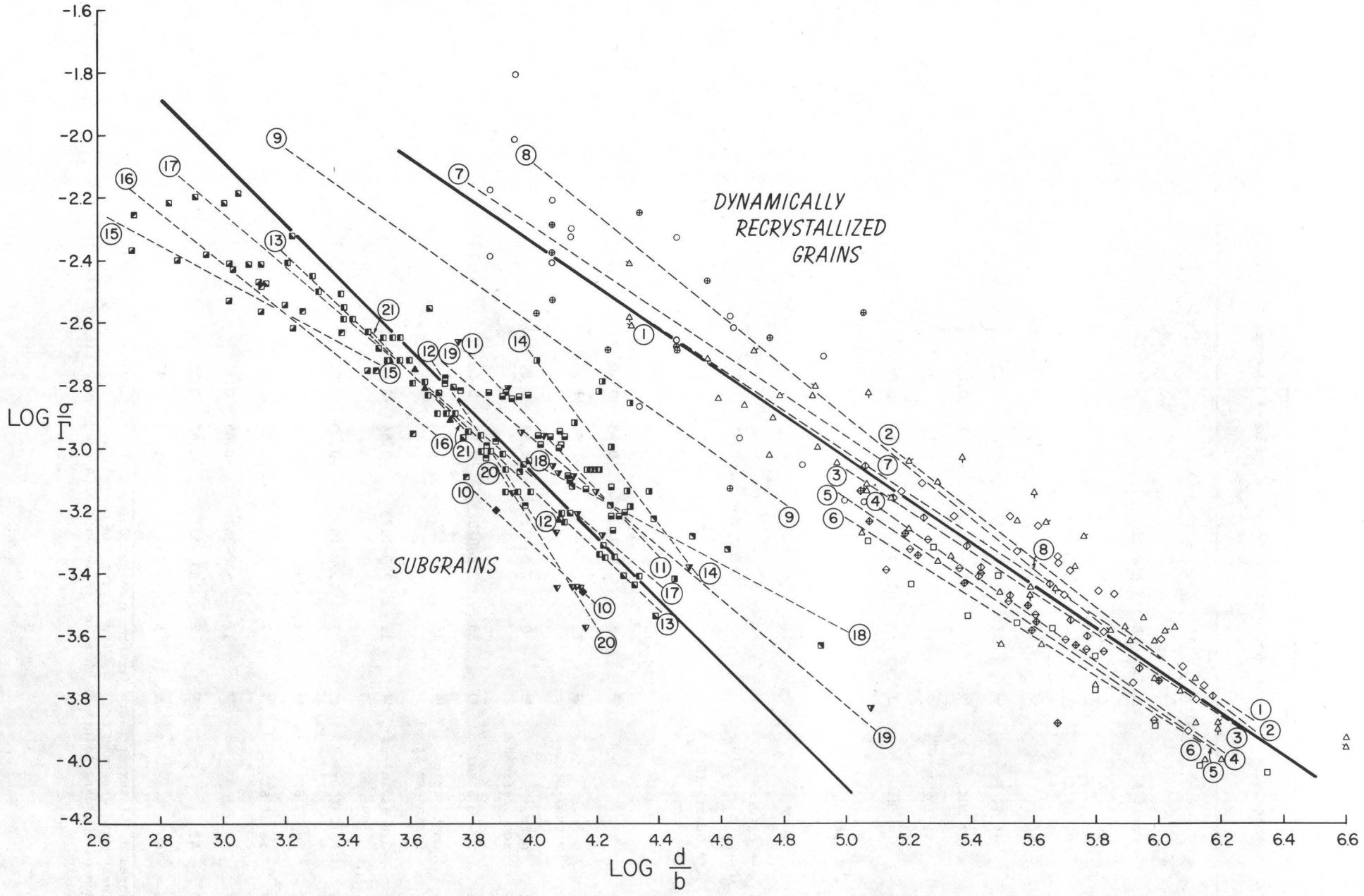

Figure 2. Non-dimensionalized plot of experimentally determined stress vs. subfrain size and recrystallized grain size for steady state creep. The key to the symbols is in Table 3. Dashed lines are unweighted linear regressions to individual data sets. Each solid line is a best fit to the respective groups of data for subgrains and recrystallized grains. The slope of the solid line is taken to be the mean of the slopes of the data sets in each group. The theoretical equation fits the solid lines exactly for physically reasonable values of the empirical parameters.

limit on the mean value of log σ/Γ; and the second error defines the dependence of the intercept on changes in slope [28]. Thus the equations that best fit the data are for subgrains:

$$\log \frac{\sigma}{\Gamma} = 0.91 - \log \frac{d}{b} \tag{22}$$

and for recrystallized grains

$$\log \frac{\sigma}{\Gamma} = 0.38 - 0.68 \log \frac{d}{b} \tag{23}$$

The data plotted in Figure 2 include considerable variation in temperature (Table 3) and strain both within and between individual data sets. Figure 2 indicates, therefore, that these variables cannot be very important in the correlation, and this is consistent with the theoretical results.

The theory includes four independent parameters, ϕ_s, ϕ_r, α, β, for which values must be chosen. Although independent limits can be set for these variables (16), the best values are determined empirically. Equations (14) provide four equations, two each for the subgrain and the recrystallized grain structures, by which values of the parameters can be determined if p_s, p_r, $\log K_s$ and $\log K_r$ are known. The test of the theory is whether the values of the parameters determined by using (21) in (14) are within the independently established limits given in (16).

Rearranging (14) gives

$$\phi = \frac{p}{2p-1} \tag{24}$$

$$\frac{1}{p} \log K + \log \phi - \frac{0.301}{\phi} - 0.414 = \frac{1}{p} \log \alpha + \left(1 - \frac{1}{\phi}\right) \log \beta \tag{25}$$

ϕ_s and ϕ_r are easily calculated from (24) using p_s and p_r from (21). Then using first $\log K_s$ and then $\log K_r$ from (21), equation (25) becomes a simple pair of linear equations with two unknowns, $\log \alpha$ and $\log \beta$. The solutions are:

$$\phi_s = 1 \pm 0.03$$

$$\phi_r = 1.89 \pm 0.15$$

$$\alpha = 1.57 \pm 0.33$$

$$\beta = 0.89 \begin{matrix} -0.55 \\ +2.46 \end{matrix} \tag{26}$$

where the errors indicate the extreme values of the parameters obtained by using the extremes indicated in (21). Although the value for β is slightly low, the error is heavily skewed toward higher values, and the agreement with expected values is therefore reasonable. All other values in (26) are within the independently expected limits, and the theory is therefore in excellent agreement with the data. Introducing (26) into (13) and (14) gives exactly the equations (22) and (23). These are plotted as solid lines through the data in Figure 2.

If the values for the parameters given in (21) and (26) are introduced into equation (20), the predicted misorientation angle θ depends on stress for nucleating subgrains according to

$$\theta_s = 2 \sin^{-1}[0.27\frac{\sigma}{\Gamma}] \quad \text{or} \quad \log \sin\frac{\theta}{2} = -0.57 + \log\frac{\sigma}{\Gamma} \tag{27}$$

and for nucleating recrystallized grains according to

$$\theta_r = 2 \sin^{-1}[0.23(\frac{\sigma}{\Gamma})^{0.53}] \quad \text{or} \quad \log \sin\frac{\theta}{2} = -0.64 + 0.53 \log\frac{\sigma}{\Gamma} \tag{28}$$

Equations $(27)_2$ and $(28)_2$ are plotted in Figure 3 with some data on the variation of subgrain misorientation with stress [30, 31, 32]. It is clear that the theoretical relation for nucleating subgrains predicts a misorientation more than an order of magnitude smaller than is observed at steady state. This result is consistent with the qualitative theoretical expectation discussed in the previous section. The optimum size of the subgrains is established at the stage of subgrain nucleation when the misorientation, given by (27), is very low. Once the subgrain boundary and the subgrain size are established, any dislocation can lower its self-energy by becoming part of the boundary. Thus the boundary is a dislocation sink, and as strain increases, dislocations join the boundary and the spacing decreases below the theoretical value, giving higher misorientation angles at constant subgrain size. This increase of misorientation with strain is indicated in Figure 3 by the data plotted as circles [31] near which the values of strain are given. A similar increase of misorientation angle with strain in subgrains in aluminum is indicated by the data of Exel and Warrington [33, Fig. 8]. In this case, the misorientation increases until a strain of about 0.10 at which point the subgrain misorientation becomes roughly independent of strain. A model of subgrain boundary migration, collision and annihilation [33, 34] can account adequately for the steady state misorientation achieved. It does not, however, account for the increase in steady state misorientation with stress that the data in Figure 3 may suggest.

The definition of what constitutes a newly recrystallized grain is somewhat ambiguous. Generally such grains are recognized by their high angle boundaries. For equation (28), however, the implicit criterion is size. Because subgrains can grow or coalesce into recrystallized grains it would be difficult in practice to recognize exactly when a grain should be considered a newly recrystallized grain. Thus as a predictor of any physically available measurement, equation (28) is of doubtful use. It is noteworthy, however, that the predicted misorientation of nucleating recrystallized grains is close to the observed steady state misorientations of subgrains and that it has approximately the same stress dependence (Fig. 3). This is at least consistent with the observation that subgrains can be nucleation sites for recrystallization [10, 11].

These ideas and the observations on subgrains require that individual subgrains be viewed as transient parts of a substructure that is continously being annihilated and reformed [33, 34]. This model of subgrains provides the following features:

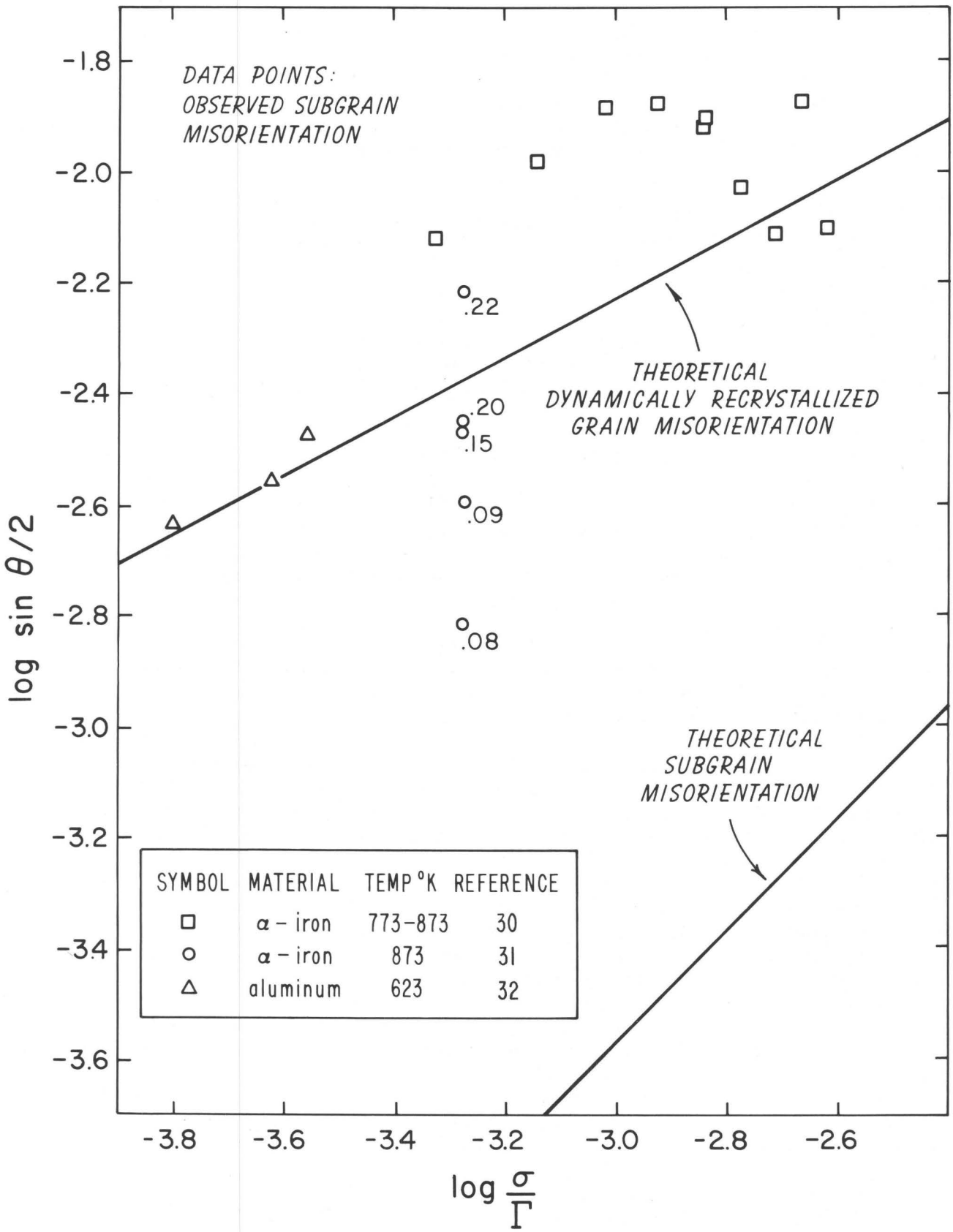

Figure 3. Variation of observed steady state subgrain misorientation with stress compared with the theoretical predictions for nucleating subgrain and recrystallized grain misorientations. The numbers beneath the data of Garofalo et al. [31] (circles) are the strains at which the measurements were made. These data are not steady data except possibly for the point at a strain of 0.22.

1) Subgrains nucleate from a nearly random distribution of dislocations. The size is determined by the energy considerations discussed above at the earliest states of the process by which dislocations order themselves into walls.

2) Because dislocation self-energy is lowered when a dislocation joins a wall, the subgrain boundary acts as a dislocation sink and tends to collect dislocations. This causes an increase in subgrain misorientation with increasing strain at constant subgrain size until a steady state misorientation is established by the migration, collision, and annihilation of walls of opposite sign [33, 34]. There is no theoretical prediction, however, that steady state subgrain misorientation should be dependent on stress, and the suggestion of such a dependence in Fig. 3 indicates the need for more extensive and detailed study.

3) The migration of subgrain boundaries with consequent coalescence or annihilation results in subgrain growth. Ideally when a subgrain has grown to more than twice its original dimension, new small equiaxed subgrains develop inside having initially a low misorientation, and a size given by equation (22). The size and shape of the subgrain population is thereby maintained at a steady state distribution, accounting for the success of equations (13) and (14).

4) Wide variation in observed subgrain misorientation in any one specimen is expected because the subgrains boundaries that formed at different times have experienced different amounts of strain and have collected different numbers of dislocations at any given instant.

5) As subgrains grow older, their boundaries tend to increase in misorientation and to expand, becoming filled in with newer, smaller, less misoriented subgrains. The older boundaries with the greater misorientation may define the larger subgrains observed optically in transmitted polarized light [35] or in reflected light from a chemically treated surface [1]. The smaller less misoriented subgrains would be the ones observed in transmission electron microscopy and are close to the size predicted theoretically. This provides a possible explanation for the disparity between subgrain size data collected by optical methods and those collected by electron optical methods [1].

6) Under some circumstances, the larger, more highly misoriented subgrains may become the nucleation sites for recrystallization. The misorientation and its stress dependence predicted by equation (28) for nucleating recrystallized grains coincides well with the observed steady state misorientation available in subgrains (Fig. 3). This is therefore consistent with the nucleation of recrystallized grains at subgrains.

This version of the theory does not explicitly account for the energy contribution to the process of dynamic recrystallization from the subgrain boundaries that are wiped out by the recrystallization. Attempts at further improving the assumptions of the theory to account for this are currently in progress.

Summary

Equations are derived relating the applied differential stress during steady state creep to both the subgrain size and the dynamically recrystallized grain size. It is assumed that the total dislocation strain energy in a closed boundary is equal to the total dislocation strain energy in the enclosed volume, and that the energy relations can be approximated by edge dislocations, simple tilt boundaries, and isotropic elasticity. This energy equality defines a unique grain size which is a function of volume dislocation density. Stress is introduced through the well-known relation between differential stress and dislocation density. The resulting equations can also be used to obtain a relation between the applied differential stress and the misorientation of nucleating subgrains and dynamically recrystallized grains.

The distinction between subgrains and dynamically recrystallized grains is provided by the value of a single parameter ϕ, which is the ratio of total dislocation length in the closed boundary to that in the enclosed volume at nucleation. By a geometrical argument, the value of ϕ can be linked to the fact that a subgrain boundary coexists with a steady state dislocation density in the volume, whereas a newly recrystallized grain boundary encloses a volume that has been swept free of dislocations.

Data on subgrain size and recrystallized grain size for a variety of metals and silicates are used to determine empirically the best values for the adjustable parameters in the theory. These values fall within the range of values expected independently for a variety of materials. The theory is therefore in good agreement with observation.

The equations relating the misorientation of nucleating subgrains to differential stress do not describe the observed steady state subgrain misorientation. This is because the process that defines the subgrain size is different from the one that produces a steady state misorientation, and the theory does not apply to the latter. After nucleation, subgrain boundaries act as dislocation sinks and misorientation increases with strain. An approximate steady state misorientation is reached and maintained by subgrain boundary migration, coalescence, and annihilation [33, 34]. This observed steady state subgrain misorientation is approximately the same as that calculated to be appropriate for the nucleation of recrystallized grains. This is consistent with the ability of subgrains to act as nucleation sites for recrystallization.

Acknowledgment

I am indebted to A. K. Mukherjee for conversations in which he suggested the basic assumption on which the theory is based.

References

1. J. E. BIRD, A. K. MUKHERJEE and J. F. DORN, *Quantitative Relation Between Properties and Microstructure*, p. 255. Proc. Intl. Conf., Haifa, Israel (1969).

2. D. L. KOHLSTEDT and C. GOETZE, *J. Geophys. Res.* 79, 2045 (1974).

3. J. WEERTMAN, *ASM Trans.* 61, 681 (1968).

4. O. D. SHERBY and C. M. YOUNG, *Rate Processes in Plastic Deformation of Materials*, p. 497. Am. Soc. Metals (1975).

5. M. J. LUTON and C. M. SELLARS, *Acta Met.* 17, 1033 (1969).

6. R. BROMLEY and C. M. SELLARS, *The Microstructure and Design of Alloys*, p. 380. Proc. 3rd Intl. Conf. on the Strength of Metals and Alloys, v. 1 (1973).

7. G. GLOVER and C. M. SELLARS, *Metal. Trans.* 4, 765 (1973).

8. R. L. POST, Jr., Ph.D. Thesis, UCLA (1973).

9. J.-C. C. MERCIER, D. A. ANDERSON and N. L. CARTER, *Pure and Appl. Geophys.* (in press) (1977).

10. R. D. DOHERTY and R. W. CAHN, *J. Less-Common Metals* 28, 279 (1972).

11. T. H. BELL and M. A. ETHERIDGE, *Tectonophys.* 32, 235 (1976).

12. D. L. HOLT, *J. Appl. Phys.* 41, 3197 (1970).

13. J. H. GITTUS, *Phil. Mag.* 35, 293 (1977).

14. R. SANDSTRÖM and R. LAGNEBORG, *Acta Met.* 23, 387 (1975).

15. Z. S. BASINSKI, *Phil. Mag., Ser. 8* 4, 393 (1959).

16. J. P. HIRTH and J. LOTHE, *Theory of Dislocations*. McGraw-Hill, New York (1968).

17. D. L. KOHLSTEDT, C. GOETZE, and W. B. DURHAM, *Physics and Chemistry of Minerals and Rocks*. R. J. G. Strens, ed., p. 35. John Wiley & Sons, New York (1976).

18. C. J. SMITHELLS, *Metals Reference Book*, v. 2. Butterworths, Washington (1962).

19. S. P. CLARK, *Handbook of Physical Constants, Revised Edition*, Geological Society of America, Inc., New York (1966).

20. S. K. MITRA and D. McLEAN, *Metals Sci. Jour.* 1, 192 (1967).

21. A. GOLDBERG, *J. Iron and Steel Inst.* 204, 268 (1966).

22. F. GAROFALO, *Fundamentals of Creep and Creep Rupture in Metals.* MacMillan Co., New York (1965).

23. F. GAROFALO, O. RICHMOND, W. F. DOMIS and F. von GEMMINGEN, *Joint Intl. Conf. on Creep*, p. 1. Inst. Mech. Eng., London (1963) (Referenced in [24]).

24. C. M. YOUNG and O. D. SHERBY, *J. Iron and Steel Inst.* 211, 640 (1973).

25. C. R. BARRETT, W. D. NIX and O. D. SHERBY, *ASM Trans. Quart.* 59, 3 (1966).

26. H. J. McQUEEN, W. A. WONG and J. J. JONAS, *Can. J. Phys.* 45, 1225 (1967).

27. P. W. CHEN, C. T. YOUNG and J. L. LYTTON, *Rate Processes in Plastic Deformation of Materials*, p. 605. Am. Soc. Metals (1975).

28. J. E. PRATT, *J. Materials* 1, 77 (1966).

29. R. L. WINE, *Statistics for Scientists and Engineers*, Prentice-Hall Inc., Englewood Cliffs, N. J. (1964).

30. A. ORLOVA, M. PAHUTOVA and J. CADEK, *Phil. Mag.* 25, 865 (1972).

31. F. GAROFALO, L. ZWELL, A. S. KEH and S. WEISSMANN, *Acta Met.* 9, 721 (1961).

32. V. I. BETEKHTIN and M. M. MYSHLYAYEV, *Phys. Metals Metallog.* 24, 81 (1967).

33. S. F. EXEL and D. H. WARRINGTON, *Phil. Mag.* 29, 1121 (1972).

34. D. H. WARRINGTON, *Nuclear Metal.* 20, 672 (1976).

35. C. B. RALEIGH and S. H. KIRBY, *Mineral. Soc. Amer. Spec. Pap.* 3, 113 (1970).

FLOW STRESS FROM MICROSTRUCTURES OF MYLONITES: EXAMPLE AND CURRENT ASSESSMENT.

John M. Christie and Alison Ord

Department of Earth and Space Sciences

University of California, Los Angeles

ABSTRACT.

Several recent studies have attempted to determine the flow stresses during geological deformations from the microstructures of rocks, utilizing quantitative estimates of such structural parameters as grain size, subgrain size and dislocation density. The basis for these stress determinations is the apparent correlation between flow stress and microstructures in experimental deformation studies of several crystalline materials. Estimates of flow stresses are presented for a group of quartz-bearing mylonitic rocks from the Coyote Mountain mylonite zone, near Borrego Springs, California, using the grain sizes and dislocation densities of quartz grains. Neglecting complexities in the geological history of the rocks, flow stresses inferred from grain sizes range from 16 to 74 MPa (160 to 740 bars), whereas those derived from dislocation densities range from 214 to 82 MPa, respectively, for the same rocks. Stress estimates by the two methods are not well correlated and may differ by an order of magnitude for the same rock. The major causes of the inconsistencies are considered to be (1) inadequacy of the currently available experimental data and (2) complexity of the thermomechanical history of the rocks. These problems are discussed and the potential value of the methods is assessed.

It appears likely that the rocks were subjected to flow stresses ($\sigma_1 - \sigma_3$) of 100 MPa (1 Kilobar) or more during mylonitization.

INTRODUCTION

Extensive microstructural studies of metals deformed by hot-working (that is, at temperatures where recrystallization accompanies deformation) have shown that recrystallized grain size (Luton and Sellars, 1969; Glover and Sellars, 1973; Bromley and Sellars, 1973), sub-grain size and dislocation density (Bird et al., 1969) vary systematically with the steady state flow stress and are independent of temperature and total strain (after a small critical strain). These studies have been reviewed by Twiss (1977), who also derived an approximate theoretical relationship between recrystallized grain size, sub-grain size and flow stress.

Several experimental studies on olivine single crystals deformed at high temperatures (Goetze and Kohlstedt, 1973; Kohlstedt and Goetze, 1974; Kohlstedt et al., 1976; Durham et al., 1977) indicate a consistent relationship between dislocation density and flow stress. Post (1973, 1977) and Mercier et al. (1977) have demonstrated that recrystallized grain size and sub-grain size vary monotonically with flow stress in experimentally deformed dunite samples. These authors and others (Kirby and Wegner, 1979) have used the experimental correlations between stress and microstructural parameters to infer flow stresses in the mantle from the microstructures of dunite in xenoliths from volcanic rocks and diatremes and from ultramafic massifs.

In principle, these techniques may be used to determine flow stresses in crustal rocks from orogenic belts or from the deeper parts of major fault zones provided that adequate experimental data are available on the relevant minerals to provide a reliable correlation between flow stress and microstructural parameters. At present limited experimental data have been published for dislocation density in calcite in experimentally deformed Yule Marble (Goetze and Kohstedt, 1977) and these data have been employed to derive flow stresses for calc-mylonite (Lochseitenkalk) from the Glarus overthrust (Briegel and Goetze, 1978). Similarly, experimental correlations between flow stress and both grain size (Mercier et al., 1977) and dislocation density in quartz have been used to infer the flow stresses during mylonitization of quartzites along the Moine Thrust, N. W. Scotland (Weathers et al., 1978; Cooper et al., 1978, Kohlstedt et al., this Conference).

Similar microstructural measurements on mylonitic rocks from a movement zone cutting granitic rocks, gneisses and migmatites at Coyote Mountain, near Borrego Springs, California are summarized below. Flow stresses are inferred from grain sizes and from dislocation densities in quartz layers in the mylonites. Incompatibilities between the two sets of stresses are discussed and problems inherent in making reliable interpretations of flow stress from microstructural data are assessed.

THE COYOTE MOUNTAIN MYLONITE ZONE

General Statement

The Coyote Mountain mylonite zone, near Borrego Springs, California (Theodore, 1967, 1970) cuts gneisses, migmatites and granitic rocks, which are locally converted to mylonitic rocks, showing varying degrees of development of mylonitic lamination and reduction of grain size. Mylonitic rocks are present in a zone several kilometers wide but mylonitization is not complete within this zone; lenses of relatively undeformed gneisses and migmatites are separated by zones of mylonitic rocks. Theodore (1970) demonstrated from the mineral parageneses that mylonitization took place, at least partly, under amphibolite facies conditions, at temperatures between 580 and 660°C.

The microstructures of six samples showing varying degrees of mylonitization were studied in detail (Ord et al., 1979) using standard petrographic methods, reflected light microscopy of etched, polished surfaces and transmission electron microscopy (TEM). The rocks varied from slightly mylonitic gneisses, with weak development of foliation and lineation (924, 925), to a blastomylonite (755) with well-developed lamination and lineation and very fine grain size. Progressive textural changes could be traced in the suite of samples: (a) Lenses of quartz show increasing elongation and reduction of grain size; all of the quartz is, however, recrystallized to more or less equant grains which show little undulatory extinction and no deformation lamellae. (b) Feldspar porphyroclasts are highly strained and commonly fractured. They show slight evidence of recrystallization to extremely fine equant grains in a thin "rind" at their margins. (c) Mica porphyroclasts in the coarser samples are bent or kinked and in the fine-grained rocks the mica is completely recrystallized to fine-grained aggregates parallel to the foliation. The textures of three of the samples, representing slight, moderate and maximum degrees of mylonitization, are shown in Figure 1.

The TEM examination revealed that only quartz was suitable for complete microstructural analysis. The feldspar porphyroclasts contained high densities of planar defects (twins, exsolution lamellae, or stacking faults) of two orientations which obscured the dislocations in TEM images. The small recrystallized feldspar grains contained variable but lower densities of planar and linear defects. In general, the grain sizes of the minor recrystallized feldspar grains were an order of magnitude smaller than those of quartz grains.

Methods of examination

Standard thin sections were prepared from each sample, oriented (A) perpendicular to the foliation and lineation and (B) perpendicular to the foliation and parallel to the lineation, for petrographic examination and preliminary estimates of grain size.

Slabs of the same orientations (A and B) were mechanically polished, then etched with ammonium bifluoride solution to reveal grain boundaries, sub-grain boundaries and dislocation etch pits. Because of the extreme anisotropy of the rate of solution in different crystallographic directions in quartz it was necessary to employ sequential etches to produce etch structures in grains of all orientations. The cumulative etching times varied from 15 minutes to 2 hours.

Grain sizes in quartzose layers of the rocks vary considerably with the degree of purity of the layer. The grain size is maximal (and uniform) in pure quartz layers, decreasing with increasing proportions of other phases, notably micas. This is a well-known phenomenon in quartz-mica aggregates (Hobbs et al., 1976, p. 112-113). The grain size of the quartz is approximately equal to the spacing of the mica grains and is controlled by the high grain boundary energy of mica relative to quartz. In this study grain size estimates were made only in pure quartz layers by the method of linear intercepts (Smith and Guttman, 1953) on etched sample surfaces of both orientations, and were consistent with similar estimates made on thin sections between crossed polarizers on a polarizing microscope. It is emphasized that such measurements should be made in monomineralic layers because of the general tendency of other phases to limit grain growth. Details of the etching procedures which were developed by M. W. Wegner are described elsewhere (Wegner, in preparation).

The grain size (D) given here represents a somewhat arbitrary "mean grain dimension." It is derived from statistical counts of "linear intercepts"; that is, the number of intersections of grain boundaries per unit length with lines in three mutually perpendicular directions [parallel to the lineation (l), transverse to the lineation in the foliation (t) and normal to the foliation (n)]. The geometric mean of these three quantities $N(n,t,l)$ is $\overline{N}_L$. The ratio (S/V) of grain boundary area (S) to volume (V) of a polycrystal, an important structural parameter, is exactly twice $\overline{N}_L$ (Smith and Guttman, 1953). The mean grain dimension (D) is derived through the arbitrary assumption that all of the grains are cubes with shared faces of edge length D ($S/V = 3/D$), so that $D = 3/2\ \overline{N}_L$.

In principle, sub-grains can be measured by the linear intercept method if the sizes are in the microscopic range. Sub-grains are present in some quartz grains in the Coyote Mountain mylonites and are well delineated by the etching methods (Figure 2).

Surface etch pits corresponding to the emergence of dislocations are present on the surfaces of grains etched for appropriate times. In these rocks they are so closely spaced that the pits interfere with each other and are difficult to count. This is consistent with the dislocation densities determined by TEM observations (below), in the range 0.5 to 20 x 10^9 cm per cm^3. The maximum dislocation densities that can be counted reliably by optical examination of etch-pits are in the range 10^6 to 10^7 cm^{-2}.

Electron-transparent "foils" of both orientations (A and B) were

prepared from sections of each rock by ion milling and examined at 200 kV in a JEM-200 transmission electron microscope. Representative areas were photographed at magnifications of 10,000 to 20,000 times. Diffraction conditions were adjusted by tilting the specimen to provide optimum contrast of all the dislocations. Diffraction contrast (tilting) experiments were carried out in a few crystals to determine if all the dislocations were in contrast, but this procedure could not be carried out routinely because it is too time-consuming and the rate of degradation (vitrification) of the quartz crystals in the electron beam was relatively rapid.

Intersections of dislocations with both sample surfaces were counted in 15 to 25 micrographs from each foil. The value n was obtained by dividing the number of intersections (x) by twice the area of the image ($n = x/2A$). This value n would represent the dislocation density if all dislocations were perpendicular to the foil surfaces. However, if the dislocations are randomly oriented, n underestimates the true dislocation density by a factor of $\frac{4\pi}{3}$ (McCormick, 1977). In the samples under study the dislocations were randomly oriented, to a good approximation. Hence the dislocation densities (N) quoted below are:

$$N(cm^{-2}) = \frac{4\pi}{3} \cdot \frac{x}{2A}$$

where x is the number of intersections in area A (cm^2) of the foil.

Summary of Microstructural Data

The textures of the mylonitic rocks are represented by the optical micrographs of three samples, including one of the coarsest (925) and one of the finest grained (755), in Figure 1. Estimates of recrystallized grain size in pure quartz layers in the six samples are listed in Table 1. The standard deviations of estimates from different linear counts are between 20 and 32 percent. The grain sizes vary from 208 μm in the coarsest mylonitic gneiss (925) to 22 μm in the blastomylonite (755).

Sub-grains are well developed in some of the quartz grains in the mylonites, as shown in the micrograph of etched grain surfaces in Figure 2. However, it was not practical in the Coyote Mountain mylonites to obtain statistical measurements of their sizes as sub-grains were present in small numbers (2-5) in only a small fraction of the suitably etched quartz grains (<20 percent). It is worth noting that the sub-grain size in these rocks is generally too large to be measured by TEM methods, so that the etching procedure is the best method of determining sub-grain size in these and most other quartz-bearing rocks.

Typical dislocation sub-structures in three of the rocks are illustrated in Figures 3, 4 and 5. The dislocation configurations are qualitatively similar in all samples, although the dislocation densities differ considerably between samples. Dislocation networks and other sub-boundaries are

widely spaced at the TEM scale. The free dislocations are uniformly distributed and they are commonly curved and, to a good approximation, randomly oriented. Triple nodes are relatively common, as are dislocation loops of all sizes. These features are characteristic of metals and minerals either deformed at relatively high temperatures (hot-worked) or partially recovered by annealing after cold-working. The curved dislocations, triple nodes, net-works and small loops all signify extensive climb and interaction of dislocations, which may occur in both creep and annealing.

Dislocation densities (N) for the six samples, estimated with the assumption of random orientation as described above, are listed in Table 2. The standard deviations, based on counts in different micrographs in each sample, provide a measure only of the homogeneity of dislocation density in different regions of quartz in the sample. They do not reflect probable errors in the estimates. Such errors may be present because of (a) out-of-contrast dislocations in some plates, (b) non-random orientation of dislocations and (c) counting errors due to overlap of dislocations. These errors should be similar in all samples and are estimated to be less than ± 30 percent.

Flow Stresses Inferred from Microstructures

It has been shown that several metals deformed by hot-working undergo dynamic recrystallization (e.g. Bromley and Sellars, 1973) and this process has also been demonstrated in quartzite (e.g. Tullis *et al.*, 1973; Ardell *et al.*, 1973). Under these conditions, the recrystallized grain size is related to the flow stress by an equation of the form:

$$(\sigma_1 - \sigma_3) = A.D^{-m},$$

where A and m are constants. On the basis of rather limited data on quartzites deformed in hydrous assemblies, Mercier *et al.* (1977) have obtained the relation:

$$(\sigma_1 - \sigma_3) = 381.D^{-0.71}$$

where stress is in MPa and D is in μm. The theoretical relationship derived by Twiss (1977) has slightly different values for A (= 603 MPa) and m (= 0.68). These are shown graphically in Figure 6. The difference between the two functions is small, amounting to differences in estimated flow stresses for a given grain size of less than a factor of two (Table 1). If it is assumed that the textures of the rocks developed during steady state flow, without later modification by transient deformation or annealing, then using the experimental relationship of Mercier *et al.* (1977), the inferred flow stresses $(\sigma_1 - \sigma_3)$ vary between 9 and 42 MPa, or, using Twiss' (1977)

theoretical relationship, between 16 and 74 MPa.

The dislocation density in many materials deformed at moderate to high temperatures is also controlled by the applied stress and is independent of temperature and strain (Bird et al., 1969). Few experimental data are available for quartz in spite of the fact that several TEM studies have been made on experimentally deformed quartz crystals and aggregates. The reason for this paucity of data is that in many of the experimentally deformed samples the flow stresses were high and resulting dislocation distributions were extremely heterogeneous and dislocation densities were too high to determine with adequate precision (Ardell et al., 1973). The most reliable experimental data are those of McCormick (1977) for synthetic quartz crystals of high hydroxyl content deformed in creep and at constant strain-rate at atmospheric pressure.

The model commonly used to account for the relationship between dislocation density and applied stress is based on the argument that when recovery processes control the deformation rate, the dislocation density will increase until the internal or "back stresses" due to dislocation interactions with obstacles increase to the value of the applied stress. Then deformation can only proceed, by further dislocation generation and motion, as existing dislocations are removed by recovery. This yields a relationship of the form:

$$N = \left[\frac{\tau}{\mu b/2\pi(1-\nu)}\right]^2$$

where τ is the applied shear stress on the slip planes, μ is the shear modulus, ν is Poisson's ratio and b is the Burgers vector of the dislocations.

Cooper et al. (1978) and Weathers et al. (in press) have used a relation between flow stress and dislocation density N of the form:

$$(\sigma_1 - \sigma_3) = \alpha\ \mu\ b\ N^{0.5}$$

with values of $\alpha = 3.0$, $\mu = 44$ GPa and $b = 0.5$ nm. McCormick (1977) showed that the dislocation densities in synthetic crystals of two different hydroxyl contents are related to stress by:

$$N = 1.60\ (\pm\ 0.89)\ \times\ 10^4\ (\sigma_1 - \sigma_3)^{1.51(\pm 0.12)}$$

where stress is in bars, or

$$(\sigma_1 - \sigma_3) = 1.64\ \times\ 10^{-4}\ N^{0.66}.$$

where stress is in MPa. These relations are compared in Figure 7. McCormick showed that the observed dislocation densities in his crystals were smaller by over an order of magnitude than those predicted by the "back stress" model mentioned above.

The flow stresses inferred from the dislocation densities in the mylonites (Table 2) vary between 214 and 82 MPa, using McCormick's (1977) relation, and 283 and 137 MPa, using the relation assumed by Weathers et al. (in press). These stresses are considerably larger than those inferred from the grain size data (Table 1), as shown by the graphical comparison in Figure 8. Only for the blastomylonite (755) do the stresses derived from grain size and dislocation density show reasonable consistency (74 and 82 MPa if the stress-microstructure relations of Twiss (1977) and McCormick (1977) are used.

Sub-grain sizes are difficult to estimate in the Coyote Mountain mylonites because sub-grain boundaries are present in relatively few of the grains. Experimental data are not yet available for the variation of sub-grain size with flow stress. It should be noted that sub-grains are uncommon in single crystals and quartzites deformed experimentally even at relatively high temperatures. This is inconsistent with the fact that such boundaries are relatively well-developed and common in recrystallized quartz tectonites.

Limited data from samples 925 and CM-13 indicate that the average sub-grain sizes are only slightly smaller than the grain sizes: in sample 925 the sub-grains are approximately 3 percent smaller than the grains and in sample CM-13 approximately 16 percent smaller. According to the theoretical correlation of Twiss (1977), these sub-grain sizes would indicate differential stresses of only 1.5 and 1.0 MPa for 925 and CM-13, respectively. These stress values are smaller, by an order of magnitude, than those derived from grain sizes and more than two orders of magnitude smaller than those inferred from dislocation densities. These observations further emphasize the inconsistency of the stress values derived from different microstructural parameters.

DISCUSSION

It is evident that there is not a simple correlation between the stress values inferred from the grain sizes and dislocation densities of quartz in the Coyote Mountain mylonites. If the experimental and theoretical stress-microstructure "calibrations" are taken to be correct the flow stresses derived from grain sizes are a few tens of MPa, those from sub-grain sizes are of the order of 1 MPa and those inferred from dislocation density are a few hundred MPa. A significant feature of the data (Figure 8) is that the finest-grained rock (755) has the lowest dislocation density (and similar flow stresses, ~ 80 MPa, are inferred from both grain size and dislocation density), but the rocks with coarser grain sizes, suggesting lower flow stresses, have significantly higher dislocation densities. There are several plausible explanations for these inconsistencies. The

most likely reasons are: (a) inaccuracy or inappropriateness of the experimental stress-microstructure relations and (b) complexity of the thermomechanical history of this and other major fault zones.

Experimental stress-microstructure relations

The experimental data on the relationship of microstructural parameters, such as grain size and dislocation density, to applied stress are still very limited for quartz. Most of the experiments on dry natural quartz crystals and quartz polycrystals have been done in solid pressure-medium deformation apparatus. In general, high axial thermal gradients make the temperature determinations imprecise and the precision and accuracy of differential stress measurement in many solid confining media are uncertain (Tullis, 1971). Moreover, extensive TEM studies done on these materials deformed at temperatures up to 800°C (Ardell et al., 1973) indicate great heterogeneity in dislocation distribution and dislocation densities too high to count. Similar heterogeneity was observed in synthetic quartz crystals deformed in gas confining medium (Morrison-Smith et al., 1976). By contrast, the dislocation distribution in wet synthetic crystals deformed at atmospheric pressure (McCormick, 1977) was uniform and the data yielded a good correlation between stress and dislocation density; this correlation is used above. However, data on dislocation density are still lacking for polycrystalline quartz. We hope to remedy this lack with new data on quartzite and novaculite, deformed in wet and dry environments at temperatures from 800° to 1000°C, in improved sample assemblies in the Griggs solid-medium apparatus. Samples from these experiments are currently being analyzed.

The effect of small amounts of dissolved water (amounting to only 0.5 percent by weight in extreme cases) in promoting flow of quartz crystals is well-known (Griggs and Blacic, 1965). This hydrolytic weakening is spectacular in laboratory experiments and is likely to be very significant in the flow of rocks in the crust. It has already been postulated that it is important in the deformation of mylonites (Riekels and Baker, 1977). As yet there are no systematic data on the microstructure-stress relations in rocks deformed under "wet" and "dry" conditions. It is not clear that consistent relationships exist between applied stress and grain size, sub-grain size or dislocation density, independent of water content or activity of H_2O. Until such data are available we consider that applications of the microstructures to stress determination should be made with extreme caution. We consider it likely, in rocks deformed during prograde metamorphism (that is, dehydration of hydrous assemblages), that the partial pressure of H_2O would be high and data obtained for experiments under these conditions would be appropriate (if different from the "dry" experiments).

Experiments on metals and minerals indicate that the dislocation density is quite sensitive to changes of stress during deformation or to hydrostatic annealing. Grain size should be relatively stable to such changes and sub-grain size should be less so, but considerably more stable than dislocation density. (Sub-grain boundaries are less energetic, and therefore less mobile during annealing, than grain

boundaries and the relative stability of these features should be checked experimentally.) Thus if a mylonitic rock in a fault zone were deformed in steady state so that the micro-structures all equilibrated with the applied stress, it would be necessary to quench it rapidly under the same stress to preserve the microstructures related to the steady, high-temperature deformation. This is very unlikely for mylonitic rocks deep in a fault zone, as is demonstrated by the structural complexity of well-studied examples. It is probable that low-stress or hydrostatic annealing will occur, if the fault becomes inactive, or that subsequent non-steady (transient plastic or brittle) deformation will occur during the long period of temperature decay.

In view of the long time intervals involved in the records of activity of fault zones and in their subsequent uplift and cooling histories, it is important to have reliable data on static annealing effects on mineral aggregates. Qualitative data on quartz aggregates have been obtained, indicating that the kinetics of recovery and grain growth are profoundly affected by the water content of the material (Green et al., 1970). Preliminary data on recovery kinetics of quartzite annealed in a dry argon atmosphere have been reported (Cooper and Kohlstedt, 1979) but further data are essential on the rates of grain growth and recovery, at high temperatures and different activities of H_2O, to interpret the grain size data in detail.

Complexity of the history of fault zones

This factor is certainly a major one in accounting for differences in flow stresses inferred from grain size and dislocation density or other microstructural parameters. The sensitivity of dislocation substructures, sub-grain boundaries and recrystallized grain size to annealing varies greatly, as noted above. Most major mylonite zones contain structural evidence, in the orientations of lineations and minor folds, of several different episodes of deformation. The field structures may vary in style from plastic to cataclastic, indicating superposed deformations under different conditions of temperature, pressure and differential stress (etc.). Thus it is unlikely, in general, that the different microstructures would all record the same aspects of the stress or thermal history.

Theodore (1967, 1970) demonstrated that the Coyote Mountain mylonites formed, at least in part, under sillimanite-grade conditions at temperatures ~ 600°C and pressures in the range 340 to 700 MPa. This corresponds to depths between 11 and 23 km. During the history of uplift and cooling of the rocks the microstructures may have been modified by either hydrostatic annealing or one or more episodes of high stress. Regional structural evidence (Theodore, 1970) suggests one identifiable episode of deformation (of Eocene or pre-Eocene age) after the mylonitization occurred between early Late Cretaceous and Eocene time.

The only comparable data at present available on stresses derived from microstructures are for the Moine Thrust zone in north-west Scotland.

The flow stresses derived from the grain sizes in mylonitic quartzites are ~ 50 MPa (Weathers et al., 1978) and those inferred from dislocation densities are ~ 100 MPa (Cooper et al., 1978). It should be noted that these rocks contain prograde phase assemblages of greenschist facies (Christie, 1960 1963), so that the temperatures were lower and the likelihood of significant annealing during cooling were therefore less. It may be significant that in the Moine thrust-zone the stresses inferred from grain size are lower than those derived from dislocation density, as in the present study.

CONCLUSION

The inconsistencies in the flow stresses inferred from the different quantitative microstructural parameters in the Coyote Mountain mylonites suggest caution in the application of these stress-microstructure relations as "paleopiezometers." The data obtained in this instance offer no refinement of existing estimates of stress in major fault zones from other sources.

It is our assessment that the relatively high stresses inferred from dislocation density (100-200 MPa) are probably reliable and date from a high stress pulse late in the history of the rocks. The stresses obtained from grain and sub-grain sizes (10-100 MPa) are probably underestimates, in that these parameters were almost certainly affected by hydrostatic or low-stress annealing episodes during the thermal peak and extended cooling history of these relatively high-temperature mylonitic rocks. An assessment of the data suggests that flow stresses ($\sigma_1 - \sigma_3$) were probably of the order of 100 MPa (1 Kb) or more during the mylonitization and during subsequent transient high stress episodes of the history.

It is essential that more extensive and accurate experimental data on (a) the relationship between steady state stress and grain-size, sub-grain size and dislocation density (and possibly other microstructural parameters) and (b) the kinetics of annealing of these microstructures be obtained for quartz aggregates before inferences on flow stress can be drawn with confidence. When such data are available, the prognosis is good that certain details of the thermo-mechanical history can be resolved from study of several types of microstructures in the same rocks. The probability will be greatly improved if similar data are obtained for other co-existing phases. In particular, the feldspars appear to offer the greatest promise, despite their structural complexity and experimental intractability.

ACKNOWLEDGMENT

The microstructural studies of the Coyote Mountain mylonites summarized here were done by the authors in collaboration with Mary W. Wegner, Department of Earth and Space Sciences, U.C.L.A.,who developed the etching procedures

and advised us on the use of these techniques. This assistance is gratefully acknowledged. This work was done under NSF Grant No. EAR 77-23163.

REFERENCES

Ardell, A. J., J. M. Christie and J. A. Tullis (1973), Dislocation substructure in deformed quartz rocks, Crystal Lattice Defects, 4, 275-285.

Bird, J. E., A. K. Mukherjee, and J. F. Dorn (1969), Correlations between high temperature creep behavior and structure. In: Quantitative Relation between Properties and Microstructure (D. G. Brandon and R. Rosen, eds.) Proceedings of an International Conference, Haifa, Israel, 255-342.

Briegel, U., and C. Goetze (1978), Estimates of differential stress recorded in the dislocation structure of Lochseiten Limestone (Switzerland), Tectonophysics, 48, 61-76.

Bromley, R., and C. M. Sellars (1973), High temperature deformation of copper and copper-aluminum alloys, in The Microstructure and Design of Alloys, Proc. Third Internat. Conf. on Strength of Metals and Alloys, 1, 380.

Christie, J. M. (1960), Mylonitic rocks of the Moine Thrust-zone in the Assynt region, north-west Scotland, Edinb. Geol. Soc. Trans., 18, 79-93.

Christie, J. M. (1963), Moine Thrust Zone in the Assynt Region, N. W. Scotland, Univ. Calif. Publ. Geol. Sci., 40, 345-349.

Cooper, R. F., D. L. Kohlstedt, M. S. Weathers, and J. M. Bird (1978), Dislocation structure in deformed quartz grains from the Moine Thrust Fault, Scotland (Abstr.), Trans. Amer. Geophys. Union, 59, 1207.

Cooper, R. F., and D. L. Kohlstedt (1979), Dislocation recovery in naturally deformed quartz (Abstr.), Trans. Amer. Geophys. Union, 60, 370.

Durham, W. B., C. Goetze and B. Blake (1977), Plastic flow in oriented single crystals of olivine, Part II, J. Geophys. Res., 82, 5755-5770.

Glover, G., and C. M. Sellars (1973), Recovery and recrystallization during high temperature deformation of α-iron. Metallurgical Trans., 4, 765-775.

Goetze, C., and D. L. Kohlstedt (1973), Laboratory studies of dislocation climb and diffusion in olivine, J. Geophys. Res., 78, 5961.

Goetze, C., and D. L. Kohlstedt (1977), The dislocation structures of experimentally deformed marble, Contrib. Mineral. Petrol., 59, 293-306.

Green, H. W., D. T. Griggs, and J. M. Christie (1970). Syntectonic and annealing recrystallization of fine-grained quartz aggregates. In: Experimental and Natural Rock Deformation (Ed. P. Paulitsch), Springer-Verlag, Berlin, p. 272-335.

Griggs, D. T., and J. D. Blacic (1965), Quartz: anomalous weakness of synthetic crystals, Science, 147, 292.

Hobbs, B. E., W. D. Means, and P. F. Williams (1976), An Outline of Structural Geology, John Wiley and Sons, Inc., New York.

Kirby, S. H., and M. W. Wegner (1979), Dislocation substructure of mantle-derived olivine as revealed by selective chemical etching and transmission electron microscopy, Phys. Chem. Minerals, 3, 309-330.

Kohlstedt, D. L., and C. Goetze (1974), Low-stress high-temperature creep in olivine single crystals, J. Geophys. Res., 79, 2045-2051.

Kohlstedt, D. L., R. F. Cooper, M. S. Weathers and J. M. Bird (1979), Paleostress analysis of deformation-induced microstructures: Moine thrust zone and Ikertoq shear zone. This Conference.

Kohlstedt, D. L., C. Goetze, W. B. Durham (1976), Experimental deformation of single crystal olivine with application to flow in the mantle. In: Physics and Chemistry of Minerals and Rocks (Ed. R. G. J. Strens), John Wiley and Sons Ltd., London, 35-49.

Luton, M. J., and C. M. Sellars (1969), Dynamic recrystallization in nickel and nickel-iron alloys during high temperature deformation, Acta Metallurgica, 17, 1033-1043.

McCormick, J. W. (1977), Transmission electron microscopy of experimentally deformed synthetic quartz, Ph.D. thesis, Univ. of Calif., Los Angeles, 171 p.

Mercier, J.-C., D. A. Anderson and N. L. Carter (1977), Stress in the lithosphere: inferences from steady-state flow of rocks. Pure and Appl. Geoohysics, 115, 199-226.

Morrison-Smith, D. J., M. S. Paterson, and B. E. Hobbs (1976), An electron microscope study of plastic deformation in single crystals of synthetic quartz, Tectonophysics, 33, 43-79.

Ord, A., M. W. Wegner, and J. M. Christie (1979), Microstructures and flow stresses in mylonitic rocks from Coyote Mountain, California (Abstr.) Program, 9th Western Regional Meeting of Electron Microscopists, Palm Springs, April 30-May 3, 1979, p. 26.

Post, R. L., Jr. (1973), The flow laws of Mt. Burnet dunite, Ph.D. thesis, Univ. of Calif., Los Angeles, 272 p.

Post, R. L., Jr. (1977), High-temperature creep of Mt. Burnet dunite, Tectonophysics, 42, 75-110.

Riekels, L. M., and D. W. Baker (1977), Origin of the double maximum pattern of optic axes in quartzite mylonite, Jour. Geol., 85, 1-14.

Smith, C. S., and L. Guttman (1953), Measurement of internal boundaries in three-dimensional structures by random sectioning, Trans. A.I.M.E., 197, 81-87.

Theodore, T. G. (1967), Structure and petrology of the gneisses and mylonites at Coyote Mountain, Borrego Springs, California, Ph.D. thesis, Univ. of Calif., Los Angeles, 268 p.

Theodore, T. G. (1970), Petrogenesis of mylonites of high metamorphic grade in the peninsular ranges of Southern California, Geol. Soc. Amer. Bull., 81, 435-450.

Tullis, J. A. (1971), Preferred orientations in experimentally deformed quartzites, Ph.D. thesis, Univ. of Calif., Los Angeles, 344 p.

Tullis, J. A., J. M. Christie and D. T. Griggs (1973), Microstructures and preferred orientations of experimentally deformed quartzites, Geol. Soc. Amer. Bull., 84, 297-314.

Twiss, R. J. (1977), Theory and applicability of a recrystallized grain size paleopiezometer, Pure and Applied Geophysics, 115, 227-244.

Weathers, M. S., D. L. Kohlstedt, J. M. Bird, and R. F. Cooper (1978), Microstructure of deformed quartzite from the Moine Thrust fault, Scotland, Trans. Amer. Geophys. Union, 59, 1207.

Weathers, M. S., R. F. Cooper, D. L. Kohlstedt, and J. M. Bird (1979), Differential stress determined from deformation-induced microstructures of the Moine Thrust zone, J. Geophys. Res. (In press).

Table 1. Grain Sizes (Quartz) and Inferred Flow Stresses

Spec. No.	Grain size (D) μm (± Standard deviation	Flow Stress, MPa. Mercier et al. (1977)	Twiss (1977)
924	208 (±43)	9	16
925	127 (±30)	12	22
868	122 (±24)	13	23
CM-13	97 (±27)	15	27
897	79 (±22)	17	31
755	22 (±7)	42	74

Table 2. Dislocation densities (Quartz) and Inferred Flow Stresses

Spec. No.	Dislocation density (N) cm^{-2} (±Standard deviation)	Flow Stress, MPa. McCormick (1977)	Weathers et al. (1979)
924	18.4 (±7.5) x 10^8	214	283
925	8.3 (±3.3) "	126	190
868	16.6 (±8.2) "	199	269
CM-13	14.2 (±7.8) "	180	249
897	9.9 (±4.7) "	142	208
755	4.3 (±2.0) "	82	137

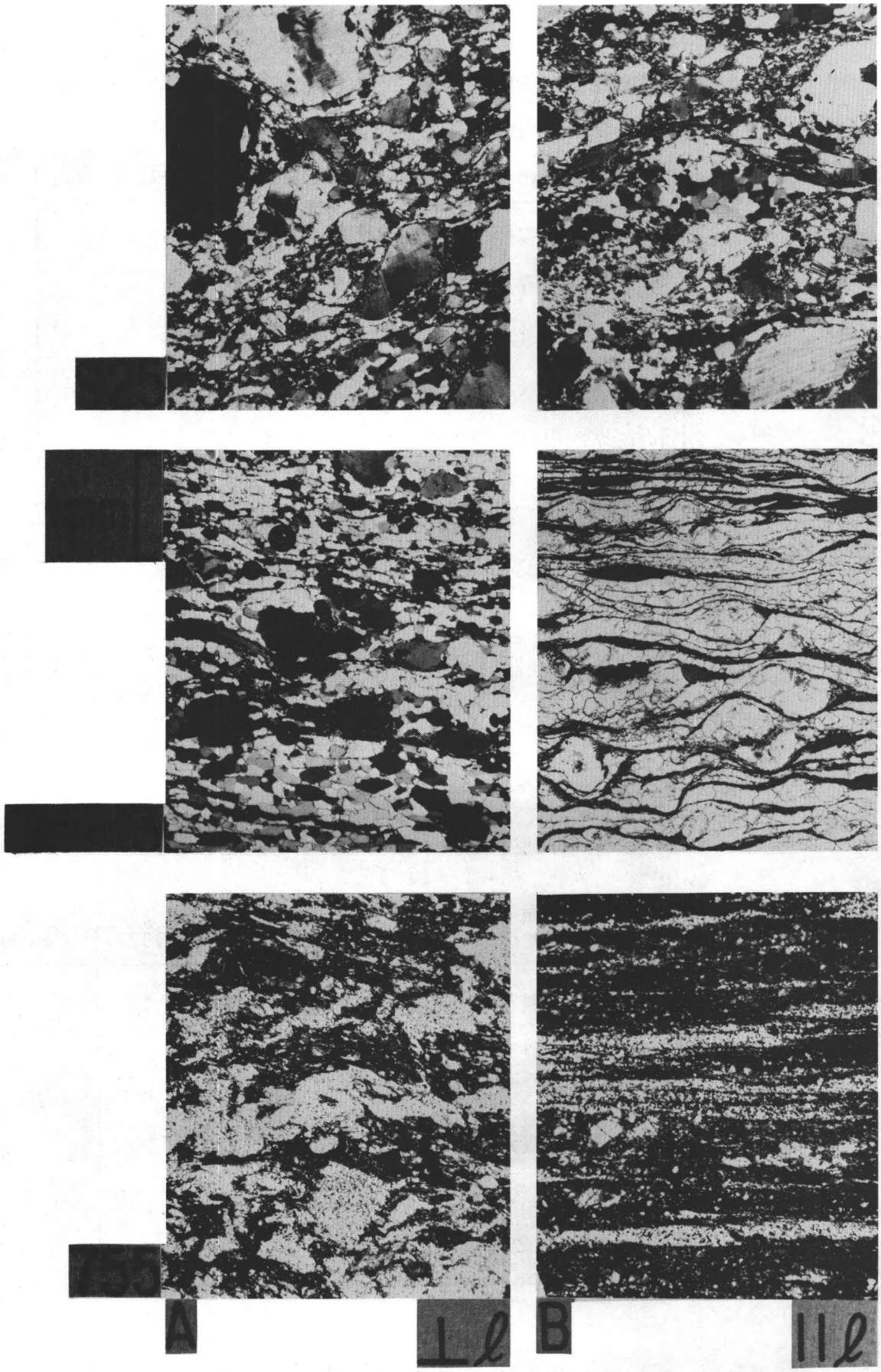

Figure 1. Optical micrographs of samples 925, CM-13 and 755. Sections are all perpendicular to foliation and either perpendicular to lineation ($\perp \ell$) or parallel to lineation ($\| \ell$). All micrographs except CM-13 ($\| \ell$) were taken with crossed polarizers.

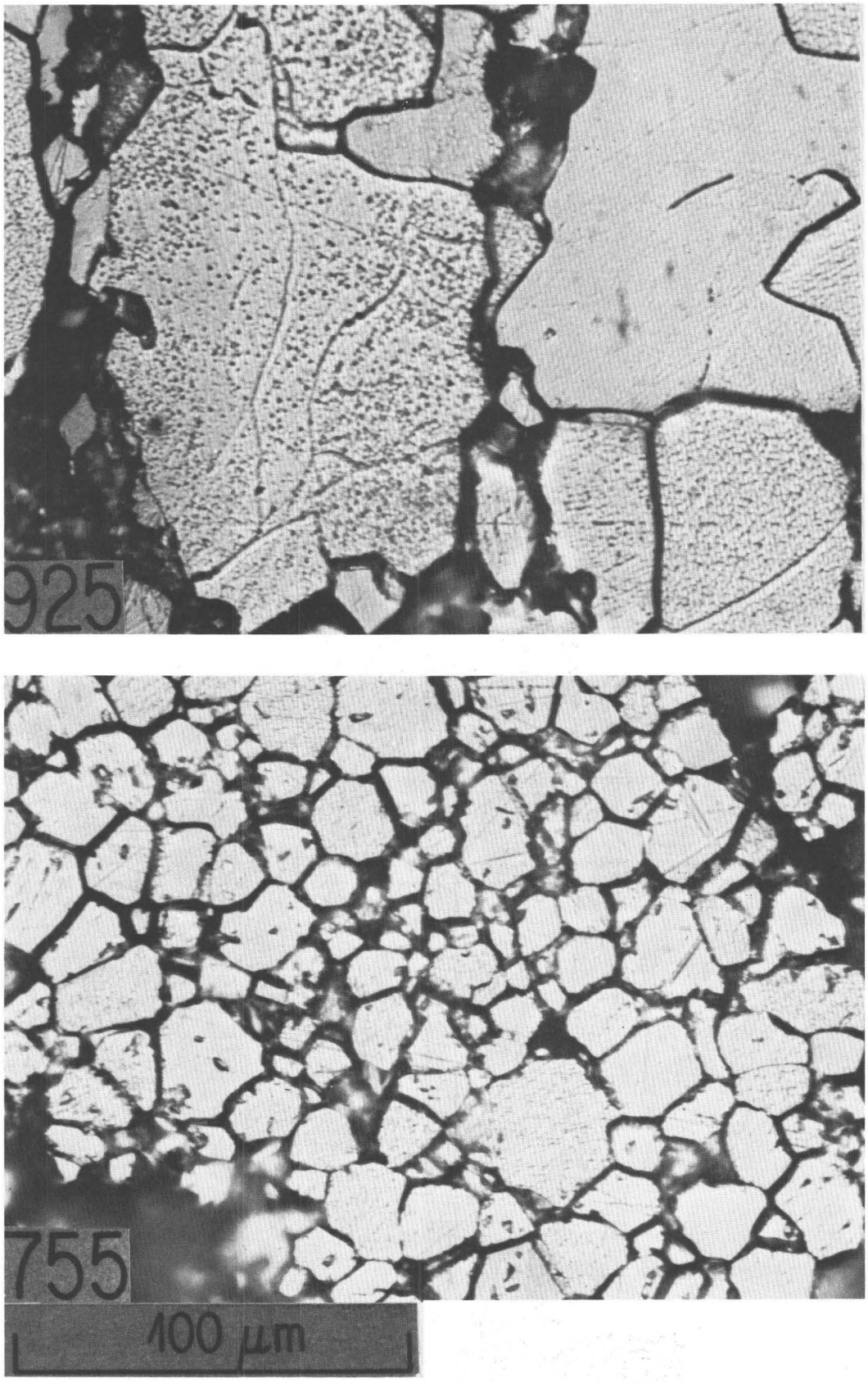

Figure 2. Optical micrographs of etched surfaces showing grain boundaries, sub-grain boundaries and dislocation etch pits. Reflected light.

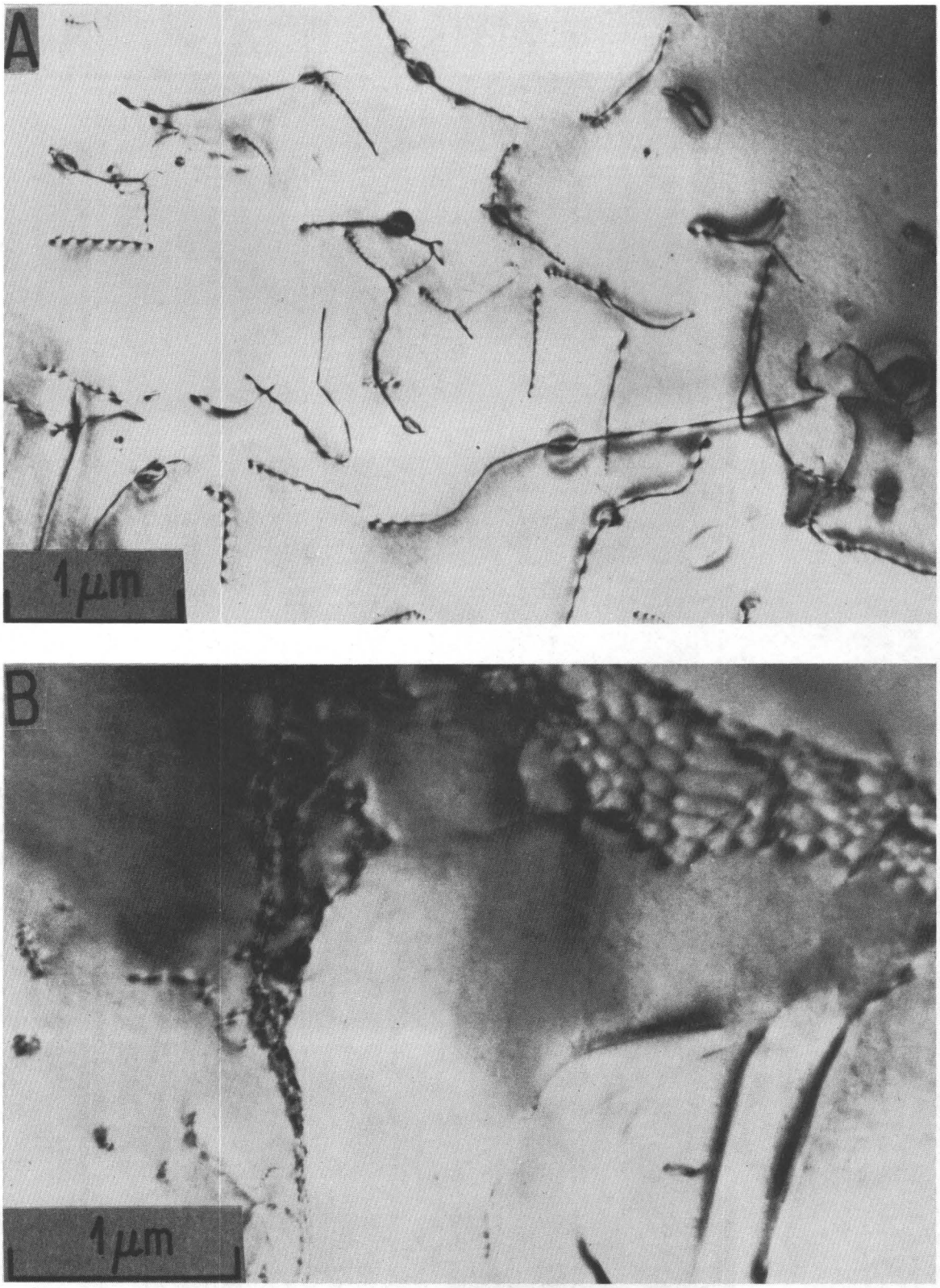

Figure 3. Transmission electron micrographs showing dislocation substructures in sample 925. The micrograph at the top shows dislocations, triple nodes and small dislocation loops. A sub-grain boundary consisting of a hexagonal network is shown at the bottom.

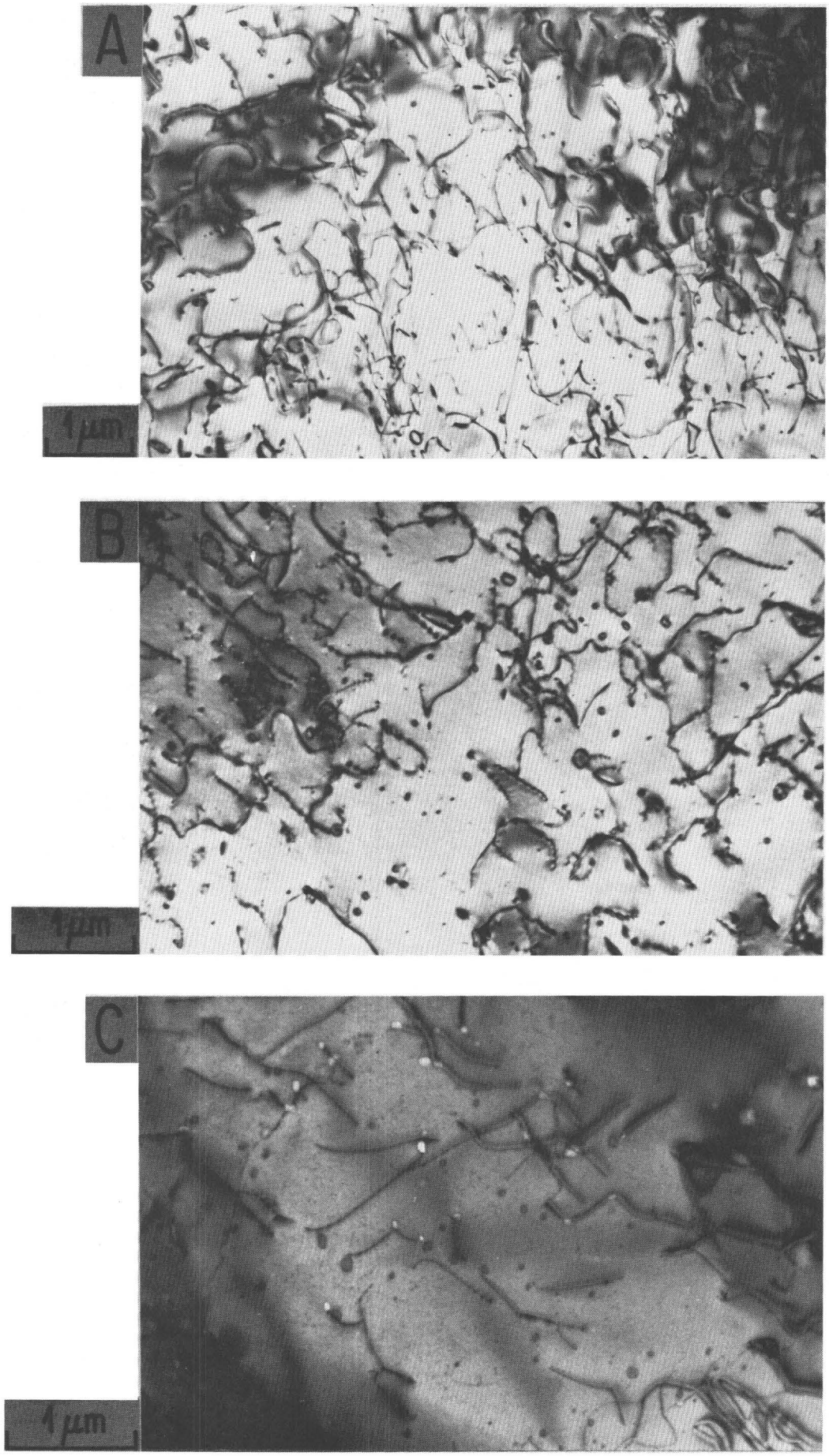

Figure 4. TEM micrographs of dislocation substructures in sample CM-13. Note bubbles, probably of precipitated water, in micrograph at bottom.

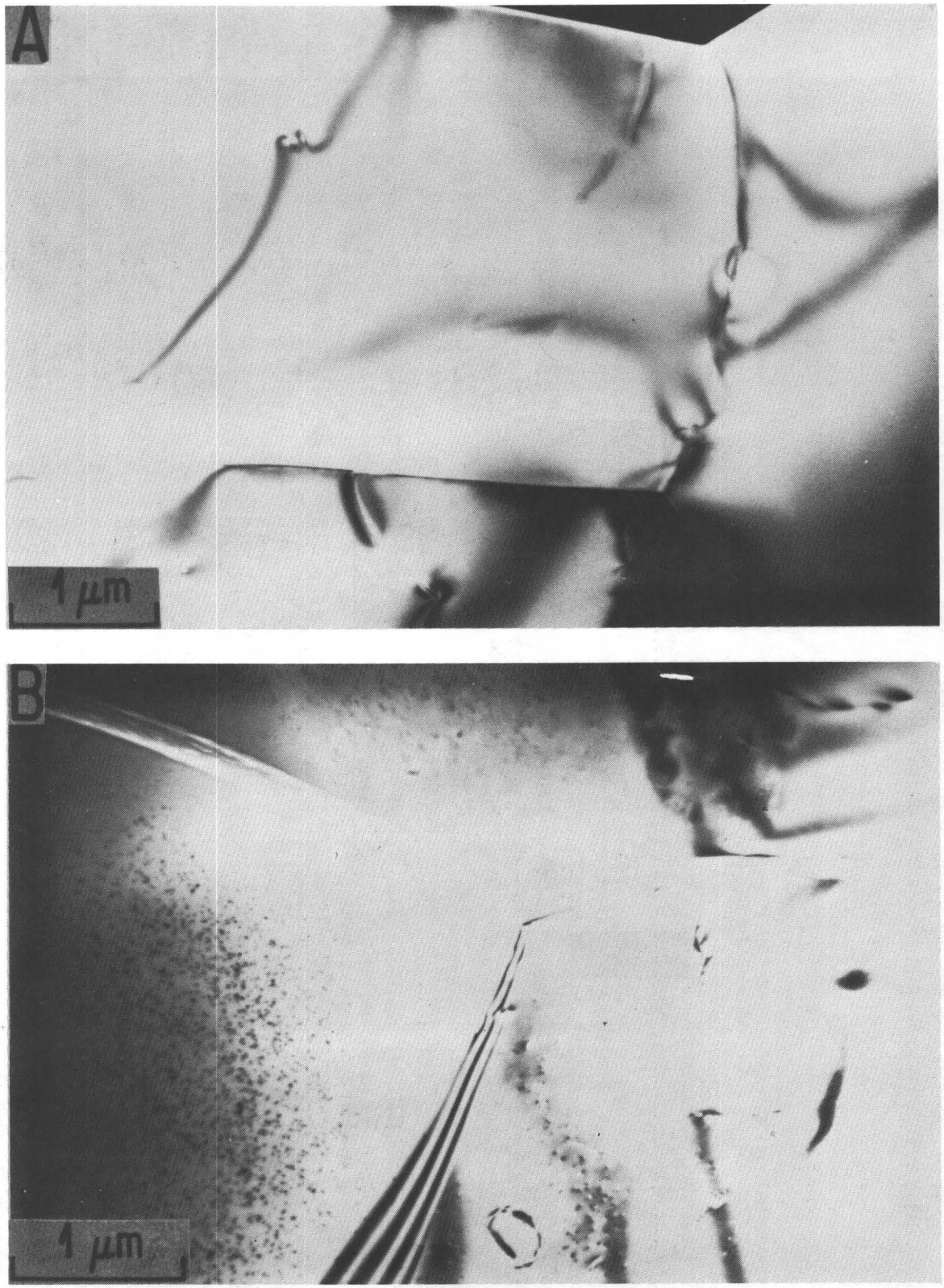

Figure 5. TEM micrographs showing grain boundaries and free dislocations in sample 755. Dark spots in micrograph at the bottom are electron beam damage. Note cavities in the grain boundary at top left of micrograph at the bottom.

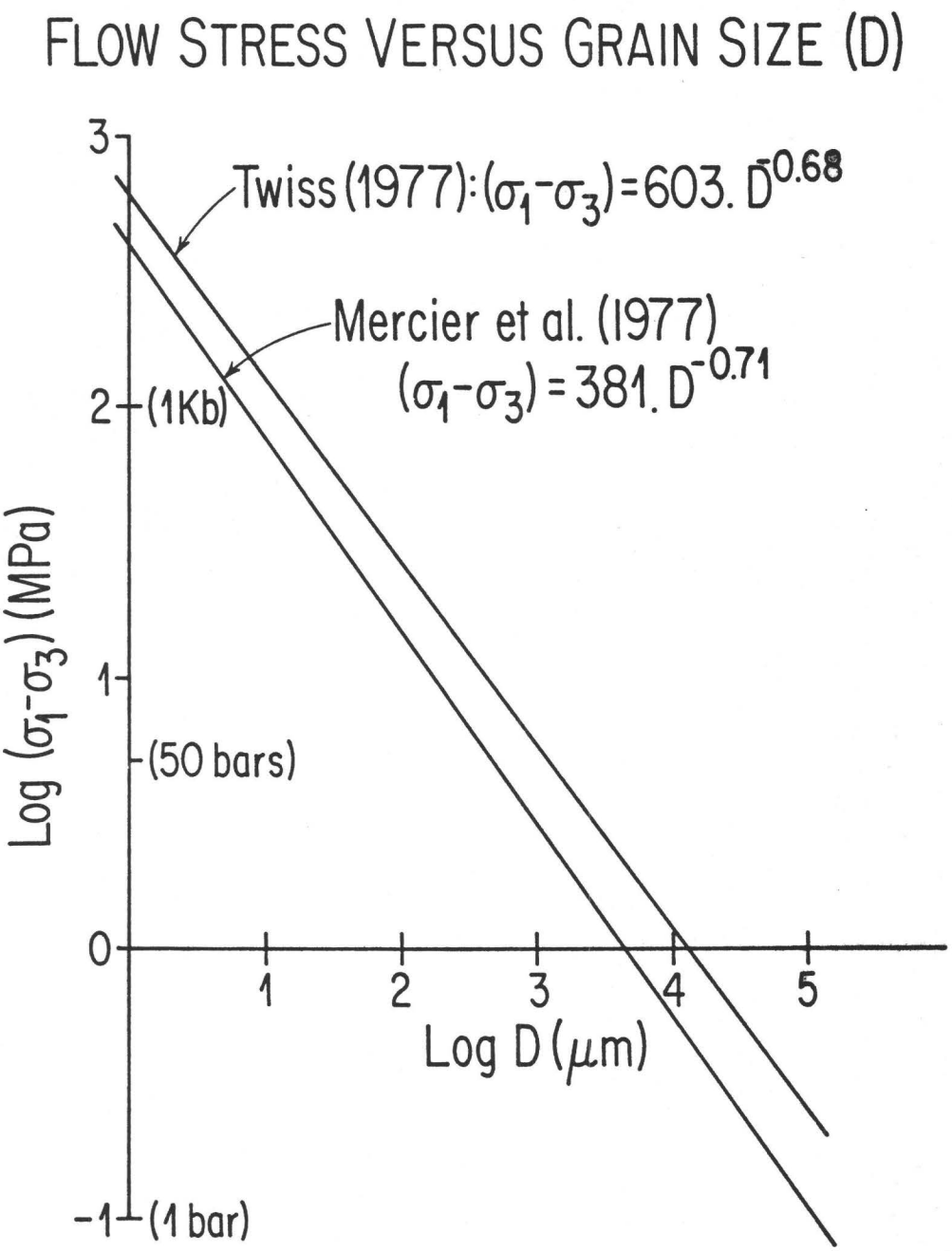

Figure 6. Relationship between steady state flow stress and grain size in quartzite, after Twiss (1977) and Mercier et al. (1977).

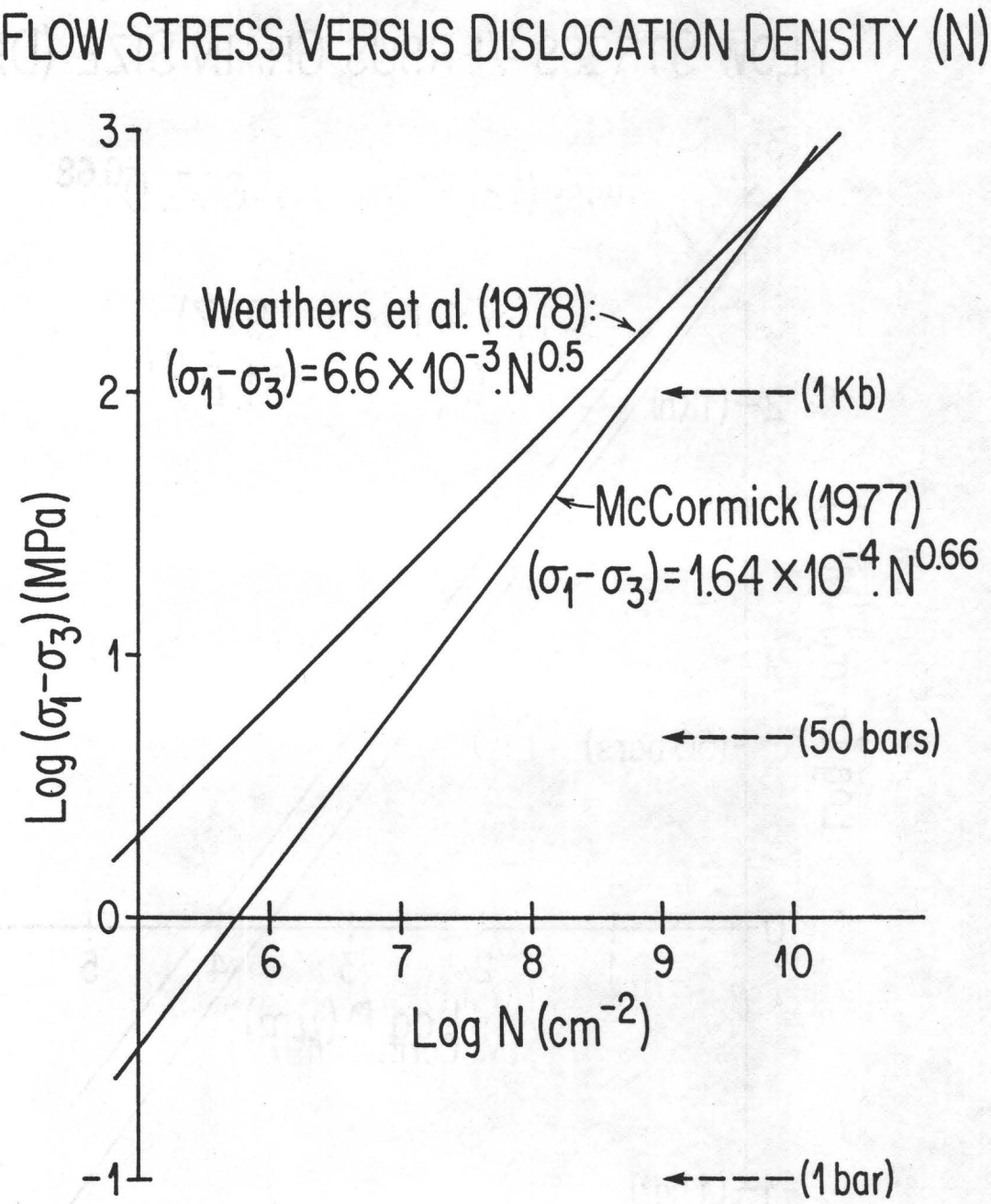

Figure 7. Relationship between flow stress and dislocation density in quartz, after McCormick (1977) and Weathers et al. (in press).

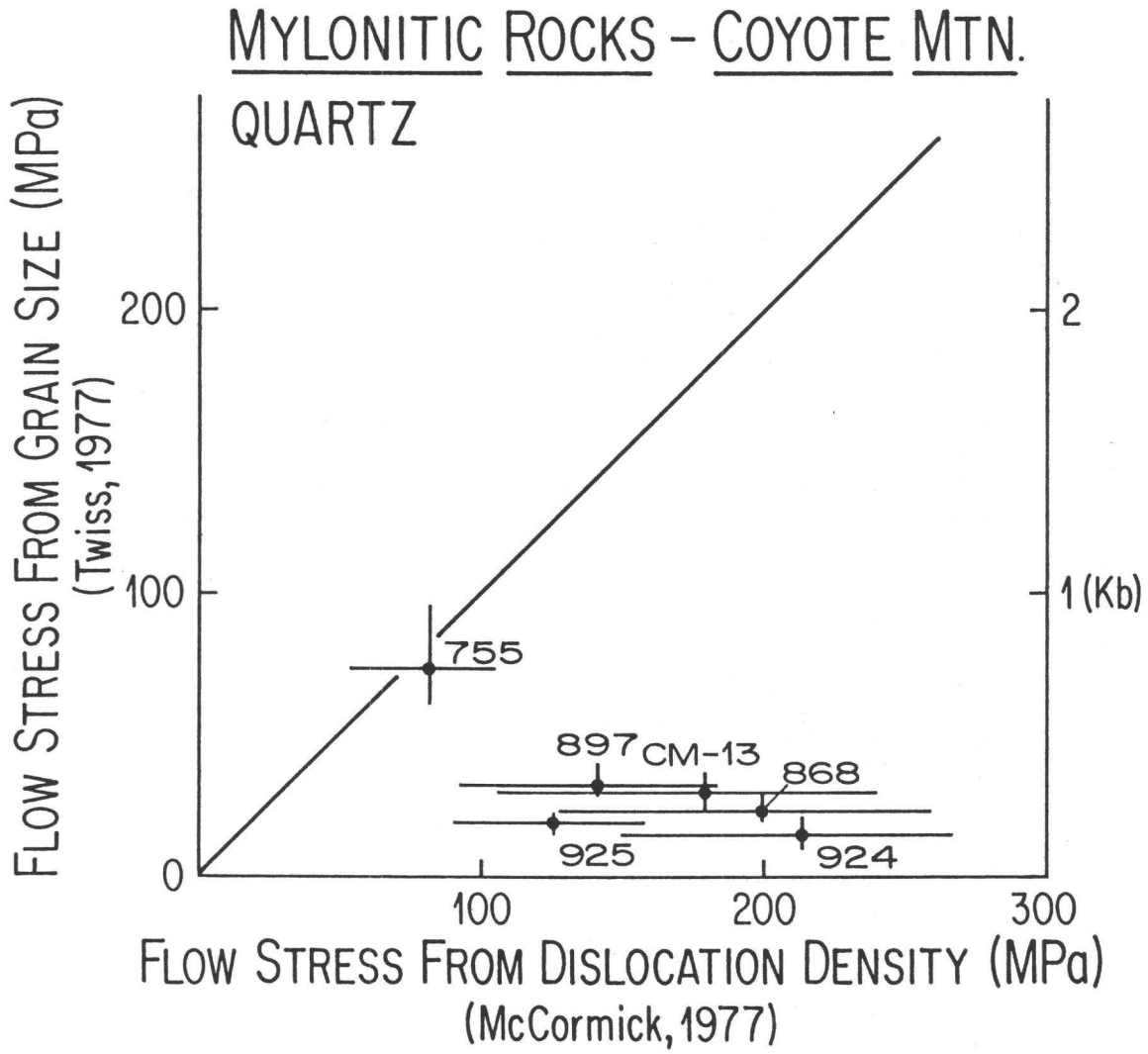

Figure 8. Comparison between flow stresses inferred from grain sizes and dislocation densities of quartz in the Coyote Mountain mylonites, using the relations of Twiss (1977) and McCormick (1977), respectively.

THE USE OF MECHANICAL TWINNING IN MINERALS AS A MEASURE OF SHEAR STRESS MAGNITUDES

Terry E. Tullis
Department of Geological Sciences
Brown University
Providence, Rhode Island 02912

INTRODUCTION

An important unresolved problem is the level of shear stress that accompanies motion on faults at all levels within the crust. Conflicting and equivocal arguments on the resolution of this question come from different quarters. For example, the absence of a sharp heat flow anomaly across the San Andreas fault has been used to suggest that the shear stresses cannot be over a few hundred bars (Brune, et al., 1969). On the other hand, it is possible that heat transported by flowing ground water could broaden the anomaly sufficiently to counter this argument (Hanks, 1977, p. 454-455). Coefficients of friction determined from laboratory experiments on rocks (e.g. Byerlee, 1978) are about 0.6, suggesting that at depths of 5 to 10 km the frictional resistance to sliding of dry rock should be in the range of several hundred bars to a few kilobars. Unfortunately, we lack knowledge of the pore fluid pressure and a high pore fluid pressure would reduce these stresses dramatically, by reducing the effective normal stress across the frictional sliding surfaces. The possible presence of clay minerals in fault zones could also reduce the stresses considerably since some clays have much lower coefficients of friction (Byerlee, 1978).

Some resolution of this question of stress magnitudes may come from a variety of in situ measurements made at the bottom of wells, such as the measurement of ambient stresses by hydraulic fracturing, the measurement of naturally occurring pore fluid pressures, and the characterization of the rock types in the fault zones. However, such measurements are difficult and expensive, and thus can only be made at a relatively few localities, even if successful. Study of features in deformed rocks from surface outcrops and from such wells may play an important role in

understanding the magnitudes of the ambiant shear stresses. One such feature that has received less attention than it deserves for estimating stress magnitudes is mechanical twinning of certain minerals.

To a first order of approximation, twinning occurs when the shear stress reaches a critical value on a twin plane in the twin direction and correct sense. Unlike the case for slip of crystals, twinning is basically an athermal process and so the critical shear stress does not depend strongly on temperature or strain rate. Unlike the case for frictional sliding, it is independent of pore fluid pressure. Consequently, laboratory determinations of this critical shear stress, many of which have been done, may have wide and direct applicability to interpreting stress levels in the natural setting - few difficulties would seem to stand in the way since extrapolations are not involved. The principal questions concern the relationship between the critical shear stresses for twinning and those that can be supported by a polycrystalline (possibly polyphase) aggregate where twinning may or may not be the principal deformation mechanism. Fortunately, this is amenable to laboratory experimentation and much relevant data already exists.

Application of this method to deciphering stress levels in a natural setting have already been made by Jamison and Spang (1976) who also calibrated their values by studying experimentally deformed limestone. Other examples of measurements exist in the literature that could perhaps be reinterpreted in this way. Future studies of these types would be very useful. This paper briefly reviews the process of twinning, pointing up some possible pitfalls in its usefulness, reviews the data on twinning in rock forming minerals already in hand, and shows how it seems very promising for resolving the question of whether shear stress levels are of the order of ten to a few hundred bars or a few kilobars. In some

instances already described in the literature it seems the stresses may be over a kilobar.

CHARACTERISTICS OF TWINNING

The mechanical twinning considered here is that which occurs with a change of form by an approximation to simple shear in a particular sense and direction on a given crystallographic plane. The resulting twinned portion of the crystal bears a mirrored crystallographic orientation to the untwinned portion across the twin plane. The twin is consequently easily identifiable by examination in a polarizing microscope. It is possible that twinning without a change in form might also be useful for determining stress magnitudes, but the only twin of this type in a common rock forming mineral, Dauphine twins in quartz, seem to occur at such low stresses that they might not be too useful in resolving the present controversy over stress levels related to faulting (Tullis, 1970; Tullis and Tullis, 1972).

Critical Shear Stress for Twinning

It is clear from study of mechanical twinning in minerals and in metal crystals that twins occur in crystals when there is a sufficiently high shear stress on the twin system in the proper sense and that if this is not the case they do not occur. Consequently it is a plausible hypothesis that a critical shear stress exists for twinning as is well known to exist for slip in crystals. In fact it is generally tacitly assumed in the geological literature that a critical shear stress does exist for twinning (e.g. Turner, et al., 1954, p. 889; Jaimson and Spang, 1976, p. 868). Indeed experimental results for twinning in minerals sumarized below suggest that this is a reasonable approximation to the truth.

However, careful study of twinning in metal crystals with a variety of degrees of imperfection, suggests that depending on the details of the situation there may be a range of shear stresses necessary to cause twinning. It seems that the nucleation of twins may take about an order of magnitude more stress than that to cause them to grow and that in the case of very perfect crystals this difference may be even higher (Cahn, 1964, p. 11-13). Furthermore, the local stress that causes the nucleation of twins may result in nearly all situations from some type of stress concentration. Thus the apparent applied stress necessary to cause the twin to nucleate will depend upon the strength of the stress concentration. Because of these facts Cahn (1964, p. 11) states that "there is no such thing as a critical resolved shear stress for twinning."

However, a variety of experiments on metal crystals and minerals in which no special precautions are taken to use highly perfect crystals seem to result in a relatively uniform value for the resolved shear stress required to cause twinning. Perhaps this is because in these situations some type of stress concentrations already exist in the form of fractures, dislocation pile-ups, or pre-existing twins. Thus the stress measured may represent that necessary to cause the twin to grow when already nucleated. There is certainly some scatter in the measured critical resolved shear stresses which may be attributable to a range in the strength of the stress concentration, but as the data in Figure 1 show, they seem to be uniform enough for purposes of getting an estimate of the stresses in the crust.

Effect of Temperature and Strain Rate on Twinning

Temperature has a much lower effect on the stress necessary to cause twinning than on that necessary to cause intracrystalline slip.

This is because diffusion, the rates of which are enhanced at high temperatures, is not necessary to promote twinning, unlike the situation under many conditions for slip. Thus, the critical resolved shear stresses for twinning plotted in Figure 1 show little temperature dependence. In general it is observed in aggragates that twinning is less important at high temperatures and low strain rates than it is at low temperatures and high strain rates. This is because the stress must become high enough to cause twinning to occur and whether this is possible depends on the stress that can be supported by the slip systems. Under cold fast situations slip requires high stress and so the stress can build up high enough to cause twinning. As the temperature increases or the strain rate decreases yielding can occur by slip without the stress ever getting high enough to cause twinning.

The stress required to promote mechanical twinning is not entirely independent of temperature. Presumably greater atomic vibrations at elevated temperatures tend to aid the process of twinning because the structure may be more easily transformed from one configuration to the other in the presence of these greater vibrations (Klassen-Neklyudova, 1964, p. 67). In one study on calcite from -142° to 20°C there is a drop of about a factor of 2 in the stress but little further change up to 400°C (Klassen-Neklyudova, 1964, p. 67) while another study on calcite showed a reduction of about a factor of two going from 25° to 300°C but no further reduction in going to 800°C (Griggs, et al., 1959, p. 83-89). These reductions are much lower that the two orders of magnitude reduction in resolved shear stress for slip in going from 25° to 800°C (Griggs, et al., 1959, p. 82).

Although there is less direct information on the effect of strain rate on the critical shear stresses for twinning of minerals than on the effect of temperature, the effect of strain rate is expected to be small since the effect of temperature is small. This is because processes having a rate dependence are thermally activated, and twinning does not seem to be in this category. In addition, observations of the rates of twinning in metals show that they propogate in their own plane at about the speed of sound and in fact frequently emit audible sounds (Klassen-Neklyudova, 1964, p. 59). The rates of growth perpendicular to the twin plane is much lower, but still seem to be on the order of 1 mm/sec. Thus, twins are able to propogate easily at rapid velocities and there is no evidence to suggest that at much lower rates the stress required is less. In fact there is some evidence to suggest that twinning occupies a small fraction of the time of the deformation, occurring rapidly but discontinuously in time (Bunshah, 1964). Thus whatever the nominal strain rates, the twinning may occur in sudden increments by the transfer of elastic strain into permanent strain.

Effect of Pressure and Water Pressure on Twinning

Hydrostatic pressure would not be expected to have a significant effect upon the critical shear stress for twinning. For the one material for which good data seems to exist, calcite, this expectation is verified. Turner et al. (1954, p. 889) state that the normal stress upon the twin plane increases the critical shear for twinning by less than 1 percent of the normal stress. In fact it may be much less than this since the difference they find between atmospheric pressure and 5 kb confining pressure may be attributable to differences in experimental technique and they find no significance difference between 5 and 10 kb.

Whether water content and pressure affect the ease of twinning in crystals has not been thoroughly investigated. It would not be expected to have an influence in calcite and dolomite since there is not evidence of its affecting their slip behavior. In silicates, however, water does play a very important role in slip (Griggs, 1967) and might possibly affect twinning as well. However, since diffusion is unimportant in twinning and no silicon oxygen bonds are broken (Kirby and Christie, 1977) it is fairly likely that the water content of silicate crystals will not greatly affect their twinning behavior. Some evidence supporting this conclusion for clinopyroxene can be seen in Figure 1c. When a diopside polycrystal was deformed at about 1250°C in a gas apparatus with some water added the crystal supported less stress than when it was dry due to greater ease of slip. The dry samples showed abundant twinning, but the wet ones only a trace. Thus it seems that the stress required for twinning was unaffected by the presence of water, and that it was between the stress available in the two different situations. This is approximately the right level for the critical shear stress for twinning if the dry hypersthene data of Kolle and Blacic (1978) is extrapolated beyond 800°C.

Thus at our present level of knowledge it seems reasonable to assume water content cannot affect the critical shear stress for twinning in minerals. The matter should be investigated further.

STRESSES FOR TWINNING IN MINERALS AND THEIR AGGREGATES

The three groups of minerals that undergo mechanical twinning and have been investigated to a sufficient extent to be useful at this time are calcite, dolomite, and clinopyroxenes. These minerals form the basis for the bulk of the discussion to follow.

Considerable study has also been made of mechanical twinning in plagioclase feldspars (Starkey, 1963, 1967; Borg and Heard, 1969, 1970; Marshall and McLaren, 1977) and in clinoamphiboles (Buck and Paulitsch, 1969; Buck, 1970; Rooney, et al., 1970; Rooney and Riecker, 1973; Rooney et al. 1974, 1975; Dollinger and Blacic, 1975; Kirby and Christie, 1977). However, the situation in the plagioclases is complex and far from being understood at present. There is evidence that the structural state of the feldspar (amount of order in the cation site occupancy) has an effect on the ease of twinning, at least in certain composition ranges. The extent of order is a function of the temperature history of the crystals and hence it would not be easy to determine in what structural state a sample had become twinned. Perhaps with further study this could be useful for determining paleo-stress magnitudes because it might allow a wider range of critical shear stress to be used, if it does depend on the extent of order. Considerably more work would be needed before this could be considered seriously.

In the case of clinoamphiboles, although Rooney, et al. (1975) suggest that the critical shear stress for twinning on (101) is about 3.5 kb at 400°C and 1.5 kb at 800°C, it seems likely that this is really instead the stress required for shearing on the reciprocal (100) plane when it is in a kinking orientation (Kirby and Christie, 1977, p. 160-161). It has been suggested by Dollinger and Blacic (1975) that the stress

required for twinning on (100) is greater than that for slip in the same (001) direction on that plane and so twinning tends not to occur. It is not yet clear whether more work would show that twinning in clinoamphiboles would be a useful tool in estimating stress magnitudes in nature.

The data forming the basis for using twinning as a means to estimate the magnitude of the shear stress felt by a rock are portrayed in Figure 1a, 1b, and 1c for calcite, dolomite, and clinopyroxene respectively. A dashed line is sketched through the data for twinning of single crystals and a solid line for aggregates that contain a high proportion of twinned crystals. In each case the data have been taken from a variety of sources as indicated and in most cases each dot represents several consistent experiments on the particular material in question. The range of shear stresses plotted at each temperature for the carbonate aggregate is generally due to testing aggregates that have preferred crystallographic orientation and varying the relative orientation of the sample and the stress directions. These differences, and those between the different aggregates tested by different workers in the case of dolomite, give some idea of the range in behavior possible among superficially similar rocks.

All three minerals show the same general trends that have been referred to in a previous section: the shear stress causing twinning is relatively independent of temperature, while the shear stress supported by the aggregates decreases at higher temperatures. Note that for all the aggregates in which the constituent crystals showed twinning the shear stress supported was always somewhat higher than the critical shear stress for twinning in a single crystal. At low temperatures where the critical shear stress for slip is much higher than that for twinning the aggregates support quite a high stress. This is because slip as well as

twinning is required to allow the differently oriented crystals to deform to sufficiently arbitrary shapes that the aggregate can deform without creating voids at grain boundaries. Were the experiments carried out at even higher temperatures or slower strain rates the stress supported by the aggregates would drop to lower values than that required for twinning and twinning would no longer be seen. In the case of the highest temperature experiments on the diopside aggregate in the presence of water this has in fact apparently happened since only a few of its crystals showed only a small amount of twinning.

In the case of twinning in calcite, the critical shear stress is relatively well determined at about 100 bars. There was a difference of about a factor of two in this stress between two different batches of calcite crystals studied by Griggs et al. (1959, p. 81-85).

In the case of dolomite crystals, the two studies available show quite different results. Higgs and Handin (1959) found that twinning became much easier at high temperatures, and that at 300°C and below they could not get twinning before fracture, stating that the critical shear stress must be greater than 2 kb. Heard, et al. (1978) found that there was a slight increase in the critical resolved shear stress with increasing temperature, and that at 150°C it was 950 bars. These differences indicate that there may be considerable variation between the behavior of different crystals perhaps related to the stress concentrations available for forming twin nuclei in them, and the matter clearly deserves more study. However, a critical resolved shear stress of about 1 kb seems a reasonable approximation to the behavior.

In the case of clinopyroxene there is only one study on twinning of a single crystal (Kolle and Blacic, 1979). However, its behavior

seems quite consistent with the stress at which twinning ceases in the polycrystalline diopside aggregate. Both compositions are nearly on the diopside-hedenbergite join, the single crystal having 66 wgt percent hedenbergite and the diopside (actually a salite) having 21 wgt percent hedenbergite. This suggests that the composition does not greatly affect the critical resolved shear stress, but the data are sparse.

Considering the data of Figure 1 as a whole it seems that if abundant twinning occurs in the crystals making up an aggregate, then the shear stress it is supporting must be as high as the critical shear stress for twinning and may be higher. This also makes good theoretical sense since although it would be possible for the local stresses on a few grains to be higher than the average for the aggregate, this could not be true for most of the grains. Furthermore if rocks can be found in areas of interest that have adequate amounts of calcite, dolomite, and clinopyroxene then we may be able to say whether the shear stresses were higher than 100 bars, than 1 kb, or than 1.4 kb. These stresses are in an interesting range of helping to decide the controversy outlined in the introduction.

A more detailed analysis of the orientation of crystals in a given aggregate that show or do not show twinning on one or more possible sets of twin planes might allow a more precise determination of the stress levels felt by the aggregate. If it can be shown or reasonably assumed that the stresses have not changed their orientation through time, then the direction of the principal stresses can be determined using the dynamic analysis method of Turner (1953). This would then allow a determination of the resolved shear stress coefficients on each potential twin plane in each crystal. A plot of the proportion of potential twin planes

that actually had twinned for given intervals of resolved shear stress coefficient might allow estimating an actual value for the average applied shear stress on the aggregate instead of only a lower bound. A method somewhat related to this was used by Jamison and Spang (1976) to estimate the stresses felt by limestones deformed in the lab as well as the field. In the case of the experimental samples, they found that they were able to estimate the true stress magnitudes to within about 20 percent and for strains of 2.5 percent or less they came within 10 percent. This is certainly encouraging for further work.

INFERENCES FROM TWINNING ON STRESS MAGNITUDES DURING FAULTING

Few studies have been done using mechanical twinning to infer stress magnitudes for natural deformations. Notable is the study of Jamison and Spang (1976) in which they studied twinned calcite and dolomite in six samples from similar locations in a major thrust sheet in the Front Ranges of the Canadian Rocky Mountains. They found the differential stress to vary no more than 300 bars in all the samples, the average being a differential stress of 1250 bars or a shear stress of 625 bars.

Many investigators have found calcite twins to be common in rocks they have examined and so it seems quite reasonable that shear stresses commonly reach at least 100 bars. Detailed studies of the type done by Jamison and Spang (1976) have not been done in such cases however, and so it is not possible to do better than to give a lower limit to the stress magnitudes that existed.

The best study of the twinning of diopside in a naturally deformed rock is that of Raleigh and Talbot (1967, p. 163-164). Their

sample came from a major fault in the Palmer Area, South Australia. Dynamic analysis of the twinning indicates that it occurred as a result of east-west compression that probably coincided with early Paleozoic motion on a series of north-south trending thrust faults. Consideration of the critical resolved shear stress for twinning of clinopyroxene suggests that the shear stress in these rocks may have been equal to or greater than 1.4 kb or a differential stress of at least 2.8 kb.

CONCLUSIONS

An assessment of the shear stresses necessary to cause mechanical twinning in calcite, dolomite, and clinopyroxene suggest that they may be useful to estimate a minimum value for the highest shear stress felt during the history of a rock containing a considerable fraction of twinned crystals. Because dolomite and clinopyroxene seem to have high critical shear stresses for twinning they may be used to distinguish whether stresses reach as high as a kilobar. In some instances at least, twinning in such rocks has occurred and the differential stress in one area where thrust faulting was occurring appears to have been as high as 2.8 kb or more. More studies of such situations should be attempted and some further experimental work on calibrating the technique should be done.

ACKNOWLEDGEMENTS

I wish to thank Jan Tullis for several helpful discussions on the subject of this paper, especially concerning twinning in plagioclase feldspars. I also wish to thank Mervyn Paterson for making his apparatus

available for the high temperature experiments I did on the diopsidite. Steve Kirby and Andy Kronenberg kindly provided data on their experiments on diopsidite prior to publication.

REFERENCES CITED

Borg, I.Y. and Heard, H.C. (1969) Mechanical twinning and slip in experimentally deformed plagioclases: Contr. Mineral. and Petrol., 23, 128-135.

Borg, I.Y. and Heard, H.C. (1970) Experimental Deformation of plagioclases: in Experimental and Natural Rock Deformation. ed. Paulitsch, Springer-Verlag, Berlin, 375-403.

Brune, J.N., Henyey, T.L., and Roy, R.F. (1979) Heat flow, stress, and rate of slip along the San Andreas fault, California: J. Geophys. Res., 74, 3821-3827.

Buck, P. (1970) Verformung von Hornblende-Einkristallen bei Drücken bis 21 kb.: contrib. Mineral. Petrol., 28, 62-71.

Buck, P. and Paulitsch, P. (1969) Experimentelle Verforming von Glimmer- und Hornblende-Einkristallen: Naturwissenschaften, 56, 460.

Bunshah, R.F. (1965) Rates of deformation twinning in metals: in Conference on Deformation Twinning, University of Florida, 1963, ed. Reed-Hill, R.E., Hirth, J.P., and Rogers, H.C., p. 390-392.

Byerlee, J. (1978) Friction of rocks: Pageoph, 116, 615-626.

Cahn, R.W. (1965) Survey of recent progress in the field of deformation twinning: in Conference on Deformation Twinning, University of Florida, 1963, ed, Reed-Hill, R.E., Hirth, J.P., and Rogers, H.C., p. 1-28.

Dollinger, G., Blacic, J.D. (1975) Deformation mechanisms in experimentally and naturally deformed amphiboles. Earth and Planet Sci. Letters 26, 409-416.

Griggs, D.T. (1967) Hydrodytic weakening of quartz and other silicates: Geophys. J. 14, 19-31.

Griggs, D.T., Turner, F.J., Borg, I. and Sosoka, J. (1951) Deformation of Yule marble: Part IV- Effects at 150°C: Bull. Geol. Soc. America, 62, 1385-1406.

_____ (1953) Deformation of Yule marble: Part V- Effects at 300°C: Bull. Geol. Soc. America, 64, 1327-1342.

Griggs, D.T., Turner, F.J., Heard, H.C. (1960) Deformation of rocks at 500 to 800°C. in Rock Deformation. Geological Society of America Memoir 79, D.T. Griggs and J. Handin, eds. pp 56-61.

Handin, J. and Fairbairn, H.W. (1956) Experimental deformation of Hasmark dolomite: Geol. Soc. America Bull., 66, 1257-1274.

Hanks, T.C. (1977) Earthquake stress drops, ambient tectonic stresses and stresses that drive plate motions: Pageoph, 115: 441-458.

Heard, H.C., Wenk, H.-R., and Barber, D.J. (1978) Experimental deformation of dolomite single crystals to 800°C: EOS, 59, 249.

Jamieson, W.R. and Spang, J.H. (1976) Use of calsite twin lamellae to infer differential stress: Geol. Soc. America Bull.: 87, 868-872.

Higgs, D.V. and Handin, J. (1959) Experimental deformation of dolomite single crystals: Geol. So. America Bull.: 70, 245-278.

Kirby, S.H. and Christie, J.M. (1977) Mechanical twinning in diopside $Ca(Mg,Fe)Si_2O_6$: structural mechanism and associated crystal defects: Phys. Chem. Min., 1, 137-163.

Kirby, S.H. and Etheridge, M.A. (1979) Experimental deformation of rock forming pyroxenes: ductile strengths and mechanisms of flow: Tectonophysics, in press.

Kirby, S.H. and Kronenberg, A.K. (1980) Ductile strength of clinopyroxenite: evidence for a transition in flow mechanisms and semi-brittle behavior: J. Geophys. Res., in preparation.

Klassen-Neklyudova, M.V. (1964) Mechanical twinning of crystals: Consultants Bureau, New York, p. 213.

Kolle, J.J. and Blacic, J.D. (1979) Mechanical deformation of a single crystal hedenbergite: EOS, 60, 96.

Marshall, D.B. and McLaren, A.C. (1977) Elastic twinning in experimentally deformed plagioclase feldspars: Phys. Stat. Sol. 41, 231-240.

Raleigh, C.B., Talbot, J.L. (1967) Mechanical twinning in naturally and experimentally deformed diopside. Am. J. Sci. 265, 151-165.

Rooney, T.P., Gavasci, A.T., Riecker, R.E. (1974) Mechanical twinning in experimetally and naturally deformed hornblende, Air Force Cambridge Research Laboratories Environmental Research Papers No. 484, 21 p.

Rooney, T.P., Riecker, R.E. (1973) Constant strain rate deformation of amphibole minerals, Air Force Cambridge Research Laboratories Environmental Research Papers No. 430, 35 pp.

Rooney, T.P., Riecker, R.E., Gavasci, A.T. (1975) Hornblende deformation features, Geology 3, 364-366.

Rooney, T.P., Riecker, R.E., Ross, M. (1970) Deformation twins in hornblende. Science 169, 173-175.

Starkey, J. (1965) Glide twinning in the plagioclase feldspars: in Conference on Deformation Twinning, University of Florida, 1963, ed. Reed-Hill, R.E., Hirth, J.P., and Rogers, H.C.,pp.117-191.

_____ (1976) On the relationship of pericline and albite twinning to the composition and structural state of plagioclase feldspars: Schweiz Mineral. Petrog. Mitt., 47, 257-268.

Turner, F.J. (1953) Nature and dynamic interpretation of deformation in calcite of three marbles, Am. J. Sci. 251, 276-298.

Turner, F.J., Griggs, D.T., and Heard, H. (1954) Experimental deformation of calcite crystals: Geol. Soc. America Bull., 65: 883-934.

Tullis, J. (1970) Quartz: preferred orientation in rocks produced by Dauphine twinning: Science, 168, 1342-1344.

Tullis, J. and Tullis, T.E. (1972) Preferred orientation of quartz produced by mechanical Dauphine twinning: thermodynamics and axial experiments, in Heard, et al., eds., Flow and Fracture of Rocks., Am. Geophys Union Monograph 16, 67-82.

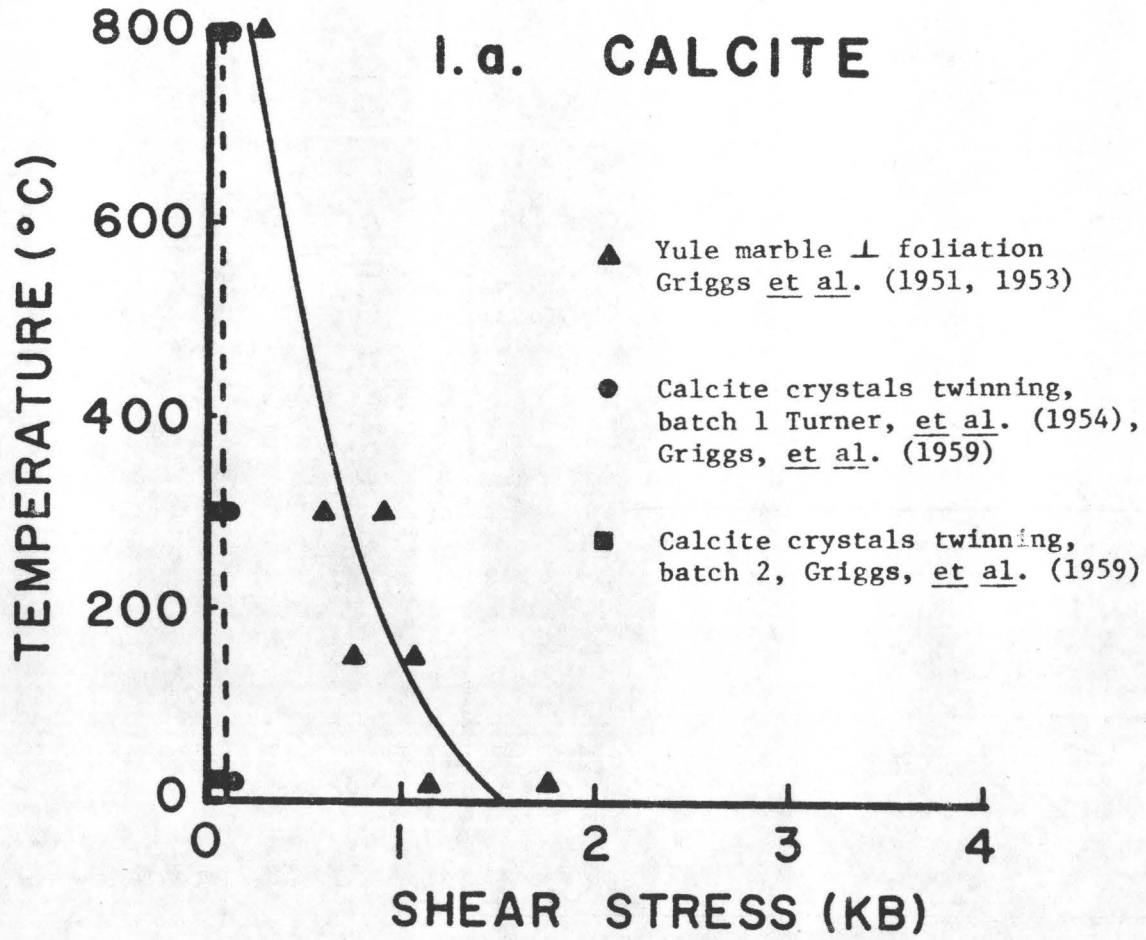
1.a. CALCITE
TEMPERATURE (°C)
800
600
400
200
0
0
1
2
3
4
SHEAR STRESS (KB)
▲ Yule marble ⊥ foliation
Griggs et al. (1951, 1953)
● Calcite crystals twinning,
batch 1 Turner, et al. (1954),
Griggs, et al. (1959)
■ Calcite crystals twinning,
batch 2, Griggs, et al. (1959)

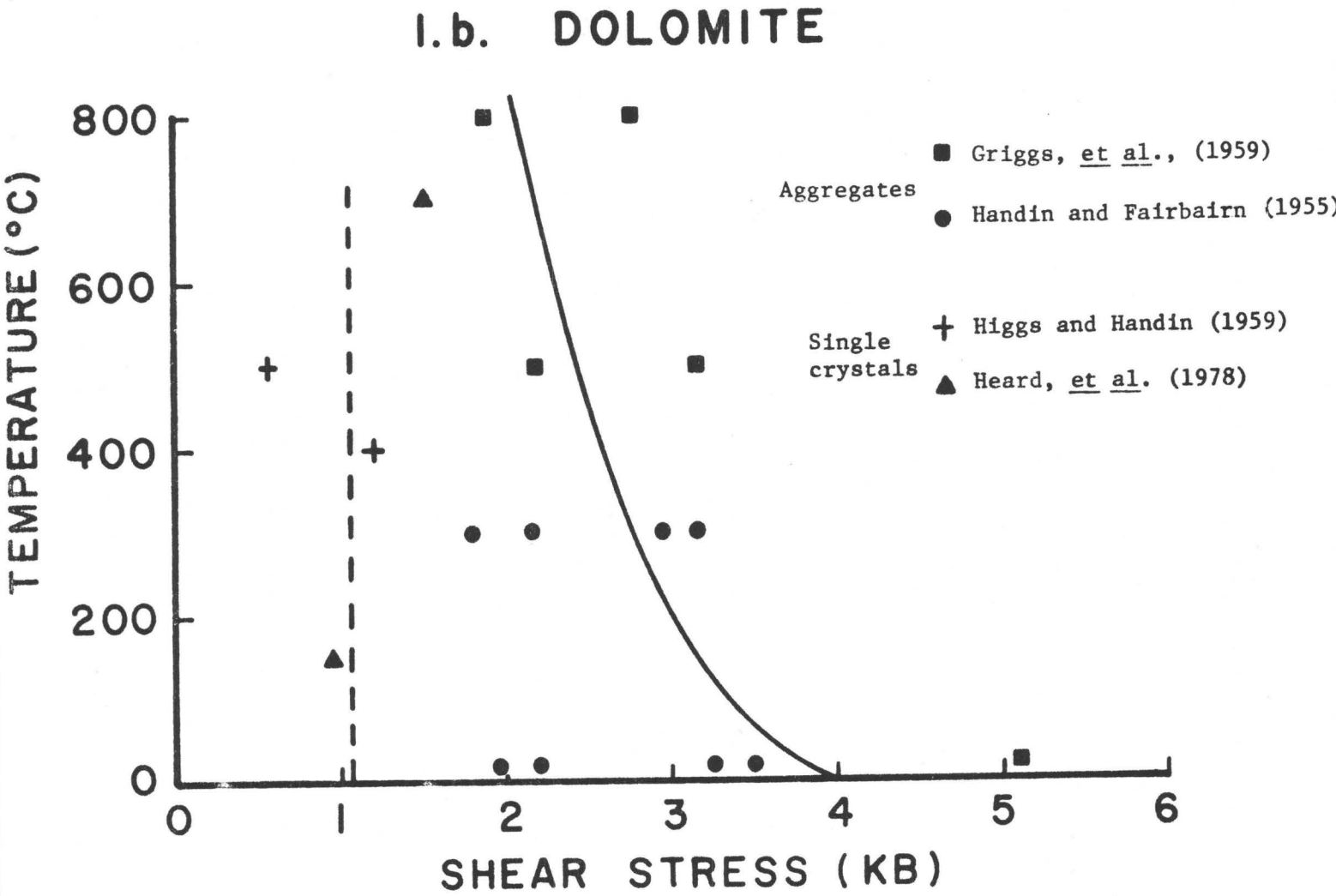
1.b. DOLOMITE
TEMPERATURE (°C)
800
600
400
200
0
0
1
2
3
4
5
6
SHEAR STRESS (KB)
Aggregates
Griggs, et al., (1959)
Handin and Fairbairn (1955)
Single crystals
Higgs and Handin (1959)
Heard, et al. (1978)

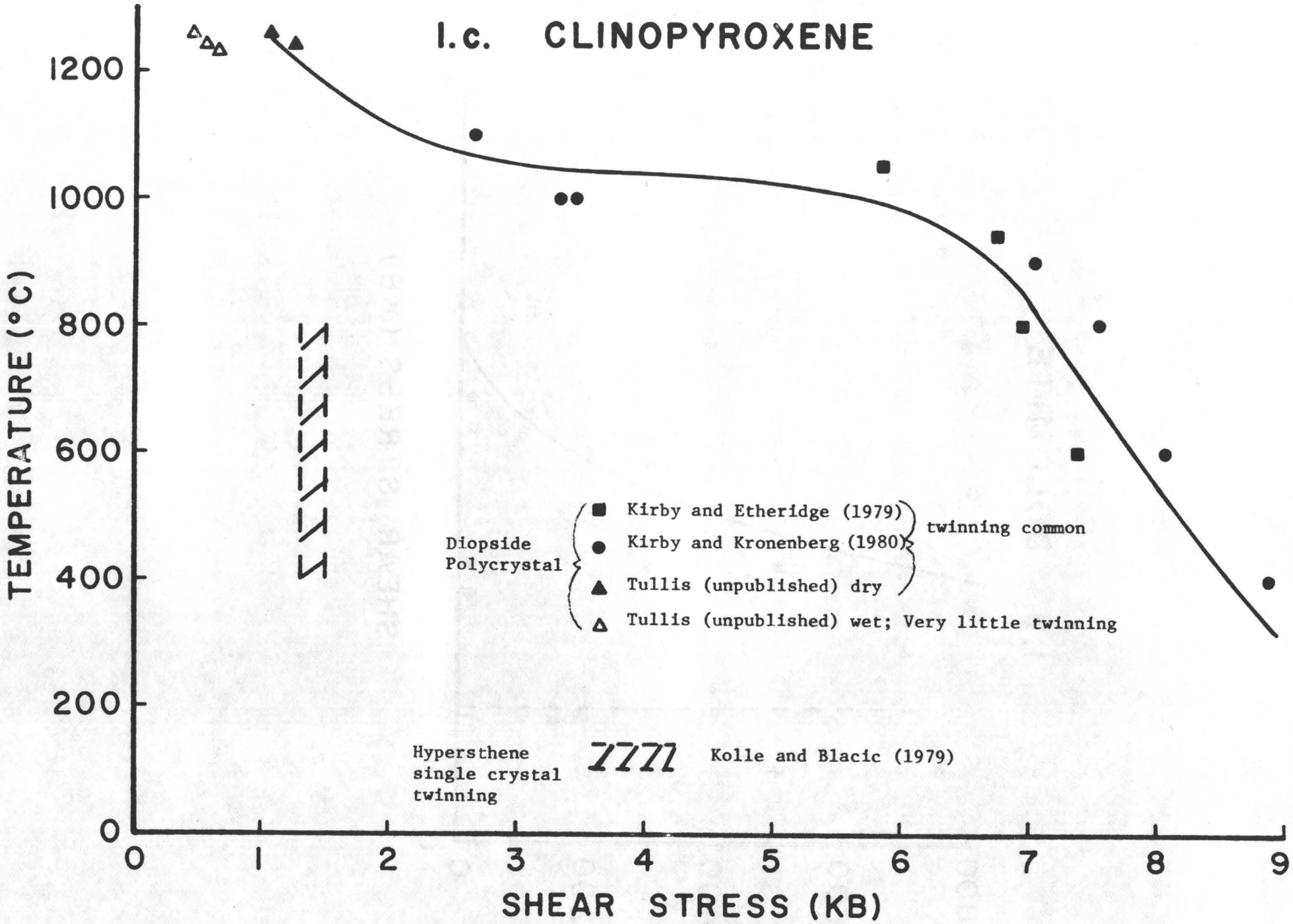
l.c. CLINOPYROXENE
TEMPERATURE (°C)
1200
1000
800
600
400
200
0
0
1
2
3
4
5
6
7
8
9
SHEAR STRESS (KB)
Diopside Polycrystal
Kirby and Etheridge (1979)
Kirby and Kronenberg (1980)
twinning common
Tullis (unpublished) dry
Tullis (unpublished) wet; Very little twinning
Hypersthene single crystal twinning
Kolle and Blacic (1979)

TECTONIC STRESSES IN THE LITHOSPHERE
CONSTRAINTS PROVIDED BY THE EXPERIMENTAL DEFORMATION OF ROCKS

by Stephen H. Kirby
U.S. Geological Survey, Office of Earthquake Studies
345 Middlefield Road, Menlo Park, CA 94025

ABSTRACT

The strengths of rocks clearly place an upper limit on the stress that can be sustained by the upper half of the lithosphere. The distribution of rock strength with depth depends on rock type, lithostatic pressure, fluid pressure, temperature, strain rate, and other factors. Laboratory data on rock rheology are generally lacking at intermediate temperatures and pressures on the important rock types expected in the lithosphere, so a definitive accounting of the strength distribution with depth in the upper lithosphere is presently unattainable. Analogies are drawn between the fragmentary strength data on silicates at intermediate temperature with the more extensive experimental data on marble and limestone and several tentative conclusions are drawn:

1. Three major regimes of rock behavior apply to carbonates and silicates:
    A. The brittle regime where changes in specimen length are accommodated by fracture and faulting.
    B. The semi-brittle regime, where stable microfracturing (cataclasis) and intracrystalline glide both occur.
    C. The ductile regime, where the mechanisms of plastic deformation dominate.
2. The brittle and semi-brittle regimes both show strong pressure effects on strength and it is shown that the transitions between the three regimes for various states of stress occur at critical values of the least principal compressive stress σ_3 for each rock type.

3. In the ductile regime, pressure effects on strength are small, and the effects of strain rate and temperature depend on the temperature interval. At low temperatures, intracrystalline dislocation glide mechanisms predominate and strength is insensitive to strain rate and temperature and is very dependent strain and time. At high temperatures, a whole host of mechanisms can occur, often diffusion controlled. Strength at high temperature is much more sensitive to temperature and strain rate and steady state (time-independent) flow predominates.

In view of the strong pressure affects on experimental rock strength at low to intermediate pressures, the conception of the lithosphere as monolithic plates of uniformly high strength is untenable. The fragmentary rheological data on the appropriate rocks and minerals suggest the following rheological structure of the lithosphere where it is inelastically deforming: A rapid pressure-driven increase in rock strength with depth culminates with a relative maximum in strength of approximately 10 $\pm$ 5 kilobars at depths which depend on the state of stress. I estimate that this critical depth is 20 to 60 kilometers. The depth at which the strength begins to decrease rapidly with depth due to the effects of temperature depends critically on the detailed thermal structure of the lithosphere. Thus, the effective thickness of high strength lithosphere is reduced by the brittle and semi-brittle processes at shallow depths, and the lithospheric plates can be considered as elastic-plastic with yield shear strengths of 3 to 8 kb and effective thicknesses of a few tens of kilometers. The weakening effects of water are reviewed and are considered likely to be small in the oceanic lithosphere but

probably dominate in the continental crust and in subduction zones where abundant pore water and water from prograde metamorphic reactions are available.

INTRODUCTION

Due to the high elastic moduli of silicate rocks, at most a few percent elastic strain can be supported by rocks of the lithosphere before additional strain occurs by brittle failure or by plastic yielding. This upper bound on stresses in the lithosphere imposed by rock strength may be estimated by laboratory determination of the effects of the parameters which control rock strength (pressure, temperature, strain rate, composition, etc.) and estimates of what values these parameters take on in the earth. In the last decade, the importance of the rheology of olivine in controlling the stress distribution in the mantle, where the behavior of olivine is expected to dominate, has been emphasized and much effort has been devoted to determining the high temperature steady state rheology of olivine. The experimentally-determined olivine rheologies have been applied to calculating the bounding strength distribution with depth in the mantle by factoring in model geotherm and pressure distributions and estimates of the likely range of geologic strain rates (See recent reviews by Carter, 1976 and Weertman and Weertman, 1975; Mercier et al., 1977; Kirby, 1977; Post, 1977). These bounding stresses, which have been extrapolated to shallow depths where temperatures and pressures are low, are oversimplified in the upper half of the lithosphere for the following reasons:

(1) At low to intermediate temperatures, the ductile rheologies of most crystalline materials are different than at high temperatures.

(2) At low confining pressures and low temperatures, brittle processes predominate in most rocks, and there are strong effects of the state of stress on rock strength.

(3) Kirby (1977) attempted to model the transition between shallow brittle behavior and deep ductile behavior by using Byerlee's (1968, 1978) universal friction law, assuming that the transition occurs where the frictional stress (determined by the lithostatic pressure and Byerlee's friction law) is exceeded by the stress derived from the high temperature steady state rheology of olivine. This preliminary approach is oversimplified for reasons stated above and because the transition between brittle and ductile behavior involves a broad region of semibrittle behavior.

In the present work, empirical relationships between the frictional strength and the critical least principal stress at the brittle to semi-brittle transition and between the ductile strength and the critical least principal stress at the semi-brittle to ductile transition are put forward. The depths of these transitions are estimated from the lithostatic pressure and a simple steady state geotherm, and model stress profiles are constructed from representative olivine rheologies. Lastly, the weakening effects of water are outlined and their likely effects are discussed in qualitative terms.

EFFECTS OF PRESSURE ON THE ROCK STRENGTH AND ON THE TRANSITIONS BETWEEN BRITTLE AND DUCTILE BEHAVIOR.

General Effects of Confining Pressure

The pioneering experiments of F. D. Adams and his coworkers, von Kármán (1911), and Griggs (1936) all demonstrated the progressive increase in rock strength and progessive suppression of brittle behavior with increasing comfining pressure P in triaxial compression tests on rocks (where the principal compressive stresses $\sigma_1 > \sigma_2 = \sigma_3 = P$). These and subsequent experiments have revealed three basic regimes of rock behavior (Figs. 1, 3, and 6):

(1) Brittle regime, where specimen shortening is accommodated by localized displacements on shear fractures or faults or on extension fractures parallel to the least principal stress. Stress drops are often observed, and ultimate strength increases rapidly with increasing confining pressure.

(2) Semibrittle regime in which strains are no longer localized on faults or fractures but distributed throughout the specimen. That brittle processes are still operating is evident from direct observation of microfractures and from large volume increases associated with microfracturing (dilatency). This last point is demonstrated by the careful measurements of volume changes in Carrara marble taken to large strains in the semi-brittle regime by Edmond and Paterson (1972; Fig. 2). Ductile processes also clearly operate since semibrittle behavior does not occur unless the

minerals of a rock in question show significant plasticity at the test temperature. For example, Tullis and Yund (1977) showed that the quartz and feldspar in Westerly granite showed no evidence of significant plasticity at $T < 400^{\circ}C$ and Schock and Heard (1974) and Tullis and Yund (1977) were unable to achieve semi-brittle behavior below this temperature even at confining pressures up to 20 kilobars. On the other hand, minerals which do show some plasticity at room temperature (halite, calcite, serpentine) can be rendered semi-brittle or ductile at low temperature by raising confining pressure. Increasing confining pressure does increase strength in this regime (Figs. 1, 2, 3 and 6B) and also increases the slope of the stress strain curve ($d\sigma/d\varepsilon$) in the post-yield region (Figs. 2 and 6A).

(3) Ductile regime is characterized by a very low pressure sensitivity of strength ($d\sigma / dP < 0.1$; Paterson, 1967), a lack of a pressure effect on the hardening rate ($d\sigma/d\varepsilon$), no significant dilatency, and by abundant evidence of intracrystalline glide or other mechanisms of plastic deformation.

Influence of the State of Stress

Even the earliest experiments by von Kármán (1911) and Böker (1915) showed that quantitatively different effects of pressure occur in triaxial compression ($\sigma_1 > \sigma_2 = \sigma_3 = \underline{P}$), triaxial extension ($\sigma_1 = \sigma_2 = \underline{P} > \sigma_3$), and triaxial torsion ($\sigma_1 > \sigma_2 = \underline{P} > \sigma_3$). The contrasts between compression and extension experiments in the classic experiments on Yule marble are shown in Fig. 3. Increasing confining pressure still increases strength $\sigma = (\sigma_1 - \sigma_3)$ in extension tests, but the rates of increase of strength with pressure are

lower, and the critical transition pressures between the three regimes are shifted to higher pressures. If we compare these strength data on the basis of the value of the least principal stress (σ_3 = $\underline{P}$ in compression and σ_3 = $\underline{P}$ - σ in extension), the two data sets correlate quite well (Fig. 4) both in absolute strength and in the transition values of σ_3. Admittedly, fracture strengths for extension and compression tests compared on this basis often do not correlate as well (see data in Heard, 1960; Handin, et al., 1967), but the critical transition values of σ_3 do correlate. This is shown in the brittle to semi-brittle transition data on Solenhofen limestone (Fig. 5). Even though the confining pressure $\underline{P}$ necessary to suppress brittle fracture varies by as much as an order of magnitude depending on the test geometry (Fig. 5A), the critical values of the least principal stress at the brittle to semi-brittle transition correspond very well for the extension and compression tests (Fig. 5B). The critical values in the torsion tests on solid cylinders deviate from the compression and extension results, and it is believed that this stems from the fact that the values at failure or yield are computed from an elastic solution and are subject to substantial error. The torsion tests on hollow cylinders, in which stress inhomogenietes are smaller and the elastic solution for σ_3 are less uncertain, support this hypothesis, since the data correspond very well to the extension and compression results.

The physical basis for the critical influence of σ_3 in the brittle to semi-brittle and the semi-brittle to ductile transitions is not known, but may be associated with the preferential opening of tensile cracks parallel to the least principal stress (where the work done against the stress state is mimimized) which have been convincingly documented in the studies of prefailure microcracking in rocks at low pressures and temperatures (see, for

example, Kranz, 1979). In any event, the effectiveness of σ_3 in the progressive suppression of brittle behavior is clear, and the effect of increasing lithostatic pressure with depth should taken into account the state of stress.

Observations in Silicates

Data on the brittle to semibrittle to ductile transitions in crystalline silicate rocks are sparse due to the high pressures necessary to suppress macroscopic failure. Tullis and Yund (1977) have rendered Westerly granite semi-brittle at temperatures as low as 500° at pressures between 5 and 10 kilobars and ductile at 900°C at pressures between 5 and 7.5 kilobars. Kirby and Kronenberg (1978 and unpublished work) have performed a series of experiments at 600°C on a clinopyroxenite at various confining pressures up to 20 kilobars (Fig. 6). The pressure effect on strength and the pressure-induced changes in mechanisms observed in marbles and other soft rocks are seen in this silicate as well (Fig. 6B). Similar behavior has been observed in orthopyroxenite (Kirby and Zateslo, 1978 unpublished) and dunite (Byerlee, 1968; Kirby and Pinkston, 1979 unpublished). All of the above experiments were performed in triaxial compression, so we have no direct measurements under other states of stress. We rely upon the analogies drawn with marbles and limestones that the principal criteria for the brittle to semi-brittle to ductile transitions are critical values of σ_3.

EFFECTS OF TEMPERATURE ON THE DUCTILE BEHAVIOR OF ROCKS

Experience in metals has shown that high temperature steady state rheology does not apply to flow at temperatures below about half the

temperature of melting T_m (Weertman and Weertman, 1970, 1975). The data on Yule marble illustrate some of these contrasts (Fig. 7A and B). At temperatures below about 400°C, flow is strongly transient (i. e., the stress strain curves monotonically rise or work harden), whereas at higher temperatures, steady state flow at constant stress can be achieved. When the strength data (differential stress σ at 10% strain) are plotted on a log σ vs 1/T basis, the contrasts in temperature, and strain rate sensitivities of strength are revealed (Fig. 7B). In the low temperature regime, strength is very insensitive to strain rate and temperature, and the behavior can be approximated by a plastic-elastic rheology with a characteristic yield stress and strong post-yield work hardening. The strain rate and temperature sensitivities of strength are clearly higher in the high temperature regime. Similar behavior is exhibited by orthopyroxene (Raleigh et al., 1971), halite (Heard, 1972), Sleaford Bay clinopyroxenite (Kirby and Kronenberg 1978; Fig. 8) and dunite (Kirby and Pinkston, unpublished data). This low temperature-high temperature transition in the ductile regime corresponds to a change in the controlling mechanism of flow: at low temperatures, intracrystalline glide (slip, twinning, etc.) occurs, whereas at high temperature, a multitude of mechanisms, many of these diffusion controlled, occur (Weertman and Weertman, 1970, 1975; Nicolas and Poirier, 1976). Thus, the transition is a fundamental property of crystalline materials. A clear strain rate dependence of the transition temperature is also evident (Figs. 7B and 9), and the flow law data indicate that the transition temperature at geologic strain rates is 600 $\pm$ 100°C for the pyroxenites (Raleigh et al., 1971; Kirby and Kronenberg, unpublished). We thus have a reasonable expectation that this low temperature ductile regime may be important in the deformation of the lithosphere.

APPLICATION TO THE EARTH

Effects of Lithostatic Pressure

The pressure due to the lithostatic load P_L is best known environmental parameter, and to a good approximation for the oceanic lithosphere:

$$P_L = \bar{\rho} g \Delta Z \simeq (0.34 \text{ kb/km}) \Delta Z \text{ (km)}$$

where $\bar{\rho}$ is the average density, taken to 3.45 g/cm (Press, 1972). In view of the importance of the least principal stress in controlling the transitions between the brittle, semi-brittle, and ductile regimes, it is likely that the effects of increasing P_L are bounded by the triaxial compression ($\sigma_1 > \sigma_2 = \sigma_3 = P_L$) and triaxial extension ($\sigma_1 = \sigma_2 = P_L > \sigma_3$) cases. The differential stress $\sigma = (\sigma_1 - \sigma_3)$ which the rock supports has an effect of reducing the least principal stress $\sigma_3 = (P_L - \sigma)$ in the extension case, an effect which must be overcome by greater depths and higher P_L. It is assumed that there is no explicit effect of the intermediate principal stress σ_2. I also defer discussion of pore pressure effects in reducing the effect of lithostatic pressure to a later section.

Following an earlier paper (Kirby, 1977), I use the universal high pressure friction law of Byerlee 1968, 1978) as a lower bound on the fracture strength:

$$\tau_f \text{ (kb)} = 0.8 + 0.6 \, \sigma_n \text{ (kb)}; \quad 2 \text{ kb} > \sigma_n < 17 \text{ kb}$$

where τ_f is the shear stress necessary to break static friction and σ_n is the normal stress. For fractures oriented at the preferred angle θ to the maximum compressive stress, this friction law can be transformed for triaxial compression:

$$\sigma_f = 2.9 + 2.1\ P_L \qquad \theta = 30^o$$

and triaxial extension

$$\tau_f = 0.9 + 0.7\ P_L \qquad \theta = 24^o$$

where σ_f is the differential stress necessary to break friction and the preferred angles θ are taken as averages from Handin's (1966) compilation of triaxial compression and extension tests. I note that the lithostatic pressure is three times as effective in increasing σ_f in compression than in extension. No strain rate or temperature effect on this brittle fracture law is incorporated, as the evidence for such effects on fracture and friction are generally lacking (Byerlee, 1978; Stesky, 1978; Paterson, 1978). No satisfactory theory permits use to predict the critical value of σ_3 at the brittle to semi-brittle transition (see review by Paterson, 1978) but we may take the ratio σ_3/σ_f (where σ_f is the frictional stress as defined above) as characteristic of this transition. Byerlee's (1968) data on Spruce Pine dunite at room temperature indicates $\sigma_3/\sigma_f \simeq 0.37$ at the transition and experiments on Balsam Gap dunite at 600°C by Kirby and Pinkston (unpublished) give $\sigma_3/\sigma_f \simeq 0.45$. These values are also typical of other silicates we have tested clinopyroxenite: Kirby and Kronenberg, 1978; Kirby and Zalesto, unpublished; Kirby and Pinkston, unpublished). These results suggest that $\sigma_3/\sigma_f \simeq 0.4$ is a good approximation to the brittle to semi-brittle transition over a wide range of temperatures. This criterion brings to mind Mogi's (1966) rule of thumb that $\sigma_3/\sigma_f \simeq 1/3$ at the transition.

For $\sigma_3/\sigma_f = 0.4$, $P_L/\sigma_f = 0.4$ for the compression case and $(P_L - \sigma_f)/\sigma_f \simeq 0.4$; $P_L = 0.4 + 1.4\sigma_f$ for extension. As expected, the critical lithostatic load at the transition is larger in extension than in compression.

A popular rule of thumb in high pressure testing of rocks in triaxial compression is that if the confining pressure exceeds the maximum differential stress sustained by the rock, then the deformation is in the ductile regime. This criterion is explored in Table I, which is a compilation of ratios of least principal stress to ductile strength σ_d for rocks. Although individual values range from 0.4 to 1.5, the data for crystalline rocks range from 0.76 to 0.9 and for dunite $\sigma_3/\sigma_f \simeq 0.8$. Taking $\sigma_3/\sigma_d = 0.8$ for the lithosphere, $P_L/\sigma_d = 0.8$ for triaxial compression case and $(P_L - \sigma_d)/\sigma_d = 0.8$; $P_L = 1.8\ \sigma_d$ for the extension case. Again, a higher lithostatic pressure is needed to suppress semibrittle behavior in the extension case than in the compression case.

Ductile Flow Law for Olivine

The available high-temperature steady-state flow law data are tabulated in Tables II and III for anhydrous and "wet" olivine, respectively and the steady state stress-strain rate relations are plotted in Fig. 10. Stress effects on steady state strain rate $\dot{\varepsilon}_s$ are very similar and are adequately represented by a thermally activated power law rheology:

$$\dot{\varepsilon} = A\sigma^n \exp\ (-\ (E^* + PV^*)/RT))$$

where A, n and E* are material constants (See Carter, 1976 and Weertman and Weertman, 1975, and Nicolas and Poirier, 1976, for reviews on rock rheology). The activation energies for steady state creep E* are systematically lower for

olivine in the presence of water, and there are large differences in the A parameter. The differences between the easy glide single crystal and dunite data are not unexpected in light of the strong contrasts between single crystal and polycrystalline mineral rheology (MgO: Weaver and Paterson, 1969; Calcite: Turner and Heard, 1965, Heard and Raleigh, 1972; Halite: Heard and Carter, 1969, Heard, 1972: Dolomite: Heard, unpublished data). We take as representative, however, the anhydrous flow law of Durham and Goetze (1977) for crystals in the "odd" orientations and the hydrous flow law of Post (1977) for dunite. An activation volume $V^* = 11$ cm /mole, which accounts for small pressure effect, is assumed based on empirical correlations (Kirby and Raleigh, 1973; Sammis et al., 1977).

For the low temperature ductile olivine rheology, I take the unpublished data of Kirby and Pinkson on Balsam Gap dunite. The strain rate sensitivity was measured at 600oC at 15 kilobars confining pressure over a range of strain rates of 10^{-3} to 10^{-6} 5 s^{-1}; temperature sensitivity of strength was measured at a strain rate 10^{-5} s^{-1} over the range 400 to 900oC. The temperature and strain rate sensitivities of strength are small and very similar to the clinopyroxenite data of Fig. 9. A transition with the high temperature rheologies at a strain rate of 10^{-14} s^{-1} occurs at about 14 kilobars stress, a value which is insensitive to the specific high temperature rheology chosen. I take the strength data at 10% strain in this low temperature regime, mindful that strong transient flow behavior is likely to be important. The resulting estimated stresses associated with the low temperature regime are lower limits for strains which exceed 10%.

Temperature Distribution

The depth to the strong fall off the ductile strength due to increasing temperature is very sensitive to the temperature distribution. Instead of explosing a wide range of geotherms, I use the steady state temperature distribution of Parsons and Sclater (1977) for the old (<120 MY) oceanic lithosphere of the deep ocean basins, with an associated heat flow of 1.1 HFU, of which 0.2 HFU represents remaining cooling of the lithosphere, 0.1 HFU a radioactive heat source, and the remaining 0.8 HFU representing a sub-lithosphere "deep" heat source. The thermal history of the old oceanic lithosphere is as simple and well-constrained as anywhere on the earth. To a good approximation, the temperature distribution is linear with a gradient of 10.7°C/km. The chosen geotherm would seem appropriate to the problem of the bending of old lithosphere in the subduction zones of the western Pacific.

CALCULATED STRESS PROFILES - ZERO PORE PRESSURE

The calculated stress profiles for a representative geologic strain rate of 10^{-14} s^{-1} are shown in Figs. 11 and 12 for the two high temperature olivine rheologies chosen. The depth of the strong falloff of strength with increasing temperature and the depth to the high temperature-low temperature transition are not strongly dependent on the specific high temperature rheology chosen because of the overwhelming high temperature sensitivities of all the flow laws. The effects of the state of stress on the depths to the brittle to semi-brittle-to ductile transitions are prominent. The low temperature ductile strength limit is eliminated in the extension case and the strength maximum is deepened to 60 kilometers. A major conclusion is that brittle processes can be important a far greater depths than previously

thought. The maximum shear stresses at the strength maxima range from about 3 to 8 kilobars and the major effects of the uncertainties in the high temperature ductile rheology and in the geotherm affect the depth of the maxima, not the stress magnitudes.

WEAKENING EFFECTS OF PORE PRESSURE

Pore pressure (in particular P_{H_2O}) reduces rock strength in a number of important ways.

(1) Effective stress phenomenon. The best known weakening effect is a purely mechanical one, involving the reduction of the effective normal stresses by the magnitude of the pore pressure. The quantitative effect of thus reducing the effective confining pressure $P_e = (P - P_{H_2O})$ is generally observed only when the fluid and rock do not chemically react, when sufficient pore water is available to saturate the porosity, and when adequate permiability exists to equilibrate the porosity (including that produced by microfracturing during deformation) to the fluid pressure (Handin et al., 1963). There is direct evidence that high pore pressures exists at relatively shallow depths in the continental crust, not only as pore water in sediments and sedimentary rocks, but also as water of dehydration in zones of prograde metamorphism, such as associated with mountain building in zones of subduction. Pore pressure effects of dehydration clearly lead to weakening and embrittlement in the experimental work done on hydrous minerals (See references in Paterson, 1978, p. 183-187). The pore pressure effects are bounded by the hydrostat (0.1 kilobar/kilometer) and

by the lithostat ($\sim$0.3 kilobars/kilometer depth). Thus without knowledge of the permeability and porosity distribution with depth, we cannot establish the explicit pore pressure weakening effect, since it can range from no effect under dry conditions to a vanishing strength at $P_{H_2O} = P_L$.

(2) Static fatigue. A specific chemical effect of water at crack tips can lead to a time dependent brittle strength at stresses less than the short term breaking strength of rocks. This chemical effect in extending cracks at stress intensities lower than that required for unstable cracking, termed stress corrosion, is thought to be responsible for delayed brittle failure and brittle creep (Scholtz, 1968; Martin, 1972; Scholtz, 1972; Martin and Durham, 1975) and a clear effect of the partial pressure of H_2O up to liquid water saturation has been shown (Martin, 1972; Scholz, 1972; Atkinson, 1979 a and b).

(3) Hydrolytic weakening. Two minerals, quartz and feldspar, which are very important in the Earth's crust, are extremely strong and brittle under dry conditions at crustal temperatures and pressures (Griggs, 1967; Tullis and Yund, 1977; Tullis et al., 1979). This is in spite of the fact that crustal rocks containing these and other minerals under metamorphic conditions show clear evidence of ductility under relatively low inferred tectonic stresses. It has been demonstrated that very small concentrations of water dissolved in the quartz structure (< 0.1 weight percent) can lead to one or two orders of magnitude reduction in strength (Griggs and Blacic, 1965; Griggs, 1967). The hydrolytic weakening effect, as it is

termed, is apparently due to hydrolysation of the Si - O - Si framework by water at dislocations, which produces a chemical weakening promoting intracrystalline slip. The magnitude of the weakening effect is proportional to the concentration of H_2O in solid solution (Griggs, 1974; Kirby et al., 1977; Kirby and McCormick, 1979). Indirect evidence suggests that the equilibrium solubility of water in silicates increases with increasing P_{H_2O} (Kirby, 1975; Paterson and Kakulawala, 1979; Tullis et al., 1979; Kirby and McCormick, 1979; Hobbs et al., 1979). Thus evaluation of the hydrolytic weakening effect in the earth is interior requires data on the equilibrium solubility of water in silicates, for which we have no data.

(4) Pressure solution. It is well known that P_{H_2O} promotes the solubility of silicates in water, and mass transport through pore solutions from stressed grain contacts to pore-grain contacts has long be considered an important mechanisms of deformation under low grade metamorphic conditions. Although there is abundant field and some laboratory evidence for the operation of this type of deformation, there is little or no data which characterize the rheological effects of P_{H_2O} to constrain theories of flow (see review by Robin, 1978).

(5) It is well known that at high temperature, the presence of small amounts of water promotes recrystallization and other processes associated with bulk crystal diffusion (see, for example, Hobbs, 1968). It is difficult to separate these effects from the mechanical effects of hydrolytic weakening.

In summary of the above points, although the major weakening mechanisms of water are clearly identified, the data and or insight are generally lacking which would permit evaluation of their relative contributions in the earths interior. In view of the probable low crustal temperatures (T< 500oC) and the observations cited above, it is likely that P_{H_2O} plays a major if not dominating role in limiting the stresses in the Earth's crust. Evidence for strong P_{H_2O} effects in the oceanic lithosphere is not as persuasive. In fact, two lines of evidence suggest that the weakening effects of P_{H_2O} may be lacking there. First, several kilometers of oceanic crust are extracted from the mantle part of the lithosphere by partial melting at the oceanic ridges. Partial melting is very efficient at removing volatiles from solid solution, grain boundaries, and from hydrous minerals, since the solubilities of volatiles, such as water, are orders of magnitude higher in silicate melts than in the corresponding silicate minerals. This would tend to milk off what water might be brought by return flow from subduction zones. It is possible that seawater could percolate through fractures deep into the mantle part of the lithosphere. The evidence is generally lacking for such deep penetration in ophiolite sequences, which are generally considered as exposed sections of oceanic lithosphere. Clear evidence is seen for chemical interaction of sea water with the pillow basalts and deeper gabbroic equivalents, but little little evidence for such interactions in the harzburgites, the uppermost part of the mantle (R. Coleman, 1977 and pers. comm. 1979). The harzburgites are generally very refractory and very dry. Thus, the weakening effects of water are not likely to be very important in reducing the stress profiles calculated in Figs. 11 and 12.

Acknowledgements

I thank Andreas Kronenberg, Theodore Zateslo, and John Pinkston for permission to use unpublished data on the strength of ultramafic rocks.

REFERENCES

Atkinson, B. K. (1974), Experimental deformation of polycrystalline galena, chalcopyrite and pyrrhotite. Inst. Mining Metallurgy Trans., Sec. B., 83, 19-28.

Atkinson, B. K. (1975), Experimental deformation of polycrystalline pyrite: Effects of temperature, confining pressure, strain rate,and porosity. Econ. Geol. 70, 473-487.

Atkinson, B. (1979), A fracture mechanics study of subcritical tensile cracking of quartz in wet environments, Teconophysics (in press).

Böker, R. (1915), Die Mechanik der bleibenden Formanderung in kristallinisch aufgebauten Korpern, Ver. dtsch. Ing. Mitt. Forsch. 175, 1-51.

Byerlee, J. D. (1968), Brittle-ductile transition in rocks. J. Geophys. Res. 73, 4741-4750.

Byerlee, J. (1978), Friction in rocks, Pageoph, 116, 615-626.

Carter, N. L. (1976), Steady state flow of rocks, Rev. Geophys. Space Phys. 14, 301-360.

Carter, N. L., and Ave'Lallement, H. G., (1970), High temperature flow of dunite and peridotite, Geol. Soc. Amer. Bull. 81, 2181-2202.

Carter, N. L., and Heard, H. C. (1976). Steady state flow of rocks. Rev. Geophys. Space Phys. 14, 301-360.

Coleman, R. G. (1977), Ophiolites: Ancient Oceanic Lithosphere?, Springer Verlag, 229p.

Durham. W. B., and Goetze, C., 1977, Plastic flow of oriented single crystals of olivine 1. mechanical data J. Geophys. Res., v. 82, 5737-5753.

Edmond, J. M. and Paterson, M. S., (1972), Volume changes during the deformation of rocks at high pressures, Int. J. Rock Mech. Min. Sci., 9, 161-182.

Goetze, C., and Brace, W. F.(1972), Laboratory observations of high temperature rheology of rocks, Tectonophysics, 13, 583-600.

Griggs, D. T. (1936), Deformation of rocks under high confining pressures, J. Geol. 44, 541-577.

Griggs, D. T. (1967), Hydrolytic weakening of quartz and other silicates, Geophys. J. R. Astron. Soc. 14, 19-31.

Griggs, D. T. (1974) A model for hydrolytic weakening in quartz, J. Geophys. Res., 79, 1655-1661.

Griggs, D. T. and Blacic, J. D. (1965), Quartz, anomalous weakness of synthetic crystals. Science, 147, 292-295.

Handin, J. (1953), An application of high pressure in geophysics: experimental rock deformation. Trans. Am. Soc. Mech. Eng. 75, 315-324.

Handin, J. (1966), Strength and ductility. In: Handbook of Physical Constants. Revised ed. Clark, S. P. (ed.). Geol. Soc. Am. Memoir 97, pp. 223-289.

Handin, J., Hager, R. V., Friedman, M., Feather, J. N. (1963), Experimental deformation of sedimentary rocks under confining pressure: pore pressure effects. Bull. Am. Assoc. Petrol. Geol. 47, 717-755.

Handin, J., Heard, H. C., Magouirk, J. N. (1967), Effects of the intermediate-principal stress on the failure of limestone, dolomite, and glass at different temperatures and strain rates. J. Geophys. Res. 72, 611-640.

Heard, H. C. (1960), Transition from brittle fracture to ductile flow in Solenhofen limestone as a function of temperature, confining pressure, and interstitial fluid pressure. In: Rock Deformation. Griggs, D., Handin, J. (eds.). Geol. Soc. Am., Memoir 79, 193-226.

Heard, H. C. (1972), Steady state flow in polycrystalline halite at 2 kilobars. Geophys. Monograph 16, 191-210.

Heard, H. C. and Raleigh, C. B. (1972), Steady state flow of Yule marble. Geol. Soc. Am. Bull., 83, 935-956.

Heard, H. C., Abey, A. E., Bonner, B. P., and Duba, A., (1975), Stress-strain behavior of polycrystalline NaCl to 3.2 GPa, Lawrence Livermore Laboratory, Rept. UCRL-51743, 16 p.

Hobbs, B., (1968), Recrystallization of single crystals of quartz, Tectonophysics, 6, 353-401.

Hobbs, B. , Tullis, T. E. (1979), The influence of pressure on hydrolytic weakening in quartz, Trans. Am. Geophys. Union 60, 370.

Kármán, T. von (1911), Festigkeitsversuche unter allseitigem Druck. Z. Verein. Dtsch. Ing. 55, 1749-1757.

Kirby, S. H. (1975), Creep of synthetic alpha quartz. Ph. D. Thesis, U.C.L.A.

Kirby, S. H. (1977), State of stress in the lithosphere: Inference from the flow laws of olivine, Pure Appl. Geophys. 115, 245-258.

Kirby, S. H., (1978), Rheology of olivine: a critical review, Trans. Am. Geophys. Union, 59, 374.

Kirby, S. H., and Kronenberg, A., (1978), Ductile strength of clinophyroxenite: evidence for a transition in flow mechanisms, Trans. Am. Geophys. Union, 59, 376.

Kirby, S. H. and McCormick, J. (1979), Creep of hydrolytically-weakened synthetic quartz crystals oriented to promote $\{2\bar{1}\bar{1}0\}$ <0001> slip. Bull. Miner, 102, 124-137.

Kirby, S. H., McCormick, J., and Linker, M. (1977), The effect of water concentration on creep rates of hydrolytically-weakened synthetic quartz single crystals. Trans. Am. Geophys. Union 58, 1239.

Kirby, S. and Raleigh, C., (1973), Mechanisms of high temperature solid-state flow in minerals and ceramics and their bearing on the creep behavior of the mantle. Tectonophysics 19, 165-194.

Kohlstedt, D. L, and Goetze, C., (1974), Low-stress high-temperature creep in olivine single crystals. Journ. Geophys. Res. 79, 2045-2051.

Kohlstedt, D., Goetze, C., Durham, W. B., (1976), Experimental deformation of single crystal olivine with application to flow in the mantle, in The Physics and Chemistry of Minerals and Rocks, edited by R. G. J. Strens, pp 35-49, Wiley, London, 697p.

Kranz, R. (1979), Crack growth and development during creep of Barre Granite. Int. J. Rock Mech. Min. Sci. 16, 23-35.

Martin, R. J. (1972), Time-dependent crack growth in quartz and its application to the creep of rocks. J. Geophys. Res. 77, 1406-1419.

Martin, R. and Durham, W. (1975), Mechanisms of crack growth in quartz, J. Geophys. Res. 80, 4837-4844.

Mercier, J.-C., Carter, N. L., Anderson, D. (1977), Stress in the lithosphere: Inferences from steady-state flow of rocks. Pure and Appl. Geophys. 115, 199-226.

Mogi, K. (1966), Pressure dependence of rock strength and transition from brittle fracture to ductile flow. Bull. Earthquake Res. Inst., Tokyo Univ. 44, 215-232.

Nicolas, A. and Poirier, J.-P. (1976), Crystalline Plasticity and Solid State Flow in Metamorphic Rocks, Wiley.

Parsons, B. and Sclater, J. G., (1977), An analysis of the variation of ocean floor bathymetry and heat flow with age, J. Geophys. Res. 82, 803-827.

Paterson, M. S. (1967), Effect of pressure on stress-strain properties of materials. Geophys. J. R. Astron. Soc. 14, 13-17.

Paterson, M. S. (1978), Experimental Rock Deformation-The Brittle Field, Springer, 254 p.

Paterson, M. S. and Kululawala, K. (1979), The role of water in quartz deformation, Bull. Miner. 102, 92-98.

Paterson, M. S., Weaver, C. W. (1970), Deformation of polycrystalline MgO under pressure. J. Am. Ceram. Soc. 53, 4634-471.

Post, R. (1977), High temperature crep of Mt. Burnet Dunite, Tectonophysics, 42, 75-110.

Press, F.(1972), The earth's interior inferred from a family of models in The Nature of the Solid Earth (ed. E. C. Robertson) pp. 147-171 (McGraw-Hill, New York), 677 p.

Raleigh, C. B., Kirby, S. H., Carter, N. L. and Ave'Lallemant, H. G. (1971). Slip and the clinoenstatite transformation as competing rate processes in enstatite, J. Geophys. Res. 76, 4011-4022.

Robin, Y. F., (1978), Pressure solution at grain-to-grain contacts. Geochimica et Cosmochimica Acta, 42, 1383-1384.

Rutter, E. H. (1972), The influence of interstitial water on the rheological behaviour of calcite rocks. Tectonophysics 14, 13-33.

Schock, R. and Heard, H. C. (1975),Static mechanical properties and shock loading response of granite. J. Geophys. Res. 79, 1662-1666.

Scholz, C. H. (1968), Mechanism of creep in brittle rock. J. Geophys. Res. 73, 3295-3302.

Scholz, C. H. (1972), Static fatigue of quartz, J. Geophys. Res. 77, 2104-2114.

Tullis, J. A., Shelton, G., and Yund, R. (1979), Pressure dependence of rock strength: implications for hydrolytic weakening. Bull. Mineral. 102, 110-123.

Tullis, J., Yund, R. A. (1977), Experimental deformation of dry Westerly granite, J. Geophys. Res. 82, 5705-5718.

Turner, F. J. and Heard (1965), Deformation in calcite crystals at different strain rates, Univ. Calif. Publ. in Geol. Sciences 46, 103-126.

Weaver, C. W., Paterson, M. S. (1969), Deformation of cube, oriented MgO crystals under pressure. J. Am. Ceram. Soc. 52, 293-302.

Weertman, J. and Weertman, J. R. (1970), Mechanical properties, strongly temperature-dependent, in Physical Metallurgy (ed. R. W. Cahn), 983-1010.

Weertman, J. and Weertman, J. R. (1975), High temperature creep of rock and mantle viscosity, in Ann., Rev. of Earth and Planet, Sci., Vol. 3 (ed. F. A. Donath) 293-315.

Table I

DUCTILE STRENGTHS AND LEAST PRINCIPAL STRESSES AT THE SEMI-BRITTLE TO DUCTILE TRANSTION IN ROCKS

MATERIAL	T, °C	DUCTILE STRENGTH$ kb	σ_3, kb	σ_3/σ_d	REFERENCE
Solenhofen limestone	20	6.9	6	0.9	Edmond and Paterson (1972)
Carrara Marble	20	5.7	6	1.05	Edmond and Paterson (1972)
Carrara Marble	500	1.7	0.7	0.4	Rutter (1972)
Yule Marble	20	3.5	5.1	1.5	Handin (1966)
Halite	23	0.8	0.3	0.4	Heard et. al. (1975).
	20	0.8	0.8	1.0	Handin (1966)
Galena	200	3.8	2.7	0.7	Atkinson (1974)
	300	2.7	2.7	1.0	Atkinson (1974)
	400	1.6	1.5	0.9	Atkinson (1974)
Pyrrhotite	300	1.4	2	1.4	Atkinson (1974)
	400	0.8	1.0	1.2	Atkinson (1974)
Clinopyroxenite	600	17.4	14.	0.8	Kirby & Kronenberg (1978)
Orthopyroxenite	600	14.0	13.	0.9	Kirby and Zateslo (unpubl.)
Dunite	600	16.1	12.	0.8	Kirby and Pinkston (unpubls.)
Granite	600	18.0	12.5	0.7	Tullis and Yund (1977)
Periclase MgO	750	3.0*	2.	0.7	Paterson and Weaver (1964)

$Differential stress at 10% strain unless otherwise noted.
*Value picked at yield.

SUMMARIZED FLOW LAW DATA FOR OLIVINE - NOMINALLY ANHYDROUS

FORM OF THE FLOW LAW: $\dot{\varepsilon} = A\sigma^n \exp[-(E^*+PV^*)/RT]$

DATA SOURCE	SAMPLE TYPE	A, $s^{-1}kb^{-n}$	n	σ range, kb	E*+PV*, kcal/mole	T range, °C	P, kb
C and A (1970)	Mt. Burnet Dunite	$1.2X10^{10}$	4.8±0.4	1 to 9	119.8±16.6	1100-1300	15
		$(5.1X10^{9})$*	(3.3)*	1 to 9	(111)*	1100-1300	15
Post (1977)	Mt. Burnet Dunite	$7.95X10^{8}$	3.56	1 to 8	126±15	1100-1400	10-15
		$4.30X10^{8}$	3	1 to 3	126±15	1100-1400	10-15
K and R (1973)	Mt. Burnet Dunite	$1.1X10^{8}$	3	1 to 7	100±15	1100	15
	Single Crystals				E*, kcal/mole		
	Orientation						
K and G (1974)	Random	$3.6X10^{11}$	~3	0.1 to 1.5	126±2	1400-1600	10^{-3}
K, G, and D (1976)	All Data	$2.69X10^{11}$	3±1	0.1 to 1.5	125±15	1500-1600	10^{-3}
D and G (1977)	"Odd"	$1.04X10^{12}$	3.5±0.5	0.1 to 1.0	~125	1500-1600	10^{-3}
	$[110]_c$	$3.44X10^{12}$	3.6±0.3	0.2 to 0.4	~125	1200-1600	10^{-3}
	$[101]_c$	$1.22X10^{12}$	3.7±0.2	0.1 to 0.6	~125	1430-1560	10^{-3}
					~80	1200-1400	10^{-3}
	$[011]_c$	$7.59X10^{10}$	3.5±0.3	0.3 to 0.8	~125	1400-1600	10^{-3}
					~90	1200-1400	10^{-3}
	On Axis#	-	-	0.8 to 1.8	-	1500-1600	10^{-3}

Sample strain less than 1%, flow law not determined

* Corrected by Carter(1976) for sample bulging

SUMMARIZED FLOW LAW DATA FOR POLYCRYSTALLINE OLIVINE WITH WATER (WET)

FORM OF FLOW LAW: $\dot{\varepsilon} = A\sigma^n \exp[-(E^*+PV^*)/RT]$

DATA SOURCE	SAMPLE TYPE	A, $s^{-1}kb^{-n}$	n	σ range, kb	E*+PV*	T range, °C	P, kb
C and A (1970)	Mt. Burnet Dunite	6.2×10^6	2.4±0.2	1 to 7	79.9±7.5	975-1350	10-15
		(1.3×10^3)*	(2.1)*		(54)*		
Post(1977)	"	4.5×10^7	5.1±0.3	1 to 8	93.8±2.8	800-1150	5-15
		4.3×10^8	3	1 to 3	93.8±2.8	800-1150	5-15

* Corrected by Carter(1976) for sample bulging

FIGURE CAPTIONS

Figure 1. Effect of confining pressure on the strength and mode of deformation of Carrara marble tested in triaxial compression. The differential stress ($\sigma=\sigma_1 - \sigma_3$) was the ultimate strength or the stress at 5% strain.

Figure 2. Stress vs axial strain and volumetric strain vs axial strain for triaxial compression tests on Carrara marble (Edmond and Paterson, 1972). Note strong dilatency in tests at 0.5 to 2.0 kilobars confining pressure where no faulting or fractures occured and the lack of such dilatency in the tests at 6 and 8 kilobars.

Figure 3. Influence of test geometry on the confining pressure (P) effect on strength in Yule marble. Strength is ultimate strength or stress at 5% strain, averaged for the two principal orientations of cores (normal and parallel to foliation). Note elevation of brittle and semi-brittle regimes to higher confining pressures in the extension experiments. Data compiled from various sources in Handin (1966).

Figure 4. Effect of least principal stress on the strength of Yule marble for both compression and extension tests. Same data and strength criteria as Fig. 3.

Figure 5. A. Effect of temperature on the critical confining pressure P at the brittle to semibrittle transition in Solenhofen limestone for varous test geometries (Heard, 1960; Handin et al., 1967). Note striking difference in transition confining pressures for the three types of tests.

Figure Captions (continued)

B. Effect of temperature on value of least principal stress at the brittle to semi-brittle transition for various test geometries. Note correspondence of σ_3 values for compression and extension tests. The low σ_3 values for torsion tests on solid cylinders is thought to arise from deficiencies of the elastic solutions for σ_3, to which the hollow cylinder data are less sensitive. Same data as Fig. 5A.

Figure 6. Effect of confining pressure on the strength of Sleaford Bay clinopyroxenite tested in triaxial compression. (Kirby and Kronenberg, 1978, unpubl.)

A. Stress-strain curves.

B. Ultimate strength or stress at 10% strain versus confining pressure

Figure 7. Temperature effects on the strength of Yule Marble

A. Stress-strain curves.

B. Log σ versus 1/T plot.

Figure 8. Temperature effects on the strength of Sleaford Bay clinopyroxenite. Strength defined as stress at 10% strain.

Figure 9. Strain rate effects on the strength of Sleaford Bay clinopyroxenite.

Figure 10. Experimental stress-strain rate relations for steady state flow in olivine at T = 1350°C (See Table II for data sources).

Figure 11. Model stress profile using Durham and Goetze (1977) single crystal rheology and Kirby and Pinkstons (unpublished) low temperature olivine rheology for Balsam Gap dunite. See text for details of

Figure Captions (continued)

geotherm. BF = Brittle fracture regime, SB = Semi-brittle regime, and D-LT and D=HT for ductile low temperature and high temperature regimes, P_L = lithostatic pressure, equal to the vertical normal stress.

Figure 12. Model stress profile using Post's (1977) hydrous olivine rheology. Same geotherm and symbols as Fig. 11.

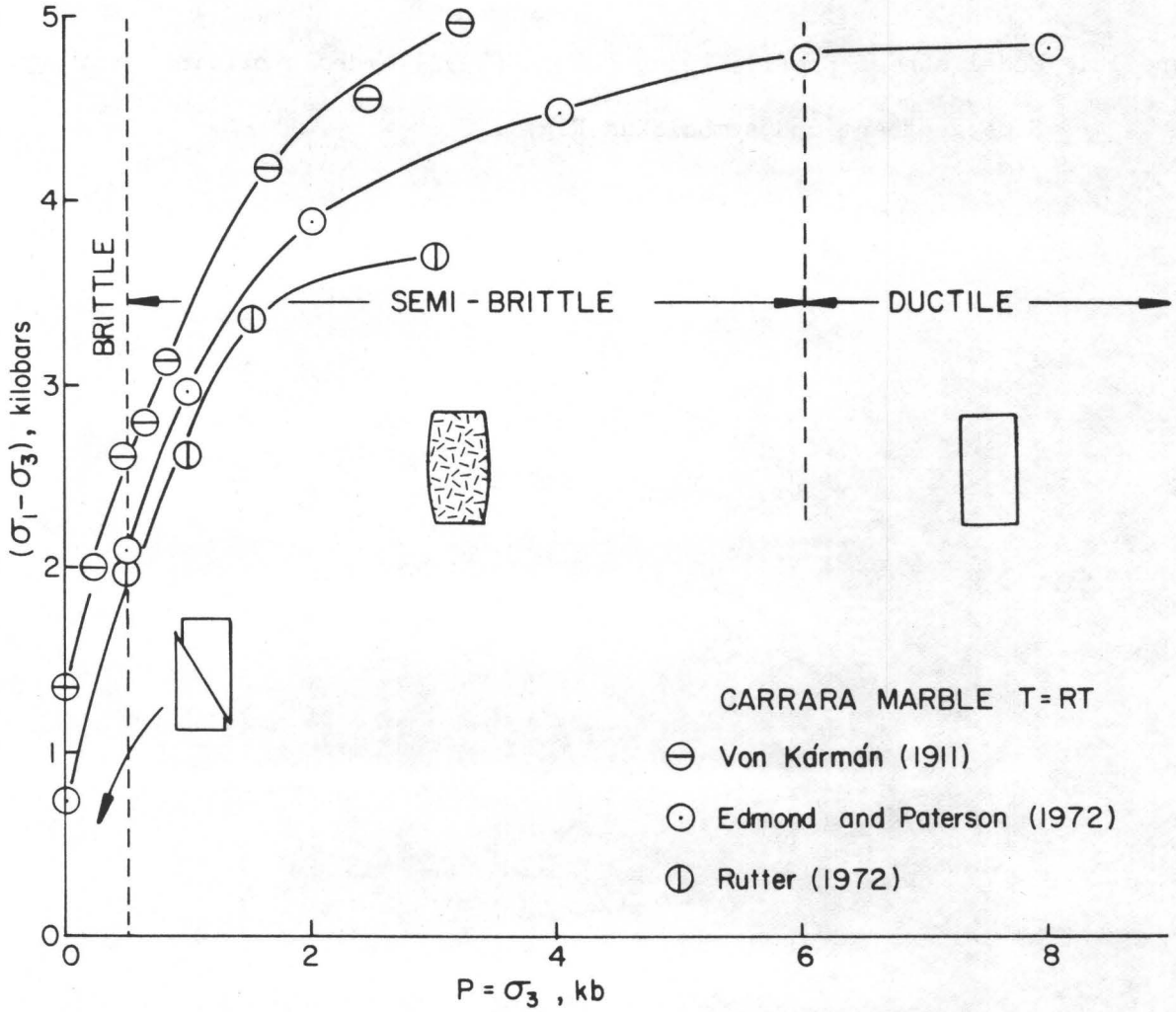
BRITTLE
SEMI - BRITTLE
DUCTILE
$(\sigma_1-\sigma_3)$, kilobars
$P = \sigma_3$, kb
0
1
2
3
4
5
0
2
4
6
8
CARRARA MARBLE T = RT
Von Kármán (1911)
Edmond and Paterson (1972)
Rutter (1972)

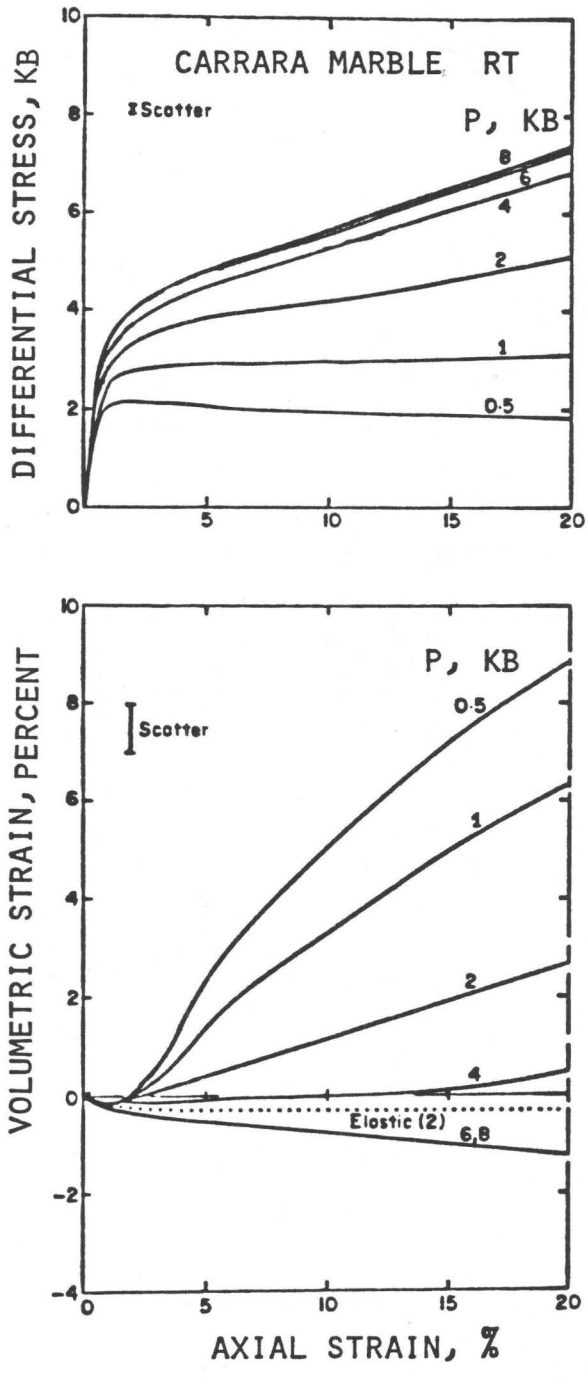
CARRARA MARBLE RT
±Scatter
P, KB
8
6
4
2
1
0.5
DIFFERENTIAL STRESS, KB
VOLUMETRIC STRAIN, PERCENT
Scatter
Elastic (2)
6,8
AXIAL STRAIN, %

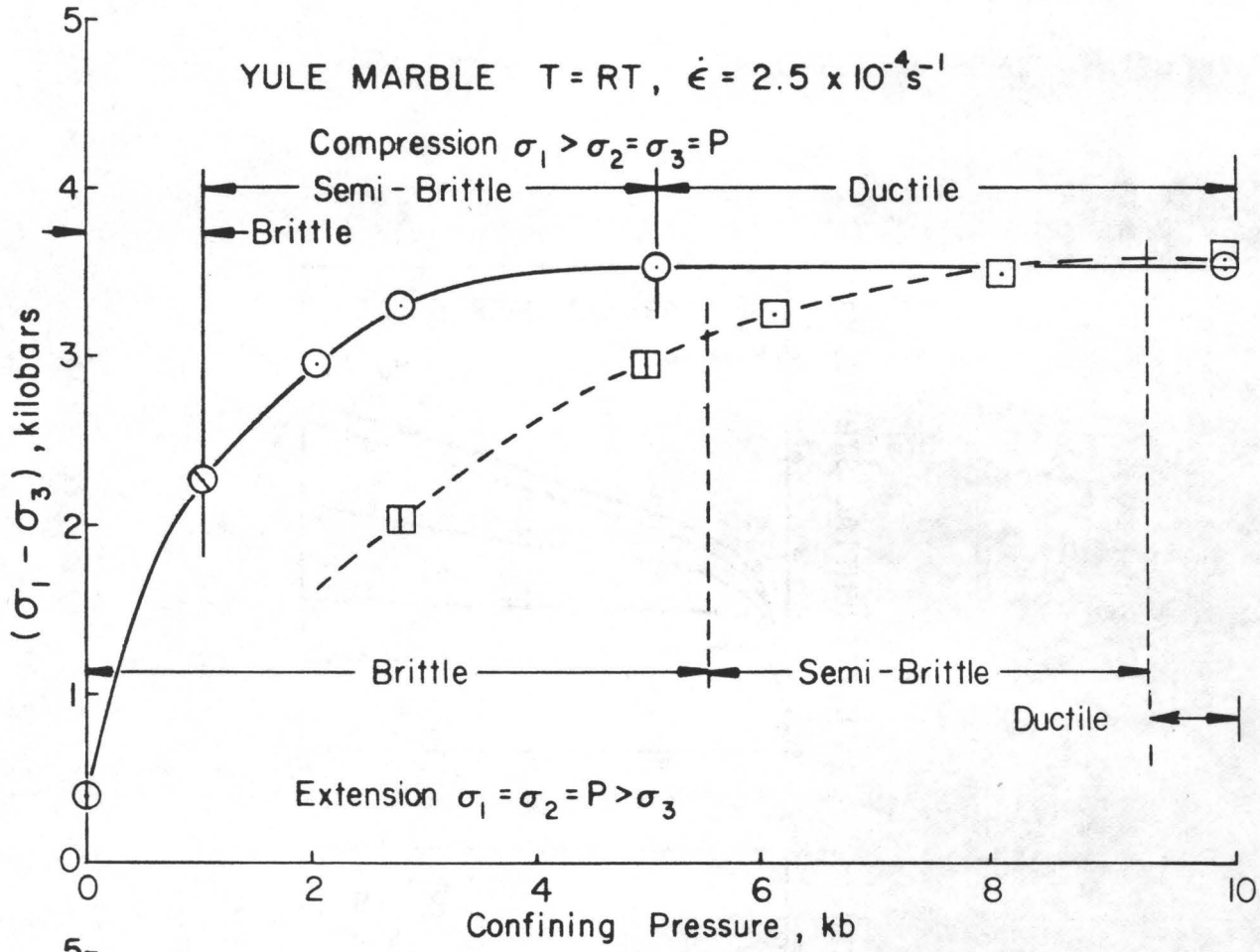
YULE MARBLE T = RT, $\dot{\epsilon}$ = 2.5 x $10^{-4}s^{-1}$
Compression $\sigma_1 > \sigma_2 = \sigma_3 = P$
Semi - Brittle
Ductile
Brittle
Brittle
Semi - Brittle
Ductile
Extension $\sigma_1 = \sigma_2 = P > \sigma_3$
$(\sigma_1 - \sigma_3)$, kilobars
Confining Pressure, kb
0
2
4
6
8
10
1
2
3
4
5

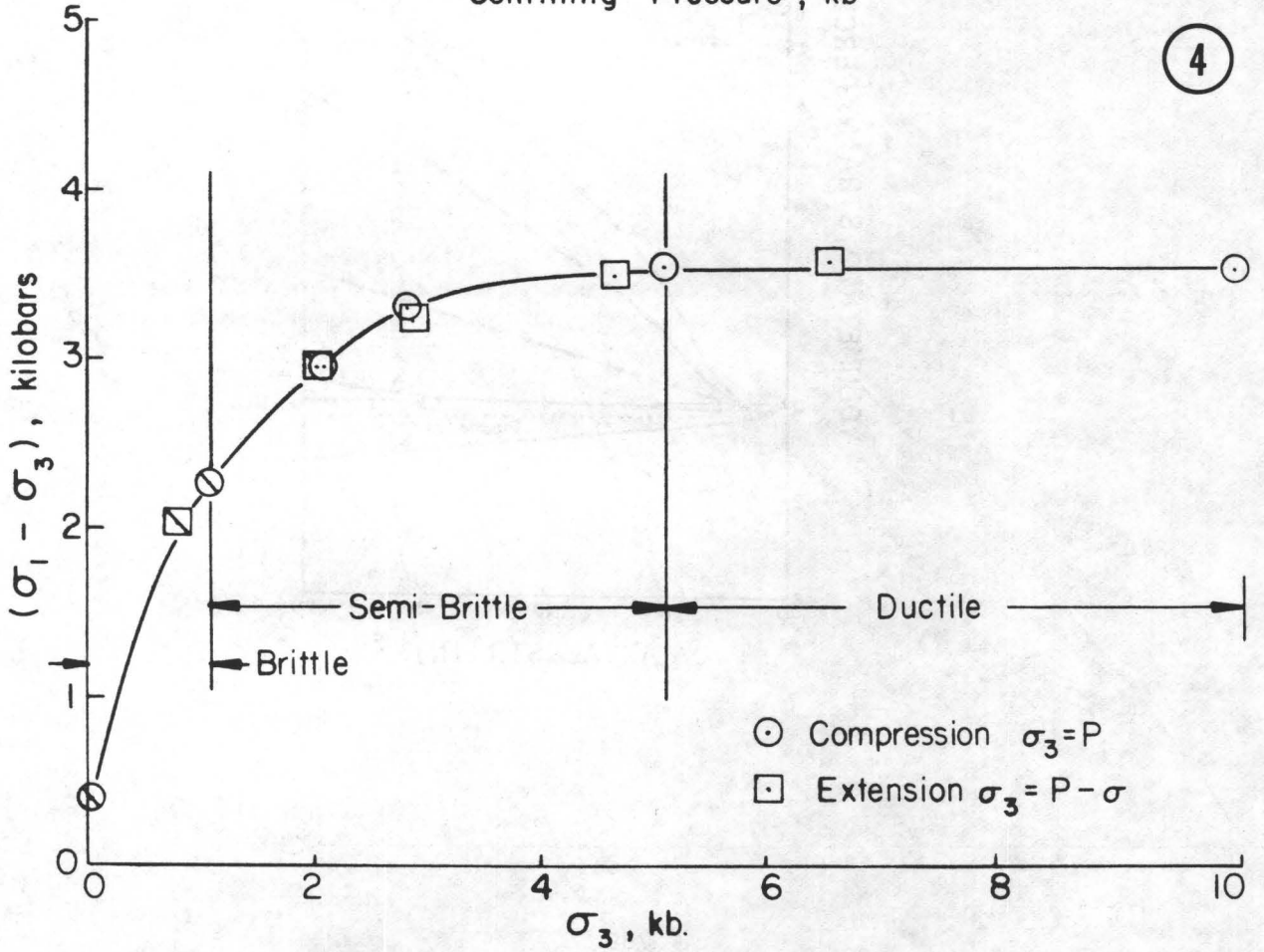
Semi-Brittle
Ductile
Brittle
Compression $\sigma_3 = P$
Extension $\sigma_3 = P - \sigma$
$(\sigma_1 - \sigma_3)$, kilobars
σ_3, kb.
0
2
4
6
8
10
1
2
3
4
5

SOLENHOFEN LIMESTONE

HEARD (1960)

HANDIN ET AL. (1967)

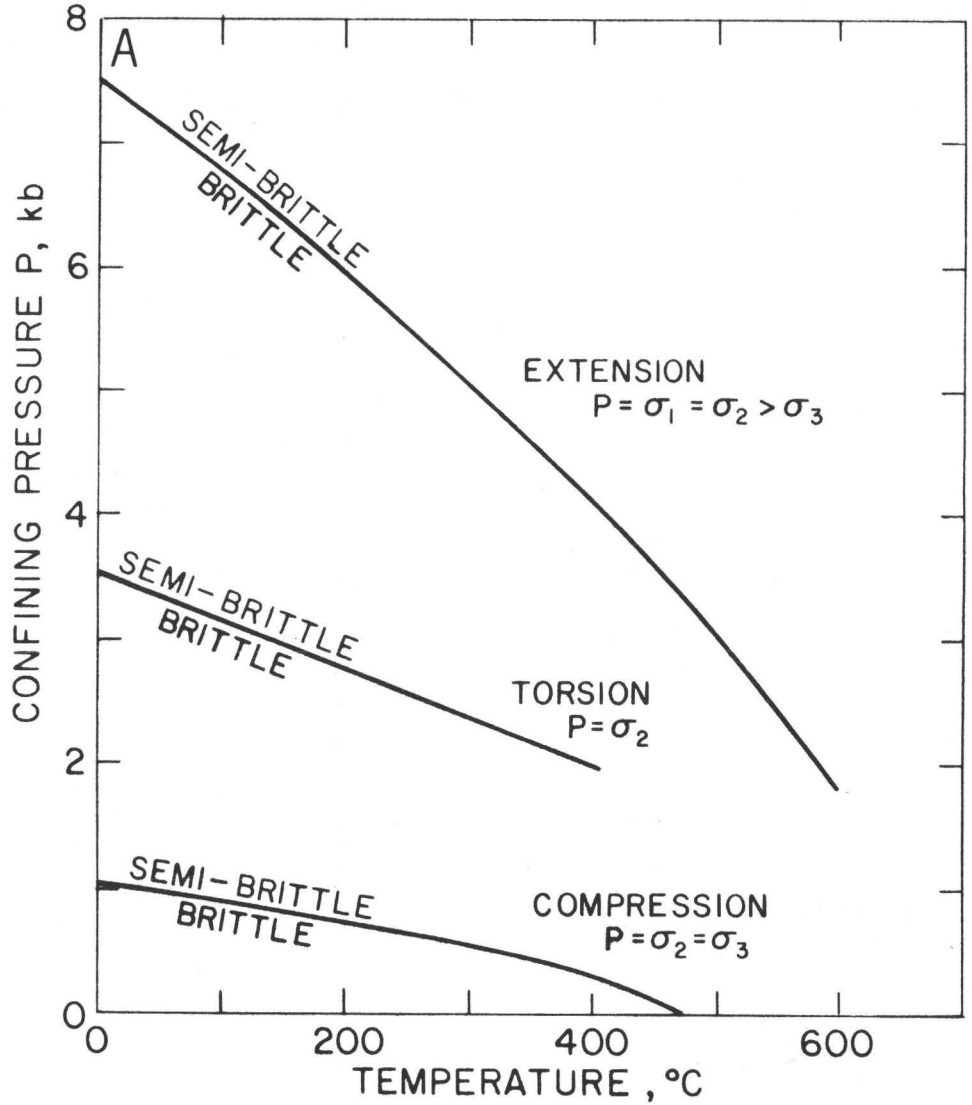

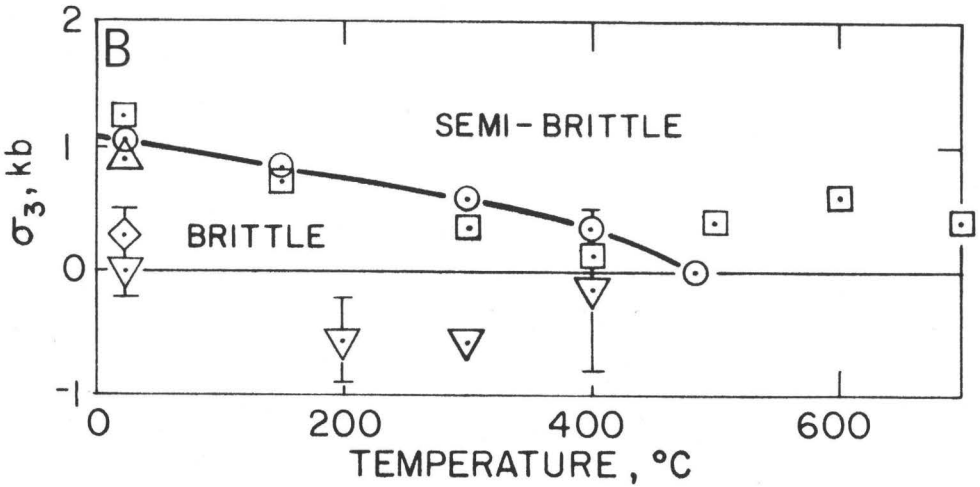

- ⊙ COMPRESSION $\sigma_3 = P$
- ⊡ EXTENSION $\sigma_3 = P - \sigma$
- △ TORSION OF HOLLOW CYLINDERS
- ▽ TORSION OF SOLID CYLS. } ELASTIC SOLUTION FOR σ_3
- ◇ TORSION + COMP. SOLID CYLS. } ELASTIC SOLUTION FOR σ_3

761

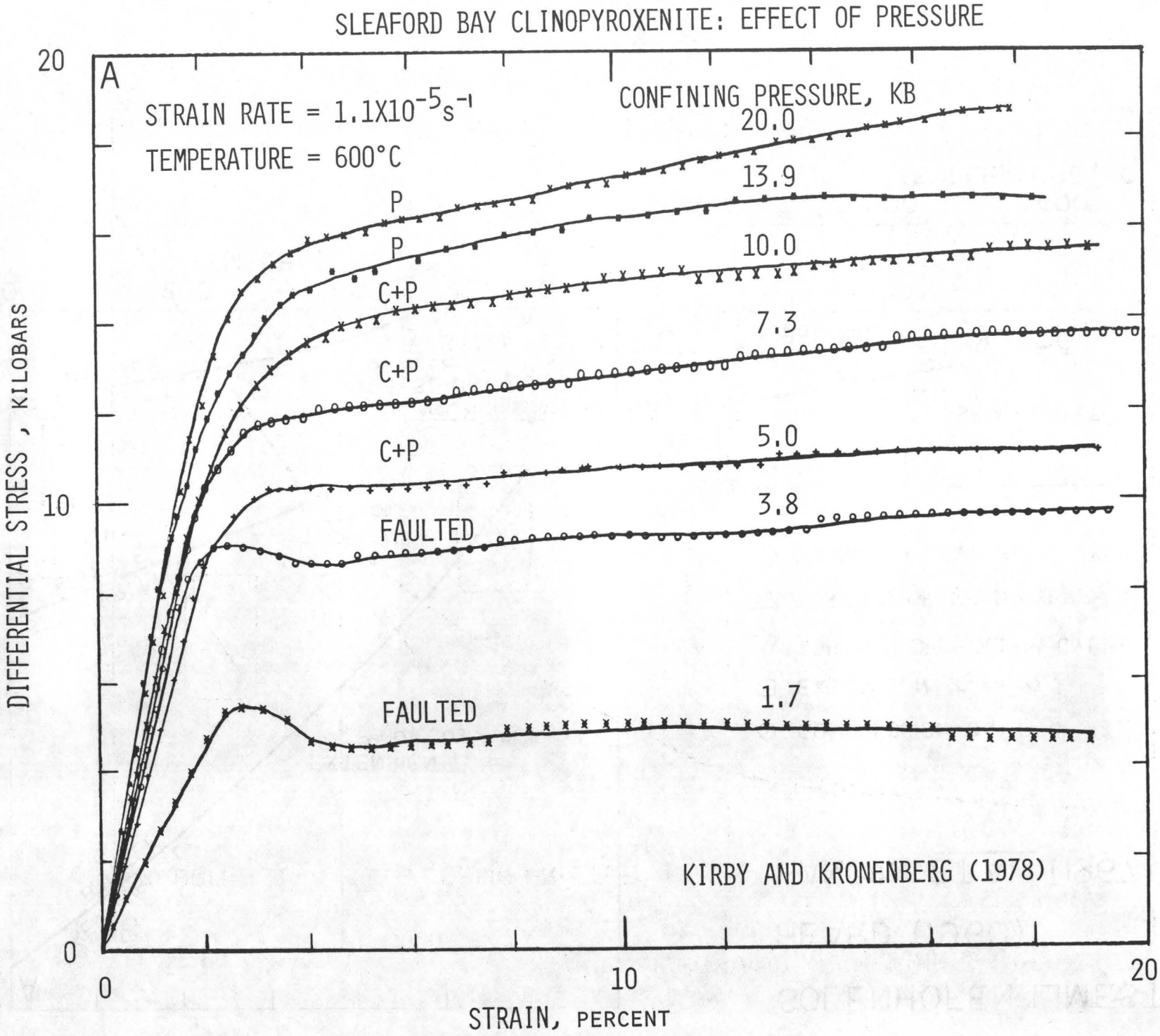
SLEAFORD BAY CLINOPYROXENITE: EFFECT OF PRESSURE
A
STRAIN RATE = 1.1X10^{-5}s^{-1}
TEMPERATURE = 600°C
CONFINING PRESSURE, KB
20.0
13.9
10.0
7.3
5.0
3.8
1.7
P
P
C+P
C+P
C+P
FAULTED
FAULTED
KIRBY AND KRONENBERG (1978)
DIFFERENTIAL STRESS , KILOBARS
STRAIN, PERCENT
0
10
20
0
10
20

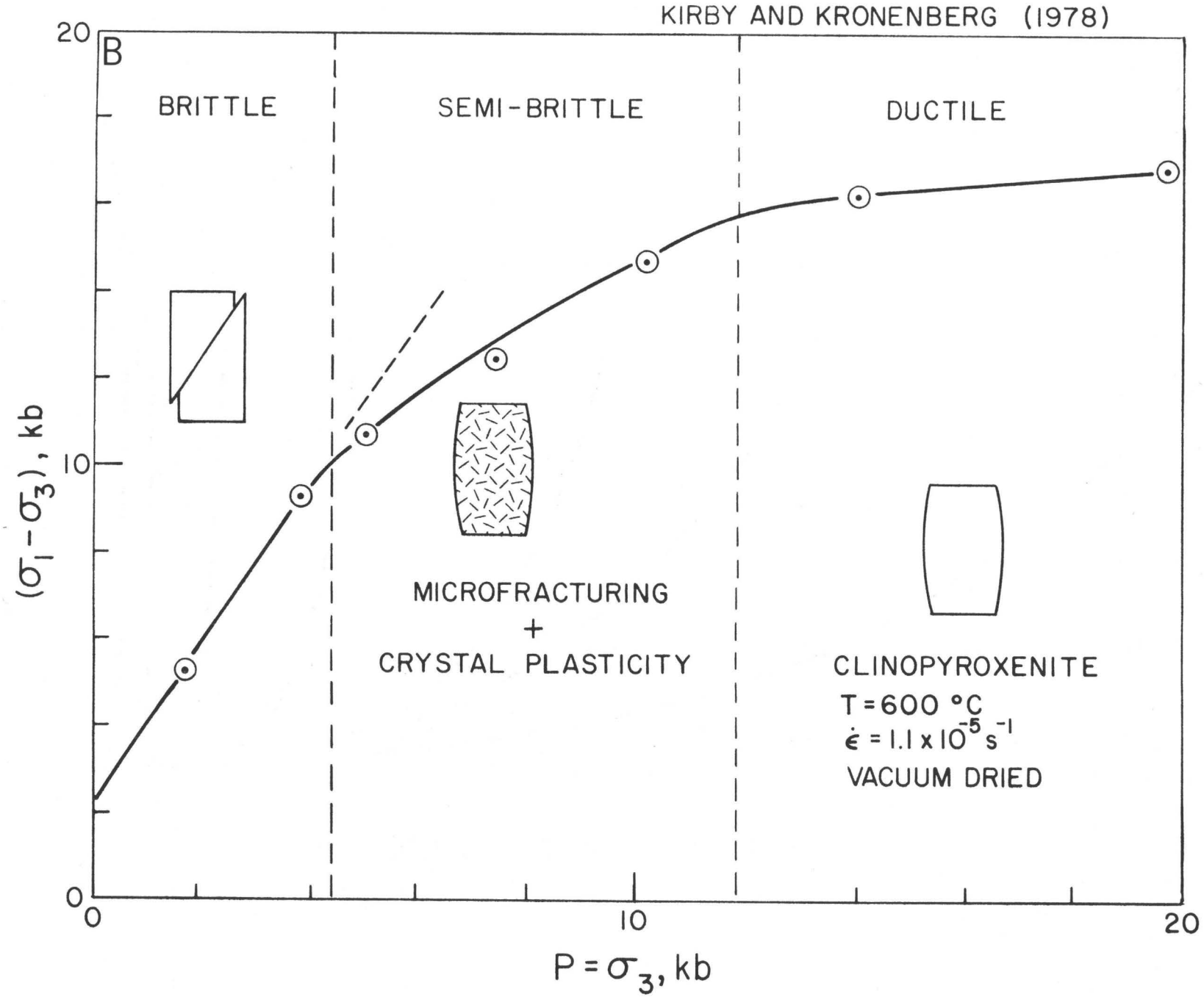
KIRBY AND KRONENBERG (1978)
B
BRITTLE
SEMI-BRITTLE
DUCTILE
MICROFRACTURING
+
CRYSTAL PLASTICITY
CLINOPYROXENITE
T = 600 °C
$\dot{\epsilon} = 1.1 \times 10^{-5}\ s^{-1}$
VACUUM DRIED
$(\sigma_1 - \sigma_3)$, kb
$P = \sigma_3$, kb
0
10
20

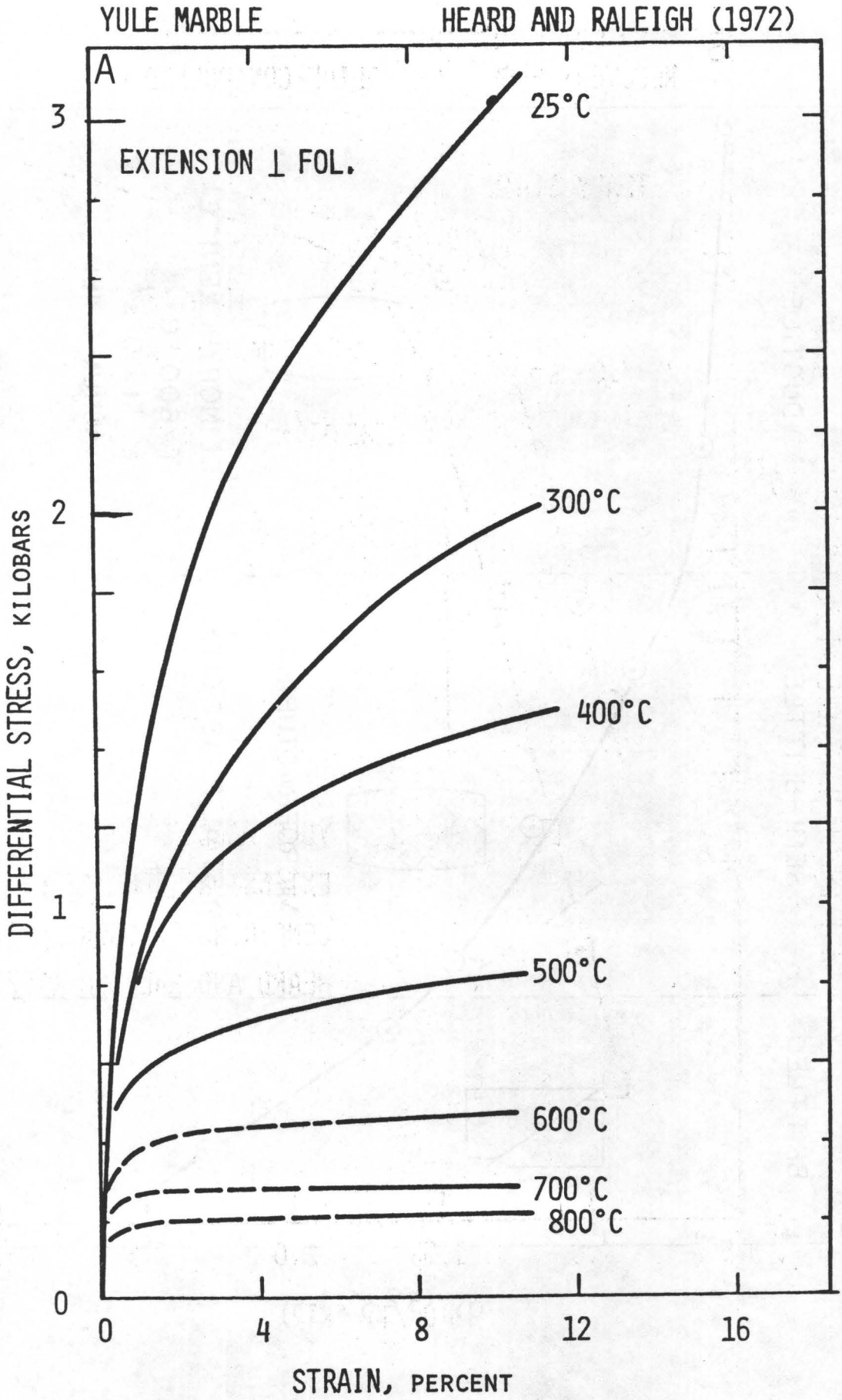
YULE MARBLE
HEARD AND RALEIGH (1972)
A
EXTENSION ⊥ FOL.
25°C
300°C
400°C
500°C
600°C
700°C
800°C
DIFFERENTIAL STRESS, KILOBARS
STRAIN, PERCENT
0
1
2
3
0
4
8
12
16

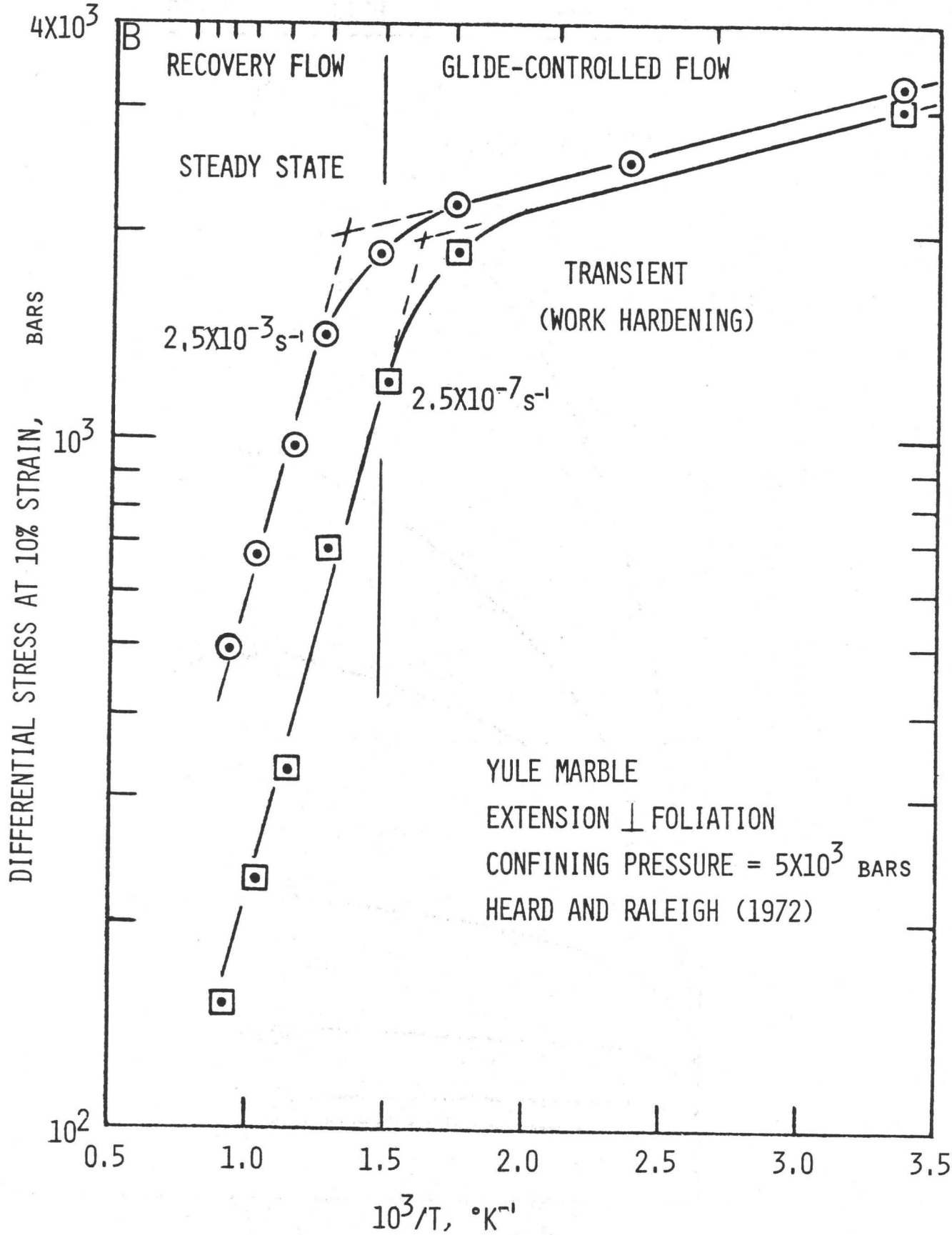
B
RECOVERY FLOW
GLIDE-CONTROLLED FLOW
STEADY STATE
TRANSIENT
(WORK HARDENING)
2.5X10⁻³s⁻¹
2.5X10⁻⁷s⁻¹
YULE MARBLE
EXTENSION ⊥ FOLIATION
CONFINING PRESSURE = 5X10³ BARS
HEARD AND RALEIGH (1972)
DIFFERENTIAL STRESS AT 10% STRAIN, BARS
4X10³
10³
10²
0.5
1.0
1.5
2.0
2.5
3.0
3.5
10³/T, °K⁻¹

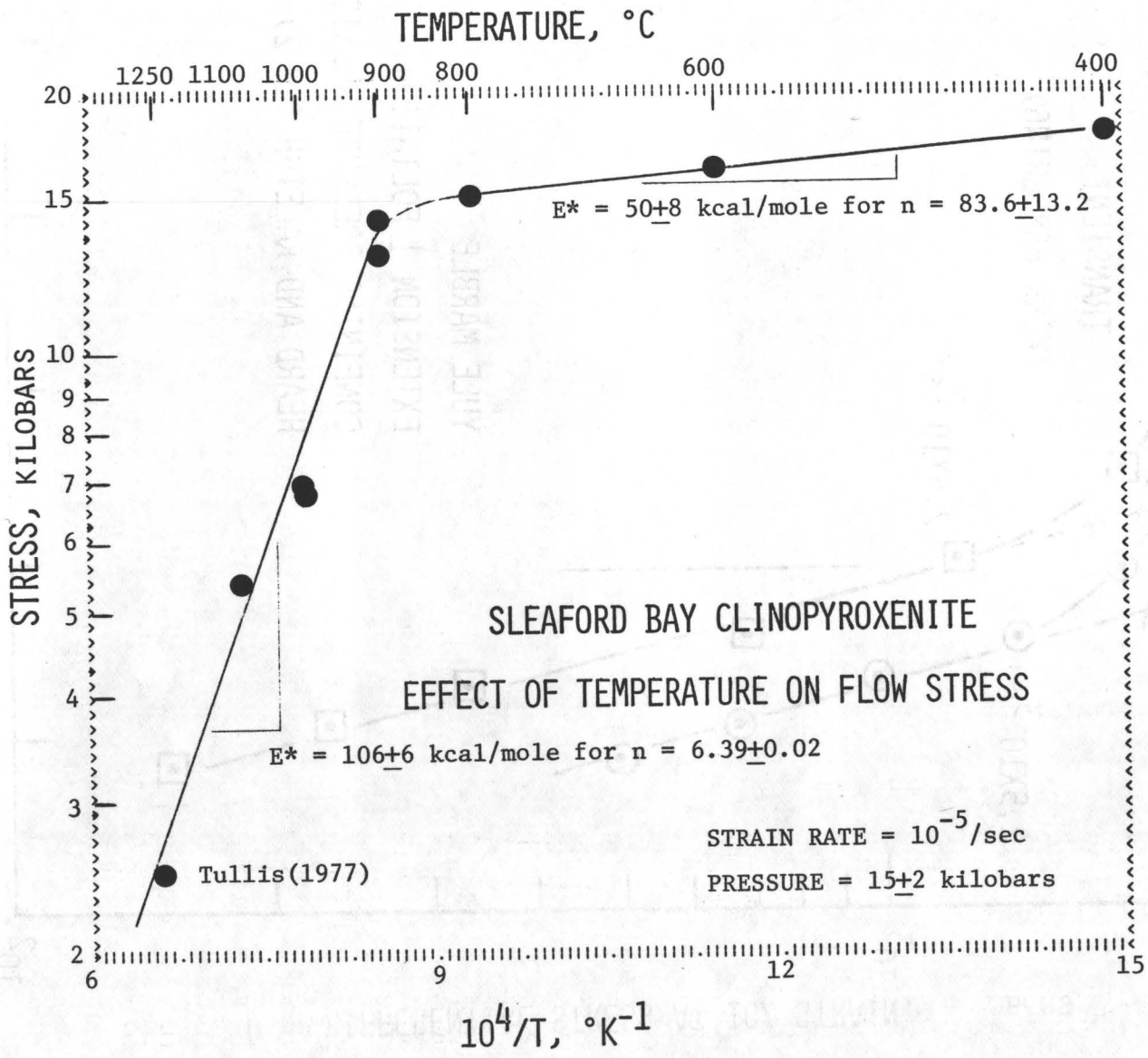
TEMPERATURE, °C
1250 1100 1000 900 800 600 400
20
15
10
9
8
7
6
5
4
3
2
STRESS, KILOBARS
E* = 50±8 kcal/mole for n = 83.6±13.2
SLEAFORD BAY CLINOPYROXENITE
EFFECT OF TEMPERATURE ON FLOW STRESS
E* = 106±6 kcal/mole for n = 6.39±0.02
STRAIN RATE = 10^{-5}/sec
PRESSURE = 15±2 kilobars
Tullis(1977)
6 9 12 15
$10^4/T$, °K^{-1}

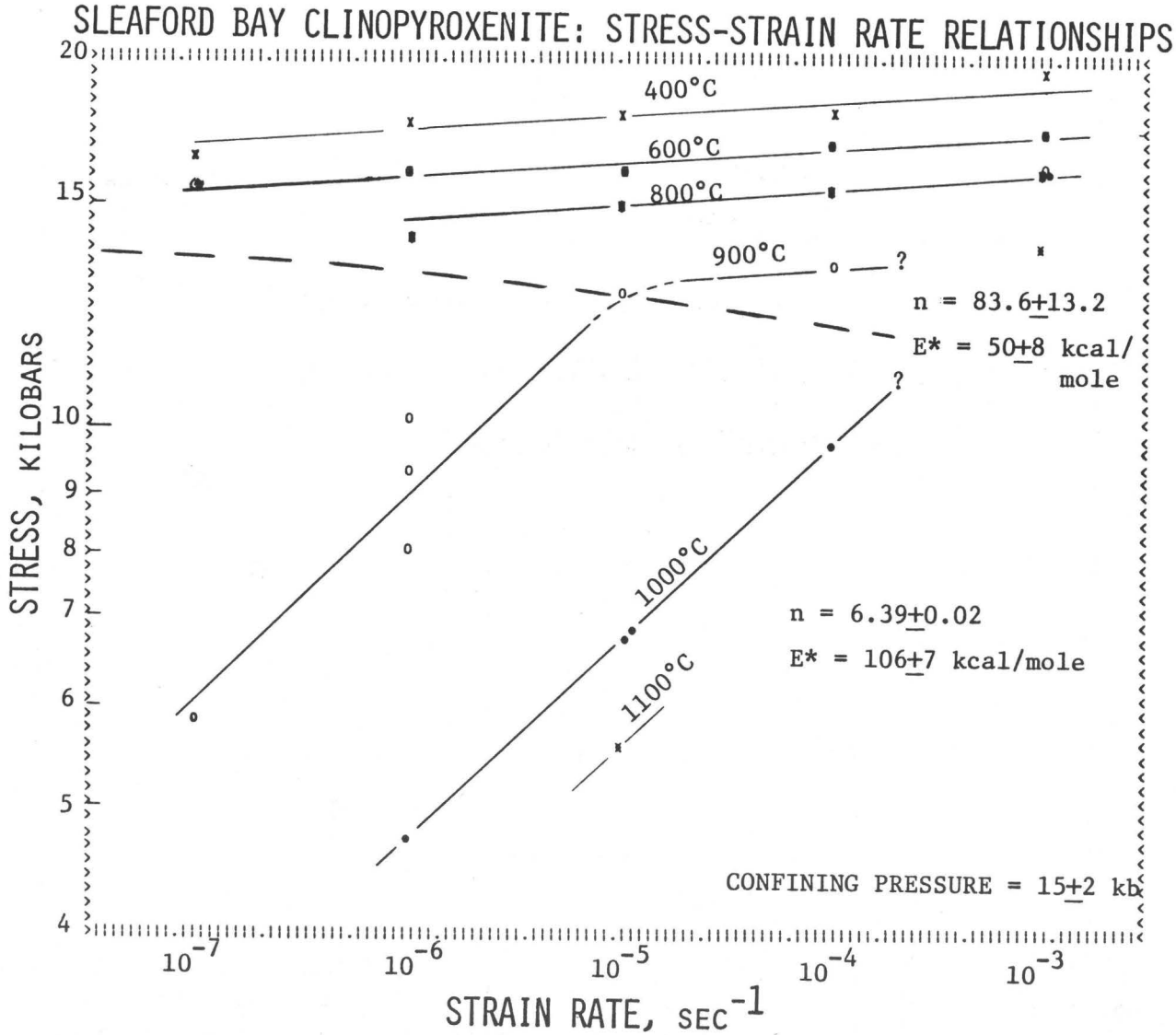
SLEAFORD BAY CLINOPYROXENITE: STRESS-STRAIN RATE RELATIONSHIPS
400°C
600°C
800°C
900°C
n = 83.6±13.2
E* = 50±8 kcal/mole
1000°C
1100°C
n = 6.39±0.02
E* = 106±7 kcal/mole
CONFINING PRESSURE = 15±2 kb
STRESS, KILOBARS
STRAIN RATE, SEC-1
20
15
10
9
8
7
6
5
4
10-7
10-6
10-5
10-4
10-3

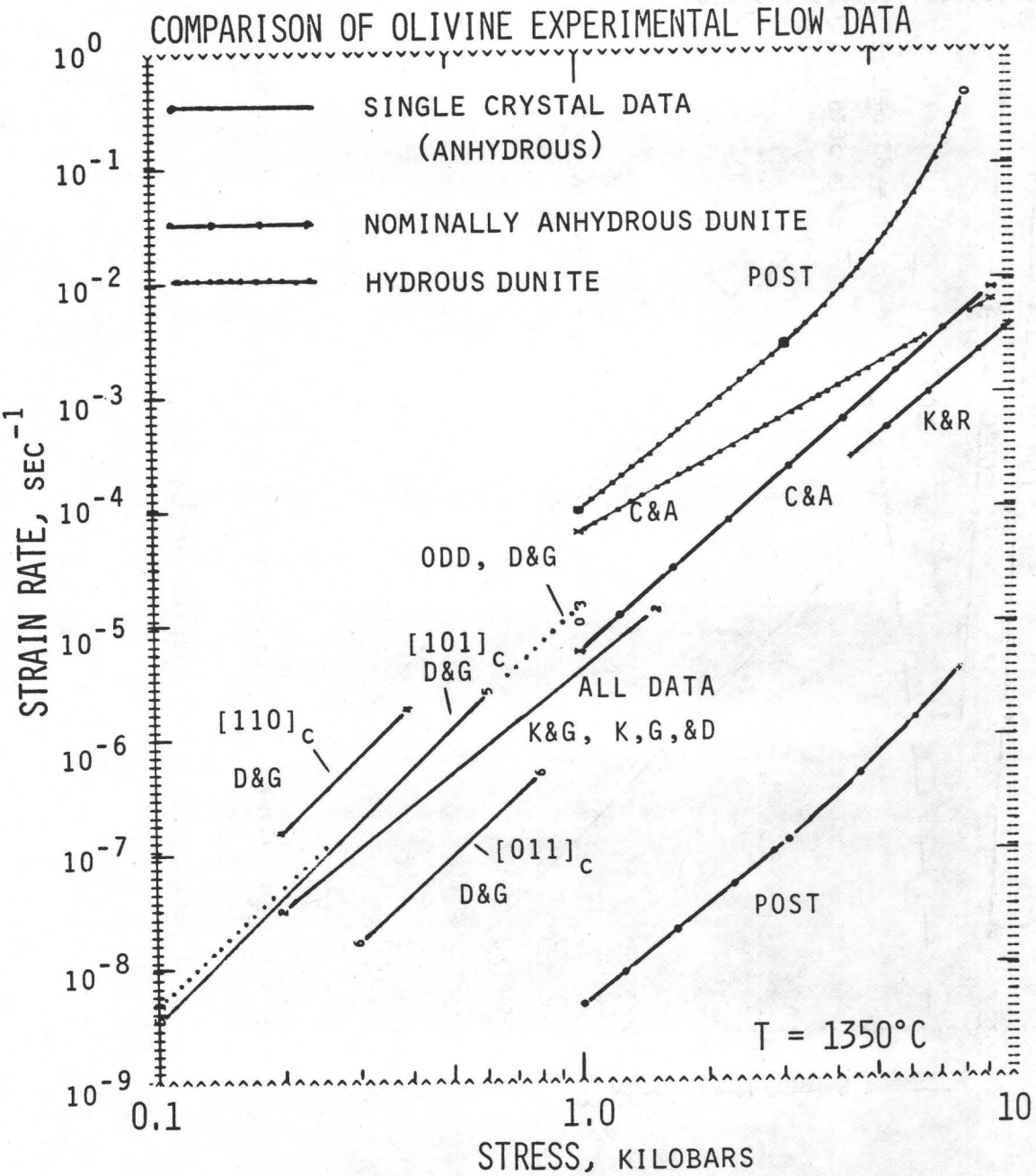
COMPARISON OF OLIVINE EXPERIMENTAL FLOW DATA
SINGLE CRYSTAL DATA
(ANHYDROUS)
NOMINALLY ANHYDROUS DUNITE
HYDROUS DUNITE
POST
K&R
C&A
C&A
ODD, D&G
[101]c
D&G
ALL DATA
K&G, K,G,&D
[110]c
D&G
[011]c
D&G
POST
T = 1350°C
STRAIN RATE, SEC-1
STRESS, KILOBARS
10^0
10^-1
10^-2
10^-3
10^-4
10^-5
10^-6
10^-7
10^-8
10^-9
0.1
1.0
10

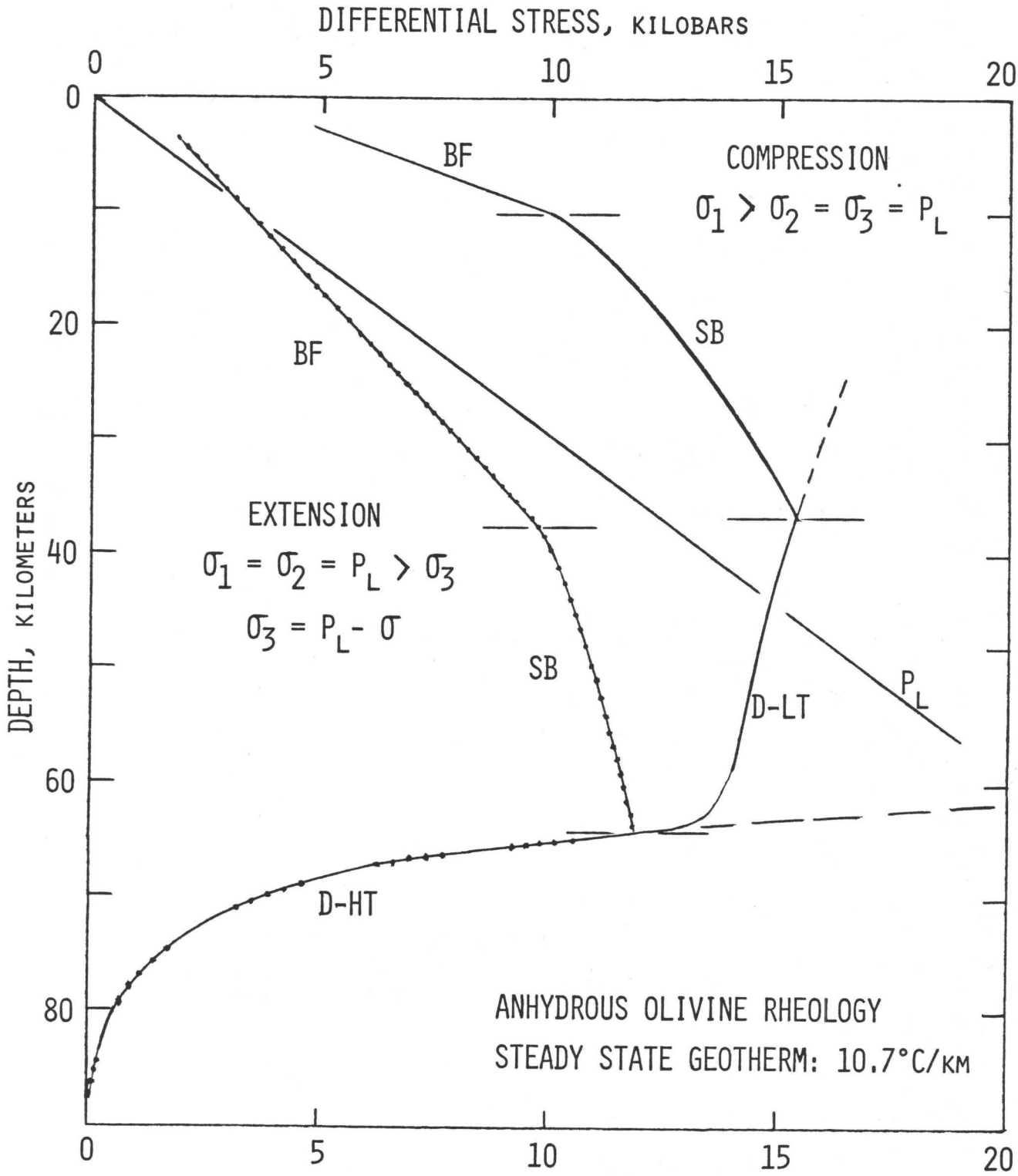
DIFFERENTIAL STRESS, KILOBARS
0
5
10
15
20
DEPTH, KILOMETERS
0
20
40
60
80
BF
COMPRESSION
$\sigma_1 > \sigma_2 = \sigma_3 = P_L$
SB
BF
EXTENSION
$\sigma_1 = \sigma_2 = P_L > \sigma_3$
$\sigma_3 = P_L - \sigma$
SB
D-LT
P_L
D-HT
ANHYDROUS OLIVINE RHEOLOGY
STEADY STATE GEOTHERM: 10.7°C/KM

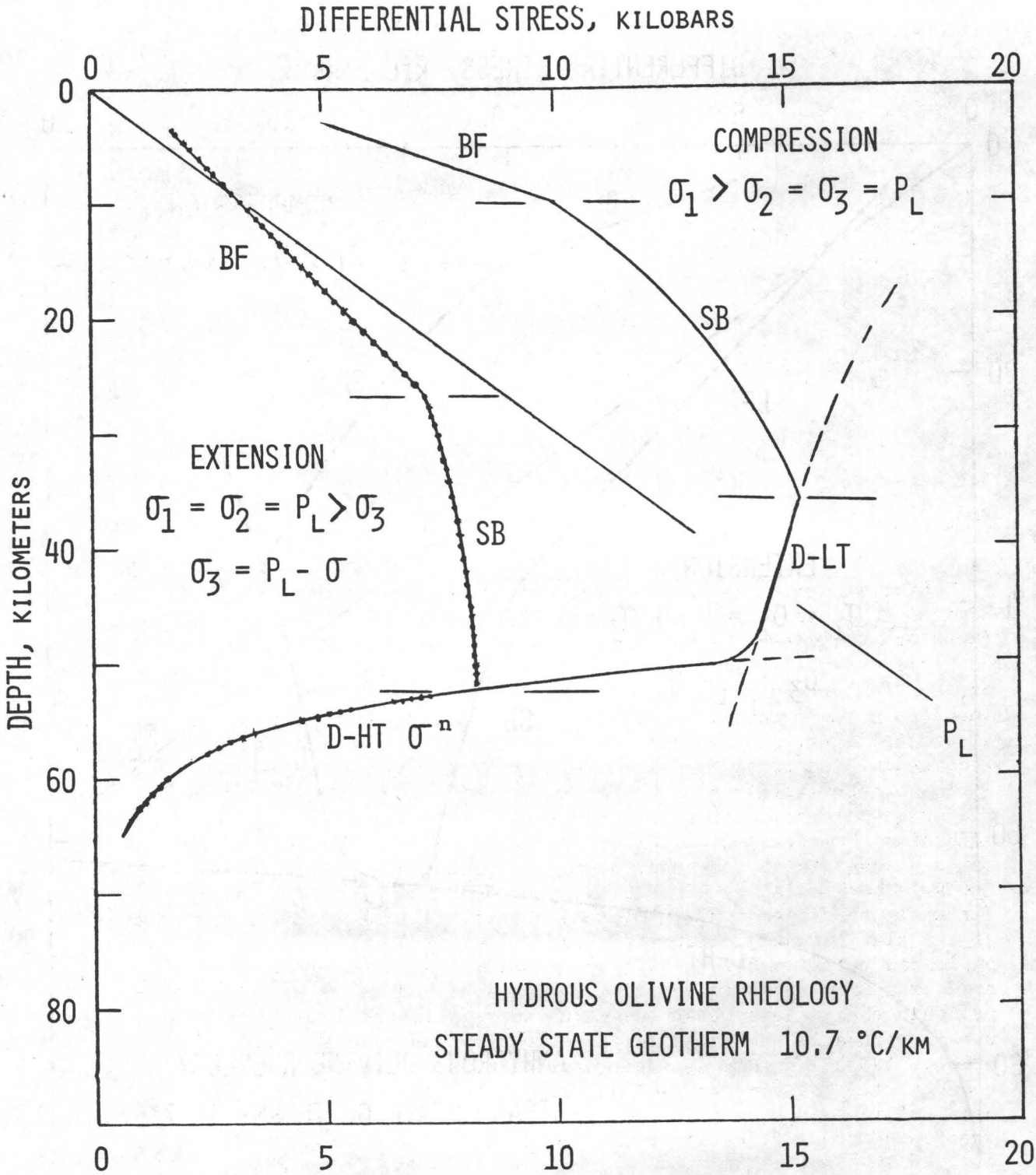
DIFFERENTIAL STRESS, KILOBARS
0
5
10
15
20
DEPTH, KILOMETERS
0
20
40
60
80
BF
COMPRESSION
$\sigma_1 > \sigma_2 = \sigma_3 = P_L$
BF
SB
EXTENSION
$\sigma_1 = \sigma_2 = P_L > \sigma_3$
$\sigma_3 = P_L - \sigma$
SB
D-LT
D-HT σ^n
P_L
HYDROUS OLIVINE RHEOLOGY
STEADY STATE GEOTHERM 10.7 °C/KM

MAGNITUDE OF THE CONTINENTAL LITHOSPHERIC STRESSES INFERRED FROM RHEOMORPHIC PETROLOGY

J-C.C. Mercier

Institut de Physique du Globe, Place Jussieu
75230 Paris, France

Abstract.

Stress magnitudes may be estimated through application of geological thermobarometers (Mercier, 1980) and of grain-size piezometers (Ross *et al.*, 1980). Discontinuities in grain-size profiles based on series of peridotite xenoliths from some representative localities can hardly correspond to abrupt changes in stress conditions at depth, inasmuch as no geochemical difference is observed across the textural discontinuities. The latter are thus regarded as artifacts resulting from reaching a critical temperature or stress beyond which the dominant recrystallization mechanism drastically changes. Indeed, the grain-size piezometer is very sensitive to the recrystallization mechanism (Poirier and Guillopé, 1979) and, whereas recrystallization through subgrain rotation has been recognized in some natural peridotites (*e.g.* Nicolas *et al.*, 1972), the experimental data available so far apply to grain-boundary-migration recrystallization. On the basis of two significantly different grain-size profile discontinuities, an empirical relationship $\{\sigma=74.5/D\}$ is inferred for the grain-size resulting from subgrain rotation. Upon application of this new relationship when relevant, stress magnitudes estimated from deep samples remain virtually unchanged relative to previous results (Avé Lallemant *et al.*, 1980), as well as their implications as regards large scale convection. However, revised magnitudes for the uppermost mantle may be significantly increased to a record value of 45 MPa (450 bars) for the Basin-and-Range Province, with stresses in the lower crust possibly reaching up to 80 MPa.

Introduction.

Though subgrain-size and dislocation-density piezometers historically have been the first ones applied to the rheomorphic study (*i.e.* the comprehensive geochemical and textural study of rocks aimed at the quantification of their original *in-situ* rheological properties) of mantle peridotites (*e.g.* Raleigh and Kirby, 1970; Goetze, 1975), such microstructural features record mostly the late high-stress deformations related to the emplacement (Avé Lallemant *et al.*, 1980) whether it corresponds to volcanic-conduit boring-processes for xenoliths, or to low-temperature deformations related to the intrusion of orogenic massifs or to the obduction of ophiolites. Furthermore, at least for xenoliths, an important annealing of the induced microstructure may result from the transport to the surface by the host lava, and use of these piezometers must await a better understanding of the kinetics of annealing through experimentation (*e.g.* Ricoult, 1978).

On the other hand, grain-sizes are quite stable and the original pre-emplacement grain-size can often be readily identified, though a careful study of a representative suite of samples from a given locality may be necessary to fully appreciate the significance of the whole textural spectrum. These techniques have been reviewed in much detail by Avé Lallemant and others (1980) and will not be discussed any further. One should, however, keep in mind that tectonites representative of high-temperature deformations related to phenomena characterized by a large time-constant relative to the geological time-scale (*e.g.* as for mantle convection) imply strain-rates too low to develop optically strained textures, as is also observed experimentally (Figure 1A; Avé Lallemant *et al.*, 1980). There is no time-dependency of the grain-size or grain-size distribution (Ross *et al.*, 1980) and once the starting material has recrystallized and attained textural equilibrium, no optically visible substructure develops, thereby implying continuous nucleation and grain growth.

All depths estimated in this paper are based on Mercier's (1980) revised single-pyroxene thermobarometer, and errors for both depths and grain-sizes were calculated according to Avé Lallemant and other's (1980) scheme. Errors on other parameters are inferred from those on depth and grain-size. S.I. units (1 GPa = 10 kbar) are used throughout this paper, whose scope is arbitrarily limited to continental regions, including Precambrian cratons, continental rifts and broad extension zones with crustal and lithospheric thinning. Oceanic data have been voluntarily left out of the present discussion as they are currently under full revision through the comparative study of xenoliths from oceanic basalts and kimberlites, and of various ophiolites.

Grain-size profile discontinuities.

Although the overall trends observed are still a general increase of grain-size with depth, in agreement with earlier results (Mercier, 1977a; Mercier *et al.*, 1977; Coisy, 1977; Coisy and Nicolas, 1978), detailed investigation of selected xenolith populations show that in many instances (Avé Lallemant *et al.*, 1980), the grain-size first increases very rapidly and, at a given depth which depends on the tectonic environment under study (Figures 2 and 3), this grain-size drops suddenly to about half its value and, then, increases again with depth, yielding an apparent discontinuity. Despite a careful investigation of phase compositions, modes and parageneses, no significant differences could be found below and above this trend inversion. There is no phase transformation ascribed to these depths which could release a fluid phase capable of modifying the growth or nucleation rates of the crystals. Since a stress discontinuity (Figures 4 and 5) seems very unlikely, if not impossible, for such a rather homogeneous medium, one has to question the validity of the piezometer and, more precisely, whether it can be of general use whatever the local physical conditions. Recent studies on nickel (Sellars, 1978) and halite (Guillopé and Poirier, 1980; Poirier and Guillopé, 1979) have shown experimentally that one could identify two mechanisms for recrystallization, grain-boundary migration (GBM) and subgrain rotation (SGR), one of which is strongly dominant depending on the physical conditions. Using textural and/or mechanical criteria, these authors have mapped the temperature-stress field for each mechanism (Figure 6). An attempt is made here to use these results to test the working hypothesis according to which the grain-size profile discontinuities would correspond to critical temperature and/or stress values for a switch of dominant mechanism to occur.

According to Sellars (1978) and Guillopé and Poirier (1980), recrystallization proceeds through grain-boundary migration (GBM) at high temperatures and stresses, and through subgrain rotation (SGR) at either low temperatures, low stresses, or both. This is in full agreement with many qualitative observations made for many years: for instance, for high-stress deformations related to the intrusion of orogenic massifs, neoblasts are no more than rotated "fragments" of the porphyroclasts (Nicolas *et al.*, 1972) and olivine tablets of the granuloblastic textures from Dreis (Germany) result from rotation and/or torsion of elongated subgrains with well-developed (010) subboundaries (Mercier, 1972). On the other hand, experimental granuloblastic textures are characterized by equant grains without optically visible substructures whatever the finite strain is, implying that GBM recrystallization is dominant. Evidence for GBM recrystallization in natural rocks does exist too, though sparser, *e.g.* when neoblasts

(small relative to the paleoblasts) produce a lace-like texture (Black-Rock Summit, Nevada; Mercier, 1977a) also observed in high-temperature - high-stress experiments) and when interpenetrative bulging occurs at subboundary-boundary junctions (some Hawaiian samples; Mercier, 1972). Of course, there are many samples without good criteria for identification of the dominant recrystallization mechanism, but all the samples for which the mechanism could be identified are in agreement with the above hypothesis. In particular, sampling-related GBM recrystallization is observed for all the infra-cratonic samples studied which plot below the discontinuity (Figure 5) to the exclusion of the other samples, and the Dreis-type textures do correspond to the shallowest peridotite facies for continental extension zones (CEZ).

Since two well-characterized discontinuities corresponding to significantly different physical conditions are available, one may infer an empirical $D \leftarrow \theta \rightarrow \sigma$ relation for SGR recrystallization from the experimentally determined relation applying to GBM recrystallization. Thus, referring to the high- and low-stress ends of the discontinuity materialized by a dashed line on the apparent-stress profiles (Figures 4 and 5) as points α and β, respectively, one may write, at point α,

$$\sigma_\alpha = 4.81\ D_\alpha^{-0.787}$$

and at point β,

$$\sigma_\beta = A\ D_\beta^{-n}$$

(σ in GPa and D in μm) and since $\sigma_\alpha = \sigma_\beta$ according to the present hypothesis,

$$A\ D_\beta^{-n} = 4.81\ D_\alpha^{-0.787}$$

By replacing D_α and D_β by their optimum values for the Basin-and-Range Province and the Southern Africa data (Table 1), one gets a system of two equations with two unknowns, A and $\underline{n}$, which, once solved, yields

$$\sigma = 74.5 / D$$

for SGR recrystallization (*i.e.* mostly for low-temperature samples). Due to the errors involved in localizing the discontinuity (see Table 1), the A parameter may vary according to the preferred fit (*e.g.* an earlier fit yielded A=40.9; Mercier, 1979), though the present value is now considered as the best approximation, until experimental data become available. Preliminary experiments (Ross, pers. comm., 1979) are qualitatively in agreement with the above equation, *i.e.* for olivine, the grain-size should be larger for SGR than for GBM recrystallization, whereas the opposite has been observed for halite (Guillopé and Poirier, 1980).

On a normalized temperature-stress diagram (Figure 6), the line joining the two points based on the discontinuities is slightly, but significantly negative in slope, in agreement with theoretical considerations and earlier results on other materials. Olivine values for the melting temperature T_m and the shear modulus μ are computed on the basis of Kirby and Raleigh's (1973) and Kumazawa and Anderson's (1969) data (T_m and T in °K; P and μ in GPa), respectively,

$$T_m = 1248.(P + 9.00)^{0.24}$$

$$\mu = 83.00 - 0.013\ T + 1.79\ P$$

When plotting together all the available data on such a plot, it is possible to infer a rough boundary between the two fields, though the high-stress branch of this pseudo-hyperbolic boundary may have a greater slope (in absolute value) as will be discussed further. The present interpretation of the discontinuities also yields realistic normalized critical temperatures and stresses relative to experimental data on nickel and halite. The large number of observations in favor of this model allows its tentative use for estimating lithospheric stresses on the basis of olivine grain-sizes.

Estimates of rheological parameters.

Profiles illustrating the variations with depth of the various rheological parameters, *i.e.* deviatoric stress, strain-rate and equivalent viscosity, can be constructed by computing independently values for each parameter and for each sample, and by fitting these data. However, fits of data derived from one another through logarithmic equations cannot be equivalent, and only an optimum stress profile, eventually taking into account some constraints imposed by the strain-rate/viscosity plots, should be used. Strain-rate and viscosity profiles are then computed from this stress curve and the relevant geotherm (Mercier, 1980).

Although all the xenoliths used in the present study are samples from infracontinental mantle, they fall into three groups, each of them being characterized by its own chemical and textural features. Samples representative of the infracratonic mantle are xenoliths from kimberlites, all from Southern Africa. Their phase chemistry defines a continental geotherm similar to Clark and Ringwood's (1964) theoretical one. The other samples were brought up by alkali basalts and correspond to infracontinental regions with an abnormally high thermal gradient. The first group, referred to as "continental extension zones" (CEZ), corresponds to the most abundant type of xenoliths in basalts. Their phase chemistry defines an oceanic-like geotherm indistinguishable from those determined for oceanic islands (Mercier, 1980). However,

this geotherm may be an inherited feature and may not be related to the present tectonics, the only extension zones sampled so far being paleo-orogenic regions. The third group, illustrated by a handful of localities, is represented by xenoliths in quaternary volcanics on the rifts themselves and may correspond to a late evolutive stage of the upper mantle beneath rifts. Most samples are not in equilibrium as a result either of an extremely fractionated partial melting (Mercier, 1977a) or of a cumulitic origin (Berger, 1978) though the textures are now metamorphic. From the few equilibrated samples available and by analogy with peridotites of similar bulk composition from other types of environments (*e.g.* Vourinos ophiolites, Greece; Mercier, 1980), these samples would be equilibrated along an extremely steep geotherm, implying dry melting near 100 km.

The various rheological parameters are estimated through the use of the following equations, where P and σ are given in GPa, T in °K, $\dot{\varepsilon}$ in s^{-1} and η in poises (1 poise = 0.1 SI poiseuille):

* stress for SGR recrystallization (this paper)

$$\sigma = 74.5\ D^{-1}$$

* stress for GBM recrystallization (Ross *et al.*, 1980)

$$\sigma = 4.81\ D^{-0.787}$$

* strain-rate (Post, 1977; Ross *et al.*, 1979)

$$\dot{\varepsilon} = 2.69\ 10^{12}\ \sigma^{3.2}\ \exp\{-(63000+1610P)/T\}$$

* equivalent viscosity

$$\eta = 10^{10}\ \sigma/3\dot{\varepsilon}$$

Stress estimates for samples from the Basin-and-Range Province, Southwestern U.S., a typical extension zone with lithospheric thinning, are extremely high for the shallowest facies (up to 70 MPa; SGR recrystallization; Figure 7) and result in higher strain-rates near 56 km depth (Figure 8) than anywhere else, down to the greatest depths sampled (*ca* 80 km). If these estimates are correct, there would be an important sub-horizontal flow within the seismic "lithosphere", just under the crust, and possibly involving the base of the latter, too. This would explain the formation of textures with small scattered spinel (Mercier and Nicolas, 1975), which would indicate an important finite strain. This zone may also be related to underthrusting of the Southwestern U.S. by oceanic lithosphere, a model called upon by Helmstaedt (*e.g.* Helmstaedt and Doig, 1975) to explain the existence at shallow depths of C-type eclogites and of serpentinized peridotites under the Colorado Plateau (Mercier, 1977a). Last, lateral flow zones of this type can easily be accomodated in a regional rifting model as they allow return flow to relieve the excess volume caused by diapiric upwelling evidenced by rift-type poikiloblastic mantle (Mercier, 1977b).

However, one cannot yet discard the possibility that the uppermost samples (above 57 km) fall in the GBM temperature/stress field because of the closeness of the boundary to the inferred physical conditions for high-stress samples (Figures 6 and 14). Still more detailed work is needed to solve this problem. In any instance, plots of the strain-rates and/or equivalent viscosities calculated for individual samples yield very well defined S-shaped patterns indicating that the sudden stress increase above 57 km first results in a sudden increase in strain-rate, but that within a few kilometers the considerable temperature drop easily overcompensate the effect of the rising stress, apparently yielding low and negligible strain-rates above 50 km, in accord with the concept of lithosphere.

Stress estimates for the infracratonic mantle beneath Southern Africa (Figure 9) vary from 15 MPa around 80 km depth to 5 MPa at 140 km, and then decrease slowly with depth to reach 4 MPa near 240 km. In terms of stresses, one could therefore consider a "lithosphere" 140 km thick. Though this depth also corresponds to a break in the strain-rate curve (Figure 10), this may be an accidental effect of the increasingly dominant temperature term at depth. The deepest strain-rates attained are only slightly above 10^{-14}/s and therefore reasonable, considering the size of the calculated error and that the fit is poorly constrained at its ends.

Whereas the discontinuities in the grain-size plots (Figure 2 and 3) were evident artefacts, grain-sizes for rift-type mantle (Figure 11) do not show any indication of crossing the boundary between SGR and GBM fields. There is a continuum in the textures from the relatively fine-grained ones to poikiloblastic samples for which pyroxenes and spinels of ordinary size occur as inclusions within centimeter-sized poikiloblasts of olivine; this behavior shows that GBM recrystallization was important for the genesis of the textures. However, *once* large poikiloblasts are formed, they seem to break apart in a way reminiscent of that of the Dreis samples (except for the one-and-a-half order-of-magnitude difference in the grain-size), with rotation/torsion of tablets limited by well-developed (010) subboundaries. The reason for such a surprising behavior, with the deepest samples recrystallizing through SGR, is best shown in Figure 6: in the present case, the textural trend encounters a critical stress instead of a critical temperature. In the absence of any clear discontinuity in the grain-size plot (Figure 11), all the coarse poikiloblastic textures are regarded here as recrystallizing through SGR, though the constructed profiles (Figure 12) are independent of the convention chosen because the stresses dealt with are very small. Strain-rate estimates (Figure 13) vary from 10^{-16}/s near 42 km depth to 10^{-14}/s at 58 km. and remain close to 10^{-14}/s thereafter. However, the latter trend is not significant according to the calculated profile (Figure 16).

In conclusion, stresses always decrease with depth for the uppermost mantle to which one has access through xenoliths, but strain-rate variations do not follow such a uniform pattern. For the only deep sample available, *i.e.* the infracratonic mantle, the strain-rate remains at all times smaller than, or close to 10^{-14}/s, thereby yielding a physically reasonable model.

Rheological parameter profiles.

Profiles calculated from the optimum stress curves and the local geotherms for various rheological parameters, are given in digitalized form in Table 2. Grain-size profiles inferred from the stress fits (Figure 14) closely follow the variations observed for the individual data plots (Figures 2, 3 and 11). Though grain-size is not really a rheological parameter, such profiles are given here because representative dimensions of grains for mantle rocks often provide important information for rheological models encompassing depths greater than those illustrated by xenoliths. Natural textures undergoing simultaneous recrystallization of several phases and, in particular, the textures of peridotite-charnockite banded xenoliths (Mercier, 1972) from Puy Beaunit, France, provide strong evidence that the grain-size of silicates is not very sensitive to mineral species, as also indicated by experiments and theoretical considerations (Twiss, 1977; 1980). Accordingly, grain-sizes for deep-crustal charnockites (Figure 14) from two CEZ regions (Massif Central, France: Leyreloup, 1974; Basin-and-Range Province, U.S.A.: Padovani and Carter, 1977) and from a paleo-orogenic region (Southern Africa, periphery of cratons: Griffin *et al.*, 1979) should provide some constraints on the physical properties of the lower crust and uppermost mantle at the Moho.

The stress profiles based on olivine grain-sizes (Figure 15) are shown together with tentative stress estimates for deep-crustal charnockites, assuming a $D \leftrightarrow \theta \leftrightarrow \sigma$ relation close to that for dry olivine in the absence of data (dry experimental conditions required) on any mineral phase typical of charnockites. The high stresses inferred (50 to 80 MPa) agree well with the textures (*e.g.* neoblast scattering) and structures (*e.g.* microfolds) of either rock type, which suggest that an appreciable amount of flow has once taken place despite the relatively low temperature of equilibration (600 to 700°C). An alternative stress profile (Figure 15) illustrates the effect of double-crossing the GBM/SGR field boundary: the maximum stresses would then become of the order of 20 MPa which, though it may seem more reasonable, fails to explain how the textures formed. Furthermore, the former high values are in accord with Kirby's (1980) experimental data allowing stresses up to 1.2 GPa for high-temperature flow of

peridotites (T>685°C), the only flow regime of interest for the continental uppermost mantle since Moho temperatures should be about 750°C for CEZ and 700°C for cratons (Mercier, 1980). These stresses are also in the range of the approximate or maximum values accepted for the oceanic lithosphere on the basis of local isostatic compensation (∿40 MPa; Lambeck, 1980), of lithospheric flexures (<300 MPa; Watts *et al.*, 1980) and of global gravity (<200 MPa; McNutt and Parker, 1980). In any instance, interpretation of charnockites is complicated by the fact that these rocks are equilibrated at shallow depths. The equilibria observed (very high thermal gradient) could therefore be metastable and could correspond to conditions which existed tens or hundreds of millions of years ago, especially in the case of the paleo-orogenic regions. Clearly, much experimental work is therefore needed on the kinetics of textural and chemical equilibration, as well as on appropriate piezometers and on the rheology of such rocks.

Strain-rate and equivalent-viscosity profiles (Figures 16 and 17) are shown independently to emphasize that differences in shapes are negligible and, therefore, that the double-scaling of Figures 8, 10 and 13 is justified. Whereas the infracratonic profiles are exactly as expected from the individual data plots (Figure 10), the profiles for rift-type mantle are significantly different from the trends observed in Figure 13: the strain-rate/viscosity profiles imply that deformation is limited to a narrow zone in the depth range 55-60 km, which is in complete agreement with the diapiric models proposed earlier (Mercier, 1977a; 1977b). For continental extension zones, a similar pattern is observed as a result of constraining the stress fit at its shallowest end (Figure 7) according to the strain-rate data (Figure 8). This thin and shallow region which accomodates significant flow within the seismic lithosphere may result from drag at the base of the crust during early stages of continental rift opening.

Once strain-rate profiles are obtained for the uppermost mantle, a maximum velocity relative to the Earth's surface can generally be computed for any point of this mantle (Figure 18). The velocity would be a true relative velocity if the flow plane were horizontal with an homogeneous sense of shear all the way to the surface (*i.e.* the plates are dragged by flow in the material below). Reversing this sense of shear would imply a zone of extremely small stresses and coarse grain-sizes (*e.g.* poikiloblastic textures of the rift-type mantle; Figure 1F) at some intermediate depth, which has not

been observed. The mantle is texturally homogeneous at all depths over large areas (Mercier, 1977a; Mercier *et al.*, 1977), therefore favoring large convection cells and dominantly horizontal flow for such areas. The relative velocities inferred would then describe the dynamics of the upper part of such mantle cells. Accordingly, the velocity estimates for the infracratonic mantle are only slightly larger than those expected for a dragged-plate model (from 10 to 30 cm/yr, depending on the model geometry), which is in reasonable agreement with the dynamic data (spreading rates, relative plate velocities). However, a push-pull counterflow model could explain the values obtained as well.

Conclusions.

Stress estimates derived through rheomorphic studies combining phase geochemistry and quantitative textural analysis yield realistic rheological models for the uppermost mantle. Deviatoric stresses in the mantle forming the lower lithosphere commonly have magnitudes of 10 to 20 MPa (100-200 bars) and may even reach 80 MPa for some extensional zones. The overall trend of decrease in stress and increase in strain-rate is confirmed, though more complex patterns emerge from detailed studies coupled with the introduction of a new grain-size piezometer for low-stress and/or low-temperature favies which recrystallize through subgrain rotation. In particular, these revised data show that significant steady-state deformation can take place in the lithosphere, either though formation of an horizontal flow zone or as an envelope to diapirs. Significant flow may involve both the uppermost mantle and the lowermost crust, but the lack of data on the rheological behavior of dry charnockites prevents any quantitative evaluation for the latter. Only the infracratonic data yield precise information on large scale mantle flow, though the velocities calculated do not provide sufficient ground for a definite choice between a dragged-plate or push-pull model. The quantitative rheological model for the lithosphere-asthenosphere transition is expected to provide useful constraints for modelling plate motions. Realistic finite-element diapiric models for rift evolution can also be produced on the basis of the present data on CEZ and rift zones.

Acknowledgments.

I wish to thank C. Mercier-Ronnat for drafting the illustration.

REFERENCES

Avé Lallemant H.G., Experimental deformation of clinopyroxene, *Tectonophys., in press,* 1980.

Avé Lallemant H.G., N.L. Carter, J-C.C. Mercier and J.V. Ross, Rheology of the uppermost mantle: inferences from peridotite xenoliths, *J. Geophys. Res. 85, in press,* 1980.

Boyd F.R., Ultramafic nodules from the Frank-Smith kimberlite pipe, South Africa, *Carnegie Inst. Washington Yearb. 74,* 525-528,1974.

Clark S.P.Jr. and A.E. Ringwood, Density distribution and composition of the mantle, *Rev. Geophys. Space Phys. 2,* 35-68, 1964.

Coisy P., Structure et chimisme des péridotites en enclaves dans les basaltes du Massif Central: modèles géodynamiques du manteau supérieur, *3rd Cycle Doct. Thesis, Univ. Nantes, France,* 1-118, 1977.

Coisy P. and A. Nicolas, Structure et géodynamique du manteau supérieur sous le Massif Central, France, d'après l'étude des enclaves des basaltes, *Bull. Minéral. 101,* 424-436, 1978.

Goetze C., Sheared lherzolites: from the point of view of rock mechanics, *Geology 3,* 172-173, 1975.

Griffin W.L., D.A. Carswell and P.H. Nixon, Lower-crustal granulites and eclogites from Lesotho, Southern Africa, *In* "The mantle sample: inclusions in kimberlites and other volcanics", F.R. Boyd and H.O.A. Meyer eds., *Amer. Geophys. Union,* 59-86, 1979.

Guillopé M. and J-P. Poirier, Dynamic recrystallization during creep of single crystalline halite: an experimental study, *J. Geophys. Res. 85, in press,* 1980.

Helmstaedt H. and R. Doig, Eclogite nodules from kimberlite pipes of the Colorado Plateau: samples of subducted Franciscan-type oceanic lithosphere, *Phys. Chem. Earth 9,* 95-111, 1975.

Kirby S.H., Tectonic stresses in the lithosphere: constraints provided by the experimental deformation of rocks, *This volume* and *J. Geophys. Res. 85, in press,* 1980.

Kirby S.H. and C.B. Raleigh, Mechanism of high-temperature solid-state flow in minerals and ceramics and their bearing on creep behavior of the mantle, *Tectonophys.19,* 165-194, 1973.

Kumazawa M. and O.L. Anderson, Elastic moduli, pressure derivatives and temperature derivatives of single crystal olivine and single-crystal forsterite, *J. Geophys. Res. 74,*5961-5972.

Lambeck K., Estimates of the finite strength of the lithosphere from isostatic considerations, *This volume* and *J. Geophys. Res. 85, in press,* 1980.

Leyreloup A., Les enclaves catazonales remontées par les éruptions néogènes de France: nature de la croûte inférieure, *Contr. Mineral. Petrol. 46,* 17-27, 1974.

McNutt M. and R.L. Parker, Implications of global gravity for the state of stress in the Earth's crust and upper mantle, *This volume and J. Geophys. Res. 85, in press,* 1980.

Mercier J-C.C., Structure des péridotites en enclaves dans quelques basaltes d'Europe et d'Hawaii: regards sur la constitution du manteau supérieur, *3rd Cycle Doct. Thesis, Univ. Nantes, France,* 1-229, 1972.

Mercier J-C.C., Natural peridotites: chemical and rheological heterogeneity of the upper mantle, *Ph.D. Thesis, S.U.N.Y. Stony Brook, NY,* 1-669, 1977a.

Mercier J-C.C., Textural evidence for upper-mantle diapirism, *abstr., EOS 58,* 506, 1977b.

Mercier J-C.C., Etat de contrainte du manteau supérieur, *abstr., Soc. Géol. France., R. Ann. Sc. Terre 7,* 324, 1979.

Mercier J-C.C., Single-pyroxene thermobarometry: a reappraisal. *J. Geophys. Res. 85, in press,* 1980.

Mercier J-C.C. and A. Nicolas, Textures and fabrics of upper-mantle peridotites as illustrated by xenoliths from basalts. *J. Petrol. 16,* 454-487, 1975.

Mercier J-C.C., D.A. Anderson and N.L. Carter, Stress in the lithosphere: inferences from steady-state flow of rocks. *Pure Appl. Geophys., PAGEOPH 115,* 199-226, 1977.

Nicolas A., J-L. Bouchez, F. Boudier and J-C.C. Mercier, Textures, structures and fabrics due to solid-state flow in some European lherzolites. *Tectonophys. 12,* 55-86, 1971.

Nixon P.H., ed., Lesotho kimberlites, *Lesotho Nat. Dev. Co., Maseru, Lesotho,* 1-350.

Padovani E.R. and J.L. Carter, Aspects of the deep crustal evolution beneath South Central New Mexico, *Am. Geophys. Union Mono. 20,* 19-55, 1977.

Poirier J-P. and M. Guillopé, Deformation-induced recrystallization of minerals, *Bull. Minéral. 102,* 67-74, 1979.

Poirier J-P. and A. Nicolas, Deformation-induced recrystallization due to progressive misorientation of subgrains, with special reference to mantle peridotites, *J. Geol. 83,*707-720, 1975.

Raleigh C.B. and S.H. Kirby, Creep in the upper mantle, *Mineral. Soc. Amer. Spec. Pap. 3,* 113-121, 1970.

Ricoult D., Recuit expérimental de l'olivine, *3rd Cycle Doct. Thesis, Univ. Nantes, France,* 1-55, 1978.

Ross J.V., H.G. Avé Lallemant and N.L. Carter, Activation volume for creep in the upper mantle, *Science 203,* 261-263, 1979.

Ross J.V., H.G. Ave Lallemant and N.L. Carter, Stress-dependence of recrystallized grain and subgrain size in olivine, *J. Geophys. Res. 85, in press,* 1980.

Sellars C.M., Recrystallization of metals during hot-deformation, *Phil. Trans. Roy. Soc. London A-288,* 147-158, 1978.

Twiss R.J., Theory and applicability of a recrystallized grain-size paleopiezometer, *Pure Appl. Geophys., PAGEOPH 115,* 228-244, 1977.

Twiss R.J., Static theory of size variation with stress for subgrains and dynamically recrystallized grains, *This volume* and *J. Geophys. Res. 85, in press,* 1980.

Twiss R.J. and C.M. Sellars, Limits of applicability of the recrystallized grain-size geopiezometer, *Geophys. Res. Lett., in press,* 1980.

Watts A.B., J.H. Bodine and M.S. Steckler, Observations of flexure and the state of stress in the oceanic lithosphere, *This volume* and *J. Geophys. Res. 85, in press,* 1980.

- - - - - - - - - - -

Table 1. Physical conditions at the depths of the textural discontinuities*.

Parameter	Basin & Range	Southern Africa
Z (km)	65.6 ± 0.4	147.5 ± 7.5
P (MPa)	2025. ± 13.	4727. ± 250.
T (°C)	1121. ± 3.	1212. ± 28.
σ (MPa)	6.9 ± 1.2	5.8 ± 0.5
D_α (μm)	4110.	5095.
D_β (μm)	10844.	12848.
T_m (°K)	2220. ± 0.5	2340. ± 10.
T/T_m	0.628 ± 0.001	0.635 ± 0.014
μ (MPa)	68503. ± 62.	72156. ± 811.
σ/μ (10^{-3})	0.101 ± 0.003	0.008 ± 0.001

* *Symbols and units as defined in the text.*

Table 2. Physical state of the upper mantle as inferred from xenolith phase-compositions and textures*.

Prof. Id.	Z km	P GPa	T °C	σ MPa	D mm	$\dot{\varepsilon}$ /s	η p
IC.r	70	2.17	873	15.7	4.75	2.8 -19	1.9 +26
	80	2.50	927	15.6	4.78	2.4 -18	2.2 +25
	90	2.83	976	15.2	4.90	1.3 -17	3.9 +24
	100	3.16	1022	14.2	5.25	4.7 -17	1.0 +24
	110	3.49	1065	12.3	6.06	1.1 -16	3.8 +23
	120	3.82	1106	9.6	7.76	1.6 -16	2.1 +23
	130	4.15	1145	7.6	9.80	2.0 -16	1.2 +23
	140	4.48	1184	6.4	11.64	3.0 -16	7.2 +22
IC.m	150	4.81	1221	5.8	5.10	5.0 -16	3.8 +22
	160	5.14	1257	5.5	5.45	9.2 -16	2.0 +22
	170	5.47	1292	5.2	5.85	1.6 -15	1.1 +22
	180	5.80	1327	5.0	6.15	2.7 -15	6.2 +21
	190	6.13	1362	4.7	6.66	4.1 -15	3.8 +21
	200	6.46	1395	4.5	7.03	6.5 -15	2.3 +21
	210	6.79	1429	4.3	7.45	9.7 -15	1.5 +21
	220	7.12	1462	4.2	7.68	1.5 -14	9.3 +20
	230	7.45	1494	4.0	8.17	2.1 -14	6.3 +20
	240	7.78	1527	4.0	8.17	3.4 -14	4.0 +20
CE.r	50.0	1.512	978	45.0†	1.66	2.5 -15	6.0 +22
	52.5	1.594	1004	44.4†	1.68	6.3 -15	7.0 +22
	55.0	1.675	1028	38.0	1.96	9.0 -15	1.4 +22
	57.5	1.757	1052	19.5	3.82	2.4 -15	2.7 +22
	60.0	1.840	1074	12.5	5.96	1.2 -15	3.5 +22
	62.5	1.922	1096	9.3	8.01	8.8 -16	3.5 +22
	65.0	2.005	1116	7.3	10.21	7.5 -16	3.2 +22
CE.m	67.5	2.087	1136	6.3	4.59	8.2 -16	2.5 +22
	70.0	2.170	1154	5.5	5.45	9.2 -16	2.0 +22
	72.5	2.252	1172	4.8	6.48	9.3 -16	1.7 +22
	75.0	2.335	1189	4.3	7.45	1.0 -15	1.4 +22
	77.5	2.417	1206	3.8	8.72	1.1 -15	1.2 +22
	80.0	2.500	1221	3.5	9.68	1.2 -15	9.5 +21
RR.m	42.5	1.262	1005	7.6	3.61	3.5 -17	7.2 +23
	45.0	1.345	1044	7.4	3.71	1.3 -16	1.8 +22
	47.5	1.427	1080	7.3	3.77	4.4 -16	5.6 +22
	50.0	1.510	1116	7.2	3.84	1.3 -15	1.8 +22
	52.5	1.592	1150	7.1	3.94	3.5 -15	6.8 +21
	55.0	1.675	1183	6.8	4.16	7.9 -15	2.9 +21
	57.5	1.757	1215	6.1	4.78	1.3 -14	1.5 +21
	60.0	1.840	1246	4.8	6.48	1.4 -14	1.1 +21
RR.r	61.0	1.873	1257	4.0	18.63	1.0 -14	1.3 +21
	62.5	1.922	1275	2.0	37.25	1.8 -15	3.8 +21

** Profile identifications: IC = infracratonic, CE = continental extension zone, RR = ridge/rift type; r and m respectively indicate whether the SGR or GBM σ/D relation has been used in the calculations.*

† Data based on the strain-rate fits to individual data.

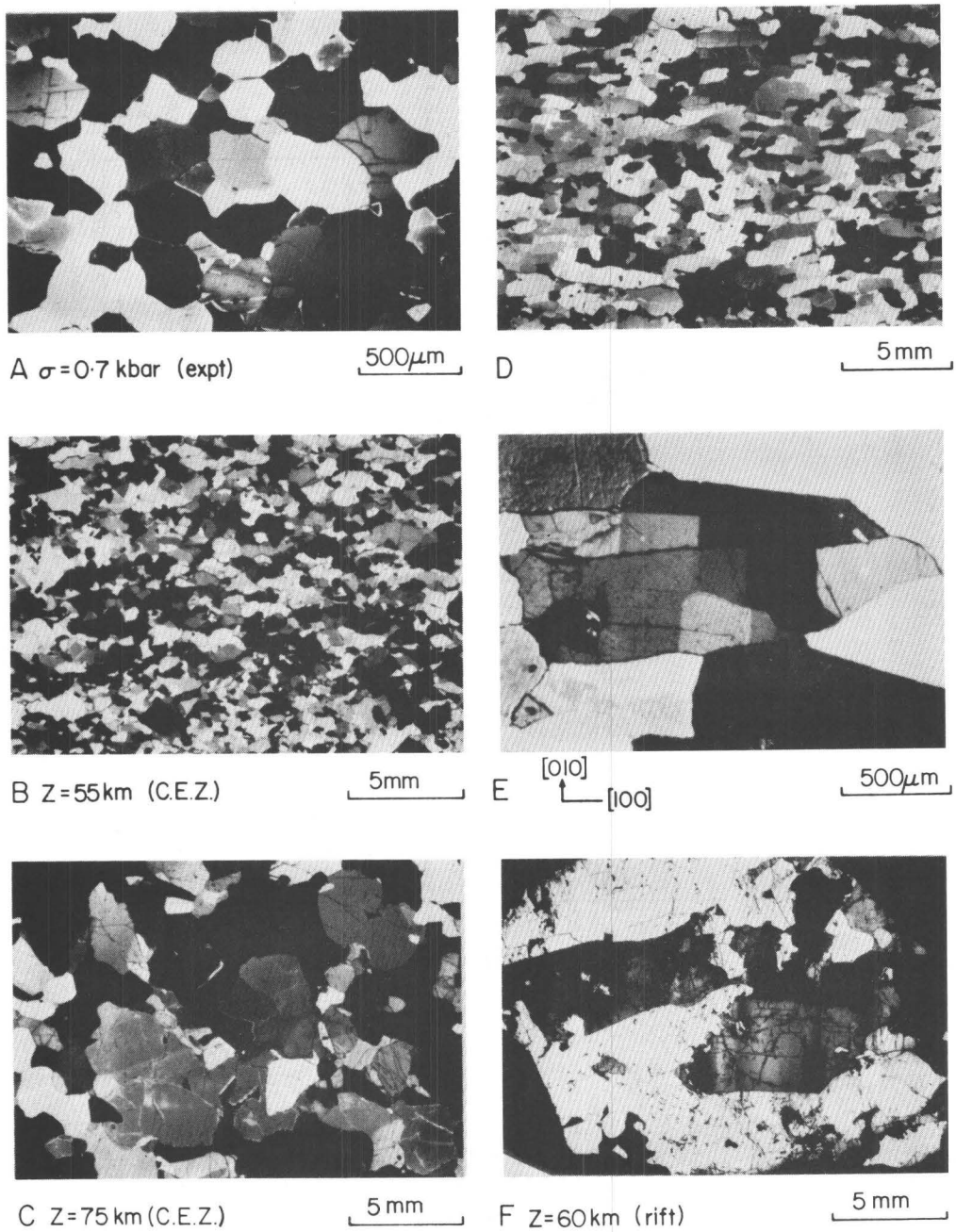

Figure 1. Homogranular textures (peridotites).
A - Dynamically recrystallized Mount-Burnet dunite (experiment).
B - Granuloblastic xenolith; Kilbourne Hole, NM, U.S.A.
C - Granoblastic xenolith, deeper facies; Kilbourne Hole, NM.
D - Granuloblastic xenolith with tablet-shaped crystals typical of SGR recrystallization; Nunivak Island, Alaska.
E - Formation of three SGR tablets in a natural olivine (xenolith from Dreis, Germany) pre-dates (100) subboundaries ascribed to late deformation related to volcanic-conduit opening.
F - "Fine-grained" poikiloblastic xenolith; Borée, France.

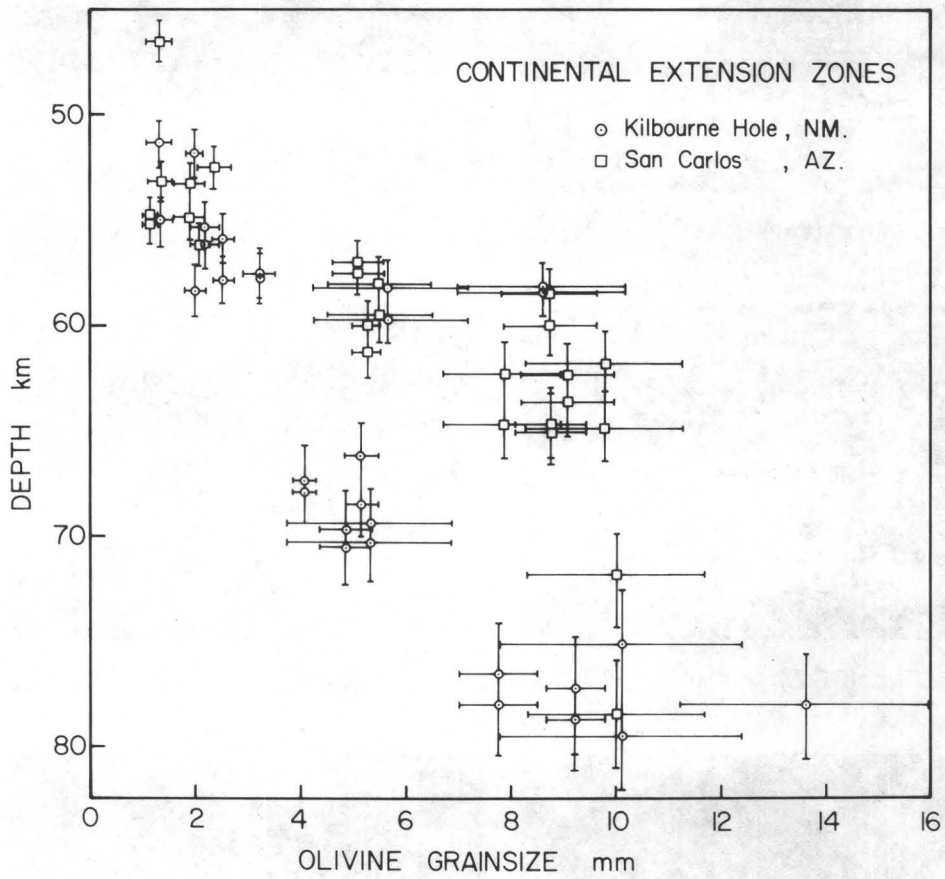

Figure 2. Olivine grain-size as a function of depth for Basin-and-Range (C.E.Z.) xenoliths. As for the other grain-size plot (Figure 3), no profile has been drawn not to influence the reader on whether the discontinuity is real. Note however that such plots must be inspected vertically, *e.g.* from top to bottom, since the relation between depth and the other parameters (grain-size, stress, strain-rate or viscosity) may not be bijective (as illustrated here). Probe analyses and the depth/pressure relation used here are from Avé Lallemant and others (1980).

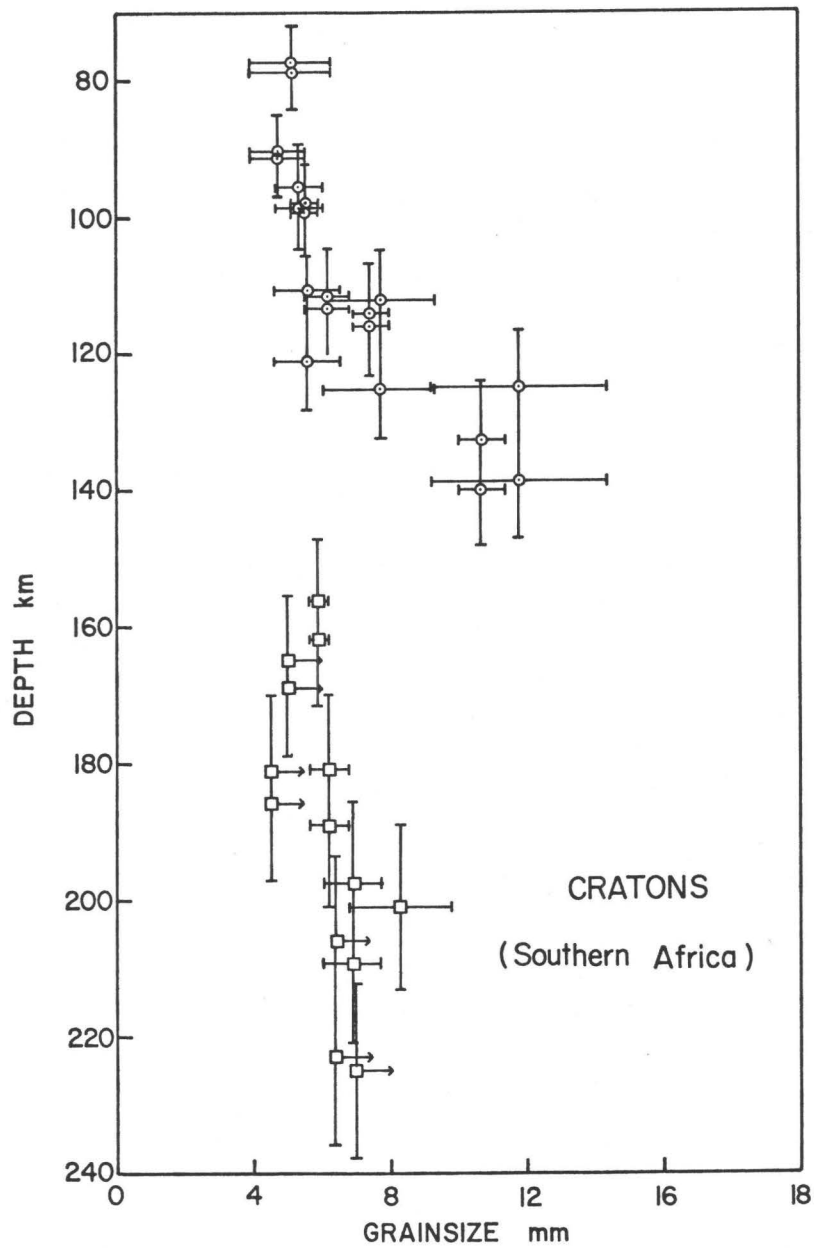

Figure 3. Olivine grain-size as a function of depth for xenoliths from Southern-Africa kimberlites (infracratonic mantle). Samples are from Frank Smith (FRB) and KaO, Letseng-la-Terae, Liqhobong, Matsoku, Mothae and Thaba Putsoa (all PHN). Probe analyses used for depth calculations are given in Boyd (1974) for FRB samples and in Nixon (1973) for PHN samples. Grain sizes represented by symbols with arrows may be underestimated by as much as 20% owing to important late recrystallization (See Avé Lallemant et al., 1980). Grain sizes used for stress calculations were approximately corrected for this effect. Porphyroclastic samples are represented by squares and granoblastic ones by circles.

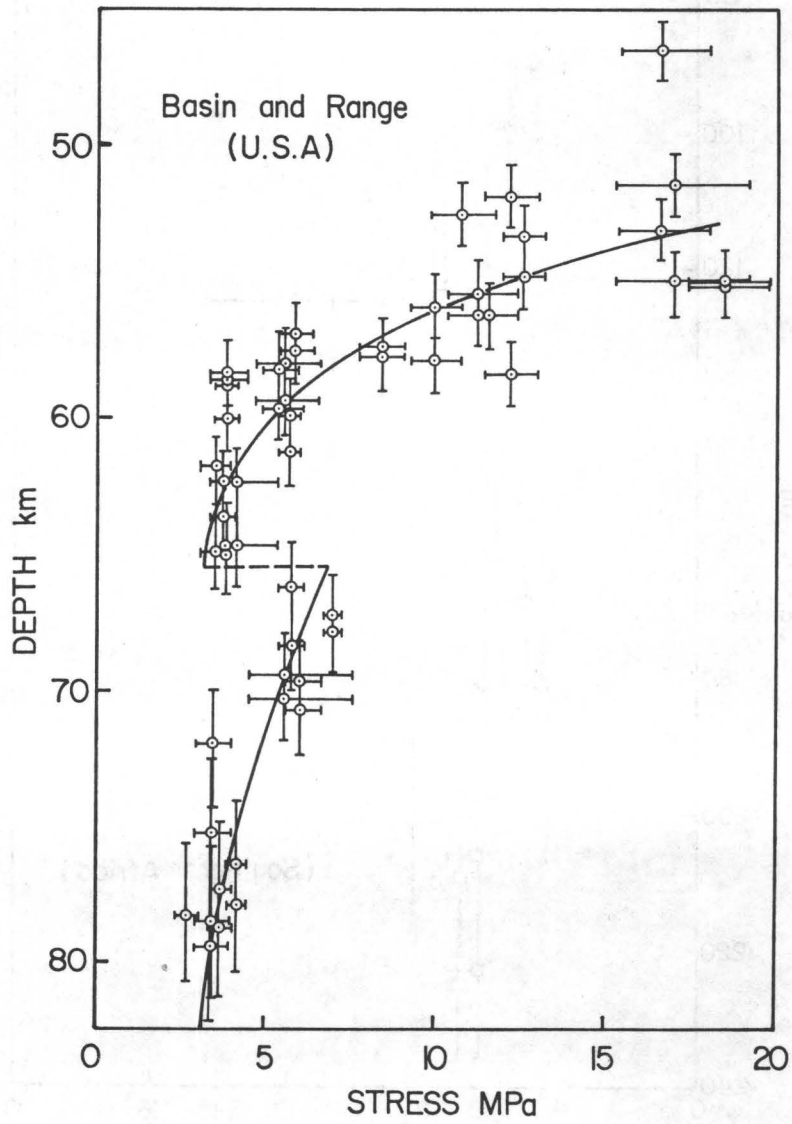

Figure 4. Deviatoric stress as a function of depth for the Basin-and-Range Province (C.E.Z.). These stresses were all computed by using Ross and others' (1980) piezometer for GBM recrystallization. The profile drawn here has been optimized by taking into account constraints from other plots (Avé Lallemant *et al.*, 1980). Physical conditions at the depth of the discontinuity are listed in Table 1.

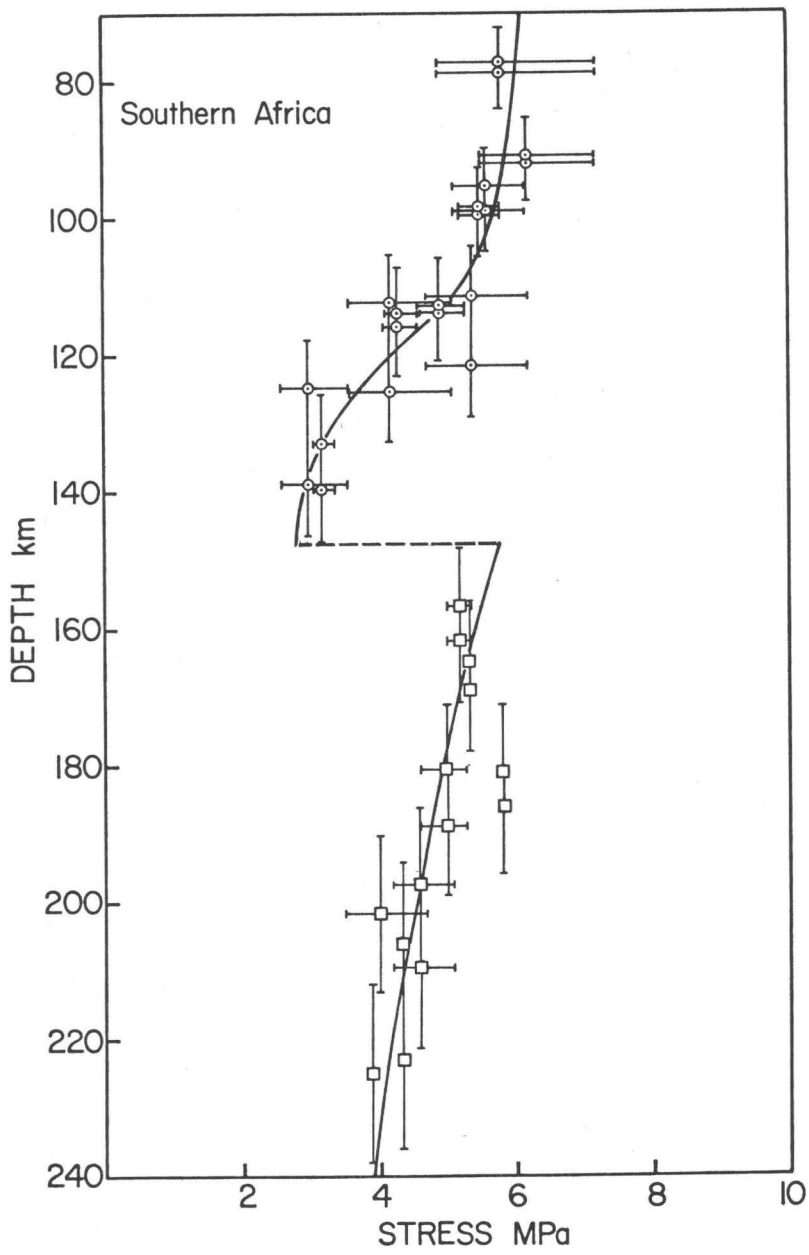

Figure 5. Deviatoric stress as a function of depth for Southern Africa (infracratonic mantle). Conventions as in Figure 4.

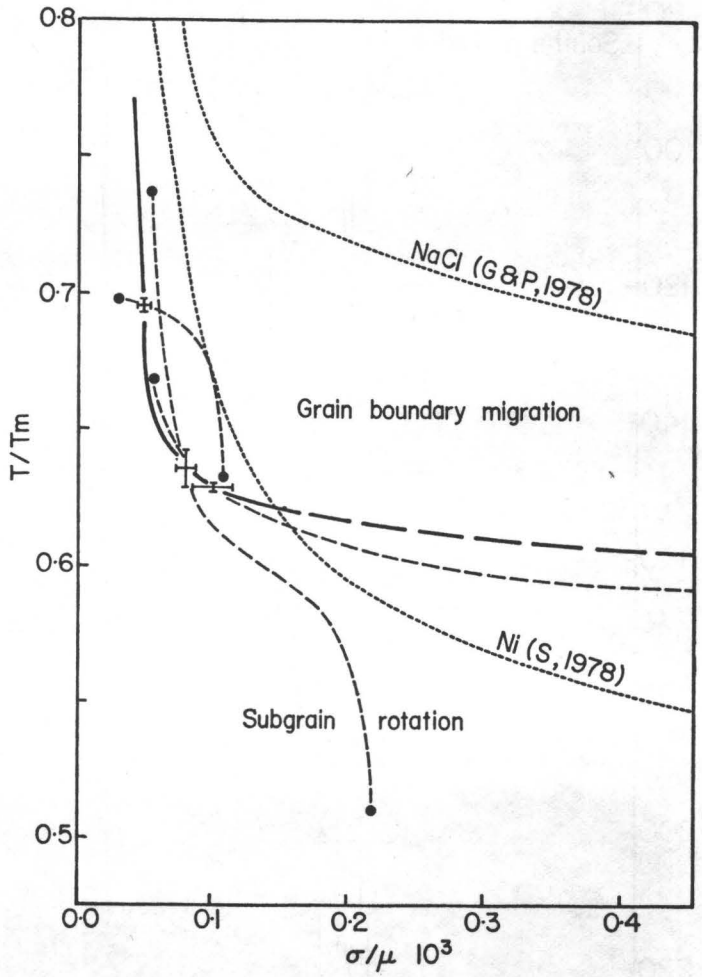

Figure 6. Grain-boundary migration and subgrain rotation as dominant recrystallization mechanisms. The boundary inferred for olivine in the present study is shown by a bold line (dashed where tentative). The error bars are calculated from observed transitions in suites of natural textures (See the text). Short-dashed lines ending at solid circles illustrate the domains of natural conditions encountered in the present study for steady-state deformation of the mantle. Dotted lines are for experimental data on halite (Guillopé and Poirier, 1980) and nickel (Sellars, 1978).

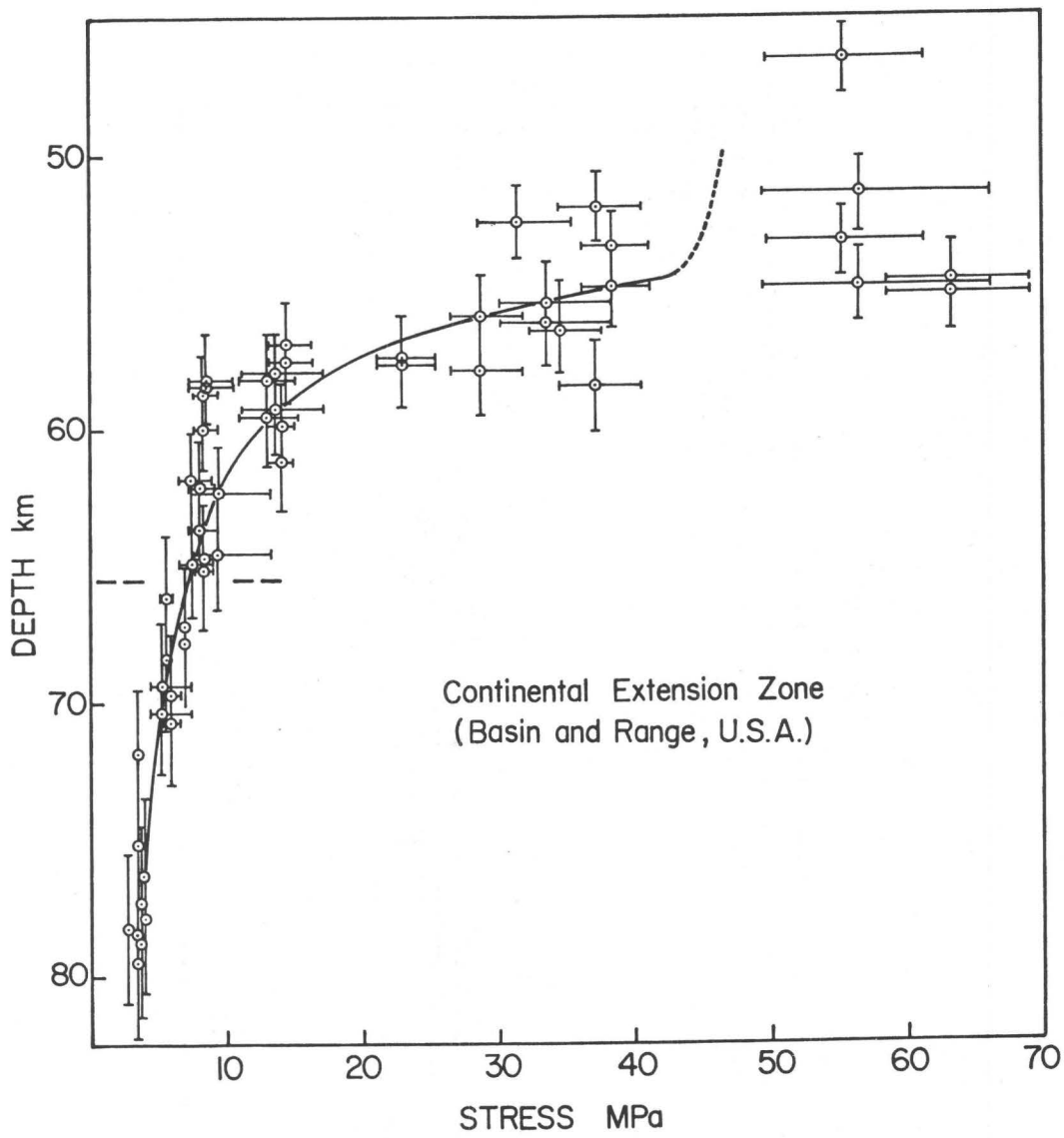

Figure 7. Corrected stress estimates for the Basin-and-Range Province (C.E.Z.). Estimates for shallow samples (above the dashed line) are based on the SGR olivine grain-size piezometer (this study) whereas estimates for deep samples are obtained by using Ross and others' (1980) GBM piezometer. Depth calculations as in Figure 2. Stress estimates greater than 20 MPa could be overestimated if the textural trend was crossing the SGR/GBM boundary twice. The shallowest part of the stress profile (dotted line) is inferred from the strain-rate plot (Figure 8) which implies a strong curvature near 55 km and almost constant stresses (∿45 MPa) above the latter.

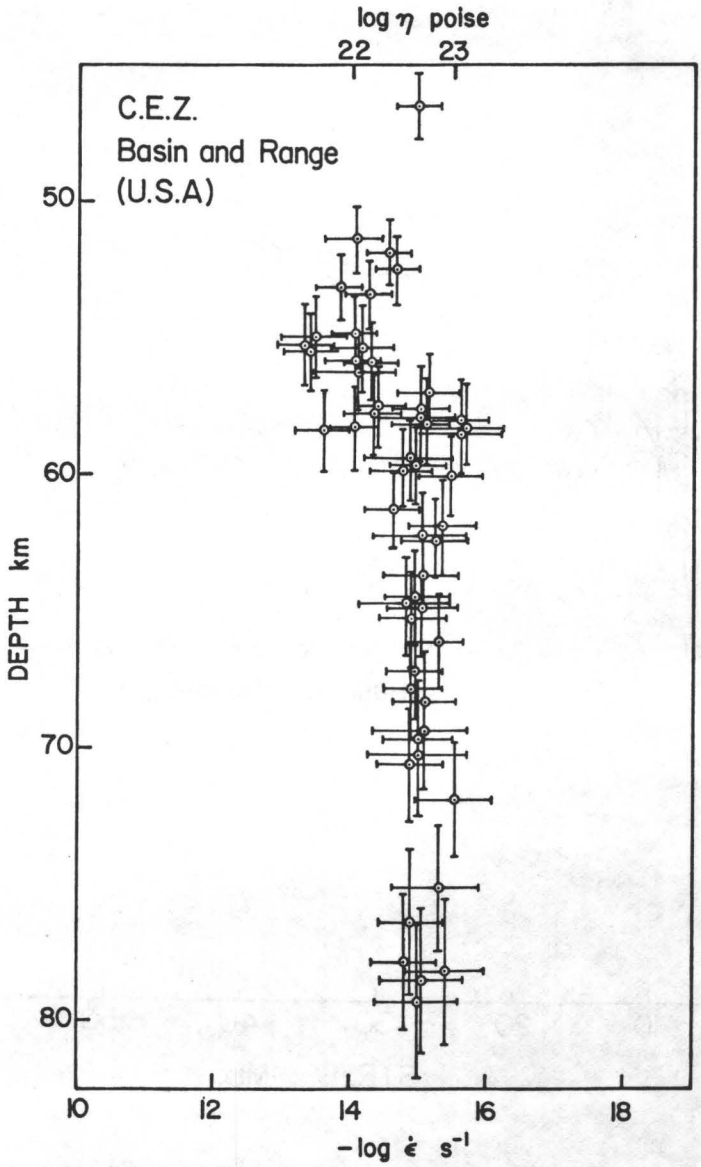

Figure 8. Strain-rates as a function of depth for the Basin-and Range Province (C.E.Z.). These estimates are based on the stresses shown in Figure 7. The viscosity scale has been calculated as an average over the whole range of depths illustrated by the samples studied. The trend above 55 km is used to infer the shallowest part of the stress profile (Figure 7).

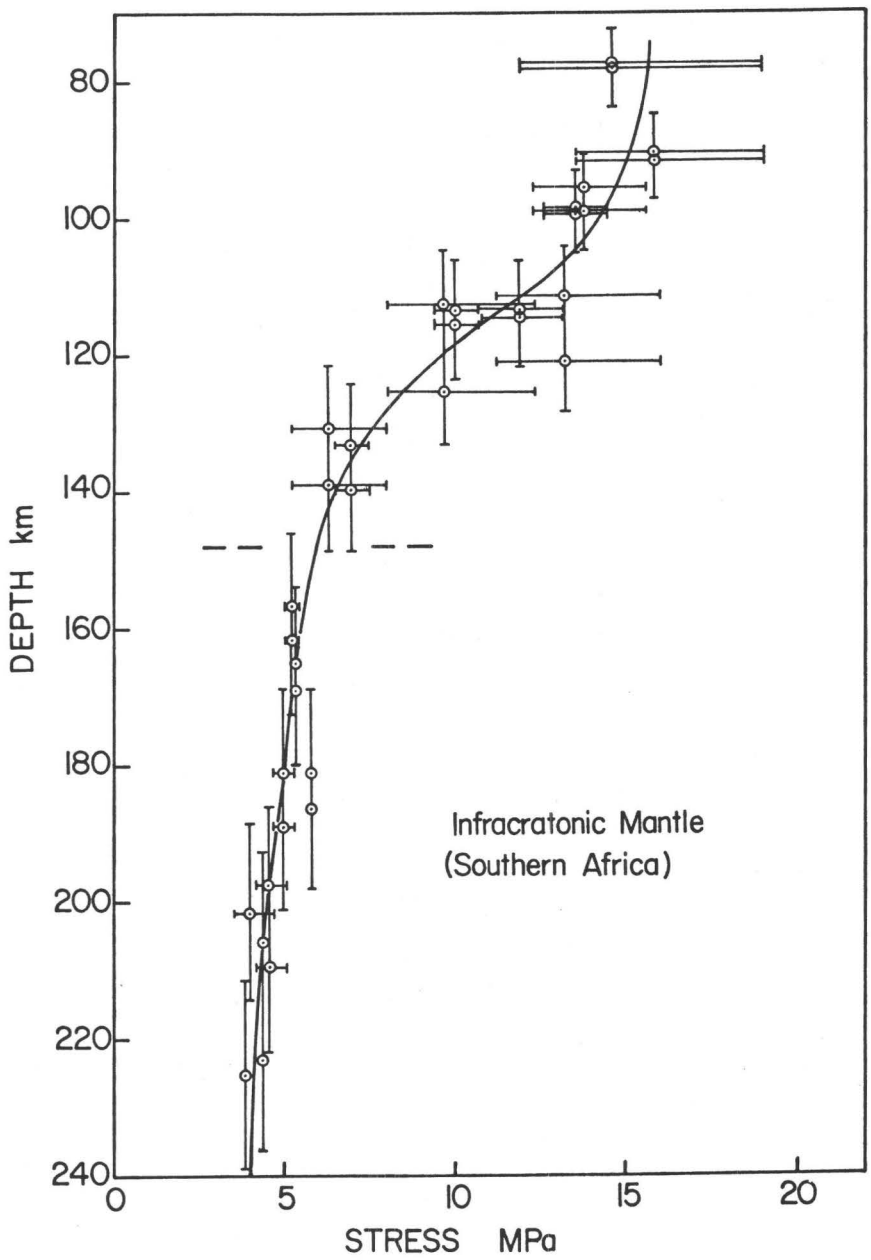

Figure 9. Corrected stress estimates for Southern Africa (infracratonic mantle. Conventions as in Figure 7.

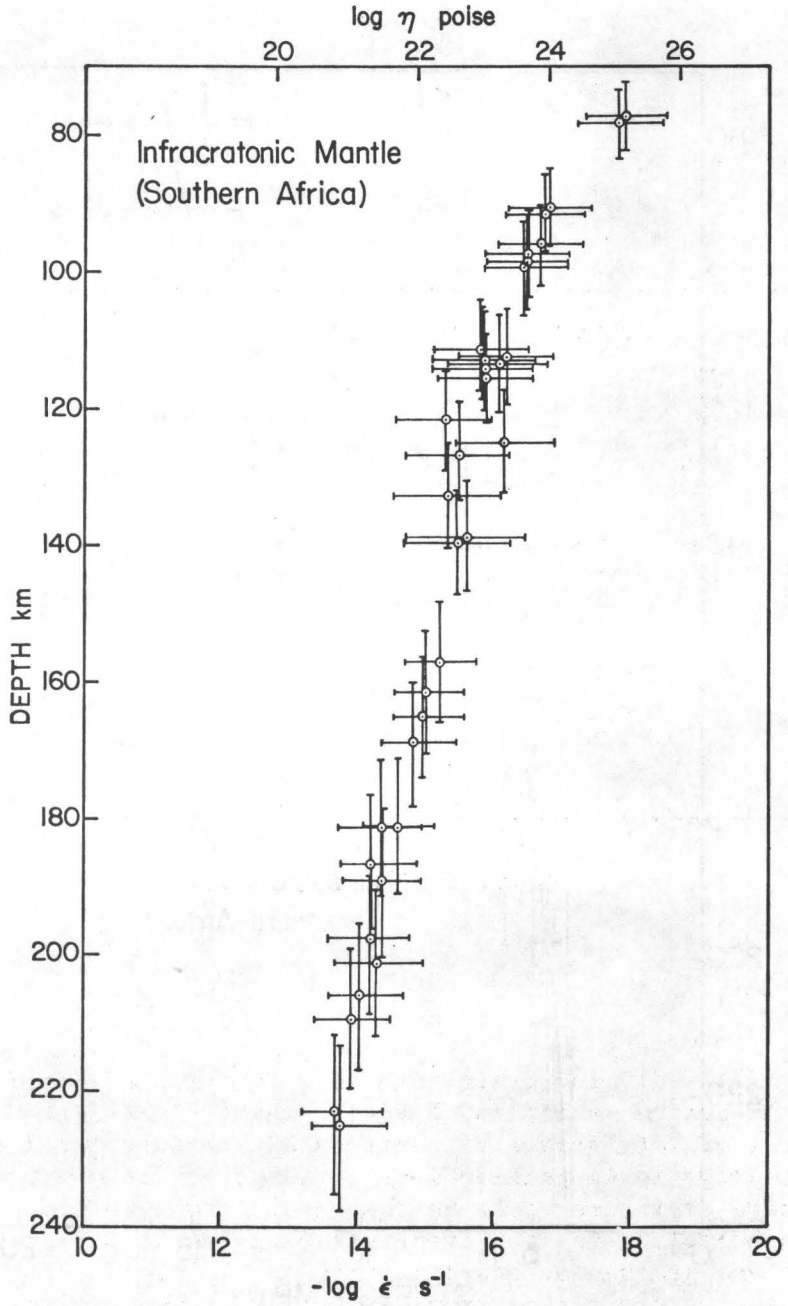

Figure 10. Strain-rates as a function of depth for Southern Africa (infracratonic mantle). Conventions as in Figure 8. The inflection near 150 km is real (Figure 16) and results from the temperature effect on strain-rate becoming dominant below this inflection.

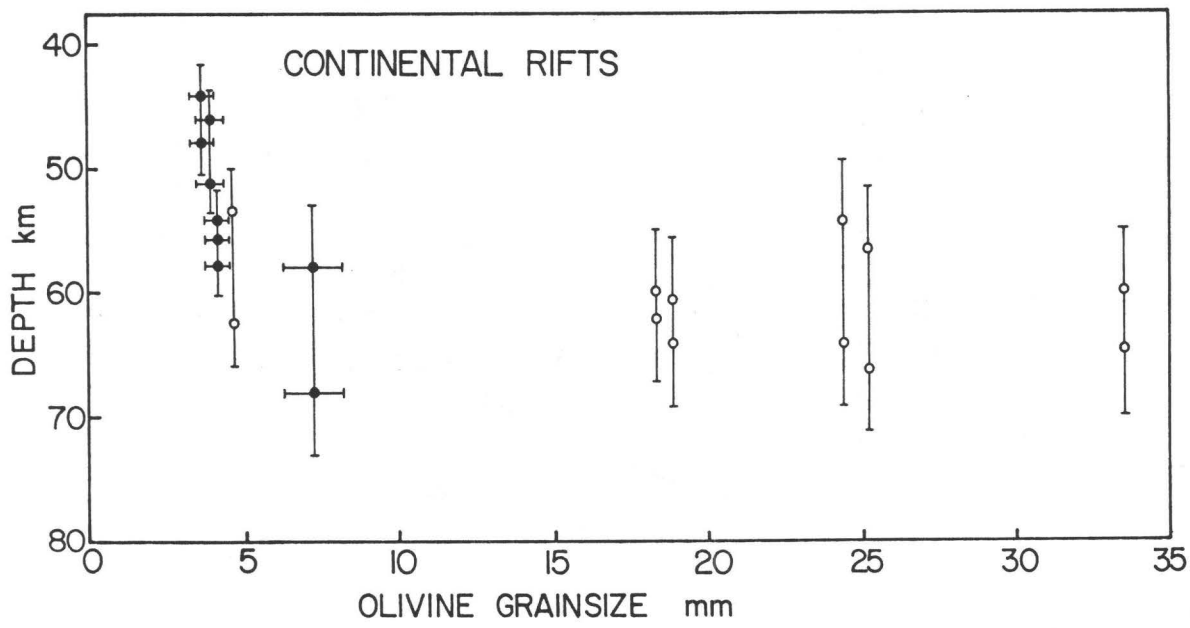

Figure 11. Olivine grain-size as a function of depth for poikiloblastic-series xenoliths (Borée, France; Black-Rock Summit, Nevada) typical of late stages of continental rifting. Open circles stand for nearly single-poikiloblast peridotites for which no significant standard deviation could be computed. Probe analyses used for depth calculations are given in Avé Lallemant and others (1980). Though no grain-size discontinuity is visible, textural studies show that a transition from GBM to SBR mechanisms (with increasing depth) occurs for grain sizes of about 10 mm, in full agreement with Twiss and Sellars' (1980) calculations according to which GBM is unlikely to yield grain sizes of 10 mm or coarser.

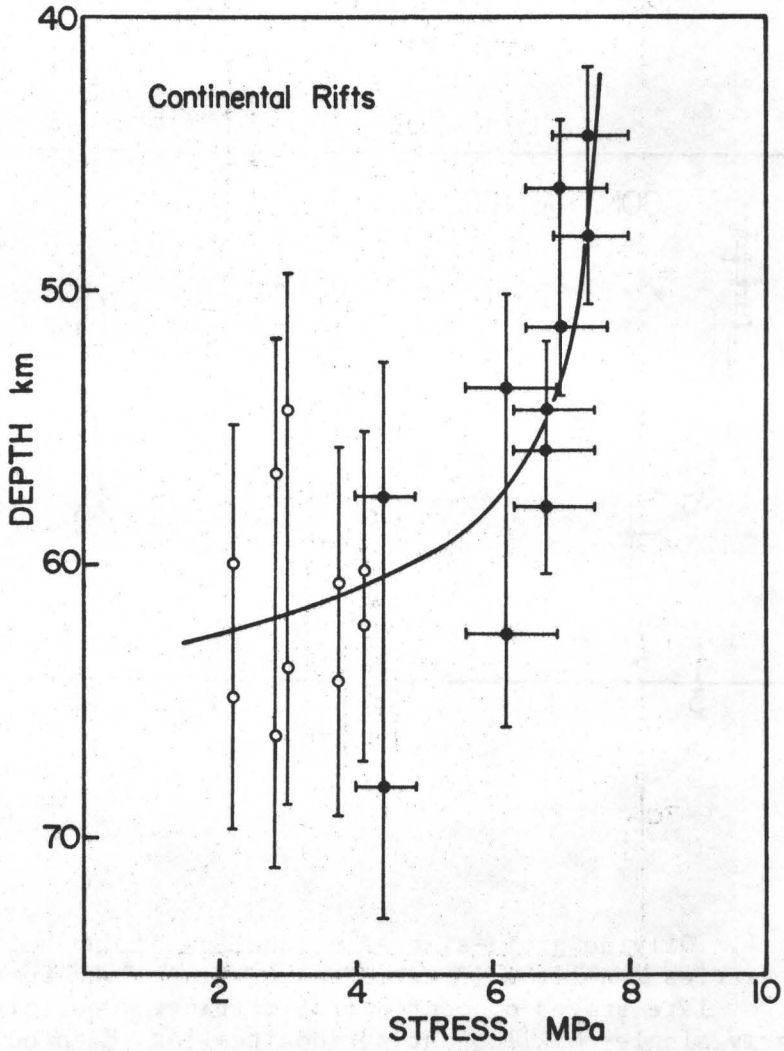

Figure 12. Corrected stress estimates for poikiloblastic-series xenoliths (rifts). Open symbols represent estimates based on the SGR piezometer and solid ones those based on the GBM piezometer.

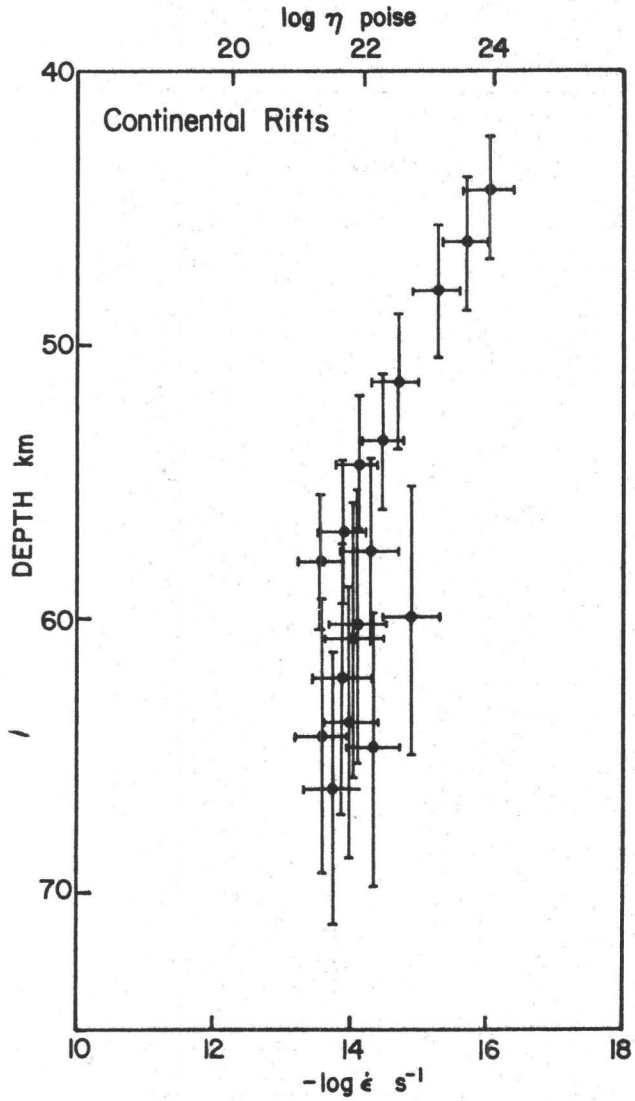

Figure 13. Strain-rate as a function of depth for the poikiloblastic series xenoliths (rifts). Conventions as in Figure 8. Although strain-rate appears to be nearly constant below 55 km, this trend is not significant according to the calculated profile (Figure 16).

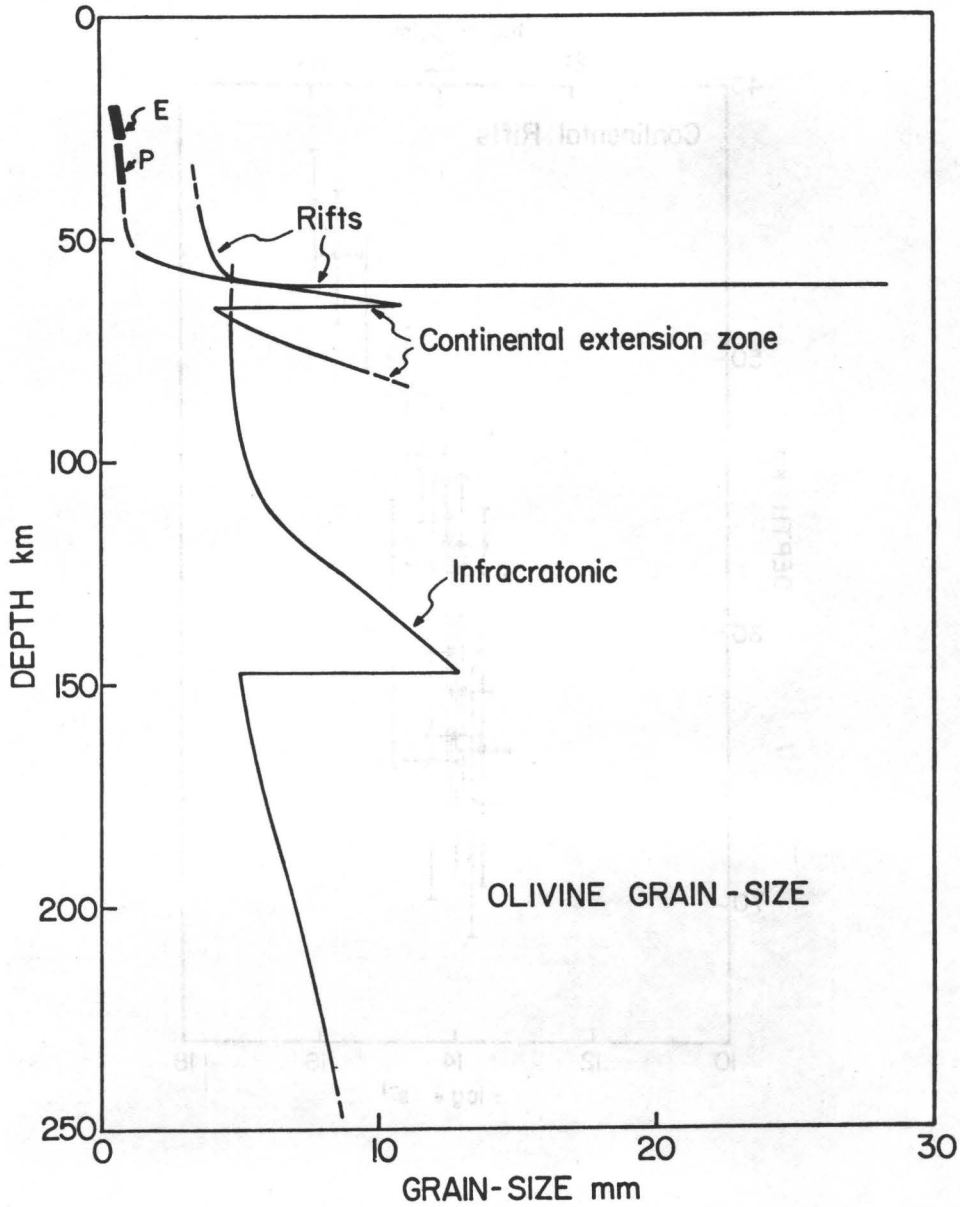

Figure 14. Grain-size profiles for peridotites. Most samples have average grain-sizes in the range 5 to 12 mm, the latter value being certainly close to the representative grain-size for depths greater than those illustrated by the xenoliths. Grain-sizes for charnockites from extension zones (E; Leyreloup, 1974; Padovani and Carter, 1977) and from paleo-orogenic regions (P; Griffin *et al.*, 1979) are given for comparison.

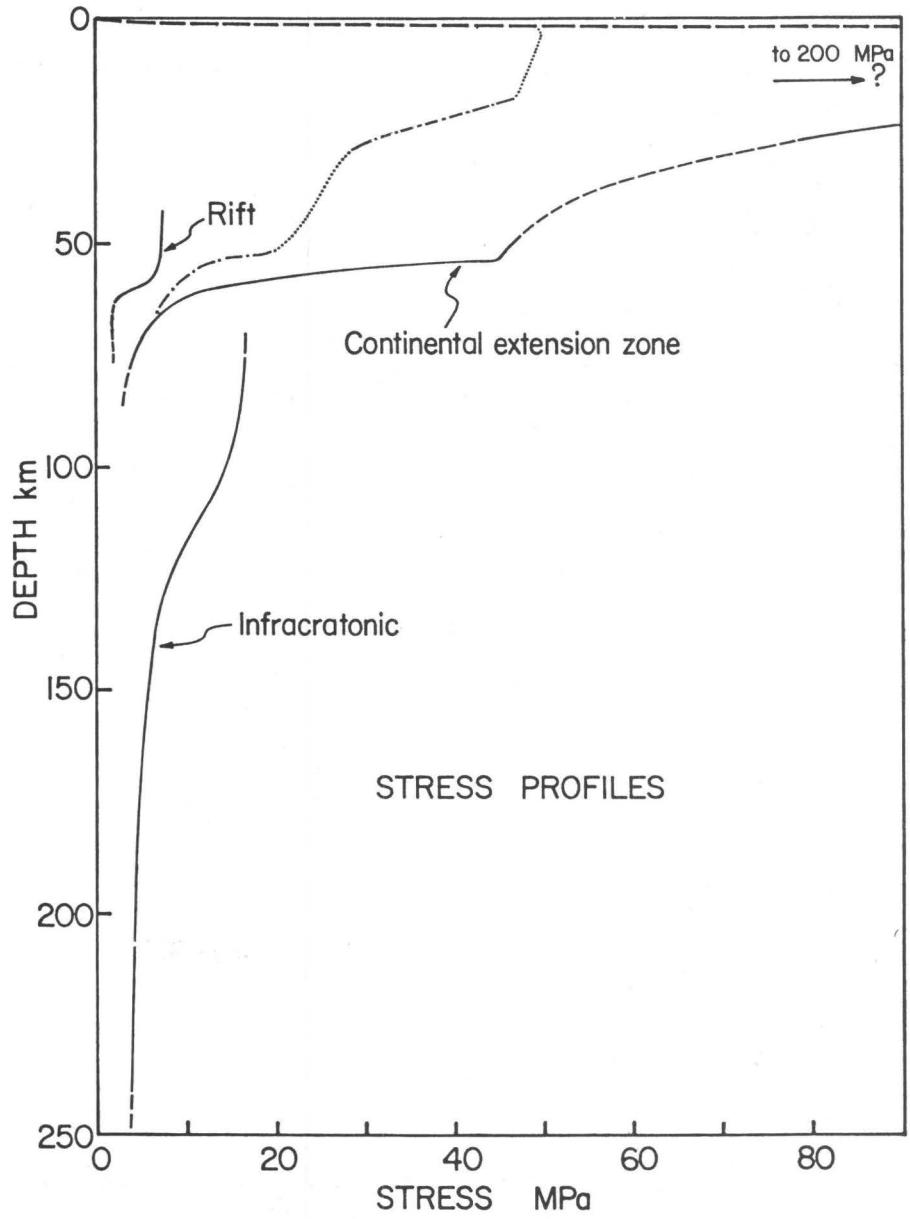

Figure 15. Stress profiles. These simple fits to the corrected stress estimates (except for the C.E.Z. profile above 55 km), are used for calculating all the other profiles. High C.E.Z. stresses (45 MPa) near 55 km are supported by independent evidence (See the text). However, if the textural trend was crossing the GBM/SGR boundary a second time near $\sigma/\mu = 0.3\ 10^{-3}$ (Figure 6), stresses for the shallowest samples would be reduced to <20 MPa (dash-dot line). Long-dashed lines show the subsurface yield strength of rocks. Deep-crustal stresses are tentatively estimated from charnockite grain-sizes, assuming a D/σ relation close to that for olivine.

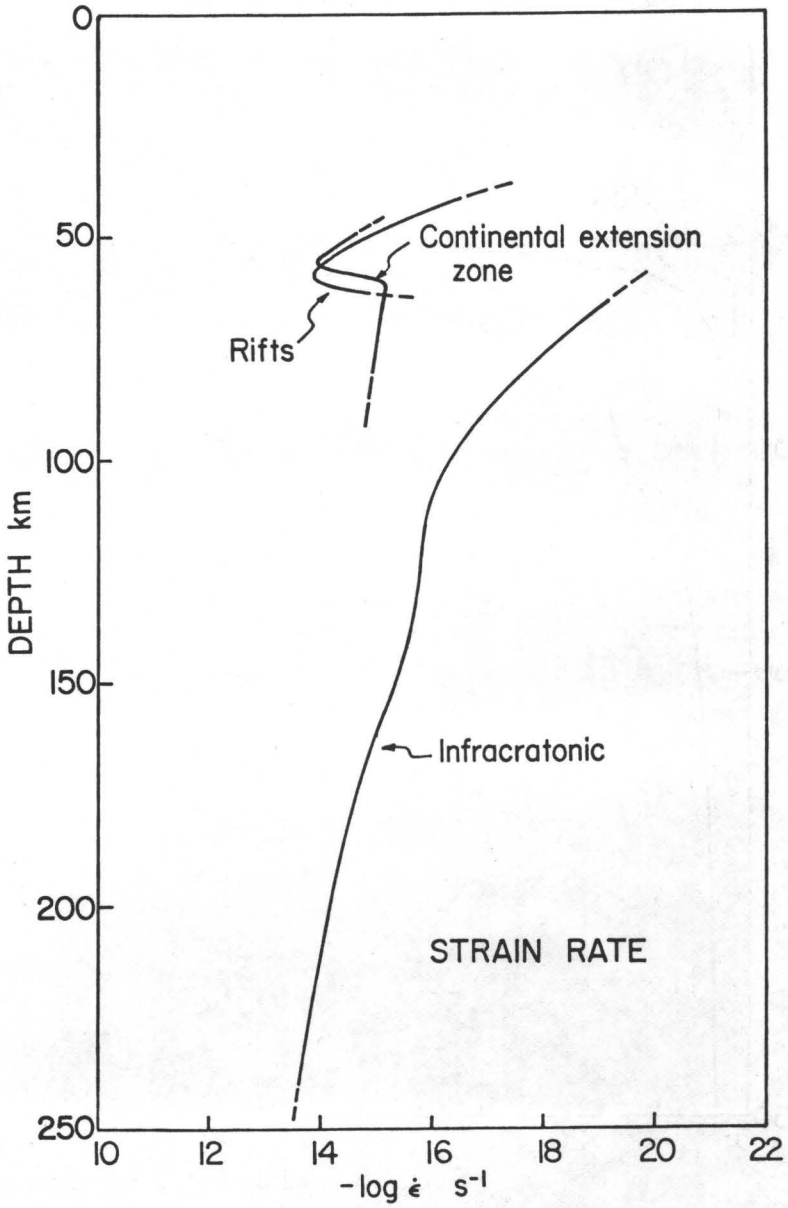

Figure 16. Strain-rate profiles. The progressive increase of strain-rate from 50 to 250 km for the infracratonic mantle, confirms that there is no decoupling at the lithosphere/asthenosphere boundary (Mercier *et al.*, 1977). For continental rifts, only a narrow layer seems to flow at an appreciable rate, in agreement with the diapiric model proposed earlier (Mercier, 1977a; 1977b) and, for C.E.Z. regions, some (horizontal?) flow would occur within the seismically-defined lithosphere. Since all strain-rates are smaller than or close to 10^{-14}/s, the present results are reasonable and likely to closely approximate the real physical properties of the uppermost mantle.

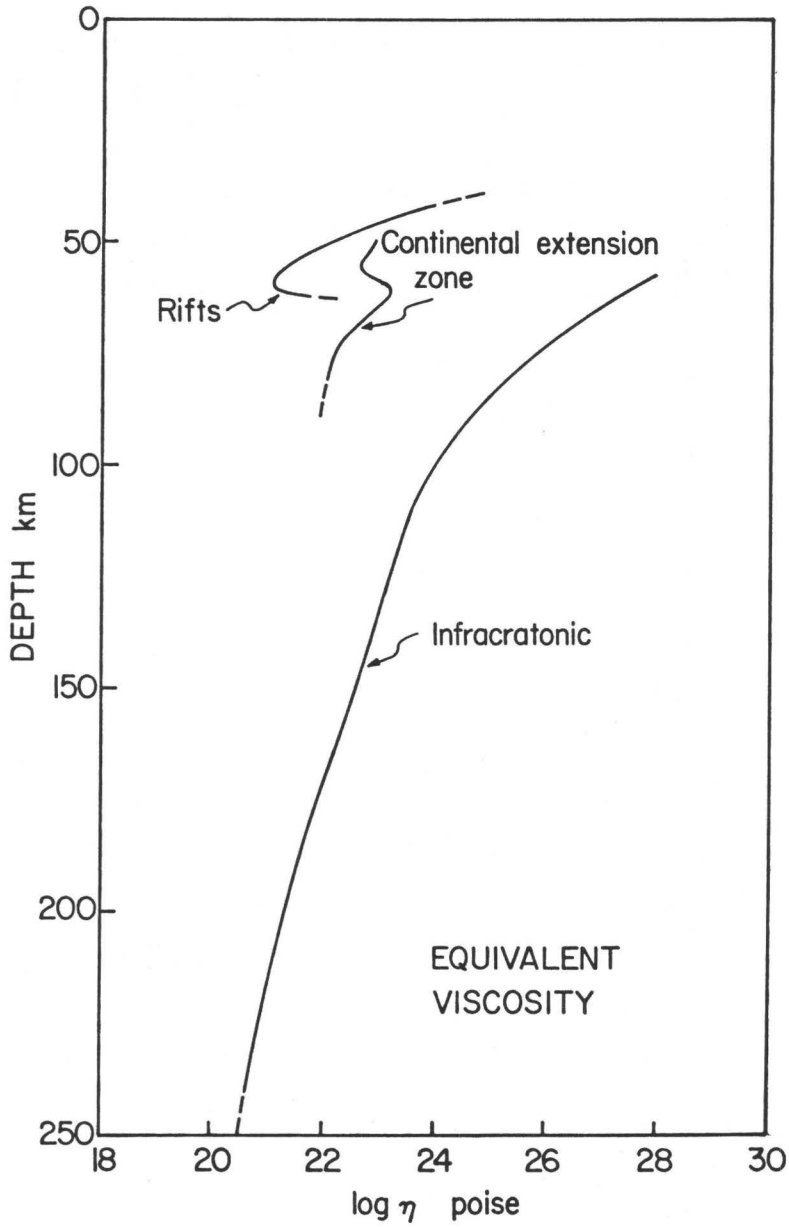

Figure 17. Equivalent viscosity profiles. The trends are nearly identical to those observed for the strain-rates, which justifies calculation of the average-viscosity scales added to the strain-rate plots.

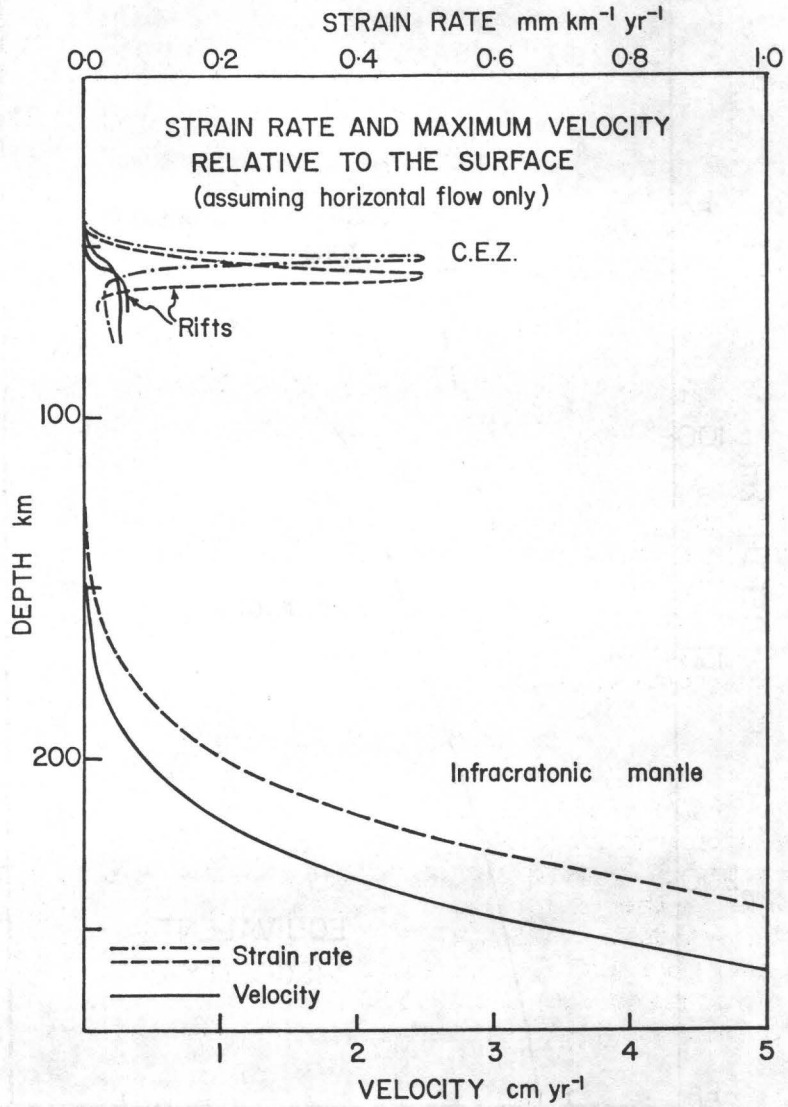

Figure 18. Strain-rates and maximum velocities relative to the surface (*i.e.* as if the mantle were to flow horizontally for the regions under study). The velocity curves are derived through 1-km-increment integration of the strain-rate curves. Considering the large errors resulting from the integration process, the velocities for the infracratonic mantle agree well with average spreading rates and plate velocities.

Limits on Crustal Stress Imposed by Laboratory Experiments

W.F. BRACE

Department of Earth and Planetary Sciences
Massachusetts Institute of Technology
Cambridge, Massachusetts 02139

Abstract

Laboratory measurements of rock strength provide limiting values of crustal stress, provided one effective principal stress is known. Fracture strengths are too variable to be useful; however, rocks at shallow depth are probably fractured so that frictional strength may apply. A single linear friction law, termed Byerlee's law, holds for all materials except clays, to pressures of more than 1 GPa, temperatures to 500° and over a wide range of strain rate. Byerlee's law, converted to maximum or minimum crustal stress, is a good upper or lower bound to observed in situ stresses to 5 km, for pore pressure hydrostatic or sub-hydrostatic. Byerlee's law combined with the olivine flow law provides a maximum stress profile to about 50 km. Stress will be close to zero at the surface and at 50 km, and average between 130 and 360 MPa for hydrostatic pore pressure. Some new permeability studies of crystalline rocks suggest that pore pressure will be low in the absence of a thick agrillaceous cover.

INTRODUCTION

Stresses in the Earth cannot exceed the strength of rocks. Therefore measurements of rock strength can be used to set limits on stress in the Earth. Here we review what is known about strength of rocks, particularly in the upper, colder parts of the crust where brittle failure limits the stress. Following the recent work of Goetze and Evans [1979], we give limiting stresses as a function of depth, noting the strong influence of pore pressure. We test these stresses to about 4 km using published in situ stress and plausible assumptions about pore pressure.

It is important to keep in mind the limitations of laboratory measurements in any discussion of crustal stress. They provide only one thing, namely the maximum stress difference which rocks can support at some pressure, temperature and strain rate. Call this maximum stress difference, or strength, S, where $S = |(\sigma_1-\sigma_3)|$. Provided one of the principal stresses, σ_1 or σ_3 is known at some point in the Earth, then the maximum or minimum value of the other can be calculated from laboratory values of S. We will note below the difficulties involved in estimating any one the principal stresses.

LABORATORY STRENGTH MEASUREMENTS

Brittle Fracture

For the present discussion we need only consider the magnitude of S for rocks and how it varies with the pressure, temperature and strain

rate encountered in crustal rocks. The subject has been most recently reviewed by Paterson [1978], Jaeger and Cook [1976], and Ohnaka [1973]. We will not present the data but only comment on the general trends. Assuming crystalline rocks are of greatest interest, the compilation by Ohnaka [1973] is particularly useful (Figure 1). These are room temperature results but illustrate several features which hold generally:

(1) $\underline{S}$ has a marked dependence on pressure.
(2) The pressure dependence, although of the same sign, varies unsystematically with rock type.
(3) $\underline{S}$ at any one pressure can vary by a factor of up to 5, depending on rock type.

Temperature and strain rate dependence of $\underline{S}$ also vary among the different crystalline rocks (Figure 2). Fortunately these effects are rather small for brittle behavior. Paterson [1978] showed that thermal weakening, if considered thermally activated, has an activation energy of less than 1 kcal mole^{-1}. Brace and Jones [1971] found a weak strain-rate sensitivity (Figure 3); $\underline{S}$ increased 5 to 20 percent per 10^3 increase in strain rate.

Given the five-fold variation in $\underline{S}$ at any pressure and the other smaller although equally unsystematic variations with temperature and strain rate, we conclude that laboratory measurements of fracture strength are almost useless in the present context. One way out of this may be to consider the influence of fractures.

Evidence for fractures (joints, faults, bedding foliation, and the like) in rocks to 5 or 10 km depth was summarized by Brace [1972]. The evidence was of two types, direct observation in mines and drill holes, and inference from measured electrical or fluid conductivity. Without repeating all the arguments, the evidence for a water-filled, interconnected pore space seemed compelling at least to about 5 km. Recent deep resistivity measurements [Nekut et al., 1977] suggest the same conclusion to 20 km, and a recent study of crustal permeability argues for high conductivities to 8 km [Brace, 1979, in press]. High fluid conductivity necessitates interconnecting fractures, since crustal porosity in crystalline terrains must be a percent or less.

The lower depth limit for interconnected pore space is unknown. Plastic flow appears to be one limiting factor [Brace, 1972] and "healing" of cracks another [Batzle and Simmons, 1977]. Nothing is known about depths at which the latter becomes significant. Plastic flow of silicate rocks appears to begin at temperatures around 500 to 600°C [Goetze and Brace, 1972; Tullis and Yund, 1977; Paterson, 1978]. Perhaps it is safe to assume that interconnection of fractures and other pore space disappears below depths at which these temperatures are reached.

If there is a region of fractured rock, extending to perhaps 25 km, we need to consider the effect on $\underline{S}$. Fortunately experimentalists have turned to this question in recent years, with a result that will be very useful for the present discussion.

Rock Strength During Frictional Sliding

If rock is fractured, frictional sliding will occur on the fractures before the stress reaches the level to cause brittle fracture of the mass as a whole. S of fractured rock is determined, therefore, by frictional resistance. Frictional resistance has been measured in the laboratory for a wide range of rock type, pressure and temperature. One might expect at least as wide a variation in friction as fracture strength, with additional factors such as surface roughness playing a role. However, this does not turn out to be the case under geologic conditions. One of the most significant recent discoveries in rock mechanics is the virtual independence of friction on rock type, displacement and surface conditions [Barton, 1976; Byerlee, 1978]. First noted by Byerlee [1968], frictional resistance can be fitted by a simple bilinear relation over a range of normal stress from about 3 MPa to 1.7 GPa:

$$\tau = 0.85\ \bar{\sigma}_n\ , \qquad 3 < \bar{\sigma}_n < 200\ \text{MPa}$$

$$\tau = 60 \pm 10 + 0.6\ \bar{\sigma}_n, \qquad \bar{\sigma}_n > 200\ \text{MPa} \qquad (1)$$

where τ and $\bar{\sigma}_n$ are shearing and normal stress at which frictional resistance is overcome on a fracture. This simple relationship, which we shall refer to as Byerlee's law, seems to hold for all geologic materials except certain clay minerals (Figure 4). More recent work on shearing resistance of pure clays (Wang et al., 1979, in press) bear this out, although it is likely that in all of the experiments done with clay, the samples were undrained, a condition which would lower the strength.

The effect of temperature on friction was reported by Stesky et al. [1974] for a gabbro (Figure 5) and granite. The stresses are independent of temperature to 500° for the granite and 400° for the gabbro. Other silicate rocks will probably behave similarly. The effect of sliding rate is also small, comparable to the effect on fracture strength [Stesky, 1975; Dieterich, 1972] up to the same temperature levels.

The role of pore pressure needs special attention. Most mechanical behavior of rocks is determined by effective stress $\bar{\sigma}_{ij}$ where

$$\bar{\sigma}_{ij} = \sigma_{ij} - \alpha P_p \delta_{ij}$$

where σ_{ij} are the total macroscopic stresses, and P_p the pore pressure [see reviews by Paterson, 1978; Brace, 1972]. Empirically, α is close to 1 for fracture and friction of silicate rocks, although it may depart significantly for some elastic and transport phenomena. For example, α of 4 has been reported for permeability in sandstone [Zoback and Byerlee, 1975]. Thus, in equation (1), pore pressure in included by noting that

$$\bar{\sigma} = \sigma_n - P_p \qquad (2)$$

We will adopt this concept in what follows. Measured in situ stress is usually reported as total stress, and (2) will be used to relate laboratory strength criteria such as equation (1) to calculated crustal stresses.

ESTIMATE OF CRUSTAL STRESS

Crustal Stress from Byerlee's Law

Byerlee's law is expressed in equation (1) in terms of the stress components on the fracture. In terms of the principal effective stresses it becomes

$$\sigma_1 \simeq 5\,\bar{\sigma}_3, \qquad \bar{\sigma}_3 < 110 \text{ MPa}$$

$$\bar{\sigma}_1 \simeq 3.1\,\bar{\sigma}_3 + 210, \qquad \sigma_3 > 110 \text{ MPa} \qquad (3)$$

A plausible assumption in fractured rock is that fractures of all orientations exist. Regardless of their orientation, then, once the principal stresses reach the values in equation (3), frictional sliding occurs somewhere. In fractured rock, therefore, these values represent the maximum permissible stresses, regardless of rock type (neglecting clays), temperature to 500°, and details of fracture geometry and gouge thickness.

Below we compare reported in situ stress with the limiting values given by equation (3). To do this one principal stress must be known, and pore pressure must be known. Usually the vertical stress, which is known, is taken to be either σ_1 or σ_2, and pore pressure to be hydrostatic.

It is interesting to compare measured crustal stress with the limiting stresses predicted from Byerlee's law, using plausible assumptions about pore pressure. The recent compilation of McGarr and Gay [1978] is particularly convenient for this.

Horizontal stresses in southern Africa (Figure 6) are available from a number of overcoring measurement in deep mines [McGarr and Gay, 1978]. The two solid lines marked BY-HYD in this figure are computed from Byerlee's law, assuming hydrostatic pore pressure; one line corresponds to horizontal σ_1 and the other to horizontal σ_3. Most of the measured values are contained within these lines, as they should be if Byerlee's law correctly gives the limiting value of crustal stress. However, a better fit is obtained if pore pressure is assumed to be zero, giving the two curves marked BY-DRY. Since these deep mines are often reported to be "dry" [McGarr et al., 1975], perhaps $P_p=0$ is reasonable. If P_p had the maximum value, equal to the total vertical stress, then the horizontal stresses should fall along the lines marked LITH.

Stresses have been measured in the U.S. primarily by hydraulic fracturing in sedimentary basins (Figure 7). Except for two points, all measurements of the minimum compression fall correctly to the right of Byerlee's law with hydrostatic pore pressure. The two points refer to crystalline rocks in South Dakota (H) and near Denver (RMA); they could be explained by slightly subhydrostatic pore pressure.

Measurements from deep Canadian mines in crystalline rocks are collected in Figure 8 [McGarr and Gay, 1978]. Byerlee's law for hydrostatic pressure (BY-HYD) is seen to enclose most of the data points, as

does the upper branch in the African example (Figure 6). This would imply imminent thrust faulting in these two areas, at these depths. Proximity to the lower branch (the deeper African measurements, for example) implies imminent normal faulting.

We conclude that Byerlee's law satisfactorily brackets most measured values of horizontal crustal stress to about 4 km, for hydrostatic pore pressure. In one area where the stresses measured exceed the hydrostatic branch of Byerlee's law, dry rocks and, therefore, reduced pore pressure, are plausible.

McGarr and Gay (1978) made a similar comparison of measured stresses and an experimentally derived failure criterion. They used the Coulomb criterion which, in the same form as equation (1), was

$$\tau = 0.6\ \bar{\sigma}_n$$

and found that over a fairly broad region of the Gulf Coast this criterion was met for hydrostatic pore pressure.

Extrapolation below 4 km

Byerlee's law appears to satisfactorily predict maximum or minimum horizontal stress to about 4 km and it is of interest to extrapolate the law to greater depths. Eventually temperature effects will play a greater role, and to take these into account we need to consider rock plasticity. We follow Goetze and Evans [1979] and use experimental studies of olivine based on the assumption that properties of this mineral will control the stress levels in the lower crust and upper mantle.

Current understanding of the flow law of olivine was summarized by Goetze (1978) and the strength, $S = \sigma_1 - \sigma_3$, is shown as a function of temperature in Figure 9; all these experimental data have been adjusted to a common strain rate of 10^{-5}sec^{-1}.

Strength in the ductile regime is probably independent of pore pressure so this complication can be avoided. However, strength is dependent on strain rate and temperature; Goetze and Evans argued that for a bending lithospheric slab $\dot{\varepsilon} \equiv 10^{-15}\text{sec}^{-1}$; their derived geotherm agreed with published geotherms. The maximum and minimum horizontal stresses that can be supported as a function of depth are shown in Figure 10. The curving portions, marked OL, come from the olivine flow law [Goetze, 1978, equation 7] extrapolated to 10^{-15}sec^{-1}, and using a linear geotherm $T = 350 + 15x$, where x is depth and T is degrees in k. The linear portions, marked BY-HYD, are from Byerlee's law (equation (3)) with hydrostatic pore pressure. Maximum stresses can be shown another way (Figure 11) in terms of the horizontal minus the vertical stress. The influence of pore pressure other than hydrostatic is shown by the lightly dotted lines with different λ values; λ is the ratio of the pore pressure to the total vertical stress.

DISCUSSION

Figure 11 illustrates graphically the limits within which crustal stress must lie based on the assumptions (a) that rocks are fractured and that friction on fractures controls the stress at shallow depths, and (b) that the creep properties of olivine control the stress below about 25 km and (c) that the effective stress principle operates for friction but not for creep. There are several implications worth noting.

(1) There is a region of high strength between the surface and about 50 km depth. The lower limit is temperature-dependent; 100° would shift the zero-stress region about 10 km.
(2) The crust has close to zero strength at the surface and at depths below about 50 km. This is important in any discussion of bending in a lithospheric slab [Goetze and Evans, 1979].
(3) Assuming that the full strength of a crustal section is attained and that horizontal stresses have the values as given in Figure 11, then average stress could reach about 130 MPa or 360 MPa depending on whether horizontal extension or compression was occurring.
(4) The level of pore pressure (as shown by the value of λ) has great influence on crustal stress levels. For example, if the rocks are dry (λ=0, as in Goetze and Evans [1979]), then average values could reach 250 or 500 MPa. If pore pressure were lithostatic (λ=1), then crustal stress would be zero; in other words, the total stress would be hydrostatic and equal to the vertical stress.

What is known about pore pressure level at depth? Unfortunately almost nothing, so that this parameter is almost totally unconstrained at this time. One new inference may be drawn from a recent analysis of crustal permeability [Brace, 1979, in press]. Crystalline rocks to about 8 km appear to have a permeability comparable to that of sandstone. Bredehoeft and Hanshaw [1968] found that pore pressure under these circumstances could not be much different than hydrostatic, for times relevant to most geologic phenomena. The same conclusion applies here for crystalline rocks which outcrop at the surface. They concluded that high pore pressure required a thick argillaceous section to act as an impermeable blanket. This may be generally true not only for sedimentary but also for crystalline rocks.

Acknowledgments. Part of the work reviewed here was supported by the National Science Foundation under contracts No. 76-12479 and No. 77-13664. Brian Evans made helpful suggestions.

REFERENCES

Barton, N., The shear strength of rock and rock joints, Int. J. Rock Mech. Min. Sci., 13, 255-279, 1976.

Batzle, M.L., and G. Simmons, Geothermal systems: rocks, fluids, fractures, Amer. Geophys. Un. Monograph No. 20, 233-242, 1977.

Brace, W.F., Pore pressure in Geophysics, Amer. Geophys. Un. Monograph No. 16, 265-273, 1972.

Brace, W.F., Permeability of crystalline and argillaceous rocks: status and problems, Int. J. Rock Mech. Min. Sci., in press, 1979.

Brace, W.F., and A.H. Jones, Comparison of uniaxial deformation in shock and static loading of three rocks, J. Geophys. Res., 76, 4913-4921, 1971.

Bredehoeft, J.D., and B.B. Hanshaw, On the maintenance of anomalous fluid pressure, Geol. Soc. Amer. Bull., 79, 1097-1106, 1968.

Byerlee, J.D., Brittle-ductile transition in rocks, J. Geophys. Res., 73, 4741-4750, 1968.

Byerlee, J.D., Friction of rocks, PAGEOPH, 116, 615-626, 1978.

Dieterich, J.H., Time-dependent friction in rocks, J. Geophys. Res., 77, 3690-3697, 1972.

Goetze, C., The mechanisms of creep in olivine, Phil. Trans. R. Soc. Lond. A., 288, 99-119, 1978.

Goetze, C., and W.F. Brace, Laboratory observations of high-temperature rheology of rocks, Tectonophysics, 13, 583-600, 1972.

Goetze, C., and B. Evans, Stress and temperature in the bending lithosphere as constrained by experimental rock mechanics, Geophys. J., in press, 1979.

Griggs, D.T., F.H. Turner, and H.C. Heard, Deformation of rocks at 500 to 800°C, Geol. Soc. Amer. Memoir 79, 39-104, 1960.

Jaeger, J.C., and N.G.W. Cook, Fundamentals of Rock Mechanics, 585 pp., John Wiley & Sons, Inc., New York, 1976.

McGarr, A., and N.C. Gay, State of stress in the Earth's crust, Ann. Reviews of Earth & Plan. Sci., 6, 1978.

McGarr, A., S.M. Spottiswoode, and N.C. Gay, Relationship of mine tremors to induced stresses and to rock properties in the focal region, Bull. Seismol. Soc. Amer., 65, 981-993, 1975.

Nekut, A., J.E.P. Connerney, and A.F. Kuckes, Deep crustal electrical conductivity; evidence for water in the lower crust, Geophys. Res. Lett., 4(6), 239-242, 1977.

Ohnaka, Mitiyasu, The quantitative effect of hydrostatic confining pressure on the compressive strength of crystalline rocks, J. Phys. Earth, 21, 125-140, 1973.

Paterson, Mervyn, Experimental Rock Deformation: The Brittle Field, Springer-Verlag, New York, 254 pp., 1978.

Stesky, R.M., The mechanical behavior of faulted rock at high temperature and pressure, PhD Thesis, Massachusetts Institute of Technology, 197 pp., July 1975.

Stesky, R.M., W.F. Brace, D.K. Riley, and P.Y.F. Robin, Friction in faulted rock at high temperature and pressure, Tectonophysics, 23, 177-203, 1974.

Tullis, Jan, and R.A. Yund, Experimental deformation of dry Westerly granite, J. Geophys. Res., 82, 5705-5718, 1977.

Wang, C.Y., N.H. Mao, and F.T. Wu, Mechanical properties of clays at high pressure, J. Geophys. Res., in press, 1979.

Zoback, M.D., and J.D. Byerlee, Permeability and effective stress, Amer. Assoc. of Petrol. Geol. Bull., 59, 154-158, 1975.

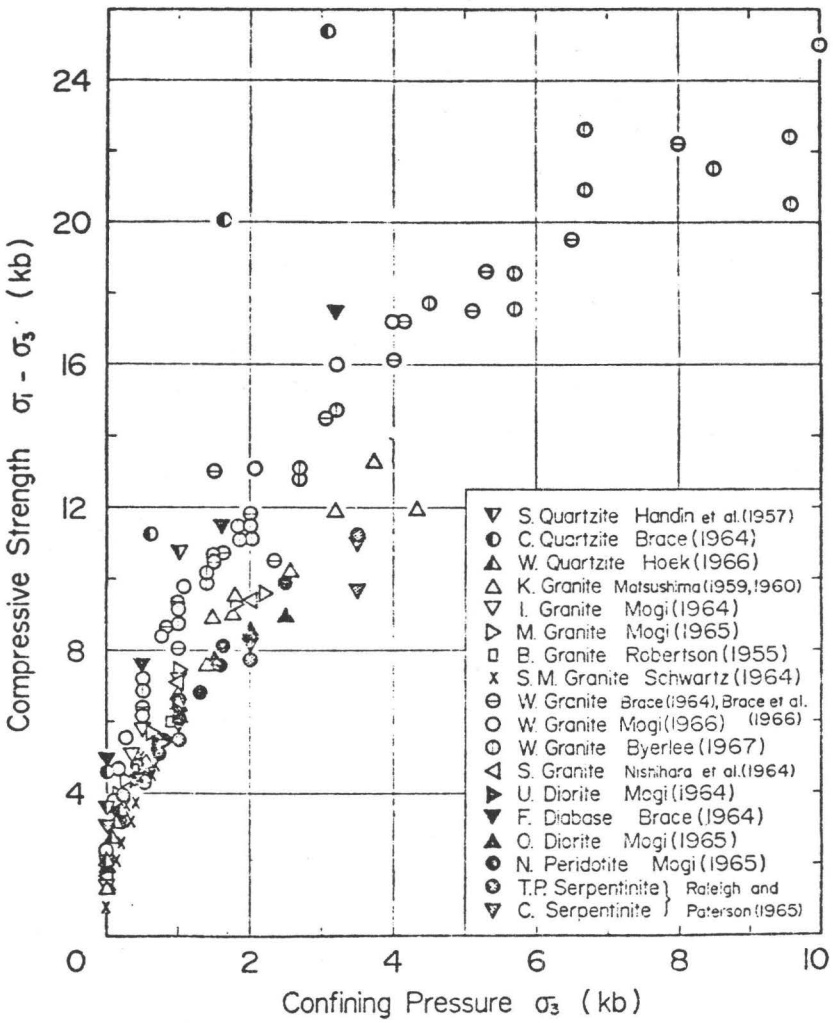

Fig. 1: Compressive fracture strength of silicate rocks as a function of pressure [Ohnaka, 1973].

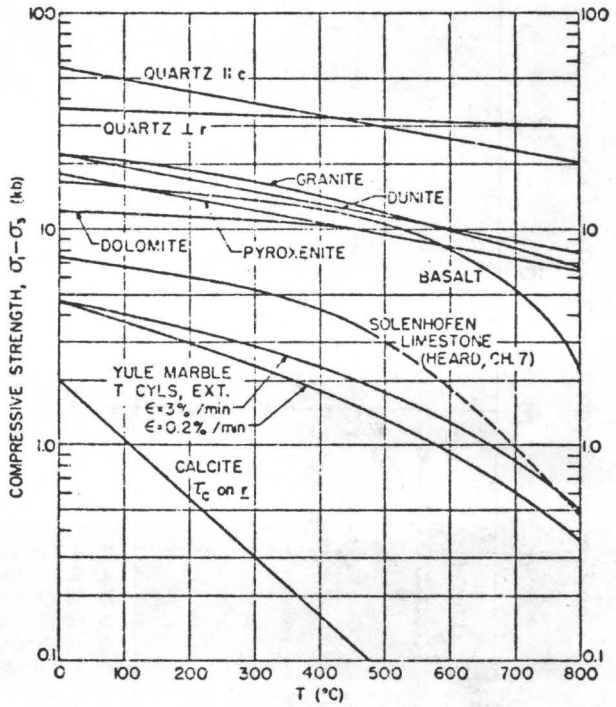

Fig. 2: Effect of temperature on the fracture strength of several rocks [Griggs et al., 1960].

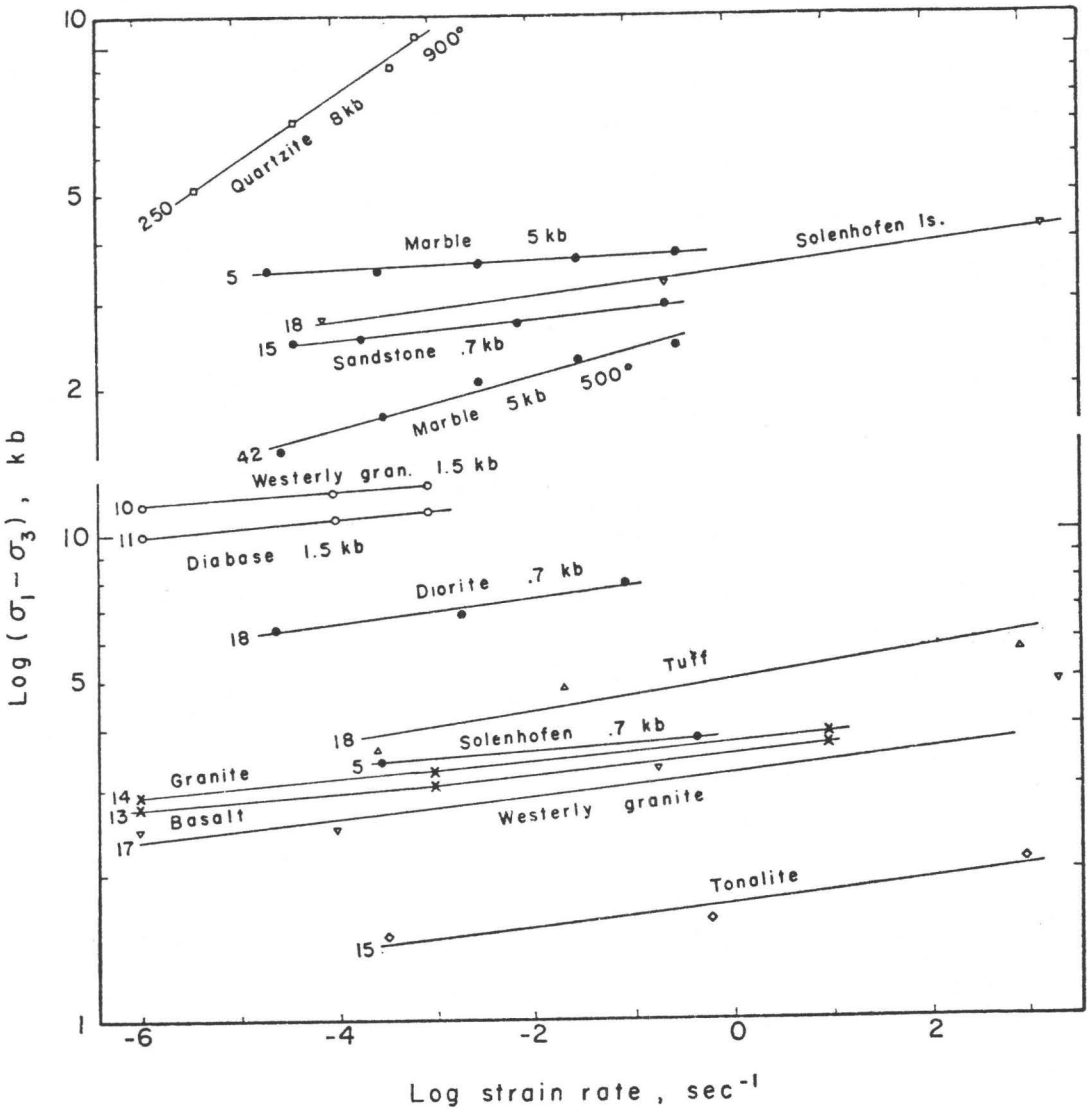

Fig. 3: Effect of strain rate on fracture of various rocks [Brace and Jones, 1971]. Except as noted on the lines, all measurements were made at room pressure and temperature. The numbers at the left end of each line through the data points reflect the slope of that line; the number is the percent increase in stress difference per 10^3 increase in strain rate.

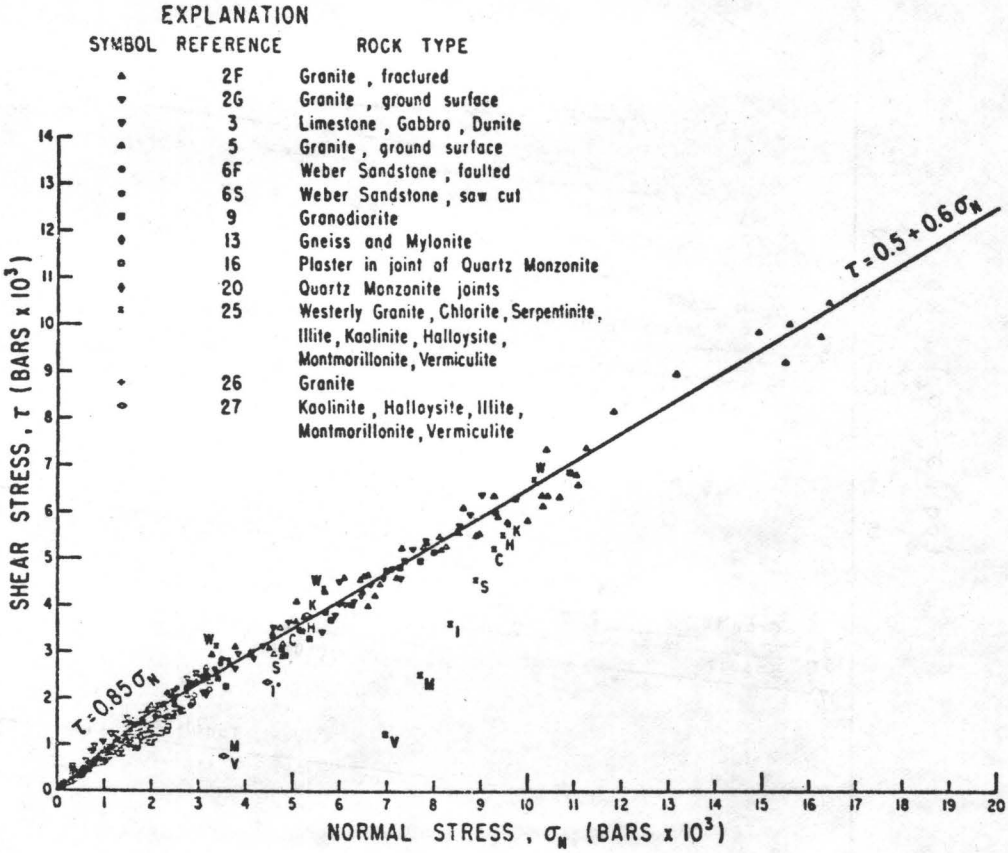

Fig. 4: Shear stress vs normal stress at maximum friction for a variety of rock types [Byerlee, 1968].

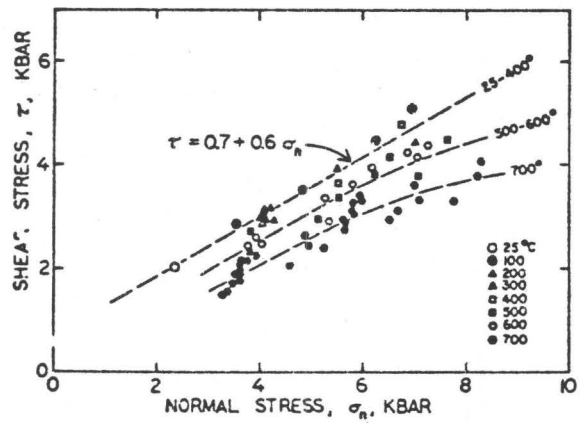

Fig. 5: Effect of temperature on maximum friction of faulted gabbro [Stesky et al., 1974].

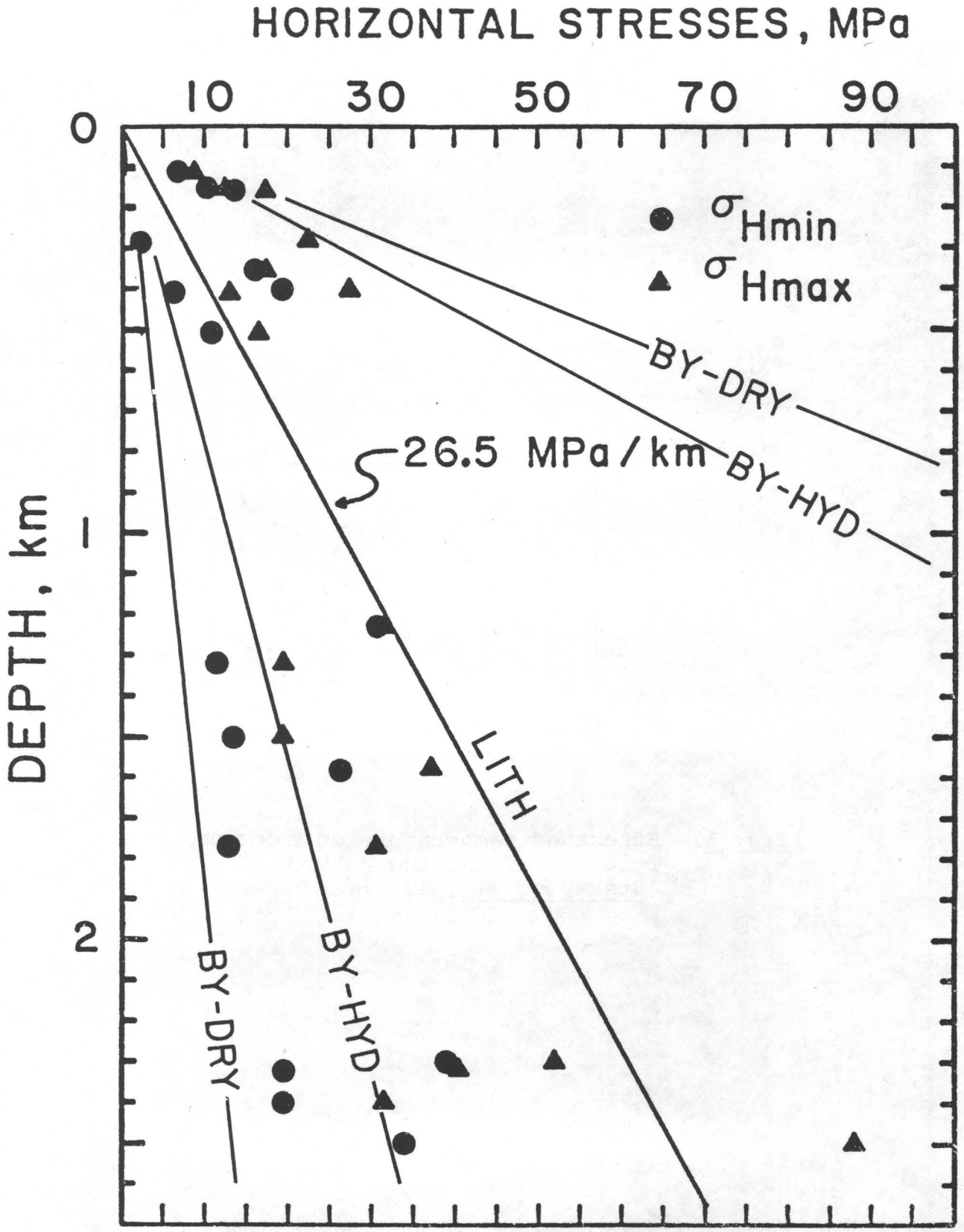

Fig. 6: Total horizontal stresses measured in southern Africa [McGarr and Gay, 1978]. The vertical total stress gradient (26.5 MPa/km) is shown along with Byerlee's law (BY) for hydrostatic pore pressure (HYD) and zero pore pressure (DRY).

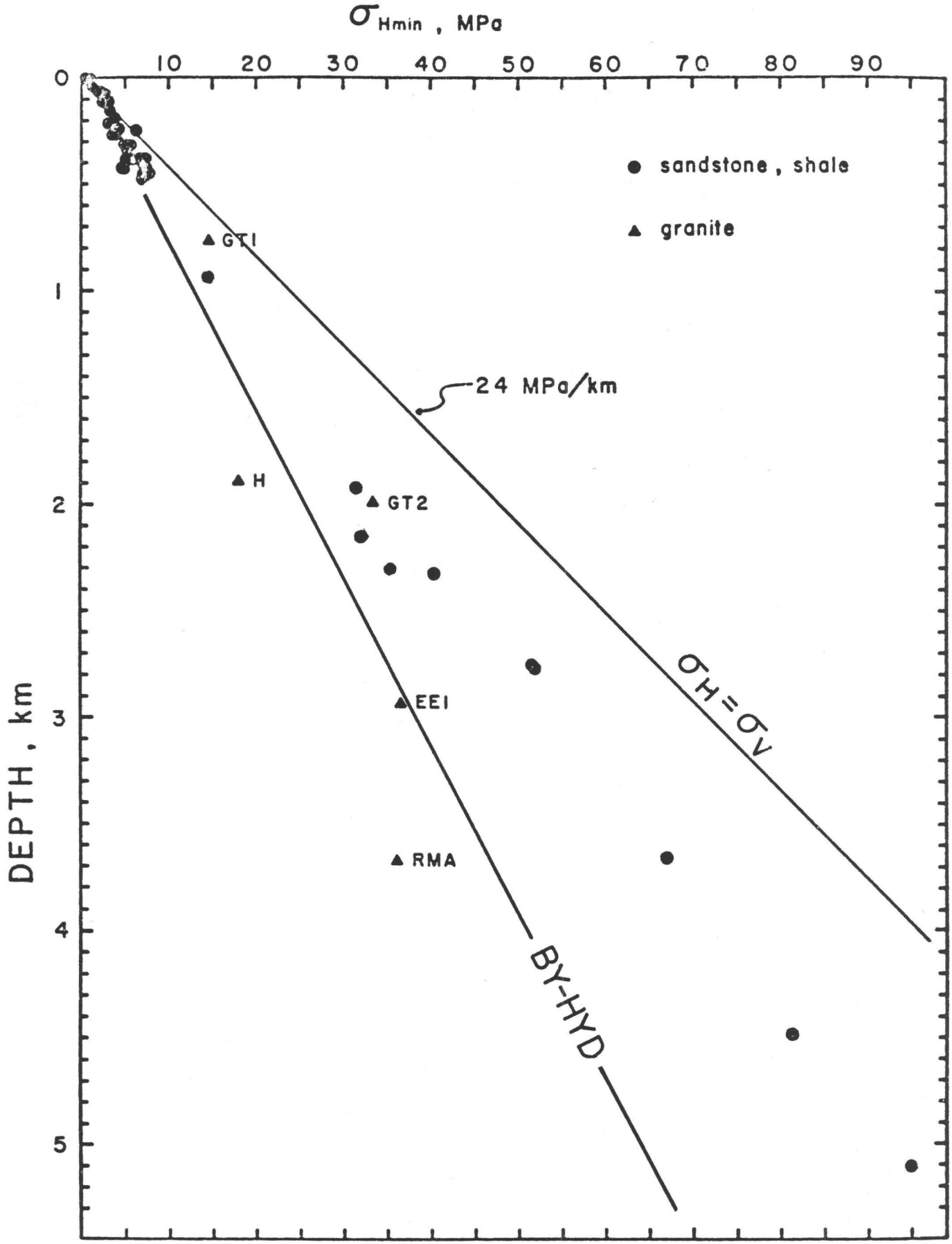

Fig. 7: The minimum total horizontal stress measured in U.S. Symbols as in Fig. 6 [McGarr and Gay, 1978].

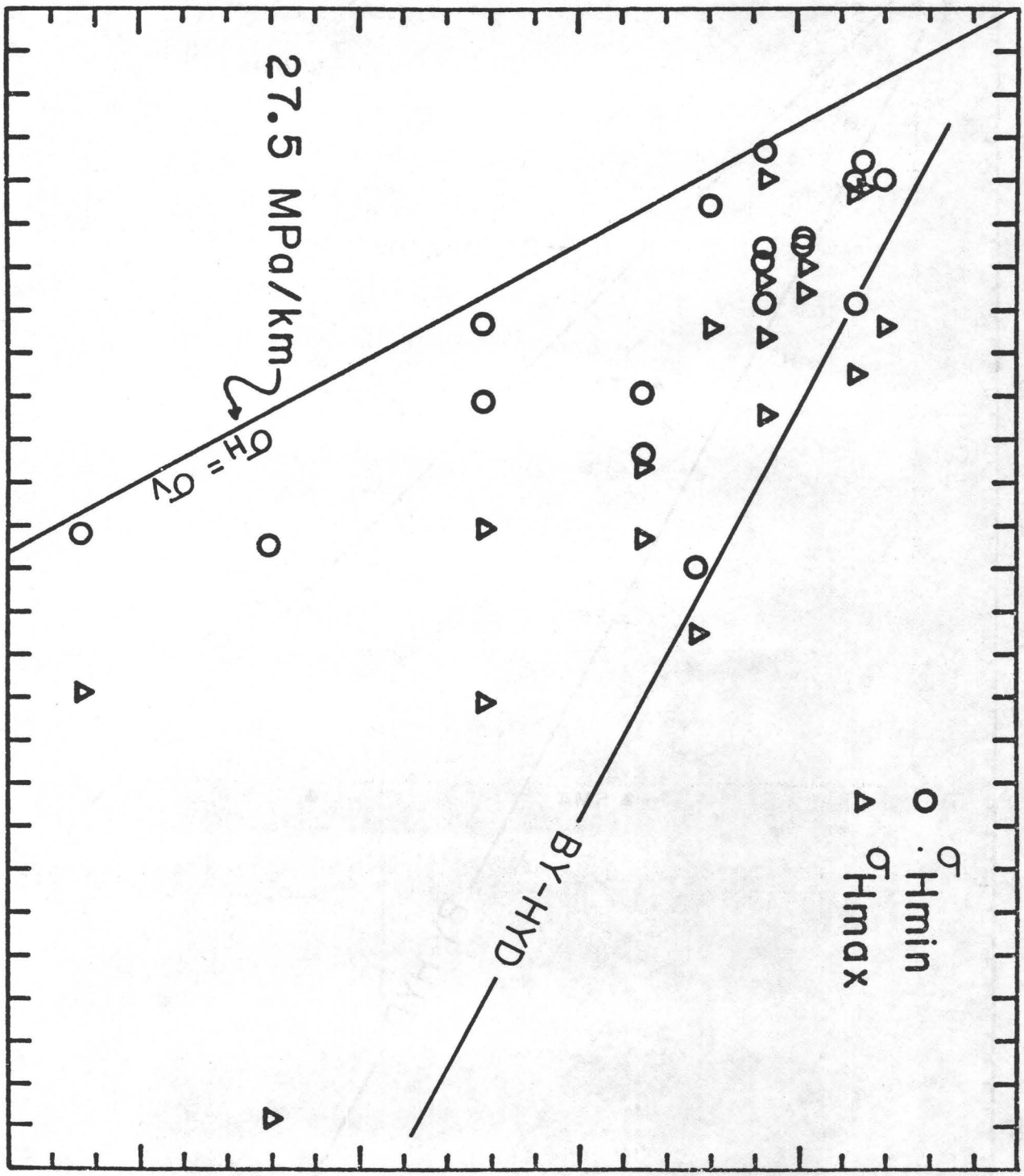

Fig. 8: Total horizontal stresses measured in Canada [McGarr and Gay, 1978]. Symbols as in Fig. 6.

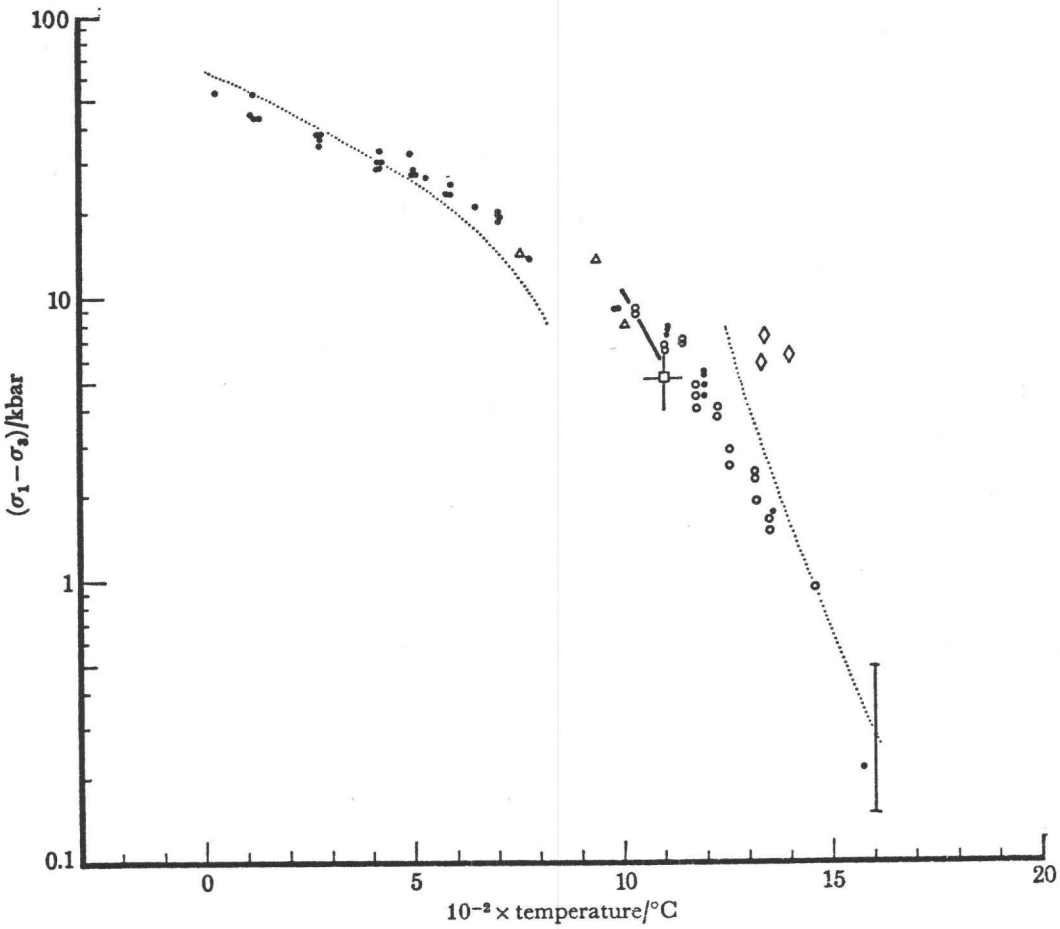

Fig. 9: Experimental creep data for dry olivine aggregates [Goetze, 1978] corrected to a common strain rate of 10^{-5} sec^{-1}.

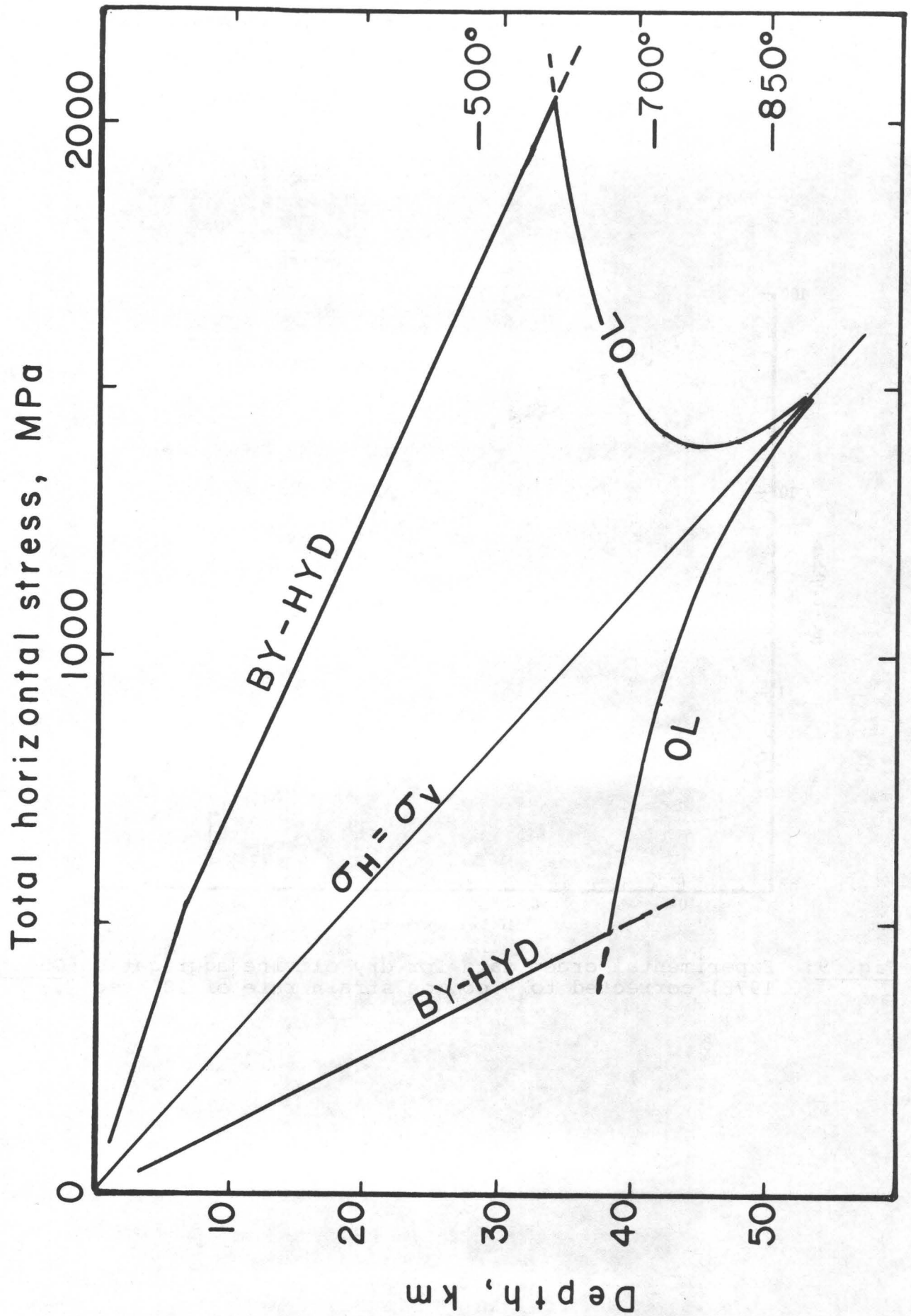

Fig. 10: Limiting values of total horizontal stress as a function of depth, based on Byerlee's law with hydrostatic pore pressure (BY-HYD) and the olivine flow law (OL) adjusted to a strain rate of 10^{-15} sec^{-1}.

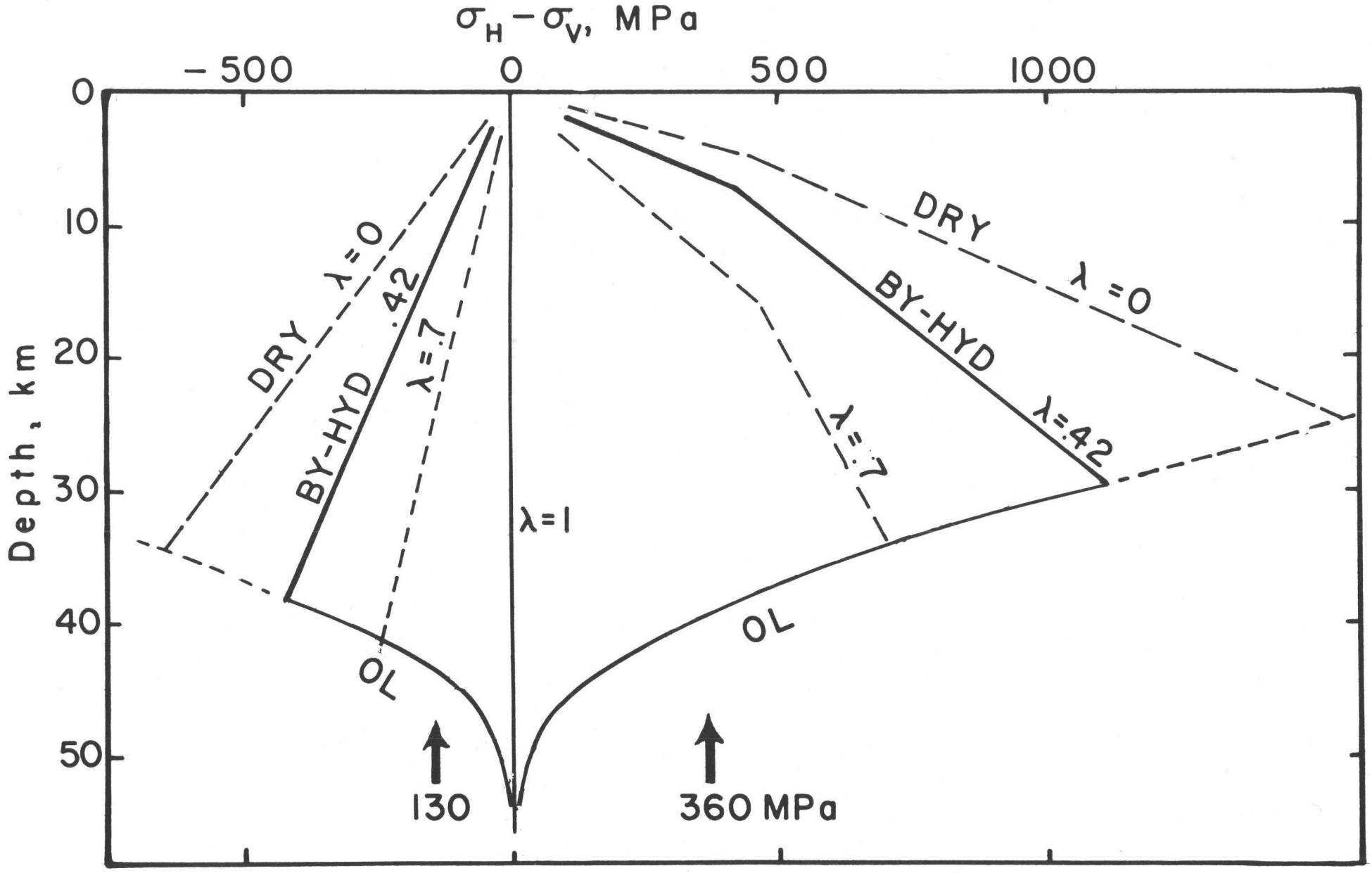

Fig. 11: Difference between maximum or minimum horizontal stress and the vertical stress as a function of depth. Values of λ give pore pressure level. Arrows at bottom give mean stresses for HYD cases.

STRENGTHS OF FAULT ZONE MATERIALS ABOVE 15 KILOMETERS DEPTH AND TECTONIC STRESSES

by

Francis T. Wu
Department of Geological Sciences
State University of New York
Binghamton, New York 13901

ABSTRACT

Fault zones observed at surface and down to a depth of 2 kilometers consist of breccia of various sizes and composition, often not related to the wall rock in the vicinity and altered to various extent, sand-silt size rock particles and clays such as montmorillonite, illite, chlorite and kaolinite etc. The fine-grained portion is commonly referred to as fault gouge. The variations in the relative amounts of breccia and gouge and the types of minerals present in the gouge, as well as pore pressure render fault zones highly heterogeneous. Based on the geochemistry of clays, it is highly possible that the fault zone constitution down to depths of 12-15 kilometers will remain basically the same. Individual fault zones observed may attain widths from a few centimeters to a few kilometers; the width in general correlates with the length of the fault and the total displacement along the fault.

The various materials in the fault zone have diverse strengths. Of the strengths of intact rocks, rock on rock contacts and the clay gouge, the gouge is the weakest. A montmorillonite-rich gouge could be more than an order of magnitude weaker than the intact rocks and about one order of magnitude weaker than the rock on rock frictional contacts. Illitic, chloritic and kaolinitic gouges could be twice or three times as strong as montmorillonitic gouge. Thus, based on available experimental data, if gouge in a fault zone is extensive enough to form a connected body, the strength of the zone would be in the order of a few hundred bars to 800 bars. Pore pressure, temperature and dehydration reaction effects could lower the strength further.

INTRODUCTION

Considering the constitution of fault zone as a whole will allow us to provide an additional constraint on the state of stress in the crust as the major fault zones are stress relief valves for the crust. Although it has not been possible to observe the interior of active fault zones at depth where earthquakes are generated, it is possible to infer the mineralogical composition of the zones from exhumed inactive fault zones, as well as surface, tunnel or drill hole samples in active fault zones (Wu et al., 1979), and our knowledge concerning the behavior of clays under moderate temperature and pressures (up to 400°C and 400Kb).

In general, the fault zones have been found to be very heterogeneous; the hetergeneities include fault zone material differences, geometry of the zone as well as pore pressure differences. One would imagine that under such circumstances, several release mechanisms may operate there, and the search for one unifying mechanism that starts all faulting is probably unrealistic. So far relatively little is known about the mechanical behavior of the fault zone materials. It is generally agreed that brittle or earthquake-like behavior of such materials exist above a level of about 12 to 15 km in a continental crust and below it flow dominates and mylonites are the products of continuous faulting. At present, most of the major continental earthquakes have been found to occur along pre-existing faults that are mature, i.e., displacements have been recurring along such faults with some regularity; in such fault zones mechanical comminution and hydrothermal alteration could conceivably have created a very substantial amount of intrafault materials that are distinctive mineralogically from the surrounding rock. In the oceanic crust or in and around the subduction zone weaknesses may arise due to the presence of hydrothermally altered rocks or subducted sediments.

As the weakest link in a chain controls the strength of a chain, our attention should focus on the determination of the mechanical properties of the weaker materials or mechanisms that would weaken the fault zone materials. Experimental evidences are accumulating that some of the commonly observed fault gouge components are almost one order of magnitude weaker than frictional resistance under the crustal pressure conditions. There are a number of fault zone conditions and many different types of fault zone materials yet to be simulated in the laboratory studies.

While single focal mechanism tells precious little of the direction of the tectonic stresses not to mention the magnitude, a group of earthquakes in a very small area with diverse focal parameters allow us to delimit the direction of the maximum compressive stress; if we adopt certain laboratory derived failure criteria, we can then estimate the teconic stresses needed to activate the faults.

These and other faulting related topics are discussed in the present report.

CHARACTERISTICS OF FAULT ZONES

It is interesting to ponder how the first continental earthquakes took place when the continents were faultless. Perhaps such a state never existed; as the primordial continents drifted and accreted while the earth was cooling down; they were badly broken to start with. In any case, most of the modern day shallow earthquakes on the continent are known to be associated with established fault zones and no "virgin earthquakes" has been confirmed.

Many of the major active continental faults are either present day or ancient plate boundaries. Thus, San Andreas fault is a present day boundary, although its location is probably determined by the ancient subduction as revealed by the presence of Mesozoic melange, ultrabasics, etc.; the A-erh-Chin fault in Sinkiang, China and the Chi-lien fault complex of Kansu, China are apparently late and early Paleozoic plate boundaries respectively (Li et al., 1978). Some faults seem to be located in the middle of a block without apparent major geological discontinuities across it; these are probably a result of presence of tectonic stress and static propagation of ruptures. It is evident that such processes as intrusion of igneous bodies and the hydrothermal reactions in the country rock may weaken the crust.

Throughout geological times, as the crustal stresses changed, the motion along a fault may change in response. Such shifts are thought to have taken place along the A-erh-Chin and Chi-lien faults and the Tanlu faults in China (Chang, et al., 1974; figure 1). Changing from strike-slip to dip-slip fault must involve the smoothing out and the broadening of the fault zone, as the asperities will be eliminated by motions of the fault different in directions and incorporated into the fault zone.

As many of the large shallow earthquakes are generated within a range of about 2.5 kilometers to 15 kilometers below the surface, knowledge concerning the constitution of fault zones at those depths is needed in order to understand the earthquake processes. But our primary evidence of the characteristics of fault zones is obtained from outcrops of these zones near the surface, in relatively shallow tunnels (down to about 2 kilometers) and from core samples in recently started drill holes (Liechti and Zoback, 1979). Probably the inactive zones we observe at the surface actually represent, in most cases, fault zones at depth during their active phases, but because the zones had, most likely, undergone changes, such as consolidation and metamorphism, that took place after the activities had ceased, the mineralogy, the amount of water present, the grain size, the microscopic structures of the materials will not be the same as those during the time of activity. Thus, in using information from shallow outcrops of active or inactive fault zones, interpretation becomes important. The definition of cataclastic rocks by Higgins (1971) is aimed for use in describing available fault zone outcrops and should be used with care when discussing active fault zones at depth. For example, the term cataclasites is used by Higgins to distinguish from gouge by the criteria of presence of

"primary cohesion". The molecular bonds among clay particles are certainly "primary" and we know that clay powder under 1 or more kb confining pressure can become solid mass, especially if some drainage can be provided.

The major active and inactive fault zones observed in surface outcrops or in tunnels are in general broad zones in which a number of parallel or subparallel faults are grouped around the main fault zone. The rocks in the immediate vicinity of the main zone are usually intensely jointed. Some of the close-in joints may be filled with slickend-sided fine grained materials identical in mineralogy and appearance to those in the fault zone. The transition from the country rock to the fault zone is not always clear-cut and seldom can one define a single plane of discontinuity. Close to the country rocks, relatively large breccia are common. They tend to decrease in size further inside the fault zone. Figure 2 summarizes our observations of the general appearance of a part of a fault zone; the breccia "b" include rocks from the walls close by and rocks that are quite foreign to the local outcrops of wall rocks. These breccia could be quite fresh but may also be badly fractured internally and deeply altered such that they disintegrate quite easily. Sedimentary rocks caught in the fault zone sometimes show tight folding (figure 3), while similar rocks in the surrounding area are only jointed, indicating the softening of rocks inside the fault zone.

The breccia are sometimes in contact with each other but more often than not they are surrounded by fine-grained gouge. In various parts of a fault zone gouge may become dominant, reaching a few meters in thickness. The gouge is a mixture of small pebbles, sand-silt-sized rock particles and clays; the clay content of gouges range from a few percent up to 50 percent in 30cm cubes. Common clay minerals such as montmorillonite, illite, chlorite, kaolinite and mixed-layer clays have all been found in gouges (Wu, 1978). The temperature stability fields of these minerals are somewhat different; chlorite can exist to 450°C, montmorillonite and illite are stable up to about 400°C and kaolinite to about 250°C. Thus, depending on the local geothermal gradient and the availability of water, clays can conceivably exist in fault zones down to a level of ten kilometers or more (Roberson, et al., 1979). The model of fault zones filled with crushed materials, with a good portion of clay gouge, is consistent with the interpretation of the low velocity and the relatively low density nature of the zone (Wang et al., 1978).

MECHANICAL PROPERTIES OF FAULT ZONE MATERIALS

Of the fault zone materials, we know the strengths of the intact rocks and the frictional strengths of the rock on rock contacts reasonably well (Ohnaka, 1978, Byerlee, 1978 among others); data accumulated over many years in several laboratories delimit the properties under crustal conditions quite clearly. On the other hand, works on simulated gouges have just begun (Wang et al., 1979a,

1979b); the stress strain behavior of the clays are found to be markedly different from rocks or frictional contacts in several ways, but as the fluid drainage conditions, strain rates, temperatures, initial textures, as well as the particular composition of gouge, be it 30% montmorillonite and 70% kaolinite or 50% montmorillonite and 50% montmorillonite and illite mixed layers, etc., are all factors that may influence strongly the properties of gouge, the need for extensive work in clays and natural gouges is self evident.

Figure 4 summarizes the relevant data. The intact rocks are at least twice as strong as the frictional contacts for many different strain rates and types of rocks and, for frictional contacts, the surface conditions. The montmorillonite clays under the undrained conditions and at a strain rate approximately 10^{-5}/sec, the strength is below 325 bars. Recent data (figure 5) on hectorite, a trioctahedral smectite that is stable under higher temperature (up to 500°C), under 10^{-3}/sec strain rate show a strength of 600 bars; such clays are structurally more stable and the increased strength may be a consequence of this stability. But the effect of strain rate is very important. The dependence of stress-strain characteristics on strain rate is shown clearly in the case of kaolinite; at 10^{-4}/sec the curve is almost a straight line beyond 10% strain, while under 10^{-5}/sec the curve tends to flatten more beyond 40% strain (Wang et al., 1979b). It is interesting to observe that smectites, montmorillonite and hectorite are weaker than the others and peak strength and strain softening phenomena occur.

As Stesky et al (1974) have shown that temperature affects the frictional strengths very little in the 25-400°C range. For rocks, the general trend is an exponential decay in strength with increasing temperature, but again in the 25°-400°C range the drop is insignificant. Temperature effects on the strengths of clays above 500°C are not yet experimentally known. That clay should weaken under increasing temperature is deduced from thermal activation considerations (Mitchell, 1976). One additional thermal effect for clays within the range of 100°C-400°C is the dehydration or possibly even dehydroxylation reaction. Beyond 400°C, many clays will change into micas etc. with loss of water. Whether such reaction will cause sudden stress drop will depend on the rate of reaction and the permeability. Also, whether rehydration can happen when water becomes available again is an important consideration if one invokes this reaction for the recurrence of earthquakes in the same fault zone.

Clay materials are also known to creep extensively and the creep rate depends on the temperature as

$$\dot{\varepsilon} \sim e^{-E/RT}$$

where E has been found, under a few bars confining pressure and less than 50°C, to be 15-30 kcal/mole (Mitchell, 1976). Phenomenon such as creep fracture, i.e., extensive creep occurs before rupture could be one of the important processes in the fault zone.

In a mature fault zone as depicted in figure 2, the gross behavior of the fault zone can be described as follows, based on our knowledge of the mechanical behavior of the fault zone materials. As the tectonic shear stress is applied in a new cycle of activity, the fault zone materials will initially undergo a large amount of straining, resulting in the relative rotation and translation of the fault breccia as well as distortion of the gouge among the breccia, thus disorienting the slip planes and the alignment of clay particles developed in the previous cycles. As the stress gradually increases, failure may occur in various points in the fault zone, where the material in the zone contains more smectites or the pore pressure is abnormally high or both. Such failure will be arrested and only a small earthquake will take place if the failure conditions have only been attained locally. Some of the slipping could occur along old existing planes, but as these planes are likely to have distorted and rotated into less advantageous direction with respect to the existing stress, new slip planes are likely to be created. In other words, in each episode, the stress strain curve will assume the strain softening characteristics shown in figure 5, instead of having only the residual strength, the strength along zones with clay platelets rotated into the slipping direction (Wu et al., 1979). On the other hand, if the zone as a whole has been strained to near the peak strength at most of the points inside the zone, then a slight displacement at one point may cause a chain reaction as the displacement at one point will cause stress concentration on neighboring point and enable that point to reach the unstable strain softening portion of the constitutive relation. As Stuart (1978) and Rudnicki demonstrated theoretically that strain softening is one of the possible ways to induce fault instability and sudden displacement along the fault,

For a major fault zone, the characteristics of the fault zone materials will change from place to place due to the change in the nature of the country rocks, the chemistry of the pore solution, the pore pressure, temperature, etc. In addition, the fault zone usually varies in width from section to section; it may be so narrow that two sides of the fault zone are interacting across the fault zone, such that the "asperity" has to yield before large displacements can occur. Certainly, the wide fault zone was probably created as the original asperities of various sizes are incorporated into the fault zone. As a result of the heterogeneity, the propagation of rupture is likely to include decelerations and accelerations. And the inhomogeneous strain of the fault zone will lead to continuous adjustment in the zone, whereby aftershocks may be generated, until the strain has attained equilibrium everywhere in the fault zone.

Two aspects concerning the experimental data on clays should be mentioned. We have used whole samples of compressed clay powder instead of thin clay wafers between saw cut rock plugs used by other investigators (Summers and Byerlee, 1976; Shimamoto, 1977). The rationale is that in fault zones exceeding a few meters wide, the gouge is usually massive enough that the properties of gouge itself

are important. On the other hand, in gouge filled joints the wafer analog is more appropriate. The other aspect is that only undrained conditions were used both in sample preparation and triaxial tests. Without doubt, the pore pressure condition in the sample is one of the most important parameters in controlling the strength and creep characteristics. Future experiements on controlled pore pressure experiment is most important. As far as the pore pressure in the fault zone itself, no direct knowledge is yet available. The very fact that hydrous minerals exist indicates an ubiquitous presence of pore solution and the low seismic velocity has also been taken to indicate high pore pressure. Questions as to whether the gouge would consolidate right after an earthquake, whether it would dilate and absorb water and whether with very low permeability, massive gouge would behave as though undrained are to be explored further.

The problem of faulting in oceanic crust is somewhat different, as the oldest oceanic crust is Cretaceous and the older crust is presumably consumed or incorporated into continental crust. New oceanic crust is created at the ridge through successive igneous intrusions and extrusions. Studies of exhumed oceanic crusts, ophiolites, DSDP (Deep Sea Drilling Project) cores and bottom dredging samples indicate that extensive metamorphism, changing basalts and gabbros to metabasalts, metagabbros and serpentinites, and hydrothermal alteration, generating clays and other hydrons minerals (Stern et al., 1976; Donnelly et al., 1979). These processes take place mainly near the spreading center, but hydrothermal fluid circulation may exist a considerable distance away from the axis. The alteration is particularly noticeably along intrusive or extrusive contacts (Salisbury, et al., 1979). Thus the new crust is permeated with weaknesses at the start. In addition, the fracture zones (transform faults) are loci of brecciation as well as hydrothermal alteration (Stern et al., 1976). Except along the fracture zones, the zones of weakness are probably discontinuous giving the oceanic crust strength.

The material strengths of the hydrothermally altered rocks will be the same as those of fault zones, on the other hand, as Raleigh and Patterson (1965) and Murrel and Ismail (1976) have shown that under high temperature, the action of shear stress may facilitate dehydration to take place, decreasing the strength of hydrous rocks by an order of magnitude and causing the material to behave brittly. Figure 7 illustrates the strength variations as a function of depth with a geothermal gradient of 25°C/km. It is seen that beyond 20 km, the strengths of the hydrated rocks decrease to the same order as those of clays under low temperatures.

The shallow normal faulting near the trench represent probably tensile failure along the weaknesses mentioned. The deeper earthquakes within the slab can conveniently be explained by the dehydration or melting. The shallow underthrust may be facilitated by the presence of subducted sediments as well as the hydrous minerals in the top part of the oceanic crust resulting from hydrothermal alteration.

FOCAL MECHANISMS AND TECTONIC STRESSES

As McKenzie (1959) and others have pointed out, the focal mechanism solutions of earthquakes only put very mild constraints on the direction not to mention the magnitude, of the earthquake-generating tectonic stresses when an individual earthquake is considered. We can easily imagine that because of the great contrast in strengths of intact and faulted rocks, repeated motions may take place along the existing faults without developing new ones, and the direction of the relative motion of the two sides of the fault (together with the orientation of the fault plane the local mechanism solution is completely determined) may relate closely to the past history of motion along the fault rather than the current state of stresses. Depending on the actual strength of the fault at the time of earthquake, the orientation and magnitude of the tectonic stress may vary widely and yet cause movements on different faults.

On the other hand, if we have a region of small enough areal extent, so that the tectonic stress there can be considered homogeneous, and in this region a number of faults in different orientations exist (these faults may include those that have had extensive movements or are zones with abundant hydrous minerals or are contacts between rocks of very different properties). Then after these faults have been activated, the sense of motion on these faults should allow us to narrow down direction of tectonic stresses. Also, with laboratory data on the strengths of fault zone materials, we may constraint further the direction and the magnitude of tectonic stresses needed to activate the faults.

For this study, we have used earthquake data from the vicinity of Taiwan where in an area of not more than 10^4 km^2, nine M 6 earthquakes took place since 1965, and good focal mechanism solutions have been obtained for them. Based on geological and geophysical investigations in this area, we expect the tectonic stresses here to be quite homogeneous (Wu, 1978b); the major plate boundary is further to the north and west and no major topographical or structural features is present nearby.

Let a right handed Cartesian coordinate system be associated with a fault plane such that X_1 is in the direction of the normal ($\vec{n}$) to the fault plane, X_2 in the direction of the displacement ($\vec{u}$) of the X_1 half space and X_3 is in the direction of the $\vec{n}\times\vec{u}$, the null vector (see figure 8). Also, let us choose a right-handed Cartesian coordinate system (X_1,X_2,X_3) for the principal stresses.

$$\begin{bmatrix} \sigma_1 & 0 & 0 \\ 0 & \sigma_2 & 0 \\ 0 & 0 & \sigma_3 \end{bmatrix} = \begin{bmatrix} S_1 & 0 & 0 \\ 0 & S_2 & 0 \\ 0 & 0 & 0 \end{bmatrix} \qquad -S_2 \text{ II}$$

where $S_1 = \sigma_1 - \sigma_3$, $S_2 = \sigma_2 - \sigma_3$ and $II = \begin{bmatrix} 1 & 0 & 0 \\ 0 & 0 & 0 \\ 0 & 0 & 1 \end{bmatrix}$

For simplicity, we shall choose $\sigma_3 = \sigma_2$ then

$$S = S_1 \begin{bmatrix} 1 & 0 & 0 \\ 0 & 0 & 0 \\ 0 & 0 & 0 \end{bmatrix} - S_3 \, II$$

The stresses in the fault plane coordinate system can be obtained by the transformation

$$S^1 = A^{-1} \; S \; A$$

where $A = a_{ij'}$, $i = 1, 3$; $j' = 1, 3$ and a_{ij} is the direction cosine between the X_i and X_j1 axes. $A^{-1} = A^t$. It can be seen that when $\sigma_2 = \sigma_3$ the spatial orientation of these two axes does not enter into the problem. In our study, the stresses on the fault plane are

σ_n = normal stress = $a_{11'} \, a_{11'} \, S_1 + S_3$

τ_{12} = shear stress in the direction of $-\vec{u}$

= $a_{11'} \, a_{12} \; S_1$

By simply requiring that for all earthquakes $\tau_{12} > o$, we may find the directions of tectonic stresses that are consistent with all the focal mechanisms. We could also impose a condition

$\tau_{12} < f(\text{depth})$

based on laboratory data then we may find the direction as well as the magnitude of stresses consistent with the mechanisms. In this case, when S_1 has a component in the opposite direction to the motion vector, the condition evidently is not satisfied. But even when S_1 has a component in the direction of the motion vector, it may not be enough to overcome friction. Thus if S_1 is not large compared to the strength of the fault, the region in which S_1 can lie will be smaller than the previous case when the strength of the fault is zero, and the possible region for S_1 can be narrowed down. At the same time, we can also estimate a minimum S_1 consistent with the criterion.

In figure 9, the circles beside each number show the region (shaded) of S_1 poles for which $\tau_{12}>0$ (they are exactly the same as the original focal mechanisms with the shaded areas as dilatation and blank areas as compression). The circle to the lower right of the previously mentioned circles are the results of successive superposition, where the shaded region is common to all the previous solutions. Thus to the southeast of Taiwan the direction of the maximum compressive stress is in the vicinity of S60°E with a plunge of about 10°. This direction agrees amazingly well with the geological structures on the island, the neotectonics there and the results of geodetic survey.

If we impose the "Byerlee's law" (Byerlee, 1978), i.e., set

$$\tau_{12} < 0.5 + 0.6\sigma_n$$

we find that S_1 has to be of the order of 60kb before all earthquakes are activated. If we use Murrel and Ismail's data (figure 7), about 20kb is needed mainly due to the shallow (<15 km) events, as the dehydration has not set in by then. If we use a combination of clay data and dehydration data then the stress can be lowered down to within 1 kb.

CONCLUSIONS

In regions where major mature faults are present in the direction of maximum tectonic shear stress, the shear stress in the region cannot exceed the shear strength of the fault zone. If our interpretation of the constitution of the fault zones at depth is correct, then the shear stress in the crust could be 300 bars if chlorite clays are present, based on available low temperature, high pressure laboratory data. As lower strain rate, higher temperature and higher pore pressure all tend to lower the strength of gouge, the stress could be lower than the numbers mentioned above. Besides, faulting is a dynamic process that involves the propagation of an instability which could be induced, for example, by sudden release of water by dehydration of hydrous minerals such as clays.

We should emphasize that the research on fault zone and the mechanical properties of fault zone materials is not yet sufficient; only through the study of many fault zones in different country rocks and tectonic settings and of the mechanical properties of likely fault zone materials under various physical conditions can we understand more fully the problems of faults and faulting.

ACKNOWLEDGEMENT

The research in this report is prerformed under the support of USDI-USGS-EHRP contracts: 4-08-0001-16802 and 14-08-0001-18213. Assistance by Robert Albert and Michael Muller is greatly appreciated. My colleague H. Roberson contributed toward my understanding of the geochemistry of clay. Dr. R. Martin generously provided his laboratory facilities for our gouge experiments.

REFERENCES

Byerlee, J. D., Friction of Rocks, PAGEOPH, 116, 615-626, 1978.

Chang, W. Y., and Members of the Tectonics maps committee, Institute of Geology, Academy of Sciences, China, Preliminary note on the basic tectonic features and their developments in China, Scientia Geologica Sinica, no. 1, 1974.

Higgins, M. W., Cataclastic Rocks, USGS Prof. Paper 687, 1-97, 1971.

Li, C. Y., Y. W. Liu, B. O. Zhu, I. M. Feng, and H. Q. Wu, The tectonic history of Qingling and Qilian mountains (in Chinese), Geological Contributions for International Exchange, volume 1, p. 174-187, 1978.

Liechti, R., and M. D. Zoback, Preliminary analysis of clay gouge from a well in the San Andreas Fault zone in Central California, Proc. of Conf. VIII. Analysis of actual Fault zone in Bedrock, USGS Open-file report 79-1239, 268-275, 1979.

Mckenzie, D. P., The relation between Fault Plane solutions for earthquakes and the directions of the principal stresses, Bull. Seism. Soc. Am., 59, 591-601, 1969.

Mitchell, J. K., Fundamentals of Soil Behavior, Wiley & Sons, N. Y., 1976.

Murrel, S. A. F., and I. A. W. Ismail, The Effect of decomposition of hydrous minerals on the mechanical properties of rocks at high pressures and temperatures, Tectonophysics, 31, 207-258, 1976.

Ohnaka, M., The quantitative effect of hydrostatic confining pressure on the compressive strength of crystalline rocks, J. Phys. Earth, 21, 125-140, 1973.

Raleigh, C. B. and M. S. Patterson, Experimental deformation of serpentinite and its tectonic implications, Jour. Geophys. Res., 70, 3965-3985, 1965.

Roberson, H. E., F. T. Wu and R. Albert, Clay minerals in fault gouge from deep mines in Idaho, to be presented at 1979 Fall National AGU Meeting.

Salisbury, M. H., T. W. Donnelly, and J. Francheteau, Geophysical Logging in DSDP Hole 417D, manuscript for DSDP reports, 1979.

Shimamoto, T., Effects of fault gouge on the frictional properties of rocks: An Experimental study, Texas A&M Univ., 1977.

Stern, C., M. J. DeWitt, A. J. R. Lawrence, Igneous and metamorphic processes associated with the formation of Chilean ophiolites and their implication for ocean floor metamorphism, Seismic Layering and Magnetism, Jour. Geophys. Res., 81, 4370-4380, 1976.

Stesky, R. M., W. F. Brace, D. K, Riley, and P. Y. F. Robin, Friction in faulted rock at high temperature and pressure, Tectonophysics, 23, 177-203, 1974.

Stuart, W., Quasi-static earthquake mechanics, Rev. of Geophys. and Space Phys., 17, 1115-1120, 1979.

Summers, R., and J. D. Byerlee, A note on the effect of fault gouge composition on the stability of frictional sliding, Int. J. Rock Mech. Min. Sci., 14, 155-160, 1977.

Wang, C. Y., W. N. Lin and F. T. Wu, Constitution of the San Andreas Fault zone at depth, Geophys. Res. Letters, 5, 741-744, 1978.

Wang, C. Y., N. H. Mao and F. T. Wu, The mechanical property of montmorillonite clay at high pressure and implications on fault behavior, Geophysical Res. Letters, 6, 476-478, 1979a.

Wang, C. Y., N. M. Mao, and F. T. Wu, Mechanical properties of clays at high pressure, Jour. Geophys. Res. (submitted), 1979b.

Wu, F. T., L. Blatter and H. Roberson, Clay gouge in the San Andreas Fault System and their possible implications, PAGEOPH, 113, 87-96, 1975.

Wu, F. T., Mineralogy and physical nature of clay gouge, PAGEOPH, 116, 655-689, 1978a.

Wu, F. T., Recent Tectonics of Taiwan, J. Phys. Earth, 26, Suppl. S265-299, 1978b.

Wu, F. T., H. E. Roberson, C. Y. Wang and N. H. Mao, Fault zones, Gouge and mechanical properties of clay under high pressures, USGS-EHRP Conference VIII, 1979.

TABLE I FOCAL MECHANISMS USED.(Wu, 1978b)

No.	Date	Origin Time	Lat.	Long.	Plane 1 Az.Pi	Plane 2 Az. Pi	Dep km	P Az.Pi	T Az.Pi	Type
5	170565	171932.8	22.41	121.26	14.4	106.32	80	155.20	55.26	SS
11	260268	105015.0	22.76	121.47	290.50	130.40	8	302.6	185.69	T
12	141170	075820.0	22.82	121.36	82.50	250.40	26	75.5	165.83	T
13	040172	031650.7	22.50	122.07	290.30	53.42	6	85.5	346.57	T
14	250172	020624.0	22.50	122.37	71.0	161.0	29	116.0	26.0	SS
17	240472	095721.2	23.60	121.55	130.40	339.48	29	247.2	340.68	T
18	220972	195727.4	22.37	121.16	6.5	265.70	8	203.40	355.45	T
20	230375	073236.5	22.74	122.80	148.7	237.3	21	103.5	193.5	SS
22	230375	160149.2	22.70	122.57	140.0	230.5	6	95.4	185.4	SS

*Katsumata and Sykes (1969).

FIGURE CAPTIONS

Fig. 1 The changing nature of faulting through geological ages along major fault zones in China (adapted from Chang, et a., 1974). Tanlu fault and Ta-pieh mountains (eastern China) in a late Paleozoic, b. and c. in Mesozoic and Cenozoic (these two patterns alternated) and d. present.

Fig. 2. Schematic representation of a part of a fault zone; b. denotes fault breccia, lines indicate the slip planes in the gouge and the thick lines indicate a more prominent slip plane.

Fig. 3. The tight folding within a block of wall rock caught in a fault zone (Polaris fault in northern Idaho at 4300 ft. level).

Fig. 4. Peak shear strengths of intact rock (within the two curves on top, from Ohnaka 1978, rock on rock frictional contact ("the Byerlee's law", from Byerlee, 1978) and whole clay samples (from Wang et al., 1979a, and 1979b).

Fig. 5. Shear stress vs. longitudinal strain for hectorite at 10^{-3}/sec strain rate.

Fig. 6. Shear stress vs. longitudinal strain for well crystallized kaolinite at 10^{-4}/sec strain rate.

Fig. 7. Strength of hydrous rocks (Ismail & Murrel, 1976).

Fig. 8. Coordinate system for fault plane, stresses and displacement.

Fig. 9. Focal mechanisms in the vicinity of Taiwan.

Fig. 10. Successive superposition of regions of admissible maximum compressive stress axes to obtain a small region for P axes that satisfies all solutions. There are nine pairs of circles; the one on the left is the focal mechanism solution with region of admissible P as shaded areas; the one on the right represents the superposition of the shaded regions of the present and previous solutions.

Figure 1

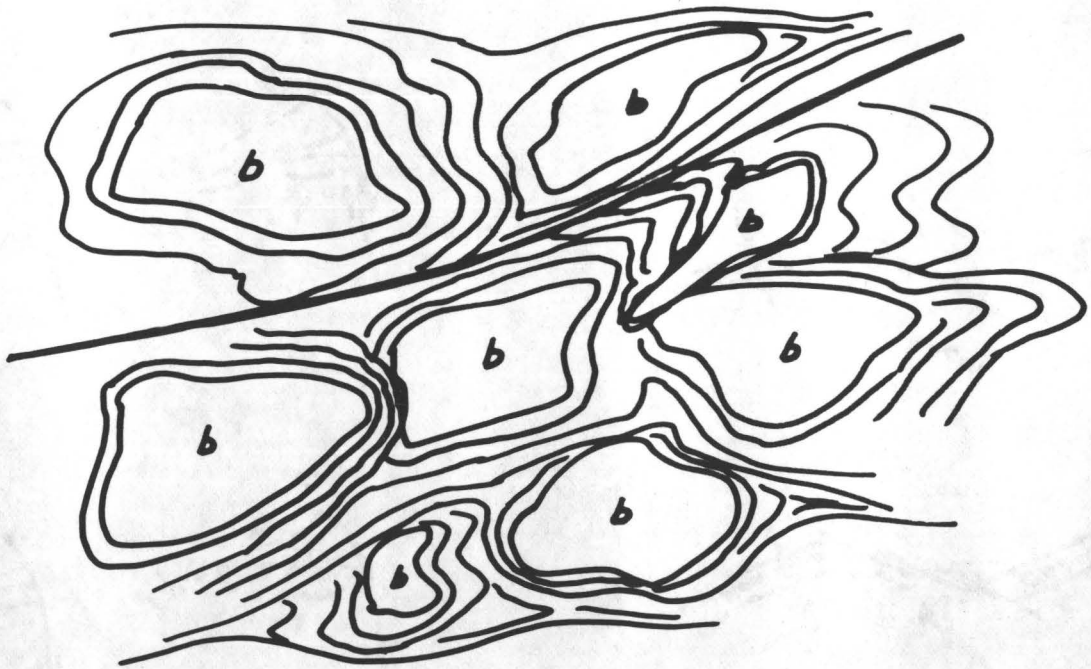

Figure 2

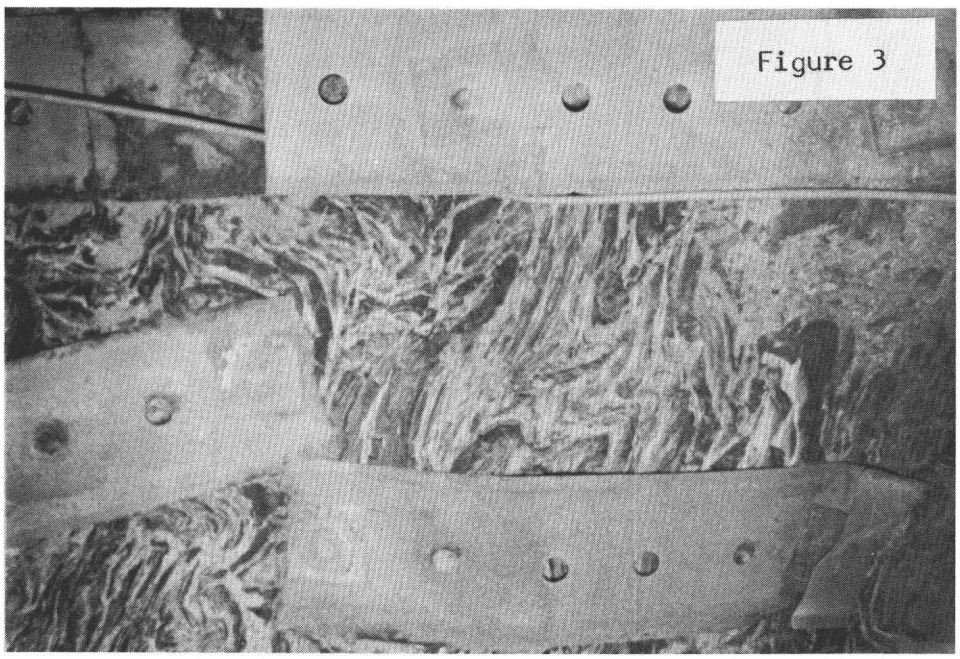

Figure 3

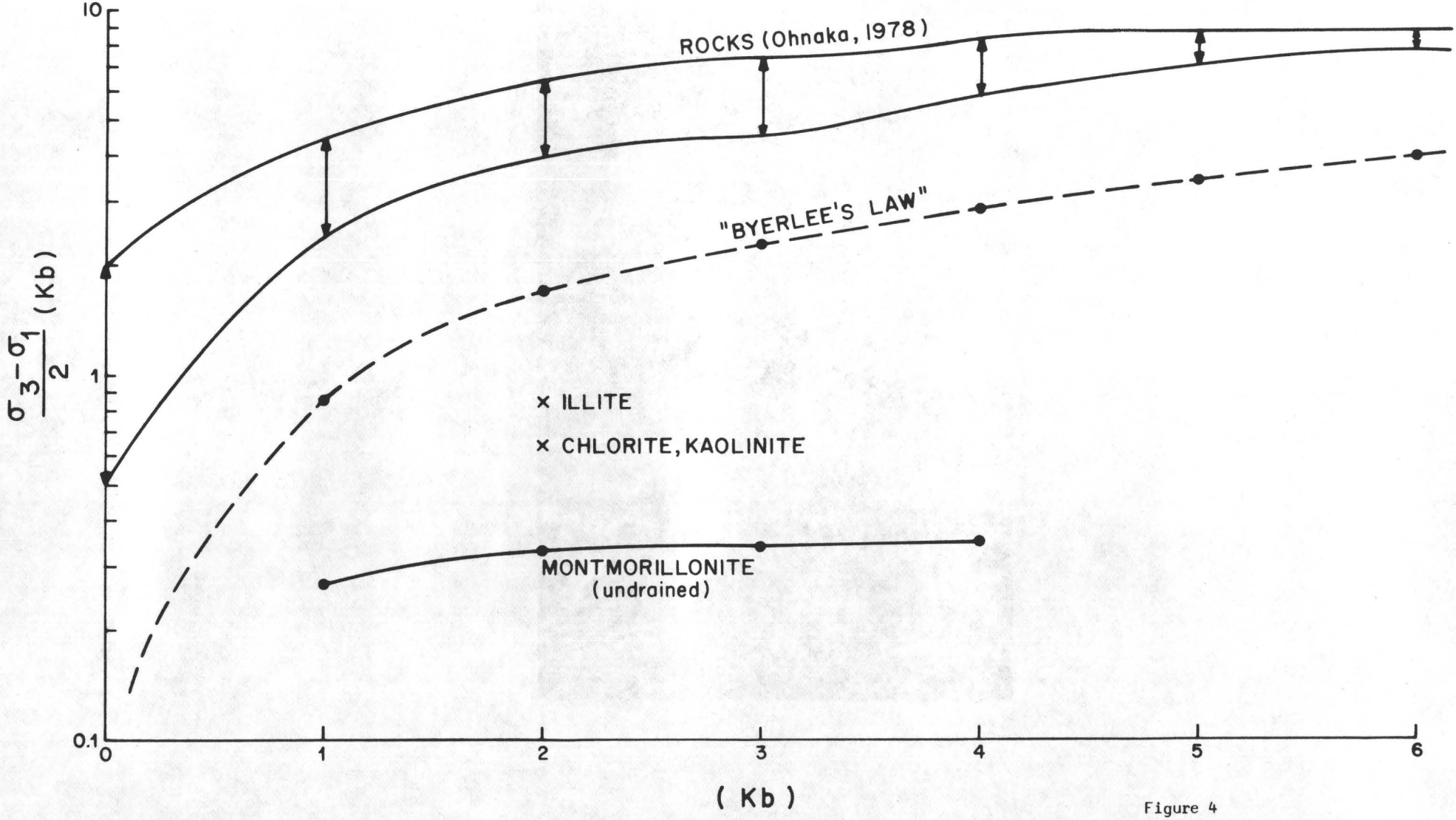
10
1
0.1
$\frac{\sigma_3-\sigma_1}{2}$ (Kb)
ROCKS (Ohnaka, 1978)
"BYERLEE'S LAW"
× ILLITE
× CHLORITE, KAOLINITE
MONTMORILLONITE
(undrained)
0
1
2
3
4
5
6
(Kb)

Figure 4

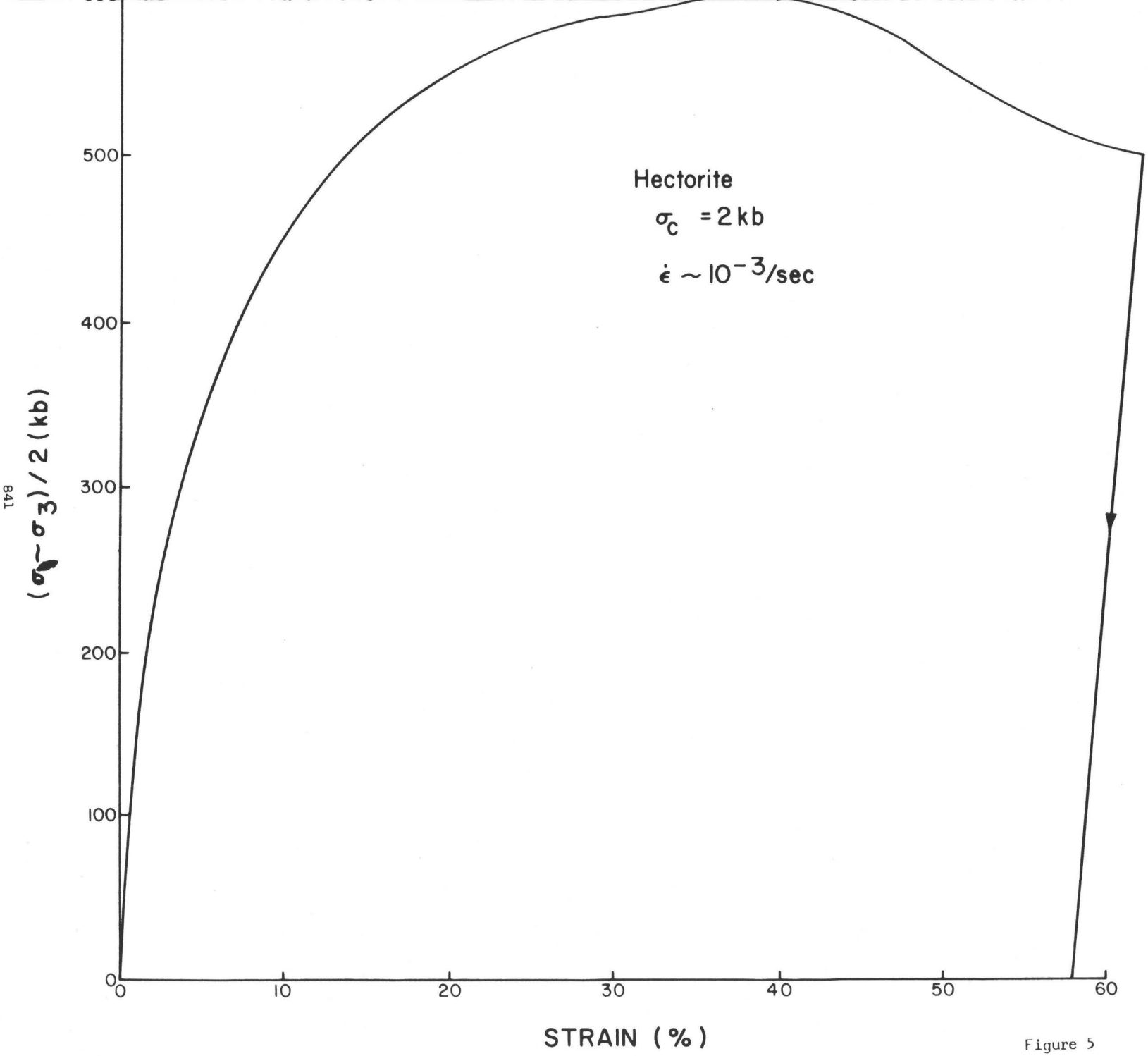
Hectorite
σ_c = 2 kb
$\dot{\epsilon} \sim 10^{-3}$/sec
$(\sigma_1 - \sigma_3)/2$ (kb)
STRAIN (%)
0
100
200
300
400
500
0
10
20
30
40
50
60

Figure 5

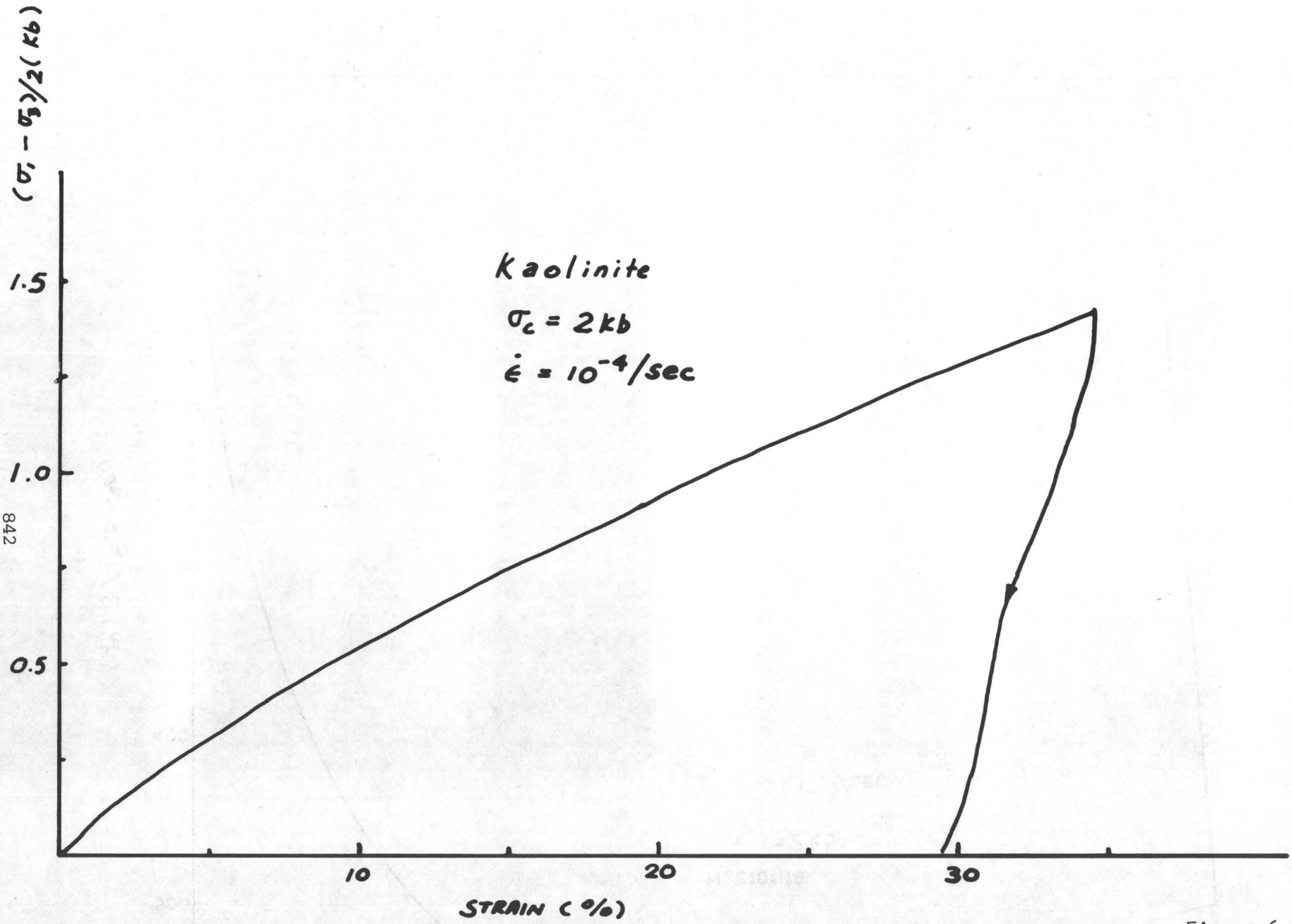
Kaolinite
σ_c = 2kb
$\dot{\epsilon}$ = 10^{-4}/sec
$(\sigma_1 - \sigma_3)/2$ (kb)
1.5
1.0
0.5
10
20
30
STRAIN (%)

Figure 6

Figure 7

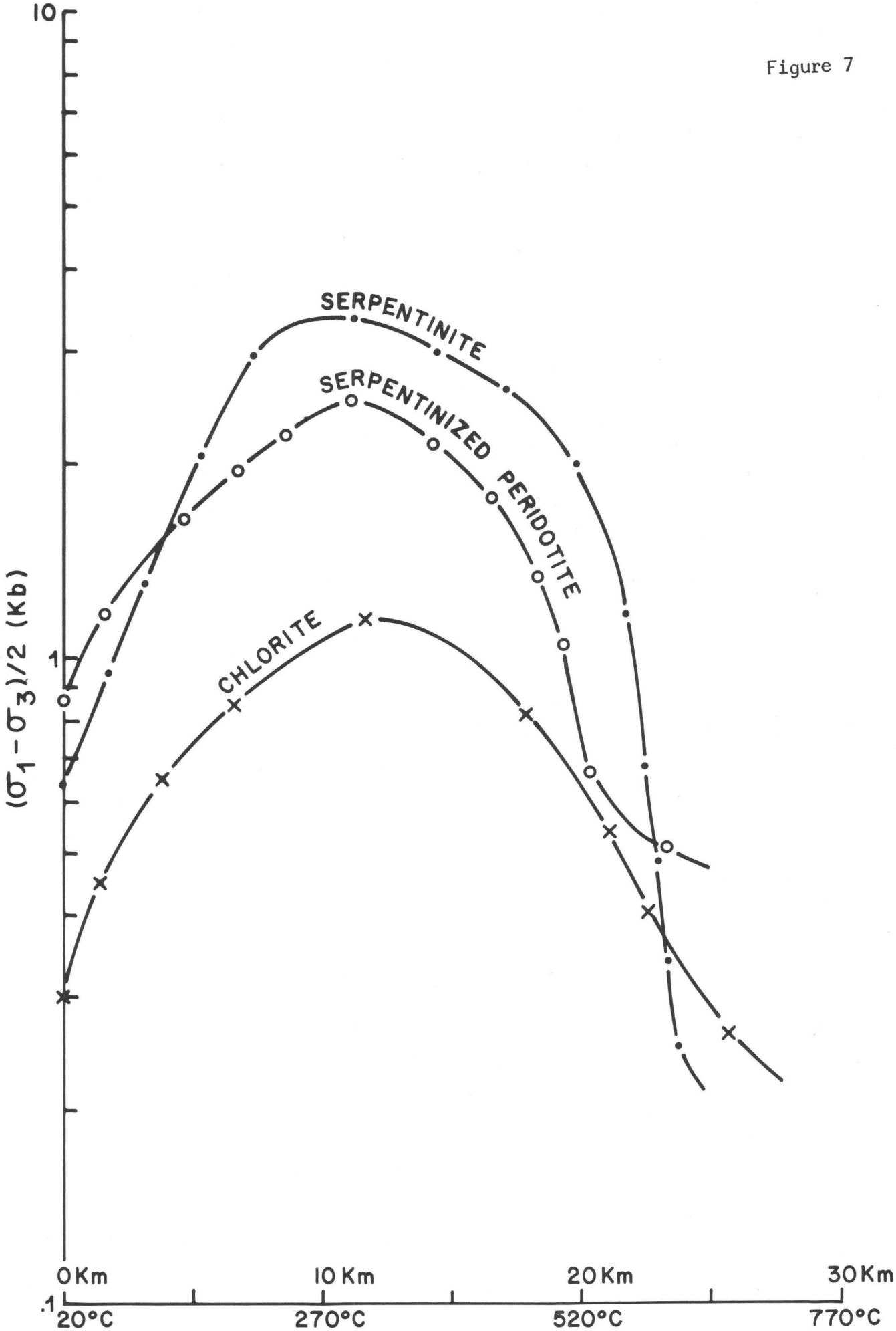
10
1
.1
$(\sigma_1 - \sigma_3)/2$ (Kb)
SERPENTINITE
SERPENTINIZED PERIDOTITE
CHLORITE
0 Km
10 Km
20 Km
30 Km
20°C
270°C
520°C
770°C

$$S' = \begin{bmatrix} -S'_1 & & \\ & -S'_2 & \\ & & -S'_3 \end{bmatrix}$$

$$S_1 > S_2 = S_3$$

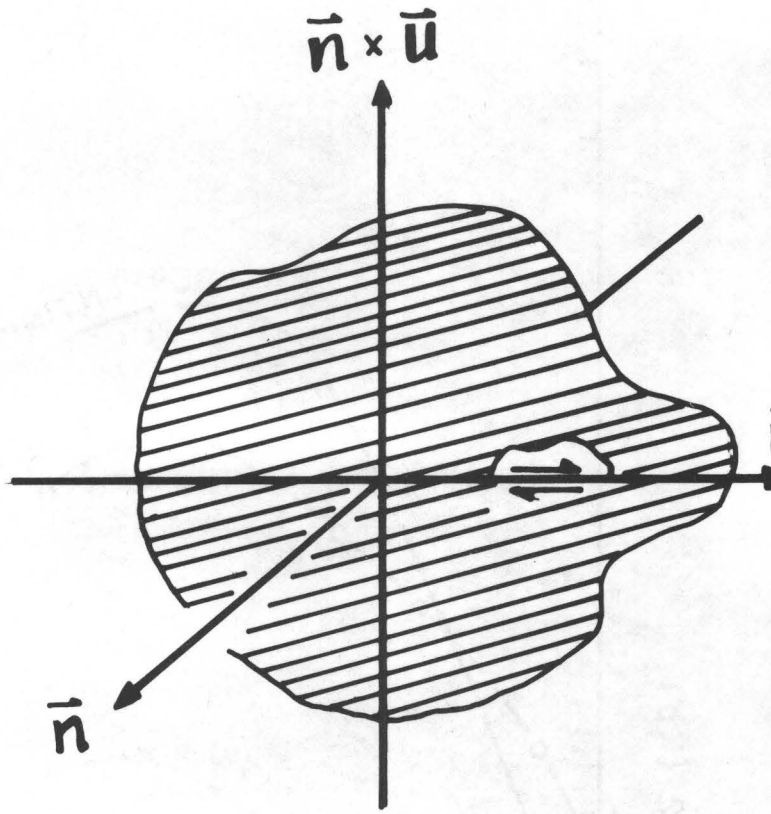

$$S = A^{-1} S' A$$

$$\vec{F} = S \cdot \vec{n}$$

$$S_{12} = \vec{F} \cdot \vec{u}$$

FOR SLIPPING

$$S_{12} < 0$$

OR

$$|S_{12}| \geq C_o + \mu |\sigma_n|$$

Figure 8

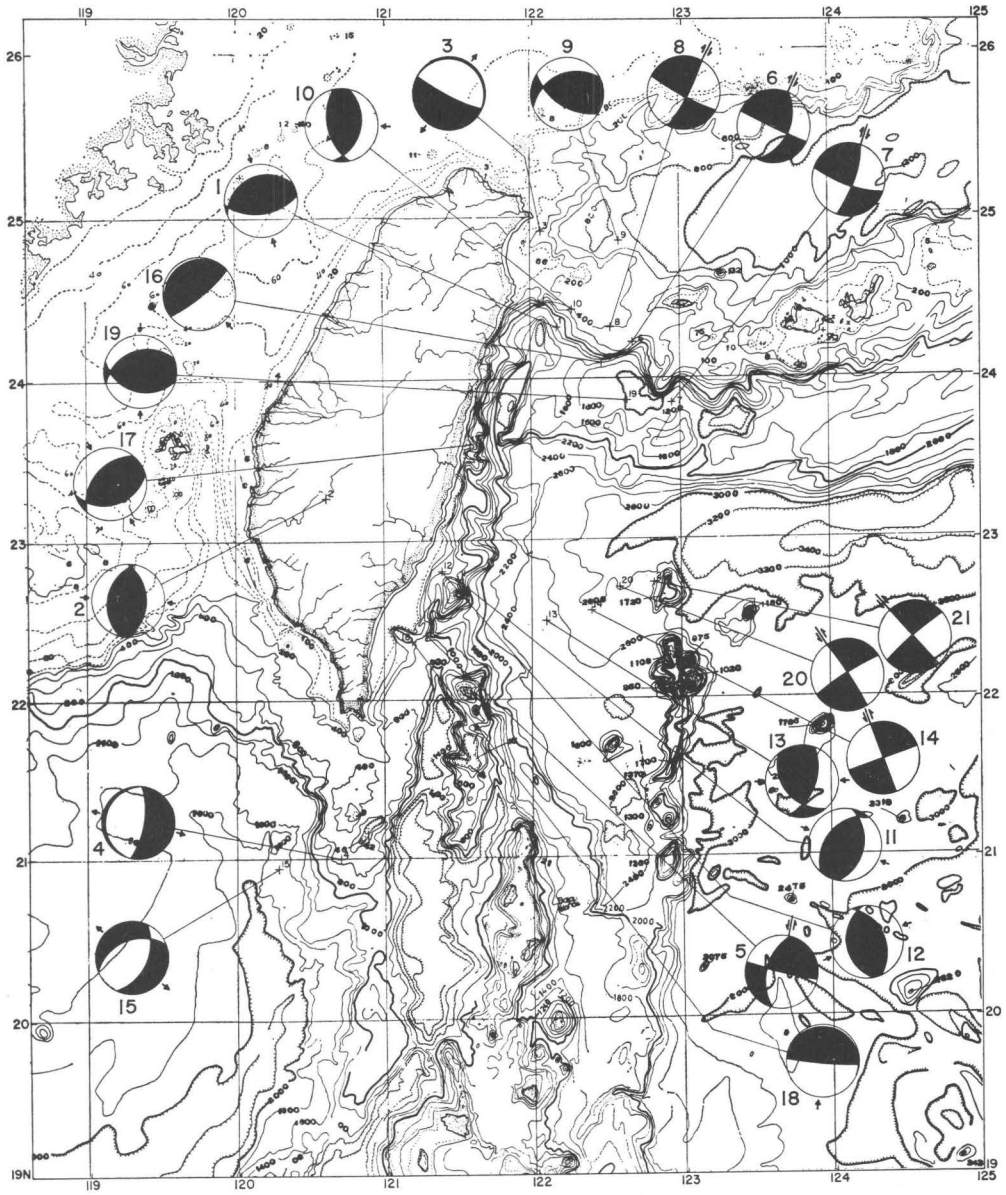
119
120
121
122
123
124
125
26
25
24
23
22
21
20
19N
1
2
3
4
5
6
7
8
9
10
11
12
13
14
15
16
17
18
19
20
21

Figure 9

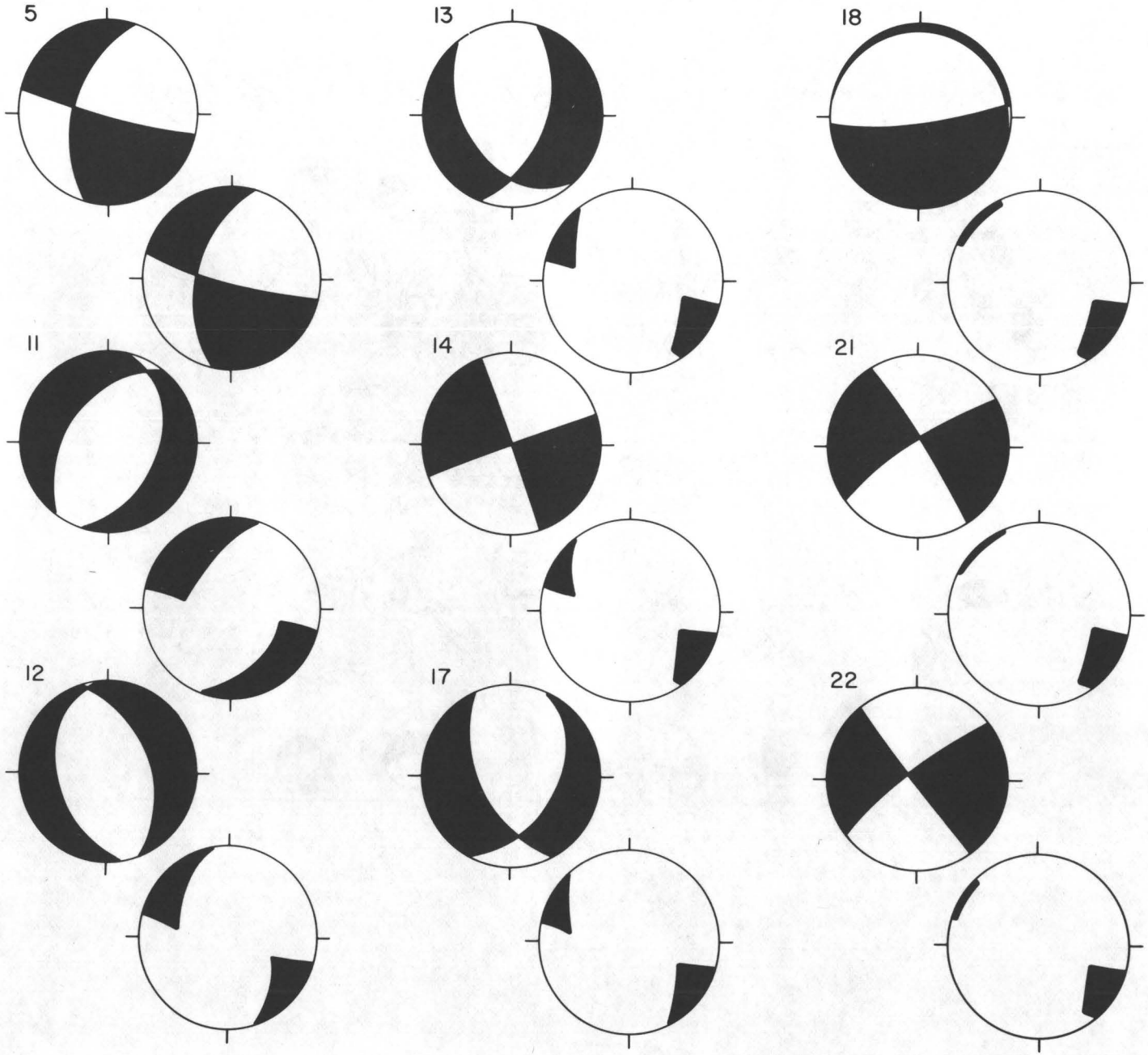

Figure 10

THE CONVERSION OF HEAT INTO MECHANICAL WORK BY MANTLE CONVECTION

Dan McKenzie
Department of Geodesy & Geophysics
Madingley Rise, Madingley Road
Cambridge CB3 OEZ, England

Gary Jarvis
Department of Physics, University of Toronto
Toronto, Ontario M5S 1A7, Canada

ABSTRACT

The rate at which heat is converted into mechanical work by a convective system can be estimated from the thermal expansion coefficient, the specific heat, and the depth of the layer if the convective heat flux is known. The heat flux from the mantle is reasonably well known, as is the rate of plate creation. The depth of the layer involved is more controversial, as is the thickness of the brittle layer beneath island arcs. Reasonable estimates for these two parameters yield mean stresses on plate boundaries of between 100 and 200 bars, with a probable upper bound of about 500 bars. These estimates are consistent with seismically determined stress drops.

INTRODUCTION

The shear stress acting on plate boundaries represents a resistive force against which work must be done to maintain the plate motions. This work must be supplied by the forces which maintain the motions, which are now generally believed to be bouyancy forces resulting from temperature induced density differences. Provided the efficiency with which the convective motions can convert heat into mechanical work is known, the convective heat transport can be used to estimate the available work and hence the upper limit on the mean shear stress acting on the plate boundaries. The advantage of this approach is that the stress estimate depends on parameters which are easier to measure than the stress itself, and is independent of the details of the flow. The principal difficulty with the argument concerns the contribution which phase changes make to the bouyancy forces, and hence with whether their contribution to the driving forces should be included. The other difficulty is the depth to which the convection associated with plate motions extends. If the whole mantle is involved the work available is greater than if the upper mantle alone maintains the motions. Various new arguments (see below) now support the older seismological evidence that the flow is confined to the mantle shallower than 700 km. If these arguments are correct, then the principal uncertainty in the calculations below concerns whether or not the olivine-spinel phase change in the sinking slabs occurs under equilibrium conditions, or whether the olivine is carried some distance into the spinel field before transformation occurs. This question is of considerable interest at present. Since the seismic velocity changes associated with the transformation are large, it should be possible to detect them using travel times of P and S waves. Furthermore, the pressures and temperatures involved are within the range of laboratory techniques, and hence the kinetics of the reaction can be investigated. Various attempts to discover large velocity

anomalies in the sinking slabs have not yet convincingly detected variations larger than those expected from the temperature differences (Mitronavas and Isacks,1971; Pascal et al., 1973; Solomon and Paw u, 1975; Hasegawa et al., 1978), and therefore it seems probable that the transformation does not occur in equilibrium. This conclusion is not compatible with Sung's (1976) laboratory investigation of the reaction kinetics, though the rates he determined may have been increased by the shear stress in his pressure cell. More work is required on both these problems. If the transformation does not occur in equilibrium then the arguments below place a probable upper limit on the mean stress of between 150 and 500 bars.

CONVERSION OF HEAT INTO MECHANICAL WORK

The equation which governs the conservation of thermal energy in a fluid is

$$\rho C_p(\partial_t T + \underline{u}\cdot[\underline{\nabla}T-(\underline{\nabla}T)_s]) = k\nabla^2 T + H + \tau_{ij}\frac{\partial u_i}{\partial x_j} \qquad (1)$$

where ρ is the density of the fluid, C_p the specific heat at constant pressure, T the absolute temperature, $\underline{u}$ the fluid velocity, $(\underline{\nabla}T)_s$ the adiabatic temperature gradient, k the thermal conductivity, H the rate of internal heat generation and τ_{ij} the deviatoric stress tensor. The derivation of (1) requires the second law of thermodynamics, but does not make any assumptions about the relationship between stress, strain and strain rate. If (1) is integrated over a volume V, we obtain in steady state

$$\int_V \rho C_p \underline{u}\cdot\underline{\nabla}T\, dV - \int_V \rho C_p \underline{u}\cdot(\underline{\nabla}T)_s dV = \int_S k\underline{\nabla}T\cdot\underline{dS} + \int_V H dV + \int_V \tau_{ij}\frac{\partial u_i}{\partial x_j} dV \qquad (2)$$

In steady state, conservation of mass requires

$$\underline{\nabla}\cdot\rho\underline{u} = 0 \qquad (3)$$

Hence the first term in (2) can be written

$$\int_S \rho C_p T\underline{u}\cdot\underline{dS} \qquad (4)$$

If the surface S is chosen such that $\underline{u}\cdot\underline{dS}$ vanishes everywhere this integral is zero. Since the total energy must be conserved if no mechanical work is done on V, the heat flux through S must equal the rate of internal heat generation. Hence

$$\int_S -k \underset{\sim}{\nabla} T \cdot d\underset{\sim}{S} = \int_V H dV \tag{5}$$

and (2) reduces to

$$\Phi = \int_V \tau_{ij} \frac{\partial u_i}{\partial x_j} dV = -\int \rho C_p \underset{\sim}{u} \cdot (\underset{\sim}{\nabla} T)_s dV \tag{6}$$

The left hand side of the equation is the rate of dissipation of mechanical energy. In steady state flow this term must equal the rate of release of potential energy: the right hand side of (6). The adiabatic gradient can be written

$$(\underset{\sim}{\nabla} T)_s = \frac{\alpha T}{\rho C_p} \underset{\sim}{\nabla} p \tag{7}$$

where α is the thermal expansion coefficient and p the pressure. Unlike the first term in (2) the right hand side of (6) cannot be converted into a surface integral. Substitution of (7) gives

$$\int_V \frac{\alpha T}{\rho} \rho \underset{\sim}{u} \cdot \underset{\sim}{\nabla} p = \int_V \frac{\alpha T}{\rho} \underset{\sim}{\nabla} \cdot \rho \underset{\sim}{u} p \, dV \tag{8}$$

but, because T/ρ is not constant, this integral cannot be transformed using Green's theorem. If the pressure is little changed by the flow

$$\underset{\sim}{\nabla} p \approx -\rho g \underset{\sim}{e}_z \tag{9}$$

where $\underset{\sim}{e}_z$ is a unit vector in the vertical direction. Hence (6) becomes

$$\Phi = \int_V \rho g \alpha T w \, dV \tag{10}$$

where $w = \underset{\sim}{u} \cdot \underset{\sim}{e}_z$. If g, α and c_p are constant (10) can be written

$$\Phi = \frac{g\alpha}{C_p} \int \langle \rho C_p w T \rangle A \, dz \tag{11}$$

where the bracketed term is the horizontally averaged convective heat flux and A is the area of the layer. In a vigorously convecting fluid with a high Rayleigh number nearly all the heat is carried by convection. The only regions where this is not true are in the thin thermal boundary layers. Hence we can set

$$\langle \rho C_p w T \rangle \approx F + Hz \tag{12}$$

where F is the heat flux through the base of layer of depth d. (11) now gives

$$\Phi \approx \frac{g\alpha d}{C_p}(F + \tfrac{1}{2}Hd)A \qquad (13)$$

If the total heat flux through the upper surface is f then

$$f = (F + Hd)A \qquad (14)$$

And

$$\Phi \approx \frac{g\alpha d}{C_p}\left(\frac{F + \tfrac{1}{2}Hd}{F + Hd}\right)f \qquad (15)$$

putting $\mu = \frac{Hd}{F + Hd}$ and the temperature scale height $H_T = \frac{C_p}{g\alpha}$ gives

$$\Phi \approx \frac{d}{H_T}(1 - \tfrac{1}{2}\mu)f \qquad (16)$$

This expression was obtained by Hewitt *et al.* (1975), whose derivation depended on the change in the pressure due to the flow being small, and the flow being steady state. A recent numerical invesigation of convection in layers in which $d = O(H_T)$ by Jarvis and McKenzie (1979) has shown that the perturbation to the pressure is small when $d \ll H_T$ and that (16) holds even when the temperature is time dependent. Hence (16) should provide an excellent estimate of the total mechanical work done by convective forces. This investigation also showed that most of the dissipation occurred near the rising and sinking regions, and was associated with vertical not horizontal motions. Jarvis and McKenzie estimated the ratio of energy transport across horizontal planes by mechanical work to that by convection & conduction of heat, and showed that this ratio did not exceed 2.5% even when $d = H_T$.

This discussion suggests that it is useful to make three estimates of the rate at which the mantle can do mechanical work. In the first two cases we will assume that all the dissipation occurs on plate boundaries. Since we do not know whether phase changes are important we will consider two extreme cases. The first, case A, assumes that the whole mantle is convecting and that the phase changes contribute to the bouyancy forces. The appropriate value of H_T can then be estimated from the density variation between top and bottom of the mantle. If H_T and Grineisen's parameter Γ are constant the density variation with depth is given by

$$\rho(z) = \rho_o \exp (d-z)/\Gamma H_T \qquad (17)$$

Taking the density at the top of the mantle to be $3.3 Mgm^{-3}$, that at the bottom to be $5.5 Mgm^{-3}$, and $\Gamma = 1.2$ gives $d/H_T = 0.6$. We further assume that all the heat convected to the surface is generated within the layer, and hence that $\mu = 1$.

The second case , B, we will consider is convection confined to the upper mantle when the phase changes do not contribute to the bouyancy forces. $\frac{d}{H_T}$ may then be estimated from α and C_p to be about 0.1, and μ is taken to be 0.5.

The final case,C, uses the numerical result that the mechanical work available to drive the horizontal motions is about 2.5% of the total heat flux, and that this value depends little on $\frac{d}{H_T}$. Unlike cases A and B, case C depends on the relationship between stress and strain and on the geometry of the flow. Therefore the stresses for case C are estimates, not upper bounds as they are in the other two cases.

To estimate the work available we need the total convective heat flux. The best estimate of the total heat flux is that of Sclater et al. (1979) of $4 \times 10^{13} W$, and of this about 85% comes from the mantle. Hence the convective transport f is about $3.4 \times 10^{13} W$. This gives estimates of the rate of mechanical working for three cases from (16) of

$$\begin{aligned} &1.0 \times 10^{13} W \text{ case A} \\ &2.6 \times 10^{12} W \text{ case B} \\ &8.5 \times 10^{11} W \text{ case C} \end{aligned} \qquad (18)$$

Further progress requires knowledge of the rate of plate movement and the surface area of plate boundaries. The detailed studies

of plate motions which are now available provide a good estimate of the rate of creation of surface area of $3km^2a^{-1}$ (Chase, 1972) or about $10^3cm^2s^{-1}$. If this surface area is created by movement on a fault of dip θ cutting a lithosphere of thickness a, the length of the fault measured down the dip is $\frac{a}{\sin\theta}$. To produce a horizontal displacement rate of s the fault must move at a rate of $\frac{s}{\cos\theta}$, hence if the mean shear stress is τ the rate of working/unit length of the boundary is

$$\frac{\tau as}{\sin\theta\cos\theta} = \frac{2\tau as}{\sin 2\theta} \qquad (19)$$

Hence

$$\Phi \geq \int_L \frac{2as\tau}{\sin 2\theta}\, dl \qquad (20)$$

where the integral is taken round all plate boundaries. Since most seismic energy is released by thrusting on faults dipping beneath island arcs, we will ignore the contribution made by ridges and transform faults to the right hand side of (20), and assume that τ and θ are constant for all arcs. Hence (20) becomes

$$\tau \leq \frac{\Phi \sin 2\theta}{2a\int_L sdl} \qquad (21)$$

$\int_L sdl$ is the rate of destruction of surface area. Reasonable estimates of a and θ are 100 km and 10° respectively, and these estimates give

$$\begin{aligned} &\tau < 1.8 \text{ kb} \quad \text{case A} \\ &\tau < 450 \text{ bars} \quad \text{case B} \\ &\tau \sim 150 \text{ bars} \quad \text{case C} \end{aligned} \qquad (22)$$

If instead we choose $\theta = 45°$, which maximises $\sin 2\theta$, the estimates become

$$\begin{aligned} &\tau < 5.0 \text{ kb} \quad \text{case A} \\ &\tau < 1.3 \text{ kb} \quad \text{case B} \\ &\tau \sim 420 \text{ bars} \quad \text{case C} \end{aligned} \qquad (23)$$

Though a thickness of the brittle layer of 100 km is an overestimate on transform faults, in island arcs the subduction of cold oceanic plate must cool the overthrusting wedge and hence increase its thickness.

DISCUSSION

The estimates obtained from the efficiency arguments above show that the depth to which the convection extends is of considerable importance in estimating the upper bound on the stress. The principal reason why various authors argued that the flow is confined to the upper mantle have been summarized by Richter (1979) and were mostly seismological. Recently two new arguments have lead to the same conclusion.

The first depends on the post-glacial deformation of North America. Though Peltier and Andrews (1976) showed that the surface movement agreed with that expected from a mantle of uniform viscosity of 10^{22} poise, Peltier and Wu (personal communication) have recently shown that the same model does not reproduce the observed gravity field. The fit is improved if the lower mantle viscosity is increased to 10^{24} poise, and may improve further with even larger values.

The second argument concerns the geochemical evolution of the mantle, which O'Nions et al., (1979) have argued is more depleted in Rubidium than would be expected if the Rubidium in crust has been extracted from the whole mantle. They argued that only about half the mass of the mantle has been involved in plate creation, and that the lower part of the mantle has been isolated from the upper throughout geological time.

These two arguments support the older one based on seismology and suggests that only the upper mantle is involved. Hence the stress estimates from cases B and C are at present more probable than that from A. This argument suggests an upper bound on the mean shear stress of about 500 bars and probable values of between 100 and 200 bars. These estimates are of the mean stress on rapidly moving plate boundaries, and do not exclude either small regions of high stress on these boundaries, or extensive regions of high stress in plate interiors not associated with deformation. In terms of the present debate about the magnitude of the shear stress on plate boundaries only case A produces an upper bound in the high stress regime. The preferred models involving only upper mantle convection gives estimates of mean stress which are comparable with the stress drops observed seismically.

ACKNOWLEDGEMENTS

This investigation resulted from a number of conversations with Peter Molnar, who had already attemped to use thermodynamics to estimate the shear stress from the heat flux. Research on mantle convection at Cambridge is supported by a grant from the Natural Environmental Research Council.

REFERENCES

Chase C. G. 1972 The n-plate problem of plate tectonics *Geophys. J. R. astr. Soc.* 29, 117.

Hasegawa A., Umino N. and Takagi A. 1978 Double-planed deep seismic zone and upper-mantle structure in the Northeastern Japan Arc. *Geophys. J. R. astr. Soc.* 54, 281.

Hewitt J. M., McKenzie D. P. and Weiss N. O. 1975 Dissipative heating in convective flows. *J. Fluid Mech.* 68, 721.

Jarvis G. T. and McKenzie D. P. 1979 Convection in a Compressible Fluid with an Infinite Prandtl Number *J. Fluid Mech.* (in press).

Mitronovas W. and Isacks B. L. 1971 Seismic Velocity anomalies in the Upper mantle beneath the Tonga-Kermadec Island Arc. *J. geophys. Res.* 76, 7154.

O'Nions R. K., Evensen N. M. and Hamilton P. J. 1979 Geochemical modelling of mantle differentiation and crustal growth J. geophys Res. (in press).

Pascal G., Dubois J., Barazangi M., Isacks B. L. and Oliver J. 1973 Seismic Velocity anomalies beneath the New Hebrides Island Arc: Evidence for a Detached Slab in the Upper Mantle. *J. geophys. Res.* 78, 6998.

Peltier W. R. and Andrews J. T. 1976 Glacial-Isostatic Adjustment - I. The forward problem *Geophys. J. R. astr. Soc.* 46, 605.

Richter F. M. 1979 Focal mechanisms and seismic energy release of deep and intermediate earthquakes in the Tonga-Kermadec region and their bearing on the depth extent of mantle flow. *J. Geophys. Res.* (in press).

Sclater J. G., Jaupart C. and Galson D. 1979 The heat flow through the oceans & continents. *Rev. Geophys. Space Phys.* (in press).

Solomon, S. C. and Paw *U*, K. T. 1975 Elevation of the olivine-spinel transition in subducted lithosphere: seismic evidence. *Phys. E. Planet. Int.* 11, 97.

Sung C. M. 1976 Kinetics of the olivine-spinel transition in the system Mg_2SiO_4 - Fe_2SiO_4: experimental results & geophysical implications. *EOS Trans. Am. Geophys. Union* 57, 1020.

MECHANICS OF SUBDUCTED LITHOSPHERE

Geoffrey F. Davies

Department of Earth and Planetary Sciences and
McDonnell Center for the Space Sciences
Washington University
St. Louis, MO 63130

ABSTRACT

Some simple models of the mechanics of subducted lithosphere, combined with observations of Benioff zones, challenge some commonly accepted views of descending lithospheric slabs. Benioff zones usually deviate substantially from planarity, but are not highly contorted. Subducted lithosphere usually becomes aseismic within 15% of the time for which the lithosphere cooled before subduction; deviations from this usually involve additional seismicity just above 650 km depth, and only in a few cases involve a deficiency of seismicity caused by the cessation of seismicity at 650 km. These observations tend to favor the idea that subducted lithosphere penetrates the lower mantle. Negative buoyancy forces in slabs are large, but the upper mantle probably cannot offer substantial viscous or hydrodynamic resistance. Thus, slabs which do not penetrate to 650 km must be supported by large shallow inter-plate frictional stresses, with perhaps some additional tensional stress from attached plates. Some mechanisms which have been proposed to resist slabs which penetrate to 650 km depth seem feasible, but the slab would be subjected to very large compressional stresses if it were substantially supported in this way. It is likely that such a slab would rapidly buckle; this is not evident in Benioff zones, and in any case the slab would no longer be supported. It is possible that the negative buoyancy due to phase changes has been over-estimated, but this will not avoid all problems. Other options seem less attractive. Thus, the possibilities should be considered that inter-plate stresses at subduction zones are large, and that deep focal mechanisms reflect local intra-slab stresses rather than the average stress through the slab.

INTRODUCTION

Although subduction zones seem to be the sites of fundamental geophysical and geological processes, very little quantitative consideration seems to have been given to the mechanics of subducted lithosphere. For example, among the significant questions concerning subduction zones is the relation between the negative buoyancy of subducted lithosphere, the inter-plate frictional stresses which give rise to the great shallow earthquakes, and the net force acting to drive or resist the motion of the attached plate (e.g., Elsasser, 1969; Forsyth and Uyeda, 1975; Chapple and Tullis, 1977; Hanks, 1977; Davies, 1978). Also, the interpretation of deep earthquake focal mechanisms by Isacks and Molanr (1971), that deeply penetrating lithospheric slabs are in down-dip compression, is important to the mechanics of the slabs, and hence to the above question, and also to the controversy over whether or not the lower mantle is involved in plate dynamics (Davies, 1977; O'Connell, 1977; Richter and McKenzie, 1978). It is thus significant that some simple calculations to be presented here cast considerable doubt on some conventional views of subducted lithosphere.

Before discussing the mechanics of subducted lithospheric slabs, some observations of Benioff zones are reviewed, and these are interpreted in the light of basic ideas of the thermal evolution of slabs. Many of the forces which have been hypothesized to act on slabs are then discussed in turn, and their magnitudes estimated. Finally, these estimates are assembled into some simplified exploratory models of slab mechanics, and the results of these models are evaluated.

GEOMETRY OF BENIOFF ZONES

Most of our information about subducted lithosphere comes from earthquake hypocenters and focal mechanisms (Isacks, Oliver and Sykes, 1968; Isacks and Molnar, 1971), and it is useful to review what these do and do not tell us. Figure 1 reproduces Isacks and Molnar's (1971) summary figures of their observations and interpretation. Figure 2 is a more recent interpretation of the shape of the Tonga-Kermadec Benioff zone from Billington (1979), and Fig. 3 is a recent cross-section of the Tonga Benioff zone (Isacks and Barazangi, 1978), to remind us that the surfaces of Figs. 1 and 2 are inferred from clouds of hypocentral points.

Benioff zones can be characterized as curved surfaces with radii of curvature of several hundred kilometers and with some resolvable irregularities on a scale of 100 km. Approximately planar zones are clearly exceptional; some zones with linear profiles in Fig. 1 (e.g., Honshu, Kuril, Peru) are less obviously planar when viewed in three dimensions (Chiu et al., 1979). On the other hand, the contortions are not extreme, even in the deepest parts. The lack of continuity between the intermediate and deep parts of some zones has often been noted, and this is a clear suggestion (but not proof) of fragmentation. There is no clear suggestion of a piling up, either by folding or fragmentation, around 650 km depth, as might be expected if a descending lithospheric slab encountered greater resistance at this depth (see especially Fig. 2). This interpretation should not be overstated, but it is notable that the Tonga slab is the clearest (perhaps the only) case in which focal mechanisms indicate compression through most of its depth, and yet the contortions evident in Fig. 2 are not readily interpreted as resulting from resistance to the slab near 650 km depth.

Figure 4 shows sketches depicting a variety of imagined fates of subducted lithosphere. The fates differ depending on the response of the slabs to internal stresses and depending on whether or not the slab penetrates into the lower mantle at a depth of about 650 km (indicated by the horizontal dashed line). In Fig. 4a, the slab simply descends into the mantle until it warms enough to be assimilated. In Fig. 4b, the slab is flexed by variations in normal forces as a function of depth, as would be caused, for example, by elevation of phase boundaries within the slab which would increase the vertical gravitational body force in the slab. Figure 4c depicts a piece of slab which has detached and sunk faster than the rest of the slab, as suggested by the lack of continuity in some Benioff zones. Figure 4 d-f suggest various responses to the slab being unable to penetrate the lower mantle. In Fig. 4d, the slab fractures under compression. Fig. 4e, it buckles under compression. Figure 4f has been suggested as a response to the fact that many ocean trenches migrate oceanward (Chase, 1979): any part of the slab may descend vertically and be laid on a "bottom" without significant deformation. Figure 4g is a variation on 4c: the slab may be fractured during subduction and the Benioff zone may just be the locus of independently settling fragments. Figure 4h depicts an attempt by Richter and McKenzie (1978) to explain quantitatively how compressive stresses might be produced in a slab which does not penetrate the lower mantle: the compression is the result of dynamic flow pressure at the end of the slab, where it becomes "fluid," and they found it necessary that the slab penetrate essentially intact to within 100 km of the bottom before becoming fluid.

Of these possibilities, Fig. 4(e) seems to be the least consistent with observations, as discussed above, especially as the folding of the slab ought to produce observable seismic activity. Figure 4h seems unreasonable for reasons discussed below. Figures 4a,b,d,f,g would be consistent with observations if the extensions or detached parts of the slab are aseismic. In Figs. 4d and f this might result from relief of stresses which exist in the main slab, but the interpretation in Fig. 4c suggests that detached segments can remain seismically active. Also, it will be suggested later that slab seismicity may not be primarily a result of large-scale slab stresses. The stress-relief argument cannot apply to Fig. 4g, since the slab is already fragmented. The rather sudden cessation of seismicity near 650 km depth can be explained in Figs. 4a and b by invoking the effect of phase changes within the slab, which might change the mechanical properties of the material enough to remove it from the regime of brittle behavior.

HEATING OF SUBDUCTED LITHOSPHERE AND LENGTH OF BENIOFF ZONES

It is important to bear in mind the great thermal inertia of subducted lithosphere. The calculation by Schubert et al. (1975) of the thermal structure of a slab descending at 8 cm/yr with a dip of 45° shows that at a depth of 650 km the slab is still as much as 800°C cooler than the surrounding mantle. Molnar et al. (1979) have shown that the down-dip lengths of several Benioff zones are consistent, within 30% accuracy, with the idea that earthquakes cease when the slab reaches a critical temperature. Using the solution of McKenzie (1969) for a slab warming in a constant-temperature mantle, they estimate this critical temperature to be 800 $\pm$ 100°C, which is still only about half of the temperature at 600 km depth. The same solution shows that at sufficient depth the thermal anomaly of the slab decays exponentially with time, t (or equivalently, with distance, x, down the slab):

$$T_o - T_m = (2T_o/\pi)e^{-x/\lambda} = (2T_o/\pi)e^{-t/\tau}, \qquad (1)$$

Where T_o is the temperature of the surrounding mantle, T_m is the minimum slab temperature at a given x, λ is a characteristic length, $\tau = \lambda/v$ is a characteristic time, v is the subduction velocity, and

$$\tau = \rho C_p H^2/2\pi^2 k. \qquad (2)$$

Here ρ is density, C_p is specific heat, H is slab thickness and k is thermal conductivity. For H = 100 km and other numerical values as given in Table 1, τ = 16 Ma (16 million years). For v = 100 mm/yr, this gives λ = 1600 km. These values only restate the conclusions of Isacks et al. (1968) and Molnar et al. (1979), but they serve to emphasize that the thermal anomaly of the slab will persist long after the slab becomes aseismic: there will still be an $\sim$ 400°C anomaly 30 Ma after subduction of 100 km-thick lithosphere.

It is instructive to replot the data of Molnar et al. (1979) in terms of lithosphere residence times rather than lengths. The time for which subducted lithosphere is seismic is just $t_s = L/v$, where L is the length of the Benioff zone. In Fig. 5, this is plotted against age of lithosphere at subduction, t_c (i.e., the time for which the lithosphere cooled). Since lithospheric thickness is given approximately by (Parker and Oldenburg, 1973; Molnar et al. 1979)

$$H\ (km) = 10\sqrt{t_c(Ma)}\ , \qquad (3)$$

we see from equation (2) that τ and t_c should be linearly related:

$$\tau = 0.16\ t_c\ . \qquad (4)$$

The line $t_s = \tau$ is included in Fig. 5. Figure 5 shows that t_s ranges between about 5 Ma and 15 Ma, and that it has a clear positive correlation with t_c, as we should expect from the results of Molnar et al. (1979). For lithosphere of a given age, the largest values of t_s approach τ.

Figure 5 shows perhaps more clearly than the plots by Molnar et al. (1979) that the Aleutians, Kuril and Tonga plot substantially below the other zones. They noted that for the Aleutians this might be because the sea floor age decreases towards the Aleutian trench, so that the subducted lithosphere is younger than it would otherwise be. This also applies to the Kuril zone and to the Honshu zone, although the effect in the latter case might be small because the sea floor isochrons are oblique to the trench (Hilde et al., 1976). For Tonga, the Benioff zone might be limited by phase changes in the slab, since the zone extends to 680 km depth. Thus, reasonable hypotheses exist to explain some of the lower values of t_s in Fig. 5, and the remainder can be approximated to within about 20% by

$$t_s = 0.15\ t_c\ . \qquad (5)$$

In other words, the period for which subducted lithosphere remains seismic is about 15% of the age of the lithosphere at subduction.

It is notable that of the zones represented in Fig. 5, only the Tonga zone requires the phase change hypothesis to explain its shorter than expected length. In the cases of South America and New Zealand, there is also deep seismicity which ceases near the mantle phase boundary at 670 km, but this seismicity is not continuous with the shallower seismicity, and the shallower seismicity is in accord with equation (5). The puzzle in South America and New Zealand is not that there is no seismicity just below the phase boundary, but that there is seismicity just above the phase boundary. Of the zones not represented in Fig. 5, the only ones which are continuous to 650 km, and which are therefore likely to require the phase change hypothesis, are the Marianas and Eastern Indonesia (Fig. 1 and Cardwell and Isacks, 1978); the remaining deep zones are not continuous with shallower zones, and probably represent seismicity additional to that predicted by equation (5). Thus, although much has been made of the sudden cutoff of seismicity near 650 km depth since it was discussed in the context of plate tectonics by Isacks, Oliver and Sykes (1968), it is really only true of two or three Benioff zones. The remaining deep zones are better characterized as a resurgence of seismicity above 650 km.

STRESSES AND EQUILIBRIUM OF PLANAR SLABS

As a first step in considering the machanics of subducted lithosphere, it can be approximated as a planar slab. The stresses within the slab can then

be related to the forces acting on it by invoking the requirement for equilibrium of the total slab. The stability of the planar configuration will be discussed in the next section.

The forces which have been proposed to act on lithospheric slabs include gravitational buoyancy due to temperature differences and phase changes, interplate friction at the subduction zone, viscous drag from the surrounding mantle, and viscous forces or hydrodynamic pressure acting on the "leading edge" of the slab. These forces and estimates of their magnitudes will be discussed individually, and they will then be assembled into some simple mechanical models of slabs.

Thermal Buoyancy (F_T)

The negative buoyancy of a cold slab is quite large, sufficient to produce several kilobars of stress within the lithosphere. McKenzie (1969) calculated the total force per unit length of trench for the case of a slab with an initial linear temperature profile:

$$F_T = g\alpha T_o \rho^2 H^3 C_p v(\sin \delta)/24k \qquad (6)$$

where the subscript T denotes (negative) thermal buoyancy, g is the acceleration due to gravity, α is the volume thermal expansion coefficient and δ is the dip of the slab. For H = 200 km, v = 100 mm/yr, $\delta = 60°$ and other parameter values given in Table 1, this gives 0.9×10^5 GPa.m (0.9×10^{17} dyne/cm). If this were supported by a stress, σ, within the slab, then

$$\sigma_T = F_T/H \ , \qquad (7)$$

which yields, for the above case, σ = 0.9 GPa (9 kbar). This is larger even than McKenzie (1969) calculated, since he used H = 50 km and T_o = 800°C, which are quite conservative values. (A unit for F which some might find easier to assimilate is the force per unit length produced by a stress of 1 kbar acting over a thickness of 1 km: 1 kb.km = 100 GPa.m = 10^{14} dyne/cm.)

Equations (6) and (7) and the values in Table 1 can be combined to yield the useful formula

$$\sigma_{T(GPa)} \approx 10^{-6} H^2(km)v(mm/yr) \approx 10^{-4} t_c(Ma)v(mm/yr) \ , \qquad (8)$$

where equation (3) was used in the last step to relate H to lithospheric age, t_c.

Schubert et al. (1975) numerically calculated the gravitational body force due a slab subducting at 80 mm/yr and their results integrate to give $F_T \approx 2.5 \times 10^4$ GPa.m. They state that the initial slab geotherm corresponded to a surface heat flow of 34 mW/m^2 (0.8 μcal/cm^{2}sec), but this is incompatible with the isotherms illustrated in their Fig. 11, which would correspond to a heat flow of about 70 mW/m^2. Using the heat flow-age correlation of Parsons and Sclater (1977), this corresponds to an age of 60 Ma and H $\approx$ 75 km. Assuming this to be correct, their values imply $\sigma_T \approx$ 0.3GPa, while equation (8) yields

$\sigma_T \approx 0.5$ GPa. Since they used a more realistic initial geotherm, and since their body force was only given to 800 km depth, this discrepancy is not serious, and it can be concluded that McKenzie's model gives results which are as accurate as is justified by the uncertainties in the parameters of Table 1.

It will be useful for later to express these results in terms of the average body force, f, per unit surface area of the slab (i.e, per unit length of trench and per unit length down the slab). If $F_T(L)$ is the total force due to a length L of slab, then

$$f_T = F_T(L)/L \approx \sigma_T H/L. \tag{9}$$

Thus, if L = 1600 km, $F_T(L) = 6\times10^4$ GPa.m, then $f_T \approx 0.04$ GPa (400 bar).

Buoyancy Due to Phase Changes (F_{PH})

Schubert et al. (1975) calculated the negative buoyance force, f_{PH}, due to the upward displacement within the cold slab of the olivine-spinel phase change. They found a maximum displacement of 160 km up the slab, a maximum body force of 0.13 GPa, and a mean body force $f_P \approx 0.1$ GPa, giving a total of $F_P \approx 1.6\times10^4$ GPa.m. This, of course, is a significant addition to the negative buoyancy of the slab.

Schubert et al. (1975) also calculated a positive buoyancy due to the hypothesized spinel to oxides phase change at 650 km, the positive buoyancy being due to the calculated negative Clapeyron slope, dT/dP, of this phase change. However, the phase change at 670 km depth probably involves the high pressure perovskite phase of $MgSiO_3$ (Liu, 1977) and the thermodynamics of this phase are unknown. In any case, Jackson et al. (1974) showed that dP/dT of the spinel-oxides transition is probably zero or slightly positive. Because of these uncertainties, and because it is difficult to separate the effects of this transition from those of postulated higher mantle viscosity at this depth, this phase change will not be considered explicity here.

Inter-Plate Friction (F_F) and Slab-Plate Force (F_{PL})

If the zone of interplate earthquakes has a down-dip width W, and an average shear stress of f_F acts across the zone, then

$$F_F = Wf_F. \tag{10}$$

Unfortunately f_F is highly uncertain and W is quite variable. However, W, f_F and the dip δ are not independent of each other. Thus, it is observed that the zone of intraplate earthquakes usually extends to a depth, h, of 80-100 km depth (Engdahl, 1977; Pascal et al., 1978; Barazangi and Isacks, 1979). Thus

$$W = h/\sin\delta\ . \tag{11}$$

Furthermore, the maximum value of f_F will be limited by the strength of the overthrust wedge, and will depend on δ. For very shallow dips, this relationship is simple. Referring to Fig. 6(a), the equilibrium of the overthrust wedge requires that

$$Wf_F \approx h\sigma_H = W\sigma_H \sin\delta ,$$

i.e.,

$$f_F \approx \sigma_H \sin\delta, \qquad (12)$$

where σ_H is the average horizontal deviatoric compressive stress. Thus, although W and f_F are quite variable, F_F is given approximately by

$$F_F \approx H\sigma_H . \qquad (13)$$

Of course, σ_H is not well determined either, but estimates of its maximum value are possible. Bird (1978) estimated a maximum of 0.7×10^4 GPa.m for lithosphere containing 35 km of continental crust, using estimates of the rheology of quartz and olivine, and an estimated strain rate and geotherm. Such estimates are quite sensitive to temperature, assumed strain rate, crustal thickness and uncertainties in rheology. Bodine et al. (1979) and Watts et al. (this volume) made estimates several times larger than this for 80 Ma-old oceanic lithosphere in the context of flexure under a vertical load. Thus a representative upper limit on F_F would be 10^4 GPa.m, with an uncertainty of at least a factor of two. For h = 100 km, this implies σ_H = 0.1 GPa (1 kbar), with mid-lithospheric stresses considerably higher than this average value.

Whether stresses across faults approach these maximum values is a matter of controversy. If fluid pore pressure in the fault zone approaches the lithostatic pressure, then the strength of the rock may be considerably reduced, and it is clear that some such mechanism must operate some of the time. For example, if the dip is very small, as in Alaska, then f_F must be considerably less than σ_H: if $\delta = 10°$, f_F is only 17% of σ_H, according to equation (12). Also, Bird (1978) has used the force balance on the Tonga and Mariana arcs, which are sites of back-arc spreading, to estimate that f_F is only about 20 MPa (200 bar). In the case of Tonga, the average dip of the fault zone down to 100 km depth is about 30°, W ≈ 200 km, and so $F_F \approx 0.4 \times 10^4$ GPa.m, and the Marianas are probably similar. On the other hand, Bodine and Watts (1979) conclude that the horizontal compressive stress in the lithosphere seaward of the Mariana and Bonin arc varies considerably: while it is probably small at the Marianas, it might be several kilobars at the Bonin arc. One source of this variation might be variations in the frictional resistance in the subduction zone. Thus, f_F may be larger in the Bonin arc (and others) than in the Marianas.

Models of the driving forces of plate motions have been used to constrain estimates of inter-plate friction. Forsyth and Uyeda (1975) and Chapple and Tullis (1977) concluded that the net force on plates at trenches, F_{PL}, is small and tensional. Forsyth and Uyeda assumed that inter-plate friction is small and invoked resistance to the slab at depth to balance most of the negative buoyancy of the slab. On the other hand, Chapple and Tullis (1977) removed deep resistance from consideration by including the "slab pull" due only to the upper part of the slab with tensional focal mechanisms. Their models still required inter-plate friction of the order of a few hundred bars (F_F about 0.5×10^4 GPa.m). Unfortunately, there may be considerable additional

non-uniqueness in this approach, since greater inter-plate friction can be offset to a large extent by invoking mantle driving stress on the base of plates (Davies, 1978). Some recent studies have concluded that the net force on plates at trenches is a pull comparable to the net effect of gravitational sliding off ridges (Richardson, 1978; Hager, 1979; Aggarwal, 1979). The latter can be estimated relatively accurately (Lister, 1975): for lithosphere which subsides until it is 70 Ma old, the net force per unit length of ridge is about 0.3×10^4 GPa.m.

The relationship between interplate friction and the net force on the plate depends on how much of the latter is transmitted to the subducted slab. The situation is depicted in Fig. 6(b). If σ_{PL} is the net average stress in the place and σ is the part of this which is transmitted to the slab, then the force balance requires, to a sufficient approximation,

$$H\sigma_{PL} = Wf_F + H\sigma \ . \qquad (14)$$

At this point it does not seem to be possible to constrain either σ_{PL} or f_F to within much less than an order of magnitude. For the purposes of the modelling to follow, two values of each will be assumed; further constraints or potential constraints will emerge from the models. For σ_{PL}, we will assume either 0.1 GPa or -0.03 GPa (300 bars, tensional). For f_F, 0.1 GPa or 0.02 GPa. W will be taken to 150 km.

Mantle Resistance on Slab Sides (F_V)

If the slab is descending faster than the surrounding mantle, then a shear stress acting on the surfaces of the slab will resist its descent. It is possible that the slab is descending slower than the surrounding mantle, for example if the surrounding mantle is actively convecting and the slab is encountering strong resistance elsewhere, but we will see that the problem is to account for sufficient resistance to the slab. Consequently, the conservative assumption will be adopted that mantle motion is driven only by the motion of the slab. The resulting resistance will be referred to (not very appropriately) as viscous resistance.

Some estimates of the magnitude of F_V can be made by assuming that the mantle has a linear viscous rheology. The limitations of this assumption will be discussed below. Thus,

$$\sigma_V = \eta\varepsilon \ , \qquad (15)$$

where η is viscosity and ε is strain rate.

A crude estimate of σ_V derives from considering the length-scale of the flow driven in the mantle. If the slab drives a circulation cell of radius r, then ε is of the order of v/r (strain rate is the same as velocity gradient). σ_V will be larger for smaller values of r, so a conservative value for r is 300 km, corresponding to a cell the size of a Benioff zone, as indicated schematically in Fig. 7(a). For v = 100 mm/yr, this gives $\varepsilon \sim 10^{-14}$ s^{-1} and

$$\sigma_V \sim \eta v/r \sim 10 \text{ MPa (100 bar)} \ , \qquad (16)$$

where viscosity, η, is taken to be 10^{21} Pa.s (10^{22} poise, Table 1). If this stress acts over a length $2r$ = 600 km of slab, then, counting both sides of the slab,

$$F_V = 4r\sigma_V = 4\eta v \sim 10^4 \text{ GPa.m} , \tag{17}$$

which is small compared to the negative buoyancy of the slab estimated above. Note that F_V is independent of r, although σ_V is not.

This value of F_V is likely to be an upper limit, for three reasons. First the mantle will also be driven by other influences: convection (Davies, 1977a; Parsons and McKenzie, 1978) or the motion of the overlying plate (Davies, 1977b). Second, the upper mantle viscosity may be somewhat less than was assumed, especially in the low viscosity layer (e.g., Carter, 1976). Third, a more realistic, nonlinear, rheology (Carter, 1976) would yield flow more concentrated near the slab which would thus lower the effective viscosity and probably σ_V.

A more rigorous estimate of F_V can be obtained from a simple solution for flow in a viscous fluid driven by a periodic tangential boundary velocity. Such solutions were used by Davies (1977a,b) in discussions of the flow under moving plates, and more details of the derivation are given there. Two-dimensional flow in a viscous, incompressible fluid can be described by a stream function, ψ, which satisfies the biharmonic equation:

$$\left(\frac{\partial^2}{\partial x^2} + \frac{\partial^2}{\partial z^2} \right)^2 \psi = 0. \tag{18}$$

Velocity components are given by

$$v_x = - \frac{\partial \psi}{\partial z} , \quad v_z = \frac{\partial \psi}{\partial x} , \tag{19}$$

and the shear stress component σ_{xz} is

$$\sigma_{xz} = \eta \left(\frac{\partial^2 \psi}{\partial x^2} - \frac{\partial^2 \psi}{\partial z^2} \right) \tag{20}$$

Now consider the geometry sketched in Fig. 7(b), and suppose that a vertical sinking slab is simulated by the vertical boundary condition $v_z = V \sin Az$, where V is a constant and A is a wave number, considering only the boundary segment between $z = 0$ and $z = \pi/A$. The horizontal boundaries at these depths are assumed to be stress-free. The solution of (18) which satisfies these conditions is

$$\psi = Vxe^{-Ax} \sin Az , \tag{21}$$

which yields

$$\sigma_{xz}(0,z) = -2\eta AV \sin Az . \tag{22}$$

Integrating this from z = 0 to z = π/A, and counting both sides of the slab,

$$F_V = -2 \int_0^{\pi/A} \sigma_{xz}(0,z)dz = 8\eta V = 4\eta \bar{v}_z \quad , \tag{23}$$

which is the value given by equation (17). This confirms the rough estimate given by equation (17). Of course, the geometry of Fig. 7(b) is still quite idealized, so equation (23) should still be regarded as a rough estimate.

A significant limitation of the above estimate is that it neglects dissipation in the corners of the flow region. In fact, in the ideal case of Newtonian viscosity and a constant velocity boundary, the solution is singular at the corners and F_V sums to infinity. With a realistic rheology, F_V would be finite and the resistance would be strongest at the corners: therefore, it can be regarded as contributing to F_F at the top of the slab or F_R (discussed below) deeper in the mantle. For the present discussion, the important point is that σ_V is not very large along those parts of the slab away from any mantle boundary.

Resistance to the "Leading Edge" of a Slab

A rather common assumption has been that resistance from the mantle is concentrated at the "leading edge" of slabs (e.g., Smith and Toksöz, 1972; Forsyth and Uyeda, 1975), which presupposes that the leading edge is blunt. In a steady state subduction zone in which the slab is thermally assimilated back into the mantle, the slab will thin steadily until either the resistance to the leading edge is insignificant or the slab is so thin that it buckles and does not transmit stress back up the slab, or both. Since the record of marine magnetic anomalies shows that most existing subduction zones have absorbed thousands of kilometers of lithosphere, we must conclude that this steady state applies to most slabs, and that the initiation of a new subduction zone, as modelled, for example, by Toksöz et al. (1971) and Smith and Toksöz (1972), is exceptional. A blunt leading edge might still result from fracturing of the slab, as suggested in Figs. 4(c) and (d). As discussed earlier there is no clear evidence supporting Fig. 4(d), and furthermore it would probably apply only to those two or three slabs (Tonga, Mariana, Eastern Indonesia) which clearly penetrate to 650 km, and even then would produce an episodic resistance: this seems an unlikely source of the kind of general resistance postulated by Forsyth and Uyeda (1975). While there is some evidence in support of Fig. 4(c), the upper Benioff zones in such cases are not obviously shortened (e.g., South America and New Zealand, Fig. 5), and in any case the upper parts of such slabs are interpreted to be in tension (Fig. 1a), and therefore not subject to major resistance at their leading edges.

The viscous resistance to a blunt leading edge of a sinking slab can be estimated from Oseen's formula for the resistance to a circular cylinder moving in a viscous fluid (Batchelor, 1967). The drag per unit length on a cylinder is

$$F = 2\pi C\eta v \quad ,$$

where

$$C = 2/\log(7.4/Re) \quad ,$$

and Reynolds number, Re, is

$$Re = 2\rho av/\eta \quad ,$$

where ρ is the fluid density and a is the cylinder radius. Taking a = 20 km and v = 100 mm/yr gives $Re = 4\times10^{-22}$ and $C \approx 0.1$. Thus, to a sufficient approximation, the leading edge drag is

$$F_{LE} = 0.6\eta v \quad . \tag{24}$$

For v = 100 mm/yr, this gives $F_{LE} \approx 0.2\times10^{4}$ GPa.m, which is not a large resistance.

Richter and McKenzie (1978) investigated a model in which the slab descends intact to near the bottom of the upper mantle and then becomes fluid simultaneously across its thickness (Fig. 4h). This is clearly an unreasonable model of the thermal assimilation of a slab, since the slab will warm and become fluid from the sides rather than at the end. Since, in their model, the end of the slab does not move, neither is it a good model of a slab being fractured as in Fig. 4(d). Therefore, their conclusion that resistance at the leading edge of slabs is due to a hydrodynamic back-pressure due to the supposed proximity of the end of the slab to the bottom of the upper mantle seems to be unreasonable.

Richter and McKenzie (1978) also point out that entry of a slab into the mantle will be opposed by a hydrodynamic pressure associated with driving the return flow in the mantle. The magnitude of this pressure is strongly constrained by the observed gravity field and geoid: the geoid deviates from the hydrostatic spheroid by less than 100 m, with free-air gravity anomalies less than 100 mgal. (Gaposchkin and Lambeck, 1971). An excess pressure of 1MPa (10 bar) would give rise to an elevation of 40m and a gravity anomaly of about 4 mgal. It is unlikely that excess pressures could exceed 10 MPa without being evident in the gravity field. The force resisting a slab due to an excess pressure, ΔP, is just $F = H\Delta P$, where H is the slab thickness. For H = 100 km, this gives $F = 0.1\times10^{4}$ GPa.m. This is a negligible resistance in the present context; it was a significant resisting force in the model of Richter and McKenzie (1978) only because their driving buoyancy forces are unrealistically small.

Although large resistance forces might act below 650 km in the mantle, as discussed below, the above discussion indicates that no good reason has been proposed to expect that the "leading edges" of most slabs are acted on by substantial resistance forces above 650 km.

Deep Mantle Resistance (F_R)

Several sources of resistance to slabs which penetrate below 650 km depth have been hypothesized: an increase in "viscous" resistance, and positive buoyancy due either to a depressed phase boundary within the slab or a change in the surrounding mantle composition.

Although the reasons for thinking that the phase boundary at 650 km is depressed in the slab have been questioned, as discussed earlier, the possibility cannot be excluded. Likewise, some chemical stratification in the mantle cannot be excluded, although the evidence does not require it (Davies, 1974; Liu, 1977; Anderson, 1979). The buoyancy force due to a density contrast $\Delta\rho$ extending for a length l down the slab is $F = glH\Delta\rho$. A force of $F = 10^4$ GPa.m would be produced with $\Delta\rho = 0.5$ g/cm^3 and $l = 40$ km (as in a phase change) or $\Delta\rho = 0.05$ g/cm^3, $l = 400$ km (chemical change); both values of l are rather large, but may not be impossible.

Significant resistance could be exerted on the sides of a slab (as distinct from the end) by a mantle layer of considerably higher effective viscosity below 650 km. Although interpretations of post-glacial rebound data do not favor a higher viscosity lower mantle (Cathles, 1975; Peltier, 1976), a layer one or two hundred kilometers thick cannot be excluded. Such a layer was advocated by McKenzie and Weiss (1975). Davies (1977a) and Sammis et al. (1978) have shown that it is unlikely that such a layer could have a high enough viscosity to prevent penetration by mantle convection, but the shear stresses acting on a penetrating slab might still be large. These stresses can be estimated from equation (16) if a suitable strain rate can be obtained. The calculations of flow in layered viscosity fluids by Davies (1977a) show that for moderate viscosity contrasts (1 to 3 orders of magnitude), the flow through a thin higher viscosity layer tends to be as nearly vertical as possible. Assuming this geometry, schematically illustrated in Fig. 7(c), the appropriate velocity gradient will be of the order of v/r, where $r \approx 3000$ km. i.e., about half the average width of a plate. For $v = 100$ mm/yr and $\eta = 10^{23}$ Pa.s, the resulting shear stress is 0.1 GPa (1 kbar). If a length $l = 100$ km of the slab interacts with the layer, the resulting force, counting both sides of the slab, is $F = 2\times10^4$ GPa.m. In other words, a layer 100 km thick in which the viscosity is two orders of magnitude greater than in the upper mantle could exert a considerable resistance on the slab.

Although the estimates in this section show that these sources could give rise to large resistance forces, they all remain speculative. Consequently, they will not be distinguished in the modelling to follow, but will be represented by a force, F_R, which can be of the order of 10^4 GPa.m, or a stress, f_R, which can be of the order of 0.1 GPa and acts over a length of 100 or 150 km of the slab.

Dependence of Forces on Lithospheric Age and Subduction Velocity

The buoyancy and viscous forces discussed above depend on the subduction velocity, v, and the age of the lithosphere at subduction, t_c. It will be convenient for this and subsequent studies to express these dependences in convenient units and approximate form. The units will be: v in mm/yr, t_c in Ma, lengths in km, f in GPa and F in GPa.m.

The length L_s, of a seismic Benioff zone is, using equation (5),

$$L_s = vt_s = 0.15\ vt_c \quad . \tag{25}$$

From equations (8) and (9), for a slab dipping at about 45°, the force due to thermal buoyancy of the seismically active part of the slab gives

$$f_T = 4\times10^{-3}\ t_c^{1/2} \quad , \tag{26}$$

$$F_T = 0.6\ vt_c^{3/2} \tag{27}$$

The buoyancy due to a phase change is proportional to the thermal anomaly and thickness of the slab, and this yields the same dependence on v and t_c as for F_T. Although the phase change displacement is proportional to the thermal anomaly, it is never very large, so it is convenient to assume that it is always 100 km, and to attribute all of the variation to f_{PH}. Using the results of Schubert et al. (1975) to calibrate, this yields

$$f_{PH} = 2.5\times10^{-6}\ vt_c^{3/2} \quad , \tag{28}$$

with $F_{PH} = 10^5 f_{PH}$.

Equation (17) shows that F_V depends on v, so f_V depends on v/l, i.e., on t_c.

Thus

$$f_V = 1/t_c \quad , \tag{29}$$

$$F_V = 150v \quad . \tag{30}$$

Some Simple Slab Models

Let us now explore some simple mechanical models of slabs using these approximations to the various forces. A further simplification will be to assume that each f is constant over that portion of the slab on which it acts. If f is the local sum of those stresses acting at a position, x, down the slab, then the cumulative force at that position due to all stresses between the surface and x is

$$F(x) = F_{PL} + \int f\,dx \quad . \tag{31}$$

Taking forces down the slab to be positive, a positive value of F will correspond to the slab being in down-dip compression at that point. At some point, x = L, the slab will become warm enough that it cannot withstand significant stresses, so

$$F(L) = 0 \quad . \tag{32}$$

Usually, L will be greater than L_S of equation (25). Here, $L-L_S$ will be taken to be 100 to 150 km, the conclusions to follow not being very sensitive to this value. Equation (32) is equivalent to requiring the forces on the slab to balance, and this condition allows one parameter to be left unspecified. In the models below this will be either f_R or f_F.

Now consider a slab descending at about 45° with v = 60 mm/yr and t_c = 100 Ma, so that L_s = 900 km. The Benioff zone would then extend almost to the 650 km transition zone. Assume that the slab extends another 150 km into the lower mantle, so that L = 1050 km. The forces predicted for this slab are listed in Table 2, models 1 - 4. Two values each are assumed for F_{PL} and f_F, as listed; f_F is assumed to act on the top 150 km of the slab. f_R is then determined from equation (32). The variation of F down the slab for these four models is shown in Fig. 8. The negative thermal and phase change buoyancies are so strong that they are chiefly opposed by F_R: if distributed through 150 km f_R must be 2 to 4 kbar to support the slab. As a result, most of the slab is strongly in compression, except for model 2, in which more of the load is taken by F_{PL} and f_F. The peak compressions of 2.5 to 5×10^4 GPa.m. would, if distributed over 50 km thick slabs (a generous assumption, at that depth) imply compressive stresses of 0.5 to 1.0 GPa, which must be considered likely to fracture the slab. Whether such stresses are just those necessary to account for the resurgence of seismicity at these depths, or whether they would severly disrupt the slab, as depicted in Fig. 4(d), is clearly an important question. However, a more severe constraint, to be discussed in the next section, is that such stresses would probably severely buckle the slab, as in Fig. 4(e). If this is true, then model 2, or models in which f_F is even larger, are to be favored. This will be discussed further below.

Before considering such questions further, it is very instructive to consider slabs which do not penetrate as deeply. As discussed earlier, such slabs will encounter only moderate resistance from the mantle, and so equation (32) can still be applied to a reasonable approximation if F_{LE} is neglected. If v = 30 mm/yr and t_c = 100 Ma, then L_s = 450 km. Taking L = 550 km, the predicted values of f are given in Table 2 as model 5; f_F is determined from the requirement that $F_{PL} \approx 0$. Model 5 is illustrated in Fig. 9: this slab is under strong extensional stresses, and f_F is required to be about 0.2 GPa. Model 6 (Table 2 and Fig. 9) is for a younger slab being rapidly subducted: v = 60 mm/yr and t_c = 50 Ma. The pattern of stresses is similar to that of model 5. Note that because of the dependences of f_T and f_V on t_c, equations (26) and (29), the effect of f_T, is considerably reduced by f_V in this case (it should be born in mind that f_V is likely to have been over-estimated here because of the large viscosity assumed). The tensional stresses are qualitatively consistent with the tensional focal mechanisms of intermediate-depth earthquakes. If the slab is both young and slowly subducted (v = 30 mm/yr, t_c = 50 Ma; model 7 in Table 2 and Fig. 9), then L_s = 250 km, and the slab may not reach the 400 km phase transition. As a result, the downward forces are greatly reduced, and either f_F must be small (Fig. 9) or F_{PL} large in order for the slab to descend. The behavior of the Juan de Fuca plate, in which subduction has apparently slowed and the plate has begun to attach to the North American plate, seems to be consistent with this result. Unless the downward forces have been greatly over-estimated, the slabs of models 5 and 6 must be supported either by large inter-plate friction (f_F) or a strong tensional plate force (negative F_{PL}).

BUCKLING OF SLABS

If an elastic plate is compressed in its plane, it may buckle. Buckling is an instability: if the plate is initially perfectly planar, it is metastable and will not buckle. A small deviation from planarity may grow if the compressive stress is sufficient, but there is also a critical stress necessary to initiate buckling. The buckling will be opposed by the flexural rigidity of the plate. In the case of a lithospheric slab, the buckling will also be resisted by the surrounding mantle. Davies (1979) has considered the buckling instability in the case of an elastic plate surrounded by a viscous fluid and derived a buckling growth time τ_B:

$$\tau_B = 2\eta\lambda/\pi(F - 4\pi^2 D/\lambda^2) \qquad (33)$$

where λ is the wavelength of the buckle, F is the compressive force and D is the flexural rigidity of the plate. Note that τ_B is negative (the buckle will not grow) if $F < 4\pi^2 D/\lambda^2$. It is useful to define a critical wavelength, λ_c:

$$\lambda_c^2 = 4\pi^2 D/F \quad . \qquad (34)$$

For a given force, buckling can only occur for $\lambda > \lambda_c$. The buckling time has a minimum value at

$$\lambda_M = \sqrt{3}\,\lambda_c \quad , \qquad (35)$$

when

$$\tau_M = 3\eta\lambda_M/\pi F \quad . \qquad (36)$$

We have seen (Figs. 1-3) that slabs contain ample irregularities which would serve to initiate buckling, and the results in Fig. 8 show that large compressive stresses are likely to occur in at least the lower 500 km of the plate in those models. The largest buckle wavelength which could occur in this region is thus $\lambda \approx 1000$ km. Studies of the flexure of lithosphere prior to subduction (Hanks, 1971; Turcotte et al., 1978; Bodine and Watts, 1979; Watts et al, this volume) have yielded flexural regidities $D \approx 0.4 - 2.0 \times 10^{23}$ Nm, and both plastic flow and slab heating are likely to reduce these. Taking the larger value and requiring $\lambda_c > 1000$ km, equation (34) yields

$$F < 0.6 \times 10^4 \text{ GPa.m} \quad , \qquad (37)$$

i.e., F must be less than this value to avoid buckling the slab. Larger values of F would permit smaller scale buckling, which could then be easily accomodated within the lower part of the slab.

Not only the scale, but the growth time of the buckles must be considered: if the growth is too slow, the slab may pass through the compressive zone before buckles develop. If v = 60 mm/yr, the slab will move 600 km in 10 Ma. A reasonable upper limit on τ is thus about 3 Ma $\approx 10^{14}$ s. Using the values of Table 1 in equation (36), buckling with $\lambda \geq 1000$ km will be avoided only if

$$F < 1.4 \times 10^4 \text{ GPa.m} \quad , \qquad (38)$$

which is comparable to condition (37).

These results suggest that the slab will rapidly buckle under the stresses shown in Fig. 8: taking $F = 3 \times 10^4$ GPa.m as a representative value, and the values of Table 1 equations (35) and (36) yield $\lambda_M = 900$ km, $\tau_M = 0.90$ Ma, even with the large value assumed for the flexural regidity. This buckling can be avoided only if either $D > 10^{24}$Nm (which makes $\lambda_c > 1000$ km) or $\eta > 3.5 \times 10^{21}$ Pa.s (which makes $\tau_M > 3$ Ma). The former condition seems unlikely, since the lithosphere should be strongest before subduction. It may be possible that the viscosity of the mantle between about 300 km and 650 km depth is larger than 10^{21} Pa.s (10^{22} poise), but it seems unlikely in view of the studies of post-glacial rebound (Cathles, 1975; Peltier, 1976) which have always yielded viscosities no greater than about 10^{21} Pa.s in the upper mantle.

If conditions (37) and (38) are valid, they severely constrain the models of the slab of Fig. 8. If we take a representative limit on F of 10^4GPa.m, and adjust f_F and f_R accordingly, the result is model (8) of Table 2 and Fig. 10. The required magnitude of F_R is reduced, but now f_F must average 0.2 GPa for 150 km down the slab, which is a very large value. f_F can be reduced, but must still be large, if F_{PL} takes some of the load. f_F could also be reduced if the downward forces have been over-estimated. It is unlikely that the thermal buoyancy is much less than estimated here. It is possible that F_{PH} has been over-estimated for deeply penetrating slabs, however, since the low temperatures within the slab may inhibit the kinetics of the olivine-spinel phase change, and hence reduce or cancel the average upward displacement of the change in the slab (Sung and Burns, 1977). In model 9 (Table 2 and Fig. 10) F_{PH} has been assumed to be zero, to illustrate this possibility: f_F is thereby reduced to about 0.1 GPa. It is notable that even in this case the upper part of the slab is in tension; it is difficult to see how the constraints (37) and (38) can be met for a slab which is in compression through most of its depth (in which case $\lambda_c = 2000$ km would be allowed), as proposed by Isacks and Molnar (1971) for Tonga.

CONCLUSIONS

Observations of Benioff zones show that although most of them show substantial departures from planar geometry, there is little evidence for severe disruption of subducted lithosphere by fracturing or buckling. The demonstration by Molnar et al. (1979) that Benioff zone lengths correlate with (vt_c) can be recast to show that subducted lithosphere becomes aseismic within about 15% of the time for which it cooled prior to subduction. It is then clear that the more common deviation from this rule involves additional seismicity just above 650 km depth, and only in a few cases does it involve a shortening of the Benioff zone caused by the absence of seismicity below 650 km. These observations weaken some of the conventional arguments for the idea that lithospheric slabs do not penetrate the lower mantle.

It is possible to estimate the magnitudes of the main forces acting on subducted lithosphere with sufficient accuracy to permit some first-order modelling of the mechanics of subducted slabs. Negative buoyancies due to low temperatures and phase changes within the slab probably provide large downward forces. The upper mantle cannot provide substantial resistance to descending slabs unless its viscosity is much higher than has been inferred from post-glacial rebound data. Consequently, slabs which do not penetrate to 650 km must be supported mainly by a combination of tensional stress from

the attached plate and inter-plate friction at the subduction zone; in either case, large (kilobar) interplate frictional stresses seem to be required. Although several proposed mechanisms for resisting slabs which penetrate to 650 km depth are feasible, the slabs must be able to sustain very large down-dip compressive stresses if this deep resistance is to support much of the load of the slab. It is not obvious that a slab could sustain such stresses (0.5 - 1.0 GPa) without fracturing, producing obvious disruption, but it is not likely, according to the preceeding calculations, that the slab could avoid being severely buckled. In either case, the results should be evident in Benioff zones, and the load of the slab would no longer be sustained. Thus it is hard to avoid the conclusion that deeply penetrating slabs must also be supported by large inter-plate frictional stresses.

The above conclusion can be avoided if part of the upper mantle has significantly higher effective viscosity than has been thought. This would inhibit buckling, and also provide some direct viscous resistance to the descent of the slab, especially for slow subduction. Some careful exploration of models will be necessary to decide whether this can be done without violating the constraints of the post-glacial rebound data. The conclusion can be avoided or weakened if the negative buoyancies have been substantially over-estimated. This is a distinct possibility for phase change buoyancy (Sung and Burns, 1978), especially since temperatures at 400 km depth in a rapidly subducting slab can be as low as 600°C (Schubert et al., 1975). Thermal buoyancy could be counteracted if the slab has an intrinsic density less than the surrounding mantle, due either to a bulk chemical difference or to a difference in mineral assemblage due to stratification within the slab (e.g., Anderson, 1979). Such a slab would eventually become positively buoyant as it warmed, and would thus eventually rise. Such a scenario would be more appealing if there were any positive indication of such behavior in Benioff zones.

Potential implications for seismology are twofold: stresses in shallow seismic zones may be large, as has been advocated by Hanks (1977) and Aki (1978), and deep focal mechanisms may not be as readily interpretable in terms of slab stresses. The deep focal mechanisms unquestionably indicate down-dip compression in many deep slabs. The question is whether these reflect total slab stresses, or perhaps are localized in some atypical part of the slab. For example, stresses generated by warming, bending or phase changes could be large and would vary rapidly across a slab, with one or more changes in sign of down-dip components.

The observations of the Tonga Benioff zone are especially important. If the slab is indeed in down-dip compression for most of its depth, and if the conclusions stated above are correct, then the compressive stress must be everywhere small, and this implies a very delicate balance of large forces down the entire slab.

The potential implications for models of plate driving forces are also considerable. First, the models of Chapple and Tullis (1977) and Davies (1978), incorporating substantial inter-plate friction, are favored over those of Forsyth and Uyeda (1975), in which slabs were supposed to be resisted within the mantle. Second, there may be considerable variation in the net force on

plates from trenches, as the balance between large opposing forces fluctuates. This may be evident in the Bonin-Mariana transition, for example, as discussed by Bodine and Watts (1978). Third, although these models raise considerable uncertainties in the mechanics of subduction zones, they also demonstrate that many of the forces are reasonably predictable, so that some careful modelling of plate dynamics might yield some useful constraints.

REFERENCES

Aggarwal, Y.P., Global estimates of interplate stresses, seismic efficiency and basal shear stresses (abstract), EOS, Trans. Amer. Geophys. Union, 60, 390 (1979).

Aki, K., Stress drop and energy release in an earthquake estimated by the use of the barrier model (abstract), EOS, Trans. Amer. Geophys. Union, 59, 326 (1978)

Anderson, D.L., The upper mantle transition region: eclogite?, Geophys. Re. Lett., 6, 433-436 (1979).

Barazangi, M. and Isacks, B.L., Subduction of the Nazca plate beneath Peru: evidence from spatial distribution of earthquakes, Geophys. J. Roy. Astron. Soc., 57, 537-556 (1979).

Batchelor, G.K., An Introduction to Fluid Dynamics, Cambridge University Press, 615 pp. (1967).

Billington, S., The morphology and tectonics of the subducted lithosphere in the Tonga-Fiji-Kermadec region from seismicity and focal mechanism solutions, Ph.D. Thesis, Cornell University (1979).

Anderson, D.L., The upper mantle transition region: eclogite?, (in press).

Barazangi, M. and Isacks, B.L., Subduction of the Nazca plate beneath Peru: evidence from spatial distribution of earthquakes, Geophys. J. Roy. Astron. Soc., 57, 537-556 (1979).

Batchelor, G.K., An Introduction to Fluid Dynamics, Cambridge University Press, 615 pp. (1967).

Billington, S., Private communication (1979).

Bird, P., Initiation of intracontinental subduction in the Himalaya, J. Geophys. Res., 83, 4975-4988 (1978a).

Bird, P., Stress and temperature in subduction shear zones: Tonga and Mariana, Geophys. J. Roy. Astr. Soc., 55, 411-434 (1978b).

Bodine, J.H. and Watts, A.B., On lithospheric flexure seaward of the Bonin and Mariana trenches, Earth Planet. Sci. Lett., 43, 132-148 (1979).

Bodine, J.H., Steckler, M.S. and Watts, A.B., Observations of flexure and the rheology of the oceanic lithosphere (abstract), EOS, Trans. Amer. Geophys. Union, 60, 393 (1979).

Cardwell, R.K. and Isacks, B.L., Geometry of the subducted lithosphere beneath the Banda Sea in eastern Indonesia from seismicity and fault plane solutions, J. Geophys. Res., 83, 2825-2838 (1978).

Carter, N.L., Steady state flow of rocks, Rev. Geophys. Space Phys., 14, 301-360 (1976).

Cathles, L.M. III, The Viscosity of the Earth's Mantle, Princeton University Press, New Jersey, 390 pp. (1975).

Chapple, W.M. and Tullis, T.E., Evaluation of the forces that drive the plates, J. Geophys. Res., 82, 1967-1984 (1977).

Chase, C.G., Extension behind island arcs and motions relative to hot spots, J. Geophys. Res., 83, 5385-5387 (1978).

Chiu, J.M., Isacks, B. and Cardwell, R.K., Three-dimensional configurations of descending lithosphere (abstract), EOS, Trans. Amer. Geophys. Union, 60, 388 (1979).

Davies, G.F., Limits on the constitution of the lower mantle, Geophys. J. Roy. Astr. Soc., 38, 479-503 (1974).

Davies, G.F., Whole mantle convection and plate tectonics, Geophys. J.R. Astr. Soc., 49, 459-486 (1977a).

Davies, G.F., Viscous mantle flow under moving lithospheric plates and under subduction zones, Geophys. J. Roy. Astron. Soc., 49, 557-563 (1977b).

Davies, G.F., The roles of boundary friction, basal shear stress and deep mantle convection in plate tectonics, Geophys. Res. Lett., 5, 161-164 (1978).

Davies, G.F., Why doesn't subducted lithosphere buckle?, (submitted for publication, 1979).

Elsasser, W.M., Convection and stress propagation in the upper mantle, in The application of modern physics to the earth and planetary interiors, 223-246, ed. S.K. Runcorn, Wiley-Interscience, New York (1969).

Engdahl, E.R., Seismicity and plate subduction in the central Aleutians, in Island Arcs, Deep Sea Trenches and Back-Arc Basins, M. Talwani and W.C. Pitman, III (editors), American Geophys. Union Maurice Ewing Series 1, 259-272 (1977).

Forsyth D. and Uyeda, S., On the relative importance of the driving forces of plate motion, Geophys. J.R. Astr. Soc., 43, 163-200 (1975).

Gaposchkin, E.M. and Lambeck, K., Earth's gravity field to the sixteenth degree and station coordinates from satellite and terrestrial data, J. Geophys. Res., 76, 4855-4883 (1971).

Hager, B.H., Oceanic plate motions driven by lithospheric thickening and subducted slabs, Nature (1978).

Hanks, T.C., The Kuril trench-Hokkaido rise system: large shallow earthquakes and simple models of deformation, Geophys. J. Roy. Astr. Soc., 23, 173-189 (1971).

Hanks, T.C., Earthquake stress drops, ambient tectonic stresses and stresses that drive plate motions, Pure and Appl. Geophys., 115, 441-458 (1977).

Hilde, T.W.C., Isezaki, N. and Wageman, J.M., Mesozoic sea-floor spreading in the North Pacific, in The geophysics of the Pacific Ocean Basin and its Margin, G.H. Sutton, M.H. Manghnani and R. Moberly (editors), American Geophysical Union Geophysical Monograph 19, 205-226 (1976).

Isacks, B.L. and Barazangi, M., Geometry of Benioff zones: Lateral segmantation and downwards bending of the subducted lithosphere, in Island Arcs, Deep Sea Trenches and Back-Arc Basins, M. Talwani and W.C. Pitman III, eds. Maurice Ewing Series 1, Amer. Geophys. Union, Washington, D.C. (1977).

Isacks, B. and Molnar, P., Distribution of stress in the descending lithosphere from a global survey of focal mechanism solutions of mantle earthquakes, Rev. Geophys. Space Phys. 9, 103-174 (1971).

Isacks, B., Oliver, J. and Sykes, L.R., Seismology and the new global tectonics, J. Geophys. Res., 73, 5855-5899 (1968).

Jackson, I.N.S., Liebermann, R.C. and Ringwood, A.E., Disproportionation of spinels to mixed oxides: significance of cation configuration and implications for the mantle, Earth Planet. Sci. Lett., 24, 203-208 (1974).

Lister, C.R.B., Gravitational drive on oceanic plates caused by thermal contraction, Nature, 257, 663-665 (1975).

Liu, L., Mineralogy and chemistry of the earth's mantle above 1000 km, Geophys. J. Roy. Astr. Soc., 48, 53-62 (1977).

McKenzie, D.P., Speculations on the consequences and causes of plate motions, Geophys. J. Roy. Astr. Soc., 18, 1-32 (1969).

Molnar, P. Friedman, D. and Shih, J.S.F., Lengths of intermediate and deep seismic zones and temperatures in downgoing slabs of lithosphere, Geophys. J. Roy. Astr. Soc., 56, 41-54 (1979).

O'Connell, R.J., On the scale of mantle convection, Tectonophysics, 38, 119-136 (1977).

Parker, R.L. and Oldenburg, D.W., A thermal model of oceanic ridges, Nature, 242, 137-139 (1973).

Parsons, B. and McKenzie, P., Mantle convection and the thermal structure of the plates, J. Geophys. Res., 83, 4485-4496 (1978).

Parsons, B. and Sclater, J.G., An analysis of the variation of ocean floor bathymetry and heat flow with age, J. Geophys. Res., 82, 803-827 (1977).

Pascal, G., Isacks, B.L., Barazangi, M. and Dubois, J., Precise relocations of earthquakes and seismotectonics of the New Hebrides island arc, J. Geophys. Res., 83, 4957-4974 (1978).

Peltier, W.R., Glacial-isostatic adjustment-II. The inverse problem, Geophys. J. Roy. Astr. Soc., 46, 669-706 (1976).

Richardson, R.M., Intraplate stress and the driving mechanism for plate tectonics, Ph.D. Thesis, Massachusetts Institute of Technology (1978).

Richter, F. and McKenzie, D., Simple plate models of mantle convection, J. Geophys., 44, 441-471 (1978).

Sammis, C.G., Smith, J.C., Schubert, G. and Yuen, D.A., Viscosity-depth profile of the earth's mantle: effects of polymorphic phase transitions, J. Geophys. Res., 82, 3747-3761 (1977).

Schubert, G., Yuen, D.A. and Turcotte, D.L., Role of phase transitions in a dynamic mantle, Geophys. J. Roy. Astr. Soc., 42, 705-735 (1975).

Smith, A.T. and Toksöz, M.N., Stress distribution beneath island arcs, Geophys. J. Roy. Astr. Soc., 29, 289-318 (1972).

Sung, C. and Burns, R.G., Kinetics of the olivine-spinel transition: implications to deep focus earthquake genesis, Earth Planet. Sci. Lett., 165-170 (1976).

Toksöz, M.N., Minear, J.W. and Julian, B.R., Temperature field and geophysical effects of a downgoing slab, J. Geophys. Res., 76, 1113-1138 (1971).

Turcotte, D.L., McAdoo, D.C. and Caldwell, J.G., An elastic-perfectly plastic analysis of the bending lithosphere, Tectonophys., 47, 193 (1978).

TABLE 1

PARAMETER VALUES USED IN THIS PAPER.

ρ	mantle density	3.3 Mg/m^3
C_P	specific heat	10^3 J/kg°C
k	thermal conductivity	3.3 W/m°C
κ	thermal diffusivity	10^{-6} m^2/s
T_0	upper mantle temperature	1400°C
α	volume coefficient of thermal expansion	3 x 10^{-5}°C^{-1}
η	upper mantle viscosity	10^{21} Pa.s (10^{22}P)
ν	kinematic viscosity	3 x 10^{17} m^2/s
g	acceleration due to gravity	10 m/s^2
H	lithosphere thickness (unless specified otherwise)	100 km
D	flexural rigidity of lithosphere	2 x 10^{23} Nm

TABLE 2

PARAMETERS, FORCES AND STRESSES OF MODELS OF SUBDUCTED LITHOSPHERE SHOWN IN FIGURES 8-10

Model	v mm/yr	t_c Ma	L_S km	L km	F_{PL} 10^4GPam	f_F GPa	f_T GPa	f_V GPa	f_{PH} GPa	f_R GPa
1	60	100	900	1050	-0.3	0.02	0.04	0.01	0.15	0.28*
2	60	100	900	1050	-0.3	0.1	0.04	0.01	0.15	0.20*
3	60	100	900	1050	1.0	0.02	0.04	0.01	0.15	0.36*
4	60	100	900	1050	1.0	0.1	0.04	0.01	0.15	0.28*
5	30	100	450	550	0	0.18*	0.04	0.01	0.08	----
6	60	50	450	550	0	0.11*	0.03	0.02	0.10	----
7	30	50	250	350	0	0.02*	0.03	0.02	----	----
8	60	100	900	1050	0	0.21*	0.04	0.01	0.15	0.10*
9	60	100	900	1050	0	0.11*	0.04	0.01	0	0.10*

* Determined from the force balance condition, equation (32).

(a)

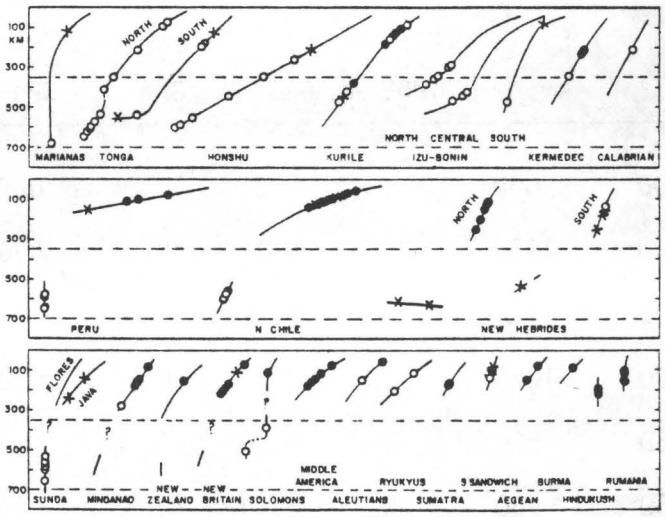

(b)

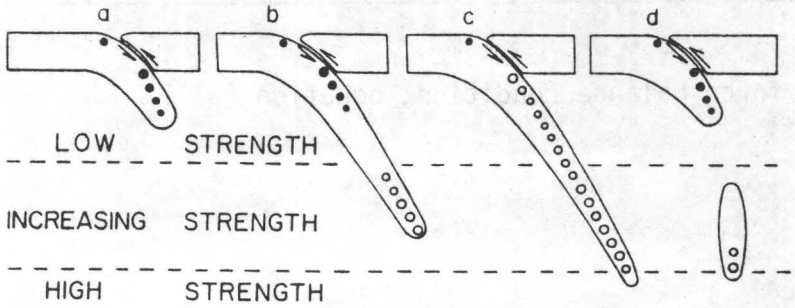

Figure 1: (a) Summary cross-sections of Benioff zones from Isacks and Molnar (1971). Symbols denote focal mechanisms; open circles: down-dip compression, solid circles: down-dip tension, crosses: other. (b) Schematic explanation, from Isacks and Molnar (1971), of the observation in part (a).

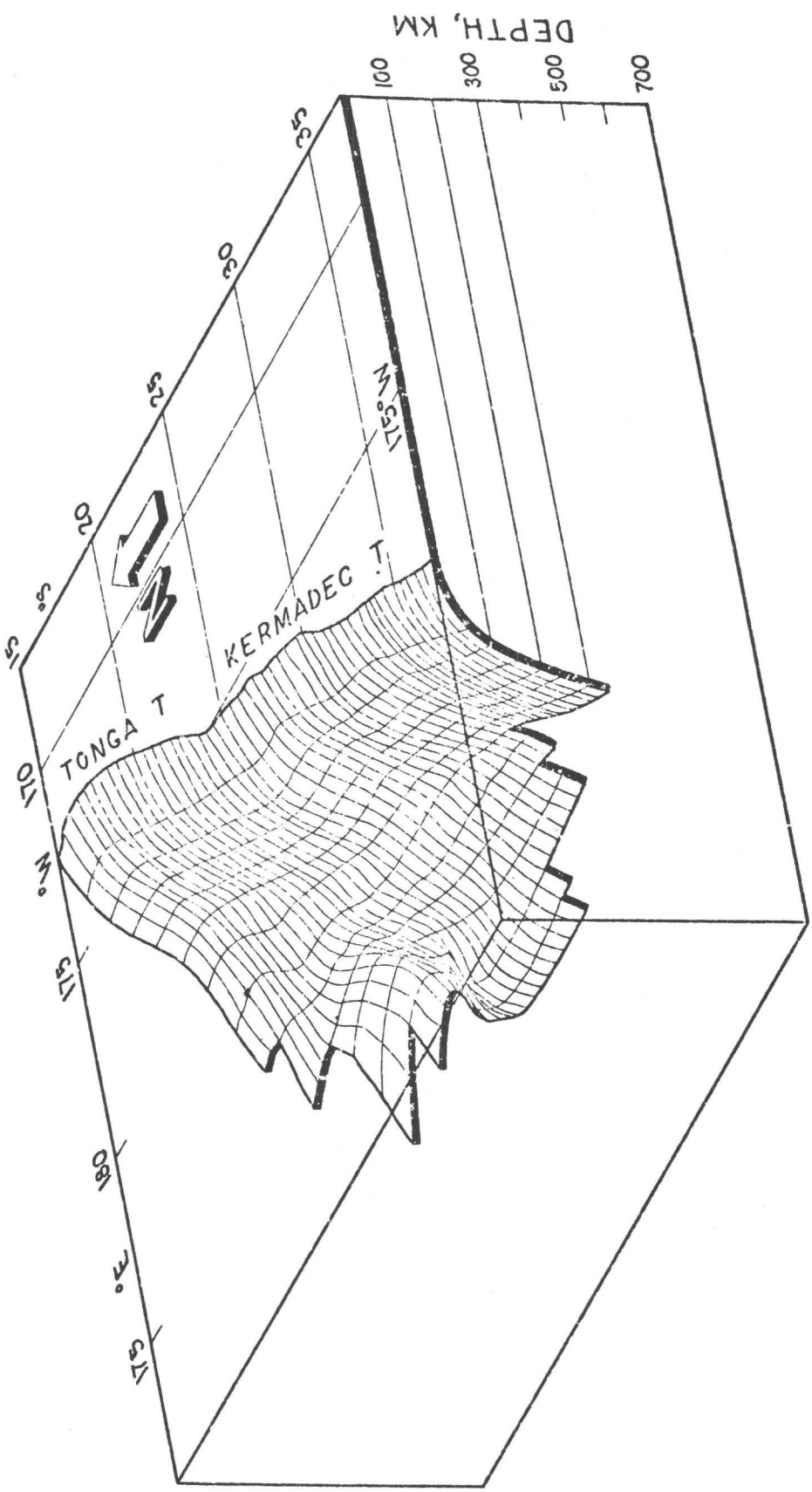

Figure 2: Block diagram of the Tonga-Kermadec Benioff zone, from Billington (1979).

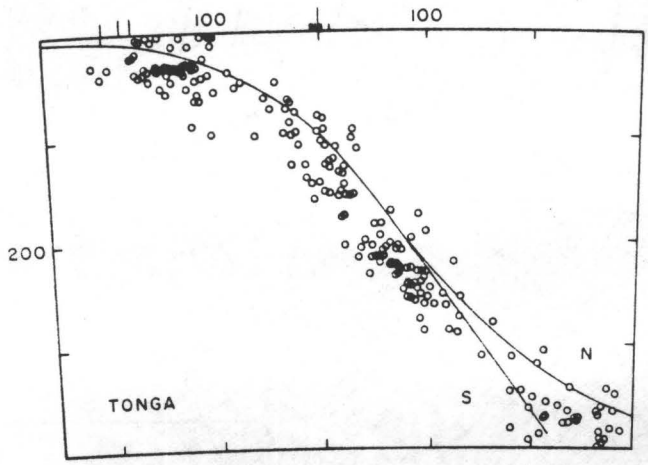

Figure 3: Earthquake hypocenters projected onto a cross-section of the Tonga Benioff zone, from Isacks and Barazangi (1977).

Figure 4: Hypothetical fates of subducted lithosphere. Lower horizontal line indicates 650 km depth in the mantle. (a) simple subduction and assimilation into the deep mantle, (b) moderate bending of slab due to variations in normal forces, such as negative buoyancy due to phase changes, (c) detachment under tension and faster sinking of a piece of slab, (d) compressional fracture of slab, (e) buckling of slab, (f) laying of slab at bottom of upper mantle due to trench migration, (g) fragmentation of slab during subduction, with independent descent of pieces, (h) assimilation of slab near bottom of upper mantle (Richter and McKenzie, 1978).

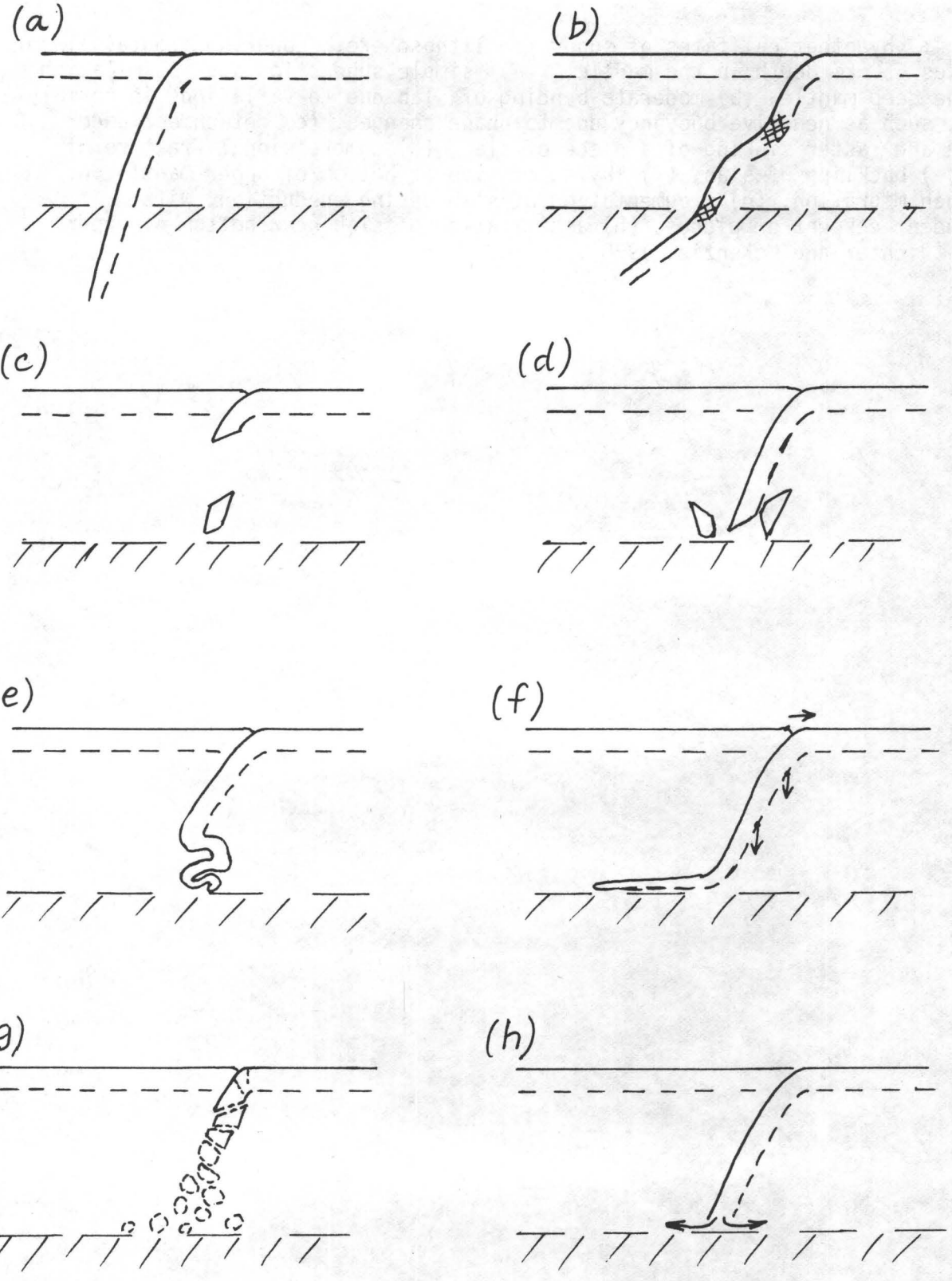
(a)
(b)
(c)
(d)
(e)
(f)
(g)
(h)

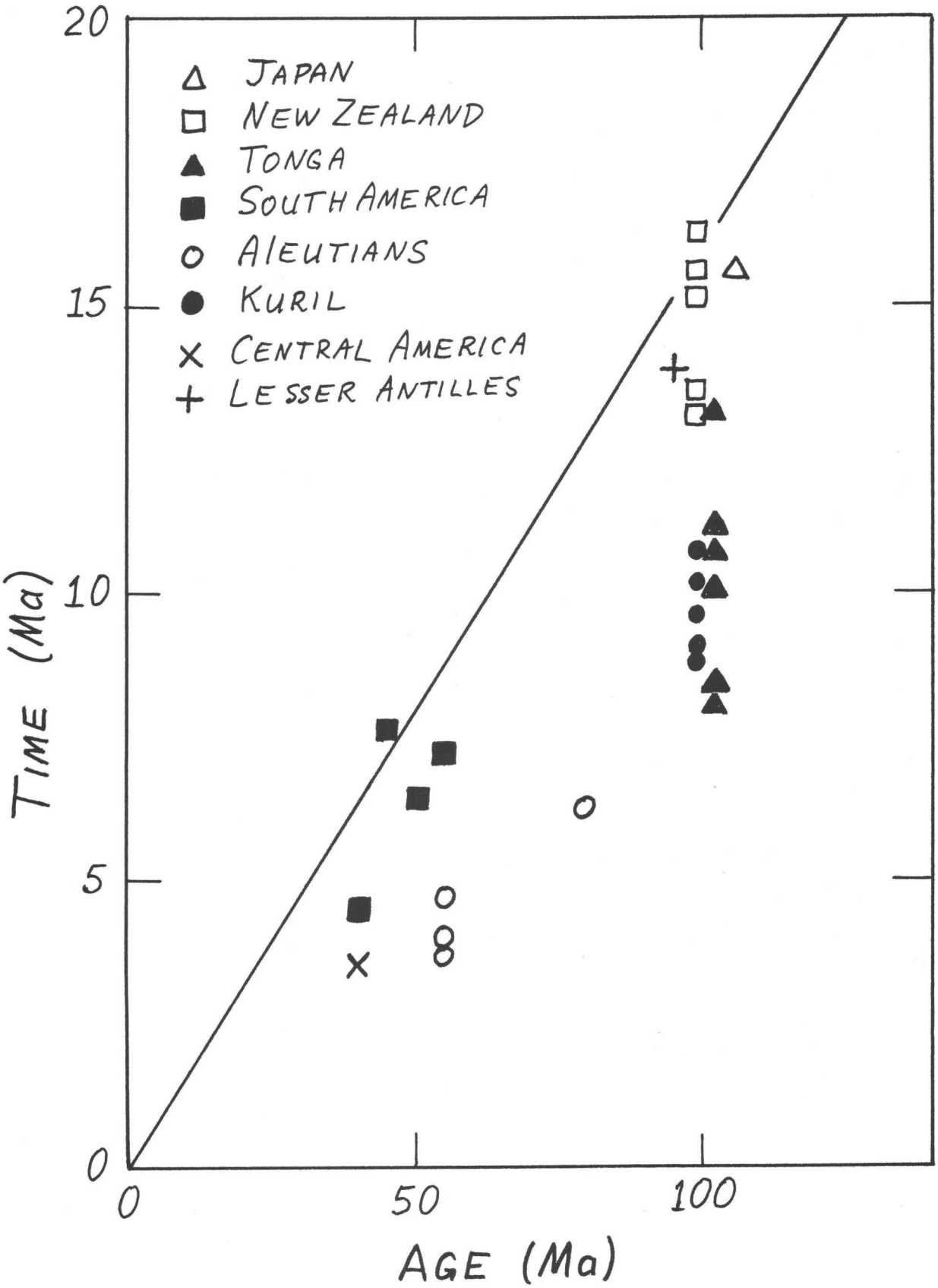

Figure 5: Residence time of subducted lithosphere in Benioff zone versus age of lithosphere at subduction. Data from Molnar et al. (1979).

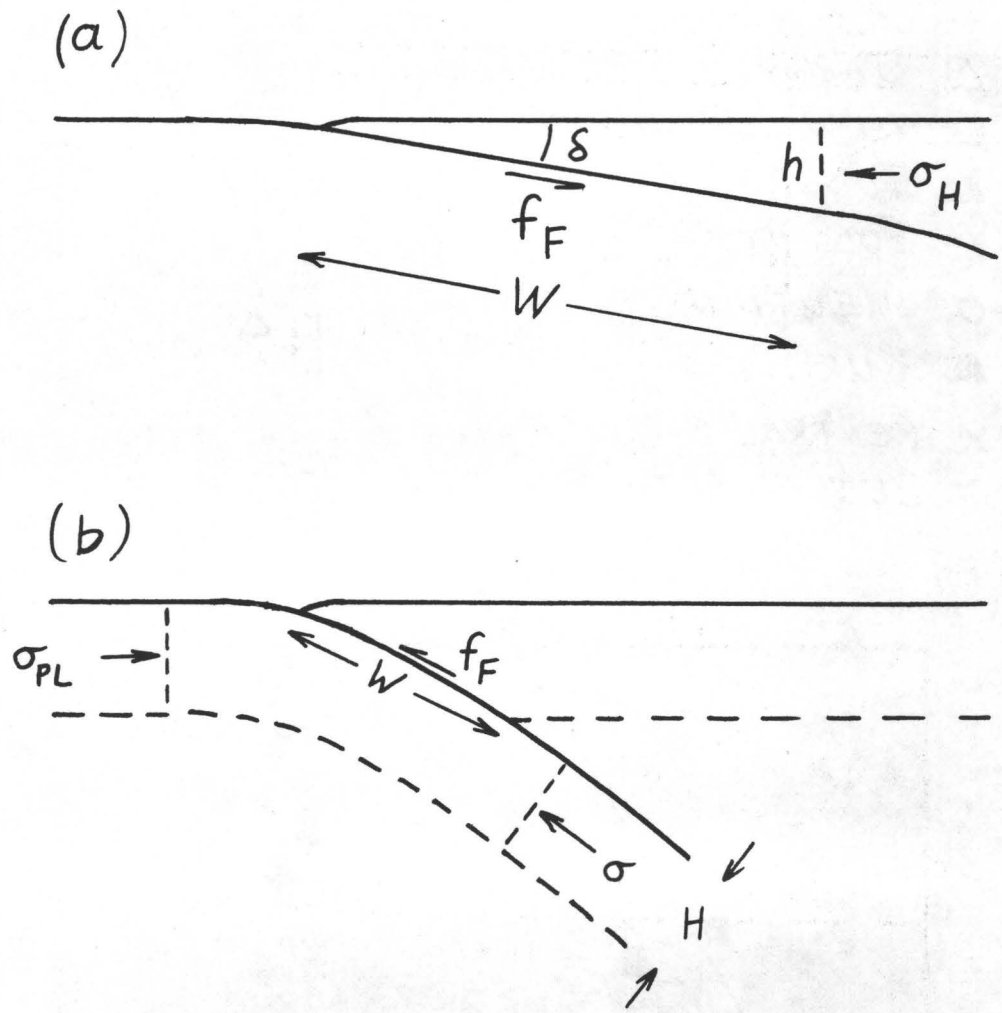

Figure 6: Schematic mechanics of subduction zones. (a) Balance of forces on an overthrust wedge with shallow dip, δ. f_F is interplate frictional stress and σ_H is horizontal normal stress component in the wedge. (b) Balance of forces on lithosphere during subduction. σ_{PL} is the horizontal normal stress in the plate before subduction and σ is that part of σ_{PL} which is transmitted to the subducted slab.

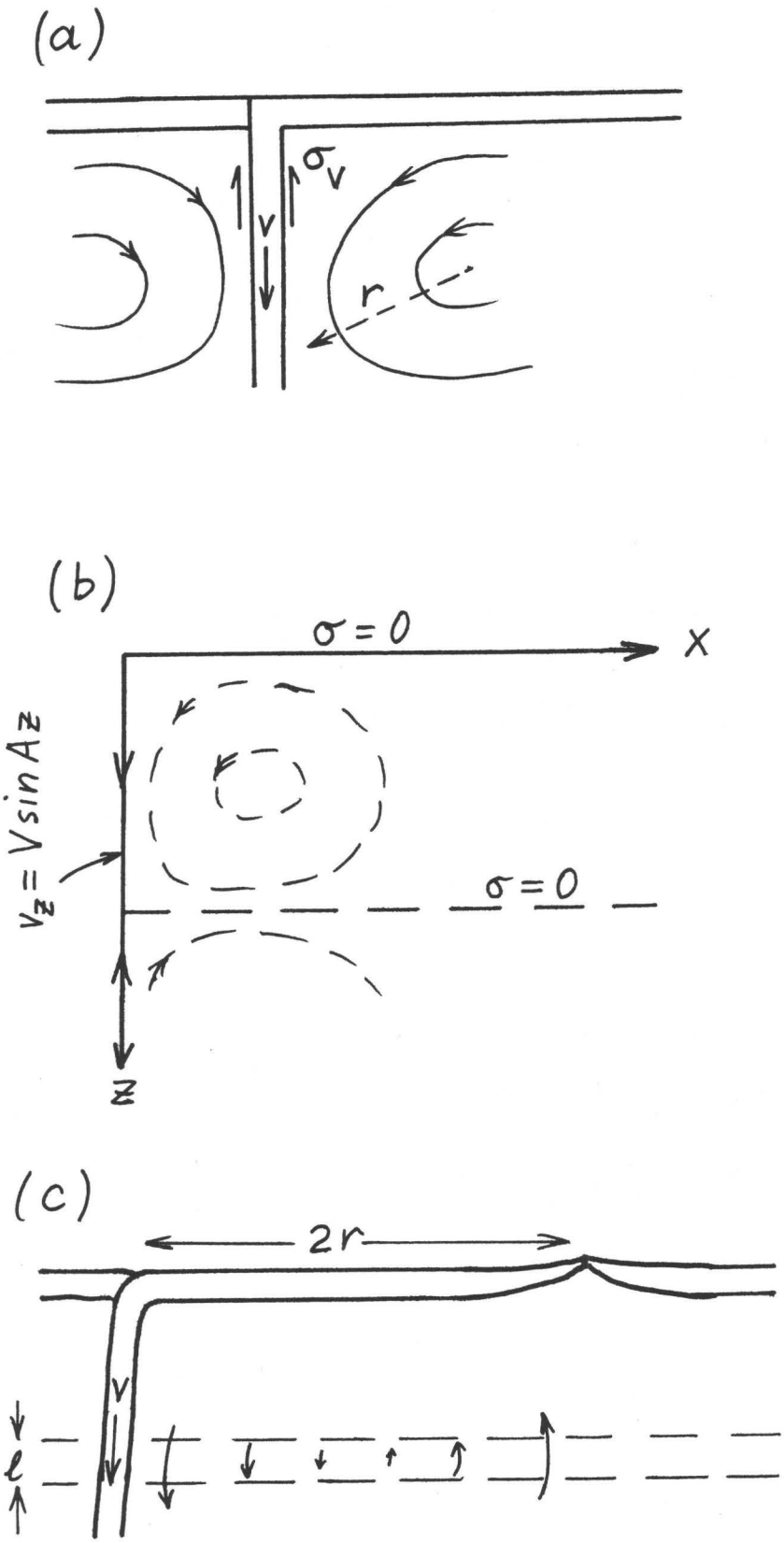

Figure 7: Sketches of the interaction of descending slabs with surrounding viscous mantle. (a) Length scale, r, and viscous shear stress, σ_V, of mantle flow induced by slab descending with velocity v. (b) Coordinates and boundary conditions for the calculation of flow induced in a viscous fluid by a vertical boundary with a spatially periodic tangential velocity. (c) Length scale, 2r, of hypothetical flow through a thin high viscosity layer in the presence of a descending slab and a spreading ridge.

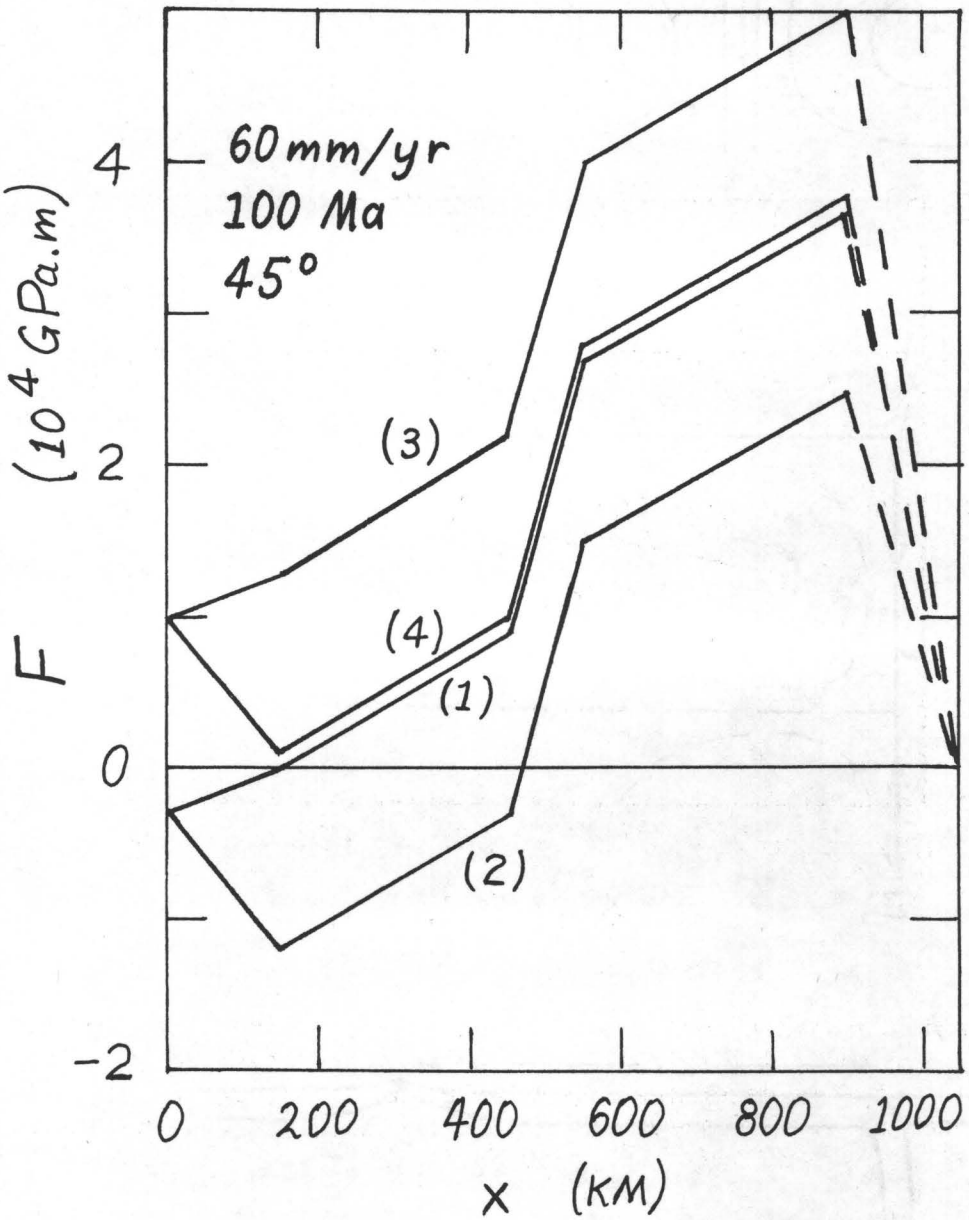

Figure 8: Cumulative down-dip force per unit length of trench, F, from the trench to a distance, x, down the slab for 100 Ma old lithosphere subducted at 60 mm/yr at 45° dip. In these cases, two values each of the plate force, F_{PL}, and inter-plate friction, f_F are assumed, and the deep resistance, F_R, is determined from the assumption that F(1050) = 0. All forces are given in Table 2. Model numbers are in parentheses. Positive F corresponds to down-dip compression, negative F to down-dip tension.

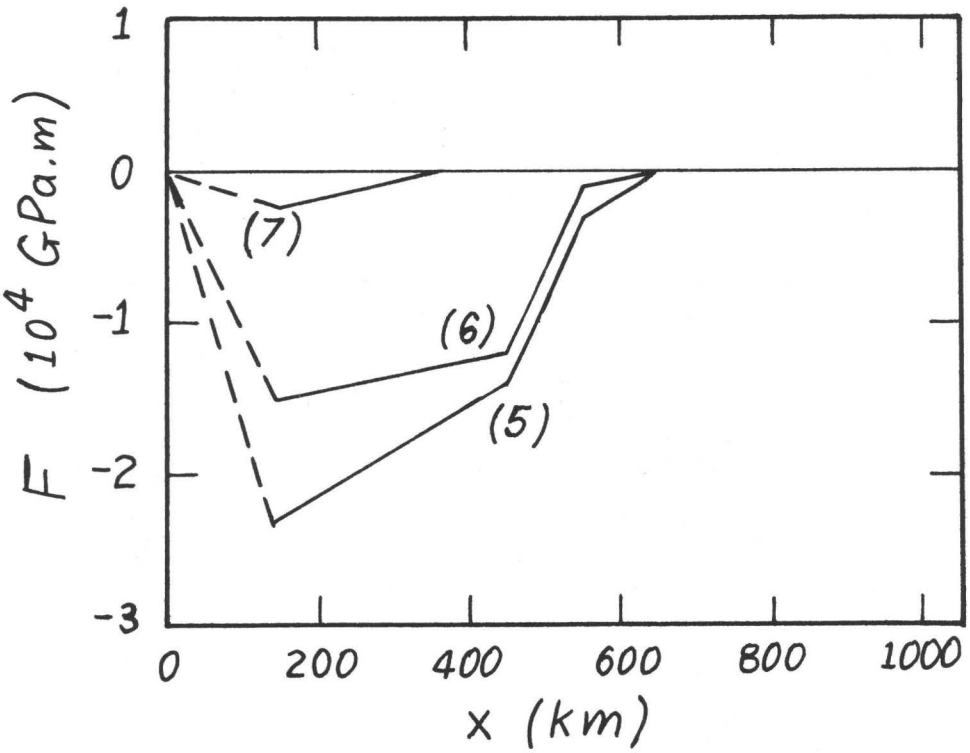

Figure 9: Cumulative down-dip force, as in Figure 8, for lithosphere of different ages and subduction rates. All forces and parameters are given in Table 2. The interplate friction, f_F, is determined from the assumption that the plate force, F_{PL}, is zero. Model 5: v = 30 mm/yr, t_c = 100 Ma. Model 6: v = 60 mm/yr, t_c = 50 Ma. Model 7: v = 30 mm/yr, t_c = 50 Ma.

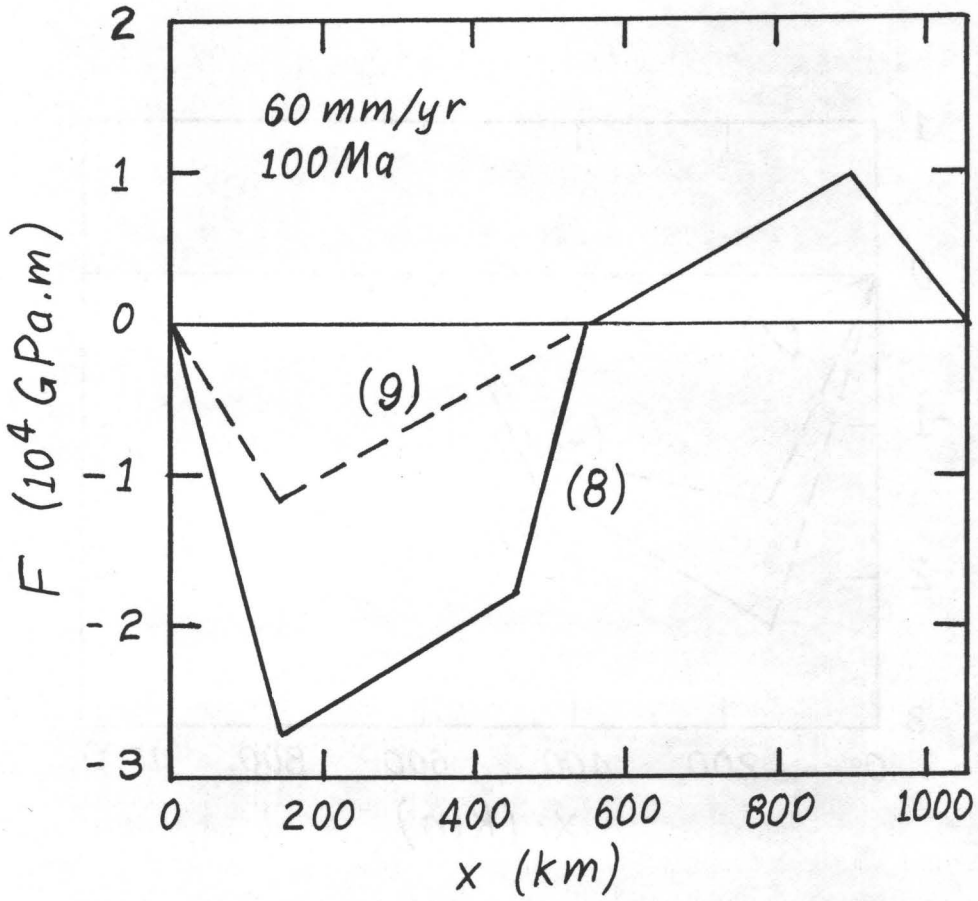

Figure 10: Cumulative down-dip force, as in Figure 8, for 100 Ma old lithosphere subducting at 60 mm/year and 45°. In these models, F is required to be less than 10^4 GPam to avoid buckling the slab and f_F and f_R are determined by assuming F_{PL} = 0 and F(1050) = 0. In model (9) the negative buoyancy due to the olivine-spinel phase change, f_{PH}, is also assumed to be zero.

IMPLICATIONS OF REGIONAL GRAVITY FOR STATE OF STRESS IN THE EARTH'S CRUST AND UPPER MANTLE

by

Marcia McNutt*
Department of Geology & Geophysics
University of Minnesota
Minneapolis, Minnesota 55455

and

R. L. Parker
Institute of Geophysics and Planetary Physics
Scripps Institution of Oceanography A-025
La Jolla, California 92093

* present address: United States Geological Survey MS 77
345 Middlefield Road
Menlo Park, California 94025

ABSTRACT

Gravity anomalies, a measure of the earth's departure from hydrostatic equilibrium, can be used to estimate the stress necessary to support surface topography and internal density anomalies. The stress levels obtained depend upon the rheological model assumed for the earth, but the gravity anomalies and surface deformations restrict the class of permissible models. Regional gravity anomalies, in the wavelength range from 20 to 2000 km, are best suited for crust and upper mantle stress studies because their source lies in the upper 100 km of the earth. Regardless of the model assumptions and analysis techniques, the stress implications from the regional gravity field are rather consistent. The majority of continental and oceanic topographic features were formed on weak crust incapable of maintaining large stress differences. As a result the features are locally compensated, and maximum stress differences are on the order of the weight of the load. However, large, isolated volcanoes in the oceans appear to have been formed on already cooled, thickened lithosphere. The gravity anomalies and surface deformation from these features demonstrate that the earth's outer 30 to 40 km is capable of regionally supporting stress differences in the 100 MPa range.

INTRODUCTION

Seismologists tell us that above the core the mantle reacts like an elastic solid to the passage of earthquake waves. The effective seismic rigidity, or resistance to deformation by shearing stresses, is comparable to the strength of steel, but these rigidity estimates only apply to short period stresses of relatively small magnitude. The rigidity may be much smaller for large stresses of long duration, and in general the problem discussed here is one of determining the earth's "permanent" resistance to shearing stresses as a function of depth, amplitude, and wavelength of the disturbance. This question is fundamental in that it bears on many other geophysical problems, such as the development of mountain chains, long-term vertical motions of the earth's surface, the internal temperature distribution, the scale and rate of convection, and other aspects of earth dynamics.

From an historical viewpoint, the first estimates of stress in the earth were based on gravity anomalies. The fact that stress differences exist cannot be denied. Topographic features alone represent a departure from hydrostatic equilibrium, and the earth's reaction to the surface load according to certain rheological laws provides a means of distributing the stresses over depth within the earth. Gravity anomalies are most often used to estimate the earth's reponse to surface stress, and thus the stress issue naturally becomes involved with the question of isostatic compensation. The discussion of stress within the earth must not be limited to that which is topographically induced, however, because gravity anomalies also tell us that there exist mass anomalies, and therefore deviatoric stresses, that are unrelated to existing surface elevations.

The purpose of this paper is to review estimates of earth strength based on gravity observations, although consideration will also be given to studies of isostatic compensation based on surface deformation. We will begin with a brief discussion of Jeffreys' (1924 plus later editions) work, because his ideas have in some way influenced the thoughts of almost all subsequent investigators. The second section concentrates on strength estimates derived from measurements of the longest wavelength components of the earth's gravity field, while the following two sections deal with oceanic and continental studies of a more regional dimension. Finally the results for the earth are compared to stress estimates for the moon and Mars based on recent elevation and gravity measurements by space probes.

JEFFREY'S WORK

Given only a surface distribution of topography, Jeffreys (1976) describes three approaches for determining stress:

1) Assume an earth rheology and mechanism for isostatic compensation. Apply the load, allow the earth to respond, and calculate the stress.
2) Assume the dynamic processes that form the topography, and work out the stress consequences.
3) Calculate all possible stress distributions consistent with the surface load. The distribution that attains the least maximum stress difference provides a lower bound for the strength of the earth.

The first two methods are examples of the "forward" problem in geophysics, and therefore the stress answers are no more valid than the

assumptions. The first method is often used to test the plausibility of various rheologies, using predicted stress levels, gravity anomalies, and surface deformation as a measure of the model's acceptability. The second approach is rarely used due to a lack of information on the fundamentals of orogeny. The third type of analysis is an example of the true "inverse" problem in that the results depend only on the observations, not on the assumptions. It should be remembered that the bound itself is the only quantity of importance in the inverse approach. The stress distribution that attains the least maximum stress may not resemble that of the earth since it was not required that the solution result from any known or even plausible earth behavior.

Jeffreys begins with the first approach, assuming an elastic rheology for the earth. This is basically a Bouguer theory corrected for earth elasticity and makes no assumption of isostatic compensation by requiring that the stress be hydrostatic below some depth. The value of this approach is two-fold. An analytic solution can be easily obtained, thus avoiding tedious numerical calculation of stress distributions. Secondly, as Jeffreys argues, the elastic theory uncorrected for isostasy gives a better estimate of the lower bound on the stress differences because the entire earth contributes to the support of the load. If we assume that the interior of the earth is hydrostatic, and thus supports no stress differences below a certain depth, the maximum stress difference in the overlying elastic layer must increase to compensate for the loss of support from below. Jeffreys also finds that the least maximum stress difference given by the elastic theory is not much more than the value determined by the inverse approach. The reason for this perhaps surprising result is that any nonelastic solution for stress within the eath must increase the total strain energy per unit volume (Castigliano's Principle) even if it does reduce the maximum deviatoric stress. Thus while the inverse approach finds stress solutions which decrease the maximum of a function, it does so at the expense of increasing the volume integral of that same function. The result is that stress values almost comparable with the maximum are spread over a greater volume.

The first case considered by Jeffreys is that of a surface harmonic load resting on an incompressible elastic sphere (Fig. 1a). Let s_n equal the root mean square variation of the topographic stress of degree n as given in terms of fully normalized spherical harmonics. The maximum stress difference in the sphere from the applied normal stress is given by $k_n s_n$ and is located at a depth of approximately $1/n$ times the sphere's radius. Using the values for k_n and depth from Jeffreys (1943) and the topography coefficients for the earth from Balmino et al. (1973) we can construct the following table of maximum stress differences $\Delta\sigma_n$ and distance from the center of the earth in fraction of earth radius that the stress maximum occurs.

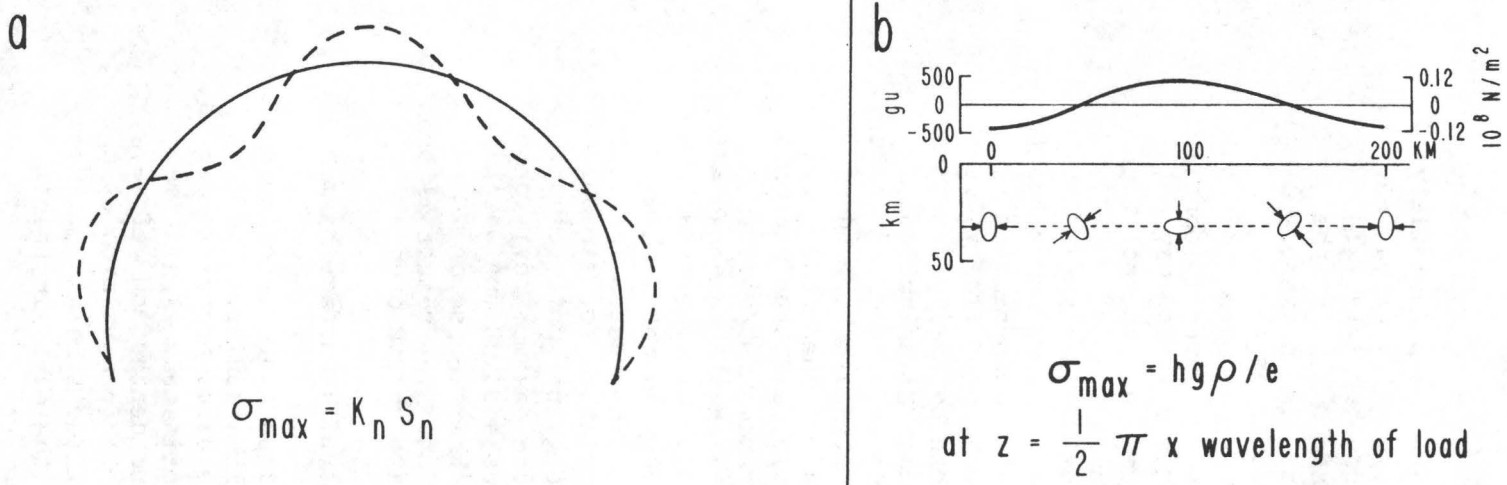

Figure 1. Models used by Jeffreys to calculate stress in the earth from surface loading. a. Harmonic loading on an elastic earth. Maximum stress (σ_{max}) depends on the root mean square of the topographic stress (s_n) and a multiplicative factor (k_n) which depends only on harmonic degree. b. Harmonic loading on a flat earth. Orientation of stress ellipsoid is also shown. c. Loading on an elastic plate overlying a fluid (from Banks et al., 1977). d. Airy compensation.

TABLE 1

n	k_n	s_n (MPa)	$\Delta\sigma_n$ (MPa)	r/a
2	3.03	21.3	64.6	0
3	1.70	23.4	39.8	.591
10	1.13	9.6	10.8	.895
30	1.025 1.040	3.4	3.4	.966

(note: 10^6 Pa = 10 bars)

The numbers in this table reveal a theme that reappears in many later studies. For degrees higher than n=10 , the maximum stress difference is less than 10 MPa and occurs at approximately lithospheric depth. Although estimates of the strength of the earth vary (Lambeck, 1972) the 10 MPa necessary to support the topographic stress assuming an elastic rheology is well within even the most conservative estimates. The low order harmonics do present a problem, however. While it may be possible for rocks to withstand stress differences of 70 MPa, it is unlikely that the requisite strength is present in the mantle between the lithsophere and the core. If we require that the support for the low order harmonics lie in the lithosphere, the maximum stress difference can increase to several hundred MPa's.

For features less than a few hundred kilometers in horizontal scale, Jeffreys adopts a flat earth model shown in Fig. 1b. Given a normal stress distributiom with harmonic form

$$p_{33} = g \rho \cos(kx)$$

where ρ is the load density, the maximum stress difference is in the neighborhood of $2g\rho/e$ and occurs at a depth of $1/2\pi$ times the wavelength of the load. The stress solutions for loads modelled as raised strips with rectangular or triangular section are similar, and in general the greatest stress difference in the elastic theory is between 1/2 and 2/3 times the range of the load stress and the greatest strength is needed at a depth of about 1/4 times the width of the load. Using these approximate equations for the Himalayas, assuming a height difference of 5 km between peaks and troughs and a chain width of 100 km, Jeffreys estimates that stress differences reach 450 MPa at depths of 20 to 30 km if the mountains are elastically supported.

The above flat earth treatment can be modified to include the effects of isostasy by assuming that the elastic support resides only in a thin elastic plate overlying a fluid that can support no shear stresses (Fig. 1c). For loads with horizontal scale less than T , the thickness of the plate, the above solution holds because the region of appreciable stresses resides above the fluid. For loads whose wavelength is long compared to the thickness of the elastic layer the thin plate equations from elastic plate theory can be applied. Jeffreys considers a case in which the plate is 50 km thick. The equivalent flexural rigidity,

$$D = \frac{E T^3}{12(1-\nu 2)} \qquad (1)$$

where E is Young's modulus and ν is Poisson's ratio, corresponding to this T value is 9×10^{23} Nm. The support from the plate leads to departures from perfect local isostasy for short wavelength loads, but longer wavelength loads are nearly locally compensated. For a 1 km amplitude harmonic load of density 2500 kg/m^3 and wavelength 450 km, the maximum stress difference in the plate reaches 300 MPa. In general, for a floating crust the maximum stress may be as much as ten times the amplitude of the surface stress. Jeffreys concludes that if mountains are supported by a floating elastic plate, laboratory measurements on the strength of rocks indicate that inequalities 5 km in height should cause fracture of the crust. If strength is uniform with depth to about half the horizontal scale of the features, igneous rocks can support 5 km high inequalities.

Taking again the case in which strength is uniform with depth, nonelastic solutions do not reduce the maximum stress significantly. The greatest improvement is found for harmonic loads of degree 2 and 3, for which the reduction in necessary strength is from 5 to 30 percent. However, for two-dimensional harmonic loading on a planar boundary, the reduction in the maximum stress difference from the elastic solution is only about 7 percent.

A familiar example of a nonelastic solution for a floating crust is the Airy isostatic mechanism, shown in Fig. 1d. Compensation for surface features is achieved by thickening the crust below elevated regions. For perfect isostatic equilibrium, the vertical pressure from the load is balanced by the buoyancy pressure from fluid displaced by a root of depth w :

$$wg\Delta\rho = hg\rho$$

where $\Delta\rho$ is the density difference between the fluid and the crust and h is the land elevation of density ρ . The maximum stress difference in the crust for this compensation distribution is equal to the magnitude of the load. For small wavelength features the elastic solution described above gives a smaller stress maximum, but for wavelengths longer than 2.6T the Airy mechanism is optimal. Therefore the local isostasy statement that mass per unit area is constant does not lead to the smallest maximum stress differences in all cases. If the definition of isostasy is amended to require that the maximum stress difference be minimized in addition to all stresses be hydrostatic below the compensation depth, then the Airy mechanism would not be acceptable. However, free air gravity anomalies in the minimum stress state would be larger than what is actually observed. Although the Airy mechanism better agrees with observations because the compensation is total and extends to all wavelength features, the model is unrealistic. The requirement that small changes in the load produce vertical motion of crustal blocks which rigidly oppose any horizontal movement implies that crustal material is infinitely anisotropic to deformation.

Artyushkov (1973, 1974) has elaborated on this point. While local isostasy only requires that vertical forces equilibrate, the true stable position of the crust balances vertical forces, horizontal forces, and all moments. Deviatoric stresses cannot be homogeneously distributed over depth if a layer is locally compensated. Departures of a locally

compensated crust from true equilibrium are inversely proportional to the characteristic horizontal scale of the topography or density inhomogeniety. Thus appreciable displacements of the crust from isostasy will only occur for very narrow features.

Given only the horizontal and vertical structure of lithospheric density inhomogenieties, Artyushkov (1973) devises a method of estimating deviatoric stress averaged over the lithospheric thickness. These stresses arise from lateral density and thickness inhomogenieties in an isostatically compensated crust. For example, the orientation of stress vectors on crustal elements is shown in Fig. 2 for two isostatic ridge crest models. For similar examples of areas with strong crustal structure, estimates of the average deviatoric stress are given below.

TABLE 2

Feature		Stress (MPa)	T (km)
Mid-ocean ridge			
	crest	-24.	50
	margin (East Pacific Rise)	-55.	50
	margin (Mid-Atlantic Ridge)	-140.	50
Continents			
	margin	10.	80
	3 km uplift } supported by	60.	80
	5 km uplift crustal root	110.	80
	2 km uplift - supported by	200.	80
	low density mantle		

It should be emphasized that only the product of average stress times lithospheric thickness (T) is determined by Artyushkov's analysis and the result depends on the assumed density structure. However, from deep seismic sounding and gravity data it is possible to resolve some of these details of crustal structure.

Further data is needed in order to determine the actual stress distribution within the lithosphere. In particular, the tectonic implications of the stresses in Table 2 depend primarily on the horizontal and vertical viscosity distribution in the lithosphere, which we are only beginning to understand. Nevertheless, Artyushkov (1973) proposes an entire scheme of global tectonics in which horizontal motions are driven by lateral spreading of crustal density and thickness inhomogenieties. Continued differentiation of the core releases buoyant material that ascends from the mantle and forms the roots for new uplifts. Thus chemical differentiation provides the driving mechansim. At present there is little support for Artyushkov's proposal. For example, since it is not possible to fix all ridge crests with respoect to the lower mantle, it becomes difficult in Artyushkov's scheme to explain the continued existence of individual ridge systems over long geologic time spans. Many other mechanical, geochemical, and observational objections could be listed, but they do not directly bear on the results of Table 2. The fact remains that in regions of relief on internal density interfaces as well as on the earth's surface deviatoric stresses exist, and they might well be on the order of hundreds of MPa's.

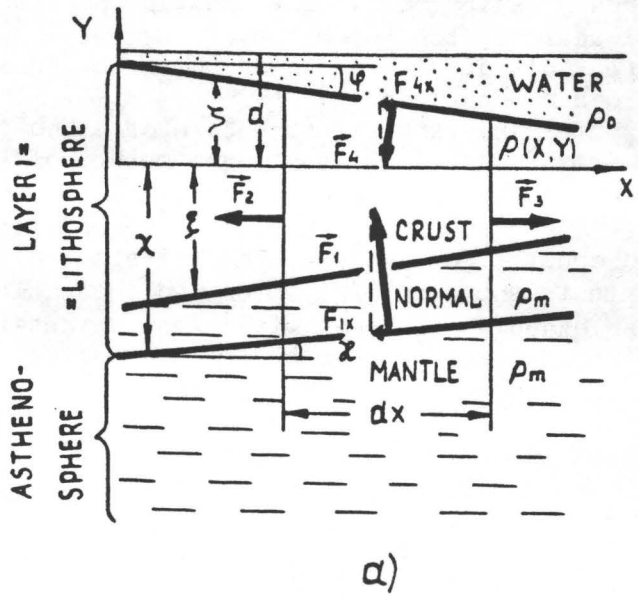

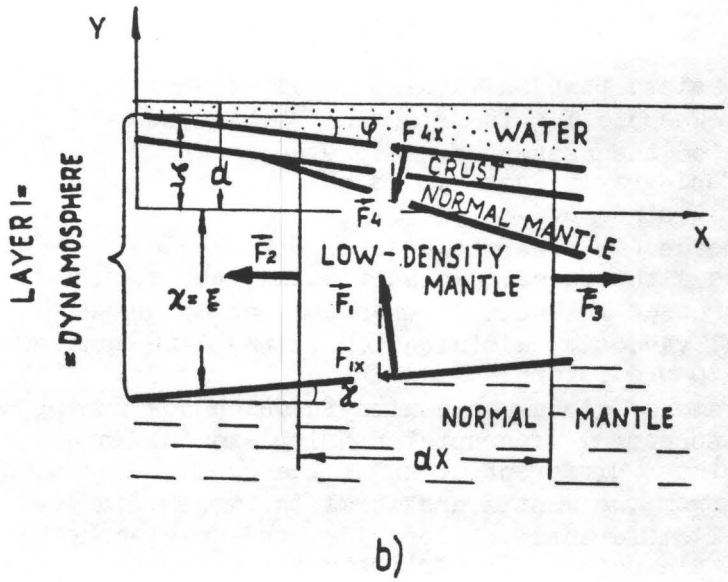

Figure 2. Forces on crustal interfaces caused by assymetry in boundaries for two possible density structures beneath oceanic ridge crests. (From Artyushkov 1973.)

GLOBAL STUDIES

We have but two alternatives for explaining the global gravity field. The anomalies must be maintained either by flow in the mantle or by the finite strength of the lithosphere. Evidence from seismology, isostatic compensation, and glacial rebound studies confirms the existence of an extremely weak asthenosphere underlying the lithosphere. While it is not yet possible to entirely discount finite strength in the lower mantle, the attenuation of upward continued potential fields makes it unlikely that any but the longest wavelength anomalies would have source depths greater than 900 km. The implied stresses from the mass anomalies would need to be unrealistically large to explain any detail in the anomaly field. The first step in identifying the origin of global gravity anomalies is therefore to determine the depth of the causative masses. Any gravity anomalies that are shallow enough to be supported by the lithosphere then provide an estimate of strength in the crust and upper mantle.

A method adopted by several investigators (Guier & Newton, 1965; Allen, 1972; Khan, 1977) for determining source depths for low degrees of the global gravity field is based on the assumption that the gravity anomalies are produced by randomly distributed density variations. The assumption of a white spectrum for the density variations is sufficiently strong to allow for a unique inversion for either the depth from which the density anomalies should extend uniformly downward, or the depth of a single density interface concentrating the anomalies. The results are dependent on the particular set of potential coefficients used (Higbie & Stacey, 1971), but a recent analysis by Khan (1977) shows that the latest satellite and combination solutions, WGS 72, GEM 7, GEM 8, and PGS 110, are consistent up to degree 10 or 11.

Assuming a single density interface, the source depths according to Khan (1977) are

600-800 km for n=2 to n=11,
300-600 km for n=11 to n=30.

Slightly shallower depths are found on the assumption of a disordered mantle below the specified depth:

150-370 km for n=2 to n=11,
150-450 km for n=11 to n=30.

Only the anomalous part of C_2^0 relative to the best-fitting satellite reference ellipsoid was used in the analysis. The non-hydrostatic part of C_2^0 is about an order of magnitude greater than the next largest coefficient, and tends to bias the third and fourth degree components towards greater depth.

We would conclude from Khan's analysis that the major contribution to the global gravity field is from sublithospheric depth, and therefore must be maintained by convection. However, Goodacre (1978) has questioned the assumption that density variations are uncorrelated within the earth. The fact that for different n values slightly different source depths are indicated may reflect the existence of several warped discontinuity surfaces, but it also may result because the spectrum of the density variations is not flat. As an example, Goodacre (1978) considers the earth's surface topography. The amplitude spectrum is not white; it varies as $(2n+1)^{-\frac{1}{2}}$ (Balmino et al., 1973). Using the potential coefficients for the gravity field from the topography, the

depth estimate for the topography on the assumption that the density variations have a flat spectrum is a few hundred kilometers, rather than the expected zero depth. There is no reason to believe that internal density variations are any more random than those at the surface, and therefore the above depth estimates may be meaningless. Overall, this approach to interpreting the global gravity field is not too promising since it involves virtually untestable assumptions concerning the statistical behavior of inhomogenieties deep within the mantle.

While the above procedure was designed to estimate directly source depth for gravity anomalies, McKenzie (1967) posed the problem in another manner. If we suppose that gravity anomalies are supported by the lithosphere, then what stresses are implied? McKenzie then rejects a lithospheric source for anomalies that require stresses above an assumed ultimate strength. He restricts discussion to gravity anomalies that are produced by uncompensated warping of an elastic lithsophere (Fig. 3), which could reasonably apply to subducting plates and broad lithospheric swells. Although it might be argued that these large scale plate deformations are a consequence of mantle flow, the only concern here is whether the lithosphere can maintain the configuration once it has been established.

McKenzie's relationship for the maximum shearing stress, σ_{max}, in a harmonically deformed plate with thickness T and density ρ is

$$\sigma_{max} = \frac{\rho a \Delta g}{3} H(k') \qquad (2)$$

where $H(k') = 1/e, \quad k' > 2$
$3/4k', \quad 1 < k' < 2$
$3/4k'^2, \quad k' < 1$

and $k' = kT/2$ is the non-dimensional wavenumber of the deformation. The amplitude of the gravity anomaly caused by the deformed plate, Δg, is measured peak-to-trough, and a represents the earth's radius. The corresponding relationship in terms of geoid height anoamly, ΔG, is

$$\sigma_{max} = \frac{2ga\rho\Delta G}{3T} k' H(k') .$$

From observed gravity and geoid anomaly amplitudes and wavelengths, McKenzie constructs the following table.

TABLE 3

Feature	Wavelength (km)	Δg (gu)	σ_{max}(MPa) T = 50 km	σ_{max}(MPa) T = 100 km
Mid-Continent Gravity High	80	1000	2.2	2.2
Hawaiian Ridge	140	3000	12.	6.7
Tonga Trench	300	5000	83.	22.
Puerto Rico Trench	300	5000	83.	22.
		ΔG (m)		
Geoid	6000	100	6800.	1700.

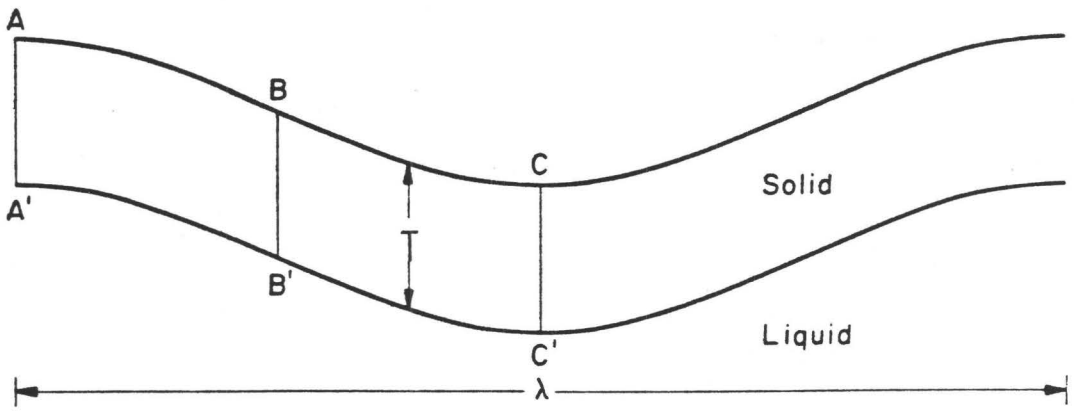

Figure 3. McKenzie's two-dimensional model of a flexed lithosphere. Harmonic distortion of the elastic, incompressible layer is supported by an internal stress field. The layer of thickness T floats on an inviscid half space. (From McKenzie, 1967.)

The decision as to whether the support for these features is derived from the lithsophere hinges on the choice for its ultimate strength. McKenzie cites laboratory experiments by Griggs et al. (1960) that produce shear failure in dunite at 400 MPa of stress. He rejects this strength estimate in favor of the 20 MPa implied by earthquake stress drops (Brune & Allen, 1967). As McKenzie admits, there is little justification for this choice. The amount of stress drop during a seismic rupture can only be a lower bound on the shear strength of the lithsophere. Based on his choice of 20 MPa, both the Hawaiian swell and the Mid-Continent Gravity High can be supported by a 50 km thick elastic lithosphere. A 100 km thick elastic lithosphere is necessary to maintain the subduction zone gravity anomalies against shear failure. The longer wavelength anomalies represented in the satellite gravity field and the geoid, however, require 100 MPa or more of stress even for a 100 km thick lithosphere. McKenzie concludes that these anomalies must be maintained by flow in the mantle and may be a consequence of small temperature inhomogenieties.

Kaula (1969, 1972) continues with McKenzie's theme that the support for the satellite gravity anomaly field must lie below the lithosphere and entails flow in the mantle. He proposes a tectonic classification of the long wavelength gravity anomalies corresponding to degrees n=6 to n=16 based on an association with tectonic features such as subduction zones, ridge crests, orogenic belts, sedimentary basins, and areas of Pleistocene glaciation. Of the eleven classifications, six are currently active tectonic features. If indeed the lithosphere is incapable of supporting statically the gravity anomalies over these features, then the magnitude and sign of the gravity anomalies provides information concerning mantle convection.

For the expected large Prandtl (high viscosity and low conductivity) conditions in the mantle, gravity anomalies can be maintained in the steady state by Lagrangian accelerations and decelerations of mass. Kaula finds that by invoking certain conbinations of boundary conditions at the earth's surface, viscosity variations, fractionation conditions, flow patterns, and driving mechanisms for this Lagrangian mass transport he can explain qualitatively most of the variation in global gravity as a function of tectonic province. Several features such as the Antarctic negative and the gravity highs associated with intraplate volcanism remain troublesome. While Kaula's arguments for varying the convection parameters seem reasonable, his study points out the complex relationship one might expect between convection and surface tectonics.

Lambeck (1972) challenges the assumption that the anomalies observed in the satellite gravity field cannot be supported by the lithosphere. His greatest objection is with McKenzie's 20 MPa stress limit, which he considers to be too low by at least a factor of four based on P wave data (Wyss, 1970). Other problems with McKenzie's (1967) analysis are
1) use of a two-dimensional geometry. Satellite gravity contours are generally circular for feature thousands of kilometers in extent.
2) an error in Eq. (2) which uses ρ , the density of the lithosphere rather than $\bar{\rho}$, the mean density of the earth.
The effect of using a two-dimensional rather than a circular geometry is to overestimate the stress by a factor of four, while the density error causes an underestimate by a factor of two. Thus Lambeck concludes that the stress estimates in Table 3 are overestimated by a factor of two.

For a three-dimensional geometry, Lambeck obtains the expression

$$\sigma_{max} = \frac{\sqrt{2}}{3} \bar{\rho} \, |\Delta g| \, \frac{(.67+.27/k'^2)}{(1-T/(\sqrt{2}ak'))} \, , \; k'<1 \, , \qquad (3)$$

in place of McKenzie's Eq. (2). From Eq. (3) and the gravity field solution of Gaposchkin & Lambeck (1971), he constructs the following table of average maximum stress arising from gravity anomalies of degree n' and higher assuming they are supported by a 100 km thick lithosphere.

TABLE 4

n'	σ_{max} (MPa)	n'	σ_{max} (MPa)	n'	σ_{max} (MPa)	n'	σ_{max} (MPa)
4	875.	8	166.	11	84.	14	49.
5	487.	9	129.	12	70.	15	39.
6	313.	10	103.	13	59.	16	31.
7	219.						

With Lambeck's preferred 100 to 150 MPa estimate for the critical strength of the lithosphere, it is possible to statically support anomalies of degree 8 or 9 and above. This value for strength is comparable to the 120 to 170 MPa estimate by Jeffrey's (1976) for the lithospheric strength necessary to support the Himalayas on a floating crust.

In particular, Lambeck (1972) emphasizes the point that the broad positive anomalies described by harmonic degrees n=8 and n=9 over spreading centers need not be maintained by convective forces, as assumed by Kaula (1972). The role of the lithosphere as a boundary of finite strength cannot be ignored when interpreting global gravity. In all fairness to McKenzie, Lambeck remarks that McKenzie declared the lithosphere incapable of sustaining gravity anomalies at a time when the satellite solution only included terms up to degree eight.

Like McKenzie (1967) and Lambeck (1972), Chase also favors the forward approach to modelling the long wavelengths of the gravity and geoid anomalies. Rather than considering the effects of a warped lithosphere, he attributes the anomalies to uncompensated point masses at depth. Much of the geoid character in harmonics 10 through 20 can be explained by positive mass anomalies in the world-wide subduction zone system. The stresses implied by the uncompensated mass range from a minimum 22 MPa for the Zargos to a maximum 162 MPa for the Ryukuyu Trench, assuming a 100 km thick plate. The required mass excess is, in most cases, less than the amount predicted by thermal plate models (e.g. McKenzie, 1969). Thus stress estimates based on a mathematical formulation of density excess in a subducting slab will be larger than those consistent with the gravity field. Although the models of McKenzie, Lambeck, and Chase are useful for estimating stress implied by the global gravity field, the models are static and thus do not answer the question of whether the lithosphere alone supports its anomalous mass and sustains its deformation. Nevertheless, the reoccurring theme from these studies is that for a variety of plausible anomaly sources, gravity anomalies with wavelengths between 5000 and 1000 km require that the earth in some way (convectively or otherwise) maintain stress from 20 MPa up to almost 200 MPa.

OCEANIC STUDIES

The vast improvement in satellite and surface ship gravimetry fostered new attempts in the mid-1970's to determine the source of long wavelength gravity anomalies (Anderson et al., 1973; Menard, 1973; Weissel & Hayes, 1974; Sclater et al., 1975; Watts, 1976). These investigations all center on oceanic observations in order to avoid the gravitational complexities of continental crustal structure and tectonic history, and they share a common line of reasoning. Numerical simulations of mantle convection in a Newtonian fluid (e.g. McKenzie et al., 1974) predict a positive surface elevation and gravity anomaly over rising convection limbs for both high and low Rayleigh number flow. Thus positively correlated gravity and depth anomalies provide a strong case for convection in the mantle, particularly when lithospheric sources for the anomalies can be ruled out. Although the calculation of residual depth anomalies is tedious since it involves systematically correcting bathymetric data for sediment loading and the empirical age-depth relationship (Sclater et al., 1971), the remainder of the analysis consists of simply calculating regression lines of gravity on bathymetry.

Table 5 summarizes the results from the marine studies. For each region listed the wavelengths and amplitudes of the depth and gravity anomalies are given, along with the slope of the (linear) relationship between gravity and topography, when available. The stress estimates were calculated from Eqs. (2) and (3) after applying the density correction previously discussed to McKenzie's relation. When gravity anomaly amplitudes were not reported, stress estimates were based on depth anomalies using

$$\Delta\sigma_{max} = \sqrt{2}\, g\rho\Delta h(.67+.27/k'^2) \qquad \text{(Lambeck, 1972)}$$

and

$$\Delta\sigma_{max} = 3/4\, g\rho\, \Delta h/k'^2 \qquad \text{(McKenzie, 1967).}$$

Maximum stresses based on Δh are likely to be overestimated, for the low regression slopes from the other studies on Table 5 indicate at least partial compensation for the lithospheric warps. On the other hand, due to the offsetting effect of the compensation, the maximum gravity anomalies underestimate the lithospheric deformation. Particularly when the compensation is far below the surface, the entries in Table 5 based on gravity can underestimate stress at intervening levels.

In general the stresses from McKenzie's equations are about a factor of two larger than the estimates according to Lambeck due to the different geometries assumed for the load. The assumption of a lineated gravity high (McKenzie) is most appropriate for the North Atlantic ridge crest, but would be questionable for the other examples.

Anderson et al. (1973) claim that the .33 gu/m correlation holds for the world-wide ocean ridge system. However, on an ocean-by-ocean basis (see their Fig. 3) the correlation is only convincing for the Atlantic and the Southwest Indian Ridge, and even the Indian Ocean correlation disappears if the data from the Madagascar plateau is removed. In addition, Watts (1976) questions the reliability of the results in Anderson et al. (1973), Menard (1973) and Weissel & Hayes (1974) which

TABLE 5. SUMMARY OF LONG WAVELENGTH DEPTH & GRAVITY ANOMALY STUDIES

LOCATION	WAVE-LENGTH (KM)	ΔH (M)	ΔG (GU)	SLOPE (GU/M)	LAMBECK σ_{MAX} (MPA)	McKENZIE σ_{MAX} (MPA)	SOURCE
NORTH ATLANTIC RIDGE CREST, 30° N TO ICELAND	7000		+ 700	.33	1580	3010	ANDERSON ET AL., 1973
NORTHEAST PACIFIC	500-2000	± 300	VISUAL CORRELATION		16.9-145	16.7-268	MENARD, 1973
AUSTRALIAN-ANTARCTIC DISCORDANCE	900	- 100	VISUAL CORRELATION		12	18	WEISSEL & HAYES, 1974
NORTH ATLANTIC	2000		500	.34	95.5	17.6	SCLATER ET AL., 1975
CENTRAL PACIFIC HAWAIIAN SWELL	2200		150	.20-.22	34.3	63.7	WATTS, 1976

are all based on the SE 2 gravity field (Gaposchkin & Lambeck, 1971). A comparison of the SE 2 field with sea surface data and the more recent GEM 6 (Lerch et al., 1974) solution reveals that anomaly peaks can be offset as much as 900 km, half the wavelength of interest, in the SE 2 field.

Only Sclater et al. (1975) and Watts (1976) justify mantle (convective) sources for the anomalies by systematically ruling out possible lithospheric causes. From Table 5, however, only the ridge crest anomaly in the North Atlantic, presumably related to the Icelandic hot spot, clearly requires too much stress to be maintained by the lithosphere according to Lambeck's criteria.

In any case, it is unlikely that analysis of very long wavelength gravity and topography anomalies will provide much information concerning the strength of the lithosphere. Regardless of whether or not the lithosphere could support the observed gravity anomalies, the agreement between theoretical calculations and observed regression slopes favors convective support. The case for convection could be made even more convincing by comparing the ratio of Fourier transforms of the gravity and bathymetry data to the theoretical admittance from convection models:

$$Z(k) = G(\vec{k})/H(\vec{k})$$

(McKenzie, 1977) where upper case variables denote Fourier transforms of gravity g and topography h and k is the modulus of $\vec{k}$. Most of the analyses in Table 5 computed the regression from $5° \times 5°$ data averages, and thus give an admittance estimate at only one k value.

In addition, from what is known of lithospheric behavior through isostatic compensation and glacial rebound studies, it is uncharacteristic of the lithosphere to sustain indefinitely uncompensated warps thousands of kilometers in extent without some incentive from below. Even if we do suppose that upward flexures are caused by rising low density material from the mantle, the gravity anoamlies are too ambiguous to define the distribution of the load. The magnitude of the deviatoric stresses associated with the observed surface strain could be several tens of MPa's or several hundreds of MPa's depending on how the support is applied.

In the oceans, about 50 percent of the power in the gravity spectrum is related to the compensation of oceanic features (Watts, 1978; Cochran, 1979; McNutt, 1979). These gravity anomalies, in the wavelength range from 20 to 1000 km, are distinctly of lithospheric origin and thus pertain more directly to the problem of lithospheric strength. The studies of lithospheric properties using isostatically compensated features fall into two categories: statistical analysis of distributed loads (Dorman, 1979; Cochran, 1979; McNutt, 1979) and direct modelling of isolated seamounts (Gunn, 1943; Walcott, 1970b; Watts & Cochran, 1974; McNutt & Menard, 1978; etc.). While the statistical approach allows an estimate of flexural rigidity in areas where the analysis would otherwise be hopelessly complex, the analysis of larger isolated loads is more likely to put an upper bound on the maximum deviatoric stress in the lithosphere.

Large positive free air gravity anomalies over oceanic seamounts flanked by encircling troughs almost demand elastic stresses in the

support of isolated oceanic features. Dynamic support for the moat-arch configuration is unlikely. Models proposed in order to explain the bathymetry, gravity anomalies, and deformation of the Moho boundary in the vicinity of large islands and seamounts assume that the athenosphere behaves overloading time scales (> 30,000 years) as an inviscid fluid and that the lithosphere has one of the following rheologies:

1) perfectly elastic (Gunn, 1943; Walcott, 1970b; etc.)
2) elastic with discontinuity at a free edge under the load (Walcott, 1970b; Watts & Cochran, 1974)
3) viscoelastic
4) layered viscoelastic with viscosity increasing with depth (Suyenaga, 1977, 1979)
5) elastic-perfectly plastic (Liu & Kosloff, 1978).

The trend in recent years as seen in this list towards increasing complexity and number of free parameters in the models has been dictated more by dissatisfaction with the implied stresses than by refinement in the observations. As an example, consider the thin plate equation:

$$D\ \nabla^4 w(\vec{x}) + \Delta\rho\ g\ w(\vec{x}) = P$$

where D is the flexural rigidity given by Eq. (1), w is the plate deflection, $\Delta\rho$ is the density contrast for materials overlying and underlying the plate, and P is the applied load. The most general homogeneous solution for a two-dimensional line load geometry is

$$w = \exp(-x/\alpha)\ [A\cos(x/\alpha) + B\sin(x/\alpha)] + \exp(x/\alpha)\ [C\cos(x/\alpha) + D\sin(x/\alpha)]\ . \qquad (4)$$

The flexural parameter α is related to D by

$$\alpha^4 = 4D/(\Delta\rho g).$$

The boundary condition that $w \to 0$ as $x \to \infty$ sets $C=D=0$. For a continuous plate (Fig. 4) we also require $dw/dx=0$ at $x=0$, from which we obtain:

$$w = \exp(-x/\alpha)\ A[\cos(x/\alpha) + \sin(x/\alpha)]\ .$$

This is the solution for plate deflection under a line load on a continuous elastic sheet. The value of A is determined by the isostatic condition:

$$P = 2\int_0^\infty \Delta\rho g\ w(x)\ dx\ .$$

And therefore

$$A = \frac{P}{2\Delta\rho g\alpha}\ .$$

The bending stress σ_x is proportional to d^2w/dx^2:

$$\sigma_x = \frac{-2EzA}{\alpha^2}\ \exp(-x/\alpha)\ [\cos(x/\alpha) - \sin(x/\alpha)],$$

where E is Young's modulus and z is the vertical distance within the

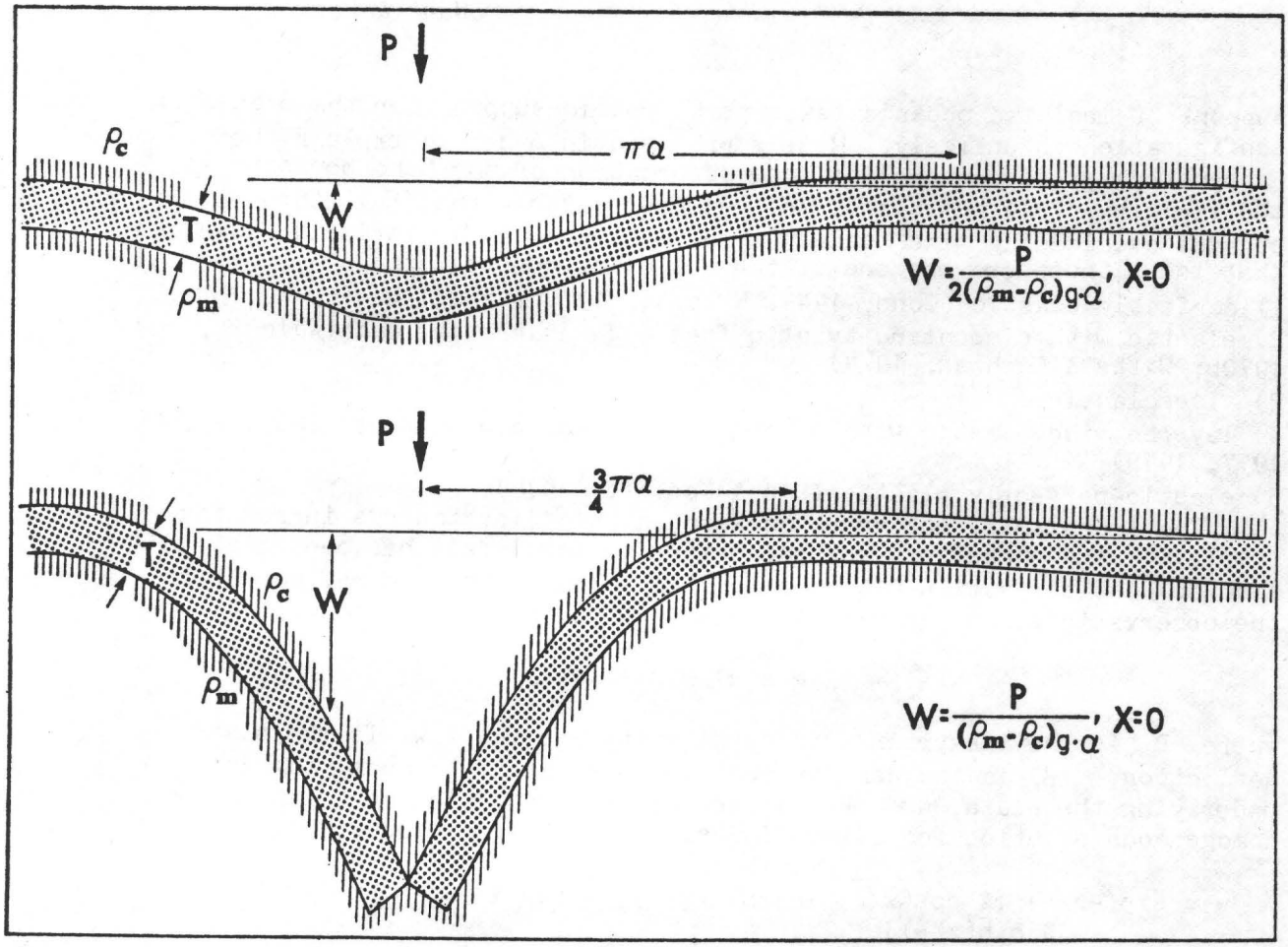

Figure 4. Examples of two elastic plate models. Upper model: continuous elastic plate of thickness T . ρ_c is the density of the material overlying the lithosphere and ρ_m is the density of the asthenosphere. Lower model: elastic plate fractured under the load axis. (From Walcott, 1976.)

plate from the neutral plane. The maximum for this function occurs at x=0 and is given by

$$\sigma_{x\ max} = \frac{-EzP}{\Delta\rho g\alpha^3} .$$

Walcott (1976) calculates that the maximum bending stress at the base of a 60 km thick plate loaded by a seamount chain 3 km high and 30 km wide is 200 MPa. Even taking into account the three-dimensionality and distributed nature of real loads, McNutt & Menard (1978) calculate 200 MPa of stress under Tahiti using a best-fitting 14 km elastic plate thickness. Walcott (1976) considers 200 MPa to be the "crushing strength of rock" and predicts that failure should occur.

Model 2 in Fig. 4 reduces the maximum stress by removing the point of maximum curvature. The equation for the deflection is obtained from Eq. (4) by applying the boundary conditions $w=0$ as $x\to\infty$ and $d^2w/dx^2 = 0$ at $x=0$:

$$w = B \exp(-x/\alpha) \cos(x/\alpha)$$

$$B = \frac{P}{\Delta\rho g\alpha} .$$

The bending stress is

$$\sigma_x = \frac{-2EzB}{\alpha^2} \exp(-x/\alpha) \sin(x/\alpha)$$

and reaches its maximum at $x/\alpha = \pi/2$ (the first nodal point) :

$$\sigma_{x\ max} = \frac{-2EzP}{\Delta\rho g\alpha^3} \exp(-\pi/2) .$$

A load P that would produce 100 MPa of stress on a continuous plate would only produce about 40 MPa of bending stress on a fractured plate. While the discontinuous plate reduces the implied stress, Walcott (1970b) found that he was unable to simultaneously fit Moho depth, flexural wavelength, and bathymetry with one value for the flexural rigidity of the fractured plate. In addition, while during magmatic activity it might be reasonable to suppose that the lithospheric plate is weakened and possibly decoupled below the load, it is difficult to justify a free edge boundary condition once volcanic activity has ceased (Liu & Kosloff, 1978).

A viscoelastic plate also reduces stress for a given flexure profile. The behavior of a plate with viscous as well as elastic properties is to relax its elastic stresses as loading time increases. For example, for a given initial viscoelastic rigidity D_0, for loading times short compared to the viscoelastic relaxation time τ, the plate appears to be perfectly elastic. However, for loading times long compared to τ, the flexural wavelength decreases and the amplitude increases. If we were to interpret a viscoelastic plate profile in terms of the perfectly elastic equations, it would appear that the flexural rigidity was less than D_0. The important point for the implied stresses is that the observed curvature of the plate is no longer proportional to the stress because some of the strain is non-recoverable, non-elastic deformation caused by viscous flow. Thus for any $t>0$, the

stress will always be overestimated if the strain is assumed to be perfectly elastic. Nadai (1963) derives the following expression for the remaining elastic deformation w' in terms of the viscoelastic deflection w at a time t after the emplacement of the load:

$$w'(t) = w(t) - \frac{\exp(-t/\tau)}{\tau} \int_0^t w(t') \exp(t'/\tau)\, dt'. \qquad (5)$$

The reduction in maximum stress for a viscoelastic rheology as compared to an elastic one depends on the ratio t/τ, and therefore we need an estimate of τ for the oceanic lithosphere.

Walcott (1970a) interprets numerous apparent flexural rigidities, D', from continental and oceanic loading studies in terms of a viscoelastic plate model. From a trend towards decreasing D' with increasing load age, he estimates $\tau = 10^5$ years. There are several problems complicating Walcott's interpretation. Known differences in continental and oceanic crustal structure suggest that equivalent elastic thicknesses will vary. Some of the differences in D' may be due to variations in initial rigidity D_o quite apart from any relaxation. Secondly, the loading times for Pleistocene lakes Algonquin and Agassiz are less than ten thousand years. The asthenosphere cannot be treated as a fluid on such short time scales, and the loads no doubt did not reach equilibrium. Finally, the relationship between D' and D_o for a linearly viscoelastic plate is (McNutt & Parker, 1978)

$$D' = \frac{D_o \exp(-t/\tau(1+\ell^4 k^4))}{1+\ell^4 k^4 (1-\exp(-t/\tau(1+\ell^4 k^4)))} \qquad (6)$$

$$\ell^4 = \frac{D_o}{\Delta\rho g}$$

Apparent flexural rigidities can only be compared if they are determined from loads of the same wavelength $\lambda = 2\pi/k$.

A value for τ as low as 10^5 years would indeed greatly decrease the elastic stresses implied by present day loads. We can approximate the reduction in stress for a given flexural profile when interpreted in terms of a viscoelastic rather than an elastic plate model by using Eq. (5) and the equation for viscoelastic deflection at time t from a constant line load (Nadai, 1963):

$$w(x) = \frac{P}{2\Delta\rho g}\{\frac{1}{x}[e^{-y_o}\cos(y_o) - e^{-y}\cos(y)] + \frac{1}{\alpha_o}[e^{-y_o}(\cos(y_o) + \sin(y_o))][1 - \ln(\alpha_o/\alpha)]\} \qquad (7)$$

in which

$$\alpha_o^4 = \frac{4D_o}{\Delta\rho g},$$
$$y_o = x/\alpha_o,$$
$$y = x/\alpha,$$

and

$$4t/\tau = (\alpha_o/\alpha)^4 - 1 - \ln(\alpha_o/\alpha)^4.$$

The integration of Eq. (7) is not easily accomplished with the system of equations in this form. However, for small t we can estimate an upper bound for the remaining elastic deflection w' by putting a lower bound on $\int w \exp(-t/\tau)\, dt$:

$$w'(t) \simeq w(t) - e^{-t/\tau} w(0) \int_0^t e^{t'/\tau}\, dt'$$
$$\simeq w(t) - w(0)\,[1 - \exp(-t/\tau)]. \qquad (8)$$

Substituting for w from Eq. (7) into Eq. (8), we obtain

$$w'(x) \simeq P/(2\Delta\rho g)\{\tfrac{1}{x}[e^{-y_o}\cos(y_o) - e^{-y}\cos(y)] + \frac{1}{\alpha_o}[e^{-y_o}(\cos(y_o) + \sin(y_o))\,(e^{-t/\tau} - \ln(\alpha_o/\alpha))]\}.$$

The bending stress is proportional to the second derivative of w', which has a singularity at the origin. In the real world, however, we would not encounter this point of infinite viscoelastic curvature since point loads do not exist. For points other than $x=0$ the curvature remains finite and is

$$\frac{d^2w'}{dx^2} = \frac{P}{\Delta\rho g\alpha_o^3}\; y_o^{-3}(e^{-y_o}\cos y_o - e^{-y}\cos y) + y_o^{-2}(e^{-y_o}(\cos y_o + \sin y_o)$$
$$- \alpha_o/\alpha\, e^{-y}(\cos y + \sin y)) + y_o^{-1}(e^{-y_o}\sin y_o - (\alpha_o/\alpha)^2 e^{-y}\sin y)$$
$$+ (e^{-t/\tau} - \ln(\alpha_o/\alpha))\, e^{-y_o}(\sin y_o - \cos y_o)\ .$$

This expression was evaluated at the crest of the first flexure arch for values of $t/\tau = .02568$ and $t/\tau = 3.0568$, with $\alpha_o = 50$ km. In each case the stress was compared to the stress implied by a purely elastic plate with the same flexural wavelength. For the short loading time $t/\tau = .02568$ the reduction in stress for the viscoelastic rheology is 5 percent. When the loading time is on the order of three times the viscoelastic decay time, the stress reduction calculated is 15 percent, but this is only a lower bound because for large t the approximation made in evaluating the intergral in Eq. (5) is no longer valid. Therefore we may conclude that interpreting flexure profiles in terms of a viscoelastic rather than an elastic plate model leads to lower stress estimates, but the difference is only significant for loads much older than τ. If τ is on the order of 100,000 years, for loads a million years or older we could presume that appreciable stress relaxation has occurred.

However, flexural evidence from the Hawaiian-Emperor seamount chain is incompatible with a 10^5 year value for τ. Assuming an initial plate thickness of 90 km, Watts (1978) finds that the present-day 20-30 km apparent plate thickness under the island of Hawaii requires a τ value of 10^5 to 10^6 years. The older Emperor seamounts north of 40° N imply T = 10 to 20 km and $\tau = 10^6$ to 10^7 years. Watts interprets this discrepancy in viscoelastic relaxation times to mean that siginificant relaxation does not occur in the Pacific plate over 50 my time scales. He prefers a model in which flexural rigidity does not decrease in time, but is a function of the age, and therefore the thickness, of the oceanic plate when the load was applied. The lower flexural rigidites for the Emperor seamounts as compared to the Hawaiian Archipelago are explained by a younger age, and therefore a lower elastic thickness, for the Pacific plate when the Emperor chain was created 50-60 my ago. The very low flexural rigidty and thin elastic plate thickness found by Cochran (1979) and McNutt (1979) for the topography in the vicinity of Pacific spreading centers supports Watts' interpretation.

It can be shown, however, that Watts' rejection of a viscoelastic mechanism is a function of his choice of the seismic plate thickness, 90 km, for the initial elastic plate thickness. There is reason to suppose that the lithosphere relaxes to a thickness of 30 km or so on a time sale not much longer than that of the asthenosphere. If we assume that the observed flexural rigidity of Hawaii is equal to the "initial" value (following lower lithosphere relaxation), then the decrease in apparent rigidity in the Emperors can be explained by τ = 45 my, which is the value determined by McNutt & Parker (1978) for continental lithosphere. The flexural response for an elastic model with T = 15 km cannot be observationally distinguished from a viscoelastic plate model with T = 20 km , t = 50 my , and τ = 45 my (Fig. 5).

Regardless of whether or not viscoelastic relaxation does occur, the implications for stress are not affected for long decay times. For τ = 45 my or for $\tau = \infty$, no appreciable stress relaxation has occurred for Hawaii, Tahiti, and other relatively young oceanic loads. Both elastic and viscoelastic plate models predict stresses in excess of 100 MPa.

Another variation on the elastic plate model is the layered plate in which relaxation begins at the base of the lithosphere and migrates upward. This scheme is appealing from a rheological viewpoint because the temperature dependence of viscosity predicts that viscosity decreases with depth. Suyenaga (1977, 1979) uses a finite element scheme (Zienkiewicz, 1971) to investigate the time history of flexure for a plate with depth dependent viscosity. He terms this plate model "viscous-elastic" to distinguish it from the viscoelastic model whose properties are constant with depth. Suyenaga's procedure can be outlined as follows:

1) Apply a load at time zero to a plate 100 km thick and numerically calculate using the finite element method the elastic displacement and stress according to the elastic plate equations.

2) Calculate the amount of creep that will occur at any point within the plate during a time increment Δt according to a creep law based on perimental data (Weertman, 1970)

$$\dot{\varepsilon} = A\, \sigma^n \exp(-GT_m/T) \qquad (9)$$

in which

$\dot{\varepsilon}$ = strain rate
$A = 3.4 \times 10^8$ kbar^{-n} sec^{-1}
$n = 3$
$G = 30$
T_m = melting temperature at ambient pressure
T = actual temperature at depth z
σ = deviatoric stress .

The numerical constants in this empirical creep law are taken from the work of Carter (1975), Weertman & Weertman (1975), and Kirby (1977). The creep strain is estimated from the elastic stresses and homologous temperature (T/T_m) curve from Mercier & Carter (1975).

3) Assume the creep strain is an initial strain within the plate and return to step 1. When the creep strain in a plate element becomes greater than the elastic strain, the element is considered to be a fluid.

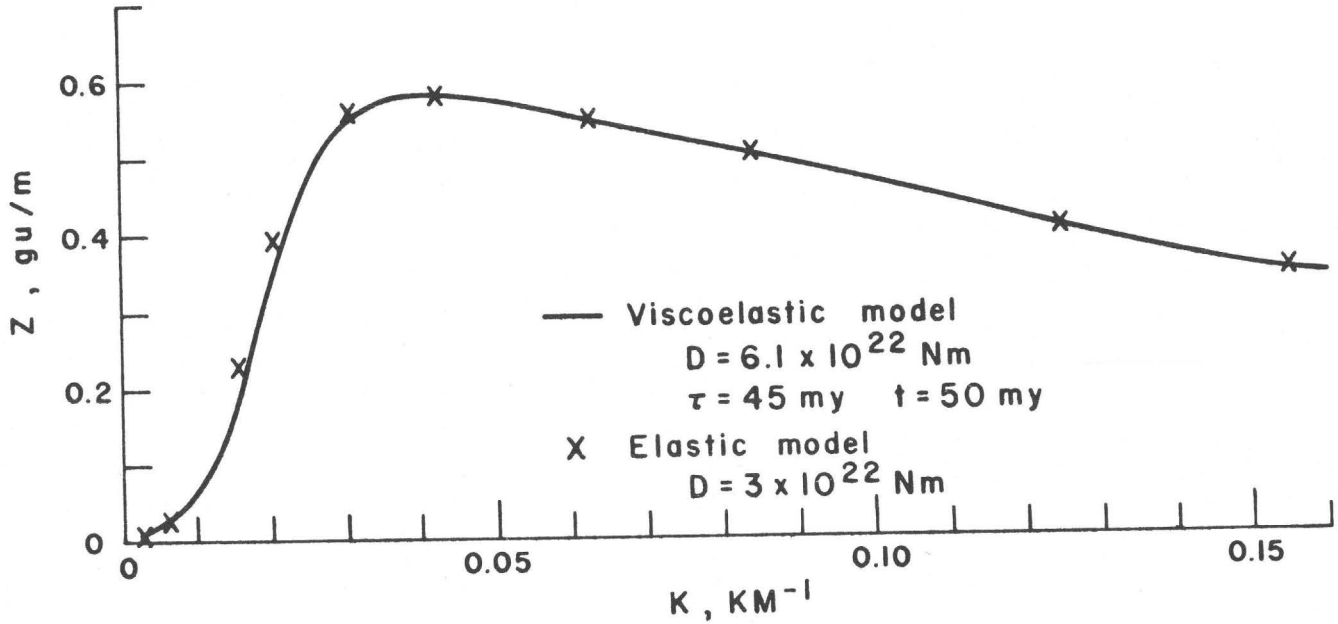

Figure 5. Comparison of responses from viscoelastic and elastic plate models. Vertical scale is the response Z defined as the ratio of the Fourier transforms of gravity and topography: $\mathfrak{F}[g]/\mathfrak{F}[h]$. Horizontal scale is wavenumber k . For all wavelengths of interest, the viscoelastic plate response is indistinguishable from an elastic plate response.

Elastic elements begin to become fluid at the base of the lithosphere first where T/T_m is a maximum, although as shown in Fig. 6a the pattern is also influenced by the stress distribution from the flexure. The flexural rigidity of the plate therefore decreases with time because the non-fluid portion of the thermal ($\sim$100 km) lithosphere that actually supports the load decreases with time. The upward spread of fluid elements practically halts after about 10^6 years at depths between 15-30 km where $T \simeq .3\ T_m$ to $.5\ T_m$ (Murrell, 1976). Below these depths stress relaxation is complete, while above relaxation is only partial and does not change appreciably over loading time scales. As a result of the partial relaxation, the stress in the upper, long-term elastic portion of the plate is less than what would be estimated from elastic theory. The evolution of the surface displacement as the fluid elements migrate upwards, shown in Fig. 6b, is similar to that of the viscoelastic lithosphere with no depth dependence in the viscosity. The important difference in the two models is that relaxation eventually ceases in a viscous-elastic lithosphere before the effective rigidity reaches zero.

The viscous-elastic model is intended to explain why the apparent elastic thickness of the oceanic lithosphere is only a fraction of its thermal thickness (Hanks, 1971, 1977). We can also estimate its long-term stress implications by considereing the strain rate at the base of the 30 km thick elastic layer assuming $T \simeq .5\ T_m$. From Eq. (9),

$$\dot{\varepsilon} = 2.4 \times 10^{-17}\ /\text{sec}$$
$$= 7.5 \times 10^{-4}\ /\text{my}$$

for a deviatoric stress of 200 MPa. In the viscoelastic plate model, it is assumed that strain rate depends linearly on stress:

$$\dot{\varepsilon} = 1/\eta\ \sigma$$
$$\eta = E\tau/3\ .$$

A strain rate similar to the viscous-elastic one would occur in the viscoelastic plate for $\eta = 8 \times 10^{24}$ N sec/m^2 or $\tau \simeq 10$ my. Thus initially the relaxation rate at 30 km depth in a viscous-elastic plate is quantitatively similar to the rate of relaxation in a viscoelastic plate with $\tau = 10$ my assuming the same stress level. A major difference in the two models is that while viscoelastic relaxation proceeds throughout the depth of the plate, in the viscous-elastic model relaxation at deep levels increases the stresses in the upper levels since less of the lithosphere supports the load. The increase in stress as the plate thins also increases the strain rate, but the factor T/T_m dominates the behavior. For example, to obtain a strain rate as high as 7.5×10^{-4} /my at a depth of 15 km where $T \simeq .3\ T_m$, the stress would have to increase to 4,400,000 MPa.

In general, the ultimate, long term stress on time scales of several hundred million years for a viscoelastic plate model would be on the order of the weight of the load (several tens of MPa) since the compensation would approach that of Airy. For a similar time scale the stress in the upper 15 km of a viscous-elastic plate would continue to increase in the range of several hundred MPa's since the low T/T_m ratio

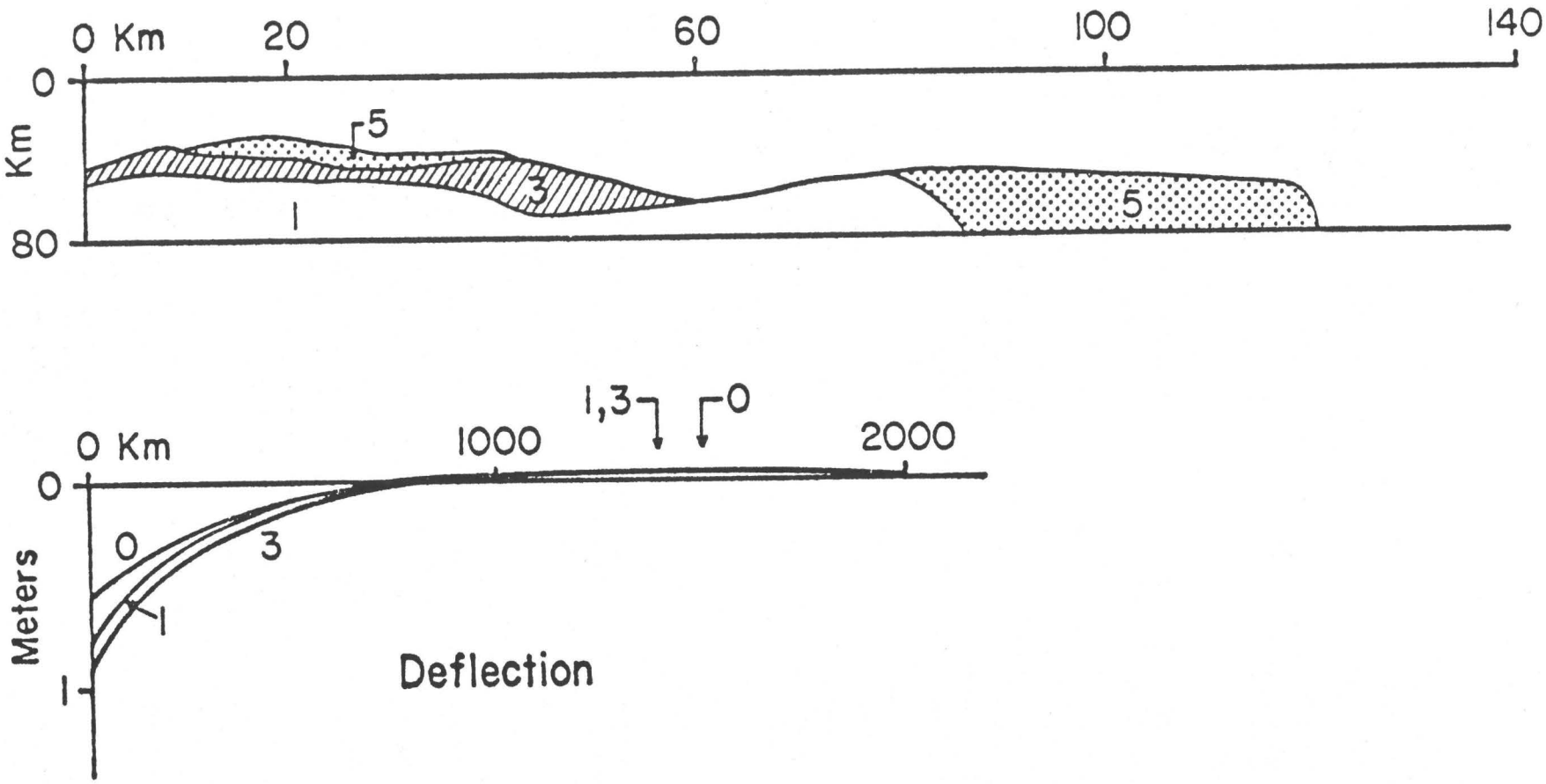

Figure 6. Creep in a finite element viscous-elastic plate under constant load. Upper diagram shows the spread of fluid elements as time progresses. The numbers indicate the extent of fluid conditions at 1, 3, and 5×10^4 years. Lower diagram shows the vertical displacement w at the plate surface. The arrows indicate the loacation of maximum displacement at 0, and at 1 and 3×10^4 years. (From Suyenaga, 1979.)

would preclude relaxation at shallow depths. In this respect, however, the stress estimate is derived more from the rock deformation experiments than from flexure modelling since the laboratory strain data was built into the model. It is perhaps significant to point out that if we were to interpret the change in flexural profile in a viscous-elastic plate in terms of a viscoelastic plate equation, it would appear that τ increases with time. This is exactly the same behavior noted by Watts (1978) along the Hawaiian-Emperor chain.

The elastic-plastic lithosphere (Liu & Kosloff, 1978) is a further refinement of plate mechanisms incorporating rock deformation data. The stress-strain relationship for an elastic-perfectly plastic material is shown in Fig. 7a. The elastic behavior is represented by the sloped line along which stress and strain are linearly proportional. At a critical stress level σ_c determined by the strain rate the material behavior is plastic. Strain increases without change in stress. The strain rate dependence of the yield stress is given by a power law equation extrapolating laboratory data to geologic loading rates (Carter, 1976):

$$\dot{\varepsilon} = A \sigma_c^n \exp(-Q/RT) \qquad (10)$$

in which Q is the activation energy and R is the gas constant. The ultimate strength of the lithosphere is equal to σ_c and depends on temperature (and thus depth) in addition to strain rate. For lower strain rates corresponding to geologic loading the yield stress is also lower.

Liu & Kosloff (1978) model flexure under the Hawaiian archipelago using an elastic-plastic lithosphere. The rate dependence of the elastic response is incorporated by using 90 percent of the elastic moduli, based on a 2 percent decrease for each three decade decrease in loading rate. The plastic part of the deformation is given by Eq. (10) using the parameters from Carter & Ave'Lallement (1970). They successfully fit a profile northeast of the island of Oahu, but there are many free parameters in the model and the fit is in no way unique. Like the viscous-elastic plate model, the implications from the stress distribution in Fig. 7b for the elastic-plastic plate are determined by rock deformation data reviewed elsewhere in this volume and cannot be taken as independent estimates of stress. Rather, this study is meant to illustrate how rock deformation data can be employed in flexure studies. For the Hawaiian ridge, at least, there appears to be no conflict between extrapolated laboratory deformation results and observed liithospheric flexure from large, long-term geologic loads.

CONTINENTAL STUDIES

The magnitude of implied stresses from topography and density inhomogenieties associated with continental structures again depends upon the rheological model assumed for the crust and upper mantle. In the ocean basins the gravity and load deformation data can be explained almost equally well by a variety of elastic, plastic, and viscous plate combinations, making it difficult to select a preferred model. On the continents, the results from the various studies that will be summarized in this section are much less consistent. More complexity in the long-term rheological models is required in order to explain the

A.

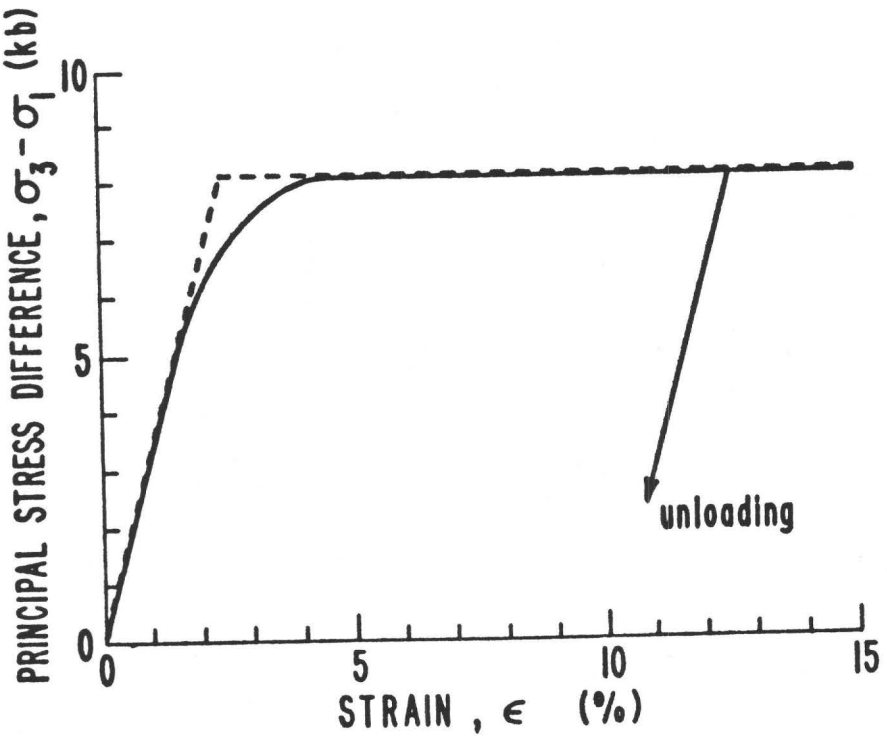

B.

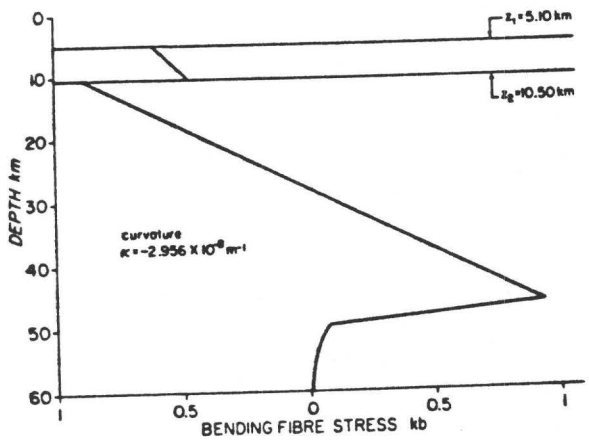

Figure 7. a. Stress-strain curve for dunite at 500 MPa confining pressure, 800° C, and 5 x 10^{-4} s^{-1} strain rate. (From Griggs et al., 1960.) b. Stress distribution associated with bending in a plate cross section with compressive fiber stress above the neutral axis and tensile fiber stress below the neutral axis. (From Liu & Kosloff, 1978).

observations under one unified theory, but perhaps there then remains a possibility of better distinguishing competing rheologies.

The results for each investigation will be given in terms of the best-fitting "effective flexural rigidity", which is the D value obtained when data is interpreted in terms of the response from a perfectly elastic, homogeneous lithosphere overlying an inviscid asthenosphere. Potential sources of variation in D are:

1) Thermal structure of the lithosphere. Creep rate increases as temperature increases, so that near ridge crests, hot spots, regions of recent orogeny, and other areas marked by high heat flow the depth to which creep strain is inhibited over geologic time scales decreases.

2) Loading time. Plate models with viscous components of deformation predict that effective rigidity should decrease with age of the load.

3) Depth of the flexure signal. Plate models with temperature and therefore depth dependent viscosity predict decreasing effective rigidity with increasing depth. If the deformation induced by the load is measured at or below the Moho the plate will appear less competent than the surface deformation would suggest.

4) Details of load application. Implicit in most loading studies is the assumption that the lithosphere passively responds to a load applied from above. A good case for this simplification can be made for sedimentary basins with distant sources. For volcanic loads the assumption is less justified. During the stage of active volcanism the plate is certianly altered and weakened in the vicinity of the conduit. Molten rock ascends from lithospheric magma chambers which continually expand and contract. Thus during load formation the lithosphere plays an active role and even after cessation of volcanism the assumption that the load did not alter the plate properties as it was applied is violated. The loading assumption is least appropriate for continental mountain belts. The details of orogeny are sketchy, but in the majority of cases deformation takes place as lithospheric plates collide. Horizontal compression and vertical uplift effect certainly the upper elastic layer and perhaps a good portion of the lithosphere.

The types of analyses fall into two categories, and perhaps not surprisingly the results divide along the same line. When the deformation from individual loads is directly modelled, the effective rigidity estimate is relatively high (10^{23} - 10^{24} Nm). Much lower rigidities (10^{19} - 10^{22} Nm) are implied by response function studies which involve a statistical analysis of gravity and topography data. The various estimates of flexural rigidity on the continents that have so far been obtained are derived from features that differ in age of the load and the lithosphere, depth of the signal, and type of load. Therefore we can test which of the four categories listed above are responsible for variation in effective rigidity, and gain insight into the non-elastic nature of the lithosphere. Table 6 summarizes the results, but most entries deserve comment.

While the sedimentary basin studies involve loading conditions which best fit the idealization in the theoretical model, the results form the Michigan Basin (Haxby et al., 1976) and the North Sea (Beaumont, 1979) are almost diametrically opposed. Haxby et al. (1976) infer from the configuration of successive sedimentary facies that the effective rigidity in the Michigan Basin has increases with time. They invoke

TABLE 6.

LOCATION	D (NM)	T-STRUCTURE	AGE(MY)	Z_s	LOAD	TECHNIQUE	SOURCE
CARIBOU MOUNTAINS	$>10^{24}$	STABLE CONTINENT	1-10	SURFACE	EROSIONAL SEDIMENTARY	DM	WALCOTT, 1970
INTERIOR PLAINS	10^{24}	STABLE CONTINENT	1-10	MOHO		DM	WALCOTT, 1970
BOOTHIA UPLIFT	2×10^{23}	STABLE CONTINENT	500	SURFACE	SEDIMENTARY	DM	WALCOTT, 1970
MCGH	2×10^{23}	RIFTING PLATES	1100	MOHO	VOLCANIC INTRUSIVE	DM	COHEN & MEYER, 1966
MICHIGAN BASIN	4×10^{23}	SUBSIDING BASIN	300	SURFACE	SEDIMENTARY	DM	HAXBY ET AL., 1976
CONTINENTAL UNITED STATES	10^{21}-10^{22}	PLATFORM & OROGENIC	50	MOHO		RF	BANKS ET AL., 1977
AUSTRALIA	$<5 \times 10^{20}$	HOT OROGENIC	200	MOHO	OROGENIC	RF	MCNUTT & PARKER, 1978
NORTH SEA	2×10^{20}	SUBSIDING BASIN	180	SURFACE	SEDIMENTARY	DM	BEAUMONT, 1979
NORTHERN INDIA	3.8×10^{24}	STABLE CONTINENT	40			DM	MOLNAR ET AL., 1979

uplift of the gabbro-eclogite phase transition caused by shoaling isotherms as the driving mechanism for gravitational subsidence of the basin. An increase in the flexural rigidity would be an expected consequence as a purely elastic lithosphere cooled and thickened to normal depths. On the other hand, Beaumont (1979) prefers a viscoelastic crustal model in order to explain the apparent decrease in flexural rigidity with time in the North Sea. In a manner expected from a viscoelastic rheology, the subsiding part of the basin narrows with time and erosion of the peripheral uplift regions results in an apparent regressive stratigraphic sequence at the basin surface. This pattern of progressively younger sediments outcropping towards the center of the basin is typical of many basins. Beaumont cautions that the parameters in his model of North Sea basin evolution are in no way unique. Initial flexural rigidity, viscoelastic decay time, and initiating mechanism for basin subsidence can all be traded off. The initiating mechanism is the parameter least well known, but it has a profound effect on the size and time history of the basin. At this stage it may not be possible to precisely determine rheological parameters from basin studies, but certainly a knowledge of lithospheric response would illuminate details of initiating mechanisms.

The rigidity estimates from the response function analyses are quite low, and merit some discussion. The technique is most useful in regions of complex topography where deformation from any one load is indistinguishable from that of another. On the assumption that isostatic compensation for a point load is linear and isotropic, the isostatic response function $Q(k)$ can be calculated from Fourier transforms of topography and Bouguer anomaly data (Dorman & Lewis, 1970):

$$G(\vec{k}) = Q(k) \cdot H(\vec{k})$$

where G and H are gravity and topography transforms and $k = |\vec{k}| = (k_x^2 + k_y^2)^{\frac{1}{2}}$. The response Q calculated from actual data sets can be directly compared to theoretical Q's from the linearized forms of regional and local compensation models. For example, for linear Airy isostasy,

$$\hat{Q}(k) = -2\pi\rho G \exp(-kz_c) \qquad (11)$$

where ρ is the density of the topography and z_c is the compensation depth. For the elastic plate compensation model,

$$\hat{Q}(k) = -2\pi\rho G \left\{ 1 + \frac{k^4 D}{\Delta\rho\, g} \right\}^{-1} \exp(-kz_c) \qquad (12)$$

where $\Delta\rho$ is the density contrast for materials overlying and underlying the plate. Fig. 8 shows examples of Eqs. (11) and (12) for identical z_c values. At long wavelengths the two response functions are equal. The elastic plate has a sharper curvature and falls off more quickly to zero at short wavelengths. The explanation for this behavior is that long wavelength features do not feel the effect of the elastic plate, and thus local and regional responses are similar. Smaller features, supported by the strength of the plate, have smaller Bouguer anomalies and therefore lower Q values than similar featues that are locally

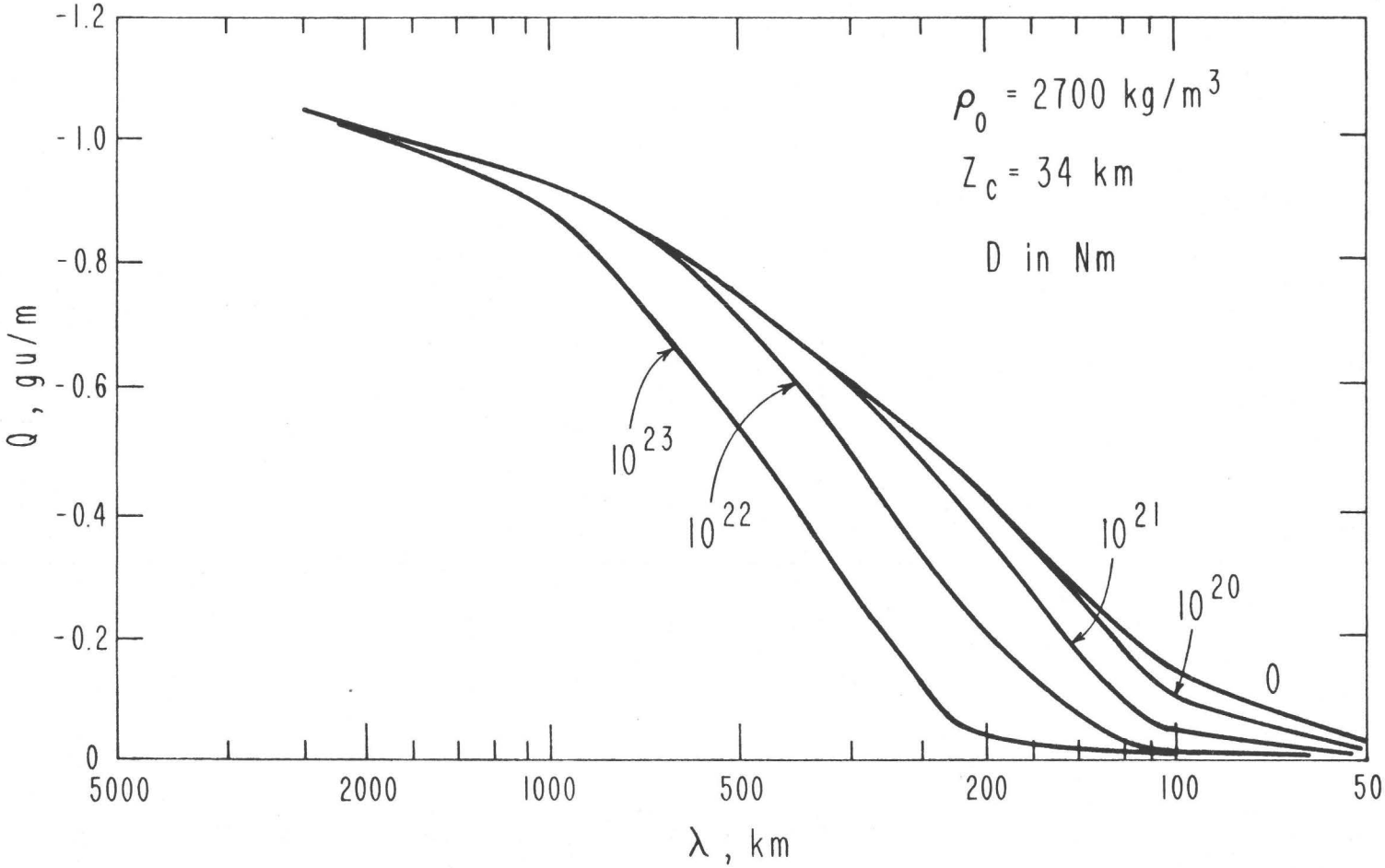

Figure 8. Theoretical isostatic response functions for five values of flexural rigidity.

compensated. Due to variations in compensation depth, curvature, rather than amplitude of the observed Q is the best estimate of elastic stresses. For example, referring to Fig. 9, at mid to long wavelengths the local compensation ($D=0$) response with a 40 km compensation depth is actually lower in amplitude than the $D=10^{22}$ Nm response with shallower compensation. On a $\ln(Q)$ versus k graph, the $\hat{Q}$ from locally compensated topography appears as a straight line. A regional $\hat{Q}$ on the same plot has strong curvature (Fig. 10).

A close relative of the isostatic response function is the free air response Z :

$$FA(\vec{k}) = Z(k) \cdot H(\vec{k})$$

where FA is the Fourier transform of the free air gravity anomaly. The Z response is most often used for oceanic surveys. The theoretical response $\hat{Z}$ is related to $\hat{Q}$ via

$$\hat{Z} = \hat{Q} + 2\pi\rho G \exp(-kz_t)$$

where z_t is the average depth from the sea surface to the topography.

There are two major drawbacks with the response function technique. The first problem is that all gravity signal is assumed to be related to compensation of topography with constant density. Density variations unrelated to topography are a source of noise, but their effect can be minimized by statistically separating out only the gravity field correlated with the topography. In regions of low topographic signal, however, the uncertainty in Q is large. A more serious problem is the necessary dimensions of the region under investigation. For the continents, the characteristic fall-off region for Q lies between 2000 km and 500 km wavelengths. The calculated Q may therefore only give an average rigidity estimate from several tectonic provinces within the survey boundary.

From the curvature in Lewis & Dorman's (1970) United States response function, Banks et al. (1977) determine that the apparent flexural rigidity in the U.S. is between 10^{21} and 10^{22} Nm. They conclude that Walcott (1970a) found higher rigidity values from other North American features because he measured the deformation at the surface rather than at the Moho. Thus Banks et al. (1977) imply that some sort of depth dependent relaxation reconciles the two rigidity estimates. When the U.S. data is interpreted in terms of a purely elastic plate, we also find an apparent contradiction. The D values for the U.S. correspond to a plate thickness of only about 10 km, which is too shallow to include the density discontinuity (i.e. Moho) which supposedly provides the gravity anomaly signal. Banks et al. suggest that the seismic Young's modulus is too large for loading time scales. Reducing E by more than an order of magnitude removes the contradiction by predicting a thicker plate, and it also reduces the implied stresses by a similar amount. The strain rate dependence in Young's modulus is similar to that inferred from a consideration of dispersion due to anelastic absorption (Liu et al., 1976), but differs greatly in the expected magnitude of the effect. Whereas Banks et al. require that the effective E for loading problems equal about 1/25th the seismic value, Liu et al. (1976) estimate that

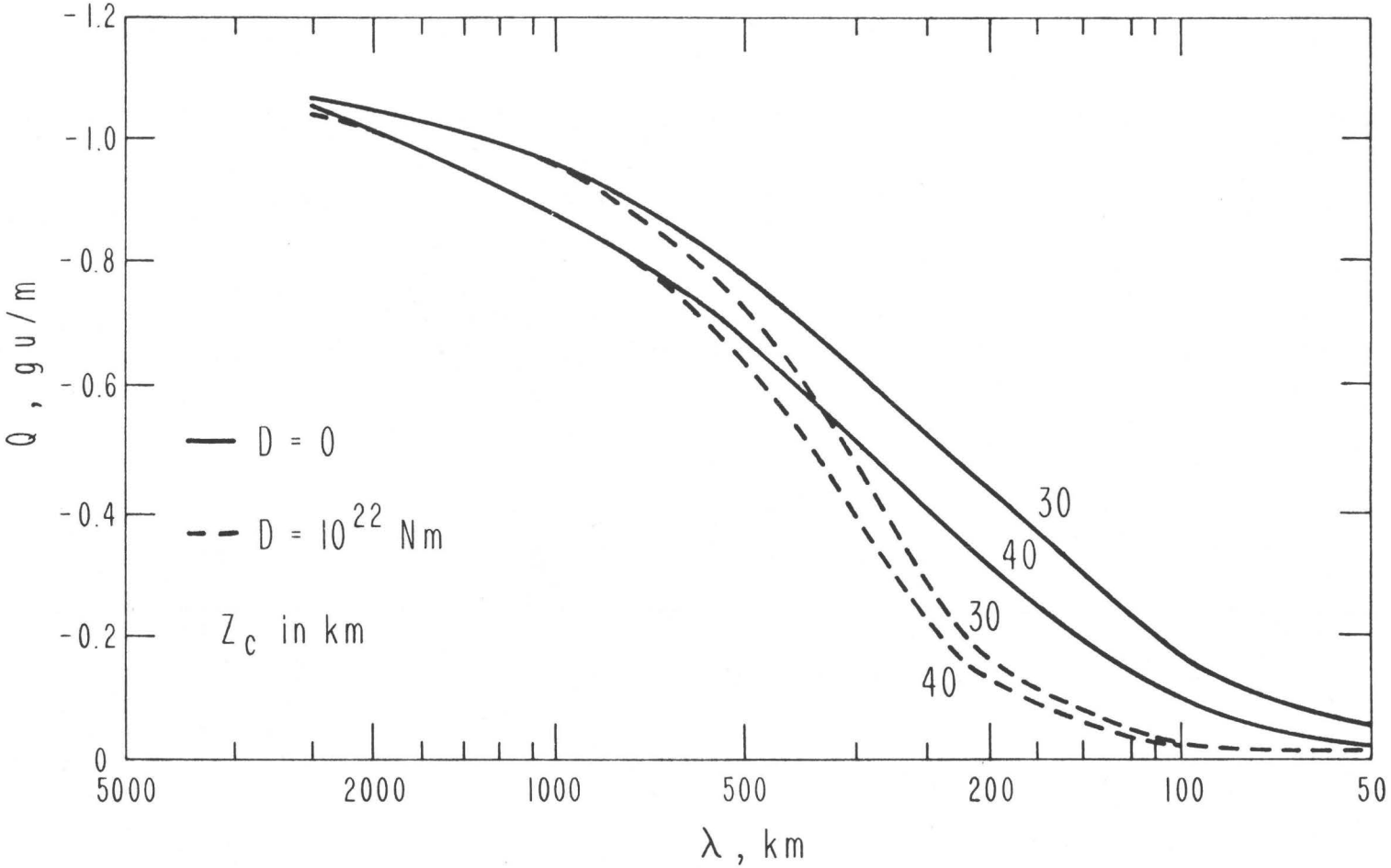

Figure 9. Theoretical isostatic response functions for local compensation (solid curves) and regional compensation with $D = 10^{22}$ Nm (dashed curves). Each response is calculated assuming two different values of compensation depth, z_c .

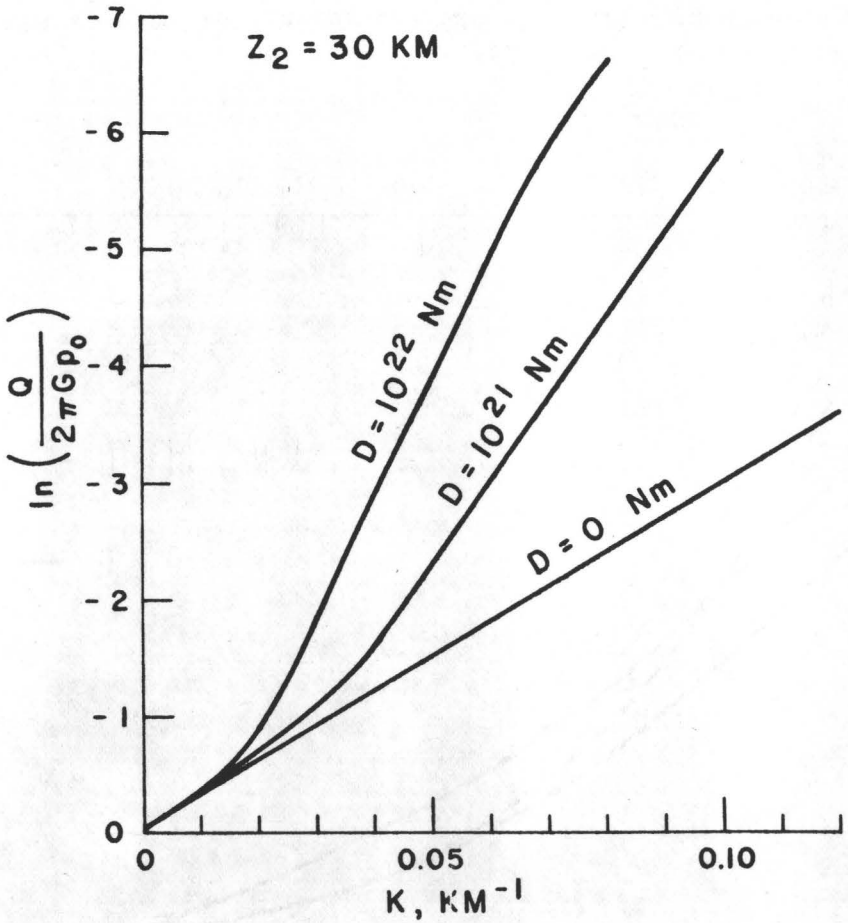

Figure 10. Comparison of a local compensation (D = 0) isostatic response with two regional elastic plate responses, plotted on a logarithmic scale. Compensation depth for all curves is 30 km.

the relaxed elastic moduli equal about 50 percent of the seismic value for linear attenuation mechanisms.

McNutt & Parker (1978) find an even lower value for apparent flexural rigidity in Australia, and invoke a viscoelastic relaxation model to explain the difference in U.S. and Australian D values. Assuming a 200 my age for the latest Australian orogeny and a 50 my age for the Laramide orogeny in the U.S., the viscoelastic relaxation time τ = 45 my. Their calculation hinges on the validity of the assumption that the response function is dominated by the signal from the most recent orogeny. This assumption is justified for Australia. When the continent is divided into Eastern, Central, and Western grids, the most coherent Q which dominates the average Q is that of the geologically youngest Eastern section. In the U.S. the results are rather surprising. Fig. 10 shows the Q calculated from the Western Cordillera of the U.S. The response resembles that of Australia in shape, and indeed the best-fitting model is local compensation at 30-35 km depth. The overall U.S. response function therefore appears to be dominated by the geologically older central plains and eastern Appalachians. This conclusion is supported by Stephenson & Beaumont's (1979) Canadian analysis. The isostatic response function from the Canadian shield (Fig. 12) is similar to that of the overall U.S., but suggests slightly higher elastic rigidity.

A possible explanation for the response function results is that orogenic regions are characterized by local compensation imposed at the time of mountain building by the same forces responsible for the topography. No further viscous relaxation is possible or even necessary since elastic stresses are not involved. This theory requires that the lithosphere be capable of deforming plastically and/or viscously at rather high strain rates when subjected to extreme heat and stress. Thus Lewis & Dorman's (1970) United States response function is a sort of crude average of signals from locally compensated orogenic topography in the west and regionally compensated topography in the eastern platform and shield areas. The higher rigidity in the eastern U.S. and Canadian shield could have a variety of implications for the rheology of more stable continental crust. No definite conclusions can be drawn until it is determined exactly which topographic loads are responsible for the response signal, but we might expect some contribution from loads analysed by Walcott (1970a), Cohen & Meyer (1966), and Haxby et al. (1976).

In general the estimates in Table 6 suggest that all four of the factors listed at the beginning of this section contribute to variation in apparent rigidity. The stress levels depend on which factors dominate, and no doubt the results will vary geographically. Thermal effects and the details of load emplacement appear to be the most important variables, but reasonably we would expect them to be closely related. From the thermal dependence of creep in Eq. (10) it is unlikely that the depth from which the signal originates would vary the apparent rigidity by more than a factor of two. The age of the load will be a critical parameter early in loading history, but will become less important for features tens of millions of years old. There is no reason to suppose at this point, however, that the stress magnitudes will be greater than those implied from oceanic studies. The largest continental

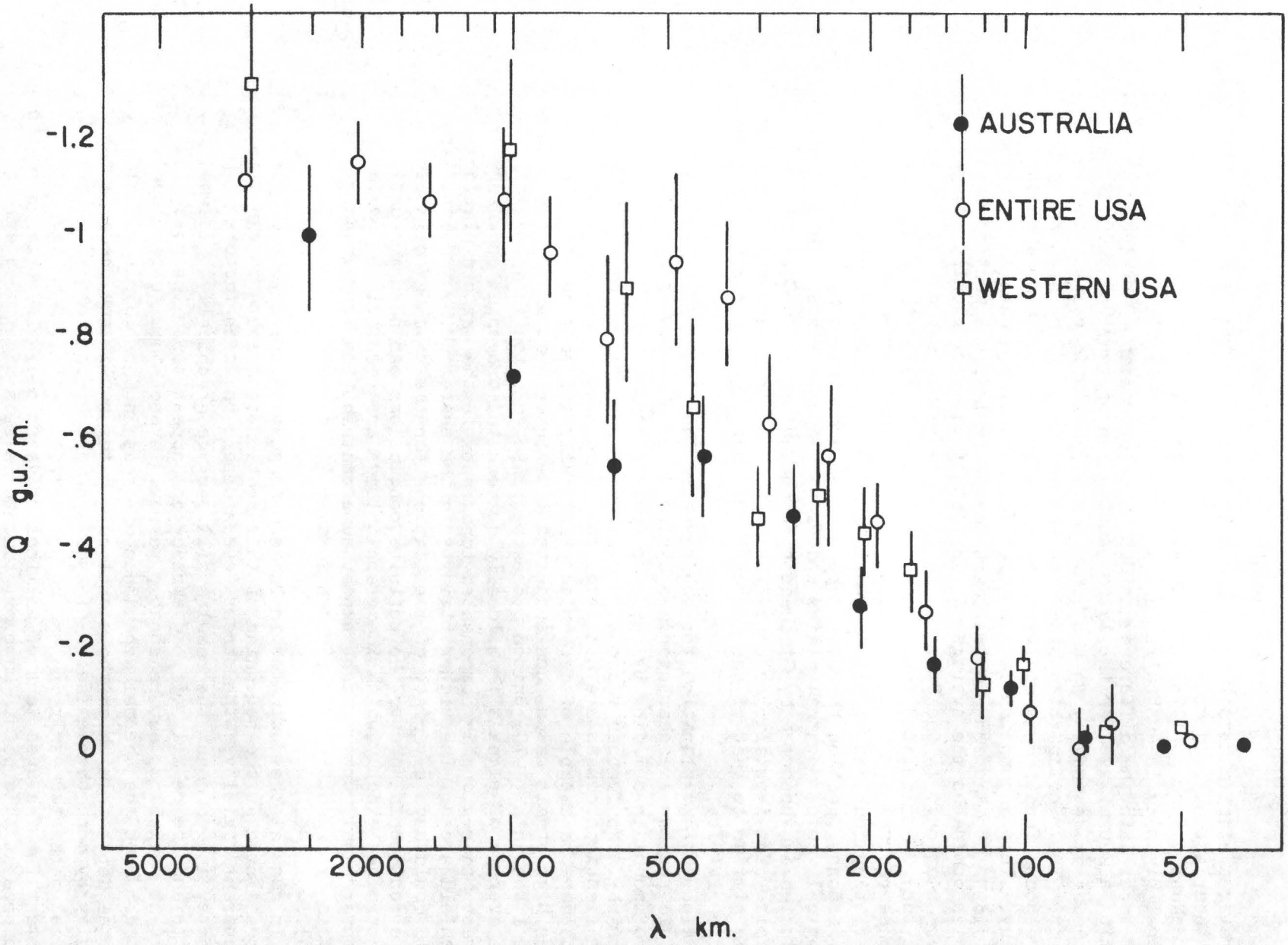

Figure 11. Comparison of observed isostatic response functions from Australia and the continental United States with the response function from only the Rocky Mountain-Basin Range section of the United States.

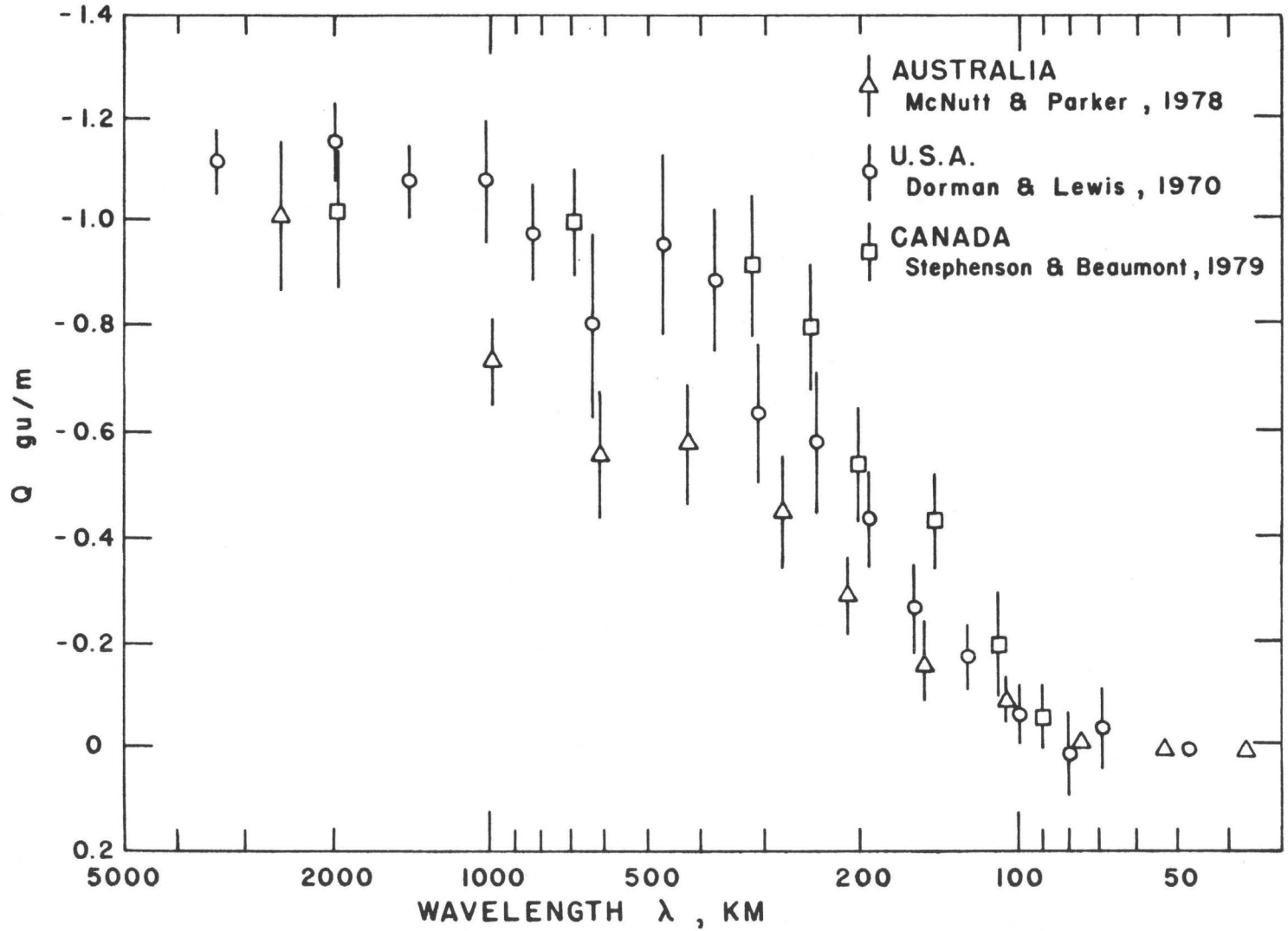

Figure 12. Comparison of United States and Australian isostatic response functions with the response from the Canadian shield. Bars indicate the standard error in each spec-ral estimate.

loads occur in orogenic regions which tend to be locally compensated, but the stress from an Airy model is less than that from the thin plate model used to describe the compensation of large oceanic features.

EXTRA-TERRESTRIAL STUDIES

Many of the same techniques used for analysing load deformation and determining stress on the earth have been applied to other planets in the solar system. The two most intensely studied from a stress viewpoint are the moon and Mars. While the remoteness of these planetary bodies makes it more difficult to interpret the geology and obtain precise measurements of gravity and topography, in at least one respect the analysis is simplified. There is no evidence from the moon, Mars, or even Mercury that since the emplacement of the oldest geologic units there has been any horizontal shifting of rigid lithospheric blocks. These bodies are considered to be "one-plate planets" (Solomon, 1978) and lack the complicated deformation patterns associated with the creation and destruction of lithospheric plates.

Solomon (1977) infers the thermal history of the moon and Mercury from the surface deformation. Early in a planet's thermal history the interior warms as core segregation progresses. The planet expands causing tensional surface features and volcanism. When differentiation is essentially complete the planet cools and contracts, producing compressional surface features and cutting off volcanic activity. For example, Mars is dominated by extensional features, indicating planetary expansion over most of its history. The absence of extensional features on Mercury places the planetary differentiation phase before the formation of the oldest surface features. The moon lacks extensive compressional or extensional features, and therefore its radius cannot have increased or decreased more than one kilometer in the past 3.8 by. The one kilometer limit is based on the assumption that a change in tangential stress of 100 MPa would be sufficient to produce observable surface faulting. Solomon (1977) finds that acceptable temperature profiles $T(z,t)$ predicting a maximum radius change of less than one kilometer over the last 3.8 by have initial profiles with melting temperatures down to 200 to 300 km depth and cold temperatures in the deep interior. However, the accumulated thermal stress in the lithosphere from the acceptable models is as high as several thousands of MPa's. In the moon's interior the thermal stresses dissipate by flow on short time scales, but the mechanism and time scale for relaxation of the lithospheric thermal stress is unknown. The solution to this problem may have important implications for the state of stress in the lithosphere and the thermal evolution of planets.

Solomon & Head (1979) combine the model for global stress on the moon with predicted stresses from lithospheric flexure in order to explain the spatial and temporal distribution of linear rilles and mare ridges. From features 3.6-3.8 by old they infer a relatively thin plate 25-50 km thick. Younger features 3-3.4 by old require a thicker plate on the order of 100 km. Note that these effective plate thicknesses are several times those found on earth, and imply that the long term elastic layer is much thicker on the moon. A thick elastic layer may be the consequence of a shallower geotherm for the moon. The observation that the compensation for younger moon features requires a thicker lithosphere

is also consistent with a viscoelastic plate mechansim, but in this case a viscoelastic explanation is unlikely. Unless the initial plate thickness at time zero is much greater than 100 km, it is difficult for loads over 3 by old but only .1 to .8 by apart in age to differ in effective plate thickness by 50 percent. From gravity and topography data, Thurber & Solomon (1978) find that the older lunar highlands are locally conmpensated while the younger mascon maria are supported by the strength of the lithosphere. Thus they also conclude that the lunar lithosphere must have increased in thickness after the formation of the highland topography.

Olympus Mons, a shield volcano situated on the Tharsis ridge of Mars, has received considerable attention recently. With a basal area of 3×10^5 km^2 and a height of 25 km, Olympus Mons represents the largest known volcanic feature in the solar system (Thurber & Toksoz, 1979). The excess mass of Olympus Mons and the other three shield volcanoes of the Tharsis dome is sufficiently large to cause a 1.2 km anomaly in the gravity equipotential surface and account for about 6 percent of the planetary oblateness J_2 (Reasenberg, 1977; Kaula, 1979). Debate has centered on whether or not the Tharsis dome volcanoes are compensated. Phillips & Saunders (1975) conclude that while older regions of Mars are locally compensated, the topography of the Tharsis region is young and mostly uncompensated. Their observation could be explained by the same scenario invoked by Solomon & Head (1979) in which the lithosphere thickens between the time of formation of young and old topography.

Thurber & Toksoz (1979) directly model the compensation of Olympus Mons using flexure theory. For an elastic plate thickness as small as 100 km the model predicts 500 MPa for the maximum extensional surface stress. Thurber & Toksoz see no evidence of surface faulting in response to the high stress, nor do they observe an arch on the order of 4 km high that would be produced by plate flexure. Their preferred model, an elastic plate approximately 200 km thick, predicts an arch amplitude of only a kilometer or two, in agreement with the topographic data, and produces maximum surface stresses of less than 100 MPa. At depth, however, the maximum stress under the load would be greater than 100 MPa. Using Jeffreys' calculation of stress underlying a triangular load resting on an elastic half space as a very rough estimate, the maximum deviatoric stress occurs at 150 km depth and equals about 200 MPa.

Thurber & Toksoz's (1979) model assumes that Olympus Mons is supported only by the strength of the Martian lithosphere. Phillips et al. (1979) argue that the implied stresses are too large and that the Tharsis region must be supported at least partially by dynamic forces from below.

There is even an indication that stress estimates based on a volume measure of excess mass from Olympus Mons may be too low. From Viking Orbiter 2 high resolution gravity data, Sjogren (1979) fails to detect any low density compensating mass for Olympus Mons. The gravity anomaly over the feature is about 20 percent greater than expected from the observed volume using a Bouguer theory, and suggests that even denser material lies beneath the volcano. Sjogren concludes, "This essentially uncompensated 600 km feature produces kilobar stresses that demand a rigid, thick lithosphere, or some rather unique scenario about very young topography obtained on a presently seismically inert planet."

CONCLUSIONS

At this point, we must in some way answer the question: What magnitude stress can the lithosphere support on geologic time scales? Due to the fundamental differences in oceanic and continental tectonic settings, the oceanic loads tend to provide a good estimate of maximum stress level, while the continents better indicate the duration of stress support. For example, from seismic refraction, surface gravity, and bathymetry studies the spatial extent and magnitude of lithospheric strain caused by the Hawaiian load is rather well documented. There exists nowhere on the continents such a classic example of lithospheric flexure. The continual overprinting of continental orogenic, volcanic, and epeirogenic episodes obscures the deformation recorded during any one event. On the other hand, since no oceanic loads are older than about 200 my, it is not possible to rule out relaxation throughout the thickness of the lithosphere on a time scale of a hundred million years. The 30 km effective elastic plate thickness supporting the Mid-Continent Gravity High (Cohen & Meyer, 1966) rather convincingly argues against upper lithospheric relaxation on the continents on billion year time scales. While it is dangerous to apply oceanic stress estimates to the continents, and assume that continental time scales are appropriate to the oceans, it appears that the upper 30 km or so of the lithosphere sustains stresses up to about 200 MPa over billion year time scales. The model results are not unique, partially due to the ambiguity of gravity data and partially due to the uncertainty in rheology, but it is unlikely that refinement in observations could drastically change these estimates. In particular, there is no conflict between empirical flow laws extrapolated from laboratory data and observed geophysical deformation data.

REFERENCES

Allen, R. R., Depth of sources of gravity anomalies, Nature Phys. Sci., 236, 22-23, 1972.

Anderson, R. N., D. P. McKenzie, J. G. Sclater, Gravity, bathymetry and convection in the earth, Earth Planet. Sci. Lett., 18, 391-407, 1973.

Artyushkov, E. V., The stresses in the lithosphere caused by crustal thickness inhomogenieties, J. Geophys. Res., 78, 7675-7708, 1973.

Artyushkov, E. V., Can the earth's crust be in a state of isostasy?, J. Geophys., 79, 741-752, 1974.

Balmino, G., K. Lambeck, W. H. Kaula, A spherical harmonic analysis of the earth's topography, J. Geophys. Res., 78, 478-481, 1973.

Banks, R. J., R. L. Parker, and J. P. Huestis, Isostatic compensation on a continental scale: Local versus regional mechanisms, Geophys. J. Roy. Astr. Soc., 51, 431-452, 1977.

Beaumont, C., The evaluation of sedimentary basins on a viscoelastic lithosphere: Theory and examples, unpublished manuscript.

Brune, J. N. and C. R. Allen, A low-stress drop low magnitude earthquake with surface faulting: The Imperial California earthquake of March 4, 1966, Bull. Seismol. Soc. Am., 57, 501-514, 1967.

Carter, N. L., High temperature flow of rocks, Rev. Geophys. Space Phys., 13, 344-349, 1975.

Carter, N. L., Steady state flow of rocks, Rev. Geophys. Space Phys., 14, 301-360, 1976.

Carter, N. L., H. G. Ave'Lallement, High temperature flow of dunite and peridotite, Geol. Soc. Amer. Bull., 81, 2181-2202, 1970.

Chase, C. G., Subduction, the geoid, and lower mantle convection, submitted to Nature, 1979.

Cochran, J. R., An analysis of isostasy in the world's oceans, 2, mid-ocean ridge crests, J. Geophys. Res., in press.

Cohen, T. J. and R. P. Meyer, The mid continent gravity high: Gross crustal structure, in The Earth Beneath the Continents, Geophys. Monogr. Ser., vol. 10, J. S. Steinhardt and T. J. Smith, eds., pp. 141-165, 1966.

Dorman, L. M., Isostatic compensation at the crest of the East Pacific Rise, submitted to J. Geophys. Res., 1978.

Dorman, L. M. and B. T. R. Lewis, Experimental isostasy 1: Theory of determination of the earth's isostatic response to a concentrated load, J. Geophys. Res., 75, 3357-3365, 1970.

Gaposchkin, E. M. and K. Lambeck, Earth's gravity field to sixteenth degree and station coordinates from satellite and terrestrial data, J. Geophys. Res., 76, 4844-4883, 1971.

Goodacre. A. K., A comment on depths of sources of anomalies in the earth's gravity field, Geophys. J. R. Astr. Soc., 55, 745-746, 1978.

Griggs, D. T., F. J. Turner and H. C Heard, Deformation of rocks at 500 to 800 C, Am. Geol. Soc. Mem. 79, Chapter 4, 1960.

Guier, W. H. and R. R. Newton, The earth's gravity field as deduced from the Doppler tracking of five satellites, J. Geophys. Res., 70, 4613-4626, 1965.

Gunn, R., A quantitative evaluation of the influence of the lithosphere on the anomalies of gravity, J. Franklin Inst., 236, 373-396, 1943.

Hanks, T. C., The Kuril Trench-Hokkaido Rise System: Large shallow earthquakes and simple models of deformation, Geophys. J. Roy. Astr. Soc., 23, 173-189, 1971.

Hanks, T. C., Earthquake stress drops, ambient tectonic stresses, and stresses that drive plate motions, Pure Appl. Geophys., 115, 330-331, 1977.

Haxby, W. F., D. L. Turcotte, and J. M. Bird, Thermal and mechanical evolution of the Michigan Basin, Tectonophysics, 36, 57-75, 1976.

Jeffreys, H., The Earth, Cambridge University Press, Cambridge, 1924, 1962.

Kaula, W. M., Earth's gravity field, relation to global tectonics, Science, 169, 982-985, 1969.

Kaula, W. M., Global gravity and tectonics, in The Nature of the Solid Earth, pp. 385-405, E. C. Robertson, ed., McGraw-Hill, New York, 1972.

Kaula, W. M., The moment of inertia of Mars, Geophys. Res. Lett., 6, 194-196 1979.

Khan, M. A., Depth of sources of gravity anomalies, Geophys. J. R. Astr. Soc., 48, 197-209, 1977

Kirby, S. H., State of stress in the lithosphere: Inferences from the flow laws of olivine, Pure Appl. Geophys., 115, 245-258, 1977.

Lambeck, K., Gravity anomalies over ocean ridges, Geophys. J. R. Astr. Soc., 30, 37-53, 1972.

Lerch, F. J., C. A. Wagner, J. A. Richardson, and J. E. Brownd, Goddard earth models (5 and 6), NASA GSVC Doc. X-921-74-145, 100 pp. Goddard Space Flight Center, Greenbelt, Md., 1974.

Lewis, B. T. R. and L. M. Dorman, Experimental isostasy 2: An isostatic model for the U. S. A. derived from gravity and topographic data, J. Geophys. Res., 75, 3367-3386, 1970.

Liu, H. P., D. L. Anderson and H. Kanamori, Velocity dispersion due to anelasticity: Implication for seismology and mantle composition, Geophys. J. Roy, Astr. Soc, 47, 41-58, 1976.

Liu, H. P. and D. Kosloff, Elastic-plastic bending of the lithosphere incorporating rock deformation data, with application to the structure of the Hawaiian Archipelago, Tectonophysics, 50, 249-274, 1978.

McKenzie, D. P., Some remarks on heat flow and gravity anomalies, J. Geophys. Res., 72, 6261-6273, 1967.

McKenzie, D. P., Speculations on the causes and consequences of plate motions, Geophys. J. R. Astr. Soc., 18, 1-32, 1969.

McKenzie, D. P., Surface deformation, gravity anomalies and convection, Geophys. J. R. Astr. Soc., 48, 211-238, 1977.

McKenzie, D. P., J. M. Roberts, and N. O. Weiss, Toward the numerical simulation of convection in the earth's mantle, J. Fluid Mech., 62, 465-538, 1974.

McNutt, M. K., Compensation of oceanic topography: An application of the response function technique to the Surveyor area, J. Geophys. Res., in press.

McNutt, M. K. and H. W. Menard, Lithospheric flexure and uplifted atolls, J. Geophys. Res., 82, 1206-1212, 1978.

McNutt, M. K. and R. L. Parker, Isostasy in Australia and the evolution of the compensation mechanism, Science, 199, 773-775.

Menard, H. W., Depth anomalies and the bobbing motion of drifting islands, J. Geophys. Res., 78, 5128-5137, 1973.

Mercier, J. C. and N. L. Carter, Pyroxene geotherms, J. Geophys. Res., 80, 3349-3362, 1975.

Molnar, P., W. P. Chen, T. J. Fitch, P. Tapponnier, W. E. K. Warsi, and F. T. Wu., Structure and tectonics of the Himalaya: A brief summary of relevant geophysical observations, C. N. R. S. colloquium on the Himalaya, in press.

Murell, S. A. F., Rheology of the lithosphere-experimental indications, Tectonophysics, 36, 5-24, 1976.

Nadai, A., Theory of Flow and Fracture of Solids, vol. 2, pp. 272-297, McGraw-Hill, New York, 1962.

Phillips, R. J., R. S. Saunders and W. B. Banerdt, Martian stress distribution: Agruments against finite support of Tharsis, J. Geophys. Res., in press.

Reasenberg, R. D., The moment-of-inertia and isostasy of Mars, J. Geophys. Res., 82, 369-375, 1977.

Sclater, J. G., R. N. Anderson, and M. L. Bell, The elevation of ridges and the evolution of the central eastern Pacific, J. Geophys. Res., 76, 7888-7915, 1971.

Sclater, J. G., L. A. Lawver, and B. Parsons, Comparisons of long-wavelength residual elevation and free air gravity anomalies in the North Atlantic and possible implications for the thickness of the lithospheric plate, J. Geophys. Res., 81, 1031-1052, 1975.

Sjogren, W. L., Mars gravity: High resolution results from Viking October 2, Science, 203, 1006-1009, 1979.

Solomon, S. C., The relationship between crustal tectonics and internal evolution in the Moon and Mercury, Phys. Earth Planet. Int., 51, 135-145, 1977.

Solomon, S. C., On volcanism and thermal tectonics on one-plate planets, Geophys. Res. Lett., 5, 461-464, 1978.

Solomon, S. C. and J. W. Head, Vertical movement in mare basins: relation to mare emplacement, basin tectonics, and lunar thermal history, J. Geophys. Res., 84, 1667-1682, 1979.

Stephenson, R. and C. Beaumont, Evidence of small scale convection in the upper mantle beneath the Canadian shield, submitted to Nature, 1979.

Suyenaga, W., Earth Deformation on Response to Surface Landing: Application to the formation of the Hawaiian Islands, Ph.D. dissertation, 147 pp., University of Hawaii, Honolulu, 1977.

Suyenaga, W., Flexure of a viscous-elastic lithosphere, submitted to J. Geophys. Res., 1979.

Thurber, C. H. and M. N. Toksoz, Martian lithospheric thickness from elastic flexure theory, Geophys. Res. Lett., 5, 977-980, 1978.

Walcott, R. I., Flexural rigidity, thickness, and viscosity of the lithosphere, J. Geophys. Res., 75, 3941-3954, 1970a.

Walcott, R. I., Flexure of the lithosphere at Hawaii, Tectonophysics, 9, 435-446, 1970b.

Walcott, R. I., Lithospheric flexure, analysis of gravity anomalies, and the propagation of seamount chains, in The Geophysics of the Pacific Ocean Basin and Its Margin, Geophys. Monogr. Ser., vol. 19, G. H. Sutton, M. H. Manghnani, and R. Moberly, eds., pp. 431-438, AGU, Washington, D. C., 1976.

Watts, A. B. Gravity and bathymetry in the central Pacific Ocean, J. Geophys. Res., 81, 1533-1553, 1976.

Watts, A. B., An analysis of isostasy in the world's oceans, 1, Hawaiian-Emperor Seamount Chain, J. Geophys. Res., 83, 5989-6004, 1978.

Watts, A. B. and J. R. Cochran, Gravity anomalies and flexure of the lithosphere along the Hawaiian-Emperor Seamount Chain, Geophys. J. R. Astr. Soc., 38, 119-141, 1974.

Weertman, J., The creep strength of the earth's mantle, Rev. Geophys. Space Phys. 13, 344-349, 1975.

Weertman, J. and J. R. Weertman, High temperature creep of rock and mantle viscosity, Ann. Rev. Earth Sci., 3, 239-316, 1975.

Weissel, J. K. and D. E. Hayes, The Australian-Antarctic discordance: New results and implications, J. Geophys. Res., 79, 2579-2587, 1974.

Wyss, M., Stress estimates for South American shallow and deep earthquakes, J. Geophys. Res., 75, 1529-1544, 1970.

Zienkiewicz, O. C., The Finite Element Method in Engineering Sciences, McGraw-Hill, London, 1971.

ESTIMATES OF THE FINITE STRENGTH OF THE LITHOSPHERE FROM ISOSTATIC CONSIDERATIONS

Kurt Lambeck
Research School of Earth Sciences
Australian National University
Canberra, 2600 Australia

ABSTRACT

Estimates of the finite strength of the crust can be obtained from a stress analysis of various tectonic problems. One of the simpler approaches, from considerations of the stress-state of isostatically compensated topography, results in average maximum stress-differences of the order of 500 bars from both local and global analyses. In so far as the Earth's topography is generally near a state of isostatic compensation, this value reflects the strength of crust subjected to loads on a geological time scale.

ESTIMATES OF THE FINITE STRENGTH OF THE LITHOSPHERE FROM ISOSTATIC CONSIDERATIONS

Introduction

The strength of the Earth's crust and lithosphere has been deduced from a variety of physical considerations; from laboratory measurements, inferences from steady-state flow, in situ measurements of strain or stress, seismic stress-drop measurements or from tectonic considerations. The resulting estimates of the maximum deviatoric stresses at which lithospheric materials begin to behave non-elastically range from a few bars to several kilobars with the tectonic arguments generally pointing to kilobar values (e.g. Jeffreys, 1970; Hanks, 1977). It is with some aspects of these tectonic stresses that we are concerned with here. The reason for this concern is two-fold: estimates of the strength of the crust is fundamental to (i) the understanding of the tectonic processes and (ii) for separating density anomalies in the lithosphere from those in the mantle.

Long wavelength gravity anomalies provide direct evidence for the non-hydrostatic state of the Earth and, by implication, for convection in the mantle. This is seen particularly in the relation between these anomalies and the kinematic expressions of convection, namely the plate margins (e.g. Kaula, 1972). Despite these correlations, however, the use of gravity data as constraints on convection models has had only a very limited success for several reasons. (i) The separation of lithospheric and mantle contributions to the anomalous density structure has not yet been achieved; (ii) the response of the boundary layers to mantle flow remains unclear; (iii) the rheological, chemical, mineralogical and thermal parameters of the mantle remain inadequately known and (iv) the full three-dimensional convection problem has not yet been solved. Inversion of gravity data for establishing the convection pattern also has not yet been successful for the same reasons, as well as due to the inherent non-uniqueness of such inversions.

Gravity data inversion and interpretation has been more successful in regional studies by elucidating specific tectonic problems which are not only of intrinsic interest but which also have global implications. Studies of the response of the lithosphere and mantle to surface loads, for example, give insight into the rheology and into the way the boundary layers in the convection problem responds to forces associated with convection. The ocean

regions have, in particular, lent themselves to studies of this kind because the thinner oceanic lithosphere may respond more directly to any underlying dynamic process than its thicker and older continental counterpart and also because the former appears to be less complex, with its main features reasonably well understood within the plate tectonics hypothesis. General investigations of the relationship between ocean bathymetry and gravity in terms of mantle convection have recently been made by McKenzie (1977) and Cochran and Talwani (1977; 1978). Studies of these relationships for specific ocean problems include the study of (i) the ocean ridges (McKenzie, 1967; Lambeck, 1972; Parker and Oldenburg, 1973; Sclater et al. 1975); (ii) Loading of the ocean lithosphere by seamounts (Gunn, 1943; Vening Meinesz, 1941; Watts and Cochran, 1974; Walcott, 1976), and (iii) flexure of the ocean lithosphere sea-wards of the ocean trench (Hanks, 1971; Watts and Talwani, 1974). Recent studies of the relationship between continental gravity, topography and crustal and upper-mantle structure are by Dorman and Lewis (1971), McNutt and Parker (1978) and Banks et al. (1977, 1978). A general review of the relations between long wavelength gravity and global tectonic processes in the terrestrial planets is given by Phillips and Lambeck (1979).

A question central to all of these studies is the finite strength of the crustal and mantle materials, for if any proposed density model results in deviatoric stresses that exceed the material strength, the plausibility of the model is severely limited. A knowledge of the rheology permits a selection to be made amongst a variety of otherwise geologically acceptable models. For example, finite strength plays a key role in separating contributions to gravity from density anomalies in the lithosphere from those within the mantle. In so far as the upper lithosphere can support some deviatoric stress elastically, this question reduces to estimating that part of the gravity field that results in deviatoric stresses that do not exceed a critical limit beyond which significant creep or failure would occur. The residual part of the gravity anomalies then provides a lower limit to those density anomalies that must be supported dynamically in the mantle. If the finite strength of the lithosphere is of the order of several kilobars then much of the Earth's gravity field can be attributed to density anomalies in the lithosphere (e.g. Lambeck, 1972) but if the finite strength is less than a few hundred bars, or if only a relatively thin part of the lithosphere can support kbar deviatoric stresses, much of the global gravity field must be due to mantle density anomalies that are dynamically supported (e.g. Kaula, 1972). Conversely, gravity studies may provide a measure of the strength of the crust if the

models can be tested in a satisfactory manner against other geophysical and geological observations.

Tectonic estimates of stress in the crust

As emphasized by Jeffreys (1970), there are several ways in which deviatoric stresses can be estimated for a particular tectonic problem. The most straightforward, but geologically not always applicable is to find a solution of the appropriate elastic equations based on the assumption that the initial state was one of hydrostatic equilibrium which was subsequently perturbed by either horizontal or vertical forces such that a steady-state situation is ultimately attained. Geophysical situations where this approach is appropriate are the passive loading of the crust by ice, water or sediments, except that the steady-state may not have been reached if recent loading histories are of a duration comparable to the relaxation times of the crust and mantle. Another situation is the loading of the crust by seamounts but as these features are a consequence of dynamic processes which remain largely unknown, the usual elastic theory may not be entirely adequate unless the loads have moved sufficiently far away from their source so that the lithosphere has cooled and elastic forces become the dominant support mechanism for the load. A third example is the flexure of the oceanic lithosphere as this layer is subducted at the oceanic trenches. In all of these cases, the models can be tested by matching the computed gravity or topography with the observed values or, in some cases, by seismic studies. The most frequent observation used is gravity but whereas gravity is sensitive to the deformation or strain it gives little constraint on the stress-state.

The second method for estimating the deviatoric stresses is to abandon the linear stress-strain relations and to search for a minimum estimate of the strength of the crust (Jeffreys, 1943; 1970). The justification of this is the presence of major faulting and thrusting in most tectonic problems, features that cannot be taken into account by conventional elastic theory. For any distribution of stress, consistent with the surface load and the boundary conditions, there is some place where the stress-differences reach a maximum value while for other stress distributions a maximum value less than this may be found. But if we find that for all consistent stress distributions a least maximum stress-difference is reached, we know that somewhere in the lithosphere this value occurs and that the material can support it. This results in a minimum estimate of the strength of the crust or lithosphere below

the load. Jeffreys finds that the stress-differences are reduced relative to the purely elastic solutions by a factor of 2 or 3 in the case of loads on an infinite half-space. In the case of loads on an elastic plate overlying a fluid half-space this reduction may be as much as an order of magnitude.

The third approach is to state the mechanism for formation and to work out both its stress state and geological and geophysical consequences. In general the mechanisms are not sufficiently well understood or constrained by other geophysical observations to make this approach viable.

Isostasy

Considerations of the isostatic state may lead to a useful global estimate of the finite strength of the crust. The isostatic state appears to be globally observed and if the finite strength of the crust greatly exceeded the stress-differences associated with this state, then either topography would be greater than observed, or the departures from isostasy would be more widespread than is observed. The state of isostasy is usually defined as a compensation of surface loads by sub-surface density anomalies distributed in such a way that below, some constant depth, pressures will everywhere be hydrostatic. The manner in which these density anomalies are distributed above this level gives rise to the specific compensation mechanism by which the isostatic state is reached. The criteria for defining this distribution may be based on the assumption of constant pressure at a given depth, as in the classical Airy and Pratt models, on a state of mechanical equilibrium being achieved, as in the regional compensation models of Vening Meinesz, or on a condition that strain-energy is minimized as done by Jeffreys.

It is generally recognized that much of the Earth's surface, both continental and oceanic, is close to the isostatic state although there are some notable exceptions to this; areas of either undercompensation or overcompensation occur due to the fact that the Earth can support non-hydrostatic stress for long periods of time and that the surface deformations are also controlled by horizontal forces in the crust and upper mantle. Isostasy also appears to be an important phenomena shaping the other terrestrial planets (Phillips and Lambeck, 1979).

In many discussions of isostasy the stress-state in the layer

is ignored, it being implied that not only are the deviatoric stresses a minimum but they are also low enough for the crust or lithosphere to be able to support them. This need not be so. The isostatic state is not a hydrostatic state and even if the isostatic state is attained, further stress-relaxation may occur such that both the load and the compensation masses are reduced through non-elastic deformation, all the while the isostatic condition being satisfied (see figure 6 of Phillips and Lambeck, 1979). An elastic plate overlying a fluid half space and loaded at both its upper and lower boundary by equal harmonic loads σ such that Airy isostasy is achieved, results in stress-differences throughout the plate that are of the order of $g\sigma$, provided that the variation of the loads along the surface is not rapid (Timoshenko and Goodier, 1970). Shear stresses are generally small but not non-zero. Typically they will reach $\ell g\sigma_\ell H/R$ where H is the thickness of the elastic plate, ℓ the degree of the harmonic load σ_ℓ, and R the radius of the Earth. Jeffreys (1943, 1970) showed that the minimum strain-energy or minimum deviatoric stress conditions results in configurations that are close to the Airy model. Thus, if a topography h of density ρ loads the crust such that Airy isostasy is approached, the maximum stress-differences that will occur in the crust are of the order

$$\tau_{max} \simeq \rho gh \qquad (1)$$

and there will be no compensation models that result in significantly lower maximum stress-differences. Only if the wavelength of the load becomes less than the thickness of the elastic layer can τ_{max} be reduced; to about one half or one third of (1).

With (1) the stress-differences required to maintain high mountains is an isostatic state will be of the order of 300 bars per kilometer of elevation. Hence for the 5km high Tibetan plateau, maximum stress-difference in excess of 1 kbar can be expected in the underlying crust if (1) is valid. If the finite strength of the lithosphere is only of the order of a few hundred bars this estimate places some severe constraints on the validity of the isostatic models. The width of the plateau is in excess of 1000 km and the height variations of the plateau proper, to the north of the Himalayas, are small. The underlying crust appears to be anomalously thick, about 75 km, yet both it and the mantle appear to be hotter and consequently weaker than in stabler regions (Bird and Töksoz, 1977). Therefore much of the support for the load must come from the finite strength of the colder upper regions of the crust. The steep slopes occurring in the Himalayas also require a considerable finite strength in the upper parts of this crust. The

topography here can be modelled by two dimensional triangular cross-section loads for which $\tau_{max} \simeq \frac{1}{2}\rho gh$, with the maximum stress-differences occurring at a depth of about L/4 where L is the width of the load. For h ≃ 5km, L ≃ 100km, τ_{max} ≃ 700 bars at 25 km depth.

One reason why these tectonic stress estimate may be too high is that the calculations do not adequately represent the true state of affairs in the crust and lithosphere in the mountain forming areas. Areas of high topography such as the Tibetan plateau or the Andes cordillera are also areas of tectonic activity and that this topography exists at all is as much a reflection of compressive forces at the plate margins as of the finite strength of the crust. Bird (1978), Molnar and Tapponier (1978) and others have argued that the Tibetan plateau is maintained by compressive forces associated with the northward motion of India relative to Siberia and Bird estimates, albeit it by a rather crude model, that the maximum stress-differences associated with the plateau may only be of the order of 400-600 bars.

As pointed out by Phillips and Lambeck (1979), that features such as the Tibetan plateau is at once in isostatic equilibrium, as is evidenced by the studies of Chang and Chen (1973) and Kono (1974), is not necessarily a contradiction with the above model involving horizontal compression since the isostatic relaxation time is relatively short compared with the time constraints associated with vertical uplift due to the horizontal compressive forces.

Clearly, tectonically active situations do not provide the best applications of the conventional stress-calculation approach along the lines of the first two methods stated earlier for, as emphasized by Crittenden (1967), to provide a significant measure of finite strength it is important that the region in question is free from contemporary and recent tectonics. Where this condition is not met a more viable alternative may be to develop specific formation models and to evaluate the associated stress state as attempted by Bird for the Himalayas and the Tibetan Plateau.

There are numerous areas where this condition is satisfied. One is in Central Australia where a parallel series of large gravity anomalies occur in a tectonically quiet area. These anomalies, of wavelength about 300 km and with a peak-to-peak amplitude of about Δg=160 milligal, are roughly equivalent to what one would expect from a surface load of

$$\sigma(x) = \frac{\Delta g_o}{2\pi G} \cos\left(\frac{2\pi}{\lambda} x\right) \qquad (2)$$

and the maximum stress difference with (1) becomes

$$\tau_{max} = g\Delta g_o/2\pi G \simeq 375 \text{ bars.} \qquad (3)$$

The tectonically quiet mid-continent gravity high in the United States has a maximum peak-to-peak amplitude of about 200 mgals and with (2) and (3) this implies maximum stress-difference of about 400 bars somewhere in the underlying crust. Birch (1964) gives an example of a gravity anomaly over Green Mountain in Vermont with resulting maximum stress-differences of some 500 bars at 10 km depth. The South Africa gravity map provides several further examples of large anomalies in tectonically quiet areas. The Trompsburg anomaly, some 100 km south of Bloemfontein, with an amplitude of nearly 100 mgals and a radius of about 50 km (Hales and Gough, 1959), requires stress-differences of the order of 250 bars in the crust and these have apparently persisted for nearly 1.9×10^9 years. The large Southern Cape anomaly (Hales and Gough, 1961) requires similar stress-differences that have persisted for about 10^8 years.

Possibly a useful global estimate of the stress-differences associated with the isostatically supported topography is obtained from (1) by using the spherical harmonic expansion of the topography, namely (see Phillips and Lambeck, 1979)

$$h = \sum_{i=1}^{2} \sum_{\ell=1}^{\infty} \sum_{m=0}^{\ell} h_{i\ell m} Y_{i\ell m}.$$

Then, with (1)

$$\tau_{max} = \rho g \left[\sum_{\ell=1}^{\infty} \sum_{m=0}^{\ell} \sum_{i=1}^{2} h_{i\ell m}^2 \right]^{\frac{1}{2}}.$$

With the equivalent rock spectrum given by Balmino et al. (1973)

$$\tau_{max} \simeq 400 \text{ bars.}$$

In so far as topography and density anomalies are initially a consequence of dynamic processes that in many instances are still

operative, the actual deviatoric stresses may be somewhat less than suggested by the application of the static theory.

Disucssion

Estimates of the average finite strength of the Earth's crust and uppermost mantle based on a variety of methods range from a few hundred bars to several kilobars. If the consensus of this volume appears to be towards the upper limit, one need only look at a recent comparable volume (Wyss, 1977) where the consensus seems to be towards the lower limit. Laboratory measurements, using large strain rates and short loading cycles will always over-estimate the strength or flow stress relevant to geological problems since any additional mechanism that operates under geological conditions, but not in the laboratory, will only reduce the long-term strength.

Possibly one reason for a trend to higher strength estimates in the renewed interest and success of the elastic plate loading calculations. Elastic solutions for the seamount loads typically indicate stress-differences of about 2 kbars per km of deflection while the deflections may attain several kilometers under such large loads as the Hawaiian Archipelago. But as noted before the gravity observations control the deformation but do not give direct information on the stress. This is well illustrated by comparing elastic (Watts, 1978) and elastic-plastic (Liu and Kosloff, 1978) solutions for the loading of the Pacific plate by the Hawaii chain. Both solutions appear to be consistent with observations but the stress-differences are significantly reduced in the latter case. Furthermore, the stress-differences can be significantly reduced, particularly in the lower regions of the plate, if the yield stress varies with depth. Lambeck and Nakiboglu (1979) discuss some possible solutions.

The considerations of isostasy in the preceding sections suggest stress-differences that are of the order of 500 bars and that this is near the finite strength of the crust, probably the upper 10 or so km, for loads operating on geological time scales. If the finite strength was much greater than this, both the departures from isostasy and the topography would be higher than is usually observed.

References

Balmino, G., Lambeck, K. and Kaula, W.M., 1973. A spherical harmonic analysis of the Earth's topography, J.Geophys.Res., 78, 478-481.

Banks, R.J. and Swain, C.J., 1978. The isostatic compensation of East Africa, Proc.R.Soc.Lond. A.364, 331-352.

Banks, R.J., Parker, R.L. and Huestis, S.P., 1977. Isostatic compensation on a continental scale; Local versus regional mechanisms, Geophys.J.Roy.Astron.Soc., 51, 341-452.

Birch, F., 1964. Megageological considerations in rock mechanics. In State of Stress in the Earth's Crust. W.R. Judd, editor, American Elsevier Pub.Co., New York, 55-80.

Bird, P., 1978. Initiation of intracontinental subduction in the Himalaya, J.Geophys.Res., 83, 4975-4987.

Bird, P. and Toksöz, M.N., 1977. Strong attenuation of Rayleigh waves in Tibet, Nature, 266, 161-163.

Chang, C. and Cheng, H., 1973. Some tectonic features of the Mt. Jolmo Lungma area, southern Tibet, China, Sci.Sinica, 16, 257-265.

Cochran, J.R. and Talwani, M., 1977. Free-air gravity anomalies in the world's oceans and their relationship to residual elevation, Geophys.J.Roy.Astr.Soc., 50, 495-552.

Cochran, J.R. and Talwani, M., 1978. Gravity anomalies, regional elevation and the deep structure of the North Atlantic, J.Geophys. Res., 83, 4907-4924.

Crittenden, M.D., 1967. Viscosity and finite strength of the mantle as determined from water and ice loads, Geophys.J.Roy.Astron.Soc., 14, 261-279.

Dorman, L.M. and B.T.R. Lewis, 1970. Experimental isostasy. I., J.Geophys.Res., 75, 3357-3365.

Gunn, R., 1943. A quantitative study of isobaric equilibrium and gravity anomalies in the Hawaiian Islands, J.Franklin Inst., 238, 373-396.

Hales, A.L. and Gough, D.I., 1959. Gravity anomalies and crustal structure in South Africa, Geophys.J.Roy.Astron.Soc., 2, 324-336.

Hales, A.L. and Gough, D.I., 1961. Isostatic anomalies and crustal structure in the Southern Cape, Geophys.J.Roy.Astron.Soc., 3, 225-236.

Hanks, T.C., 1971. The Kurile trench - Hokkaido rise system: Large shallow earthquakes and simple models of deformation. Geophys.J.Roy.Astron.Soc., 23, 173-190.

Hanks, T.C., 1977. Earthquake stress drops, ambient tectonic stresses and stresses that drive plate motions, Pure Appl.Geophys., 115, 441-458.

Jeffreys, H., 1943. The stress differences in the Earth's shell, Mon.Not.Roy.Astron.Soc., Geophys.Supp., 5, 71-89.

Jeffreys, H., 1970. The Earth, Its Origin, History and Physical Constitution, Cambridge University Press, Cambridge.

Kaula, W.M., 1972. Global gravity and tectonics, in The Nature of the Solid Earth, edited by E.C. Robertson, McGraw Hill, New York, pp.385-405.

Kono, M., 1974. Gravity anomalies in East Nepal and their implications to the crustal structure of the Himalayas, Geophys.J.Roy.Astron.Soc., 39, 283-299.

Lambeck, K., 1972. Gravity anomalies over ocean ridges, Geophys.J. Roy.Astron.Soc., 30, 37-53.

Lambeck, K. and Nakiboglu, S.M., 1979. On the loading of the ocean lithosphere by seamounts. In Magnitude of Deviatoric stresses in the Earth's Crust and Upper Mantle. J. Evernden, editor, U.S. Geol.Survey, Menlo Park.

Liu, H.P. and Kosloff, D., 1978. Elastic-plastic bending of the lithosphere incorporating rock deformation data, with application to the structure of the Hawaiian archipelago. Tectonophysics, 50, 249-274.

McKenzie, D.P., 1967. Some remarks on heat flow and gravity anomalies. J.Geophys.Res., 72, 6261-6273.

McKenzie, D.P., 1977. Surface deformation, gravity anomalies and convection, Geophys.J.Roy.Astron.Soc., 48, 211-238.

McNutt, M.K. and Parker, R.L., 1978. Isostasy in Australia and evolution of the compensation mechanism, Science, 199, 773-775.

Molnar, P. and Tapponnier, P., 1978. Active tectonics of Tibet, J.Geophys.Res., 83, 5361-5376.

Parker, R.L. and Oldenburg, D.W., 1973. Thermal model of ocean ridges, Nature, Phys.Sci., 242, 137-139.

Phillips, R.J. and Lambeck, K., 1979. Gravity field of the terrestrial planets: long wavelength anomalies and tectonics, Revs.Geophys.Space Phys., in press, 1979.

Sclater, J.G., L.A. Lawver and B. Parsons, 1975. Comparison of long-wavelength residual elevation and free air gravity anomalies in the North Atlantic and possible implications for the thickness of the lithospheric plate, J.Geophys.Res., 80, 1031-1052.

Timoshenko, S. and Goodier, J.N., 1970. Theory of Elasticity, McGraw Hill, New York, 806 pp.

Vening Meinesz, F.A., 1941. Gravity over the Hawaiian Archipelago and over the Madeira area. Proc.K.Ned.Akad.Wet., 44, 1-12.

Walcott, R.I., 1976. Lithospheric flexure, analysis of gravity anomalies and the propagation of seamount chains, in The Geophysics of the Pacific Ocean Basin and Its Margin, Amer. Geophys.Union Monograph, 19, 431-438.

Watts, A.B., 1978. An analysis of Isostasy in the World's Oceans. 1. Hawaiian-Emperor Seamount Chain. J.Geophys.Res., 83, 5985-6004.

Watts, A.B. and Cochran, J.R., 1974. Gravity anomalies and flexure of the lithosphere along the Hawaiian-Emperor seamount chain, Geophys.J.Roy.Astron.Soc., 38, 119-141.

Watts, A.B. and Talwani, M., 1974. Gravity anomalies seaward of deep-sea trenches and their tectonic implications, Geophys.J.Roy. Astron.Soc., 36, 57-90.

Wyss, M., 1977. Editor, Stress in the Earth. Pure Applied Geophysics, 115, No.1-2.

SEISMIC VELOCITY, ATTENUATION AND RHEOLOGY OF THE UPPER MANTLE

Don L. Anderson
and
J. Bernard Minster

Seismological Laboratory
California Institute of Technology
Pasadena, California 91125

Abstract

It is proposed that the seismic and rheological properties of the upper mantle in the vicinity of the low-velocity zone can be understood in terms of dislocation motions. Dislocation bowing in the glide plane has the proper relaxation strength and time scale to explain the seismic velocities and attenuation. The same dislocations climb at higher stresses and longer times and give the observed viscosity. This explains the low velocity and high attenuation found at seismic frequencies, the low viscosity inferred for short term post-seismic rebound and the higher values found for longer term uplift processes. The thickness of the "rheological lithosphere" decreases with loading time and applied stress and is different from the "seismic lithosphere" and the "thermal lithosphere". All three, however, are related and are functions of temperature. Partial melting, if it exists, does not play an important role in the seismic and rheological properties of the upper mantle.

Introduction

The upper mantle low-velocity zone (LVZ) first described by Gutenberg and supported by numerous later studies has played an important but controversial role in the modern theory of plate tectonics. It has been associated by many with the "asthenosphere", a layer of reduced strength proposed by early geologists and geodesists. Such a layer could decouple the surface lithospheric plates from the underlying mantle and explain their relatively high mobility.

In this paper we show that disloaction motions can explain both the short term (seismic) and long term (flow) properties. Under small strains the dislocations bow by glide, the time scale being controlled by kink or interstitial diffusion. At larger strains, and longer times, dislocations can bow out of their glide plane by climb, a mechanism controlled by the slower process of self diffusion. These mechanisms are controlling even if the upper mantle is partially molten.

Previous Work

Temperature, particularly relative to the melting point, plays a critical role in determining seismic velocity, attenuation and visco-

sity. One expects low seismic velocities and viscosities to be associated with higher temperature. The attenuation, for a thermally activated process, on the other hand, depends on the time scale of the measurement relative to the temperature dependent characteristic relaxation times. High temperatures, per se, do not necessarily lead to high attenuation.

The seismic velocities in the LVZ in tectonic and oceanic regions are too low to be the result only of a high temperature gradient if high frequency laboratory measurements in single crystals and dense aggregates are used as a guide. The shear velocity decreases more than the compressional velocity. This plus the high homologous temperatures inferred for the vicinity of the LVZ lead Anderson and Sammis (1970) and others to conclude that the shear modulus was relaxed. This can be accomplished by grain boundary melting but this is not the only possibility.

The low velocities in the LVZ are associated with high attenuation. This provides an additional and powerful constraint on the relaxation mechanism. There is no doubt that partial melting can provide the observed reduction in velocity, if the melt occurs in intergranular films, but the associated attenuation requires that the relaxation occurs at seismic frequencies. The seismic data provide information about the relaxation time which in turn is a function of temperature.

There have been some attempts to determine the viscosity and configuration of the grain boundary melts which are required to satisfy the seismic data but these have not been satisfactory. That partial melting is not required to explain the seismic attenuation data can be seen from the large subsolidus attenuation peaks which are observed in a variety of materials at high temperature. These have been attributed to grain boundary relaxation and motion of dislocations, i.e., mechanisms related to solid state diffusion. These have much longer characteristic times that can be provided by diffusion or flow in silicate melts and have the potential for explaining not only the seismic data but also longer time processes. Subsolidus grain boundary relaxation, in many cases, almost completely relaxes the shear stress across grain boundaries and further relaxation due to partial melting cannot occur without grain deformation. There are several recent studies which further suppress the importance of partial melting as a universal explanation of high attenuation in the upper mantle. Turcotte and Ahern (1978) and Walker et al (1978) have computed the residence time of melts in the upper mantle and concluded that these times are very short. Even a small amount of melt is unstable and quickly migrates upwards. Waff and Bulau (1978) showed that silicate melts do not wet grain boundaries and tend to occur in thin tubes at grain corners. This is contrary to the assumptions in the partial melt theories. This decreases the effectiveness of the melt in permitting grain boundary relaxation and also provides more efficient channels for magma removal. Melt in this configuration increases the permeability and the electrical conductivity. Partial melt does seem to be required to explain the high electrical conductivity in tectonic regions (Shankland and Waff, 1977).

The Low Velocity Zone

The shear velocity in the mantle decreases by about 10% between 40 and 150 km in tectonic and oceanic regions (Anderson and Hart, 1976, Cara, 1978). When corrected for temperature and pressure, using single crystal values for olivine (Kumazawa and Anderson, 1969), the remaining shear modulus defect is about 8%. This can be compared with the modulus defect, to be discussed later, associated with dislocation glide of 8%. The total modulus defect associated with dislocations when both climb and glide are allowed ranges from 11 to 14%. The climb component requires self diffusion and therefore only contributes at very high temperature, low frequency or long time. By contrast the decrease in velocity in the upper mantle under shields and non-tectonic regions can be accounted for almost entirely by the high frequency single crystal elastic constants and their pressure and temperature derivatives. The attenuation of seismic waves is much less under stable regions than under tectonic and oceanic regions. This suggests that the homologous temperatures under stable continents are lower than in the other areas.

Solomon (1972) and Nur (1971) attempted to explain upper mantle seismic attenuation in terms of a viscous grain boundary mechanism and inferred values of 10^6-10^{12} P for the "melt" at grain boundaries. These estimates are orders of magnitude greater than the range 10^3-10^4 P measured on silicate melts at the appropriate conditions. The high inferred viscosities and the very small displacements at grain boundaries, $\sim 10^{-8}$ cm at seismic strain levels, both suggest a solid state diffusional mechanism, even if the mantle in the vicinity of the LVZ is not subsolidus. With measured melt viscosities the grain boundary relaxation would occur at very high frequencies and the associated absorption peak would be outside the seismic band. This is an example of high temperatures leading to small attenuation, a situation contrary to the assumptions of many workers.

The present study does not rule out the existence of partial melt in the upper mantle. It stresses the role of temperature on the mobility of crystalline defects. Partial melting, of course, occurs at high temperatures but it is the dislocations and their associated point defects that controls the rheology rather than the presence of the melt. The relatively minor role of the melt phase has also been stressed by Goetze (1978). Guequen and Mercier (1973) have proposed a dislocation mechanism for the low-velocity, high-attenuation zone of the upper mantle.

Dislocation Mechanisms

The minerals of the mantle are assumed to contain dislocation networks. These dislocations are pinned at network nodes. They are free to bow, however, under a small applied stress and to multiply under a large applied stress. The first characteristic is responsible for transient creep and for a reduction in the shear modulus. The second characteristic is responsible for steady state creep. At low temper-

ature, short time, and high strain rates, bowing is restricted to the glide plane, a process that is rate limited by the diffusion of intersitial impurities. At high temperature dislocations can climb, a slower process that is rate limited by self diffusion. Climb contributes a further reduction to the velocity.

Relaxation mechanisms such as proposed here, lead to an internal friction peak of the form

$$Q^{-1}(\omega) = \Delta \int_{-\infty}^{\infty} D(\tau) \quad [\omega\tau/(1+\omega^2\tau^2)]d\tau \qquad (1)$$

where ω is the applied frequency, τ is a characteristic time, $D(\tau)$ is the retardation spectrum and Δ is the modulus defect, $(G_u - G_r)/G_r$, the relative difference between the high frequency, unrelaxed shear modulus, G_u, and the low frequency, relaxed modulus, G_r. The modulus defect is also a measure of the total reduction in modulus that is obtained in going from low temperature to high temperature. In our model the modulus defect is due to the additional strain contributed by dislocation bowing. The dislocations bow to an equilibrium radius of curvature which is dictated by the applied stress. The rate at which they do so is controlled by the diffusion of point defects near the dislocation and therefore is a strong function of temperature.

The retardation spectrum can be written (Minster and Anderson, 1979)

$$D(\tau) = [\alpha/(\tau_2^{\alpha}-\tau_1^{\alpha})]\ \tau^{\alpha-1} \qquad (2)$$

for $\tau_1 < \tau < \tau_2$ and zero elsewhere. τ_1 and τ_2 are, respectively, the shortest and longest relaxation times of the mechanism being considered. Ordinarily the characteristic times of various mechanisms that lead to damping are well separated so that only a single or several mechanisms contribute to the observed attenuation over a given frequency or temperature band. The characteristic times for single mechanism, however, can be spread out over a appreciable interval.

When $\alpha = 1$ equation (1) reduces to the well known Debye peak. When $\alpha = 0$, and $\tau_2 >> \tau >> \tau_1$, a frequency independent Q results (Liu et al., 1976). The more general case of $0 < \alpha < 1$ has recently been discussed (Anderson and Minster, 1979). This leads to a weak dependence, $Q(\omega) \sim \omega^{\alpha}$ for $\tau_1 < \tau < \tau_2$ and has characteristics similar to Jeffreys (1958) modification of Lomnitz's law. Outside the absorption band $Q(\omega) \sim \omega^{\pm 1}$ for $\omega\tau \lesssim 1$. This result holds for all relaxation mechanisms.

Dislocation glide for a random orientation of glide planes gives a modulus defect of 8% (Minster and Anderson, 1979). This gives a minimum Q at $\omega\tau = 1$ of 25 which is in good agreement with the seismic data (Solomon, 1972). Thus, the reduction in velocity and the attenuation caused by dislocations bowing under small stresses are in excellent accord with the seismic data. It remains to be seen if the characteristic times of this mechanism occur at seismic frequencies. For this purpose we use the theory of Friedel (1964) and Schoeck (1963). In these theories the motion of the dislocations is rate limited by the diffusion of impurities which are attached to the dislocation. Other possibilities of drag such as the drag of a Cottrell atmosphere are more appropriate for metals than for ionic crystals. We have calculated that the drag of a Cottrell cloud of impurities will only be important for higher temperatures and longer times than those considered here.

We assume that dislocations in olivine can glide in their slip plane easier than they can climb. The glide contribution to the modulus defect therefore sets in at lower temperatures. Glide motion is rate limited by the diffusion of interstitial atoms near the dislocation. The time constants is (Shoeck, 1963),

$$\tau_g \simeq \frac{kT\ell^2 C}{GD_i b^3} \qquad (3)$$

where C is the concentration of impurities or interstitial atoms on the dislocation line and D_i is their diffusivity. For purposes of illustration we assume Mg++ interstitials. The interdiffusion coeffieicent for Mg++ - Fe++ in olivine is (Misener, 1974)

$$D_i \simeq (0.52 \times 10^{-2}) \exp(-58/RT) \quad (cm^2/sec)$$

The calculated time constants are given in Table 1. They range from 55 sec at 1100 K to 0.05 sec at 1523 K. For a typical upper mantle temperature profile, therefore, the relaxation times span the seismic band. An order of magnitude decrease in dislocation length decreases the times by two orders of magnitude. A spread in the lengths of dislocations and the range of homologous temperatures for mantle minerals will spread out the characteristic time spectrum and lead to a broad absorption for seismic waves. In the above calculations we have taken C equal to 10^{-3} and the other parameters from the following analysis.

Behavior of Dislocations at Large Stresses

The bowing of dislocations has been shown to be a plausible explanation for the reduction in shear velocity and increase in attenuation in the upper mantle. We now discuss how this information can be used to determine the viscosity of the mantle. Dislocation climb is probably the dominant mode of creep in the mantle. The theory has been worked out by Nabarro (1967). The importance of climb in olivine has been discussed by Goetze (1978).

The nature and distribution of dislocations in olivine grains from naturally deformed peridotite correspond closely to the assumptions required for Nabarro's analysis for climb-limited creep (Goetze and Kohlstedt, 1973).

Consider a uniform three dimensional array of dislocations of length ℓ. Under an applied stress, σ, each dislocation climbs at a speed

$$V = 2D\sigma\Omega/kTb\pi \qquad (4)$$

where Ω is the atomic volume.

The time between multiplications (generation time) is

$$\tau = (\pi\ell bkT/2D\Omega\sigma)\ln(8\pi\ell^2/b^2G) \qquad (5)$$

where b is the Burger's vector and ℓ is the dislocation length. The time to collision between dislocations in adjacent cells (annihilation time) is

$$\tau_a = (\ell^2kT/2GD\Omega)\ln(2^{3/2}\ell/b) \qquad (6)$$

This time is related to the attraction of dislocations of opposite sign.

In the steady state dislocation multiplication and annihilation balance giving the steady state creep rate

$$\dot{\varepsilon}_{ss} = (Db\sigma^3/\pi kTG^2) \; / \; \ln(4G/\pi\sigma) \qquad (7)$$

For a distribution of initial lengths those having a critical length $\ell_c = Gb/\sigma$ first reach the critical curvature and multiply. This length dominates thereafter and gives the well known relation between dislocation density and applied stress.

The average lifespan of these dislocations is

$$\tau_a = (GkT/2\sigma^2Db) \ln (2^{3/2} \ell_c/b) \qquad (8)$$

The creep function for the relaxation spectrum (2) is

$$\varepsilon_t(t) \simeq \sigma J_u[1 + (\delta J/J_u)\Gamma(1-\alpha)\ (t/\tau_a)^{\alpha}] \qquad (9)$$

for $\tau_1 << t << \tau_2 \sim \tau_a$.

The reversible strain is

$$\varepsilon_T \simeq \sigma J_u[1 + (\delta J/J_u)\Gamma(1-\alpha)] \qquad (10)$$

The transient creep rate at $t = \tau_a$ is

$$\dot{\varepsilon}_t\ (\tau_a) = 2\sigma J_u\ (\delta J/J_u)\alpha\Gamma(1-\alpha)GDb^3/\ell_c^2\ kT\ \ln(2^3/^2G/\sigma) \qquad (11)$$

which, when equated with the steady state creep rate gives

$$\delta J/J_u \simeq [2\pi\alpha\Gamma(1-\alpha)]^{-1} \qquad (12)$$

which for $\alpha = 1/3$ (Anderson and Minster, 1979) gives

$$\delta J/J_u = 0.80$$

which is equivalent to

$$M_R/M_u = 0.56$$

The steady state dislocation length is a function of stress

$$\ell \sim Gb/\sigma \qquad (13)$$

For a distribution of dislocation lengths this is the length which under an applied stress first reaches the critical radius of curvature and starts to multiply.

Dislocation climb is rate limited by self-diffusion of oxygen where (Goetze and Kohlstedt, 1973, Ashby and Verrall, 1978),

$$D \simeq 10^3 \exp(-135/RT)\ (cm^2/sec)$$

We take $\sigma = 30$ bars, a value appropriate for stresses in the upper mantle, and compute $\ell \sim 2 \times 10^{-3}$ cm for $b = 10^{-7}$ cm and $G = 6 \times 10^{11}$ dy/cm^2. This is close to dislocation lengths observed in naturally deformed peridotite.

Table 1 summarized the time constants for glide and climb and the inferred climb viscosity as a function of temperature for olivine. The

diffusive and creep properties of many materials are similar when referenced to the melting temperature (e.g. Weertman, 1970, Ashby and Frost, 1975). In polyphase material it is the solidus of the individual phases that controls their creep properties rather than the solidus of the composite. In many discussions of mantle rheology the composite solidus is used to estimate the viscosity but this is valid only as an approximation of the properties of the minimum melting point phases, garnet and clinopyroxene. Olivine is the major phase in the upper mantle and it is more logical to use the liquidus temperature, T_ℓ, when computing the homologous temperature T/T_ℓ.

The nearest that upper mantle temperatures get to the melting point of olivine corresponds to T/T_ℓ of about 0.77. Therefore, the minimum time constant for climb, the mechanism of steady state creep, is about 2×10^7 seconds. This corresponds to a minimum steady state viscosity of about 6×10^{19} poise. This low value will occur over only a limited depth extent. The homologous temperature anywhere in the mantle below the lithosphere is likely to be less than 0.7. This corresponds to a viscosity of 10^{21} poise. Therefore, viscosities in the mantle are confined to a relatively narrow range, as observed.

Other upper mantle minerals such as pyroxene and garnet have lower melting points, and therefore higher homologous temperature, shorter relaxation times and lower viscosity, but they will not control the overall steady state creep rate unless they form a continuous network. They do contribute, however, in proportion to their volume to the seismic velocity and attenuation. In effect, they serve to spread out the seismic absorption band. They also contribute to transient creep.

The observation of transient displacement following the 1946 Nankaido earthquake is remarkably consistent with the theory. Nur and Mavko (1974) analyzed the rebound data in terms of an elastic lithosphere overlying a viscous half-space. The asthenosphere was shown to have a relaxation time of $\sim 10^8$ seconds and a relaxed shear modulus of about 0.4-0.6 times the initial shear modulus. We have shown that the dislocation strain for high stresses leads to a reduction of the shear modulus by about 50%. We will now analyse the relaxation time.

For a temperature of 1250° C for the asthenosphere we obtain from equations (8) and (13) a relaxation time of 1.4×10^8 seconds or about 5 years. Thus, both the modulus reduction and the characteristic time for dislocation bowing are compatible with the post-seismic rebound data. Mavko and Nur (1975) proposed a "melt squirt" mechanism of relaxation in order to obtain the observed time scale. We have shown that a subsolidus mechanism has the appropriate characteristics.

Transient creep and attenuation data (Anderson and Minster, 1979) and direct observations of dislocations in deformed MgO (Bilde-Sorensen, 1973) imply a distribution of dislocation lengths. The characteristic times depend on the lengths ($\tau \sim \ell^2$) as well as on the distrib-

ution of activation energies and homologous temperatures in upper mantle minerals. The rebound data is sensitive to the longest relaxation time whereas the dislocation density is a function of the mean dislocation length which for a hyperbolic or exponential distribution is controlled by the shorter lengths. A variation of 10% in E^* (T_ℓ/T) gives a four order of magnitude variation in the relaxation time, as does a two order of magnitude variation in dislocation length. Therefore, characteristic times for this mechanism can cover a broad band. The characteristic times are very much longer in the colder, relative to the melting point, regions of the Earth such as the lithosphere. This is why, in fact, the lithosphere appears rigid. The effective thickness of the lithosphere should depend on the duration of the load. For each temperature we can calculate a band of characteristic times. For shorter times the material is unrelaxed and appears rigid; for longer times the material relaxes.

For example, with the parameters used above, the 1200 K isotherm would represent the bottom of the lithosphere for processes acting over half a million year whereas the 1100 K isotherm is appropriate for 80 million years. This represents an effective thinning of the lithosphere of about 30 km.

Before proceeding along this line it is prudent to check the predictions of Nabarro's dislocation climb mechanism with steady state creep data on olivine. Kohlstedt et al. (1976) summarize creep data on dry olivine at 1400°C (Figure 1). For comparison purposes they used an activation energy of 125 kcal/mol, a value we use below. The other parameters needed to evaluate equation (7) are $b = 6 \times 10^{-8}$cm and G = 634 kb (Ashby and Verrall, 1978). The theoretical curve is labelled "Nabarro" in Figure 1. Weertman (1968) reconsidered the dislocation climb theory and obtained essentially equation (7) without the logarithmic term. This gives a slightly higher creep rate for a given stress, as shown in Figure 1. The agreement with the data is satisfactory, particularly for Weertman's theory. The curve labelled Nabarro-Herring is for intergranular diffusion. It gives much lower strain rates indicating that dislocation mechanisms predominate.

We are now encouraged to estimate the thickness of the "rheological lithosphere". Clearly it will depend on age and will thicken as the crust and mantle cools. It depends on the magnitude of the load; because of the stress dependence it will appear thicker for smaller loads. It depends on the duration of the load. At a given depth, and therefore temperature, the rheology will appear elastic for durations shorter than the characteristic relaxation time, and viscous for longer duration loads. The "thickness of the lithosphere" is therefore a more complicated concept that has been generally appreciated.

In figure 2 we present estimates of the thickness of the oceanic rheological lithosphere as a function of age of crust and duration of load. In the calculation we have used oceanic geotherms from Schubert et al. (1978) and a stress of 1 kilobar. The load time constant can be

scaled for other stresses from equation (8). The depth to the rheological asthenosphere is defined as the depth having a characteristic time equal to the duration of the load. For example, from Figure 2, a 30 million old load imposed on 80 million year old crust would yield a thickness of 45 km if the lithosphere did not subsequently cool or if the cooling time is longer than the relaxation time. A 30 million year old load on currently 80 million year old crust would give a 34 km thick rheological lithosphere with the above qualifications. The thickness of the high velocity layer overlying the low-velocity zone (the LID) is also shown in Figure 2. For load durations of millions of years the rheological lithosphere is about one-half the thickness of the seismological lithosphere. Note that the rheological thickness decreases only gradually for old loads. This is consistent with the observations of Watts et at. (1975). On the other hand the lithosphere appears very thick for young loads and the apparent thickness decreases rapidly.

We have shown earlier that the relaxed modulus is about one-half of the unrelaxed or high frequency seismic modulus. This should be taken into account when the thickness of the rheological lithosphere is calculated from flexural rigidity data. For a given flexural rigidity, calculated for example from the bathymetry near loads on the oceanic crust, the true lithospheric thickness will be slightly greater than would be computed by using the seismic modulus in the conversion from flexural rigidity to thickness.

Summary

The pronounced low-velocity zone found in oceanic and tectonic regions can be explained in terms of relaxation by dislocation glide. The time constant appears to be appropriate for explaining the absorption band at seismic frequencies. The higher stress and longer duration rheological properties can be understood in terms of dislocation climb. Both glide and climb are thermally activated processes and there is therefore a relation between the seismic and rheological properties via the temperature and pressure.

It is proposed that separate terms be used for the thermal, seismic and rheological lithospheres since these are based on different concepts. The thermal lithosphere, as studied by the variation of bathymetry and heat flow as a function of age (Parsons and Sclater, 1977) is related to cooling and involves such parameters as thermal conductivity, coefficients of thermal expansion and subcrustal heat flow. The seismic lithosphere, called the LID by Anderson and Toksoz (1963) represents that part of the upper mantle which have relaxation times for dislocation glide that are long compared to seismic wave periods. Its thickness is a function of period. The low-velocity zone is due to high temperature and is characterized by relaxation times short compared to seismic periods. The depth of minimum velcity should also be a function of period. The important parameters are dislocation densities, temperature and activation energy. In principle, seismic data could be used to determine temperature and stress state of the upper mantle.

The apparent thickness of the rheological lithosphere depends on temperature, stress and load duration. For small loads, for example, post-glacial rebound, relaxation times are longer and lithospheric thicknesses are greater than for large loads such as oceanic islands. For loads greater than thousands of years the rheological thickness is much less than the seismic thickness.

We propose that the terms "thermal lithosphere", "seismic lithosphere", or "LTD", and "rheological lithosphere" be used when the different phenomena are being discussed. Even with these qualifiers it is necessary to specify other parameters such as period, stress, stress duration, etc.

Table 1. Time constants for climb (τ_c), glide (τ_g) and viscosity for climb controlled creep (η_c) as a function of temperature and homologous temperature relative to the melting point of olivine, Fo_{g2}.

T(K)	T/T	τ_c(sec)	T_g(sec)	η_c(P)
1100	0.51	3×10^{15}	55	10^{28}
1200	0.55	2×10^{13}	7	6×10^{25}
1400	0.65	6×10^{9}	0.3	2×10^{22}
1523	0.70	10^{8}	0.05	5×10^{20}
1600	0.74	2×10^{7}	0.02	6×10^{19}
1800	0.83	2×10^{5}	0.003	6×10^{17}
2000	0.92	5×10^{3}	0.0007	2×10^{16}

References

Anderson, Don L. and Hart, R. S., 1976. Absorption and the low velocity zone. Nature, 263: 397-398.

Anderson, Don L. and Minster, J. B., 1979. The frequency dependence of Q in the Earth and implications for mantle rheology and Chandler Wobble. Geophys. J. R. astr. Soc. (in press).

Anderson, Don L. and Sammis, C., 1970. Partial melting in the upper mantle. Phys. Earth Planet. Inter., 3: 41-50.

Anderson, Don L. and Toksoz, M. N., 1963. Surface waves on a spherical Earth I. Upper mantle structure from Love waves. J. Geophys. Res., 68: 3483-3500.

Ashby, M. F. and Frost, H. J., 1975. Constitutive equations in plasticity (ed. A. Argon), p. 117, M.I.T. Press.

Ashby, M. F. and Verrall, R. A., 1978. Micromechanism of flow and fracture, and their relevance to the rheology of the upper mantle, Phil. Tran. R. Soc. Lond. A., 288: 59-95.

Bilde-Sorensen, J. B., 1973. Dislocation link length distribution in creep deformed magnesium oxide. Acta Metall., 21: 1495-1501.

Cara, M., 1979. Lateral variations of S-velocity in the upper mantle from higher Rayleigh modes. Geophys. J. R. astr Soc. (in press).

Friedel, J., 1964. Dislocations, Pergamon Press Ltd., Oxford.

Goetze, C., 1977. A brief summary of our present day understanding of the effect of volatiles and partial melt on the mechanical properties of the upper mantle. High-Pressure Research, M. Manghnani and S. Akimoto, editors, p. 3-23.

Goetze, C., 1978. The mechanisms of creep in olivine, Phil. Trans. R. Soc. Lond. A, 288: 99-119.

Goetze, C. and D. L. Kohlstedt, 1973. Laboratory study of dislocation climb and diffusion in olivine. J. Geophys. Res., 78: 5961-5971.

Guequen, Y. and J. M. Mercier, 1973. High attenuation and the low-velocity zone. Physics of the Earth and Planetary Interiors, 7: 39-46.

Jeffreys,H., 1958. Rock creep. Mon. Nat. R. astr. Soc., 118: 14-17.

Kohlstedt, D. L., C. Goetze and W. B. Durham, 1976. Experimental deformation of single crystal olivine with application to flow in the mantle, in Petrophysics: The Physics and Chemistry of Minerals and Rocks, R. G. U. Strens (ed.), pp. 35-49, John Willey, N.Y.

Kumazawa, M. and D. L. Anderson, 1969. Elastic models, pressure derivatives and temperature derivatives of single-crystal olivine and single-crystal forsterite. J. Geophys. Res., 74, 5961-5972.

Liu, H. P., Don L. Anderson and H. Kanamori, 1976. Velocity dispersion due to anelasticity; implications for seismology and mantle composition. Geophys. J. R. astr. Soc., 47: 41-58.

Mavko, G. and A. Nur, 1975. Melt squirt in the asthenosphere. J. Geophys. Res., 80: 1444-1448.

Minster, J. B. and Don L. Anderson, 1979. Dislocation mechanisms of attenuation (in preparation).

Misener, D. V., 1974. Cationic diffusion in olivine to 1400° C and 35 kbar. Carnegie Inst. Washington Publ. 634: p. 117-129.

Nabarro, F. R. N., 1967. Steady-state diffusional creep, Phil. Mag., 16: 231-237.

Nur, A., 1971. Viscous phases in rocks and the low velocity zone. J. Geophys. Res., 76: 1270-1278.

Nur, A. and G. Mavko, 1974. Postseismic viscoelastic rebound. Science, 183: 204-206.

Parsons, B. and J. G. Sclater, 1977. and analysis of the variation of ocean floor heat flow and bathymetry with age. J. Geophys. Res., 82: 803-827.

Schoeck, G., 1963. Friccion interna debido a la interaccion entra dislocaciones y atomos solutos. Acta Metall., 11: 617-622.

Schubert, G., C. Froideraux, and D. A. Yuen, 1976. Oceanic lithosphere and asthenosphere; Thermal and mechanical structure. J. Geophys. Res., 81: 3525-3540.

Shankland and H. S. Waff, 1977. Partial melting and electrical conductivity anomalies in the upper mantle. J. Geophys. Res., 82: 5409-5417.

Solomon, S.C. 1972, On Q and seismic discrimination. Geophys. J. R. astr. Soc., 31: 163-177.

Turcotte, D. L. and J. L. Ahern, 1978. A porous flow model for magma migration in the asthenosphere. J. Geophys. Res., 83: 767-772.

Waff, H. S. and J. R. Bulau, 1978. Equilibrium fluid distribution in an ultramafic partial melt under hydrostatic stress conditions. J. Geophys. Res. (in press).

Walker, D., E. M. Stolper and J. F. Hayes, 1978. A numerical treatment of melt/solid segregations: size of the eucrite parent body and stability of the terrestrial low velocity zone (in press).

Watts, A. B., J. R. Cochran and G. Selzer, 1975. Gravity anomalies and flexure of the lithosphere: a three-dimensional study of the Great Meteor Seamount, N. E. Atlantic. J. Geophys. Res., 80: 1391-1398.

Weertman, J., 1970. The creep strength of the Earth's mantle. Rev. Geophys. Space Phys., 8: 145.

Weertman, J., 1968. Dislocation climb theory of steady-state creep. Tran. Amer. Soc. Metals, 61: 681-694.

Figure Captions

Figure 1: Strain rate vs. stress for olivine (from Kohlstedt et al., 1976). Theoretical curves for dislocation climb are computed from theory of Nabarro (1967) and Weertman (1968). Also shown is theoretical curve for Nabarro-Herring diffusional creep with a stress dependent grain size. The higher stress, or tertiary creep, data is not shown.

Figure 2: Thickness of rheological lithosphere versus age of oceanic crust and duration of loading for imposed stress of 1 kilobar. For smaller stress multiply load duration time by $(1kb/\sigma)^2$. For example, the curve for 3×10^4 years for 1 kb corresponds to 33×10^6 years for 30 bars. The oceanic geotherms are from Schubert et al. (1976). The seismic thickness is from summary by Solomon (1976) and is based on measurements by Weidner (1974), Leeds et al. (1974) and Asada and Shimamura (1975).

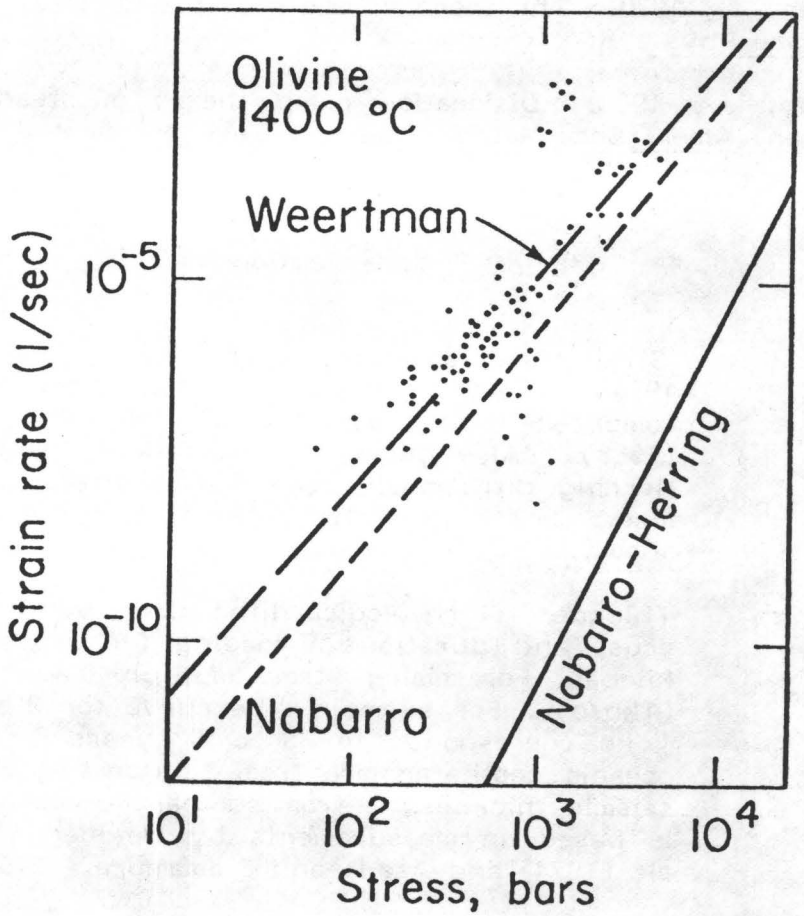
Olivine
1400 °C
Weertman
Nabarro
Nabarro-Herring
Strain rate (1/sec)
10^{-5}
10^{-10}
10^{1}
10^{2}
10^{3}
10^{4}
Stress, bars

Fig. 1

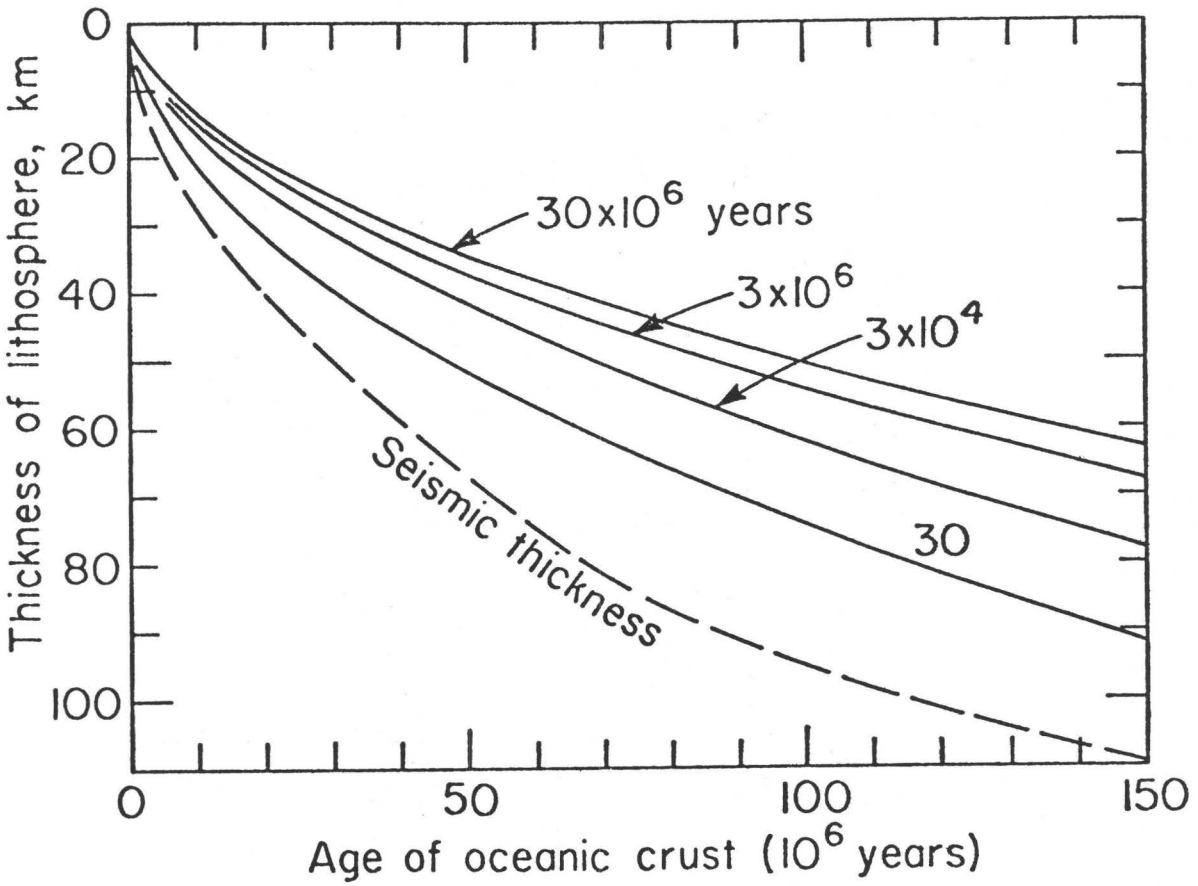
Thickness of lithosphere, km
0
20
40
60
80
100
0
50
100
150
Age of oceanic crust (10^6 years)
30×10^6 years
3×10^6
3×10^4
30
Seismic thickness

Fig. 2

EARTHQUAKE LOADING OF THE LITHOSPHERE:

REVIEW AND SPECULATIONS

Wayne Thatcher
U.S. Geological Survey, Menlo Park, California

Tokihiko Matsuda
and
Teruyuki Kato
Earthquake Research Institute, Tokyo University, Japan

John B. Rundle
Sandia Laboratories, Albuquerque, New Mexico

ABSTRACT

Applying methods similar to those used in modeling the effects of plate flexure and post-glacial rebound, the time-dependent aseismic deformation resulting from the loading of the lithosphere by the stress drop of a large earthquake can be used to estimate elastic plate thickness and effective asthenospheric viscosity. For these purposes, dip-slip earthquakes are preferable to strike-slip ones, and intraplate events produce better results than plate boundary shocks. For several large thrust earthquakes from Japan, application of this method yields effective viscosities for the uppermost asthenosphere of $2 \rightarrow 6 \times 10^{20}$ Poise and elastic plate thicknesses of 30 - 60 km. Results obtained thus far are consistent with a linear flow law for the asthenosphere, but some unique characteristics of the earthquake loading problem suggest its potential for studying departures from linear behaviour.

1. INTRODUCTION

The effect of a large earthquake in the lithosphere on flow in the asthenosphere is similar to the transient effect of glacial loading or unloading. The earthquake stress drop or the application/removal of a continental icesheet causes stress changes in the asthenosphere that relax with time by a solid-state flow mechanism. This adjustment causes time-dependent surface deformations that can be measured and used to infer something about the flow properties of the asthenosphere. Measurements of crustal uplift in previously glaciated regions have been extensively applied to infer the rheology of the earth's interior. Application of similar principles to the problem of earthquake-induced asthenospheric flow has only recently begun.

Here we describe the distinctive features of this problem (referred to hereafter as "the earthquake loading problem"), contrast it with the more familiar problems of post-glacial rebound and plate flexure, and illustrate its utility with several applications. Our previous work (Thatcher and Rundle, 1979) has applied these results to earthquake-related deformation at subduction zones. For several reasons this earlier work examined only the consistency of observations with a thrust earthquake loading model that used conventional values of lithospheric thickness and asthenospheric viscosity. The arguments may in fact be put more strongly, and here we examine a more optimum dataset and turn the argument around: i.e., given the loading model and the observed deformation, how precisely can we constrain lithospheric thickness and asthenospheric viscosity?

For several reasons we have confined our discussions to thrust faulting problems and have ignored the analytically simpler case of strike-slip

movements. First, for the strike-slip problem, the importance of asthenospheric relaxation is quite uncertain: competing deformation mechanisms produce similar movement patterns, and the magnitude of the asthenospheric effect depends critically on the precise elastic thickness of the lithosphere. This parameter must be assumed in the strike slip loading problem rather than being determined by the observations. Its value is not well-constrained by other geophysical data. Furthermore, elevation changes (most pertinent to dip-slip faulting) can be measured more precisely than horizontal strain changes, and relevant data, principally from Japan, are much more complete in regions of underthrust earthquakes.

2. GENERAL CHARACTERISTICS AND SCALING RELATIONS

Qualitative features of the deformation due to earthquake loading, post-glacial rebound, and plate flexure due to surface loads are compared in Figure 1. Similarities and differences between the earthquake loading problem and the two more familiar plate deformation problems are evident from the figure and will be referred to from time to time in what follows. Readers are encouraged to examine Figure 1 and make their own comparisons.

Figure 2 shows some quantitative modeling results plotted in a non-dimensional form which emphasizes the scaling parameters that control the spatial pattern and time-dependence for the deformation. The model consists of an elastic plate of thickness H and rigidity μ overlying a viscoelastic half-space with the properties of a Maxwell solid (instantaneous elasticity at $t = 0$, subsequently Newtonian viscous with viscosity η). Buoyant restoring forces are not included in these computations. Slip is imposed on the indicated fault segments as a step function in time at $t = 0$. The immediate

elastic vertical displacements at the free surface are shown by the solid lines, and the subsequent surface displacements due to asthenospheric readjustment to the elastic stresses imposed at t = 0 are given (for one particular time, t = 2τ) by the dashed lines. Note that the relaxation time $\tau = \frac{2\eta}{\mu}$ is merely a convenient scaling parameter here, and does not, for example, represent an exponential decay constant for surface displacements. For this loading problem, as well as for the corresponding strike-slip case (see Spence and Turcotte 1979, Figure 3), significant displacements continue well past $t \simeq 10\tau$. Details of the formulation and computational methods are given in Rundle (1978). Results shown in Figure 2 are for an infinitely long fault, but the model is equally applicable to finite faults, and we shall employ both geometries in matching data.

Three scaling parameters critically control the character of the post-slip time-dependent deformation:

1. The spatial dimension of the deformation is directly proportional to the effective elastic thickness of the lithosphere H.

2. The amount and rate of vertical displacement at any point is directly proportional to the average fault slip $\bar{u}$ that occurs at t = 0.

3. The amount and rate of vertical displacement is approximately linearly related to the effectively viscosity η of the asthenosphere.

Fortunately, deformation is not strongly dependent on the precise geometry of the faulting, which is not always well-known. As long as the downdip <u>width</u>, W, of the fault (and its length in three dimensional faults) is greater than roughly half the lithospheric thickness H, the asthenospheric effect will be important. Neither the spatial pattern nor the rate of movement are especially sensitive to the precise W/H ratio or to the fault dip if it is less than about 70°.

Differences between the relaxation effects of surface faulting and the deformation due to buried fault slip can be useful diagnostic criteria in matching models with data. The former (Figure 2a, dashed curves) produces predominantly surface downwarping and the latter (Figure 2b, solid and dashed curves) results largely in land uplift.

3. MODELING OBSERVED ELEVATION CHANGES

Model-predicted vertical displacements are compared with observations using the results of repeated first order geodetic leveling surveys. Level changes may be measured very precisely, and for our models, are very sensitive measures of asthenospheric viscosity. For example, for 4 m of displacement on the fault shown in Figure 2a, maximum post-earthquake subsidence rates are ~ 5 mm/yr if $\eta = 10^{21}$ P and ~ 800 mm/yr if $\eta = 10^{19}$ P. Elevation changes are measured to a few parts in 107, and precision of surveys made 100 years ago is comparable to that attained today by the same techniques. Thus, differential changes as small as ~ 1 mm/yr over ~ 10 km of a survey route are easily detected from repeated measurements made over timespans as short as a few years. Typical subsidence rates observed landward of subductions zones are 5 - 10 mm/yr.

In ideal situations, the procedure used in fitting observed level changes to models of earthquake loading is straightforward. Earthquake parameters (fault dimensions, dip angle, average slip) are independently determined from seismological data, geodetic measurements of the coseismic deformation, or geologic observations of surface faulting. With the loading geometry established, the observed post-earthquake level changes can be used to determine the remaining free parameters of the model: the

length-scale of the movements determines the lithospheric thickness H, the rate of subsidence constrains the relaxation time τ and hence the asthenospheric viscosity η.

As with most geophysical problems, the actual state of affairs is seldom optimum. Earthquake parameters are imperfectly known, areal coverage of geodetic surveys is incomplete, repeated surveys are infrequent, and extraneous surface deformation effects contaminate the movement of interest.

In what follows it is convenient to divide the observed deformations related to thrust faulting earthquakes into three distinct phases:

Coseismic (CO): the elastic deformation that results solely from slippage occurring at the time of the earthquake.

Postseismic (POST): transient aseismic movements observed to follow major earthquakes.

Interseismic (INTER): approximately uniform aseismic deformation that persists at constant rates between major earthquakes.

Since postseismic movements merge gradually into the interseismic pattern of deformation, the distinction between the two phases is seldom sharp. In practice, the defined duration of the postseismic interval depends largely on the dates of postearthquake surveys. Where detailed information is available, observations show that the largest transient movements occur in the first several postearthquake years, although identifiably similar deformation may persist for 20 years at lower rates.

In this paper the main modeling efforts will be focused on the longterm postearthquake deformation related to the 1896 Riku-u earthquake, an intraplate thrust event in Northern Honshu, Japan (Figure 3). First, however,

we briefly review our earlier work, which was directed towards modeling the effects of plate boundary earthquakes.

4. MODELING AT SUBDUCTION ZONES-A REVIEW

The aseismic level changes observed landward of subduction zones off Japan and elsewhere can be understood as basically a superposition of two effects, slip at depth on a plate-bounding thrust fault and the asthenospheric response to repeated surface faulting events on the upper portions of the thrust plane. Episodic buried slip downdip of the coseismic rupture can largely explain the postseismic transients, while subsidence due to the asthenospheric response to earthquake loading accounts for the interseismic movements. Smaller magnitude deformation effects due to asthenospheric relaxation occur in the postseismic interval, and steady buried slip also contributes to the interseismic movements.

Typical comparisons of modeling results with observed level changes from two regions of Japan are shown in Figures 4 and 5. More extensive comparisons and further details can be found in Thatcher and Rundle (1979). Basically the same model, shown in the third panel of Figure 4, is able to explain both sets of observations. A difference in the POST curves is due to the predominance strike-slip over reverse dip-slip movements at depth in the South Kanto region after 1923.

These results illustrate advantages and shortcomings of studying the earthquake loading problem at subduction zones. Since the faulting mechanisms of these two great earthquakes are known rather well (Ando, 1971, 1975; Kanamori, 1971, 1972), uncertainties in the loading parameters are small. However, since most of the deformation profile lies beneath the sea, the

length scale of the surface displacement pattern is quite uncertain and the effective elastic lithospheric thickness cannot be independently obtained. We have merely assumed H=60 km, a seismic estimate for Japan (Kanamori, 1970), but changes of as much as a factor of two in this parameter would not substantially alter the results. Perhaps more seriously, the several plate driving and resisting forces presumed to act as subduction boundaries (e.g. Forsyth and Uyeda, 1975) are ignored. In our model it is simplistically assumed that the net effect of these forces is to produce steady aseismic slip at the plate motion rate near the bottom of an otherwise locked thrust fault (see Figure 4, third frame, segment labeled INTER). These idealizations, though plausible, make us uneasy. Clearly a less complicated tectonic situation would be desirable.

5. ASTHENOSPHERIC RELAXATION EFFECTS FROM AN INTRAPLATE EARTHQUAKE

Several of the difficulties involved in studying plate boundary thrust earthquakes are absent for intraplate earthquakes, and the 1896 Riku-u earthquake (M=7.5) illustrates several of these advantages (for a more detailed study see Thatcher et al, 1980). This earthquake occurred in Tohoku district, Northern Honshu about 330 km west of the Japan Trench (Figure 3). Surface faulting was observed along 40 km of the Senya fault and indicated thrust motion on NNE trending fractures, with the fault plane dipping steeply to the east. Leveling surveys carried out since 1900 have been studied by Kato (1979), and his map of elevation changes for 1900-1975 is reproduced in Figure 6. The location of 1896 ground rupture is shown for reference, and the close association of the faulting to a region of localized subsidence is very clear. By 1975 this subsidence, which occurred entirely aseismically, had exceeded 35 cm. Superimposed on this is a general

pattern of progressive tilting of the eastern coast of northern Honshu towards the Japan Trench, movement similar to the interseismic deformation observed landward of the Nankai and Sagami Troughs (INTER profiles, Figures 4 and 5).

Figure 7 shows more details: surface ruptures mapped by Matsuda et al. (1979), a leveling route that crosses the Senya fault, and the surface projection of the inferred 1896 coseismic fault plane. Although neither seismological nor geodetic measurements are available for determining the earthquake parameters, the work of Matsuda et al. (1979) provides satisfactory constraints. The surface breaks show 1.4 to 3.6 m of vertical offset, and the Senya fault dips 45° to 70° to the east, so we have assumed an average coseismic fault slip of 4 m and a 45° dip. The depth of coseismic faulting is not known, but all well-located crustal microearthquakes in Tohoku district occur above 20 km depth, most of these being shallower than 15 km (Takagi et al, 1977), so we have assumed a fault depth of 15 km. The fault length, 50 km, is confined at its northern end by the extent of surface faulting, but is extended 10 km south of the southernmost rupture segment in order to produce a minor improvement in the match of the observed and computed level changes.

Both the localized subsidence near the 1896 ruptures (Figure 8) and its decaying rate since 1900 (Figure 9) support our view that asthenospheric relaxation from the 1896 earthquake is responsible for the observed deformation. The sharp downwarping gradients between -35 km and + 40 km on the observed level profiles (Figure 8) associate the downwarping unmistakably with the Senya fault and indicate an effective elastic thickness of 30 km for the lithosphere. This value agrees well with the crustal thickness of 30 km and upper mantle velocity of 7.5 km/sec obtained in this region by the Research Group for Explosion Seismology (1977). The low upper mantle

velocity, high heat flow, and Quaternary vulcanism observed here all suggest that the lithosphere may be abnormally thin in this part of Japan. The decay in the subsidence rate, plotted in Figure 9 for benchmark J8, is matched by τ = 20 years, yielding η = 2 x 10^{20} P. Uncertainties in the earthquake faulting parameters would not alter this viscosity estimate by more than about a factor of two.

The subsidence occurring further than 40 km east of the Senya fault is almost certainly due to subduction of the Pacific plate beneath the Japan Trench. Figure 10 illustrates this point by showing the difference between observed and computed level changes for 1900-1934 (from Figure 9) plotted as a function of the perpendicular distance from the Japan Trench. This residual profile is compared with level changes observed landward of two other trenches in Japan. Although the residual North Honshu profile is shifted about 50 km landward, it is otherwise rather similar to the profile for Eastern Hokkaido. As the Southwest Honshu profile shows, the distance from the trench to the slope change on each profile varies considerably from one region to another (see also Figure 5, INTER), but the association with the subduction zone is nonetheless clear.

Thus, despite several shortcomings of the Riku-u earthquake, the evidence seems to us rather strong that flow in the asthenosphere following 1896 is responsible for the observed deformation. At its eastern boundary the 1896 subsidence region abuts a zone of movement related to subduction at the Japan Trench, but is otherwise free of plate boundary complications - the subducting Pacific plate lies more than 100 km beneath the Senya fault. In addition, the recurrence interval for major earthquakes on the Senya fault is very long, 1000 years or greater (Matsuda et al, 1979), so the tectonic

loading rate is low and has a negligible effect on the observed deformation since 1896. Except for a short extension of the coseismic fault beyond the mapped surface ruptures, the earthquake loading parameters are specified independently of the observed level changes, and the modeling then predicts the deformation with plate thickness and asthenospheric viscosity being the only adjustable parameters. A linear rheology matches the observed time decay of displacement rather well (Figure 9), although data are absent for 1896-1900, and more frequent subsequent surveys would have been valuable.

6. SUMMARY AND DISCUSSION

An assessment of the earthquake loading problem indicates that it provides information that is complementary rather than redundant to that obtainable by other means. Figure 11 lists the parameters that can be obtained from earthquake loading studies, along with the merits and shortcomings of each determination.

The difference between the seismically estimated lithospheric thickness and the effective elastic thickness determined from plate flexure studies is well known. Values obtained here apply to timescales intermediate to these two extremes.

The effective viscosity of the uppermost asthenosphere can be bracketted more narrowly than is possible from post-glacial rebound studies. According to Walcott (1973, 1979) the rebound data from Fennoscandia and Arctic Canada are equally consistent with viscosities of 10^{19} to 10^{21} P. in the upper asthenosphere. Our results suggest a mean value of $\sim 5 \times 10^{20}$ P for Japan, which may be a lower bound for the world-wide average value.

Subject to several <u>further</u> caveats, this estimate is relevant to determining the magnitude of the viscous stresses that may be resisting the motion of the plates and to the viability of mantle-wide convection. The viscous stresses, however, depend on both the magnitude of upper asthenosphere viscosity and the width of the low viscosity zone, while whole-mantle convection will occur if the viscosity contrast between the upper and lower mantle is sufficiently small. Both issues then depend on the viscosity distribution below 150-200 km depth, which cannot be determined from earthquake loading studies and has not yet been firmly constrained by other means. If the long wavelength negative gravity anomalies observed in Scandanavia and Northern Canada are due to the incomplete isostatic compensation of post-glacial rebound, then Walcott (1979) suggests the lower mantle viscosity must be greater than 10^{23} P. Further refinements of this rough estimate are not yet available.

Finally, the unique nature of the earthquake loading, periodic at plate boundaries and widely spaced in time in plate interiors, provides the potential for determining both the steady-state and transient flow properties of the asthenosphere. The steady-state properties are most pertinent to mantle convection. The transients may be applicable to investigating the possibility of non-linear mantle rheology and testing the degree to which flow laws derived from solid-stage deformation of laboratory samples are matched in the earth's asthenosphere.

REFERENCES

Ando, M., A fault-origin model of the great Kanto earthquake of 1923 as deduced from geodetic data, Bull. Earthquake Res. Inst. Tokyo Univ., 49, 19-32, 1971.

Ando, M., Source mechanisms and tectonic significance of historical earthquakes along the Nankai trough, Japan, Tectonophys., 27, 119-140, 1975.

Forsyth, D., and S. Uyeda, On the relative importance of the driving forces of plate motion, Geophys. J. R. Astr. Soc., 43, 163-200, 1975.

Imamura, A., On the chronic and acute earth-tilting in the Kii peninsula, Jap. J. Astron. Geophys., 7, 31-45, 1929.

Kanamori, H., Mantle beneath the Japanese arc, Phys. Earth Planet Interiors, 3, 475-483 1970.

Kanamori, H., Faulting of the great Kanto earthquake as revealed by seismological data, Bull. Earthquake Res. Inst. Tokyo Univ., 49, 13-18, 1971.

Kanamori, H., Tectonic implications of the 1944 Tonankai and 1946 Nankaido earthquakes, Phys. Earth Planet. Interiors, 5, 129-139, 1972.

Kato, T., Crustal movements in the Tohoku district, Japan, during the period 1900-1975 and their tectonic implications, Tectonophys, in press, 1979.

Matsuda, T., Y. Ota, M. Ando and N. Yonekura, Fault mechanism and recurrence time of major earthquakes in the southern Kanto district, Bull. Geol. Soc. Amer., 89, 1610-1618, 1978.

Matsuda et al, in preparation, 1979.

Research group for Explosion Seismology, Regionality of upper mantle around Northeastern Japan as derived from explosion seismic observations and its seismological implications, Tectonophysics, 37, 117-130, 1977.

REFERENCES CONTINUED

Rundle, J. B., Viscoelastic crustal deformation by finite, quasistatic sources, J. Geophys. Res., 83, 5937-5945, 1978.

Shimizaki, K., Pre-seismic crustal deformation caused by an underthrusting oceanic plate, in eastern Hokkaido, Japan, Phys. Earth Planet. Interiors, 8, 148-157, 1974.

Spence, D. A. and D. L. Turcotte, Viscoelastic damping of cyclic displacements on the San Andreas fault, Proc. Roy. Soc. London, 365, 121-144, 1979.

Takagi, A., A. Hasegawa, N. Umino, Seismic activity in the northeastern Japan arc, J. Phys. Earth, 25, Suppl., S95-S104, 1977.

Thatcher, W. and J. B. Rundle, A model for the earthquake cycle in underthrust zones, J. Geophys. Res., 84, 5540-56, 1979.

Thatcher, W., T. Katsuda, T. Kato and J.B. Rundle, Lithospheric loading by the 1896 Riku-u earthquake, northern Japan: implications for plate flexure and asthenospheric rheology, J. Geophys. Res., 85, in press, 1980.

Walcott, R. I., Structure of the earth from glacio-isostatic rebound, Annual Revs. Earth Planet. Sci., 1, 15-37, 1973.

Walcott, R. I., Rheological models and observational data of glacio-isostatic rebound, in Morner, N., ed., Earth Rheology, Isostasy, and Eustasy, John Wiley and Sons, Chichester, in press, 1979.

FIGURES CAPTIONS

Figure 1: Comparison of deformation characteristics of asthenospheric relaxation due to reverse dip-slip faulting, postglacial isostatic rebound, and plate flexure due to applied surface loads.

Figure 2: Instantaneous elastic vertical displacement ($t = o$, solid lines) and subsequent viscoelastic response ($t = 2\tau$, dotted and dashed lines) due to slip on indicated fault segments. Faulting occurs in an elastic plate of thickness H overlying a viscoelastic (Maxwell) half-space of viscosity η. Shear modulii of plate and half-space, μ, are identical.

(a) Response to surface faulting

Dotted line μ = Maxwell viscoelastic in half-space and K, compressibility is constant; dashed line, μ = Maxwell viscoelastic in half-space and Lamé constant λ is held fixed.

(b) Response to buried sip.

(from Thatcher and Rundle, 1979, Fig. 1).

Figure 3: Location map of Japan showing major plates, subduction boundaries and location of 3 regions of recent thrust faulting where long-term post-earthquake level changes have been modeled as effects due to asthenospheric relaxation. The 1923 and 1946 events are great plate boundary earthquakes, while the 1896 shock is an interplate event.

Figure 4: Typical modeling results from southwest Japan, site of the great 1946 Nankaido earthquake (M=8.2). Top inset is a location map showing surface projection of coseismic fault planes of 1944 and

1946 earthquakes from Ando (1975), and level lines (dashed lines) and tidegage data (triangles) used to constrain modeling calculations. Remainder of figure compares observed and computed level changes between Muroto and Komatsujima, on the east coast of Shikoku. More extensive data comparisons are made in Thatcher and Rundle (1979).

Figure 5: Typical modeling results from the South Kanto district, site of the great 1923 earthquake (M = 8.1). Model is similar to that shown in Figure 4, except that coseismic fault dip is 45^{o} and asthenospheric viscosity is 6×10^{20} Poise. Again, more extensive data comparisons are made in Thatcher and Rundle (1979).

Figure 6: Level changes, 1900-1975, in Northern Honshu determined by Kato (1979). Note the 35 cm depression centered near the surface fault trace of the 1896 M = 7 1/2 Riku-u earthquake.

Figure 7: Location map of the vicinity of the 1896 Riku-u earthquake. Surface ruptures mapped by Matsuda et al (1979, in preparation) are shown by dark solid lines with teeth on upthrown side of fault. Rectangle shows surface projection of inferred 1896 coseismic fault plane, which dips 45^{o} to the ESE. Railway track symbol shows leveling route for which measured elevation changes are compared with model results in Figure 8. Leveling benchmark J8, near the 1896 surface ruptures, is also shown, and the time history of elevation changes at this point is compared with model predictions in Figure 9.

Figure 8: Comparison of observed (solid lines) and computed (dashed) cumulative post-1896 level changes on the east-west route shown

in Fig. 7. Model is shown to scale below the profile, which is projected perpendicular to the coseismic fault. Level changes are all relative to benchmark J9 for both observed and computed profiles. Modeling predicts minor uplift at J9 (~30 mm) but computed profiles have been shifted downward by predicted amount to make them directly comparable with observations. Computed movements for 1896-1900 (t = o to $t = 0.2\tau$) have been subtracted from model profiles. Modeling makes no attempt to match observed changes beyond + 40 km which are presumed to represent effects due to the subduction of the Pacific plate beneath the Japan trench (see Fig. 10).

Figure 9: Observed versus computed subsidence of benchmark J8 as a function of time (for location see Figs. 7, 8). Error bars on observations are one-standard deviation estimates of the accumulated random error of level differences betwen J9 and J8 benchmarks.

Figure 10: Residual (Observed-Computed) profile of level changes across Northern Honshu (this study) compared with observed profiles landward of the Kuril Trench in Eastern Hokkaido (derived from Shimazaki, 1974) (see map, Fig. 3) and onshore from the Nankai Trough in southwest Honshu (Imanmura, 1929). Note similarities in the shapes of the three profiles but differing distance from trench of the steep gradient in elevation change.

Figure 11: Lithosphere and asthenosphere properties obtainable from observations of time-dependent surface deformation resulting from asthenospheric relaxation due to large dip-slip earthquakes. Advantages and shortcomings of each parameter obtained.

	EARTHQUAKE LOADING	POST-GLACIAL REBOUND	PLATE FLEXURE
LOADING CHARACTERISTICS	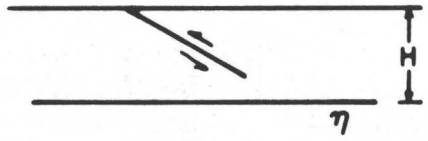 ~PERIODIC (PLATE BOUNDARY EQS) ~TRANSIENT (INTRAPLATE)	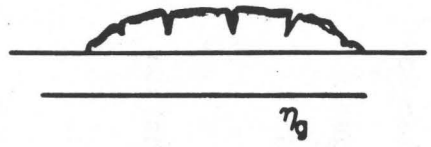 TRANSIENT	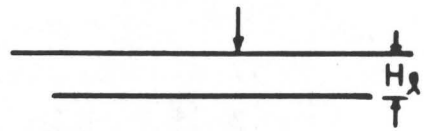 STEADY STATE
TIMESCALE	$10^0 \rightarrow 10^2$ years	$\sim 10^4$ years	$\lesssim 10^6$ years
LENGTH SCALE	~100 km	~200 → 2000 km	~100 → 1000 km
REGION	TECTONIC ZONES (~ LARGELY PLATE BOUNDARIES)	LARGELY Pε SHIELDS (EX. LAKE BONNEVILLE)	LARGELY PLATE INTERIORS (EX. OUTER RISES)
DEFLECTION	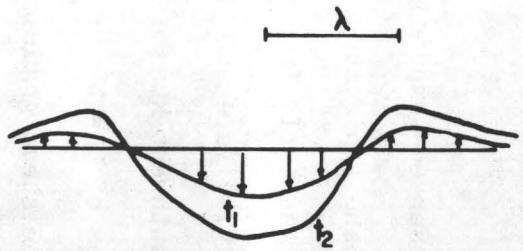 $\lambda \propto H$	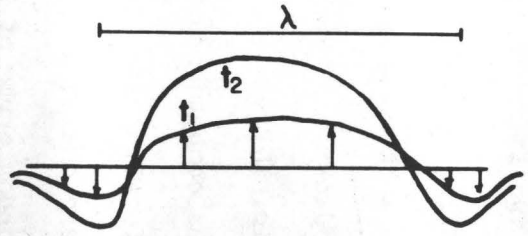 $\lambda \propto$ LOAD DIMENSIONS	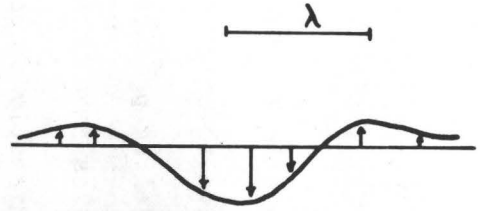 $\lambda \propto H_\chi^{3/4}$
FLOW	STEADY-STATE (RECURRENT EQS) ~TRANSIENT (INTRAPLATE EQS)	TRANSIENT (?)	NONE - ASTHENOSPHERE EQUILIBRATED
DATA CONSTRAINTS	-REPEATED GEODETIC LEVELING SURVEYS	-DATABLE UPLIFTED BEACH STRANDLINES -GEODETIC LEVELING -LONG WAVELENGTH GRAVITY ANOMALIES	- GRAVITY - TOPOGRAPHY

Fig. 1

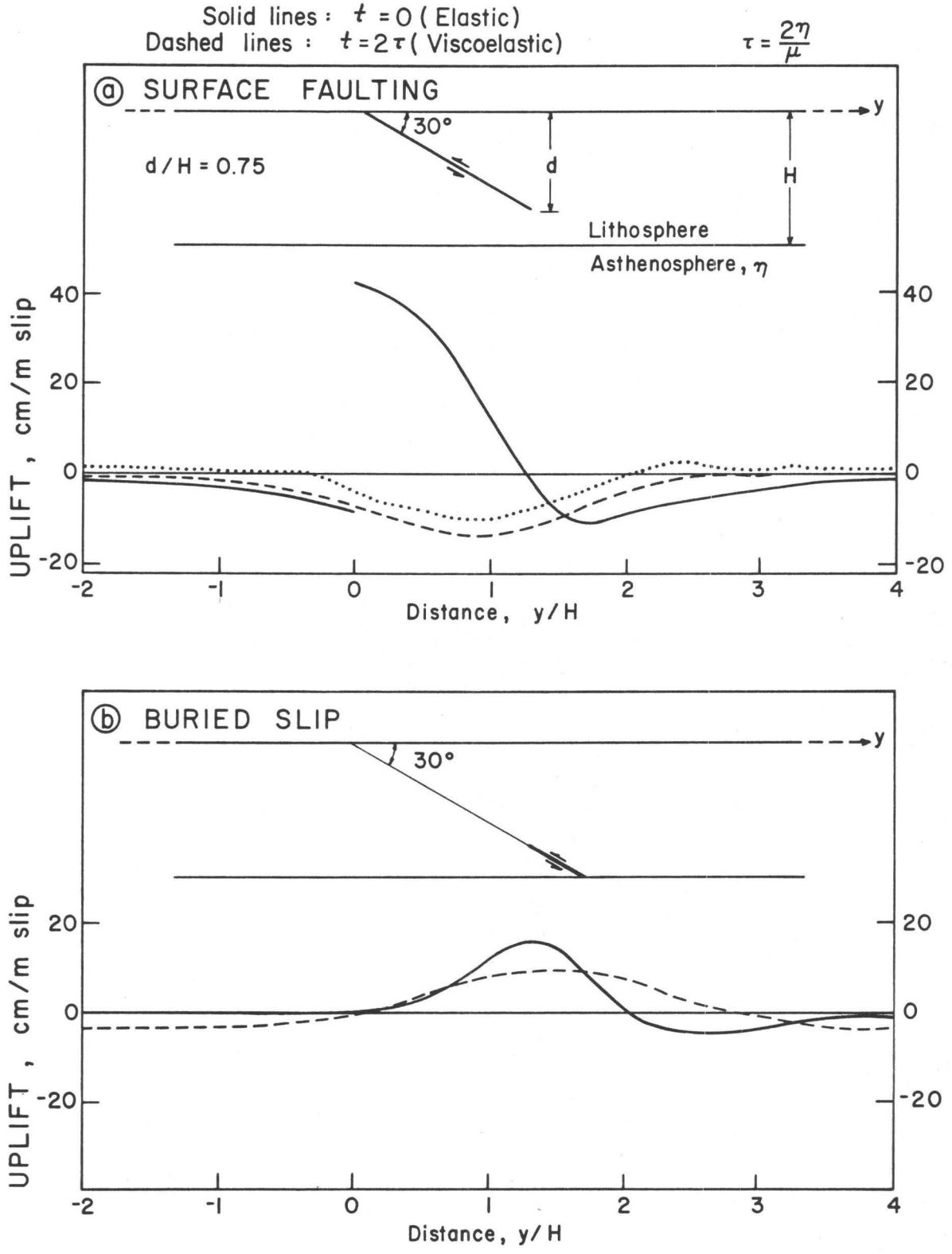
Solid lines : $t = 0$ (Elastic)
Dashed lines : $t = 2\tau$ (Viscoelastic)
$\tau = \frac{2\eta}{\mu}$
ⓐ SURFACE FAULTING
30°
y
d/H = 0.75
d
H
Lithosphere
Asthenosphere, η
UPLIFT, cm/m slip
40
20
0
-20
-2
-1
0
1
2
3
4
Distance, y/H
ⓑ BURIED SLIP
30°
y
UPLIFT, cm/m slip
20
0
-20
-2
-1
0
1
2
3
4
Distance, y/H

Fig. 2

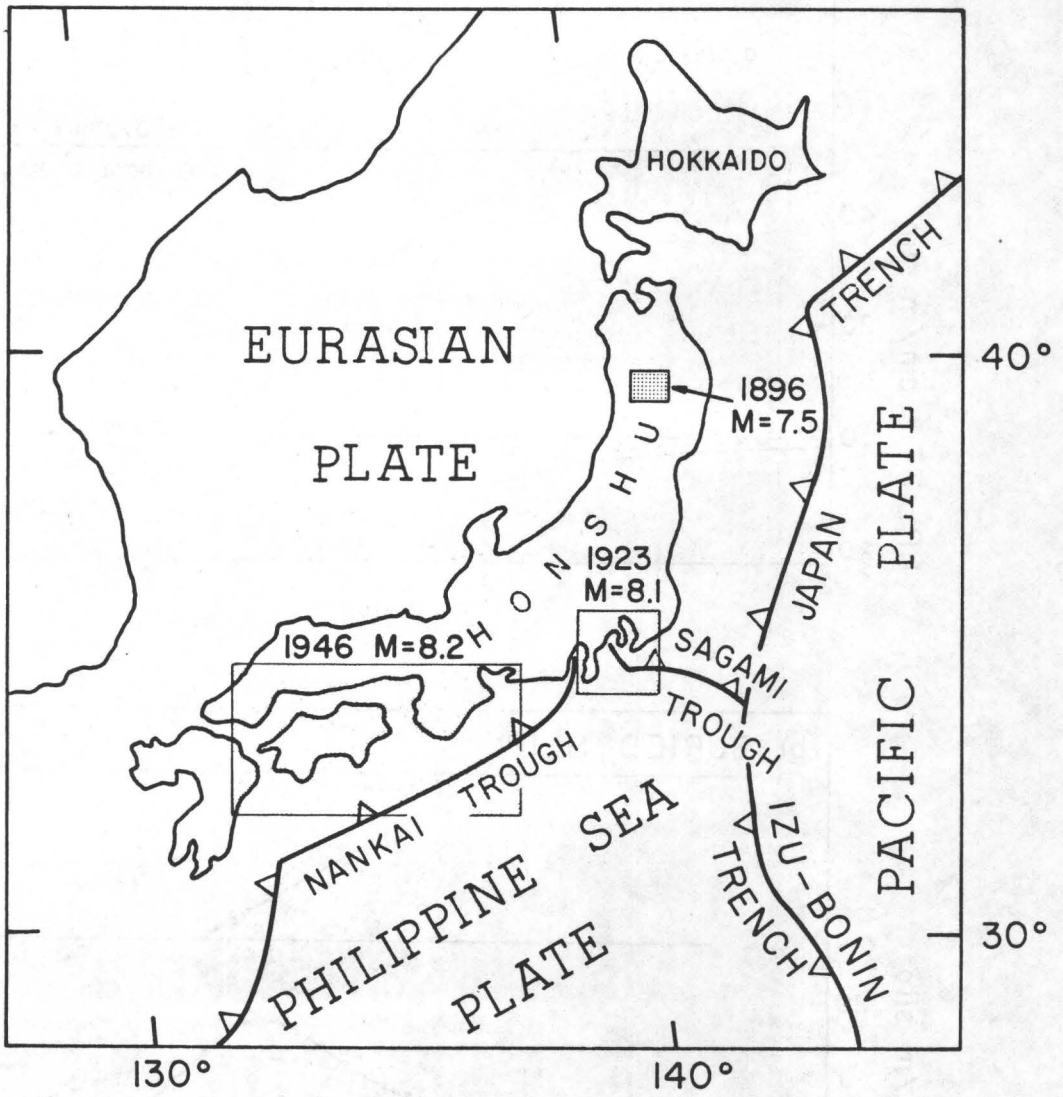
HOKKAIDO
EURASIAN
PLATE
1896
M=7.5
HONSHU
1923
M=8.1
1946 M=8.2
SAGAMI
TROUGH
NANKAI
TROUGH
PHILIPPINE SEA
PLATE
JAPAN
TRENCH
IZU-BONIN
TRENCH
PACIFIC PLATE
40°
30°
130°
140°

Fig. 3

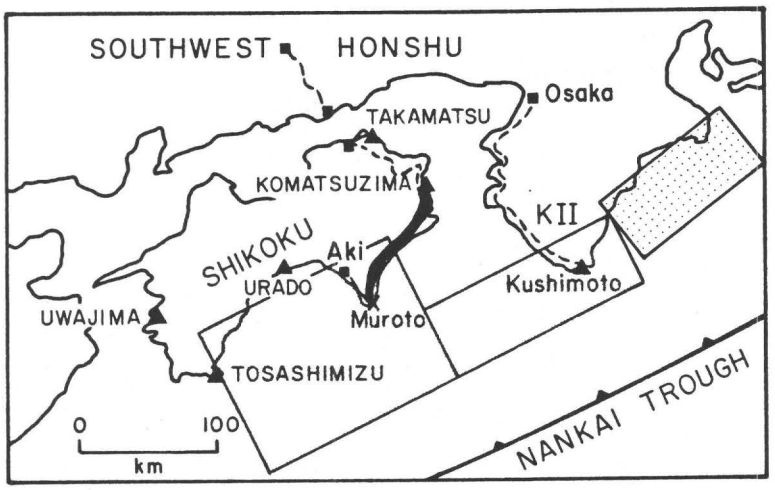
SOUTHWEST HONSHU
Osaka
TAKAMATSU
KOMATSUZIMA
KII
SHIKOKU
Aki
URADO
Kushimoto
UWAJIMA
Muroto
TOSASHIMIZU
0
100
km
NANKAI TROUGH

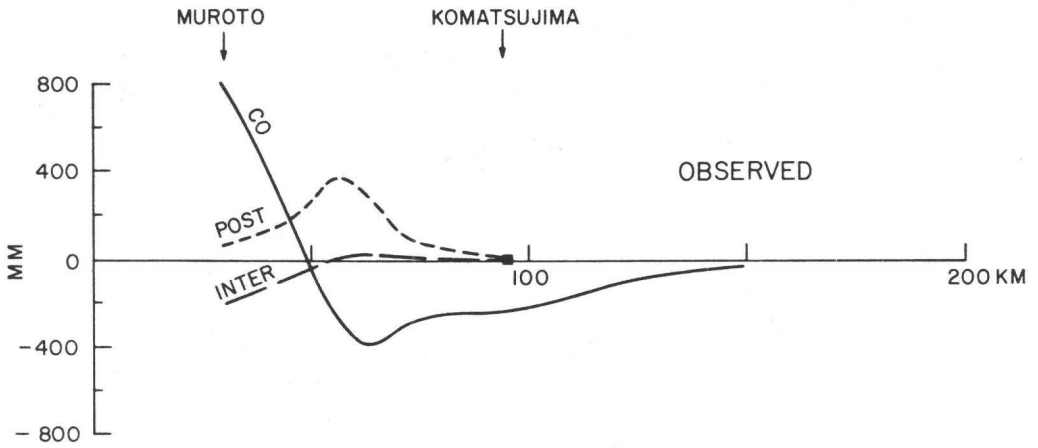
MUROTO
KOMATSUJIMA
800
400
0
-400
-800
MM
CO
POST
INTER
OBSERVED
100
200 KM

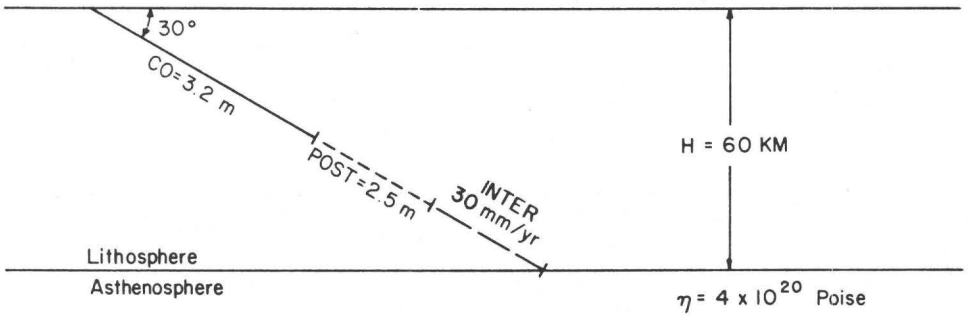
30°
CO=3.2 m
POST=2.5 m
INTER
30 mm/yr
H = 60 KM
Lithosphere
Asthenosphere
η = 4 x 10^20 Poise

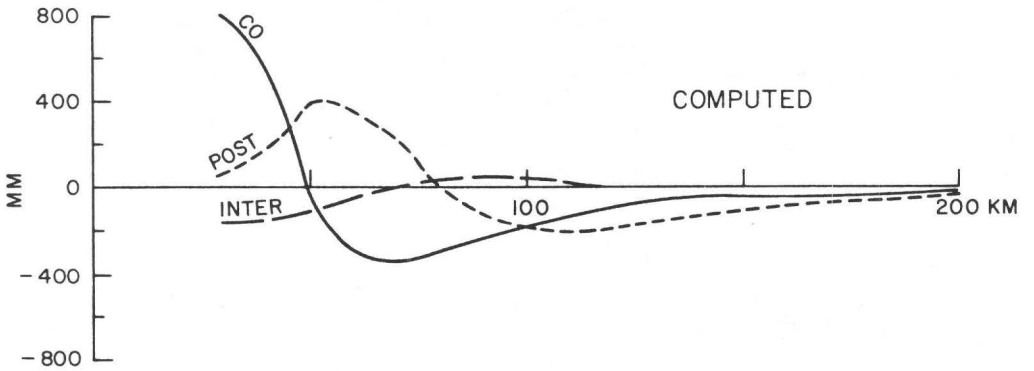
800
400
0
-400
-800
MM
CO
POST
INTER
COMPUTED
100
200 KM

Fig. 4

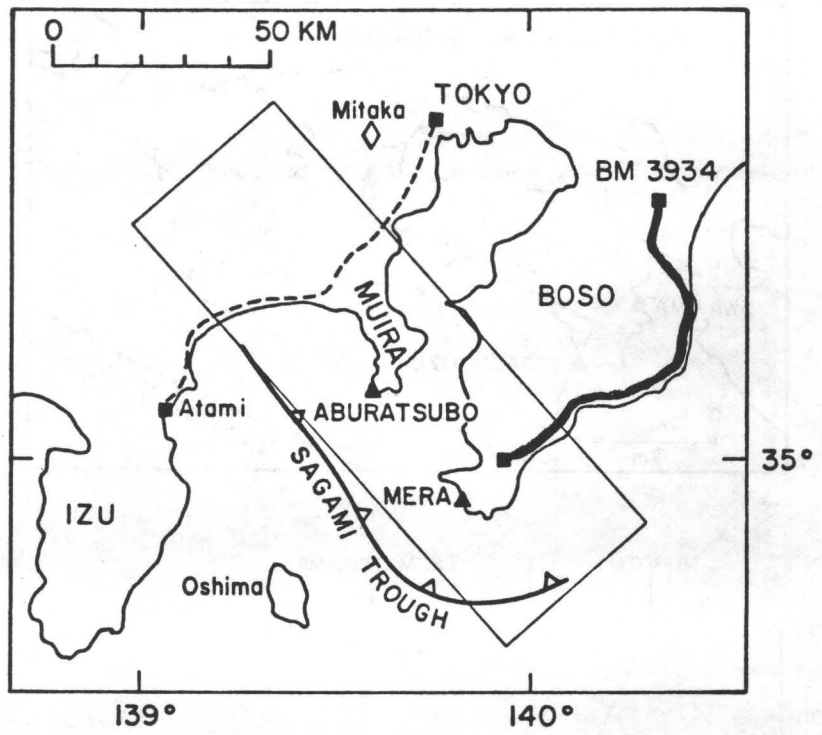
0
50 KM
Mitaka
TOKYO
BM 3934
BOSO
MUIRA
Atami
ABURATSUBO
SAGAMI TROUGH
MERA
IZU
Oshima
35°
139°
140°

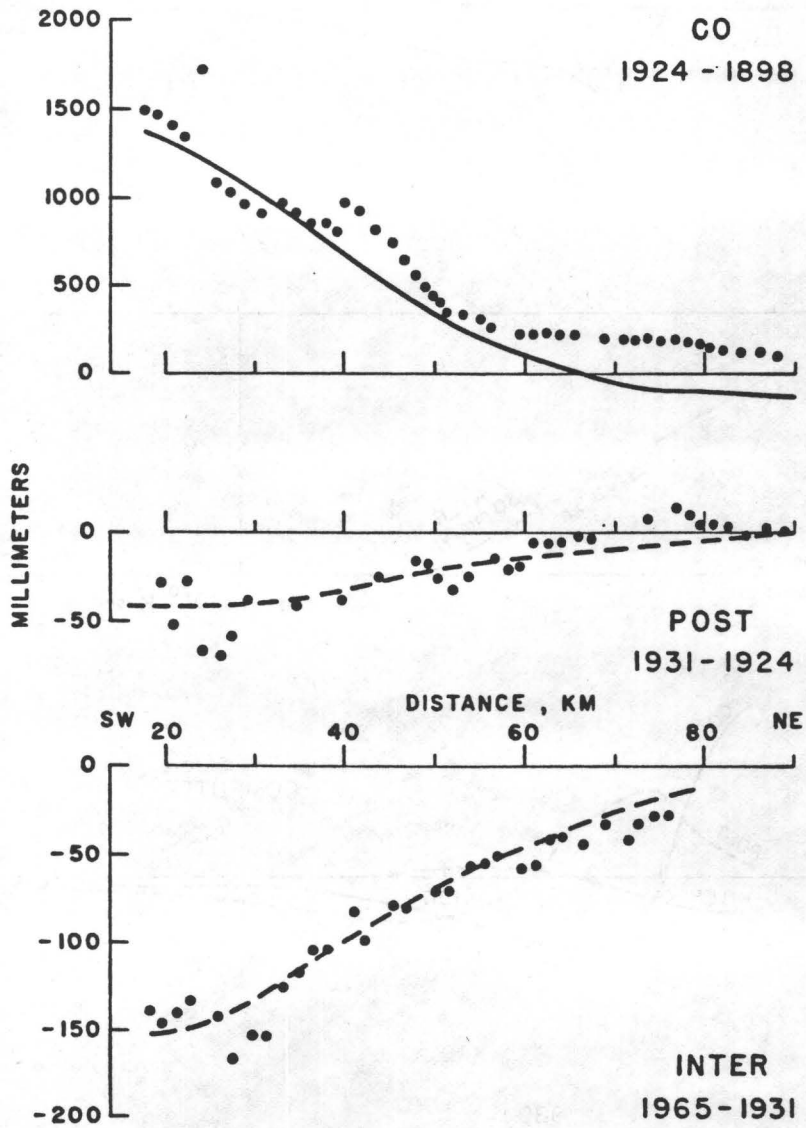
2000
1500
1000
500
0
CO
1924 - 1898
0
-50
MILLIMETERS
POST
1931 - 1924
DISTANCE , KM
SW
20
40
60
80
NE
0
-50
-100
-150
-200
INTER
1965 - 1931

Fig. 5

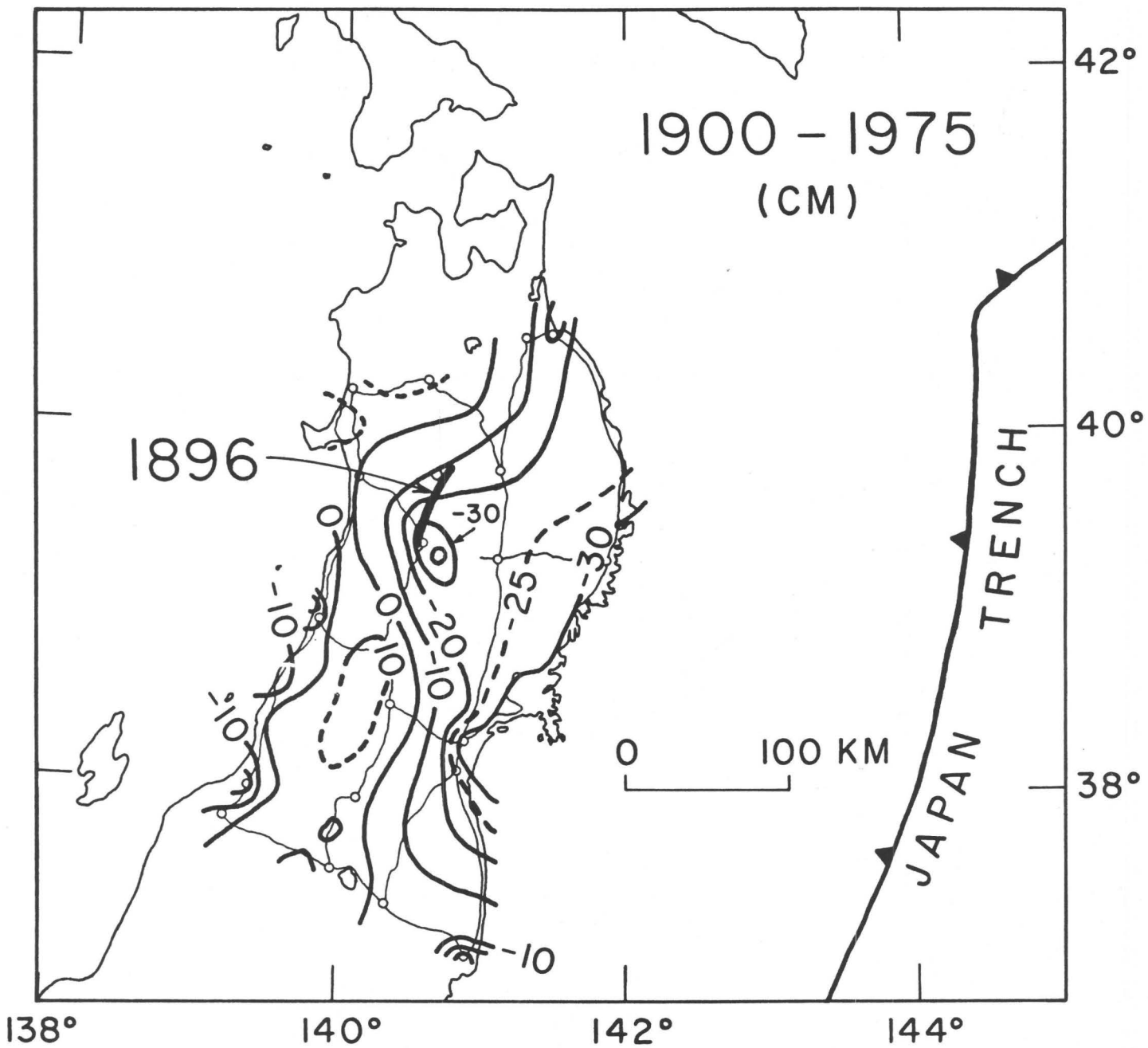
1900 – 1975
(CM)
1896
-30
0
-10
-20
-25
0 100 KM
JAPAN TRENCH
42°
40°
38°
138°
140°
142°
144°

Fig. 6

LAKE TAZAWA
J9
AKITA
JAPAN
SEA
PACIFIC
OCEAN
J8
YOKOTE
J3
KAMAISHI
40°
39°
0
50
KM
140°
141°
142°

Fig. 7

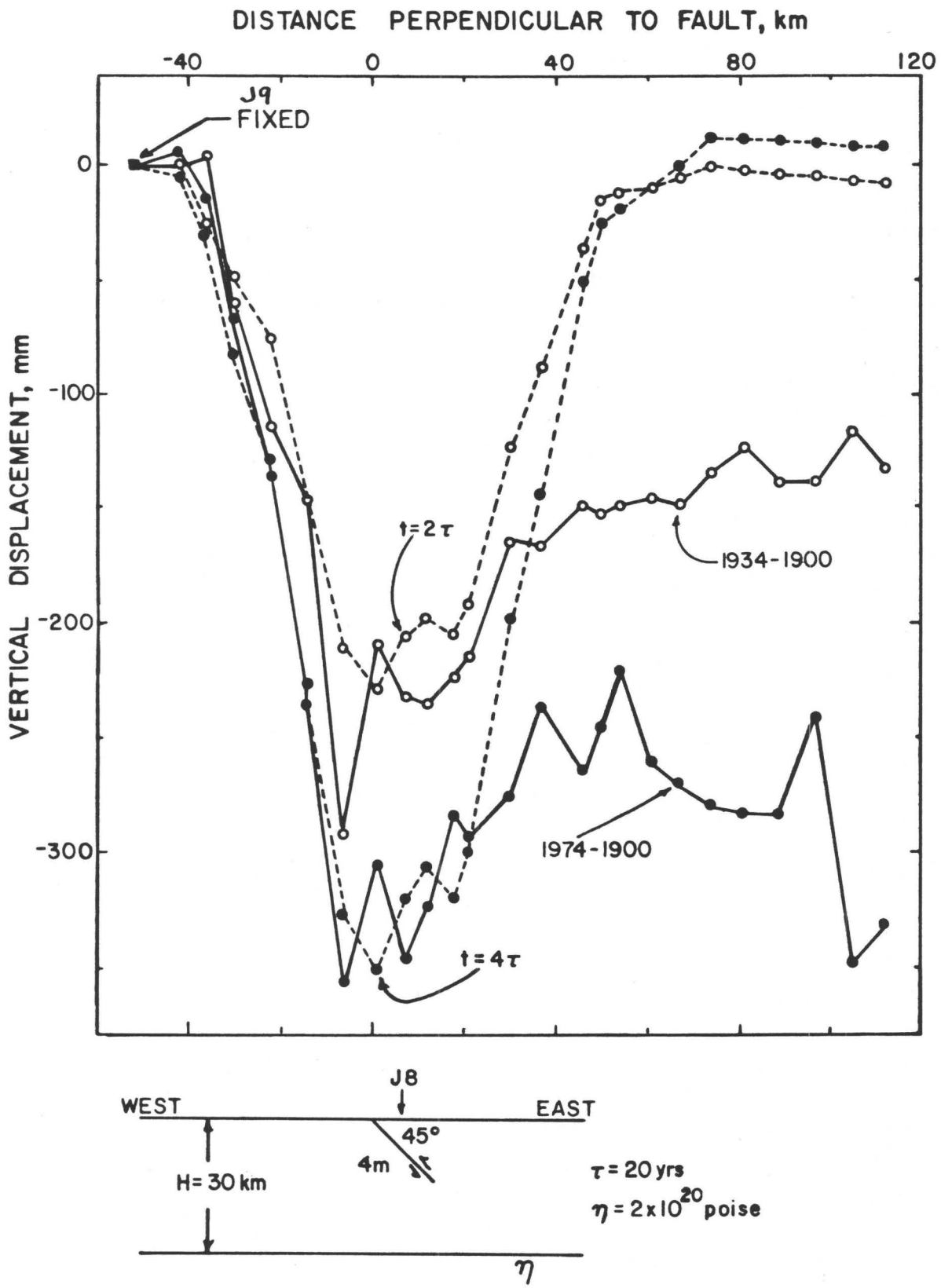
DISTANCE PERPENDICULAR TO FAULT, km
-40
0
40
80
120
J9
FIXED
0
-100
-200
-300
VERTICAL DISPLACEMENT, mm
t=2τ
1934-1900
1974-1900
t=4τ
J8
WEST
EAST
45°
4m
H=30 km
τ=20 yrs
η=2x10^20 poise
η

Fig. 8

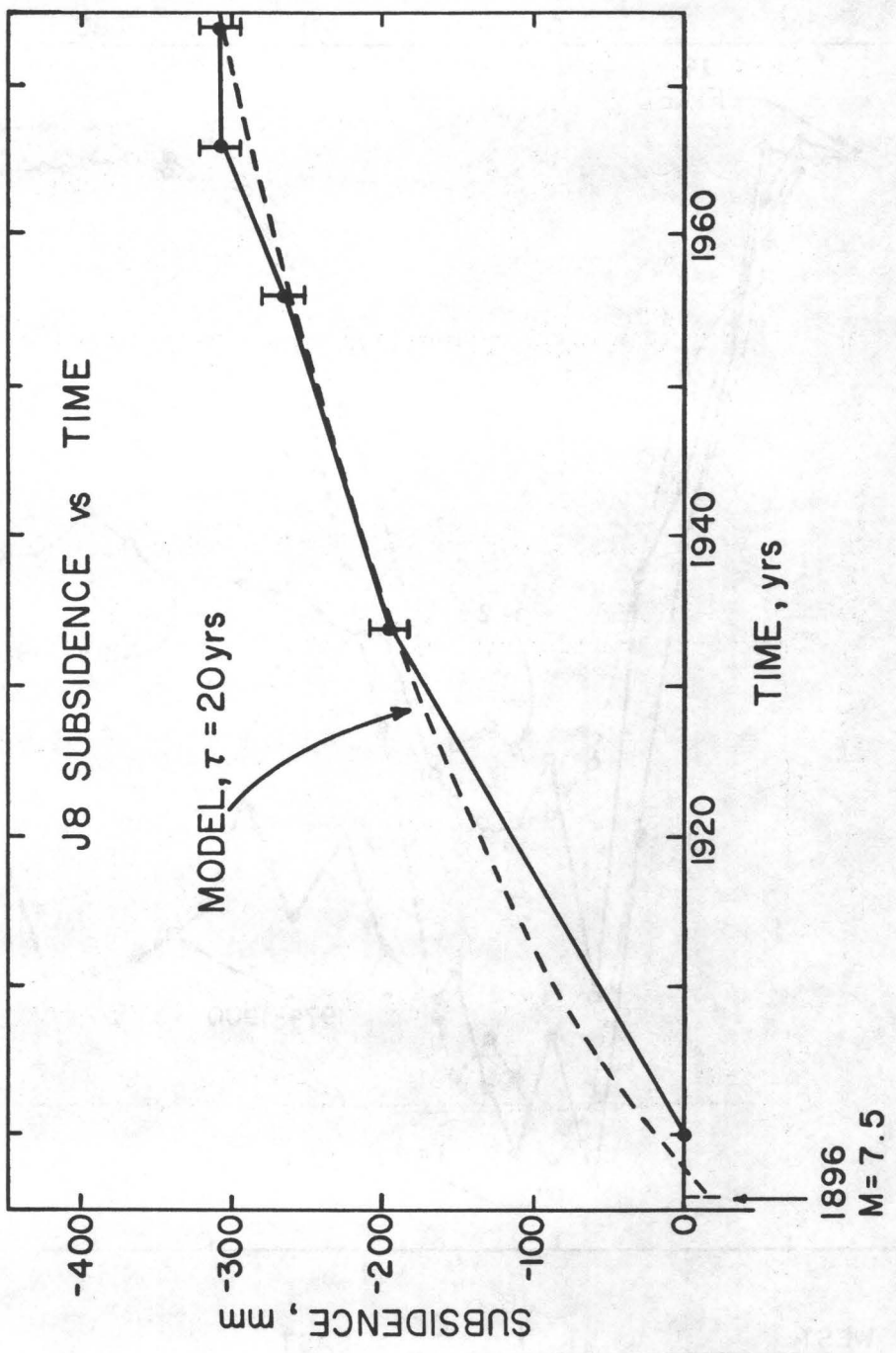
J8 SUBSIDENCE vs TIME
MODEL, τ = 20 yrs
SUBSIDENCE, mm
-400
-300
-200
-100
0
1920
1940
1960
TIME, yrs
1896
M=7.5

Fig. 9

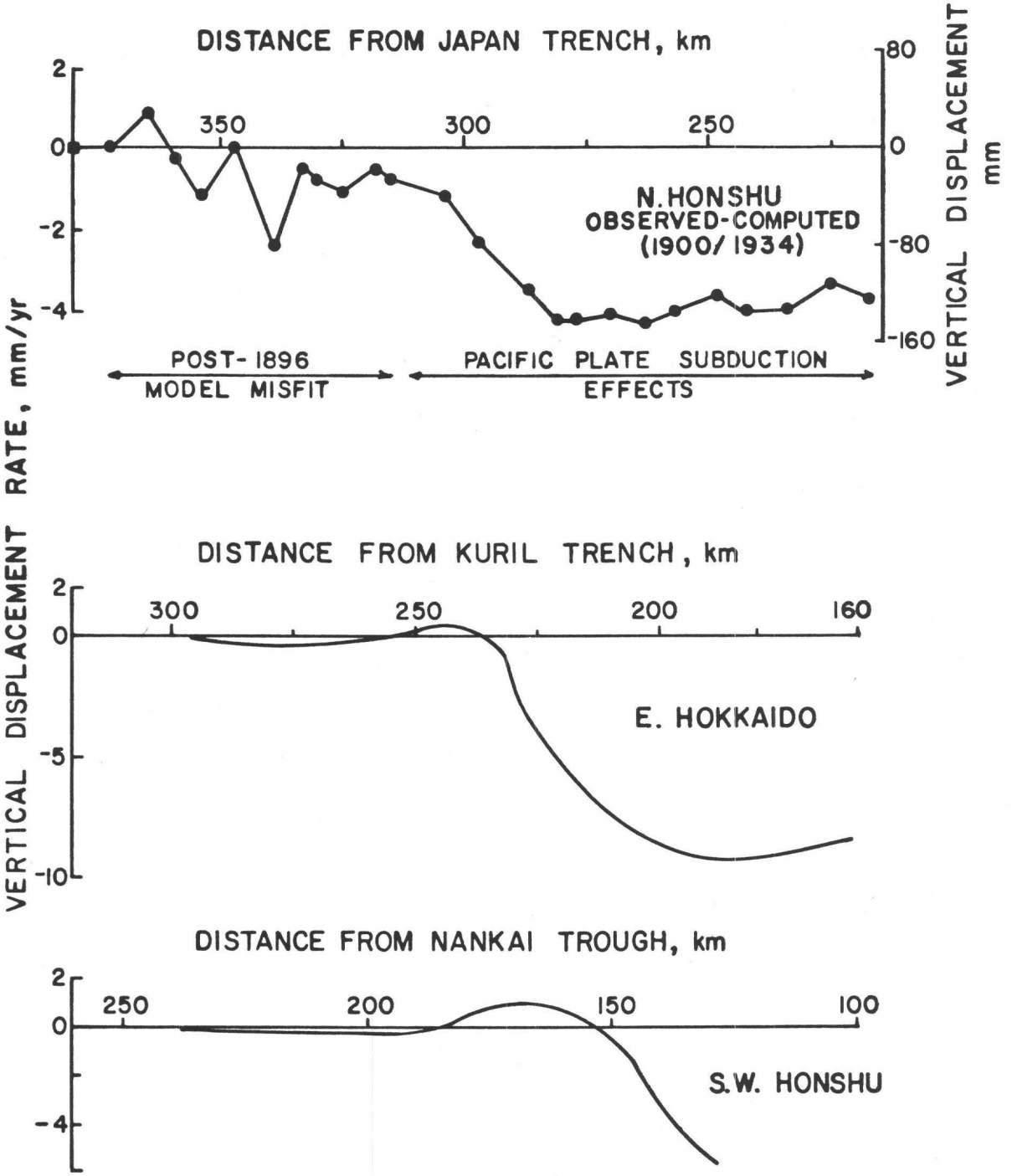
DISTANCE FROM JAPAN TRENCH, km
2
0
-2
-4
350
300
250
80
0
-80
-160
N. HONSHU
OBSERVED-COMPUTED
(1900/1934)
POST-1896
MODEL MISFIT
PACIFIC PLATE SUBDUCTION
EFFECTS
VERTICAL DISPLACEMENT RATE, mm/yr
VERTICAL DISPLACEMENT mm
DISTANCE FROM KURIL TRENCH, km
2
0
-5
-10
300
250
200
160
E. HOKKAIDO
DISTANCE FROM NANKAI TROUGH, km
2
0
-4
250
200
150
100
S.W. HONSHU

Fig. 10

EARTHQUAKE LOADING PROBLEM

PARAMETER DETERMINED	DIFFICULTIES
H, short-term elastic plate thickness, estimated from length scale of INTERSEISMIC secular deformation	– Not well-determined at trenches (most of profile beneath sea) – Possibly not directly comparable to H_ℓ from plate flexure pbs
η, effective viscosity of upper asthenosphere, estimated from rate of INTERSEISMIC secular deformation	– Faulting geometry, especially average coseismic slip, must be well-known – Possibly not directly comparable to glacial rebound values (Tectonic zone, uppermost asthenosphere)
Non-linear Rheological Parameters – immediate postearthquake deformation measurements can constrain	– POST deformation likely is contaminated by episodic aseismic slip downdip of coseismic fault
Steady-State Rheology Determined (?) – from INTERSEISMIC deformation resulting from recurrent subduction zone earthquakes – Possibly (?) more directly comparable to lab solid-state flow expts – Possibly more relevant to mantle convection (?)	Subduction Zones are Complicated – INTERSEISMIC deformation may be due to mechanisms other than asthenosphere relaxation + buried aseismic slip

Fig. 11